EURASIP Book Series on Signal Processing and Communications

UWB

Communication Systems

A Comprehensive Overview

Edited by: Maria-Gabriella Di Benedetto, Thomas Kaiser, Andreas F. Molisch, Ian Oppermann, Christian Politano, and Domenico Porcino

UWB Communication Systems

A Comprehensive Overview

A print edition of this book can be purchased at
http://www.hindawi.com/spc.5.html
http://www.amazon.com/dp/9775945100

EURASIP Book Series on Signal Processing and Communications, Volume 5

UWB Communication Systems

A Comprehensive Overview

Edited by: Maria-Gabriella Di Benedetto, Thomas Kaiser, Andreas F. Molisch, Ian Oppermann, Christian Politano, and Domenico Porcino

Hindawi Publishing Corporation
http://www.hindawi.com

A print edition of this book can be purchased at
http://www.hindawi.com/spc.5.html
http://www.amazon.com/dp/9775945100

EURASIP Book Series on Signal Processing and Communications
Editor-in-Chief: Alex Gershman

Hindawi Publishing Corporation
410 Park Avenue, 15th Floor, #287 pmb, New York, NY 10022, USA
Nasr City Free Zone, Cairo 11816, Egypt
Fax: +1-866-HINDAWI (USA Toll-Free)

ISBN 977-5945-10-0

A print edition of this book can be purchased at
http://www.hindawi.com/spc.5.html
http://www.amazon.com/dp/9775945100

Contents

Preface

Ultra-wideband (UWB) communication systems offer an unprecedented opportunity to impact the future communication world. The enormous available bandwidth, the wide scope of the data rate/range trade-off, and the potential for very-low-cost operation, which will lead to pervasive usage, all present a unique opportunity for UWB systems to impact the way people and intelligent machines communicate and interact with their environment. In particular, UWB is a promising area offering enormous advantages for short-range communications. Nevertheless, the technology still requires much work from the research community as well as solid proof of its viability in the commercial world before it can claim to be successful.

The world of UWB is changing rapidly, and it may be argued that the information contained in any general text on the subject is obsolete before the ink has dried. Even between the writing of the manuscript (Winter 2004) and the actual production, we have seen a number of interesting developments in the field. Our book attempts to provide an understanding of the (longer-term) fundamentals of UWB, the major research and development challenges, as well as a snapshot of the work in progress addressing these challenges. Due to the rapid progress of multidisciplinary UWB research, such a comprehensive overview can generally be achieved by combining the areas of expertise of several scientists in the field.

More than 30 leading UWB researchers and engineers have contributed to this book, which covers the major topics relevant to UWB. These topics include UWB signal processing, UWB channel measurements and modelling, higher-layer protocol issues, spatial aspects of UWB signalling, UWB regulation and standardisation, implementation issues, UWB applications, and positioning with UWB systems.

The book is targeted at advanced academic researchers, wireless designers, and graduate students wishing to greatly enhance their knowledge of all aspects of UWB systems. The reader should be left with a high-level understanding of the potential advantages of UWB in terms of high-data-rate communications, and location and tracking capabilities.

Due to the sheer number of authors who have contributed to this book and many others involved, it is difficult to equally thank them all, so we generally apologize for the absence of personal acknowledgements.

Introduction

This introductory first chapter by I. Oppermann is intended to give the reader a high-level understanding of the scope and the role of UWB as well as some

A print edition of this book can be purchased at
http://www.hindawi.com/spc.5.html
http://www.amazon.com/dp/9775945100

appreciation for the difficult "birth" UWB has experienced in the crowded world of communication standards. The enormous bandwidth and very low power spectral density of UWB make it difficult to detect; therefore it is potentially difficult to operate in such as way as to realise these benefits. The nature of UWB also leads to very significant technical difficulties, which are then compounded by regulatory and commercial resistance to UWB as a technology. The introduction covers some of the basic UWB signal generation techniques, working definitions of UWB, the on-going regulatory situation broad application areas and current research focus areas.

UWB propagation channels

Chapter 2 describes the propagation of UWB radiation from the transmitter to the receiver, covering the physical processes of the propagation as well as the measurement and modelling of the channels. The first section by A. F. Molisch is an introduction that outlines the basic properties of UWB propagation channels (as compared to the well-known narrowband channels) and also gives a synopsis of the subsequent sections. Section 2.2, "Measurement techniques," by J. Kunisch describes how to measure the transfer function or impulse responses of UWB channels and pays particular attention to the impact of the antennas used during the measurement. As it is desirable to isolate the impact of the channel (without the antennas), the de-embedding of the antenna effects becomes of paramount importance. Next, Section 2.3 by R. Qiu describes the fundamental propagation effects for UWB radiation. In particular, the diffraction of an ultra-wideband wave (corresponding to a short pulse) by a half-plane is a canonic problem that is analysed. It is shown that the pulse is distorted during that process; this has important consequences for the design of optimum receiver structures (matched filters). After those fundamental investigations, Section 2.4 to Section 2.6 describe statistical channel models. Section 2.4 by D. Cassioli gives an overview of measurements and models of path loss and shadowing, which describe the large-scale channel attenuation. Section 2.5 by A. F. Molisch and M. Buehrer then analyses the small-scale fading and delay dispersion effects that are caused by the multipath propagation. This section also investigates the frequency selectivity of the reflection coefficients of various materials and shows that it can lead to similar distortions of each multipath component as the diffraction effects described in Section 2.3. Finally, Section 2.6 by M. Pendergrass describes a standardised channel model established by the IEEE 802.15.3a group. This model, which is suitable for indoor environments with distances of up to 10 m, has been used for the evaluation of various high-data-rate UWB systems. Another type of system is body area networks, where various devices mounted on a human body communicate via UWB radiation. This rather unique environment gives rise to new challenges in the channel measurement and modelling. Section 2.7 by I. Z. Kovács, G. F. Pedersen, and P. C. F. Eggers describes such channels. Finally, Section 2.8 by S. Roy and I. Ramachandran gives an overview of channel estimation techniques for both OFDM-based and impulse-radio-based UWB systems.

Signal processing

This chapter addresses signal processing issues in UWB. The first three sections by I. Oppermann, M. Hämäläinen, J. Iinatti, and A. Rabbachin, present both impulse radio techniques and multiband techniques. UWB systems may be primarily divided into impulse radio (IR) systems and multiband systems. Multiband systems offer the advantage of potentially efficient utilisation of spectrum, while IR systems have the advantage of simplicity, and thus have potentially lower cost. The IR UWB concepts investigated support many modulation schemes including orthogonal and antipodal schemes. However, the basic modulation must also include some form of spectrum randomisation techniques to limit the interference caused by the transmitted pulse train. Both time-hopping (TH) and direct-sequence (DS) randomisation techniques were examined. Deciding which modulation scheme to use depends on the expected operating conditions and the desired system complexity. Section 3.4 by B. Allen, S. A. Ghorashi, and M. Ghavami introduces the application of impulses to UWB wireless transmissions. A number of candidate pulse waveforms are characterised in the time and frequency domains. The application of orthogonal pulse waveforms is introduced. These waveforms enable advanced modulation and multiple-access schemes to be implemented. The success of these schemes, however, is determined by the extent of pulse distortion caused by the transmitter and receiver circuitry and the propagation channel. Thus, distortion mitigation techniques are required. The issue of coexistence of impulse radio with other spectrum users is also discussed. Section 3.7 by I. Oppermann, M. Hämäläinen and J. Iinatti discusses synchronisation in IR systems. After a brief introduction of optimal synchronisation schemes, a more realistic approach is investigated in closer detail. Finally, the last Section by O. Albert and C. F. Mecklenbräuker presents a UWB radio testbed based on pulse position modulation (PPM) for investigating the properties of short-range data communication. The testbed is designed to realise data transmission at 6 Msymb/s over a distance of a few meters in indoor office environments. The focus of this effort is on the implementation of commercial-grade microwave circuitry and algorithms for ultra-wideband data transmission, especially concerning mobile battery-driven devices. The testbed hardware is described in detail as well as the two-stage approach used for receiver synchronisation.

Higher-layer issues: ad hoc and sensor networks

In the last few years, the increasing interest in applications based on the deployment of ad hoc networks has triggered significant research efforts regarding the introduction of the energy-awareness concept in the design of medium access control (MAC) and routing protocols. Chapter 4, which was edited by M.-G. Di Benedetto and includes contributions by L. De Nardis, S. Falco, and M.-G. Di Benedetto, investigates this issue in the context of UWB, ad hoc, and sensor networks. Progressing from the analysis of the state of the art in energy-efficient MAC and routing protocols, the chapter presents an innovative energy-aware MAC and

routing solution based on the position information provided by UWB by means of a distributed positioning protocol.

Ad hoc networks are considered as a viable solution for scenarios in which fixed infrastructure and, consequently, unlimited power sources are not available. In such scenarios, an efficient management of the limited power supply available in each terminal is a key element for achieving acceptable network lifetimes. This is particularly true for sensor networks, for which long battery duration is one of the basic requirements, given the typical size of such networks (up to thousands of terminals), as will be analysed in Section 4.1 by L. De Nardis and M.-G. Di Benedetto.

Location information is another valuable way of achieving energy awareness in ad-hoc networks. In Section 4.2, by L. De Nardis, we will first review location-aware routing protocols with a focus on power efficiency. We then address the problem of information exchange through the network by means of specifically designed protocols.

Next, we introduce in Section 4.3, by L. De Nardis, a MAC protocol that foresees a dedicated procedure for the acquisition of distance information and is tailored on UWB features.

Section 4.4, by L. De Nardis and S. Falco, analyses the effect of mobility on the behaviour of the proposed MAC and routing strategies.

Spatial aspects of UWB

The aim of this chapter is to discuss the spatial aspects of the UWB radio channel from various perspectives. In the second section by J. Kunisch, a spatial model is presented based on measurement data that was obtained in office environments with line-of-sight, non-line-of-sight, and intermediate conditions. The distinguishing feature of the ultra-wideband indoor radio channel is that certain individual paths are recognisable and resolvable in the measurements, which are adequately reflected by the proposed spatial model. Moreover, the model also covers movements of the receiving or of the transmitting antennas on a small scale (several wavelengths). In Section 5.3 by W. Sörgel, C. Waldschmidt, and W. Wiesbeck, the state-of-the-art UWB antenna array concepts and their applications are introduced. Simulation results for a linear exponentially tapered slot antenna array (Vivaldi antennas) for time domain beam steering are given, and further theoretical modelling is substantiated by experimental results. F. Argenti, T. Bianchi, L. Mucchi, and L. S. Ronga present in Section 5.4. a two-transmit-antenna scheme with orthogonal polarisation in order to uniformly cover an indoor area. A single antenna receiver results in a 2×1 MISO (multiple-input single-output) system so that space-time coding becomes applicable. The goal is to employ the polarisation diversity in order to obtain quality constant symbol detection while the receiver moves around within the covered area. Section 5.5 by A. Sibille addresses several basic issues pertaining to spatial diversity in UWB systems. It mainly concentrates on impulse-based radio, but it also evokes effects concerning frequency domain modulation schemes such as OFDM. The main subjects are the impact

of electromagnetic coupling between sensors and the impact of channel properties (like fading and angular variance) on spatial diversity. Besides the two main pillars of MIMO signal processing, namely, spatial multiplexing and space-time coding, the third and most classical one is *beamforming*, which is revisited in Section 5.6 by S. Ries, C. Senger, and T. Kaiser. Since the pulse duration is shorter than the travel time between two colocated antennas, beamforming for UWB signals has some special properties that are different from the narrowband case. For instance, because of the absence of grating lobes in the beam pattern, the spacing of the array elements is not limited by half of the wavelength, so that high resolution can be achieved with only a few array elements. At the end of this chapter the principal feasibility of direction-of-arrival (DoA) estimation is shown by an illustrative example. In Section 5.7 by W. P. Siriwongpairat, M. Olfat, W. Su, and K. J. Ray Liu, the performance of UWB-MIMO systems using different models for the wireless channels and different modulation schemes is presented. In particular, the performance merits of UWB-ST-coded-systems employing various modulation and multiple-access techniques, including time-hopping (TH) M-ary pulse-position modulation (MPPM), TH binary phase-shift keying (BPSK), and direct-sequence (DS) BPSK, are mentioned. At the end, the application of multiple transmit and/or receive antennas in a UWB-OFDM system is discussed. The last section by F. Zheng and T. Kaiser presents an evaluation of ergodic capacity and outage probability for UWB indoor wireless systems with multiple transmit and receive antennas (multiple-input multiple-output, MIMO). For some special cases, analytic closed-form expressions for the capacity of UWB wireless communication systems are given, while for other cases the capacity is obtained by Monte Carlo simulation approach. The contribution reveals that the UWB MIMO communication rate supportable by the channel increases linearly with the number of transmit or receive antennas for a given outage probability, which is reminiscent of the significant data rate increase of MIMO narrowband fading channels.

UWB ranging

One of the most innovative features of ultra-wideband technology is the very-high temporal resolution associated with the typical spread of UWB energy over large frequency bands. This feature has inspired and is still inspiring a new generation of technical developments and applications looking at the challenges of detection of the location of people and objects (people and asset tracking, smart spaces, ambient intelligence). Chapter 6 of this book introduces the reader to the basics of location technology via UWB systems. An analysis of the main potential and practical techniques with their accuracy is presented in Section 6.2 by A. Ward. In Section 6.3 by A. Ward and D. Porcino, a comparison with alternative radio-based systems is closely considered, while the main implications on the physical layer of a radio design and a sample RF link budget are discussed in Section 6.4 by D. Porcino. In the next section, results and advantages are then presented from commercial fine-grained UWB positioning systems by A. Ward, leading the discussion to operations in very challenging propagation conditions (such as metal cargos) where the signal

distortion is very significant and makes ranging calculations very difficult. These issues are part of Section 6.6 by D. Porcino. An experimental antenna-array system is then introduced in Section 6.7 by J. Sachs and R. Zetik, with test results showing the limits of what has been achieved today in terms of maximum positioning accuracy in controlled situations. In the last section by A. Ward, the important aspects of system integration of UWB positioning technology in the real world of complex buildings, hospitals, and houses are presented with attention given to the requirements that this technology will put onto system integrators and designers. This chapter guides the reader with a language suitable to comprehend the basic principles of the promising UWB ranging features, which are about to be widely explored in the commercial world.

Regulation and standardization

Since typical UWB radio may use part of the radio frequency spectrum already assigned to operative primary or secondary radio services, UWB radio devices—despite their extremely low transmission output power—may be a potential source of interference for incumbent radio services and should provide the ability to coexist with legacy radio services. In this chapter, we provide the reader with a comprehensive description of the worldwide UWB regulation and standardization framework under completion in order to elaborate on novel and effective means of spectrum management based on coexistence mechanisms instead of using conventional frequency sharing mechanisms. The first section by C. Politano is dedicated to regulation aspects for UWB communication and positioning applications to operate without requirement for individual right to use radio spectrum ("license-exempt"), and on a "no protection, no harmful interference" basis. This section introduces the UWB regulation framework elaborated under ITU-R to allow UWB devices and provides a detailed overview on the European regulatory approach in order to explain how prudent but constructive regulation rules are elaborated in this region. The second section by W. Hirt presents UWB standardization overview in the USA and in Europe. It provides the global overview of IEEE working groups mandated for wireless personal area network (WPAN) including high-data-rate (IEEE802.15.3a) and low-data-rate (IEEE802.15.4a) communication applications, and introduces the most popular UWB technology candidates identified during the year 2004. Then in this section, the European standardization process is also presented with an overview of the ETSI-TG3 working group mandated by the ECC for the definition of "harmonised standards for short-range devices (SRD) using UWB technology." The last section by R. Guiliano describes the methodology "compatibility study" for evaluating UWB interferences risk with incumbent radio services and presents some evaluation results of compatibility studies conducted for a few coexistence scenarios between UWB and UMTS, and fixed services (PP, PMP). The particular interest of this section is the description of the UWB characteristics that are impacting compatibility studies (activity factors, traffic characteristics, radio access modes) and how interference risks may be reduced by applying these features, allowing incumbent radio receivers to coexist

with UWB devices. The results of such compatibility studies have been used for the elaboration of mitigation techniques (proposed for standardization) in order to specify coexistence mechanisms to reduce UWB interferences with incumbent radio services.

Maria-Gabriella Di Benedetto, Thomas Kaiser, Andreas F. Molisch,
Ian Oppermann, Christian Politano, and Domenico Porcino
March 2006

1 Introduction

Ian Oppermann

1.1. Introduction

Ultra-wideband (UWB) communication systems have an unprecedented opportunity to impact communication systems. The enormous bandwidths available, the wide scope of the data rate/range tradeoff, and the potential for very-low-cost operation leading to pervasive usage, all present a unique opportunity for UWB to impact the way people interact with communications systems.

The spark-gap transmission experiments of Marconi in 1901 represent some of the first experiments in a crude form of impulse radio. Pioneering contributions to modern UWB radio were made by Ross and Bennett [1] and Harmuth [2]. The earliest radio communications patent was published by Ross (1973). In the past 20 years, UWB has been used for radar, sensing, military communications, and niche applications.

A substantial change occurred in February 2002 when the US Federal Communications Commission (FCC) [3, 4] issued a ruling that UWB could be used for data communications as well as radar and safety applications. This book will focus almost exclusively on the radio communications aspects of UWB.

The band the FCC allocated to communications is 7.5 GHz between 3.1 and 10.6 GHz; by far the largest allocation of bandwidth to any commercial terrestrial system. It was little wonder that efforts to bring UWB into the mainstream were greeted with great hostility. First, the enormous bandwidth of the system meant that UWB could potentially offer data rates of the order of Gbps. Second, the bandwidth was overlaid on many existing allocations, causing concern from those groups with the primary allocations. When the FCC proposed the UWB rulings, they received almost 1000 submissions opposing the proposed rulings.

Fortunately, the FCC UWB rulings went ahead. The concession was however that available power levels would be very low. At the time, the FCC made it clear that they were being deliberately cautious with the setting of the maximum power masks. If the entire 7.5 GHz band is optimally utilized, the maximum power available to a transmitter is approximately 0.5 mW. This is a tiny fraction of what is

available to users of the 2.4 GHz and 5.8 GHz ISM (industrial, scientific, and medical) bands used by wireless LAN (WLAN) standards such as IEEE 802.11 a/b/g. The power limitation effectively relegates UWB to indoor, short-range communications for high data rates, or very low data rates for longer link distances. Applications such as wireless USB and personal area networks have been proposed offering hundreds of Mbps to several Gbps with distances of 1 to 4 metres. For ranges of 20 metres or more, the achievable data rates are very low compared to existing wireless local area network (WLAN) systems.

Part of the enormous potential of UWB is the ability to move between the very high data rate, short-link distance applications and the very low data rate, longer-link-distance applications. The tradeoff is facilitated by the physical layer signal structure. The very low transmit power available means that multiple, low-energy UWB pulses typically must be combined to carry one bit of information. In principle, trading data rate for link distance can be as simple as increasing the number of pulses used to carry one bit. The more pulses per bit, the lower the data rate, and the greater the achievable transmission distance.

1.1.1. Goals and scope of this book

This book explores the fundamentals of UWB technology with particular emphasis on the physical layer (PHY) and medium access (MAC) layer. Regulatory aspects and the state of the art will also be presented. The topics addressed include UWB signal processing, UWB channel measurement and modeling, higher layer issues, UWB spatial aspects, UWB standardization and regulation, implementation issues, and UWB applications including positioning.

The goals of the early parts of the book are to provide the essential aspects of knowledge of UWB technology, especially in communications and in control applications. A literature survey examining books, articles, and conference papers presents the basic features of UWB technology and current systems.

1.2. UWB basics

Other terms associated with "UWB" include "impulse," "short-pulse," "nonsinusoidal," "carrier-less," "time domain," "super wideband," "fast frequency chirp," and "monopulse" [5].

Impulse radio communication systems and impulse radars both utilize very short pulses in transmission that results in an UWB spectrum. For radio applications, this communication method is also classified as a pulse modulation technique because the data modulation is introduced by pulse-position modulation (PPM). The UWB signal is noise-like which makes interception and detection quite difficult. Due to the low power spectral density, UWB signals cause very little interference with existing narrowband radio systems, and according to current FCC regulations, UWB signals are not necessarily regarded as radio transmissions. Depending on the attitude of national and international regulatory bodies, this should allow licence-free operation of radio systems.

Time-modulated (TM) impulse radio signal is seen as a carrier-less baseband transmission. The absence of carrier frequency is the fundamental characteristic that differentiates impulse radio and impulse radar transmissions from narrowband applications and from direct-sequence (DS) spread-spectrum (SS) multicarrier (MC) transmissions, which can also be characterized as an (ultra-) wideband technique. Fast slewing chirps and exponentially damped sine waves are also possible methods to generate UWB signals.

1.2.1. Characteristics of UWB

UWB has a number of features which make it attractive for consumer communications applications. In particular, UWB systems

(i) have potentially low complexity and low cost;
(ii) have a noise-like signal spectrum;
(iii) are resistant to severe multipath and jamming;
(iv) have very good time-domain resolution allowing for location and tracking applications.

The low complexity and low cost of UWB systems arise from the baseband nature of the signal transmission. Unlike conventional systems, the UWB transmitter produces a very short time-domain pulse which is able to propagate without the need for an additional RF (radio frequency) mixing stage. The RF mixing stage takes a baseband signal and "injects" a carrier frequency or translates the signal to a frequency which has desirable propagation characteristics. The very wideband nature of the UWB signal means that it spans frequencies commonly used as carrier frequencies. The signal will propagate well without the need for additional up-conversion. The reverse process of down-conversion is also not required in the UWB receiver. Again, this means the omission of a local oscillator in the receiver, and the removal of associated complex delay and phase tracking loops.

Consequently, UWB systems can be implemented in low-cost, low-power integrated circuit processes [6]. UWB technique also offers grating lobe mitigation in sparse antenna array systems without weakening of the angular resolution of the array. Grating lobes are a significant problem in conventional narrowband antenna arrays.

Due to the low energy density and the pseudo-random (PR) characteristics of the transmitted signal, the UWB signal is noise-like which makes unintended detection difficult. Whilst there is some debate, it appears that the low-power, noise-like UWB transmissions do not cause significant interference to existing radio systems. The interference phenomenon between impulse radio and existing radio systems is one of the most important topics in current UWB research.

UWB systems offer high data rates for communication. Hundreds of Mbps have been reported for communication links. In [6], it is estimated that the number of users in an impulse radio communication system is much larger than in conventional systems. The estimation is claimed to be valid for both high- and low-data rate communications.

Because of the large bandwidth of the transmitted signal, very high multipath resolution is achieved. The large bandwidth offers (and also requires) huge frequency diversity, which together with the discontinuous transmission makes the UWB signal resistant to severe multipath propagation and jamming/interference. UWB systems offer good LPI and LPD (low probability of interception/detection) properties which make it efficient for secure and military applications. These properties, in turn, make commercial systems more challenging to develop.

The very narrow time-domain pulses mean that UWB radios are potentially able to offer timing precision much better than GPS (global positioning system) [6] and other radio systems. Together with good material penetration properties, UWB signals offer opportunities for short-range radar applications such as rescue and anti-crime operations, as well as in surveying, and in the mining industry. One should however understand that UWB does not provide precise targeting and extreme penetration at the same time, but UWB waveforms present a better tradeoff than many conventional radio systems.

1.3. Regulatory bodies

One of the important issues in UWB communication is the frequency of operation. Due to the use of very wide spectrum range, UWB systems are not intended to operate under any specific allocation. There are many systems operating under allocated bands in the UWB signal band. Some companies in the USA are working towards removing the restrictions from the FCC's regulations for applications utilizing UWB technology. These companies have established an UWB working group (UWBWG) to negotiate with the FCC. Some other companies and organizations in the USA are examining solutions to allow existing narrowband allocated services to be protected from possible interference generated in UWB systems. Discussions on frequency allocation and protection of other radio services from interference are also taking place in Europe. Currently, there are no dedicated frequency bands for UWB applications identified by ETSI (European Telecommunications Standards Institute), in the ECC (European Communication Committee) decisions or in ITU (International Telecommunications Union) Radio Regulation treaty.

1.3.1. UWB regulation in the USA

Before the FCC's First Report and Order [3, 4], there was significant effort by industrial parties to convince the FCC to release UWB technology under the FCC Part 15 regulation limitations and allow license-free use of UWB products. The FCC Part 15 rules permit the operation of classes of radio frequency devices without the need for a license or the need for frequency coordination (47 CFR 15.1). The FCC Part 15 rules attempt to ensure unlicensed devices do not cause harmful interference to other users of the radio spectrum (47 CFR 15.5). Within the FCC Part 15 rules, intentional radiators are permitted to operate within a set of limits (47 CFR 15.209) that allow signal emissions in certain frequency bands.

Intentional radiators are not permitted to operate in sensitive or safety-related frequency bands, which are designated as restricted bands (47 CFR 15.205). UWB devices are intentional radiators under FCC Part 15 rules.

In 1998, the FCC issued a Notice of Inquiry (NOI) [7]. Despite the very low transmission power levels anticipated, proponents of existing systems raised many claims against the use of UWB for civilian communications. Most of the claims related to the anticipated increase of interference level in the restricted frequency bands (e.g., TV broadcast bands and frequency bands reserved for radio astronomy and GPS). The Federal Aviation Administration (FAA) expressed concern about the interference to aeronautical safety systems. The FAA also raised concerns about the direction finding of UWB transmitters.

When UWB technology was proposed for civilian applications, there were no definitions for the signal. The Defence Advanced Research Projects Agency (DARPA) provided the first definition for UWB signal based on the fractional bandwidth B_f of the signal. The first definition provided that a signal can be classified as an UWB signal if B_f is greater than 0.25. The fractional bandwidth can be determined using the formula [5]

$$B_f = 2\frac{f_H - f_L}{f_H + f_L}, \tag{1.1}$$

where f_L is the lower and f_H is the higher -3 dB point in the spectrum, respectively.

In February 2002, the FCC issued the FCC UWB rulings that provided the first radiation limitations for UWB, and also permitted technology commercialization. The final report of the FCC First Report and Order [3, 4] was publicly available during April 2002. The document introduced four different categories for allowed UWB applications, and set the radiation masks for them.

The prevailing definition has decreased the limit of B_f to a minimum of 0.20 defined using the equation above. Also, according to the FCC UWB rulings, the signal is characterized as UWB if the signal bandwidth is 500 MHz or more. In the formula above, f_H and f_L are now the higher and lower -10 dB bandwidths, respectively. The radiation limits set by the FCC are presented in Table 1.1 for indoor and outdoor data communication applications.

1.3.2. UWB regulation in Europe

At the time of writing, regulatory bodies in Europe are awaiting further technical input on the impact of UWB on existing systems. The process of regulation in Europe has been ongoing for a considerable time and has experienced repeated delays. The European approach is somewhat more cautious than that of the USA, as Europe requires that a new technology must be shown to cause little or no harm to existing radio services. Of course, the European organizations must take into account the FCC's decision, in full awareness of the potential benefits to

Table 1.1. FCC radiation limits for indoor and outdoor communication applications.

Frequency (MHz)	Indoor	Outdoor
	EIRP (dBm/MHz)	EIRP (dBm/MHz)
960–1610	−75.3	−75.3
1610–1990	−53.3	−63.3
1990–3100	−51.3	−61.3
3100–10600	−41.3	−41.3
Above 10600	−51.3	−61.3

consumers of achieving globally compatible conditions of radio spectrum use for UWB.

Currently in Europe, the recommendations for short-range devices belong to the CEPT (the European Conference of Postal and Telecommunications) working group CEPT/ERC/SRD MG/REC 70–03 [8].

In March 2003, the European Commission gave a mandate [9] to the European standardization organizations, with the purpose of establishing a set of harmonized standards covering UWB applications. ETSI in turn established Task Group ERM TG31A to develop a set of harmonized standards for short-range devices using UWB technology by December 2004, following the completion of spectrum compatibility studies by CEPT. The output of this group has been delayed. The standardization working groups for UWB include ERM/TG31A covering generic UWB, and ERM/TG31B which covers UWB for automotive applications at higher bands. These groups have developed two technical reports on communication and on radio location UWB applications, respectively. In the related report [10] a preliminary slope mask is presented that allows UWB communication systems to operate. This mask referred to in Figure 1.1 as the provisional CEPT/ETSI mask is supported by the UWB industry within ETSI as the starting point for studies by CEPT. ETSI should further develop two standards on communication and on radio location UWB applications.

The European Commission has further given CEPT a mandate [11] related to the development of harmonized conditions of use of UWB devices in the European Union. This mandate requires "an in-depth analysis of the risks of harmful interference of UWB on all potentially affected radio services, including via aggregation effects, as well as taking into account the existing regulatory environment."

In March 2004, the ECC (within the CEPT) established Task Group TG3 to take on the task of responding to this mandate. TG3 has produced a first report in mid-2004, which states that one key factor in the consideration of appropriate frequency bands for use by UWB is the compatibility with radio communication services using these bands in CEPT countries. The CEPT final report to the European Commission is to be approved by the ECC in April 2005.

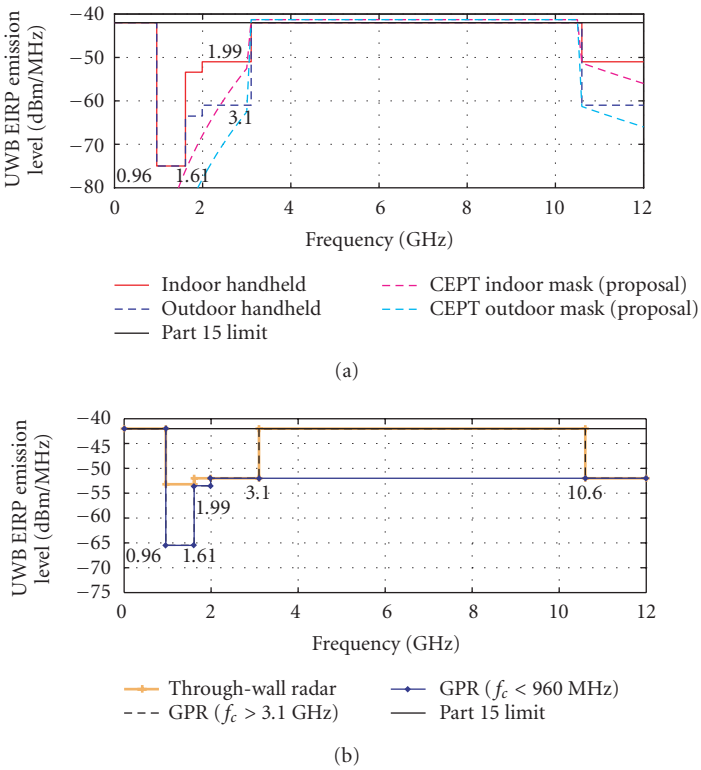

Figure 1.1. UWB radiation mask defined by FCC and one early CEPT proposal.

The CEPT has already undertaken a number of compatibility studies which indicate that limits for emissions from UWB devices for communication applications would need to be lower than the FCC limits in order to avoid harmful interference to some of the radio communication applications in CEPT countries. It is generally expected that ETSI/CEPT will follow some of the FCC's recommendations but will not necessarily directly adopt the FCC's regulations, now out of date!

Figure 1.1 shows an early proposal for CEPT/ETSI mask limits as well as the agreed FCC masks. Figure 1.1(a) represents the masks for data communication applications for indoor and outdoor uses. Figure 1.1(b) gives the FCC radiation mask for radar and sensing applications. In all cases, the maximum average power spectral density follows the limit of FCC Part15 regulations [12]. Therefore, the limit will depend on compatibility studies results made by CEPT/TG3.

1.3.3. UWB regulation within ITU

The ITU-R Study Group 1 has established Task Group 1/8 [13] to carry out relevant studies related to the proposed introduction of UWB devices and the

implications of compatibility with radio communication services. The mandate of TG 1/8 is focused on the study of

(i) compatibility between UWB devices and radio communication services (Question ITU-R 227/1);
(ii) spectrum management framework related to the introduction of UWB devices (Question ITU-R 226/1);
(iii) appropriate measurement techniques for UWB devices.

TG1-8 is to complete its work in 2005 and will present to SG1 four new recommendations on UWB characteristics, UWB compatibility with other radio services, UWB spectrum management framework, and UWB measurement techniques, respectively.

1.3.4. UWB standardization in the IEEE

1.3.4.1. IEEE 802.15.3a

The IEEE established the 802.15.3a Study Group to define a new physical layer concept for short-range, high-data-rate applications. This alternative physical (ALT PHY) layer is intended to serve the needs of groups wishing to deploy high-data-rate applications. With a minimum data rate of 110 Mbps at 10 m, this study group intends to develop a standard to address such applications as video or multimedia links, or cable replacement. Whilst not specifically intended to be an UWB standards group, the technical requirements lend themselves very much to the use of UWB technology. The study group has been the focus of significant attention recently as the debate over competing UWB physical layer technologies has raged. The work of the study group also includes analyzing the radio channel model proposal to be used in the UWB system evaluation.

The purpose of the study group is to provide a higher-speed physical layer (PHY) candidate for the existing, approved 802.15.3 medium access standard. The targeted applications are those which involve imaging and multimedia [14]. The main desired characteristics of the alternative PHY are

(i) coexistence with all existing IEEE 802 physical layer standards;
(ii) target data rate in excess of 100 Mbps for consumer applications;
(iii) robust multipath performance;
(iv) location awareness;
(v) use of additional unlicensed spectrum for high-rate WPANs (wireless personal area network).

1.3.4.2. IEEE 802.15.4

The IEEE established the 802.15.4 Study Group to define a new physical layer concept for low-data-rate applications. The IEEE 802.15 TG4 is chartered to investigate low-data-rate solutions for very low power and very low complexity systems. It is intended to operate in unlicensed, international frequency bands. Potential applications are sensors, interactive toys, smart badges, remote controls, and home automation.

One option examined by the working group is utilizing UWB technology at the air interface. The study group addresses new applications which require not only moderate data throughput, but also require long battery life such as low-rate wireless personal area networks, sensors, and small networks.

1.3.5. The multiband OFDM alliance (MBOA)

The MBOA is an alliance of industry and academic partners which aims to develop physical layer and medium access layer technologies for UWB based on OFDM techniques [15]. The stated mission of the MBOA is to develop the best overall solution for UWB-based products in compliance with worldwide regulatory requirements as well as to ensure coexistence with current and future spectrum users [15].

In practice, the MBOA is formed in response to the impasse which existed in the IEEE 802.15.3a standardization attempt. The MBOA is still heavily involved in promoting its particular standard within the IEEE, but is moving to develop product for the market irrespective of the position of the IEEE standardization process.

1.4. Applications of UWB

Even with the significant power restrictions, UWB holds enormous potential for wireless ad-hoc and peer-to-peer networks. One of the major potential advantages in impulse-radio-based systems is the ability to trade data rate for link distance by simply using more or less concatenated pulses to define a bit. Without dramatically changing the air interface, the data rate can be changed by orders of magnitude depending on the system requirements. This means however that high-data-rate (HDR) and low-data-rate (LDR) devices will need to coexist. The narrow time-domain pulse also means that UWB offers the possibility for very high positioning accuracy. However, each device in the network must be "heard" by a number of other devices in order to generate a position from a delay or signal angle-of-arrival estimate. These potential benefits, coupled with the fact that an individual low-power UWB pulse is difficult to detect, offer some significant challenges for the medium access (MAC) design.

Figure 1.2 shows the area of application for UWB with respect to existing and future networks. The low-power restricts UWB to very short-range high-data applications, or very low data rates for moderate-range applications. The power restrictions on transmission effectively prohibit UWB from most outdoor applications. The increasing trend of users to combine both cellular and ad hoc technologies (e.g., 802.11b WLAN and 2G cellular) is a strong indicator for the inclusion of high-speed short-range wireless in a comprehensive picture of future wireless networks.

UWB systems have been targeted at very HDR applications over short distances, such as USB replacement, as well as very LDR applications over longer distances, such as sensors and RF tags. Classes of LDR devices are expected to

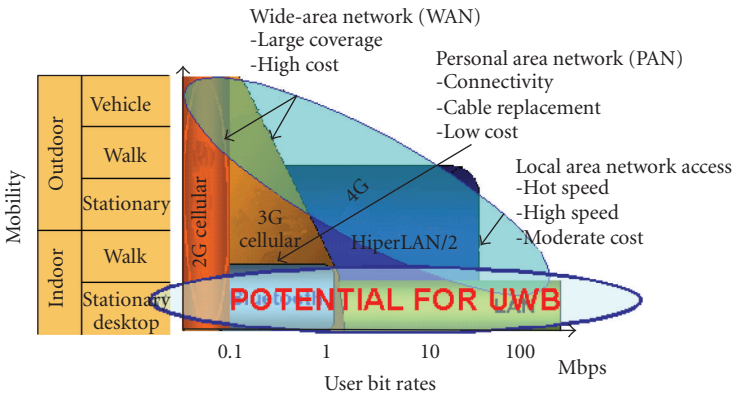

Figure 1.2. Role of UWB in future systems.

have very low complexity and very low cost. The expected proliferation of low-cost UWB devices means that solutions must be devised for devices to coexist or preferably interoperate with many different types of UWB devices with different capabilities. The complexity limitations of LDR devices may mean that very simple solutions are required. HDR devices, which are expected to have higher complexity, may have much more sophisticated solutions.

Figure 1.3 shows applications for UWB as perceived by members of the European Union project PULSERS [16]. These scenarios cover wireless local area networks (WLANs), wireless personal area networks (WPANs), sensor networks, and short-range peer-to-peer networks.

1.5. Impulse radio schemes

1.5.1. Impulse radio UWB

Time-modulated ultra-wideband (TM-UWB) communication is based on discontinuous emission of very short pulses or pulsed waveforms (monocycles), for example, one of those presented in Figure 1.4. Impulse-radio-based UWB has much in common with spread-spectrum systems. A major difference however is that the spread-spectrum "chip" is replaced by a discontinuous UWB "pulse" or monocycle transmission. The UWB pulse employed determines the bandwidth occupied by the signal.

Each pulse has the ultra-wide spectrum in the frequency domain (as presented in Figure 1.5). This type of transmission does not require the use of additional carrier modulation as the pulse will propagate well in the radio channel. The technique is therefore a baseband signaling technique. This radio concept is referred as impulse radio (IR).

One transmitted symbol is spread over N pulses to achieve a processing gain which may be used to combat noise and interference. This is similar to the approach used for spread-spectrum systems.

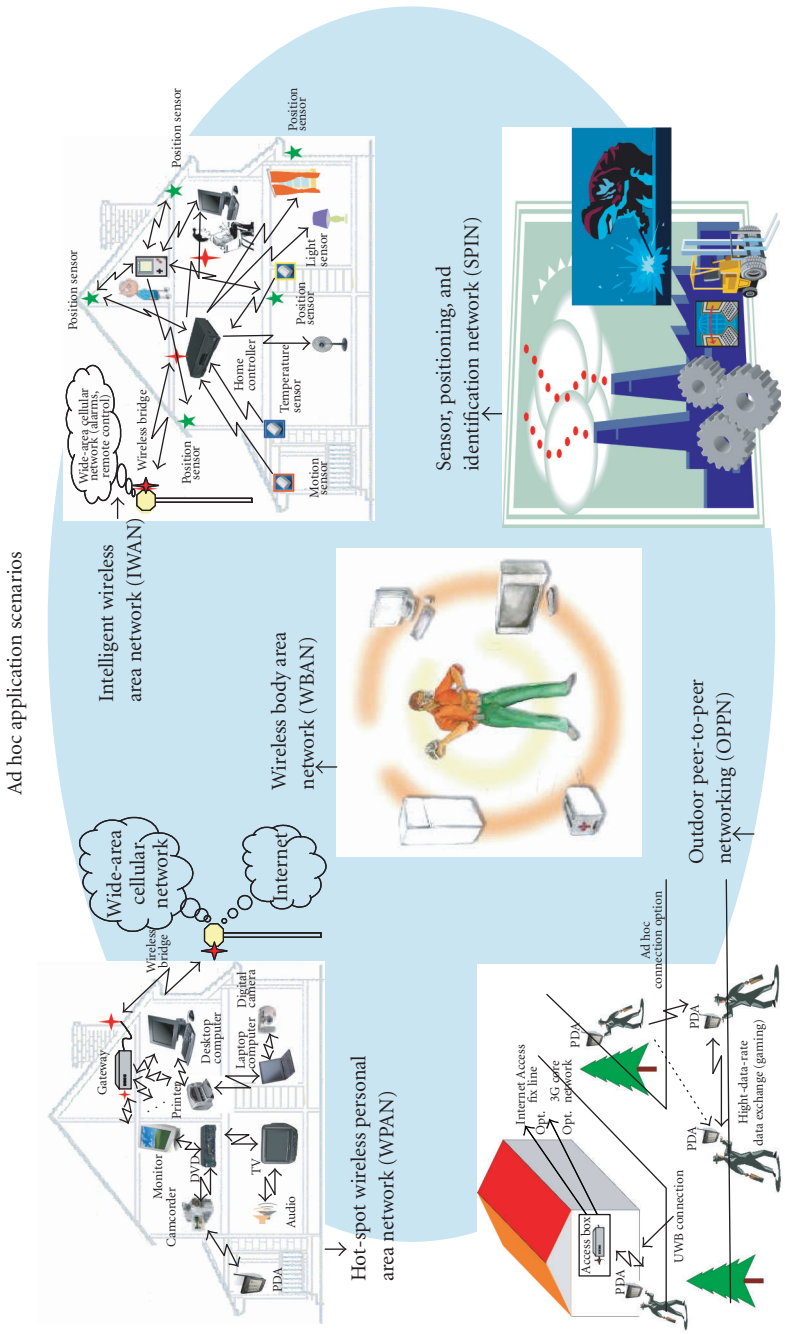

FIGURE 1.3. Applications for UWB (source: PULSERS White Paper [16]).

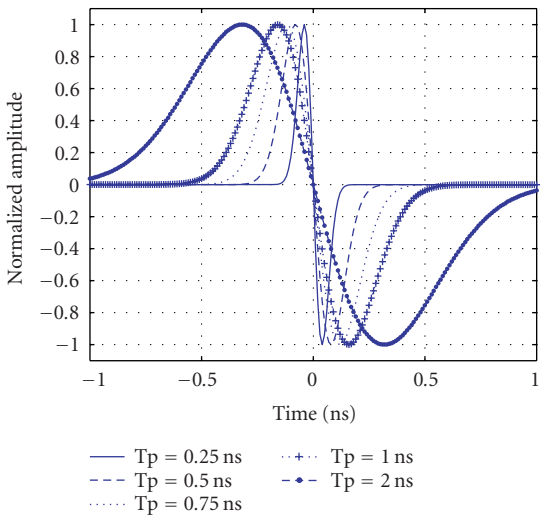

FIGURE 1.4. Gaussian monocycle in time domain.

The UWB pulse waveform can be any function which satisfies the spectral mask regulatory requirements. Common pulse shapes used in theoretical studies include Gaussian, Laplacian, Rayleigh, or Hermitean pulses. In practical systems, exact pulse shapes are extremely difficult to generate due to antenna and radio frequency matching problems. Only coarse approximations of the theoretical waveforms are available in practice.

Data modulation is typically based on simple modulation schemes such as pulse position modulation (PPM) and/or pulse amplitude modulation (PAM) [17]. A commonly proposed UWB receiver is a homodyne cross-correlator, that is, based on the architecture that utilizes a direct RF-to-baseband conversion. Intermediate frequency conversion is not needed, which makes the implementation simpler than in conventional (super-)heterodyne systems.

Unlike spread-spectrum systems, the pulse (chip) does not necessarily occupy the entire chip period. This means that the duty cycle can be extremely low. The receiver is only required to "listen" to the channel for a small fraction of the period between pulses. The impact of any continuous source of interference is therefore reduced so that it is only relevant when the receiver is attempting to detect a pulse. This leads to processing gain in the sense of a spread-spectrum system's ability to reduce the impact of interference.

The nominal centre frequency and the bandwidth of the monocycle (see Figure 1.5) depends on the monocycle's width. The -3 dB bandwidth is approximately 116% of the monocycles nominal centre frequency $f_0 = 1/\tau_p$ [6]. Considering an example monocycle duration of 0.75 nanosecond (as shown in Figure 1.4), the nominal centre frequency is 1.33 GHz and the half-power bandwidth is 1.55 GHz. The spectrum of a Gaussian monocycle is asymmetrical, as seen in Figure 1.5.

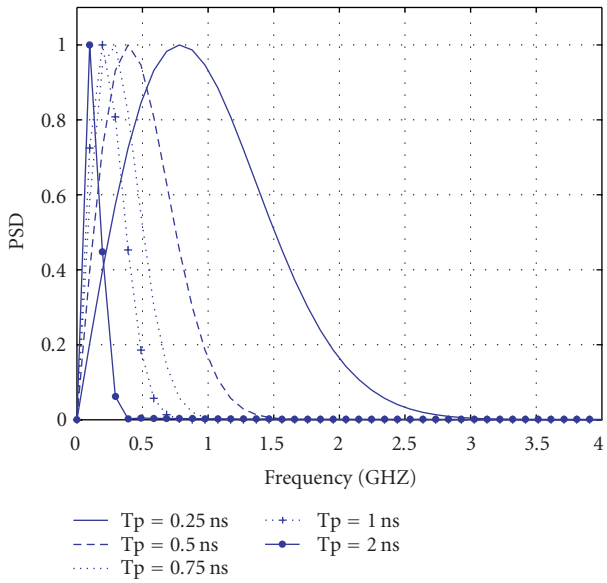

FIGURE 1.5. Gaussian monocycle in frequency domain and spectra of the Gaussian monocycle.

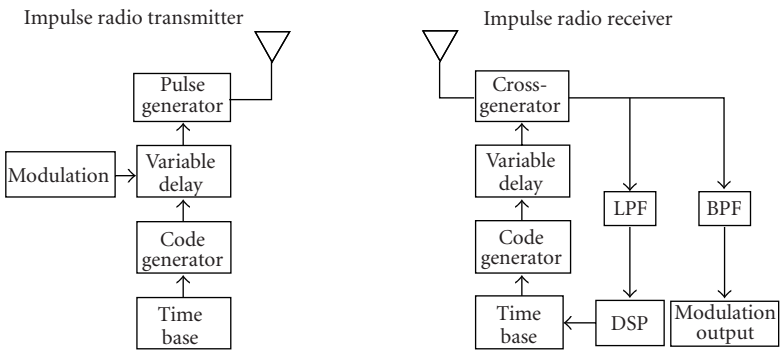

FIGURE 1.6. Block diagram of the TH-PPM UWB impulse radio concept by Time Domain Corporation.

Figure 1.6 presents a block diagram of a time-hopping UWB impulse radio concept that utilizes pulse position modulation (concept by Time Domain Corporation, USA).

1.5.2. Fast stepped frequency chirps

Both the bandwidth and spectral mask limitations must be satisfied by the UWB signal. There are many means of generating a very wideband signal. One technique is based on fast frequency chirps, which are commonly used in impulse

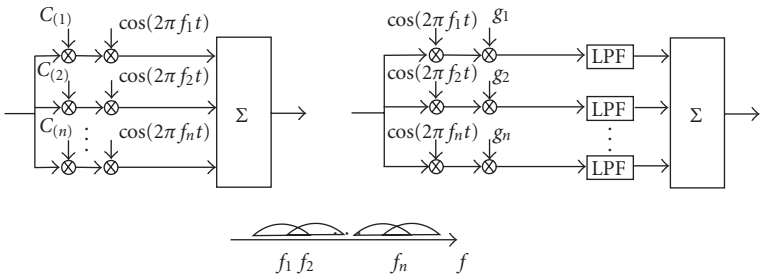

FIGURE 1.7. Block diagram and spectrum for multicarrier CDMA system.

radar applications. It is possible to generate a wideband transmission by sweeping the transmitter's oscillator in the frequency domain. A bandwidth of several hundred MHz can be achieved with ~ 10 nanosecond sweep time [18]. Wider bandwidths can be achieved using this technique, for example, ground penetrating radar (GPR) systems with 50–1200 MHz bandwidth have been documented in [19].

GPR systems based on UWB technology are suitable for object detection in, for example, landmine sweeping and avalanche rescue operations, because of the good signal penetration ability and fine spatial resolution.

1.6. Multicarrier schemes

Another approach to producing an UWB signal is to extend the techniques utilized for direct-sequence spread-spectrum or code-division multiple-access (CDMA) schemes that are used for third generation mobile systems. Wideband CDMA systems with optional multicarrier (MC) techniques can be used to fill the available spectral mask.

There are three main techniques to generate an SS-MC transmission; multicarrier CDMA, multicarrier DS-CDMA, and multitone (MT) CDMA [20]. Each of these techniques relies on, and benefits from, the properties of conventional spread-spectrum signals. However, multicarrier systems are reasonably complex to implement. In particular, multicarrier systems require several mixers or digital fast Fourier transform (FFT) techniques to place the different signal components in the required bands.

Figure 1.7 shows a block diagram for an MC-CDMA system. The original data stream is spread over the different subcarriers f_i with each chip of pseudo-random (PR) code C_i. The spectrum spreading is done in the frequency domain [20]. The signal is despread at the receiver using corresponding chips g_i of the spreading code C. In UWB applications, the individual modulated carrier needs to fulfil the 500 MHz bandwidth requirements.

Figure 1.8 shows a block diagram for a multicarrier DS-CDMA system. This method involves spreading the original data in the time domain after serial-to-parallel conversion of the data stream [20]. The system needs to obtain the 500 MHz minimum bandwidth requirement to be treated as UWB.

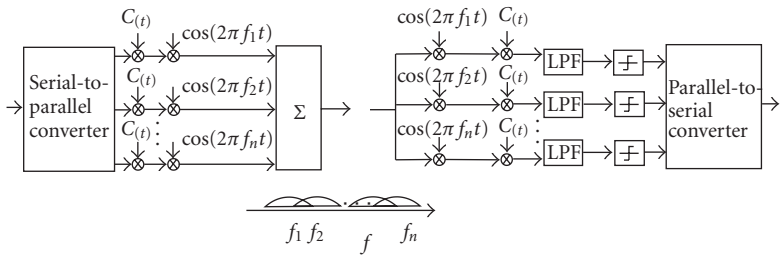

FIGURE 1.8. Block diagram and spectrum for multicarrier DS-CDMA system.

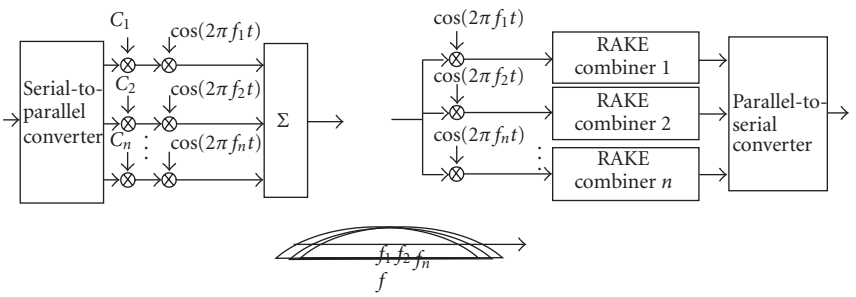

FIGURE 1.9. Block diagram and spectrum for multitone CDMA system.

Figure 1.9 shows the block diagram of a multitone-CDMA system. The bandwidth of an MT-CDMA system is smaller than in the previous multicarrier systems because of the small subcarrier spacing. This kind of multicarrier approach is the closest to the original UWB concept. However, it causes the highest self-interference due to the overlapping spectra.

Multicarrier technology is currently used in high-data-rate applications, for example, in WLAN systems such as Hiperlan2, digital audio or video broadcasting (DAB and DVB, resp.) and in asymmetric digital subscriber line (ADSL).

The advantage of multicarrier technologies over single carrier systems is that the data rate in each subcarrier is lower than for single carrier systems. This eases synchronization with the spreading sequence at the receiver, and helps to avoid intersymbol interference (ISI). The disadvantage is the increased complexity of the receiver requiring either multiple mixing stages or fast Fourier transform processing. MC-CDMA schemes spread the signal in the frequency domain. The signal consists of overlapping, relatively narrow carriers which fill the available UWB signal spectrum. MC-DS-CDMA and MT-CDMA schemes apply spreading in the time domain. MT-CDMA has a similar bandwidth to a basic DS-CDMA scheme [20] with relatively small separation of the tones used (f_1 to f_n in Figure 1.9). Consequently, the spreading factor employed for MT-CDMA schemes are much higher than for the MC schemes. The increased spreading factor increases the processing speed required at the receiver.

The conventional DS-SS technique without multicarrier properties can also be characterized as an UWB technique if the chip rate is high enough. This calls

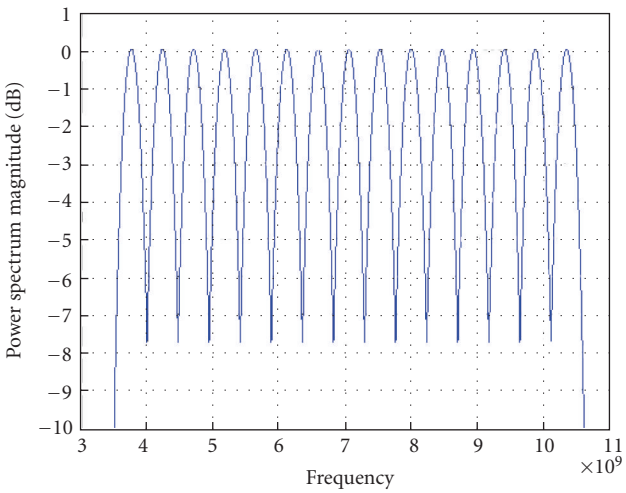

FIGURE 1.10. Multiband frequency plan and spectral plan—Group A.

for extremely fast digital signal processing which may be impractical. Issues such as synchronization will also be a significant challenge.

1.6.1. Multiband UWB

A recent proposal within the IEEE 802.15.3 Working Group for UWB signals [14] utilizes overlapping groups of UWB signals which each has a bandwidth of approximately 500 MHz. Whilst not currently the leading proposal, this technique offers an interesting insight into the potential use of the very large spectrum available. This so-called multiband UWB ensures adherence to the FCC minimum bandwidth requirements and allows efficient utilization of the available spectrum.

Figure 1.10 shows the spectrum plan for the first group of UWB signals (Group "A"). The subbands are spaced 470 MHz apart, and any number of 500 MHz signals may be utilized. This allows for flexible coexistence with existing communications systems (such as WLAN systems). Each subband is generated by a pulse with 10 dB bandwidth of ~ 520 MHz. Figure 1.11 shows the second group of UWB signals (Group "B") which overlaps the first group of UWB signals by 235 MHz. This potentially enhances the system's flexibility with respect to coexistence, interference mitigation, and multiple access.

Each group of UWB signals is divided into lower sets (subbands 1–8) and upper sets (subbands 9–15). Only 7 subbands are used in the lower set, which means that one subband can be avoided for coexistence. The upper set is used in conjunction with the lower set to increase the bit rate.

1.6.2. Multiband OFDM

A hot candidate for standardization in the IEEE 802.15.3a Group is multiband OFDM as supported by the MBOA. The technique proposed by the MBOA is to

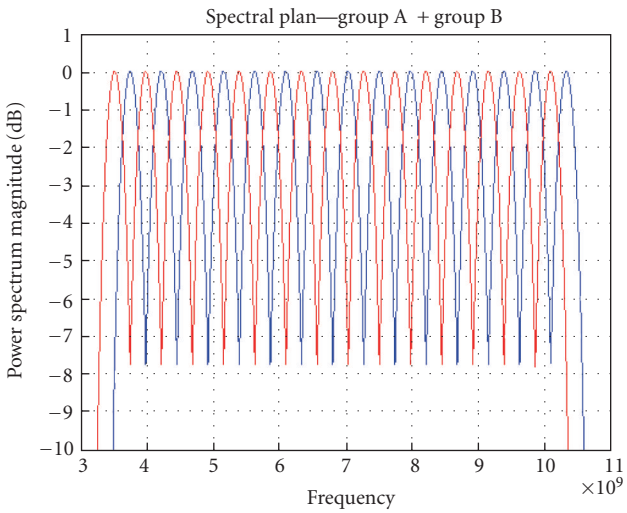

FIGURE 1.11. Multiband frequency plan and spectral plan of two overlapping frequency groups—Group A and Group B.

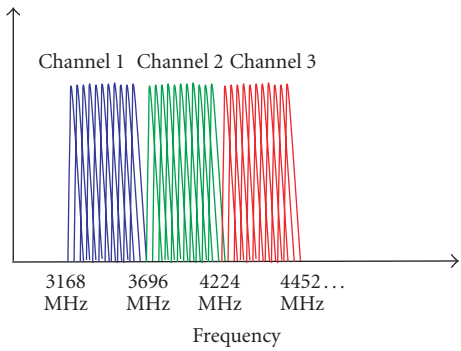

FIGURE 1.12. MBOA channel allocation scheme.

utilize OFDM techniques to produce a signal (channel) which is approximately 528 MHz wide. The signal structure is shown in Figure 1.12. The OFDM signal can be produced using standard FFT techniques [21].

1.7. Conclusions

The fact that UWB technology has been around for so many years and has been used for a wide variety of applications is a strong evidence of the viability and flexibility of the technology. The simple transmitter and receiver structures which are possible make this a powerful technology for low-complexity, low-cost communications. As will be discussed in later chapters, the physical characteristics of the

signal also support location and tracking capabilities of UWB much more readily than in existing narrowerband technologies.

The severe restrictions on transmit power, allowing less than 0.5 mW maximum power over the 7.5 GHz band in the FCC emission mask, have substantially limited the range of applications of UWB to short-distance high-data-rate, or low-data-rate, longer-distance applications. The great potential of UWB is to allow flexible transition between these two extremes without the need for substantial modifications to the transceiver. On the other hand, UWB technology emission masks outside the USA are still under discussion pending the outcome of compatibility studies with other radio services.

Whilst UWB is still the subject of significant debate, there is no doubt that the technology is capable of achieving very high data rates and is a viable alternative to existing technology for WPAN; short-range, high-data-rate communications; multimedia applications, and cable replacement. Much of the current debate centers around which PHY layer(s) to adopt, development of a standard, and issues of coexistence and interference with other radio services.

At the time of writing, no standard exists for a MAC which has been specifically developed for UWB which will support all of the unique advantages of UWB. The potential of UWB systems to offer flexible data rates, support coexistence, enable large numbers of users and positioning services are critically dependent on the capabilities of the MAC.

Research is ongoing in industry and academic consortia including the IEEE, MBOA, and in European Union Projects such as PULSERS [22]. There is work ongoing in standardization bodies to adapt, optimize, and enhance existing MACs for use over UWB. Part of the reason for the slow progress in developing a flexible, comprehensive MAC specifically for UWB is due to the inherent complications of using a physical layer signal which is difficult to detect and difficult to synchronize for intended users. Efforts have been made to develop MACs which allow efficient operation for large numbers of devices. However, this work is still at an early stage.

Acknowledgments

The author would like to thank colleagues from CWC for input to this chapter. In particular, thanks to Matti Hämäläinen and Jari Iinatti. The author would also like to thank colleagues from the Wireless World Research Forum (WWRF) Working Group (Short Range Communications) for their input related to the regulatory status section. In particular,thanks to Frédéric Lallemand and Guy Salingue. Thanks also to Therese Oppermann for careful proofreading.

Bibliography

[1] C. L. Bennett and G. F. Ross, "Time-domain electromagnetics and its applications," *Proceedings of IEEE*, vol. 66, no. 3, pp. 299–318, 1978.

[2] H. F. Harmuth, *Nonsinusoidal Waves for Radar and Radio Communication*, Academic Press, New York, NY, USA, 1981.

[3] FCC press release, Febrauary 2002, http://www.fcc.gov/Bureaus/Engineering_Technology/News_Releases/2002/nret0203.html.
[4] Federal Communications Commission (FCC), "First Report and Order in The Matter of Revision of Part 15 of the Commission's Rules Regarding Ultrawideband Transmission Systems," ET-Docket 98-153, FCC 02-48, released April 2002.
[5] J. D. Taylor, Ed., *Introduction to UWB Radar Systems*, CRC Press, Boca Raton, Fla, USA, 1995.
[6] Time Domain Corporation, "Comments of Time Domain Corporation, Docket 98-154. In the Matter of Revision of Part 15 of the FCC's Rules Regarding Ultra wide-band Transmission Systems," 1998.
[7] Federal Communications Commission (FCC), "FCC NOI: Rules Regarding UWB Transmission Systems," ET Docket No. 98-153, September 1998.
[8] CEPT/ERC Recommendation 70-03, "Relating to the use of Short Range Devices (SRD)".
[9] EC Mandate M/329 to the European Standardisation Organisations, referenced in document RSCOM03-07.
[10] ETSI TR 101 994-1 for communication and positioning applications.
[11] EC Mandate to CEPT, "Mandate to CEPT to harmonise radio spectrum use for Ultra-wideband Systems in the European Union," referenced in document RSCOM03-40 rev. 3.
[12] Federal Communications Commission (FCC), http://www.fcc.gov, (Many standards documents may be found on this site).
[13] I. Oppermann, F. Lallemand, and G. Salingue, "WWRF White Paper," chapter 5, "UWB Spectrum Landing Zones," 2004.
[14] http://www.ieee802.org/15/pub/.
[15] http://www.multibandofdm.org/about.html.
[16] "PULSERS White Paper," *WWRF Meeting*, Eindhoven, The Netherlands, December 2002.
[17] J. T. Conroy, J. L. LoCicero, and D. R. Ucci, "Communication techniques using monopulse waveforms," in *Proceedings of IEEE Military Communications Conference (MILCOM '99)*, vol. 2, pp. 1181–1185, Atlantic City, NJ, USA, October–November 1999.
[18] G. F. Stickley, D. A. Noon, M. Chernlakov, and I. D. Longstaff, "Preliminary field results of an ultra-wideband (10–620 MHz) stepped-frequency ground penetrating radar," in *Proceedings of IEEE International Geoscience and Remote Sensing (IGARSS '97)*, vol. 3, pp. 1282–1284, Singapore, August 1997.
[19] L. Carin and L. B. Felsen, Eds., *Ultra-Wideband, Short-Pulse Electromagnetics 2*, Conference Proceedings, Kluwer Academic/Plenum Press, New York, NY, USA, 1995, 605 pages.
[20] R. Prasad and S. Hara, "An overview of multi-carrier CDMA," in *Proceedings of IEEE 4th International Symposium on Spread Spectrum Techniques and Applications (ISSSTA '96)*, vol. 1, pp. 107–114, Mainz, Germany, September 1996.
[21] MBOA White paper, http://www.multibandofdm.org/, September 2004.
[22] http://www.pulsers.net/main.shtml.

Ian Oppermann: Department of Electrical and Information Engineering, University of Oulu, FIN-90014, Finland

Email: ian@ee.oulu.fi

2 UWB propagation channels

Andreas F. Molisch, Jürgen Kunisch, Robert Qiu,
Dajana Cassioli, Michael Buehrer,
Marcus Pendergrass, István Z. Kovács,
Gert F. Pedersen, Patrick C. F. Eggers,
Sumit Roy, and Iyappan Ramachandran

2.1. Introduction

2.1.1. General aspects of channel modeling

As with any other communications system, it is the *channel* that determines the ultimate (information-theoretic) performance limits, as well as the practical performance limits of various transmission schemes and receiver algorithms. For UWB systems, this channel is the ultra-wideband propagation channel. Understanding this channel is thus a vital prerequisite for designing, testing, and comparing UWB systems. Just like UWB communications itself, channel modeling for UWB is a relatively new area. And just as the interest for UWB systems has intensified in the last years, so has the importance of modeling the UWB propagation channels. In this chapter, we will give a comprehensive overview of the state of the art in this exciting area.

Quite generally, wireless channel modeling is done for two different purposes.

(i) Deterministic channel modeling tries to predict the behavior of a wireless channel in a specific environment. If a complete description of the geometry, as well as of the electromagnetic properties of the materials, of the surrounding of transmitter and receiver is given,[1] then Maxwell's equations can be solved exactly, and the channel impulse response (or an equivalent quantity) can be predicted. This approach, which had long been deemed too complicated, has become popular in the last 15 years. Ray tracing and other high-frequency approximations, as well as the advent of more powerful computers, have made it possible to perform the required computations within reasonable time.

(ii) Stochastic channel models try to model the "typical" or "canonical" properties of a wireless channel, without relating those properties to a specific location. As the most simple example, the probability density

[1]The size of the "surroundings" depends on the environment, as well as on the desired dynamic range.

function of the (narrowband) amplitude of the received signal is modeled as Rayleigh-distributed within a small area (part of a room). In contrast, a deterministic model would try to predict the exact amplitude values at each location in that part of a room.

There is an enormous amount of literature for *narrowband* wireless channels; for textbooks and overview articles, see [1–10]. However, those models cannot be easily generalized to UWB channels, due to some important basic differences in the propagation processes and the resulting models. Some of these differences are the following.

(i) Each multipath component (MPC) can lead to delay dispersion by itself, due to the frequency-selective nature of reflection and diffraction coefficients. This effect is especially important for systems with large *relative* bandwidth.

(ii) The signals are received with excellent delay resolution. Therefore, it often happens that only a few multipath components make up one *resolvable* MPC, and the amplitude statistics of such a resolvable MPC is not complex Gaussian anymore. Similarly, there is an appreciable probability that areas of "no energy" can exist, that is, (resolvable) delay intervals during which no significant amount of energy is arriving at the receiver. These issues are mostly important for systems with large *absolute* bandwidth.

By definition, a UWB channel is a more general description of nature than a narrowband channel: it is always possible to obtain a narrowband channel from a UWB channel by just filtering the UWB channel. Extrapolation from narrowband to UWB is tempting, as it allows the reuse of existing measurements. However, it is extremely dangerous, and has to be backed up by measurement data. Every aspect of narrowband channel modeling has to be questioned before it can be accepted for UWB modeling!

2.1.2. Regulatory and application-specific aspects

The frequency range of UWB systems is limited by transceiver design issues (transit frequency of semiconductor components, antenna bandwidth, etc.), as well as rulings of the frequency regulators. Channel models should be mindful of those limitations: after all, the main purpose of channel models is the design and testing of UWB systems, and as the systems face practical and legal limitations, there is no need to be overly general in the models either.

Up to now, only the regulator in the USA has issued rulings that allow the use of UWB.[2] The report and order of the FCC from 2002 [11] allows unlicensed operation of UWB communications devices in indoor environments, mainly in the frequency range between 3.1 and 10.6 GHz. The admissible power spectral density is −41.3 dBm/MHz, and considerably lower outside that band (the exact

[2]Singapore has recently established a "UWB-friendly zone," and other countries are expected to issue rulings within the next few years.

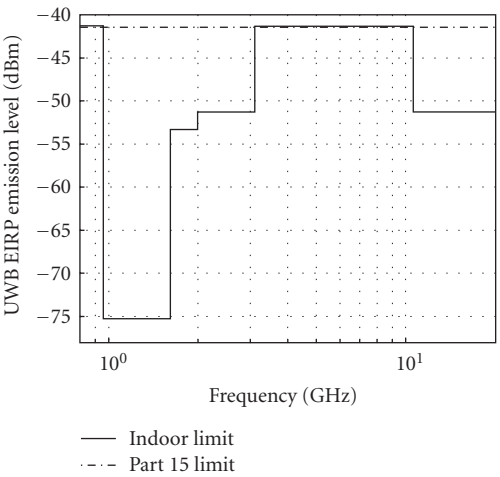

FIGURE 2.1. FCC mask for indoor communications.

mask is shown in Figure 2.1). Communications is also allowed at frequencies below 960 MHz. There are certain restrictions in the applications, as well as in peak-to-average ratios; however, those have no impact on the channel modeling. It is important that outdoor devices must not be fixed, or have a connection to power mains-only peer-to-peer communications of portable devices is allowed. These restrictions limit the frequency range in which the channel model needs to be valid, as well as the possible distance between transmitter and receiver.

The envisioned applications give us guidelines about what propagation environments are of greatest interest for UWB applications. A main point of emphasis is high-data-rate personal area networks (PANs). A typical application there is the transmission of digital TV signals via a wireless link. It follows that such high data rates, in conjunction with the limits on the power spectral density, can be performed only over short distances (on the order of 10 m), and are of interest mostly for residential and office environments. Another application of interest is sensor networks. As the data rates are much lower in this context, longer ranges are possible. Furthermore, sensor networks can be of great interest in factory environments, where "indoor" distances can be larger, and the abundance of metallic reflectors can lead to quite different propagation conditions.

Yet another application for UWB is emergency communications, possibly combined with geolocation, for example, from a building that collapsed during an earthquake, or from an avalanche. Propagation conditions in such rubble or snow environments will obviously differ considerably from "normal" environments; required distance can be up to 100 m. Outdoor UWB applications, as mentioned above, are limited to peer-to-peer communications in the USA; however, since other countries might allow fixed-location transmitters, it is worthwhile to also study the "base-station to mobile-station" scenario. Finally, communications between cars is of interest.

2.1.3. Synopsis of the chapter

A first step in understanding UWB propagation has to be measurements of UWB channels. For this task, we have two different types of measurement techniques at our disposal: frequency-domain measurements, employing a vector network analyzer, give the transfer function of the channel; alternatively, the channel can be excited with a short pulse, and a time-domain measurement of the received signal returns the convolution of the pulse with the channel impulse response. In either of those cases, the impact of the antenna on the measurement results is crucial. In fact, it is much more important than in the narrowband case, because the antenna characteristics vary significantly with the frequency, and exhibit a different response in different directions. Section 2.2 by *Kunisch* gives a detailed mathematical model for these effects, and suggests a procedure for the deconvolution of the antenna effects.

As mentioned above, a crucial property of UWB channels is the fact that each multipath component can show delay dispersion by itself. That means that a short pulse that, for example, undergoes only a single diffraction will arrive at the receiver with a larger support (extent in the delay domain) compared to the originally transmitted pulse. The reason for this is that the diffraction coefficient is frequency-dependent. *Qiu* describes in Section 2.3 the mathematics of these processes. Exact and approximate formulations, based on the uniform theory of diffraction, allow a modification of the classical Turin model, so that the impulse response in a multipath environment is now the sum of *distorted*, scaled, and delayed pulses. This has important implications for the design of correlation receivers, which are also addressed in this section. From a more experimental point of view, *Molisch and Buehrer* discuss the impact of frequency-selective reflection coefficients in Section 2.5.5. The results from these sections can be combined with classical ray tracing approaches, resulting in a deterministic channel prediction and modeling method.

For stochastic channel modeling, we have to investigate the path loss and shadowing, as well as the delay and angular dispersion of the channel. These two topics are treated in Sections 2.4 (by *Cassioli*) and 2.5 (by *Molisch and Buehrer*), respectively. While the path loss is a well-known quantity in narrowband channel modeling, Section 2.4 shows that it actually has to be treated as frequency-dependent when the relative bandwidth becomes significant. On the other hand, many narrowband measurement campaigns in different frequency bands can be reused for path loss predictions. The delay dispersion properties also show a significant dependence on the bandwidth. While the rms delay spread shows only a weak dependence on the bandwidth, the amplitude statistics and the statistics of the arrival times of the multipath properties strongly vary with the bandwidth, as well as with the center frequency of the considered signal. All the different aspects of stochastic channel modeling had an impact on the standardized IEEE 802.15.3a channel model, which is described by *Pendergrass* in Section 2.6. It was used in the downselection process for the standard for the physical layer of high-data-rate UWB communications, and is therefore restricted to modeling

short-range communications in indoor office environments. More general channel models are currently under development within the IEEE 802.15.4a group, but not yet finalized at the time of this writing, and therefore not further treated here.

All of the above considerations are for a channel without human presence—measurement campaigns (as well as the models based on them) usually try to avoid the influence of human bodies on the measurement results as much as possible. This assumption might be realistic, for example, for an antenna mounted on a DVD-player, which establishes a video link. However, it becomes untenable for "body-area network," where the antenna is placed directly on a body of a user—antenna and body become inseparable. This case requires new measurement techniques, and also new channel models. *Kovacs, Pedersen, and Eggers* describe measurement setups that are especially suitable for this situation (see Section 2.7). A main difficulty is the impact of cables between antenna and network analyzer (or oscilloscope); this problem is solved by using RF-over-fiber.

Finally, Section 2.8 by *Roy* deals with the topic of channel estimation. While it is clearly similar to the problem of measuring channels, there are also important conceptual differences. Channel estimation always must be viewed in light of the system it is being performed for, while channel measurement and modeling tries to remain as system-independent as possible. Also, channel estimation has to use a signaling structure that is similar to the signaling (modulation) of the payload data—cost considerations do not allow the building of an additional transceiver with a different structure, just to obtain channel estimates. Due to these reasons, the estimation techniques for OFDM-based UWB systems on one hand and for impulse-radio and direct-sequence CDMA systems on the other hand are quite different. Both are treated in Section 2.8.

The state of the art of UWB channel modeling is by now sufficiently advanced that it merits a review such as the one given in this chapter. The main problems and challenges for UWB channel models have been identified, and generic model structures can be established. However, we have to recognize that UWB channel models are still far less comprehensive than narrowband models—this is no wonder when we compare the duration of UWB channel research with the more than 30 years that have been spent on narrowband channels. A main gap in our knowledge is the parameterization of the models in different environments. Up to now, almost all measurements have been performed in indoor office and residential environments. Those measurements give a first indication of occurring parameters, though important questions (angular dispersion, what is the best distribution to describe fading statistics?, how do the results depend on the measurement bandwidth and center frequency?) need more thorough investigation. Parametrization for other environments, like factory halls, disaster areas, and so forth, are completely unknown, and many measurements will be required to obtain statistically reliable parametrizations. It is thus safe to say that the understanding of UWB channels has made some important advances, but much more work is required before we can claim to have a thorough understanding of this important communications medium.

2.2. Measurement techniques

2.2.1. Introduction

In this section, we will give a review of the measurement techniques that can be used to characterize UWB radio channels and discuss some of their properties. We give analytical expressions for the transfer functions of some elementary UWB radio channels. A particular problem for UWB measurements is the removal of antenna influences from radio channel measurements (de-embedding), which needs to account for specific UWB properties of antennas. For that purpose, characteristic functions are defined that describe the UWB transmission and reception properties of an antenna. A general relationship that exists for these functions is derived, to finally arrive at a formulation of the de-embedding problem suited for ultra-wide bandwidths.

What is a radio channel, in the first place? In this section, we will consider any arrangement of two or more antennas, of which at least two are coupled by far field radiation, a radio channel. If the total number of connectors of all antennas is N, the corresponding radio channel can be viewed simply as an N-port. This definition covers the cases of SISO, SIMO, and MIMO channels. This definition also includes the antennas into the channel, and consequently changing the antenna characteristic may change the properties of the channel as well. Therefore, a radio channel can be viewed as the result of combining "antennas and propagation."

The inclusion of antennas into the radio channel definition follows practical considerations regarding system design to some extent: all radio systems (including those for measuring radio channels) need to use some form of antenna, and in many cases the intended application imposes constraints on the antennas that can be used for a particular system—for example, handset antenna designers have to cope with strong restrictions related to the form factor of the handset.

This poses the problem that results obtained for a particular radio channel using a certain measurement setup in the strict sense only apply to channels incorporating the antennas used during that measurement. To use such results for systems with different antennas, some further steps are required. Consequently, it is frequently required to consider a channel concept that is independent of the employed antennas. We will refer to this type of channel as a "propagation channel"; its ports are not related to feed lines of antennas, rather they are directly related to the propagating fields.

Deriving propagation channel characteristics from measured radio channel data is a de-embedding problem which in principle can be solved if sufficient measurement data and a complete characterization of the antennas are available. However, in many cases the effort to obtain such a complete characterization is too high; that is, the effects of changing antennas cannot be easily assessed. In this case, some approaches are in common use. The most obvious way is to use the antennas of the target system for measurements—such *in vivo* measurements save the need for recalibration due to different antennas. Unfortunately, for various reasons, such measurements are often not possible.

Another approach employs antennas that are "neutral" in the sense that radio channel measurements with these antennas do not disturb the characteristics of the underlying propagation channel significantly—so these may be recovered easily. Isotropic antennas would make a good choice for this type of measurement; however, isotropic antennas exist only as a theoretical device. A frequent compromise is the use of omnidirectional antennas. Using this type of antenna at the transmitter, for example, allows to determine "unbiased" azimuth-power spectra at the receiver in the horizontal plane.

All of the above considerations are not specific to UWB radio channel measurements. However, what is specific to UWB conditions is the particular significance of frequency dependence. While it is often feasible to assume the radiation pattern to be constant over the band for (non-ultra-) wideband systems (e.g., WCDMA with a fractional bandwidth of approximately 1/400), the frequency dependence of antennas must not be neglected in UWB applications. Furthermore, the UWB radio channel may exhibit certain frequency dependencies even for "frequency-independent" antennas, which is due to the fact that an antenna cannot be frequency-independent in both transmission and reception; which in turn is caused by constraints imposed by reciprocity. Before we look into this and the implications of these frequency dependencies for the formulation of the de-embedding problem, we first give a short review of some basic measurement approaches that can be used for UWB radio channel measurements.

2.2.2. Basic measurement approaches

An important assumption for the characterization of mobile radio channels is linearity. An exhaustive treatment of time-variant linear systems has been given by Bello [12, 13] in terms of various system and correlation functions that are related by Fourier transforms. The basic measurement approaches can be directly related to several of these system functions. For example, following [12], the response $w(t)$ of a time-variant linear system to a stimulus $z(t)$ can be written as

$$w(t) = \int z(t-\xi)g(t,\xi)d\xi = \int z(t-\xi)h(t-\xi,\xi)d\xi, \tag{2.1}$$

where $g(t,\xi)$ and $h(t,\xi)$ are the input delay-spread function and output delay-spread function, respectively. Using an input signal that is localized in time, for example, an impulse $z(t) = \delta(t-t_0)$, the output signal $w(t) = g(t,t-t_0) = h(t_0,t-t_0)$ is directly related to these system functions. Occasionally, this type of measurement is referred to as a "time-domain" measurement. A common measurement setup consists of an impulse transmitter and a digital sampling oscilloscope (DSO) as receiver. This technique is intuitively appealing as a UWB measurement technique due to its conceptual simplicity in dealing with time-variant UWB channels. The downside of this approach, however, is that calibration of such a measurement setup requires additional effort that much affects its simplicity. Furthermore, care has to be applied in considering possible rms averaging of oversampled signals

performed inside the DSO, as this may affect the amplitude statistics of the signal finally delivered by the DSO.

In a similar fashion, for an input signal $Z(f)$ that is localized in frequency domain, for example, $Z(f) = \delta(f - f_0)$,[3] the input-output relationships

$$W(f) = \int Z(f - \nu)H(f, \nu)d\nu = \int Z(f - \nu)G(f - \nu, \nu)d\nu \tag{2.2}$$

allow to determine $W(f) = H(f, f - f_0) = G(f_0, f - f_0)$, where H and G are the input Doppler-spread function and output Doppler-spread function. These equations are useful for channels that are discrete in Doppler domain, that is, channels with quasiperiodic time variance, with only a few fundamental Doppler frequencies. For example, consider a single ray that passes through a fluorescent tube: the oscillating plasma inside the tube introduces a Doppler shift of multiples of twice the local power line frequency. Using a tunable CW source as transmitter and a DSO as receiver, the Doppler behavior of this type of channel can be accurately characterized over ultra-widebands.

The time-variant transfer function

$$T(f, t) = \int g(t, \xi) \exp(-j2\pi f\xi)d\xi \tag{2.3}$$

and the associated input-output relationship

$$w(t) = \int Z(f)T(f, t) \exp(j2\pi ft)df \tag{2.4}$$

are useful for "frequency-domain" measurements. For $Z(f) = \delta(f - f_0)$, we have

$$w(t) = T(f_0, t) \exp(j2\pi f_0 t), \tag{2.5}$$

and for slowly time-varying channels, that is,

$$T(f, t) \approx T(f, t_0) \quad \text{for } |t - t_0| < \frac{1}{f_0}, \tag{2.6}$$

we get

$$w(t) \approx T(f_0, t_0) \exp(j2\pi f_0 t), \tag{2.7}$$

[3]Note that to obtain a real signal $z(t) \in \mathbb{R}$, $Z(f)$ has to exhibit complex conjugate symmetry with respect to the origin; for example, $Z(f) = \delta(f + f_0) + \delta(f - f_0)$.

leading to[4]

$$W(f) \approx T(f_0, t_0)\delta(f - f_0) = T(f_0, t_0)Z(f). \tag{2.8}$$

Equation (2.8) is the quasistatic equation underlying vector network analyzer (VNA) measurements (of S_{21} for a two-port radio channel). While this technique has the major advantage that calibrated measurements of even ultra-wide bandwidths are more easily performed, this method has the serious drawback of being applicable only to quasistatic channels. At first glance, condition (2.6) seems to be not too restrictive; however, for traditional VNA architectures that employ IF filtering, f_0 has to be replaced by the IF bandwidth which will result in much stronger constraints for the permissible time variance of the channel. Furthermore, the channel must not change during a sweep over the entire band. For example, with an IF bandwidth of 300 Hz and $N = 1601$ frequency points, sweep times in the order of several seconds result. A further constraint for the maximum sweep rate is related to the delay introduced by the channel. Note that even for time-invariant channels ($T(f, t) = T(f)$) and under ideal noise-free conditions, (2.8) is only an approximation due to the finite-time interval T_M available to obtain a transfer ratio for a frequency point. For continually swept measurements, the finite sweep rate df/dt will contribute another error caused by changing the stimulus frequency during the measurement of a frequency point, thus resulting in $T(f)$ effectively getting averaged over $\Delta f \approx T_M df/dt$.

Both time-domain and frequency-domain measurements are subject to errors caused by narrowband interference. Another measurement technique that is more robust against narrowband interference employs factorizing of a signal $z(t)$ into a correlation product $z(t) = q(\tau) \otimes_{\tau,t} q(\tau) \triangleq \int q(\tau)q(\tau + t)d\tau$, where $\otimes_{\tau,t}$ denotes the correlation operator. Assume that q has the finite support $[-T/2, T/2]$.[5] For an input signal centered around t_0, $z(t - t_0)$, (2.1) can be rewritten as

$$\omega(t) = \int q(\tau) \int q(\tau + t - t_0 - \xi)g(t, \xi)d\xi\, d\tau. \tag{2.9}$$

Due to the assumed support of q, the inner integral can be nonzero only for $|t - t_0 - \xi| \le T$. Then, if $g(t, \xi)$ is slowly time-varying such that $g(t, \xi) \approx g(t_0, \xi)$ for $|t - t_0 - \xi| \le T$,

$$\begin{aligned} w(t) &\approx \int q(\tau) \int q(\tau + t - t_0 - \xi)g(t_0, \xi)d\xi\, d\tau \\ &= \int q(\tau - t) \underbrace{\int q(\tau - t_0 - \xi)g(t_0, \xi)d\xi}_{\triangleq p(\tau, t_0)}\, d\tau \qquad (2.10) \\ &= q(\tau) \bigotimes_{\tau,t} p(\tau, t_0), \qquad (2.11) \end{aligned}$$

[4]Assuming that an estimate of $W(f)$ can be determined from (2.7) during a reasonably short interval of time such that the approximation (2.6) holds.

[5]Then the support of z is a subset of $[-T, T]$, that is, z is localized around $t = 0$.

where $p(\tau, t_0)$ is the response of the channel to the shifted correlation factor $q(\tau - t_0)$. Equation (2.11) states that the channel response $w(t)$ to the input signal $z(t - t_0)$ can approximately be determined by transmitting the shifted correlation factor $q(\tau - t_0)$ instead of $z(t - t_0)$ and then performing a correlation of the channel response with the correlation factor $q(\tau)$.

The correlation method has two major advantages. First, due to the correlation at the output of the channel, interfering signals can be suppressed to some extent. Second, instead of using an impulse excitation (like it is the case for "time-domain" measurements), by proper selection of the correlation factor q, it is possible to significantly reduce the crest factor[6] of the transmitted signal. This can considerably relax the linearity requirements for the measurement setup (in particular, power amplifiers). Commonly used signals are, for example, chirps and PN-sequences.

A drawback of the correlation method, however, is that the correlation factors can be much less localized than the original signal. Therefore, the maximum achievable measurement rate is reduced, and the amount of permissible time variance is even lower.

2.2.3. The de-embedding problem

To assess the de-embedding problem associated with the transition from a radio channel to a propagation channel more specifically, what is needed in the first place is a clear definition of the propagation channel and its relation to the radio channel. Unlike the radio channel, where, for example, the antenna connectors provide convenient ports, no such obvious choice is available for the propagation channel a priori. In this section, we approach the problem by giving a simple analytical expression for the transfer function of the UWB multipath radio channel that provides a natural separation of antenna and propagation terms. A particular aspect which is of paramount importance for UWB channels is that both antenna and propagation terms have to include phases in order to preserve coherence over the entire band.

We start by introducing a generic antenna model by defining two complex characteristic functions $\mathbf{A}$ and $\mathbf{h}$ that describe the spatiotemporal transmission and reception characteristic of an antenna.[7] As will become clear below, these functions are closely related to the familiar concepts of radiation pattern and effective length.

2.2.3.1. Antenna model

The antenna definition used here comprises two elements: (a) a material distribution $\varepsilon(\mathbf{r}, \omega)$, $\mu(\mathbf{r}, \omega)$ which differs from free space only within a finite volume; (b) a port defined by a reference plane R on a waveguide (the antenna feed line). One part of the feed line up to the reference plane is considered part of the antenna. In

[6] Ratio of peak-to-average power.

[7] In the remainder of this section, a bold typeface will be used to denote vectors; a caret $\hat{}$ on top of a vector denotes a unit vector: $\hat{\mathbf{r}} \triangleq \mathbf{r}/\|\mathbf{r}\|$.

the vicinity of the reference plane, the feed line is considered to be uniform such that at the reference plane power wave amplitudes a and b (corresponding to waves approaching and leaving the antenna, resp.) may be defined by

$$\begin{aligned}\mathbf{E}_{\tan} &= \sum_n \sqrt{Z_n}\underline{\mathbf{e}}_n(x,y)\left[a_n e^{-jk_n z} + b_n e^{+jk_n z}\right],\\ \mathbf{H}_{\tan} &= \sum_n \sqrt{Y_n}\underline{\mathbf{h}}_n(x,y)\left[a_n e^{-jk_n z} - b_n e^{+jk_n z}\right],\end{aligned} \tag{2.12}$$

where $\underline{\mathbf{e}}_n$, $\underline{\mathbf{h}}_n$, and $Z_n = 1/Y_n \in \mathbb{R}$ are the normalized electric and magnetic fields tangential to the reference plane and feed-line impedance for mode n, with $\underline{\mathbf{h}}_n = \hat{\mathbf{z}} \times \underline{\mathbf{e}}_n$ and normalization such that $\int \underline{\mathbf{e}}_n \underline{\mathbf{e}}_m = \delta_{m,n}$, where the integration extends over the cross-section of the feed-line. The positive z-direction points towards the antenna and $z = 0$ on R. In the following, a single mode n is considered and for simplicity the index n is dropped. If necessary, corresponding results for several modes may be superimposed, as the modes on the considered feed-line are orthogonal.

At the reference plane, the antenna acts as a source according to $b = b^i + \Gamma a$ with the source strength b^i evoked by an incident field and the output reflection coefficient Γ due to the antenna input impedance Z_A, which in general is different from the feed-line impedance Z; a is the wave amplitude (at the reference plane) of the input signal used to excite transmission.

When transmitting, the electric field at a point $\mathbf{r}_2$ in the far-field of the transmitting antenna located at $\mathbf{r}_1$, excited at its port by a wave a, may be given as

$$\mathbf{E}_1(\mathbf{r}_2,\omega) = \sqrt{Z_0}\frac{e^{-jk_0 r_{12}}}{\sqrt{4\pi} r_{12}}\mathbf{A}(\hat{\mathbf{r}}_{12},\omega)a(\omega). \tag{2.13}$$

Equation (2.13) defines the *spatiotemporal transmit characteristic* $\mathbf{A}(\hat{\mathbf{r}}_{12},\omega)$ as function of the transmission direction $\hat{\mathbf{r}}_{12} = (\mathbf{r}_2 - \mathbf{r}_1)/\|\mathbf{r}_2 - \mathbf{r}_1\|$ (direction of departure) and the angular frequency ω; Z_0 is the free-space impedance. The dependence of $\mathbf{A}(\hat{\mathbf{r}}_{12},\omega)$ on $\hat{\mathbf{r}}_{12}$ is related to the radiation pattern and the dependence on ω describes the (temporal) filter characteristics of the transmitting antenna. Under far-field conditions, $\mathbf{A}(\hat{\mathbf{r}}_{12},\omega)\perp\hat{\mathbf{r}}_{12}$. Note that the normalization factor $(\sqrt{Z_0/4\pi})$ may be chosen arbitrarily because (2.13) is a definition (for $\mathbf{A}$).

The power flux density S corresponding to the electric field of (2.13) is given by[8]

$$S(\mathbf{r}_2) = \frac{\left|\left|\mathbf{E}_1(\mathbf{r}_2)\right|\right|^2}{Z_0} = \frac{\left|\left|\mathbf{A}(\hat{\mathbf{r}}_{12})\right|\right|^2 |a|^2}{4\pi r_{12}^2.} \tag{2.14}$$

[8]Using rms phasors.

From the power $|a|^2$ approaching the antenna, only the amount

$$P_t = |a|^2(1 - |\Gamma|^2) \tag{2.15}$$

actually enters the antenna. Isotropic radiation of P_t would produce a power flux density which on comparison with (2.14) gives the relation between **A** and the gain over an isotropic antenna as

$$G_{\text{iso}}(\hat{\mathbf{r}}_{12}, \omega) = \frac{||\mathbf{A}(\hat{\mathbf{r}}_{12}, \omega)||^2}{1 - |\Gamma(\omega)|^2}. \tag{2.16}$$

For the case of a receiving antenna at position $\mathbf{r}_1$, let

$$\mathbf{E}^i(\mathbf{r}, \hat{\mathbf{k}}, \omega) \triangleq \mathbf{E}^i(\hat{\mathbf{k}}, \omega) \exp(-jk_0\hat{\mathbf{k}}\mathbf{r}) \tag{2.17}$$

be the electric field at position **r** of an incident plane wave travelling into direction $\hat{\mathbf{k}}$, where $k_0 = \omega/c_0$ is the free-space wave number for angular frequency ω. The corresponding source strength of the receiving antenna b^i may be given as

$$b^i(\omega) = \sqrt{4\pi}\mathbf{h}(\hat{\mathbf{k}}, \omega)\frac{\mathbf{E}^i(\mathbf{r}_1, \hat{\mathbf{k}}, \omega)}{\sqrt{Z_0}}. \tag{2.18}$$

Equation (2.18) defines the *spatiotemporal receive characteristic* $\mathbf{h}(\hat{\mathbf{k}}, \omega)$ of the antenna under far-field (incident locally plane wave) conditions as function of the propagation direction $\hat{\mathbf{k}}$ of the incident field (direction of arrival[9]) and the angular frequency ω. Because $\mathbf{E}(\mathbf{r}, \hat{\mathbf{k}}, \omega) \perp \hat{\mathbf{k}}$ for plane waves, we additionally require $\mathbf{h}(\hat{\mathbf{k}}, \omega) \perp \hat{\mathbf{k}}$ to obtain a unique definition of **h**. It should be noted that **h** is defined with respect to the incident field, that is, the field without the field scattered at the antenna. Because **h** linearly maps the electric field strength to the source strength b^i, **h** acts like an effective length operator.[10]

The definitions (2.13) and (2.18) of the characteristic functions involve "nominal" antenna positions **r**. For a given physical antenna, there is some degree of arbitrariness regarding the relation of the nominal antenna position **r** and the actual material distribution that constitutes the antenna. Moving the nominal antenna position with respect to the antenna body will introduce a corresponding change in **A** and **h**.

[9]Note that by direction of arrival we designate the direction into which the arriving wave propagates.

[10]Some more relations of **A** and **h** to commonly used antenna parameters are given in Appendix 2.2.B.

2.2.3.2. Transmit and receive characteristic relation

Using the reciprocity principle, it can be shown that the transmit and receive characteristics are related by (cf. Appendix 2.2.A)

$$2j\omega\mathbf{h}(-\hat{\mathbf{k}},\omega) = c_0\mathbf{A}(\hat{\mathbf{k}},\omega), \tag{2.19}$$

where $c_0 = 1/\sqrt{\varepsilon_0\mu_0}$. Note the minus sign in front of $\hat{\mathbf{k}}$ in the left-hand side of (2.19) which is due to the definition of $\mathbf{h}$ with respect to directions of arrival, while $\mathbf{A}$ is defined with respect to directions of departure.

If (2.19) holds for all ω, the corresponding time-domain expression[11]

$$2\frac{\partial}{\partial t}\tilde{\mathbf{h}}(-\hat{\mathbf{k}},t) = c_0\tilde{\mathbf{A}}(\hat{\mathbf{k}},t) \tag{2.20}$$

illustrates the well-known temporal derivative relationship between transmit and receive impulse responses [14–21]. From (2.19) we immediately get the even better-known property that, for a given frequency, the (spatial) transmission and reception patterns are equal:

$$\frac{\mathbf{h}(-\hat{\mathbf{k}},\omega)}{\max_{\hat{\mathbf{k}}}||\mathbf{h}(-\hat{\mathbf{k}},\omega)||} = \frac{\mathbf{A}(\hat{\mathbf{k}},\omega)}{\max_{\hat{\mathbf{k}}}||\mathbf{A}(\hat{\mathbf{k}},\omega)||}. \tag{2.21}$$

A commonly encountered assumption is that UWB antennas, on transmission, differentiate the input signal. Note, however, that (2.20) only supports the statement that the impulse responses in transmission and reception are related by a temporal derivative, without further constraint regarding their particular form (cf. Appendix 2.2.C).

2.2.3.3. The ideal free-space far-field UWB radio channel

In this section, we proceed by giving expressions for the transfer function of the most simple UWB radio channel, that is, the ideal free-space far-field UWB radio channel made up by two antennas in free space and mutually in far field. Single scattering is assumed, that is, contributions that bounce back and forth between the two antennas are neglected.

For two antennas (designated by indices 1 and 2), and under the above given assumptions the transfer function

$$S_{21}(\omega) = \frac{b_2}{a_1}\bigg|_{a_2=0} = \frac{b_2^i}{a_1} \tag{2.22}$$

[11] We use $\sim$ to denote time-dependent quantities.

of the corresponding ideal free-space far-field UEB radio channel may be given in various forms by combining (2.13), (2.18), and (2.19) as

$$S_{21}(\omega) = \mathbf{A}_1(\hat{\mathbf{r}}_{12},\omega)\mathbf{h}_2(\hat{\mathbf{r}}_{12},\omega)\frac{e^{-jk_0r_{12}}}{r_{12}} \tag{2.23}$$

$$= \mathbf{h}_1(\hat{\mathbf{r}}_{21},\omega)\mathbf{A}_2(\hat{\mathbf{r}}_{21},\omega)\frac{e^{-jk_0r_{12}}}{r_{12}} \tag{2.24}$$

$$= \frac{1}{j\omega}\frac{c_0}{2}\mathbf{A}_1(\hat{\mathbf{r}}_{12},\omega)\mathbf{A}_2(\hat{\mathbf{r}}_{21},\omega)\frac{e^{-jk_0r_{12}}}{r_{12}} \tag{2.25}$$

$$= j\omega\frac{2}{c_0}\mathbf{h}_1(\hat{\mathbf{r}}_{21},\omega)\mathbf{h}_2(\hat{\mathbf{r}}_{12},\omega)\frac{e^{-jk_0r_{12}}}{r_{12}}. \tag{2.26}$$

It is important to stress that the various vectors in this equation refer to the same reference frame. In particular, if the orientation of an antenna changes with respect to that frame, the corresponding **A** and **h** will change. In the likely case that **A** and **h** are given with respect to an antenna fixed frame, the orientation of the antenna has to be accounted for by a proper transformation of **A** and **h**.

The above equation already has the desired form: the propagation aspects (delay, attenuation) are described by the $\exp(-jk_0r_{12})/r_{12}$ term while the other terms (including $2j\omega/c_0$ factors) are related to the antennas.

In particular, (2.25) illustrates the fact that for ideal "impulse radiating" antennas (where **A** is not a function of ω, cf. (2.13)) on both ends, already the most fundamental UWB channel exhibits a $1/\omega$ frequency dependency, while for "impulse receiving" antennas (where **h** is not a function of ω, cf. (2.18)) on both ends, a ω frequency trend is imposed. In all cases, this behavior is due to the reciprocity relation (2.19). While for (non-ultra-) wideband conditions the influence of these ω dependencies is small and may even be neglected (consider again the WCDMA case with a fractional bandwidth of $\approx$ 1/400), this is not the case for the UWB channel. The presence of these particular frequency trends can be considered an essential property of the UWB channel.

2.2.3.4. Extension to multipath conditions

If the transmission via a given path involves some intermediate interaction with the environment, the transfer function of that path may be modified to

$$S_{21}(\omega,\mathbf{r}_1,\mathbf{r}_2,\hat{\mathbf{k}}_D,\hat{\mathbf{k}}_A) = \mathbf{A}_1(\hat{\mathbf{k}}_D,\omega)\mathbf{h}_2(\hat{\mathbf{k}}_A,\omega)G(\omega,\mathbf{r}_1,\mathbf{r}_2,\hat{\mathbf{k}}_D,\hat{\mathbf{k}}_A), \tag{2.27}$$

where $\hat{\mathbf{k}}_D$ and $\hat{\mathbf{k}}_A$ are the directions of departure and arrival, respectively. The function

$$G(\omega,\mathbf{r}_1,\mathbf{r}_2,\hat{\mathbf{k}}_D,\hat{\mathbf{k}}_A) \tag{2.28}$$

is analogous to a scalar Green's function and describes the propagation channel for reception at $\mathbf{r}_2$ (from direction $\hat{\mathbf{k}}_A$) when transmitting into direction $\hat{\mathbf{k}}_D$

at $\mathbf{r}_1$. For example, for the ideal free-space far-field channel, there is a nonzero $G(\omega, \mathbf{r}_1, \mathbf{r}_2, \hat{\mathbf{k}}_D, \hat{\mathbf{k}}_A) = \exp(-jk_0 r_{12})/r_{12}$ only for $\hat{\mathbf{k}}_D = \hat{\mathbf{k}}_A = \hat{\mathbf{r}}_{12}$; and for a path containing an ideal specular reflection, $G(\omega, \mathbf{r}_1, \mathbf{r}_2, \hat{\mathbf{k}}_D, \hat{\mathbf{k}}_A) = \exp(-jk_0 r)/r$ is nonzero if $\hat{\mathbf{k}}_D$ and $\hat{\mathbf{k}}_A$ are the directions to and from the mirror point, and r is the total path length.

Summing over all paths, and designating the lth path with a superscript l, a general expression for the ideal UWB multipath channel transfer function is

$$S_{21}(\omega, \vec{r}_1, \vec{r}_2) = \sum_l \mathbf{A}_1\left(\hat{\mathbf{k}}_D^l, \omega\right)\mathbf{h}_2\left(\hat{\mathbf{k}}_A^l, \omega\right) G\left(\omega, \mathbf{r}_1, \mathbf{r}_2, \hat{\mathbf{k}}_D^l, \hat{\mathbf{k}}_A^l\right). \tag{2.29}$$

Like (2.23)–(2.26), both (2.27) and (2.29) can be cast into various forms.

Equation (2.29) describes a multipath channel with a discrete spectrum of paths. In general, however, a continuum of paths may exist and the summation has to be replaced by an integration.

We will refer to G as the propagation channel transfer function. The above discussion suggests to specify the "ports" of the (far-field) propagation channel by pairs $(\mathbf{r}, \hat{\mathbf{k}})$ of a position and a direction, and assuming locally plane waves. As there is potentially an infinite number of paths between two given antenna positions $\mathbf{r}_1$ and $\mathbf{r}_2$, even a SISO radio channel corresponds to a propagation channel with a potentially infinite number of ports.

For a MIMO channel with M transmit antennas at positions $\mathbf{r}_1^m$, $m = 1 \ldots M$, and N receive antennas at positions $\mathbf{r}_2^n$, $n = 1 \ldots N$, the elements of the MIMO radio channel transfer matrix are obtained from (2.29) by replacing $\mathbf{r}_1$, $\mathbf{r}_2$, $\mathbf{A}_1$, and $\mathbf{h}_2$ by $\mathbf{r}_1^m$, $\mathbf{r}_2^n$, $\mathbf{A}_1^m$, and $\mathbf{h}_2^n$, respectively. Depending on whether antennas are co-located or not, the directions of departure and arrival may have to be adapted as well.

2.2.3.5. Formulation of the de-embedding problem

The de-embedding problem can now be posed as the problem of determination of G from S_{21}, that is, solving (2.29) for G. The algebraic structure of (2.29) is similar to that of a quadratic form; we may write (2.29) as

$$S_{21}(\omega, \vec{r}_1, \vec{r}_2) = \left(\mathbf{h}_2\left(\hat{\mathbf{k}}_A^1, \omega\right), \mathbf{h}_2\left(\hat{\mathbf{k}}_A^2, \omega\right), \ldots, \mathbf{h}_2\left(\hat{\mathbf{k}}_A^M, \omega\right)\right)\underline{G}\begin{pmatrix} \mathbf{A}_1\left(\hat{\mathbf{k}}_D^1, \omega\right) \\ \mathbf{A}_1\left(\hat{\mathbf{k}}_D^2, \omega\right) \\ \cdots \\ \mathbf{A}_1\left(\hat{\mathbf{k}}_D^M, \omega\right) \end{pmatrix} \tag{2.30}$$

with $\underline{G} = \mathrm{diag}(\ldots, G(\omega, \mathbf{r}_1, \mathbf{r}_2, \hat{\mathbf{k}}_D^l, \hat{\mathbf{k}}_A^l), \ldots)$.[12] It is obvious that a single measurement of S_{21} is not sufficient to determine G.

[12] A more general form that includes path splitting (the phenomenon that a single direction of departure results in several directions of arrival, or vice versa) results in a nondiagonal $\underline{G}$.

A straightforward way is the use of double-directional measurements (cf. [22]), which essentially means that individual path transfer functions $S_{21}(\omega, \mathbf{r}_1, \mathbf{r}_2, \hat{\mathbf{k}}_D, \hat{\mathbf{k}}_A)$ of (2.27) are measured or estimated, from which $G(\omega, \mathbf{r}_1, \mathbf{r}_2, \hat{\mathbf{k}}_D^l, \hat{\mathbf{k}}_A^l)$ can be determined easily.

2.2.4. Summary

In this section, we have discussed some basic channel measurement techniques. Furthermore, the relation between radio channels, which include antennas, and propagation channels, which do not, has been given in terms of characteristic functions that describe the UWB spatiotemporal transmission and reception properties of antennas. Both transmit and receive characteristics are related due to the reciprocity principle. While the familiar fact that the spatial aspects of an antenna are the same for transmission and reception still holds under UWB conditions, this is not the case for the temporal behavior. In particular, the temporal filter responses in transmission and reception are related by a temporal derivative operator. It is essential to take this into account—for example, when de-embedding the propagation channel from radio channel measurements.

Appendices

2.2.A. Derivation of transmit-receive relation

If two solutions $(\mathbf{E}_a, \mathbf{H}_a, \mathbf{J}_a, \mathbf{K}_a)$ and $(\mathbf{E}_b, \mathbf{H}_b, \mathbf{J}_b, \mathbf{K}_b)$ of Maxwell's curl equations

$$\begin{aligned} \nabla \times \mathbf{E} + j\omega\mu\mathbf{H} &= -\mathbf{K}, \\ -\nabla \times \mathbf{H} + j\omega\varepsilon\mathbf{E} &= -\mathbf{J} \end{aligned} \tag{2.31}$$

pertain to the same material distribution within a volume V (and possibly different materials outside), then these solutions are subject to the Lorentz reciprocity constraint [18]

$$\oint_{\partial V} (\mathbf{E}_a \times \mathbf{H}_b - \mathbf{E}_b \times \mathbf{H}_a)\hat{\mathbf{n}} = \int_V (\mathbf{J}_a\mathbf{E}_b - \mathbf{K}_a\mathbf{H}_b) - (\mathbf{J}_b\mathbf{E}_a - \mathbf{K}_b\mathbf{H}_a). \tag{2.32}$$

Two such solutions are constructed as follows.

Solution (a). We consider an antenna at position $\mathbf{r}_1$ embedded in free space. In the reference plane R of the antenna port, electric and magnetic surface current densities

$$\begin{aligned} \mathbf{J}_A &= \hat{\mathbf{z}} \times \underline{\mathbf{h}}_n \sqrt{Y_n} a_n, \\ \mathbf{K}_A &= \underline{\mathbf{e}}_n \times \hat{\mathbf{z}} \sqrt{Z_n} a_n \end{aligned} \tag{2.33}$$

are impressed to excite the field of mode n travelling into the antenna with amplitude a. $\hat{\mathbf{z}}$ is normal to R and points towards the antenna. Due to this source

arrangement, no fields are excited on the field line on the other side of the reference plane. Effectively, these surface current densities constitute an ideal wave source for mode n of amplitude a connected to the input port of the antenna. The field at a point $\mathbf{r}_2$ is then given by (2.13).

Solution (b). No current densities are impressed at the antenna port. An elementary electric dipole, that is, an electric current density

$$\mathbf{J}_2 = I_2 l \delta^3(\mathbf{r} - \mathbf{r}_2)\hat{\mathbf{v}} \tag{2.34}$$

is impressed at position $\mathbf{r}_2$ (the same as for solution (a)) in the *presence* of the antenna at $\mathbf{r}_1$, leading to a total field

$$\mathbf{E}_2(\mathbf{r}) = \mathbf{E}_2^i(\mathbf{r}, \hat{\mathbf{r}}_{21}) + \mathbf{E}_2^s(\mathbf{r}, \hat{\mathbf{r}}_{21}, \mathbf{E}_2^i), \tag{2.35}$$

where $\mathbf{E}_2^s(\mathbf{r}, \hat{\mathbf{r}}_{21}, \mathbf{E}_2^i)$ is the field scattered at the antenna.

The result (2.19) is obtained by inserting the above constructed solutions into the reciprocity relation (2.32), letting $V \to \mathbb{R}^3$, assuming vanishing fields at infinity, and considering that according to the definition of $\mathbf{h}$ in (2.18) the antenna source strength b^i depends only on the *incident* field, that is, the field the elementary electric dipole would produce in *absence* of the antenna,

$$\mathbf{E}_2^i(\mathbf{r}_1, \hat{\mathbf{r}}_{21}) = -j\omega\mu_0 \frac{\exp(-jk_0 r_{21})}{4\pi r_{21}} I_2 l(\hat{\mathbf{v}} - \hat{\mathbf{r}}_{21}(\hat{\mathbf{r}}_{21}\hat{\mathbf{v}})), \tag{2.36}$$

and furthermore considering that the orientation $\hat{\mathbf{v}}$ of the elementary dipole can be chosen arbitrarily.

For $V \to \mathbb{R}^3$, (2.32) gives

$$\int (\mathbf{J}_a \mathbf{E}_b - \mathbf{K}_a \mathbf{H}_b) = \int (\mathbf{J}_b \mathbf{E}_a - \mathbf{K}_b \mathbf{H}_a). \tag{2.37}$$

For the left-hand side, we have

$$\begin{aligned}
&\int (\mathbf{J}_a \mathbf{E}_b - \mathbf{K}_a \mathbf{H}_b) \\
&\quad = \int_R (\mathbf{J}_A \mathbf{E}_b - \mathbf{K}_A \mathbf{H}_b) = a_n \int_R ((\hat{\mathbf{z}} \times \underline{\mathbf{h}}_n \sqrt{Y_n})\mathbf{E}_b - (\underline{\mathbf{e}}_n \times \hat{\mathbf{z}}\sqrt{Z_n})\mathbf{H}_b) \\
&\quad = a_n \int_R (-\sqrt{Y_n}\underline{\mathbf{e}}_n \mathbf{E}_b + \sqrt{Z_n}\underline{\mathbf{h}}_n \mathbf{H}_b) \\
&\quad = -2a_n b_n = -2a_n \sqrt{4\pi}\mathbf{h}(\hat{\mathbf{r}}_{21}) \frac{\mathbf{E}_2^i(\mathbf{r}_1, \hat{\mathbf{r}}_{21})}{\sqrt{Z_0}} \\
&\quad = 2a_n \sqrt{4\pi} j\omega\mu_0 \frac{e^{-jk_0 r_{21}}}{4\pi r_{21}} I_2 l \mathbf{h}(\hat{\mathbf{r}}_{21}) \frac{(\hat{\mathbf{v}} - \hat{\mathbf{r}}_{21}(\hat{\mathbf{r}}_{21}\hat{\mathbf{z}}))}{\sqrt{Z_0}} \\
&\quad = 2a_n \sqrt{4\pi} j\omega\mu_0 \frac{e^{-jk_0 r_{21}}}{4\pi r_{21}} I_2 l \mathbf{h}(\hat{\mathbf{r}}_{21}) \frac{\hat{\mathbf{v}}}{\sqrt{Z_0}}.
\end{aligned} \tag{2.38}$$

For the right-hand side, we have

$$\begin{aligned}\int (\mathbf{J}_b\mathbf{E}_a - \mathbf{K}_b\mathbf{H}_a) &= \int \mathbf{J}_2\mathbf{E}_1 = \int I_2 l\delta^3(\mathbf{r}-\mathbf{r}_2)\hat{\mathbf{v}}\sqrt{Z_0}\frac{\mathrm{e}^{-jk_0r_{12}}}{\sqrt{4\pi}r_{12}}\mathbf{A}(\hat{\mathbf{r}}_{12})a_n \\ &= I_2 l\sqrt{Z_0}\frac{\mathrm{e}^{-jk_0r_{12}}}{\sqrt{4\pi}r_{12}}a_n\hat{\mathbf{v}}\mathbf{A}(\hat{\mathbf{r}}_{12}).\end{aligned} \tag{2.39}$$

Combining both sides gives

$$2a_n(\omega)\sqrt{4\pi}j\omega\mu_0\frac{\mathrm{e}^{-jk_0r_{21}}}{4\pi r_{21}}I_2 l\mathbf{h}(\hat{\mathbf{r}}_{21},\omega)\frac{\hat{\mathbf{v}}}{\sqrt{Z_0}} = I_2 l\sqrt{Z_0}\frac{\mathrm{e}^{-jk_0r_{12}}}{\sqrt{4\pi}r_{12}}a_n(\omega)\hat{\mathbf{v}}\mathbf{A}(\hat{\mathbf{r}}_{12},\omega), \tag{2.40}$$

and after cancelling terms

$$2j\omega\mu_0\mathbf{h}(\hat{\mathbf{r}}_{21},\omega)\hat{\mathbf{v}} = Z_0\hat{\mathbf{v}}\mathbf{A}(\hat{\mathbf{r}}_{12},\omega). \tag{2.41}$$

This equation is valid for arbitrary $\hat{\mathbf{v}}$. Therefore, with $\hat{\mathbf{k}} \triangleq \hat{\mathbf{r}}_{12} = -\hat{\mathbf{r}}_{21}$, $r_{12} = r_{21}$, $Z_0 = \sqrt{\mu_0/\varepsilon_0}$, and $c_0 = 1/\sqrt{\varepsilon_0\mu_0}$, we get

$$2j\omega\mathbf{h}(-\hat{\mathbf{k}},\omega) = c_0\mathbf{A}(\hat{\mathbf{k}},\omega). \tag{2.42}$$

2.2.B. Relation to standard antenna parameters

In this section, we give a few common antenna parameters in terms of the transmit and receive characteristic functions **A** and **h**.

The power available from the receiving antenna is given by

$$P_{\mathrm{av}} = \frac{|b^i|^2}{1-|\Gamma|^2} = \frac{4\pi\|\mathbf{h}(\hat{\mathbf{k}})\|^2}{1-|\Gamma|^2}\frac{\|\mathbf{E}^i(\mathbf{r}_1,\hat{\mathbf{k}})\|^2}{Z_0}, \tag{2.43}$$

where matching polarization states are assumed. Hence, the well-known relation between the effective aperture (for reception of a plane wave incident from direction $\hat{\mathbf{k}}$) and the gain over an isotropic antenna (for radiation into direction $-\hat{\mathbf{k}}$) follows as (using (2.16) and (2.19))

$$A_{\mathrm{eff}}(\hat{\mathbf{k}}) = \frac{P_{\mathrm{av}}}{S} = \frac{4\pi\|\mathbf{h}(\hat{\mathbf{k}})\|^2}{1-|\Gamma|^2} = \frac{\lambda^2}{4\pi}\frac{\|\mathbf{A}(-\hat{\mathbf{k}})\|^2}{1-|\Gamma|^2} = \frac{\lambda^2}{4\pi}G_{\mathrm{iso}}(-\hat{\mathbf{k}}). \tag{2.44}$$

If the antenna port is terminated with an ideal open circuit (reflection coefficient 1), the open circuit voltage is given by

$$U^{O.C.} = \sqrt{Z}\frac{2}{1-\Gamma}b^i = \sqrt{Z}\frac{4\sqrt{\pi}}{1-\Gamma}\mathbf{h}\frac{\mathbf{E}^i}{\sqrt{Z_0}} \triangleq \mathbf{h}_{\mathrm{eff}}\mathbf{E}^i. \tag{2.45}$$

From that, the effective length follows as

$$\mathbf{h}_{\text{eff}} = \frac{4\sqrt{\pi}}{1-\Gamma}\sqrt{\frac{Z}{Z_0}}\mathbf{h}. \tag{2.46}$$

Finally, combining (2.43), (2.15), (2.22), (2.26), and (2.44) (in the form $A_{\text{eff}} = 4\pi\|\mathbf{h}\|^2/(1-|\Gamma|^2)$) and setting $\cos\varphi = |\mathbf{h}_1\mathbf{h}_2|/\|\mathbf{h}_1\|\,\|\mathbf{h}_1\|$, Friis' equation for the ratio of the power available from the receiving antenna and the power actually entering the transmit antenna [23] is obtained:

$$\frac{P_{\text{av}}}{P_t} = \frac{|b_2^i|^2}{1-|\Gamma|^2}\frac{1}{|a_1|^2(1-|\Gamma|^2)} = \frac{|b_2^i|^2}{|a_1|^2}\frac{1}{(1-|\Gamma|^2)^2} = \frac{A_{\text{eff},1}A_{\text{eff},2}}{\lambda^2 r_{12}^2}\cos^2\varphi. \tag{2.47}$$

2.2.C. Other formulations

The received wave b^i corresponds to a voltage wave leaving the antenna with amplitude $U^- = \sqrt{Z}b^i$. Introducing

$$\mathbf{h}_N(\hat{\mathbf{k}},\omega) \triangleq \sqrt{4\pi}\mathbf{h}(\hat{\mathbf{k}},\omega), \tag{2.48}$$

the receive relationship (2.18) may be written in the form

$$\frac{U^-(\omega)}{\sqrt{Z}} = \mathbf{h}_N(\hat{\mathbf{k}},\omega)\frac{\mathbf{E}_2^i(\mathbf{r}_1,\hat{\mathbf{k}},\omega)}{\sqrt{Z_0}} \tag{2.49}$$

and, in time domain,

$$\frac{\tilde{U}^-(t)}{\sqrt{Z}} = \tilde{\mathbf{h}}_N(\hat{\mathbf{k}},t) *_t \frac{\tilde{\mathbf{E}}_2^i(\mathbf{r}_1,\hat{\mathbf{k}},t)}{\sqrt{Z_0}}, \tag{2.50}$$

where $*_t$ denotes convolution with respect to t.

Similarly, considering that an input wave a corresponds to a voltage wave with amplitude $U^+ = \sqrt{Z}a$ approaching the antenna, from (2.13), (2.19), and (2.48), we get

$$\frac{\mathbf{E}_1(\mathbf{r}_2,\omega)}{\sqrt{Z_0}} = \frac{e^{-jk_0r_{12}}}{2\pi c_0 r_{12}} j\omega\mathbf{h}_N(-\hat{\mathbf{r}}_{12},\omega)\frac{U^+(\omega)}{\sqrt{Z}} \tag{2.51}$$

with various forms of the time-domain equivalent

$$\begin{aligned}\frac{\tilde{\mathbf{E}}_1(\mathbf{r}_2,t+r_{12}/c_0)}{\sqrt{Z_0}} &= \frac{1}{2\pi c_0}\frac{1}{r_{12}}\frac{\partial}{\partial t}\left(\tilde{\mathbf{h}}_N(-\hat{\mathbf{r}}_{12},t) *_t \frac{U^+(t)}{\sqrt{Z}}\right)\\ &= \frac{1}{2\pi c_0}\frac{1}{r_{12}}\left(\frac{\partial}{\partial t}\tilde{\mathbf{h}}_N(-\hat{\mathbf{r}}_{12},t)\right) *_t \frac{U^+(t)}{\sqrt{Z}}\\ &= \frac{1}{2\pi c_0}\frac{1}{r_{12}}\tilde{\mathbf{h}}_N(-\hat{\mathbf{r}}_{12},t) *_t \frac{\partial}{\partial t}\frac{U^+(t)}{\sqrt{Z}}.\end{aligned} \tag{2.52}$$

Equations (2.50) and (2.52) express both the receive and transmit operations by means of a single effective length operator $\mathbf{h}_N$. These equations correspond to those given in [16]. Note that the last form of the transmission equation (2.52) suggests that the input signal is *always* differentiated before being transmitted.

Alternatively, however, instead of using a single effective length operator $\mathbf{h}_N$, we may introduce a renormalized transmit characteristic

$$\mathbf{A}_N(\hat{\mathbf{r}}_{12},\omega) \triangleq \frac{\mathbf{A}(\hat{\mathbf{r}}_{12},\omega)}{\sqrt{4\pi}}. \tag{2.53}$$

Then, from (2.13), (2.18), (2.19), and (2.53),

$$\begin{aligned}\frac{U^-(t)}{\sqrt{Z}} &= 2\pi c_0 \int \widetilde{\mathbf{A}}_N(-\hat{\mathbf{k}},t) *_t \frac{\mathbf{E}_2^i(\mathbf{r}_1,\hat{\mathbf{k}},t)}{\sqrt{Z_0}}\,dt \\ &= 2\pi c_0 \widetilde{\mathbf{A}}_N(-\hat{\mathbf{k}},t) *_t \int \frac{\widetilde{\mathbf{E}}_2^i(\mathbf{r}_1,\hat{\mathbf{k}},t)}{\sqrt{Z_0}}\,dt,\end{aligned} \tag{2.54}$$

$$\frac{\widetilde{\mathbf{E}}_1(\mathbf{r}_2,t+r_{12}/c_0)}{\sqrt{Z_0}} = \frac{1}{r_{12}}\widetilde{\mathbf{A}}_N(\hat{\mathbf{r}}_{12},t) *_t \frac{U^+(t)}{\sqrt{Z}}. \tag{2.55}$$

Transmission equation (2.55) is equivalent to (2.52) and suggests that the input signal is *never* differentiated before being transmitted.

This is only an apparent contradiction because the actual output signal depends on two factors: the input signal and the impulse response (represented by $\mathbf{h}_N$ or $\mathbf{A}_N$). In general, $\mathbf{h}_N$ or $\mathbf{A}_N$ can introduce any filter characteristic (within constraint (2.19)). However, a few general statements regarding operations that are always or never performed on the input signal by an antenna can be made. For example, despite the apparent proportionality of radiated field and input voltage in (2.55), radiation at $\omega = 0$ is always impeded because $\mathbf{A}(\omega = 0) = 0$ due to (2.19) for finite $\mathbf{h}(\omega = 0)$.

2.3. Propagation effects

2.3.1. Introduction

The theoretical and mathematical foundation of UWB signal processing and system modeling is based on the interaction of a transmitted pulse with the transmission medium, for example, free space, buildings, furniture, trees, hills, rivers, stones, and so forth. The historical logical development of the UWB propagation processes can be conveniently divided into four stages: (1) fundamental concepts and mechanisms; (2) high-frequency approximation techniques (GTD/UTD); (3) transient and impulse-response approximations; (4) per-path pulse waveform distortion. The first physical cornerstone to understand the medium-interaction mechanisms of UWB pulse propagation and shape distortion was the work of Sommerfeld [24] on the diffraction of pulse by a perfectly conducting half-plane [24]. His solution was the first exact solution of Maxwell's equations. Lamb [25]

and Friedlander [26] also studied the pulse distortion caused by diffraction by a half-plane. These solutions provided us with good pictures of understanding the physical mechanisms of pulse diffraction [27–30]; however, these solutions were impractical in engineering and applied science. Secondly, another conceptual breakthrough was the birth of the geometric theory of diffraction (GTD) developed by Keller [31], based on the Lunberg-Kline series in 1949 [30]. Rather than seeking the exact solution for Maxwell's equations, GTD uses a generalization of Fermat's principle to find high-frequency harmonic Maxwell equation solutions for many complicated objects. The uniform theory of diffraction (UTD) was proposed in 1974 to complement GTD in situations where GTD was invalid [32]. The GTD/UTD framework has become the practical framework in narrowband radio propagation [2, 33] and will be also the foundation of our proposed framework. Thirdly, the impulse-response waveform of the finite three-dimensional target was approximated by a linear system theory in UWB radar in 1965 [34]. The chief value of the impulse response concept was to sum up the radar signature of an object in a unique manner which adds insight into the complex relationship between the target shape and radar reflectivity. A linear system is fully characterized by its impulse response. Thus, in general, the impulse response fully describes the properties of the radar target for any frequency. Finally, this concept of impulse response and scattering center widely used for a UWB radar was borrowed in 1995 [35], to describe the impulse response of a generalized multipath path in UWB wireless communications [36–40]. The resultant generalized model [41–43, 35, 44–51] extended the widely used Turin's model [52] that was first suggested in 1958. This model already finds some applications [53–60]. This section is aimed at a tutorial logical development of a unified theory based on this generalized model (also called physics-based generalized multipath model). The starting point of this theory will be Maxwell's equations. We will address all the aspects that are important from the theory and engineering point of view.

2.3.2. UWB pulse propagation physics and mechanisms

The starting point of our unified theory that takes into account pulse distortion is Maxwell's equations. Maxwell's equations are linear, as is the UWB propagation medium. Therefore, the linear system theory and Maxwell's equations are valid everywhere. We will approach our problem using exact solutions and high-frequency GTD/UTD approximations. Although we will give exact solutions for two special cases (half-plane and wedge), we will focus on developing the GTD/UTD framework that is practical in UWB communications.

GTD/UTD may be viewed as an asymptotic (wavelength $\lambda \to 0$ or $\omega \to \infty$) theory of the solutions of Maxwell's equations. The algorithms of GTD/UTD are rather simple and lead to explicit expressions for the desired quantities. The shortwave (or high-frequency) behavior of the known exact solutions (diffraction by a wedge, cylinder, and sphere) reveals that the laws of geometric optics break down only in *narrow transition regions* where diffraction fields are described by GTD/UTD coefficients. Fortunately the narrow transition regions are local, that

is, the diffracted fields only depend on the local properties of the incident waves and bodies in these regions. Fock's localization principle (1946) [61, 33] is a cornerstone of our framework. With Fock's principle, we *postulate* that the complex structures can be decomposed into separated scattering centers where each scattering center is described by an impulse response $h_l(\tau)$of the lth path. When a ray is distorted in pulse shape, we call this ray a "generalized path" to differentiate it from the conventional one used in Turin's model [52]. Therefore, all ray fields can be described by the ordinary geometric optics (GO) and GTD (UTD). All UWB signals' energy is transferred along these ray tubes. Let us consider an example to illustrate how a UWB pulse travels along a generalized path. The amplitude of a diffracted ray (u_d) is proportional to the amplitude of the inducing primary ray (u_i) *at the point of incidence* (r_0). Mathematically the diffraction coefficient $D(j\omega; t_i; t_d)$ connects u_i with u_d [61]:

$$u_d = \left(\frac{1}{\sqrt{J}}\right) \cdot e^{jks} D(j\omega; t_i; t_d) u_i, \tag{2.56}$$

where J is the Jacobian of the transformation to ray coordinates, s the eikonal defining the phase structure of the field, t_i and t_d unit vectors of the incident and diffracted rays, k the wavenumber, and ω the angular frequency. In (2.56) the coefficient of diffraction depends on the *local geometry* of the body in the vicinity of the incident ray in the case of corners and edges. Below we will use half-plane and wedge as two examples to show the method of obtaining $D(j\omega; t_i; t_d)$ using GTD/UTD. Other complicated geometric structures in engineering applications can be also worked out. For these structures, often we need trace all the significant rays to capture the major energy. Before we show the examples, let us consider the impact of the $D(\omega; t_i; t_d)$ on the incident pulse waveform.

UWB pulse waveform distortion. We can model the localized diffraction phenomenon as a linear system. The transfer function of this linear system is determined by the local diffraction coefficient $H(j\omega) = D(j\omega; t_i; t_d)$ located at the point of emanation of the ray (say r_0) on the edge or apex. When a pulse travels through a *locally located diffraction point*, the pulse is modeled as passing through an equivalent linear system of $H(j\omega)$. This point acts as a linear filter. In reality this mathematical point is a localized region (called scattering center) [62]. To apply the linear system theory, our observation must be far enough from the scattering center, for the approximation conditions of the high-frequency GTD/UTD to be valid. For a given pulse of incident waveform $p(t)$, the pulse waveform right after r_0 is $r_0(t) = p(t) \bigotimes h(t)$, where $h(t)$ is the inverse Laplace transform of $H(j\omega)$ [63]. Along the tube of this diffracted ray, the pulse waveform is in the form of $r_0(\tau - \tau_0) = r_0(\tau) * \delta(\tau - \tau_0)$, where the delay is $\tau_0 = s/c$ with c being the speed of light. In other words, it follows that

$$r(t) = p(t) \bigotimes h(t) \bigotimes \delta(t - \tau_0). \tag{2.57}$$

A linear system is distortionless if $h(t) = \delta(t)$. This condition is valid for Turin's model but generally invalid for the physics-based model. Turin's model only takes into account the effect of delays through $\delta(\tau - \tau_0)$, as included in (2.57). For example, for diffraction by a perfectly conducting (PEC) half-plane, it follows from the GTD that $h(\tau) = A_0/\sqrt{\tau}U(\tau)$ [64, 65], where A_0 is real and $U(x)$ is the unit step function. The mathematical property of this diffraction phenomenon is very far-reaching. The role of the impulse response of the PEC half-plane is the *semi-integral* of the waveform of the incident primary ray field, with a notation of $(d/d\tau)^{-1/2}$ or $(j\omega)^{-1/2}$. Fractional calculus has proven to be a very good tool to handle these problems [49, 50], see Section 2.3.A for details.

Pulse diffraction by a perfectly conducting half-plane. As an example let us consider the canonical problem of diffraction by a half-plane. This problem, first solved by Sommerfeld, is both theoretically and practically important. For monochromatic incident field $u_i = A_0 \exp(j\omega t)$, the complex-valued amplitude u of the scattered field at the distance r is given by [33]

$$\begin{aligned} u(j\omega) = u_1 \pm u_2 = A_0 e^{jkr\cos(\varphi-\varphi_0)} F\left(\sqrt{2kr}\cos\left(\varphi-\varphi_0\right)\right) \\ \pm A_0 e^{jkr\cos(\varphi+\varphi_0)} F\left(\sqrt{2kr}\cos\left(\varphi+\varphi_0\right)\right), \end{aligned} \tag{2.58}$$

where $F(x) = (e^{j(\pi/4)}/\sqrt{\pi})\int_x^\infty e^{-j\mu^2}d\mu$ and the plus and minus signs denote the **H** and **E** polarization incident fields. φ_0 and φ are, respectively, the incident and observation angles; $k = \omega/c$ is the wave number. The Fresnel function $F(x)$ can be expressed in terms of the error function erfc(x) as $F(z) = (1/2)\text{erfc}(e^{-j\pi/4}z)$ where $\text{erfc}(z) = (2/\sqrt{\pi})\int_z^\infty e^{-x^2}dx$. Using the Laplace transform of an error function, we can derive the closed form of the impulse response defined by $h(\tau) \triangleq L^{-1}\{u(j\omega)/u_i\}$:

$$\begin{aligned} h_{\text{half-plane}}(\tau) = \frac{\sqrt{2r/c}}{2\pi}\left[\frac{\cos(1/2)(\varphi-\varphi_0)}{\tau + (r/c)\cos(\varphi-\varphi_0)} \pm \frac{\cos(1/2)(\varphi+\varphi_0)}{\tau + (r/c)\cos(\varphi+\varphi_0)}\right] \\ \times \frac{1}{\sqrt{\tau - r/c}}U\left(\tau - \frac{r}{c}\right), \end{aligned} \tag{2.59}$$

where $U(t)$ is the unit step function of t. The transient exact solution is remarkably simple, compared with its time-harmonic frequency-domain solution (2.58). To compare our results with others, consider the normal incidence where $\varphi = 2\pi - \theta$ and $\varphi_0 = \pi$. Equation (2.59) reduces to

$$h_{\text{normal}}(\tau) = \frac{1}{\pi}\frac{\sqrt{2r}\sin(\theta/2)}{c\tau - r\cos\theta}\frac{1}{\sqrt{c\tau - r}}, \tag{2.60}$$

which is identical to the derivative of the unit step response results obtained by [30]. Reference [66] also obtained similar expressions.

Equation (2.59) has two singularities: (1) when $\tau + (r/c)\cos(\varphi - \varphi_0)$ and $\tau + (r/c)\cos(\varphi + \varphi_0)$ approach zeros; (2) when τ approaches r/c. We only consider the

second case where the wave front $c\tau - r$ assumes a singularity of $(1/\sqrt{\tau})U(\tau)$ if the singularity of case 1 is absent. We only have one scatter center occurring at the edge of the half-plane. If a pulse $p(t)$ propagates through this scattering center, the pulse waveform will be distorted since the impulse response of the half-plane is not a Dirac function $\delta(\tau)$.

In Keller's GTD model for the diffraction at the edge of a half-plane [64, 65], the monochromatic diffraction wave is given as

$$u_{d1} = \frac{1}{\sqrt{r}} e^{-jkr} D(\varphi, \varphi_0, k) u_i, \tag{2.61}$$

where

$$D_{s,h}(\varphi, \varphi_0, k) = -\frac{\exp(-j\pi/4)}{2\sqrt{2\pi k}} \left(\frac{1}{\cos\left[(\varphi - \varphi_0)/2\right]} \pm \frac{1}{\cos\left[(\varphi + \varphi_0)/2\right]} \right) \tag{2.62}$$

is a diffraction coefficient obtained through the first-order asymptotic approximation of the exact solution of (2.58). This first-order solution breaks down within the transition zone, known as semishadow, which is defined by the region $q \leq q_0$ where q is defined as $q = \sqrt{2kr}\cos((\varphi \pm \varphi_0)/2)$ and q_0 is the minimum value of q such that the approximation (2.62) is satisfactory within $q \geq q_0$. With the aid of a Laplace pair, from (2.62) the time-domain diffraction coefficient predicted by Keller's GTD is derived as

$$h_{s,h}(\tau) = -\frac{\sqrt{c}}{2\pi\sqrt{2}} \left(\frac{1}{\cos\left[(\varphi - \varphi_0)/2\right]} \pm \frac{1}{\cos\left[(\varphi + \varphi_0)/2\right]} \right) \frac{1}{\sqrt{\tau - r/c}} U\left(\tau - \frac{r}{c}\right). \tag{2.63}$$

Pulse diffraction by a perfectly conducting wedge. As another example, we consider the wedge. The exact transient solution to a perfectly conducting wedge is available [27] as follows (for $\Omega > \pi$ and $\phi' < \Omega - \pi$):

$$\begin{aligned} h_{\text{wedge}}(r, r'; \tau) &= \frac{\delta(\tau - |r - r'|/c)}{4\pi|r - r'|} U(\pi - |\phi - \phi'|) + \frac{\delta(\tau - |r - r'|/c)}{4\pi|r - r'|} U(\pi - \phi - \phi') \\ &\quad - \frac{c}{4\pi^2} \frac{Q(\phi, \phi', \beta) + Q(\phi, -\phi', \beta)}{\rho\rho' \sinh(\beta)} U(c\tau - D_0), \end{aligned} \tag{2.64}$$

where

$$\begin{aligned} Q(\phi, \phi', \beta) = -\frac{\pi}{2\Omega} \Bigg\{ &\frac{\sin\left[(\pi/\Omega)(\phi - \phi' - \pi)\right]}{\cosh(\pi\beta/\Omega) - \cos\left[(\pi/\Omega)(\phi - \phi' - \pi)\right]} \\ &- \frac{\sin\left[(\pi/\Omega)(\phi - \phi' + \pi)\right]}{\cosh(\pi\beta/\Omega) - \cos\left[(\pi/\Omega)(\phi - \phi' + \pi)\right]} \Bigg\}, \end{aligned} \tag{2.65}$$

Ω is the angle of the wedge. Polar coordinates (ρ, ϕ, z) and (ρ', ϕ', z') are used for observation point and source point, respectively. Equation (2.64) assumes Neumann boundary condition on the wedge faces. Parameters β, T, D_0 are defined by

$$\begin{aligned} \beta &= \cosh^{-1}\left[\left(c^2T^2 - \rho^2 - \rho'^2\right)(2\rho\rho')^{-1}\right], \\ cT &= \left[c^2\tau^2 - (z-z')^2\right]^{1/2}, \qquad D_0 = \left[(\rho+\rho')^2 + (z-z')^2\right]^{1/2}. \end{aligned} \tag{2.66}$$

There is only one scattering center in this case. The first two terms represent the geometric-optics ray fields. The third term represents the diffracted field caused by an impulse plane wave. Obviously (2.64) will predict some pulse waveform distortion if a pulse signal is diffracted by a perfectly conducting wedge. The transient responses given in (2.59) and (2.64) are valid at all observation times, thereby providing an insight into the field behavior at observation times immediately (early-time) and long (late-time) after the passage of a wavefront. The time-domain GTD (Keller's) coefficient has been derived as follows [64, 65]:

$$h_{s,h}(\tau) = A\frac{1}{\sqrt{\tau - r/c}}U\left(\tau - \frac{r}{c}\right), \tag{2.67}$$

where

$$A = \frac{\sqrt{c}}{\pi\sqrt{2}}\frac{\sin\pi/n}{n\pi}\left(\frac{1}{\cos\pi/n - \cos\left[(\varphi-\varphi_0)/n\right]} \mp \frac{1}{\cos\pi/n - \cos\left[(\varphi+\varphi_0)/2\right]}\right). \tag{2.68}$$

The two faces of wedge are $\varphi = 0$ and $\varphi = n\pi$. The impulse response obtained from UTD has been derived as [65, 64]

$$h_{s,h}(\tau) = \sum_{m=1}^{4} A_m \frac{1}{\sqrt{\pi c\tau}(\tau + X_m/c)}U(\tau), \quad \tau = t - \frac{r}{c}, \tag{2.69}$$

where A_m and X_m are time-independent parameters. For practical UWB pulses, we find that the methods (GTD, UTD, and exact) in (2.64) give us calculated pulse waveforms that are not differentiable [46]. Equations (2.67) and (2.69) can readily be shown to have a singularity of type $\tau^{-1/2}U(\tau)$ in the wavefront $\tau = t - r/c$. More generalized singularities will be given in (2.73) and (2.74) as well as (2.81) and (2.82).

2.3.3. Early-time response and asymptotic high-frequency time-harmonic solutions

Let us now investigate the relationship between the early-time response and asymptotic high-frequency time-harmonic solutions, due to its fundamental nature

in our unified theory. A basic difficulty of the GTD/UTD-based Laplace approach is that we have to justify the validity of the GTD/UTD-based high-frequency approximation for each individual scattering center [64, 63, 65]. The communications medium can be regarded as the composite interactions of separated scattering centers [54, 44, 60]. Due to the high-resolution capability of a UWB pulse signal, these scattering centers are well resolved in the time-domain. This is one of the most fundamental features of a UWB system from a signal analysis point of view. The property of each scattering center can be treated as different (or composite) mechanism corresponding to reflection, refraction, and diffraction [62]. Under the GTD/UTD framework, each mechanism is fully described by GTD/UTD coefficients. The accuracy of these time-domain GTD/UTD coefficients is not well established. Can we use the time-domain GTD/UTD coefficients to model the modern UWB communications/sensing systems? Fortunately we have already made a decisive step [46] to answer this. Compared with the exact solutions of wedge and half-plane, the time-domain GTD/UTD coefficients are shown to be *sufficiently* accurate for the modern UWB communications/sensing system modeling. This has paved the way to a more *systematic* use of the time-domain GTD/UTD coefficients as building blocks in UWB signals modeling. These closed-form solutions based on UTD/GTD provide big advantages over the conventional methodology.

The mathematical foundation of the GTD/UTD is the Kline-Luneberg expansion of the field components. The main result of this subsection is to tell us how to obtain the asymptotic series representation of the steady-state or time-harmonic solution of Maxwell's equations if we know the behavior of the corresponding pulse solution in the neighborhood of its singularities [30]. We will give the form of asymptotic series that is valid in terms of the singularities of the pulse solution. The asymptotic series is determined only by the singularities of the pulse solutions. The mathematical result of this expansion is intimately related to an Abelian theorem (Watson' lemma) in Laplace transform theory [67]. This theorem states [30] that if the original function $h(t)$ has the convergent or asymptotic form

$$h(t) \approx \sum_{n=0}^{\infty} C_n t^{\nu_n} \quad \text{for } t \text{ near } 0+ \text{ and } \nu_n > -1, \tag{2.70}$$

and $h(t) < 0$ for $t < 0$ (causal), then the image function $H(s)$ of $h(t)$ has the asymptotic form

$$H(s) \approx \sum_{n=0}^{\infty} C_n \frac{\Gamma(1+\nu_n)}{s^{\nu_n}} \quad \text{as } s \longrightarrow \infty. \tag{2.71}$$

In this theorem $s = j\omega + \sigma$ may be complex, where σ is greater than zero. This theorem connects the early-time response (the initial transient fields on and near the wavefront) and the high-frequency time-harmonic solutions. Let us assume the

field near the wavefront $t = r/c$ behaves as $h(r,t) \approx A(t - r/c)^{\beta}$, where A is time-independent and $\beta > -1$. This is the case for (2.59) and (2.63). The asymptotic behavior of the field behaves as

$$H(j\omega) \approx \exp(jkr)A\frac{\Gamma(\beta+1)}{2\pi(j\omega)^{\beta+1}}. \tag{2.72}$$

This is true for (2.62). Recall that GTD/UTD solutions are asymptotic solutions of the model problem solutions that are exact. The field behavior near $t = r/c$ is related to the time-harmonic behavior for $\omega \to \infty$.

Equation (2.72) is inadequate to describe the phenomena at times $t \approx r/c$ corresponding to the arrival of the wavefront. As described above, the wavefront fields are synthesized by the high-frequency time-harmonic wave constituents. The asymptotic expansions of the time-harmonic fields (such as obtained by GTD/UTD) can be employed to develop corresponding expansions of the transient fields for $t \approx r/c$ (early-time response), improving the leading term expressions of (2.72). A generalized version of the time-harmonic field is given by [29]

$$H(j\omega) \approx \frac{1}{2\pi}e^{-jk\Psi(r)}\left[A'(r) + \frac{1}{(j\omega)^{\beta+1}}\sum_{n=0}^{\infty}\frac{A_n(r)}{(j\omega)^n}\Gamma(\beta+n+1)\right]. \tag{2.73}$$

Then, from (2.70) and (2.71), the transient field near $t = \psi(r)/c$ is

$$h(\tau) \approx A'(r)\delta(\tau) + \tau^{\beta}\sum_{n=0}^{\infty}A_n(r)\tau^n, \quad \tau = t - \frac{\Psi(r)}{c} \geq 0. \tag{2.74}$$

The appearance of the phase $\Psi(r)$ instead of $\mathbf{r}$ generalizes the applicability of (2.72). $A_n(r)$ and $A'(r)$ are time-independent amplitudes. In (2.73) and (2.74), the first term represents the geometric-optics fields and the second term the diffracted fields.

According to (2.70) and (2.71), the time-domain ray solution (GTD/UTD) is only valid for "early to intermediate times" since these high-frequency solutions are asymptotic in the frequency domain and remain accurate for moderate to high frequencies. Again this is not a problem for UWB signals within FCC band (3.1–10.6 GHz). The transient responses in intervals close to ray arrivals times of the TD-UTD/GTD are generally strongest and are directly associated with the waves arriving from the local features of the radiating (scattering) object. The TD-UTD/GTD is based on the asymptotic (high-frequency) formulas of the time-harmonic UTD and therefore the "late-time" behavior of the TD-UTD/GTD impulse-response is expected to be erroneous [64]. But, on the other hand, if the TD-UTD/GTD impulse-response is convolved with an excitation pulse waveform that has a frequency spectrum (say FCC band) dominated by frequencies for which the time-harmonic UTD solution is expected to be accurate, then the resultant transient waveforms (per-path impulse response) predicted by the TD GTD/UTD

should be accurate also. Another reason for paying special attention to the TD GTD/UTD is that the current state of the art cannot allow us to sound the UWB channel accurately. In practical analysis, an impulse response of the UWB channel is needed. When the sounding pulses are much shorter than the practical signals to which the measured channel response signals will be applied, we can regard these measured signals as a good approximation of channel impulse response. However, this condition cannot be met for a UWB channel. In the near future, it is infeasible to use measurement equipment that has a bandwidth much larger than the practical UWB signal bandwidth (up to 7.5 GHz). This is one fundamental reason for using the TD UTD/GTD, which gives us impulse responses of each ray.

Let us now deal with some practical issues. Although in theory we assume we have the pulse solutions available, then the asymptotic time-harmonic solutions can be determined. In practice, the case is on the contrary since there are rich asymptotic time-harmonic solutions and techniques available in the literature. One question will naturally arise. Are these solutions (such as obtained by GTD/UTD) sufficiently accurate for the current UWB communications? In other words, do the early-time response of the scattering center sufficiently approximate its true time-domain response? As an example consider the time-domain GTD solution to the half-plane edge. Equation (2.63) gives the closed-form solution. If two such edges are put together to form a strip, the two edges will interact with each other. We assume that the frequency is high enough, so that the two edges can be treated as two independent scattering centers. The wavefronts from each scattering center arrive at an observation point at different times. Let the first arrival be $t = t_1$. The solution is asymptotic as $\tau_1 = t - t_1 \to 0$, although it is valid only within the time interval Δt, where $\Delta t = t - t_1$ is small. However, when the next waveform (caused by the other edge) arrives at t_2, $t_2 - t_1$ is significantly larger than Δt. The total response after t_2 will not be accurate and must be found by other methods. Therefore, one must be careful when using the time-domain GTD in a problem involving more than one scattering center or multiple scatterings. Unfortunately we always deal with multiple scatterings in modeling multipath. This problem is essential to practical applications.

Based on the comparisons between the time-domain GTD and the exact solution [46, 65], it is discovered that the useful period $\Delta t = t - t_1$ may be varied depending upon factors such as scattering structure, source point, observation point, and so forth. For example, the useful period of $\Delta t \sim 10x/c$ for the right-angle (90 degree) wedge, where x is the distance from the edge (scattering center). At high frequencies, the field tends to be localized (Fock's principle of locality). The energy tends to be localized in the scattering center (a singularity). If we have a UWB pulse of duration of T nanoseconds (ns), the condition to use the time-domain GTD to describe the pulse response of the scattering center is that the UWB pulse duration T must be smaller than the useful period of $\Delta t \sim 10x/c$, that is, $T < \Delta t \sim 10x/c$. For $T = 0.1 - 1$ nanosecond (1–10 GHz bandwidth), $x > cT/10 = 3T = 0.3 - 3$ (cm), where $c = 30$ cm/nanosecond (speed of light). In other words, the observation point must be 0.3–3 cm away from the scattering center.

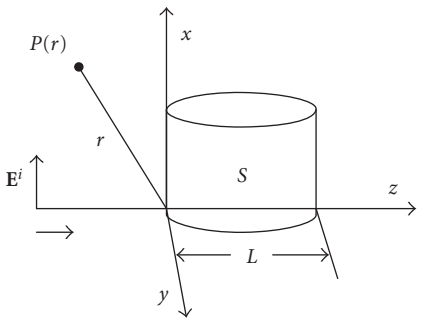

FIGURE 2.2. Coordinates of impulse-response definitions.

2.3.4. Impulse-response for electrically large objects

Before generalizing the above results in a heuristic manner to model the UWB channel (see Section 2.3.5), we must introduce the method in the literature for modeling large radar objects. The same method will be still valid for UWB pulse propagation in communications environment. Physically and mathematically the two problems are equivalent. Radar interrogation (per-path pulse response modeling) is essentially a transient process [34]. In order to simplify the calculation of radar reflectivity (per-path pulse response), one usually assumes that values obtained for a monochromatic source (time-harmonic solutions) are representative of the target (per-path pulse response) and can be used with little or no modification, to predict the return for a pulsed signal with the same carrier frequency. This assumption cannot be made for ultrashort pulses or any other UWB signaling waveform. To obtain a target reflectivity model (per-path pulse response model) applicable to all types of signal, time-domain concepts suggest use of an impulse-response waveform to characterize each radar target (per-path pulse response).

The first such attempt to estimate an impulse-response waveform in the radar scattering context was perhaps that of Kennaugh and Cosgriff (1958). Using extremely simple approximations for high- and low-frequency backscatter from conducting sphere and spheroids, estimates of the impulse-response waveform were obtained. The mathematical physical tools to attack the problems involving finite three-dimensional targets are described in Section 2.3.2. As suggested in (2.56), a linear system can be used to describe the object. We will follow [34] in the following derivations of this subsection.

To apply linear system analysis to scattering analysis problems [54, 44, 60], we first define input and output quantities as electrical field intensities at a pair of points in space and in fixed directions. As shown in Figure 2.2, the input $x(t)$ is the x-directed electric field intensities at the origin produced by a plane wave $E^i = \hat{x}x(t - z/c)$. If, now, this plane wave is incident upon an arbitrary scattering object (per-path obstacles), a scattered electromagnetic field E^s is produced. We may select an arbitrary component of this vector field at any point $P(r)$ to be the output of $y(t)$. Thus, restricting the direction and polarization of the incident

plane wave, the relationship between the $x(t)$ and $y(t)$ is that of a one-dimensional linear system. If we assume that the scatterer does not move, so that the system is time-invariant. The impulse-response waveform $h_0(t)$ is that obtained when the incident plane wave $x(t)$ is impulsive, that is, $x(t) = \delta(t)$, the Dirac delta-function. This approach is essentially the same as in Section 2.2.

Several features of the impulse-response waveform can be inferred immediately if the scattering body is of finite size:

(i) $h_0(t)$ is identically zero for $t < 0$ if the scatterer lies to the right of the xy plane, as in Figure 2.2. The linear system must be causal,

(ii) $h_0(t)$ decays exponentially for large values of $\tau = t - r/c$, where r is the distance to the observation point from the origin, as in Figure 2.1,

(iii) when $r \gg L$, where L is the maximum dimension of the scattering object, $h_0(t)$ varies with r in a given scattering direction as $r^{-1} f(t - r/c)$ for transverse components of the scattered field.

Properties of impulse-response waveform $h(t)$. The normalized impulse-response $h(t)$ and the transfer function $H(j\omega)$ are a Laplace transform pair. Here $H(j\omega)$ is related to a transverse component $E^s(t - r/c)$ of the scattering field at large r by

$$\operatorname{Re}\left\{H(j\omega)e^{j\omega(t-r/c)}\right\} = \left(\frac{2r}{c}\right)E^s\left(t - \frac{r}{c}\right), \tag{2.75}$$

the incident plane wave being given by $E^i = \hat{x}\cos\omega(t - z/c)$. We introduce the notation

$$H(s) = \int_0^\infty h(t)e^{-st}dt, \qquad H(s) = L\{h(t)\}, \qquad h(t) = L^{-1}\{H(s)\}. \tag{2.76}$$

In practice, we usually first obtain $H(j\omega)$ using the GTD/UTD asymptotic solutions, then we can replace $s = j\omega$ in $H(j\omega)$ to obtain $H(s)$. Secondly, we apply the Laplace transform pair to obtain the $h(t)$. Not all the functions have their inverse Laplace transform in closed forms. Due to the essential property of causality, a Laplace transform rather than a Fourier transform must be used, in order to guarantee that the so obtained impulse-response is physically sound. Such obtained impulse-response must be a real function. This can serve as sanity check for the analysis.

High-frequency impulse-response based on scattering centers. Let us present such a model based on the concept of scattering centers. Extensive development of high-frequency scattering theory (developed in Sections 2.3.2 and 2.3.3) traces back at least to 1940s–1960s. Experimental conditions and analytic tools were mature until 1960s, mainly driven by the study of short pulses caused by nuclear explosions. Two categories of work were performed. One was to model the impulse-response of simple shapes and composite shapes (finite three-dimensional objects). Another category was to study the radio propagation of pulse in a dispersive medium like plasma at a distance of kilometers. Here we are only interested in methods developed for the first category, especially based on experimental work [68, 69].

It is *postulated* that for a sufficiently short pulse, the solution can be represented as a sequence of pulses scattered from the resolved scattering centers. (Section 2.3.2 has discussed the conditions of validity of the time-domain GTD to model the resolved scattering centers.) This postulated solution has an approximate equivalent in the frequency domain. The back scattering amplitude at the frequency ω will be of the form

$$H(j\omega) \simeq \sum_n A_n H_n(j\omega) e^{-j2kL_n} = \sum_n A_n H_n(j\omega) e^{-j\omega\tau_n}, \quad \tau_n = \frac{L_n}{c}, \tag{2.77}$$

where A_n is the scattering amplitude, $H_n(j\omega)$ is the frequency response for the nth center, and L_n is the distance along the ray path from the first to the nth scattering center. The so-called per-path transfer function (heuristically defined in Section 2.3.5), $H_n(j\omega)$, plays the central role in characterizing the pulse waveform. The per-path delay, $\tau_n = 2L_n/c$, describes the intrapath delay that connects the localized responses. When an inverse Laplace transform is applied in (2.77) (see (2.70) and (2.71)), the early-time approximation to the impulse-response is obtained as

$$h(\tau) = \sum_n A_n h_n(\tau) * \delta(\tau - \tau_n). \tag{2.78}$$

Both $H_n(j\omega)$ and $h_n(\tau)$ have a unit energy for convenience. In general, (2.77) and (2.78) are connected by the Laplace transform. We assume that $H_n(j\omega)$ is centered about f_0 with a normal bandwidth B. If $H_n(j\omega)$ is slowly varying for $-B/2 + f_0 \leq f \leq B/2 + f$, the term e^{-j2kL_n} varies rapidly in the same band. For a special case, a simple relation can be obtained as

$$h(\tau) \simeq \sum_n A_n H_n(\omega_0)\, p\left(\tau - \frac{2L_n}{c}\right), \tag{2.79}$$

where $p(t)$ is the incident pulse. Thus the nth scattering center returns a pulse of amplitude $A_n H_n(\omega_0)$, delayed by $\tau_n = 2L_n/c$ from the first term. From a physical point of view, (2.78) and (2.79) imply that the dimensions of the scattering centers are of the order one wavelength or less. Thus, if the incident pulse contains more than several wavelengths (at the center frequency), the distortion of the scattered pulses is negligible. Refinements of (2.79) could be included by accounting for the frequency dependency of $H_n(j\omega)$ near the center frequency, as in (2.78). It should be noted that this representation in (2.78) and (2.79) may also include terms due to multiple scattering.

For high frequencies, one may approximate $H(s)$ by an expansion called Luneberg-Kline series in negative powers of s (as discussed in Section 2.3.2 and used in Section 2.3.5). Individual terms in such an expansion are related to impulse, step, ramp, and low-order discontinuities in $h(t)$. Thus, if the asymptotic

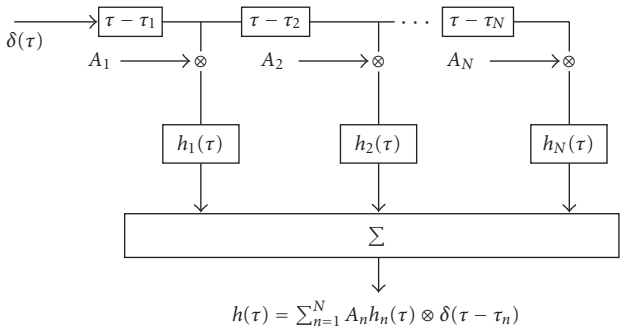

FIGURE 2.3. The structure of the generalized multipath model.

expansion of $H(s)$ contains a term $A_n s^{-n} e^{-s\tau}$, the impulse-response waveform undergoes a discontinuous jump of magnitude A_n in its $(n-1)$th-order derivative at $t = \tau$. Terms of the form $A_0 e^{-s\tau}$ in the asymptotic expansions are contributions predicted by geometric optics, giving impulses in $h(t)$ at $t = \tau$, of magnitude A_0. It is clear that low-frequency approximation serves to determine waveform shape and size, whereas high-frequency information relates to fine structure and detail in the waveform. Both are thus interpreted in a single concept that serves to predict the scattering behavior in the intermediate or resonance range of frequencies. The intuitive hypothesis that the ramp response is most closely associated with the volume and size of a scatterer suggests that, as our knowledge of response waveforms for special objects increases, we will ultimately be able to sketch, by inspection, a reasonably accurate estimate of the ramp response of any target (per-path response).

2.3.5. Generalized multipath model based on per-path pulse waveform

The methods and mathematical physical results are historically developed for UWB radar (see Section 2.3.4), but can be generalized to a UWB radio propagation channel if we treat the objects encountered by tracing a path in multipath channel modeling. This will be the philosophy adopted in this subsection. Admittedly, the state of the art in predicting or approximating impulse-response waveforms for per-path is rather primitive. It has been applied to perfectly conducting objects of simple shape [41, 42, 35, 44–51]. With a combination of theoretical and experimental techniques, the associated waveforms can be determined for other, more complex, shapes. No technique or concept can make an intrinsically difficult task simple, and the long history of channel modeling investigations indicates that this is, indeed, a difficult task. Perhaps the chief value of the per-path impulse-response concept is that it sums up the signal signature of a path (like the radar signature of an object) *in a unique manner* which adds insight into the complex relationship between each individual path response and the propagation environment. The relationship to statistical channel modeling, and some discussions of measurement results, will be present in Section 2.5.

Based on the GTD framework and principle of locality [31], we postulate that the total response is modeled by the sum of the impulse-responses of local scattering centers [35, 41, 42, 44–51]:

$$h(\tau,\theta,\varphi)=\sum_{n=1}^{N_1}a_n(\theta,\varphi)\delta(\tau-\tau_n)+\sum_{n=1}^{N_2}A_n(\theta,\varphi)h_n(\tau,\theta,\varphi)*\delta(\tau-\tau_n),\quad(2.80)$$

where N_1 and N_2 represent the number of rays without per-path pulse distortion and rays with per-path pulse distortion, respectively. The first term is of the form identical to Turin's model. The second term is more general; as a matter of fact, the first term is a special form of the second term when $h_n(\tau)=\delta(\tau)$.[13] The function $h_n(\tau)$ is defined to have unit energy. When an arbitrary pulse, $p(t)$, passes through the channel defined by (2.80), some pulses will be undistorted and some pulses will be distorted. When the duration of this pulse, T_p, is shorter than any interpath interval of (2.80), that is, $T_p<|\tau_i-\tau_j|$ for $i\neq j$, all pulses will be resolvable in time. The $h_n(\tau)$ can be obtained through exact, experimental, numerical, or/and asymptotic methods. As an example, let us take a look at the diffracted rays. The geometric optics rays can be treated as a special form of a generalized diffracted ray [30]. If in the neighborhood of the singularity $\tau=\tau_\alpha$ any field component has the behavior

$$h_n(\tau)=\begin{cases}\xi(\tau_\alpha-\tau)\displaystyle\sum_{n=0}^{\infty}\frac{C_n}{n!}(\tau_\alpha-\tau)^n, & \tau<\tau_\alpha,\\ \eta(\tau_\alpha-\tau)\displaystyle\sum_{n=0}^{\infty}\frac{D_n}{n!}(\tau_\alpha-\tau)^n, & \tau>\tau_\alpha,\end{cases}\quad(2.81)$$

where $\xi(\tau)$ and $\eta(\tau)$ are rather general, then the corresponding asymptotic frequency response has the form [30]

$$H_n(j\omega)\approx e^{-jk\psi}\sum_{m=0}^{\infty}\left\{\frac{D_m}{m!}\frac{1}{(jw)^m}\int_0^{\infty}\eta\left(\frac{t}{jw}\right)t^me^{-t}dt-\frac{C_m}{m!}\frac{1}{(-jw)^m}\int_0^{\infty}\xi\left(-\frac{t}{jw}\right)t^me^{-t}dt\right\},\quad(2.82)$$

where $\Psi(x,y,z)$ determines the wavefront at the (x,y,z) in question, that is, $\Psi(x,y,z)-ct=0$ is the discontinuity hypersurface on which $h_n(\tau)$ has a finite jump. As shown in Section 2.3.3, the behavior of the impulse-response solution in the neighborhood of its singularities does determine the asymptotic series for the corresponding time-harmonic problem. Further we learn the form of the asymptotic series in terms of the form of the singularity of the impulse-response solution. The function of (2.81) can be infinite at the singularities. The results of (2.81) and

[13]Note the properties of Dirac's function: $\delta(\tau)\otimes\delta(\tau)=\delta(\tau)$ and $\delta(\tau)\otimes\delta(\tau-\tau_n)=\delta(\tau-\tau_n)$.

(2.82) extend a known result in Laplace transform theory—the Abelian theorem ((2.70) and (2.71)).

Equation (2.82) is a special form of (2.80). Equations (2.80) and (2.82) are insufficiently generic to represent all the signals in the set of the actual physical field signals that satisfy Maxwell's equations. But they are generic enough to describe almost all the practical series obtained by GTD/GTD and other high-frequency asymptotic techniques. For a large category of physical signals, both $\xi(\tau)$ and $\eta(\tau)$ are of a form $\tau^{1/2}$, the asymptotic series contains fractional powers of $(1/\omega)$, for example, $1/(j\omega)^{m+1/2}$, where m is an integer. For diffracted signals $\xi(\tau)$ and $\eta(\tau)$ can take a more general form of $\tau(\log\tau)^m$, $\exp(-1/\tau)$, and τ^α, where α is real [30]. $\xi(\tau)$ and $\eta(\tau)$ may also have nonalgebraic singularities provided that these functions are continuous at $t = 0+$. For $\omega \to \infty$, each term of the series vanishes. This is as expected, for there is no classical diffracted geometric-optics field [30]. The leading term for large ω may well serve as the geometric optics diffracted field. For a special case, using a Laplace transform pair, we obtain

$$h_n(\tau) = \begin{cases} \dfrac{1}{\sqrt{\tau}} \displaystyle\sum_{m=0}^{\infty} \frac{D_m}{m!} (\tau - \tau_0)^m, & \tau > \tau_0, \\ 0, & \tau < \tau_0, \end{cases} \qquad (2.83)$$

$$H_n(\omega) = \sum_{m=0}^{\infty} \frac{D_m}{(j\omega)^{m+1/2}} \Gamma\left(m + \frac{3}{2}\right).$$

The primary term in (2.83) is sufficient in practice (e.g., GTD/UTD series). Now consider the physics-based generalized multipath model of a form in the following:

$$H(\omega) = \sum_{n=1}^{N} A_n (j\omega)^{\alpha_n} e^{j\omega\tau_n}, \qquad h(\tau) = \sum_{n=1}^{N} \frac{A_n}{\Gamma(-\alpha_n)} \tau^{-(1+\alpha_n)} U(\tau) \bigotimes \delta(\tau - \tau_n), \qquad (2.84)$$

where α_n is a real value, $H_n(j\omega) = (j\omega)^{\alpha_n}$, and $h_n(\tau) = \tau^{-(1+\alpha_n)} U(\tau)$. $U(x)$ is Heaviside's unit function. This model is asymptotically valid for incident, reflected, singly diffracted, and multiply reflected/diffracted ray path field. The motivation of using the function in (2.84) is its simplicity and feasibility for a large category of problems. This form can allow us to use the powerful mathematical tool of fractional calculus [70, 71] to conveniently describe our problems. Equation (2.80) gives a formal generic mathematical model for $h(\tau)$. A large category of problems can be described by per-path impulse-response $h_n(\tau)$ given by (2.81). In (2.84), we can model α_n as the random variables that can be experimentally measured. The amplitudes and delays can be statistically described similarly to the Turin's model.

As an example, in Figure 2.4, we obtain the pulse waveform distortion as a function of α for one generalized multipath defined by its impulse-response $\tau^\alpha U(\tau)$. The incident pulse waveform is the second-order derivative of a Gaussian function (corresponding to the curve of $\alpha = 0$). Usually, a matched filter is required for an optimum reception (see next subsection), so the new changed

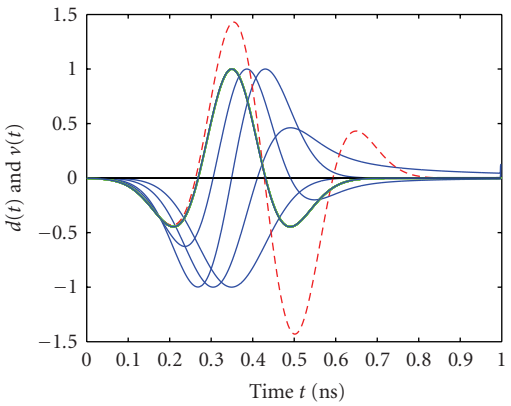

FIGURE 2.4. Pulse waveform distortion as a function of α for one generalized multipath.

waveform after the incident pulse passing through the sole generalized multipath is needed and calculated in Figure 2.4. For a pulse position modulation, a template pulse consisting of the incident pulse and its negative delayed version is used for detection. This template pulse is only proper when the pulse waveform is not changed by the channel. When a pulse is distorted by passing through a generalized multipath, then the pulse waveform is changed to a new waveform. Thus a new template formed by the new changed waveform and its delayed version should be used [47, 48].

2.3.6. Impact of propagation processes on optimum receiver structures

We will incorporate the per-path impulse-response into the optimal receiver when intersymbol interference (ISI) is present. For pulse amplitude modulation (which encompasses PSK, QAM, etc.), the transmitted signals have the same form [43] as $s(t) = \sum_{n=0}^{\infty} a_n x(t - nT)$, where a_n represents the discrete information symbol sequence with symbol duration of T, and $x(t)$ is a pulse that is bandlimited. The channel impulse-response $h(\tau)$ is illustrated in Figure 2.3 for the generalized multipath (see Section 2.3.5). The receiver signals are represented as

$$r(t) = \sum_{n=0}^{\infty} a_n y(t - nT) + n(t), \tag{2.85}$$

where $n(t)$ is AWGN. The received symbol signal waveform is $y(t) = h(t) \otimes x(t)$, consisting of a sequence of distorted pulses described by $h(t)$ defined by (2.80). It has been shown that the optimum receiver structure is illustrated in Figure 2.5. The received signal $r(t)$ first passes the matched filter followed by a sampler of sampling rate of $1/T$. The sampled sequence is further processed by a maximum likelihood sequential estimation (MLSE) detector. This receiver structure is optimal in terms of minimizing the probability of transmission error in detecting the information sequence. If we accept the condition that $y(t)$ is finite in the UWB

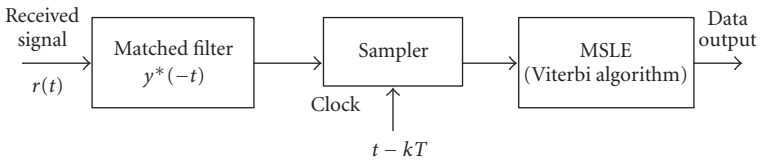

FIGURE 2.5. Optimal receiver structure in presence of ISI in an AWGN channel.

receiver, this structure can immediately be applied to our problem. The output of the matched filter is expressed as

$$q(t) = \sum_{n=0}^{\infty} a_n R_{yy}(t - nT) + v(t), \tag{2.86}$$

where $R_{yy}(t) = y(t) \otimes y^*(-t) = R_{xx}(t) \otimes h(t) \otimes h^*(-t)$ is the autocorrelation of $y(t)$ and $v(t)$ is the response of the matched filter to AWGN noise $n(t)$. $R_{xx}(t)$ is the autocorrelation of $x(t)$. Pulse distortion will affect the optimal energy collection in matched filter. The sampled values at $t = nT$ can be expressed as

$$q_k = a_k + \sum_{n=0,\, n\neq k}^{\infty} a_n R_{k-n} + v_k, \tag{2.87}$$

where a_k term represents the expected information symbol of the kth sampling period, the second term is the ISI, and v_k is the additive Gaussian variable at the kth sampling point. The sequence of q_k will be further processed by MSLE (Viterbi algorithm) before being sent to decision circuits. After pulse distortion is taken into account in the ISI through (2.86) and (2.87), all the rest of analysis follows the conventional case [43] when Turin's model rather than (2.80) is used for $h(t)$.

The suboptimum implementation of the matched filter is the Rake receiver structure. Suboptimum linear equalizers such as zero-forcing, decision-feedback, adaptive equalization can be used to replace the optimum MSLE. Since the per-path pulse waveform has been included in the channel impulse-response (illustrated in Figure 2.3), the resultant matched filter is sometimes called "generalized Rake" receiver structure [45], which is a generalization of Altes' receiver structure [72].

Appendix

2.3.A. Representation of pulse distortion using fractional calculus

Following Sommerfeld [24], Lamb [25] and Friedlander [26] analytically and numerically studied the pulse distortion caused by diffraction at a half-plane for sound pulses. Friedlander transformed Lamb's result into Abel's integral equation, which is the classical result in fractional calculus, and is thus a good starting point

for us to apply fractional calculus in UWB communications.[14] We can readily represent their formulation in terms of the Rieman-Liouville fractional differintegral $(d/dt)^{\nu}$, which can be defined as

$$(d/dt)^{\nu} f(t) \equiv {}_0 D_t^{\nu} f(t) \equiv \left[\frac{1}{\Gamma(-\nu)} t^{-(1+\nu)} U(t)\right] \bigotimes f(t), \quad \nu < 0, \tag{2.88}$$

where ν is negative and real. For fractional $\nu > 0$, the above definition can be applied with additional step ${}_0D_t^{\nu} f(t) = (d/dt)^m {}_0D_t^{\nu-m} f(t)$, where m is a positive integer large enough so that $(\nu - m) < 0$. According to (2.88), we find that $(j\omega)^{\nu} F(j\omega)$ is the Fourier transform of ${}_0D_t^{\nu} f(t)$. When ν assumes an integer value, $(d/dt)^{\nu}$ or ${}_0D_t^{\nu}$ reduces to the ordinary Riemann integral $\nu = n$, where n is an (positive or negative) integer. This new tool provides a powerful means to describe the pulse distortion. For example, for the PEC wedge and half-plane (a special case of wedge), we have $\nu = \alpha = -1/2$. For the generalized multipath signals in (2.84), we have $\alpha = \alpha_n$ for the nth path. So (2.84) can be expressed in a new form as

$$h(\tau) = \sum_{n=1}^{N} A_n \left(\frac{d}{d\tau}\right)^{\alpha_n} \delta(\tau) \bigotimes \delta(\tau - \tau_n), \tag{2.89}$$

where α_n is an arbitrary real number. When a pulse $p(t)$ passes through the channel, the new pulse is

$$r(t) = \sum_{n=1}^{N} A_n \left(\frac{d}{dt}\right)^{\alpha_n} p(t) \bigotimes \delta(t - \tau_n), \tag{2.90}$$

According to (2.89) and (2.90), after a pulse travels through a generalized multipath, its waveform will be changed and represented by the fractional differintegral $(d/dt)^{\alpha_n}$ of this pulse. The delay of this pulse is similarly modeled as in Turin's model [52] which ignores the effect of the fractional differintegral $(d/dt)^{\alpha_n}$ of this pulse on the incident pulse. The fractional differintegral has a lot of desirable properties that greatly simplify the analytical and numerical analysis of the signals in (2.90) [45].

2.4. Path loss and shadowing

2.4.1. Introduction

Path loss models give an accurate estimate of the power level as a function of the transmitter-receiver separation distance. Therefore, path loss models constitute the basis for link budget calculations, since they allow the calculation of the SNR

[14] In electromagnetics, Engheta appeared to be the first to use fractional calculus [73].

or the C/I in different locations in the area in which the assumed path loss model holds. Analysis and simulations based on link budget calculations are usually required to evaluate the coverage and the capacity of the system under test. Indeed, mobile radio systems tend to be interference limited (due to other users sharing the same/adjacent channels) rather than noise limited, and this kind of studies permits to predict the effects of the interfering signals that a user will experience from other RF sources.

This issue becomes more critical for UWB systems, since they are committed to coexist with other systems sharing the RF spectrum without significantly degrading their performance. The total interference to the radio systems can be limited reducing the number of active UWB devices in the area, that is, limiting the capacity of the UWB systems, or reducing the power emitted by each single UWB device, as the current regulation establishes.

In this context, the propagation losses may have two counteracting effects:

(i) a reduction of the interference power detected by the victim receiver, which facilitates the coexistence of UWB with other RF systems;

(ii) a degradation of the UWB signal that may be significant since the UWB transmitted power cannot exceed the threshold imposed by the current regulation; thus, the UWB communication link may be seriously compromised.

Link budget analyses based on accurate path loss models for UWB channels give deeper insights about the coexistence/capacity issues for UWB systems. Furthermore, accurate path loss models permit to design a reliable radio system with a reduced link margin.

Propagation models that predict the signal strength can be divided into two categories:

(i) *large-scale models* which predict the signal power over large transmitter-receiver separation distances (several hundreds or thousands of meters in outdoors—tens of meters in indoors);

(ii) *Small-scale models* (also called fast fading), which characterize the actual signal power over very short distances (up to 15 or 30 meters in outdoors—up to a few meters in indoors).

At the small scale, variations are very rapid and the signal may have deep fades (e.g., 30 or 40 dB) when the receiver is moved just a fraction of a wavelength of the radiated signal. Small-scale fading is due to the multipath propagation, that is, many reflected replicas of the transmitted signal combine at the receiver with a different phase (related to the different travelling distance). When the phases are close, the waves add up and the result is a gain in power, but when the phases are opposite (180° apart), then the waves cancel each other and a deep fade occurs. The small-scale models will be treated in more detail in the subsequent Section 2.5.

Large-scale propagation models, instead, predict the *local average power*, that is, the average power of the small-scale variations. Indeed, the power measurements used to develop these models are averaged over short distances. Becoming more specific, the mean value of the power level as a function of distance is provided by *path loss models*. In practice, the signal level statistically fluctuates around

the deterministic value given by the path loss laws, due to the presence of obstacles and objects around the transmitter and the receiver. This statistical behavior is referred to as the *shadowing*.

The path loss law and the shadowing behavior vary depending on the carrier frequency and the signal bandwidth. Furthermore, they strongly depend on the propagation environment. At the moment, the only available analysis which statistically models the variability of path loss and shadowing laws with the propagation environment applies to *residential environments* [74, 75].

In this chapter, we summarize the most recent contributions to measurements and path loss models for UWB channels in typical propagation scenarios [74–85]. Measurements have been conducted also within some of the projects of the IST program of the European Community, Fifth Framework [86, 87]. Furthermore, the standardization groups SG3a and SG4a, established within the IEEE 802.15 to propose PHY layers potentially based on UWB technology, are working to set up standard models of the UWB channel in order to fairly evaluate and optimize the system proposals. The propagation model for the IEEE 802.15.3a standard has been already selected and holds in residential/office environments over areas of the order of 10 m (see also Section 2.6). The model for the IEEE 802.15.SG4a, instead, is currently in progress.[15]

Most of the path loss and shadowing models for UWB channels are based on extensions of narrowband models. However, since the bandwidth of UWB signals may extend for several GHz, the frequency dependence of diffraction/reflection coefficients, dielectric constants, and so forth, can be significant in the band of interest. Some measurement campaigns over very wide bandwidths have permitted to investigate on the frequency dependence of the UWB path loss laws and some models have been proposed [76, 78, 84].

This chapter section is organized as follows. In Section 2.4.2, we describe the typical UWB scenarios based on the envisaged applications for this technology. In Sections 2.4.3 and 2.4.4, we review the measurements and models for the path loss and shadowing presented in the literature for the UWB channel. Finally, in Section 2.4.5, we discuss about the *standard* models for path loss and shadowing already adopted for the high data-rate standard (IEEE 802.15.3a) and currently in progress for the low-data-rate standard (IEEE 802.15.4a).

2.4.2. Typical propagation environments for UWB applications

The UWB propagation environments are various, since the envisioned UWB applications are numerous and each of them addresses a typical operation scenario.

(i) The use of a very wide bandwidth makes the UWB technology very attractive for *high-data-rate PANs*, including data and high-quality video transmissions. The regulation limits on the power spectral density and the quality-of-service requirements limit the coverage area of these UWB

[15] The selection of different models for these standards is necessary because they address different UWB applications which have their own scenarios and environments.

devices. Therefore, a typical propagation environment for such applications is a small area with a radius on the order of 10 m within residential or office buildings.

(ii) Low power consumption and locationing capability, instead, make UWB technology suitable for application in *sensor networks*. As the data rates are much lower in this context, larger coverage areas are served. Typical environments for sensor networks can be home/office as well as factories, grocery stores, and so forth, where "indoor" distances can be larger. However, sensor networks find applications also in the WBANs having typical ranges of 1–2 m, or as cable replacement in the vehicles, whose typical ranges are on the order of 5–10 m.

(iii) Another attractive application for UWB is *emergency communications*, possibly combined with geolocation, for example, from a building that collapsed during an earthquake, or from an avalanche. Required distance can be up to 100 m in outdoor environments.

At the moment, however, only measurement data and models for indoor office/residential environments are available; for the other environments, some campaigns are in progress, but not yet finalized.

2.4.3. Path loss laws

The path loss ($\overline{\mathrm{PL}}$) denotes the *local average* received signal power relative to the transmit power. From electromagnetic field theory, the *free-space path loss*, $\overline{\mathrm{PL}}_{\mathrm{FS}}$, is expressed as

$$\overline{\mathrm{PL}}_{\mathrm{FS}}(\lambda, d) = \left(\frac{4\pi d}{\lambda}\right)^2, \tag{2.91}$$

which is a function of the distance d and the wavelength λ of the radiated signal. The free-space path loss model, which is a square law with the transmitter-receiver distance, applies to an ideal situation in which the electromagnetic field propagates in the absence of ground/obstacles' reflections, multipath propagation, and so forth.

A more general path loss model uses a parameter, n, to denote the power law relationship between the transmitter-receiver separation distance d and the received power:

$$\overline{\mathrm{PL}}(d) \propto \left(\frac{d}{d_0}\right)^n, \tag{2.92}$$

where $\overline{\mathrm{PL}}$ is the mean path loss, n is the mean path loss exponent, which indicates how fast path loss increases with distance ($n = 2$ for free-space propagation) and d_0 is a reference distance.

Absolute mean path loss, in decibels, is defined as the path loss from the transmitter to the reference distance d_0, plus the additional path loss described by (2.92)

Table 2.1. Path loss exponents and standard deviations measured in different buildings.

Building	Frequency (MHz)	n	σ (dB)
Retail stores	914	2.2	8.7
Grocery store	914	1.8	5.2
Office, hard partition	1500	3.0	7.0
Office, soft partition	900	2.4	9.6
Office, soft partition	1900	2.6	14.1
Textile/chemical	1300	2.0	3.0
Textile/chemical	1400	2.1	7.0
Paper/cereals	1300	1.8	6.0
Metalworking	1300	1.6	5.8
Indoor to street	900	3.0	7.0
Textile/chemical	4000	2.1	9.7
Metalworking	1300	3.3	6.8

in decibels:

$$\overline{\mathrm{PL}}(d)\,(\mathrm{dB}) = \mathrm{PL}\,(d_0)\,(\mathrm{dB}) + 10 \times n \times \log_{10}\left(\frac{d}{d_0}\right). \tag{2.93}$$

Generalizing (2.91), the frequency dependence of path loss is also included [88, 86]:

$$\overline{\mathrm{PL}}(f, d) \propto d^n \cdot f^m. \tag{2.94}$$

Note that the distance dependence and the frequency dependence can have different exponents, that is, $n \neq m$.

In general, the exponent n is extracted by performing a linear regression of the path loss values expressed in dB versus the logarithm of the distance. The path loss values are computed from the experimental data by integrating the total signal power received at a given location at a distance d and then normalizing it to the transmitted power, when available, or to the signal power received at the reference distance d_0.[16] More accurate models average these values over a number of realizations to remove the effects of the small-scale statistics (see Section 2.4.3.2).

Typical values of path loss exponents and standard deviations (shadowing) for different classes of buildings are given in the literature. In general, values of $n < 2$ are given for indoor LOS propagation and $n > 2$ for indoor NLOS conditions. Table 2.1 provides a range of typical values that have been measured in the past using narrowband probing signals [1].

The presented models apply to narrowband signals and are largely employed to the analysis of narrowband systems. However, some of those models are based on measurements with probing signals having a bandwidth ranging from 200 MHz to 1 GHz and can work as starting points for UWB studies, since they characterize environments of interest for the UWB envisaged scenarios.

[16] In that case $\overline{\mathrm{PL}}(d_0) = 0$ in (2.93).

Measurements over a bandwidth of 200 MHz around 1 GHz over an area of about 50 m radius have been carried out in a high-rise office building and a three-story building with offices and laboratories, leading to an average path loss exponent of $n_{av} = 2.4$ and a lognormal shadowing with a standard deviation from 2.82 to 4.56 dB [89, 90].

Experiments have been also performed in factory buildings in LOS and OBS over distances from 25 to 75 m; the probing signal had a bandwidth of 400 MHz around 1.3 GHz [91–93]. The path loss exponents vary from 1.8 to 2.8, with an average of $n_{av} = 2.2$.

A measurement campaign at 1.5 GHz over a bandwidth of 200 MHz in a medium-size two-story building at distances up to 50 m has reported a path loss exponent of $n = 3$ or $n = 4$ [94].

In [95] a path loss model with n between 1.8 and 2.1 is provided for office environments for LOS, OBS, and NLOS for the band 4.5-5.5 GHz; furthermore, the penetration losses for walls of 10 cm and 20 cm thickness are estimated to be 16 dB and 29 dB, respectively.

Measurements in LOS conditions over a band of 400 MHz centered at 1 GHz, 5.5 GHz, and 10 GHz in an office environment (rooms are delimited mostly by smooth metallic walls) have shown path loss exponents of 1.27, 1.49, and 1.26, respectively, which seems to be quite independent from the carrier frequency [96]. Similar conclusions have been drawn in [97] for LOS conditions in a laboratory/office environment over distances up to 30 m, while the OBS measurements have shown that the path loss exponent increases with the increasing frequency. Those measurements were made at 2.4 GHz and 4.75 GHz with a probing signal of 500 MHz bandwidth and at 11.5 GHz with a bandwidth of 1 GHz, obtaining path loss exponents of, respectively, 1.86, 1.98, and 1.94 for LOS and 3.33, 3.75, and 4.46 for OBS.

Path loss exponents of 1.5, 1.7, and 1.6 have been measured at 2 GHz, 5 GHz, and 17 GHz with a 500 MHz bandwidth in LOS conditions in a laboratory and the adjoining corridor at the University of Swansea (UK); in OBS conditions, instead, the attenuation increases with frequency [98].

Many experimental and theoretical activities (currently in progress) are devoted to understand if a simple extension of those models by just changing the parameters can accurately models the UWB path loss and shadowing.

As explained in the following sections, many contributions confirmed the power law with the distance, with exponents comparable with the narrowband propagation. However, the frequency dependence of path loss becomes a critical issue in UWB channels.

2.4.3.1. Distance dependence

The distance dependence of path loss for UWB signals is usually modelled by (2.93), in which the parameter n is extracted by UWB experimental data. As in narrowband cases, the path loss exponent depends on the environment and the

Table 2.2. Parameters of the model in [74].

	LOS		NLOS	
	Mean	Std. dev.	Mean	Std. dev.
PL_0 (dB)	47	NA	50.5	NA
n	1.7	0.3	3.5	0.97
σ (dB)	1.6	0.5	2.7	0.98

propagation conditions. Some models differentiate between LOS, "soft" NLOS, also known as "obstructed" LOS, and "hard" NLOS.

LOS exponents in indoor environments range from 1.0 in a narrow corridor [86] to about 2 in an office environment [77, 81, 87].

NLOS exponents typically range from 3 to 4 for soft NLOS [77, 81, 87] and from 4 to 7 for hard NLOS [79, 86].

In [86] the path loss exponents for the three LOS, soft NLOS, and hard NLOS conditions are reported for more than sixteen scenarios in typical European office buildings for distances up to 20 m.

In [82, 74, 75] the path loss exponent is modelled as a random variable that varies from building to building in residential environments in the US for distances up to 10 m. They also found that the empirical distribution of this random variable is well approximated by a Gaussian distribution whose parameters (mean values and standard deviations) are summarized in Table 2.2.

The model in (2.93), which assumes a linear dependence between the path loss (dB) and the logarithm of distance, is usually referred to as *"single-slope" model*. In [80] the single-slope model has not given a good agreement with the experimental values, yielding a too large value for the exponent n. A more accurate model than the single-slope has been proposed taking into account separately the effect of the distance and the attenuations introduced by the walls intercepted by the direct path, that is,

$$\overline{\mathrm{PL}}_{M_w}(d)\,(\mathrm{dB}) = \overline{\mathrm{PL}}(d)\ \ (\mathrm{dB}) + M_w\,(\mathrm{dB}), \tag{2.95}$$

where M_w is the *multiwall component* [80].

Such a *multiwall model* requires to evaluate the number and the nature of the obstacles traversed by the direct path for each measurement. The model distinguishes between NLOS and hard NLOS, defining the multiwall component M_w as

$$M_w(dB) = \begin{cases} k \cdot l_1 & \text{for NLOS,} \\ l_c & \text{for hard NLOS,} \end{cases} \tag{2.96}$$

where $k = 1, \ldots, 4$ is the *number* of penetrated walls having attenuation $l_1 = 6.25\,\mathrm{dB}$ and $l_c = 26.25\,\mathrm{dB}$ is a constant accounting for the cumulative effect of the extremely heterogenous series of obstacles present in the hard NLOS link. The

number k of walls intercepted by the direct path when the distance is d can be defined looking at the considered environment [80]. The dependence on distance is still modelled by (2.93) with an exponent $n = 7.33$.

Finally, a multislope path loss model has been proposed in [99], in which the breakpoint(s) is obtained by theoretical derivations. In particular, assuming that the transmitted signal reaches the receiver through a multitude of paths, L, having different path lengths $\{d + \Delta d_i\}$, $i = 1, 2, \ldots, L$, equation (2.93) can be expressed as

$$\overline{\mathrm{PL}}(d) \propto 20\log_{10}(d) - 10\log_{10}\sum_{i=1}^{L}\left(1 + \frac{\Delta d_i}{d}\right)^{-2}. \tag{2.97}$$

Differentiating (2.97), with some algebra, the breakpoint d_{bp} is easily derived to be

$$d_{\mathrm{bp}} \approx \frac{3 - 2\Omega/20}{1 - \Omega/20} \cdot \frac{\sum_{i=1}^{L} \Delta d_i}{L}. \tag{2.98}$$

The breakpoint d_{bp} separates the region where the path loss increases of Ω dB/dec (with distance) from the region where a slope of 20 dB/dec (free space) is assumed. A dual-slope model has also been proposed in [79], obtained by fitting experimental path loss values.

2.4.3.2. Frequency dependence

In narrowband channels, the path loss at a distance d is defined as in (2.94) and is calculated from experimental data by

$$\overline{\mathrm{PL}}(d) = \frac{E\{P_{\mathrm{RX}}(d)\}}{P_{\mathrm{TX}}} = E\left\{\left|H(f_c, d)\right|^2\right\}, \tag{2.99}$$

where P_{TX} and P_{RX} are the transmitted and received power, respectively, f_c is the carrier frequency and $H(f, d)$ is the frequency response of the radio channel [100]. The values of $\{P_{RXi}(d)\}$, or the values of the $\{H_i(f_c, d)\}$, measured over a small area at a distance d from the transmitter, are averaged in order to "remove" the effects of small-scale variations of the signal level.

In wideband channels [100], the path loss is obtained by integrating the channel frequency response over the frequency band of interest $[f_1, f_2]$:

$$\overline{\mathrm{PL}}(d) = E\left\{\int_{f_1}^{f_2} \left|H(f, d)\right|^2 df\right\}. \tag{2.100}$$

Indeed, when the band of interest is such that the frequency dependence of the propagation parameters is negligible, this integration is equivalent to averaging over the multipath fading.

In a UWB channel, instead, the frequency dependence of the propagation parameters can be significant. It is well known that also the antennas' gain (or, equivalently, their effective areas) is a function of frequency, and often it is not possible in the experimental channel responses to isolate the channel behavior from the antennas responses.

Reference [100] defines a *frequency-dependent path loss* as

$$\overline{\mathrm{PL}}(f,d) = E\left\{ \int_{f-\Delta f/2}^{f+\Delta f/2} |H(\zeta,d)|^2 d\zeta \right\}, \tag{2.101}$$

where Δf is small enough that diffraction/reflection coefficients can be considered constant in Δf. The *total* (frequency-averaged) path loss may be obtained by integrating over the whole bandwidth of interest [100].

Many measurement campaigns have observed very large bands, such as 2–8 GHz [83, 101], 1–11 GHz [84], 1–13 GHz [76], and 2–12 GHz [78]. Some of the UWB models that have been developed based on these campaigns assume that the path loss dependence on frequency and distance may be expressed, similarly to the narrowband case (2.94), by the product of two independent functions of frequency and distance:

$$\overline{\mathrm{PL}}(f,d) = \overline{\mathrm{PL}_f}(f) \cdot \overline{\mathrm{PL}_d}(d). \tag{2.102}$$

Reference [84] models the frequency dependence of path loss as

$$\sqrt{\overline{\mathrm{PL}_f}(f)} \propto f^{-m}, \tag{2.103}$$

where m varies between 0.8 and 1.4.

Reference [76] instead proposes

$$\log_{10}\left(\overline{\mathrm{PL}_f}(f)\right) \propto \exp(-\delta f), \tag{2.104}$$

with δ varying between 1.0 (LOS) and 1.4 (NLOS).

In [78] the frequency dependence of path loss is modelled implicitly through the frequency dependence of the path loss exponent that gives the dependence on distance. This analysis distinguishes between LOS and NLOS path loss: in LOS conditions in the corridor, the exponent is about 1.5 and increases with the increasing frequency, while within the lab the exponent is about 1.0 and still increases with the increasing frequency; in NLOS conditions, instead, the exponent varies from 2 to 6 diminishing with the increasing frequency with a decay that is well approximated by a third-order polynomial.

2.4.4. Shadowing

Shadowing, or large-scale fading, is defined as the variation of the local attenuation around the deterministic mean value given by the path loss law.

Some measurement campaigns have shown that the UWB shadowing is fairly similar to the narrowband case. Many contributions in the literature are consistent in assuming the narrowband shadowing to be lognormally distributed, with different values of the standard deviation, since it strongly depends on the measurement environment.

To be more specific, once that the variations of the mean of the power measurements (in dB) have been fitted to a straight line, which represents the path loss model as a power of distance, there remains the task of characterizing the distribution of the samples P_i around their mean $\hat{P}_i$ at a given radial distance. In terms of the residual errors, e_i, we can write, in general,

$$P_i = \hat{P}_i + e_i. \tag{2.105}$$

At a given radial distance, it is found that the e_i's obey the normal distribution with mean = 0 dB and a standard deviation σ, that is, $N(0, \sigma)$, leading to

$$\mathrm{PL}(d)\,(\mathrm{dB}) = \overline{\mathrm{PL}}(d) + X_\sigma = \overline{\mathrm{PL}}(d_0) + 10n\log_{10}\left(\frac{d}{d_0}\right) + X_\sigma, \tag{2.106}$$

where the term $X_\sigma \sim N(0, \sigma)$ represents the shadowing.

Some UWB models also assume a lognormal distribution for shadowing [79]. For indoor conditions, the standard deviation of shadowing is easily derived from the scatter plot of the measured path loss data.

More exhaustively, [74] suggests to model the shadowing variance as a random variable; σ^2 is modeled as normally distributed with realizations that change from house to house. The total attenuation due to shadowing and path loss is then expressed as:

$$\left[\,\mathrm{PL}_0 + 10\mu_n\log_{10}(d)\right] + \left[10n_1\sigma_n\log_{10}(d) + n_2\mu_\sigma + n_2n_3\sigma_\sigma\right], \tag{2.107}$$

where n_1, n_2, and n_3 are zero-mean, unit-variance Gaussian variables, but with a recommendation to limit n_1 to the range $[-0.75, 0.75]$ and n_2, n_3 to the range $[-2, 2]$ to avoid nonphysical values of the attenuation. The other parameters (i.e., the mean values of n and σ, μ_n, and μ_σ, resp., and their standard deviations, σ_n, and σ_σ, resp.) can be found in Table 2.2.

2.4.5. Standard models for UWB path loss and shadowing

Standard models are established to fairly evaluate different system architectures, as well as to assess the benefits of different transceiver structures, alternative multiple access techniques, and so forth.

The only UWB standard model presently available has been selected by the IEEE 802.15.SG3a. The ith realization of the channel impulse-response, $h_i(t)$, is

defined as

$$h_i(t) = X_i \sum_{l=0}^{L} \sum_{k=0}^{K} a_{k,l}^{i} \delta(t - T_l^i - \tau_{k,l}^i), \tag{2.108}$$

where $a_{k,l}^i$ are the tap weights, X_i represents the lognormal shadowing, K is the number of rays within the l-th cluster, and L is the number of ray clusters. A detailed description of the model can be found in Section 2.6 as well as [102], while here we concentrate on the UWB standard models for path loss and shadowing.

The lognormal shadowing of the total multipath energy is captured by the term X_i characterized by

$$20 \log_{10}(X_i) \propto N(0, \sigma_x^2), \tag{2.109}$$

where the standard deviation σ_x is 3 dB.

The recommended path loss model is the one presented in [74, 103] and described above, even if a free-space path loss model has also been specified and has mostly been used within the standardization.

In September 2003, standardization activities started for low-data-rate UWB communications, in the IEEE 802.15.4a group, which established a channel modelling subgroup. This subgroup is currently working on formulating an appropriate UWB channel model for this standard, which presents many differences with the 802.15.3a. Specifically, the considered ranges are much larger (up to 100 m), and the environments will include factories, storage halls, and so forth. The path loss model will follow the general principles outlined above, though the exact parameters still need to be specified.

2.5. Delay dispersion and small-scale fading

2.5.1. Introduction

Delay dispersion and small-scale fading are those effects of the channel where the UWB propagation channel differs most significantly from narrowband channels. Delay dispersion is defined to occur when the channel impulse-response has a finite support, that is, lasts for a finite amount of time. Equivalently, the channel can be said to be frequency-selective, that is, the transfer function depends on the considered frequency. The impact of the delay dispersion on a specific system is given by the product of the delay spread with the system bandwidth. If that product is much less than unity, then delay dispersion has little effect on the system design [104]. The larger this product, the stronger the impact of the delay dispersion on the system performance. In UWB systems with large absolute bandwidth, this impact is consequently very high. We find the following.

(1) The available delay diversity order is very high. A Rake receiver (or equivalent structure) with a large number of fingers can effectively eliminate

fading [105]. It is well known that appropriately combining the signal copies from many independently fading processes approximates an AWGN signal [106].

(2) When Rake receivers are used, the number of fingers required to collect all multipath energy is considerable. Reference [107] observed that the number of MPCs that are within 10 dB of the maximum is 3–4 in LOS, but 15–100 in NLOS situations. Thus, practical receivers, which have a finite number of Rake fingers, suffer from suboptimal energy collection. Thus, one of the greatest strengths of UWB, namely, its fine delay resolution, can become a weakness. Solutions to this problem include the use "selective Rake receivers" that collect only the instantaneously strongest paths [108, 109], transmitted-reference schemes [108, 110], orthogonal frequency division multiplexing [111], and Rake receivers with a very large number of fingers that are made practical by using single-bit A/D converters [112].

In narrowband channels, delay dispersion stems only from the multipath propagation, that is, the arriving signal can be viewed as a sum of weighted and delayed echoes of the transmit signal. In UWB channels, delay dispersion can also stem from the fact that the interaction between the waves and a single object (e.g., diffraction at a corner) is frequency-selective, see Section 2.3. We also find two other important differences to narrowband channels:

(1) the impulse-response of the channel can become sparse, in other words, there are "empty" delay bins (bins containing no energy) between the arriving multipath components,

(2) only few multipath components fall into each delay bin; that implies that the central limit theorem is not fulfilled anymore, and the amplitude fading statistics for each resolvable bin are no longer Rayleigh.

2.5.2. Arrival statistics of multipath components

2.5.2.1. Poisson-based models

We first turn our attention to the statistics of the arrival times of the MPCs, while the path amplitudes and the distortions of each MPC by propagation effects will be treated later. The delays of the MPCs are determined by the runtime through the propagation environment. In the most simple case, where only single-interaction processes occur, those runtimes can be uniquely associated with the locations of the interacting objects (IOs).[17] For multiple interactions, the relationship becomes more complicated.

For a random model, the simplest assumption to make is that IOs are distributed in the environment uniformly according to a (multidimensional) Poisson process. This assumption leads to a distribution of the MPC arrival times T_m at

[17] In many papers, the word "scatterer" is broadly used to describe the objects that interact with the propagating waves. As the interaction processes can be specular reflection, diffuse scattering, or diffraction, we use here the more general term "interacting object" (IO).

the receiver as a *nonhomogeneous* one-dimensional Poisson process with an arrival rate that increases with delay. The increasing arrival rate arises because reflections with a large delay value arise from the many IOs located near an ellipse with large circumference, while reflections with a small delay value arise from IOs located near a smaller ellipse, which are fewer in number. In fact, in the two-dimensional case with a uniform density of IOs, the average number $m(t)$ of MPC arriving on or before t seconds after the time of arrival of the line-of-sight path is given by

$$m(t) = \frac{\pi}{4} D c^2 t \sqrt{t^2 - t_0^2}, \tag{2.110}$$

where D is the spatial density of IOs in the environment, c is the speed of light, and t_0 is the line-of-sight propagation time from the transmitter to receiver. The *arrival rate* $v(t)$ is the derivative of (2.110), given for $t > t_0$ by

$$v(t) = \frac{d}{dt} m(t) = \frac{\pi D c^2 (2t^2 - t_0^2)}{4\sqrt{t^2 - t_0^2}}. \tag{2.111}$$

Note that $v(t)$ is an increasing function of t, that is, the density of arrivals increases (on average) with increasing delay.

However, this phenomenon of increasing MPC density with increasing delay is counteracted by two other physical factors. First, the amplitudes of the MPCs decrease with delay, and second, the paths begin to overlap as their density increases. Thus, many engineers, starting with [113], have found that the more familiar *homogeneous* Poisson process, characterized by a constant arrival rate λ, suffices,

$$P(\tau_k - \tau_{k-1} > t) = \exp(-\lambda t). \tag{2.112}$$

In a slight abuse of notation, we can write that the probability density function for the arrival of path k (given a certain arrival time τ_{k-1} for the previous time) is

$$p(\tau_k | \tau_{k-1}) = \lambda \exp\left[-\lambda(\tau_k - \tau_{k-1}) \right], \quad k > 0. \tag{2.113}$$

For many environments, both indoor and outdoor, the assumption of uniformly distributed scatterers is not true. Rather, it has been observed frequently that MPCs arrive in "clusters"—that is, several MPCs arrive shortly one after the other, then there is a longer pause, and then another group of MPCs arrives.

One mathematical model that reflects this clustering is the $\Delta - K$ model, which was first suggested for the outdoor case, and popularized for the indoor case by [114]. It defines two states: state A, where the arrival rate of paths is λ, and state B, where the rate is $K\lambda$. The model starts in state A. If a path arrives at time t, then a transition is made to state B for a minimum duration Δ. If no path arrives during that time, the model reverts to state A; otherwise, it remains in state B. $\Delta - K$ models were used for UWB channels in [115, 116]. Note that both the number of clusters and the duration of the clusters become random variables in this model.

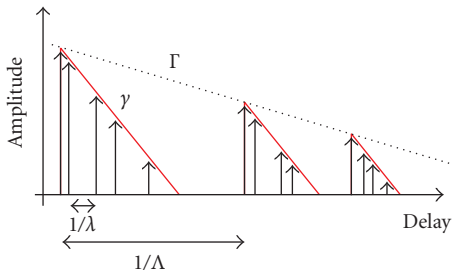

FIGURE 2.6. Principle of the Saleh-Valenzuela model.

An alternative model for the clustering is the Saleh-Valenzuela (SV) model [94], which uses the following discrete-time impulse-response:

$$h(t) = \sum_{l=0}^{L} \sum_{k=0}^{K} a_{k,l}\delta(t - T_l - \tau_{k,l}), \tag{2.114}$$

where $a_{k,l}$ is the tap weight of the kth component in the lth cluster, T_l is the delay of the lth cluster, $\tau_{k,l}$ is the delay of the kth MPC relative to the lth cluster arrival time T_l. By definition, we have $\tau_{0,l} = 0$. The distributions of the cluster arrival times and the ray arrival times are given by Poisson processes

$$\begin{aligned} p(T_l|T_{l-1}) &= \Lambda \exp\left[-\Lambda(T_l - T_{l-1})\right], \quad l > 0, \\ p(\tau_{k,l}|\tau_{(k-1),l}) &= \lambda \exp\left[-\lambda(\tau_{k,l} - \tau_{(k-1),l})\right], \quad k > 0, \end{aligned} \tag{2.115}$$

where Λ is the cluster arrival rate, and λ is the ray arrival rate. Figure 2.6 shows the different parameters and their meaning. The SV model has been used in several papers, among them [117–119].

When comparing the $\Delta - K$ model and the SV model, we find some important differences. In the $\Delta - K$ model, the number of clusters is a random variable, whose realization is determined by how often system enters into state B; in the "classical" SV model, the number of clusters is a constant that is a model parameter.[18] In the SV model, the clusters can overlap; if the product of cluster arrival rate and cluster delay spread is much larger than unity, it even becomes difficult to see with the naked eye where one cluster begins and another one ends.

Due to these reasons, the extraction of the number of clusters in an SV model is a rather ambiguous procedure. It is often a somewhat arbitrary decision whether to consider a (reasonably continuous) power delay profile as a superposition of several closely spaced clusters, or as a single cluster. This has naturally a great impact on the number of clusters as well as the intercluster decay time constants.

[18]Modifications of the SV model exist that assume the number of clusters to be a Poisson-distributed random variable.

Spatially resolved measurements, like those of [101], are helpful in resolving this ambiguity, as the directions of arrival offer an additional domain from which to determine whether MPCs are clustered or not.

The number of clusters is a function both of the measurement bandwidth, and of the considered environments

(i) Reference [79] found only one cluster for 1 GHz bandwidth in baseband in an indoor office environment.

(ii) Reference [77] found between one and three clusters for 2.4 GHz bandwidth centered around 5 GHz in indoor office environments.

(iii) Reference [75] measured mostly one cluster with a measurement bandwidth of 1.25 GHz around a center frequency of 5 GHz; for indoor residential and office environments. Two clusters were found in some special scenarios, especially corridors.

(iv) Reference [101] measured the number of clusters in offices and residential environments. As mentioned above, those measurements also used the spatial domain, which resulted in a finer resolution of clusters. They found 1–2 clusters in office LOS, up to 4 clusters in office NLOS, 1 cluster in residential LOS, and 1–2 clusters in residential NLOS. It is also interesting that the number of clusters slightly decreases for higher frequencies.

Measured cluster interarrival times are typically in the range of 10–50 nanoseconds ([118]: 45 nanoseconds in offices at baseband frequences, [117]: 16–25 nanoseconds in NLOS and 39 nanoseconds in LOS at 5 GHz center frequency, [119]: 11–14 nanoseconds mean arrival time in NLOS and 60 nanoseconds in LOS at 5 GHz center frequency.

Mean interpath arrival times, $1/\lambda$, show a wide variation, from 0.18 nanoseconds in NLOS situations to more than 20 nanoseconds in LOS situations [117]. It is noteworthy, however, that these values depend on the dynamic range of the measurement equipment, the SNR, and the evaluation procedure. Furthermore, it is difficult even with high-resolution algorithms to clearly resolve paths that have a delay difference much smaller than the inverse measurement bandwidth; thus measurements with lower bandwidth lead to higher interarrival times. Widely differing values (between 1 and 60 nanoseconds) have been reported for the intracluster decay constants γ.

Some authors have also analyzed the number of significant MPCs, by which they mean the number of MPCs that is above a certain threshold, or the number of components that carry a certain percentage (usually 90%) of the total energy. One example for such evaluations is [115], where a mean number of 36 MPCs was found for NLOS 0–4 m distance; the probability for a bin to be occupied by a "significant" MPC decreases from 0.6 for zero excess delay to 0.2 for 40-nanoseconds excess delay for a 0–4 m distance, and falling from 0.8 at 0-nanoseconds to 0 at 100-nanoseconds excess delay for NLOS at 4–10 m. Note that this is a remarkable difference to modeling all components, where the occupancy probability *increases* with increasing delay [84]. An alternative definition for the number of significant MPCs counts the MPCs that are no more than 10 dB below the maximum: [107]

measured 3-4 in LOS, but 15–30 in residential NLOS, and 50–100 in office NLOS situations.

2.5.2.2. Power delay profile

Besides the arrival times, we also have to define the power decay of the multipath components. The PDP is defined as the squared magnitude of the impulse-response, averaged over the small-scale fading [12]. When assuming furthermore that the channel is ergodic and any channel changes in the considered time scale come only from the small-scale fading, the PDP becomes [104][19]

$$P(\tau) = E_t\{\,|h(t,\tau)|^2\}, \tag{2.116}$$

where $E_t\{\cdot\}$ denotes expectation over time.

The most common model is an exponential decay, so that

$$P(\tau) = \frac{1}{\gamma_d}\exp\left(-\frac{\tau}{\gamma_d}\right)U(\tau), \tag{2.117}$$

where $U(\tau)$ is the Heaviside step function, and γ_d is the decay time constant.

In an SV-type model (2.114), where multiple clusters are present, it is usually assumed that each cluster is exponentially decaying, so that

$$E\{|a_{k,l}|^2\} = \Omega_0\exp\left(-\frac{T_l}{\Gamma}\right)\exp\left(-\frac{\tau_{k,l}}{\gamma}\right), \tag{2.118}$$

where Ω_0 is the mean energy of the first path of the first cluster, Γ is the intercluster decay time constant, and γ is the intracluster decay time constant.

Several measurement campaigns give only the rms delay spread, which is defined as the second central moment of the PDP.[20] Reference [115] shows a delay spread of 9 nanoseconds at 2 m for NLOS and 4 nanoseconds mean (delay spread) for NLOS, and a slight increase of the delay spread with distance (about 1 nanoseconds/m). Reference [120] measured rms delay spreads of 10 nanoseconds in LOS, and 22.7 nanoseconds in NLOS; the delay spread being strongly correlated with the path loss, and thus with the distance. Reference [107] measures an rms delay spread of 10.9 nanoseconds in LOS, 16.5 nanoseconds in NLOS, and 22.4 nanoseconds in hard NLOS in an office, and 12.2 nanoseconds in LOS, 9.9 nanoseconds in soft NLOS, and 12.9 nanoseconds in hard NLOS in residential. Reference [84] found a 14 nanoseconds decay time constant. All those measurements were done in the microwave range. Low-frequency (baseband) measurements in an indoor office environment indicate delay spreads around 40 nanoseconds [79]. Low-frequency measurements in outdoor forest areas show delay

[19] note that the definition of "power delay profile" in UWB channels is still subject to debate.

[20] For the case of a single cluster with exponential decay, the rms delay spread is identical to the decay time constant. However, for more general models (like SV), the rms delay spread is an insufficient description of the delay dispersion.

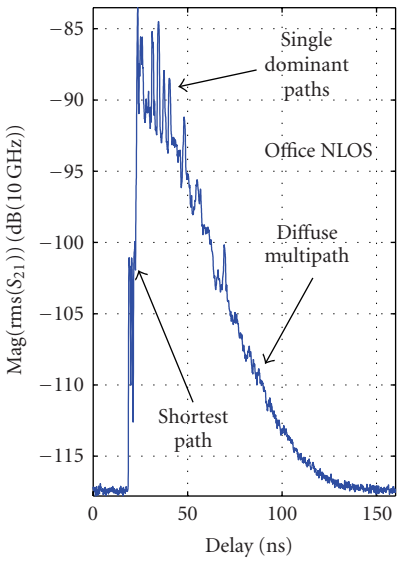

FIGURE 2.7. Measured indoor multipath intensity profile in the microwave range, from [84].

spreads between 30 and 50 nanoseconds in [121]. It is also notable that the delay spread is itself a random variable that changes between different rooms as well as different environments.

The delay spread and the PDP of ultra-wideband channels show little difference to the narrowband channels. Thus, the extensive results available from those narrowband measurements (for an overview, see, e.g., [7]) can be applied also in this case.

2.5.2.3. Semideterministic modeling

References [84, 122] have independently suggested a somewhat different modeling approach. In a first step, they establish *deterministic* components that are derived from an (existing or virtual) geometry, by means of ray tracing. For outdoor LOS environments, two deterministic components (direct wave and ground wave) are often sufficient [122], while for indoor environments, components that have undergone up to three reflections have to be taken into account [84], see Figure 2.7. In addition to the deterministic components, a Rayleigh-distributed "clutter" describes the contributions that stem from diffuse scattering and other propagation paths that are not covered by the ray tracing.

The model of [123] thus proceeds in the following steps.

(i) Compute the contributions from ray tracing in a simplified model geometry (e.g., box), taking into account up to threefold reflections. Limit the number of considered rays to K, and compute the attenuation for each of those rays from a power law d^{-n} (the parameter n is a model parameter).

(ii) Each of the rays is associated with a cluster of Rayleigh-fading MPCs; each cluster is exponentially decaying.

2.5.3. Fading of the multipath components

In the previous subsection, we have analyzed the mean behavior of the channel, that is, when averaged over measurement points within a small area. In this subsection, we analyze the statistical behavior of the amplitudes within such a small area. We can understand the occuring phenomena better by dividing the delay axis into "bins" with a width that is the inverse bandwidth. Components of the impulse-response that fall into one delay bin cannot be resolved by the system, and are thus seen as a single (but fading) component.

In conventional narrowband, bandpass wireless systems, it is well established that the amplitudes in delay bins are Rayleigh-fading

$$\mathrm{pdf}(x) = \frac{x}{\sigma^2} \exp\left(-\frac{x^2}{2\sigma^2}\right), \tag{2.119}$$

or possibly Rician-fading for the LOS component. The Rayleigh fading is created by the superposition of many multipath components within each delay bin, so that the in-phase and quadrature-phase components each are Gaussian. In UWB systems, the number of components falling within each delay bin is much smaller, which leads to a change in the statistics. Various alternative distributions have been used in the literature.

Nakagami distribution. This amplitude distribution was suggested in [79] (see Figure 2.9), and was also confirmed in [77], and by [84] for bins with large delays. The pdf of the amplitudes is given as

$$\mathrm{pdf}(x) = \frac{2}{\Gamma(m)}\left(\frac{m}{\Omega}\right)^m x^{2m-1} \exp\left(-\frac{m}{\Omega}x^2\right), \tag{2.120}$$

where $m \geq 1/2$ is the Nakagami m-factor, $\Gamma(m)$ is the Gamma function, and Ω is the mean-square value of the amplitude. The parameter Ω is the mean-square value $\Omega = \overline{r^2}$, and the parameter m is

$$m = \frac{\Omega^2}{\overline{\left(r^2 - \Omega\right)^2}}. \tag{2.121}$$

It is straightforward to extract those parameters from measured values. When the amplitude is Nakagami-distributed, then the power is Gamma-distributed.

Rice distribution. This distribution has been suggested by [83], as well as by [84] for bins with small delays in LOS situations

$$\mathrm{pdf}(x) = \frac{x}{\sigma^2} \exp\left(-\frac{x^2 + A^2}{2\sigma^2}\right) I_0\left(\frac{xA}{\sigma^2}\right), \tag{2.122}$$

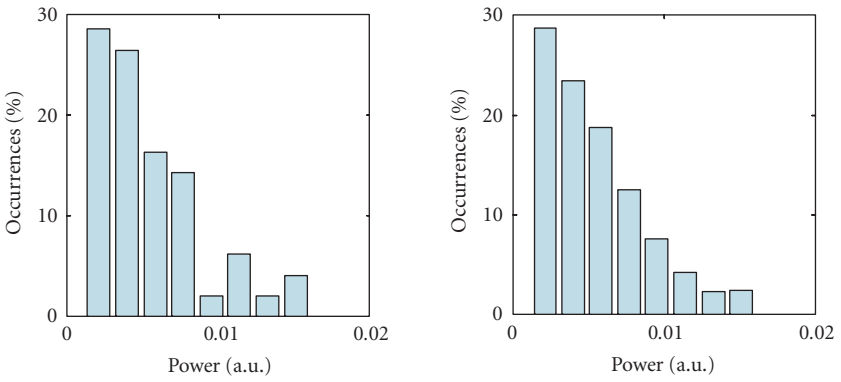

FIGURE 2.8. (a) Experimental histogram of received powers, compared to (b) a histogram derived from a theoretical Gamma distribution with $m = 3.1$.

where A is the amplitude of the dominant component, $K_r = A^2/(2\sigma^2)$ is the Rice factor, and I_0 is the zero-order modified Bessel function of the first kind. Nakagami and Rice distributions have a quite similar shape, and one can be used to approximate the other. For $m > 1$, the m-factor can be computed from K_r by

$$m = \frac{(K_\mathrm{r} + 1)^2}{(2K_\mathrm{r} + 1)}, \tag{2.123}$$

while

$$K_\mathrm{r} = \frac{\sqrt{m^2 - m}}{m - \sqrt{m^2 - m}}. \tag{2.124}$$

Note, however, that if those equations are used, the resulting pdfs have different slopes close to $r = 0$, as well as for very large r.

Lognormal distribution. The lognormal distribution has the advantage that the fading statistics of the small-scale statistics and the large-scale variations have the same form; the superposition of lognormal variables can also be well approximated by a lognormal distribution, its pdf is given as

$$\mathrm{pdf}_F(F) = \frac{20/\ln(10)}{F\sigma_F\sqrt{2\pi}} \cdot \exp\left[- \frac{\left(10\log_{10}\left(F^2\right) - \mu_\mathrm{dB}\right)^2}{2 \cdot \sigma_F^2} \right], \tag{2.125}$$

where σ_F is the variance of the local mean F, and μ_dB is the mean of the values of F in dB. The lognormal distribution was suggested by [119]; also Ghassemzadeh et al. [75] use a similar modeling approach: they model the deviation χ of the local MIP (multipath intensity profile, $|h(t,\tau)|^2$ around its expected value PDP)

as lognormal. For the LOS case, the model uses

$$\chi = \begin{cases} 0 & \text{for } \tau_i = 0, \\ C - \alpha\tau_i + S(\tau_i) & \text{for } \tau_i = i\Delta\tau, \end{cases} \tag{2.126}$$

where C is a Gaussian-distributed random variable[21] $N(-6.38, 1.98)$, $\alpha = N(-0.82, 0.25)$, S is a correlated Gaussian process with mean -0.41 dB, and the variance of S is $N(6.86, 0.92)$, all in dB (α in dB/ns). S is assumed independent from one delay to another. For the NLOS case, the result is similar

$$P_r(t) = -\alpha\tau_i + S(\tau_i), \tag{2.127}$$

where $\alpha = N(0.91, 0.13)$, S is a correlated Gaussian process with mean -0.41 dB, and the variance of S is $N(7.2, 0.88)$.

POCA and NAZU distributions. POCA and NAZU distributions, which were theoretically derived as distributions for a small number of components without (POCA) and with (NAZU) dominant component, were suggested in [124]. The POCA distribution is defined as

$$p_r(r) = \frac{2\pi K^2(2n+1)}{\sigma^2} \frac{r}{\left(a^2 - b^2\right)^{(n+1)/2}} P_n\left(\frac{a^2}{\sqrt{a^2 - b^2}}\right), \tag{2.128}$$

where $P_n(x)$ is the Legendre function,

$$\begin{aligned} K(2n+1) &= \frac{1}{\sqrt{\pi(2n+1)}} \frac{\Gamma(n+1)}{\Gamma((2n+1)/2)}, \\ a &= 1 + \frac{r^2}{\sigma^2(2n+1)} + \frac{r^4}{8\sigma^4(2n+1)^2}, \\ b &= -\frac{r^4}{8\sigma^4(2n+1)^2}, \end{aligned} \tag{2.129}$$

and n is the number of paths. The NAZU distribution adds one dominant component.

Weibull distribution. Reference [76] models the deviation χ of the local MIP around its expected value by a Weibull distribution

$$p_X(x) = \frac{\lambda}{\sigma}\left(\frac{x-\mu}{\sigma}\right)^{\lambda-1} \exp\left[-\left(\frac{x-\mu}{\sigma}\right)^{\lambda}\right] \quad \text{for } x \geq 0, \tag{2.130}$$

where the parameters σ and λ depend on the environment.

Several papers have found that the fading depth increases with increasing delay. This is also physically intuitive. For small delays, there is only a small number of possible propagation paths that have a delay within a considered delay bin.

[21] Different realizations of C should be used in different houses.

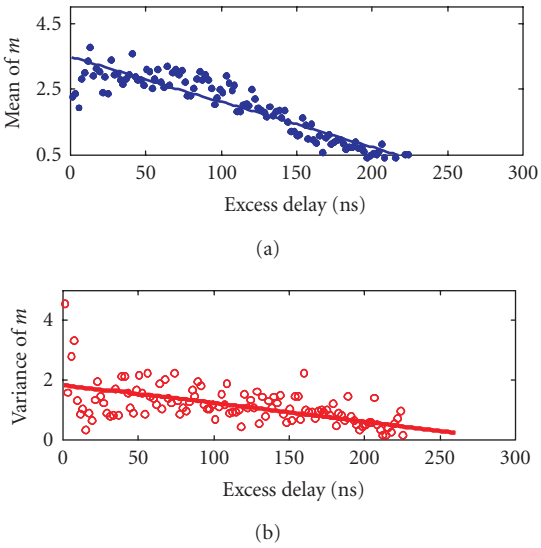

FIGURE 2.9. Mean and variance of the Nakagami m-factor as a function of the excess delay for a baseband (< 0.5 GHz) measurement (according to [79]).

For larger delays, more (but weaker) MPCs fall into one bin, so that the fading is more Rayleigh-like. Reference [79], which modeled the amplitude statistics as Nakagami, reflects this fact by treating the m-factor as a random variable whose mean and variance decrease with increasing delay. Similarly, [83] found the Rice factor to be exponentially decreasing with delay.

Apart from the amplitudes, also the phase (for passband channels) or polarity (for baseband channels) of the MPCs has to be modeled. For passband channels, a uniform phase distribution is commonly assumed. For baseband channels, the polarity of the MPCs is assumed to be positive or negative with equal probability, except for the LOS components that always have positive polarity. Another important point is whether the fading in adjacent delay bins is correlated. Reference [76] found that components immediately following the LOS have a high probability of having the same polarity as the LOS.

The above equations have described the fading of the MPCs. In most indoor models, the MPCs are grouped in clusters. These clusters can also be fading, typically due to shadowing. An example of how this cluster fading can be combined with the MPC fading is described in Section 2.6.2. As the sum of the cluster powers is the total power (assuming that the fading of the clusters is statistically independent of each other), this fading is also related to the shadowing of the total signal as described in Section 2.4.

2.5.4. Frequency-domain modeling

The previous subsections dealt with the modeling in the delay domain. Of course, it is also possible to model the channel transfer function. This was done in a purely

phenomenological approach by an autoregressive model in [125]:

$$\rho_1 H(f_i, t, d) = n_i - \rho_2 H(f_{i-1}, t, d) - \rho_3 H(f_{i-2}, t, d), \tag{2.131}$$

where n_i are i.i.d. Gaussian variables with zero mean and unit standard deviation, and the ρ_i are the parameters of the model that have to be extracted from the measurements. Autoregressive models have been suggested also for narrowband channels, but have not gained widespread popularity, due to difficulties in interpreting them physically.

2.5.5. The impact of the discrete-time impulse-response model

A fundamental assumption of the channel model given in (2.114), consistent with nearly all channel models since Turin's description of the tap-delay line model [113], is that the received signal is the sum of a finite number of scaled, phase-shifted, and delayed versions of the transmitted signal. In other words, the observed signal is a superposition of a number of undistorted versions of the transmitted pulse. However, as was discussed in Section 2.3, a UWB pulse will often exhibit frequency-dependent distortion on a per-path basis.[22] This distortion can result from propagation through materials, diffraction, the antenna, or other mechanisms. This fact is discussed in detail for diffraction mechanisms in Section 2.3; in the current subsection, we concentrate on the reflection and transmission processes and the antennas.

In this section, we will investigate the impact of this frequency dependence on the use of discrete tap channel models of the type given in (2.114). There are two basic questions that should be addressed in this discussion. (1) "What is the direct impact of our assumption on the resulting model?" (2) "How does this distortion influence our interpretation of the model?" We will address question (1) first.

As stated, there are several potential sources of pulse distortion during propagation. One such source is the distortion caused to a pulse as it passes through materials. A detailed study of the frequency-dependence of common building materials was carried out by Virginia Tech as part of the DARPA NETEX program [126, 127]. We apply the results here to demonstrate the impact that materials can have on UWB signals and the discrete-time channel model. For example, consider the impact that brick has on a UWB pulse as it passes through the material. Figure 2.10 plots the received line-of-sight pulse using a TEM horn antenna with and without the material present [126]. The original pulse has a pulse duration of roughly 300 picoseconds and a 10 dB bandwidth of approximately 7 GHz. Clearly the frequency-dependent nature of the material has caused pulse distortion as can be seen in Figure 2.10.

[22] Note that we are not referring to frequency-dependent distortion of the entire received signal. This is clearly present in even moderate bandwidth channels when the delay spread is large. We are referring specifically to per-path frequency distortion.

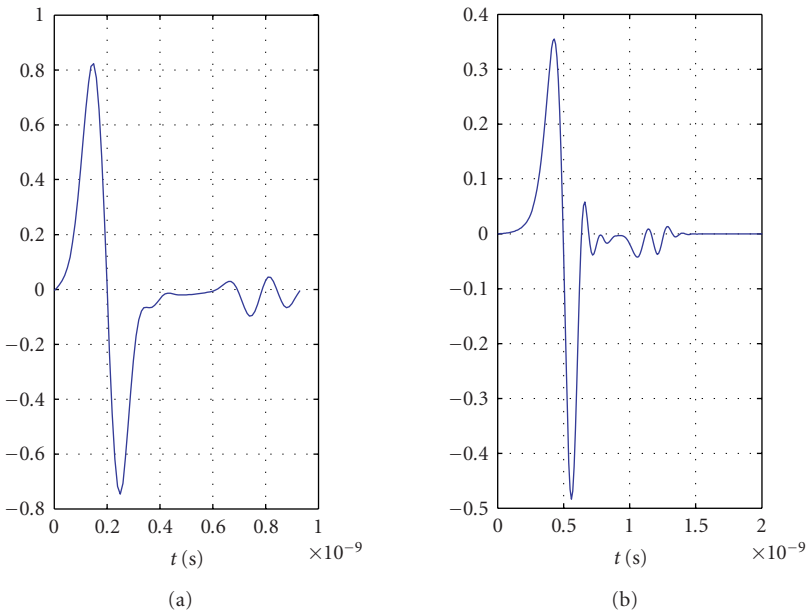

FIGURE 2.10. (a) Original and (b) distorted UWB pulse after passing through brick.

The classic tapped-delay line channel model cannot explicitly account for this distortion without modification. However, the model can account for the distortion implicitly. That is, physically, there is a single path that exhibits frequency distortion. Thus, using a single path of the form given in (2.114), we cannot represent the distorted pulse. However, the model can accurately represent the pulse if we relax the restriction that we use a single path. We will demonstrate this in a moment. However, first we must discuss the creation of tap-delay line models from measurement data.

Time-domain channel sounding techniques are discussed in detail in Section 2.2. A common method for obtaining the channel impulse-response from the measurement data is deconvolution of the pulse shape from the received data. This ignores angle-dependent antenna effects, but allows for a reasonable approximation of the channel impulse-response [126]. Typical frequency domain deconvolution techniques result in a continuous-time impulse-response due to the band-limited nature of the original measurement data. The resulting impulse-response must be binned in order to create a discrete impulse-response similar to (2.114). An attractive alternative is to perform time-domain deconvolution using the CLEAN algorithm [118, 128, 129]. A full discussion of CLEAN is beyond the scope of this work, but the algorithm is more amenable to the tap-delay line model since it assumes that the channel impulse-response is a sum of scaled and delayed impulses.

Thus, by deconvolving the undistorted pulse from the received signal, the distorted pulse shown in Figure 2.10 can be represented by a sum of scaled and

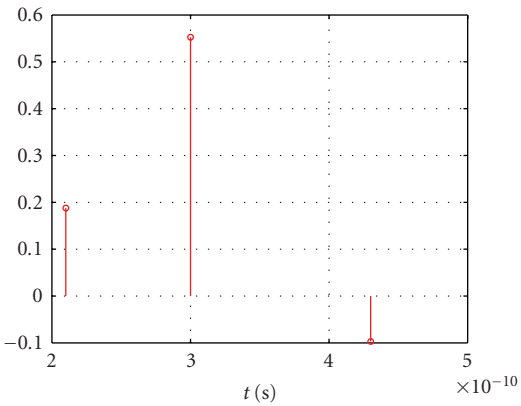

FIGURE 2.11. Discrete-tap channel model created by CLEAN algorithm using the distorted pulse after passing through plywood.

delayed versions of the line-of-sight pulse. To demonstrate this, the CLEAN algorithm was used to deconvolve the LOS (i.e., undistorted) pulse in Figure 2.10(a) from the received signal given in Figure 2.10(b). The resulting impulse-response is plotted in Figure 2.11. This impulse-response was then convolved with the undistorted pulse and plotted in Figure 2.12(b) along with received signal. We can see that the modeled signal very closely represents the true received signal (the mean square-error between the received pulse and the reconstructed pulse is $4 * 10\hat{}\{-4\}$). However, we require a 3-tap channel to do so, when the true physical channel has only a single path. Thus, frequency distortion can be modeled using the classic method, but one must take care in interpreting the results. There are not 3 true paths in the channel, despite the fact that the impulse-response contains 3 taps.

As stated, this is specifically due to the ultra-wideband nature of the pulse. For moderate bandwidths, this is not a concern. For example, compare the previously described UWB pulse with a 10 MHz Gaussian pulse centered at 5 GHz shown in Figure 2.13(a). The resulting pulse after passing through brick appears in Figure 2.13(b). The pulse is not distorted which is clear from the impulse-response generated by CLEAN shown in Figure 2.14. Thus, traditional carrier-based communication systems would typically not experience frequency-dependent distortion passing through brick. This analysis was repeated using the UWB pulse described previously for several common building materials whose frequency characteristics are presented in [126, 127]. Table 2.3 presents a synopsis of the discrete-time CIR for several of these materials. Specifically, the table presents the number of components in the impulse-response within 10 dB of the strongest component and the percent of the CIR energy in the dominant component. A large number of components reflect the fact that the discrete tap model will exhibit more "paths" than actually exist. We will refer to such paths as "phantom paths" since the model includes them to represent the per-path frequency distortion rather than independent temporal echoes. The percent energy measure describes the relative

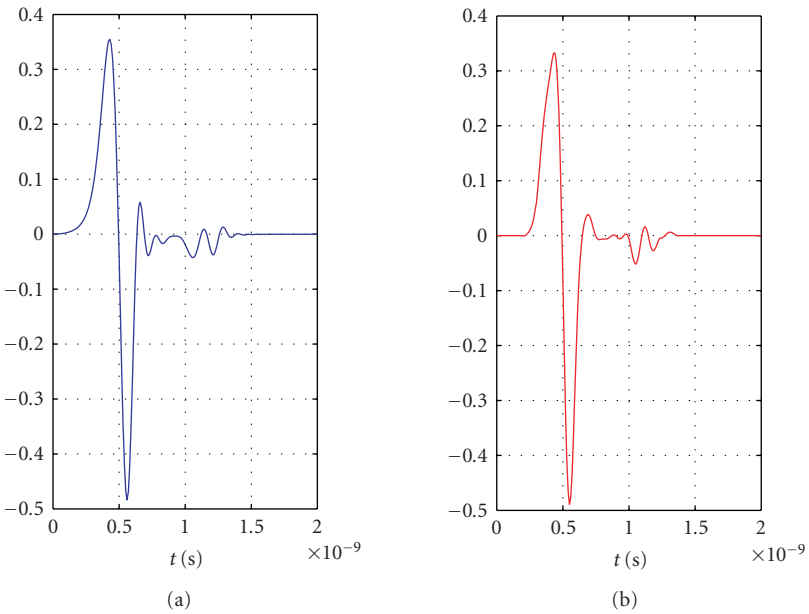

FIGURE 2.12. (a) Distorted UWB pulse after passing through brick and (b) pulse produced from CLEAN.

strength of the phantom paths. A large percent energy measure signifies that the phantom paths are weak relative to the main path which represents the actual temporal echo.

The preceding discussion can be applied to several aspects of UWB propagation. For example, consider the impact of a UWB pulse reflecting from a metalic cylinder. Such an experiment was conducted by the Virginia Tech Antenna Group (VTAG) as part of the DARPA NETEX project as explained in detail in [126]. Measurements were taken in an anechoic chamber to characterize the distortion caused by reflections from common shapes. An example of LOS pulse and the pulse received after reflecting from a hemisphere with a 6-inch diameter is plotted in Figure 2.15. The transmit and receive antennas both pointed at the hemisphere to ensure the hemisphere was in the boresight of both antennas. Additionally, non-reflected (i.e., direct) paths were removed by taking a measurement without the hemisphere present. The received pulse after reflection is essentially a single specular component (which is inverted due to the reflection) along with a resonant component as can be seen in Figure 2.15. The classic model can easily represent the specular component, but does not assume the existence of the resonant component. Again, using the CLEAN algorithm results in a discrete-time model which has significantly more than one path as shown in Figure 2.16. While the additional paths are well below the specular path (more than 12 dB), clearly the impulse-response must contain a large number of additional phantom paths in order to accurately represent the received signal. A third cause of frequency distortion was explained in detail in Section 2.3.

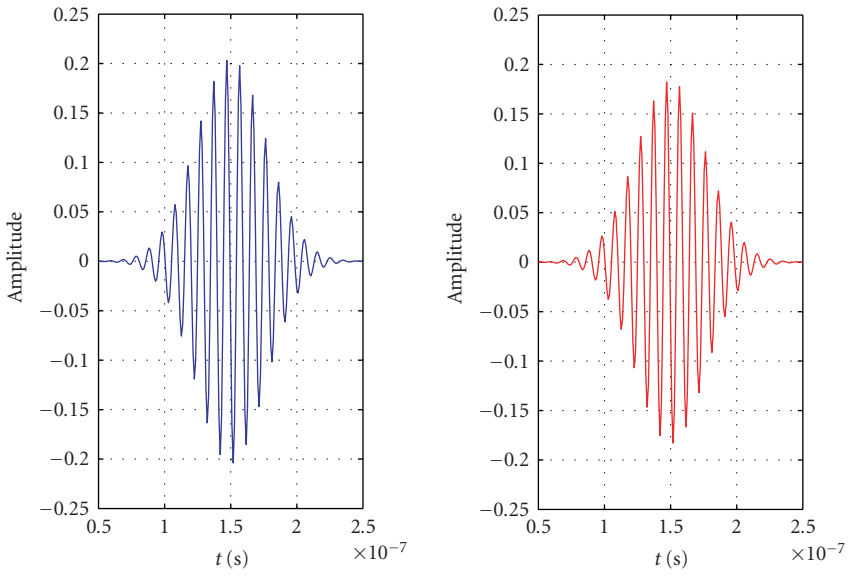

FIGURE 2.13. (a) 10 MHz pulse after passing through plywood and (b) pulse produced from CLEAN.

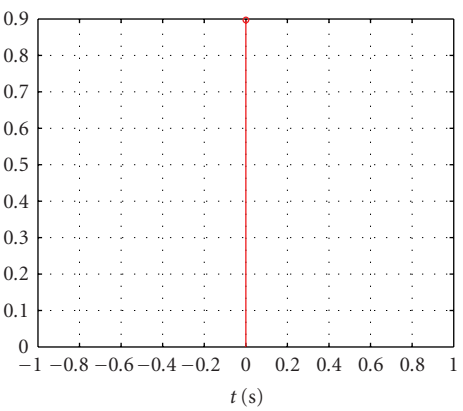

FIGURE 2.14. Discrete tap channel model created by CLEAN algorithm using the distorted 10 MHz pulse after passing through plywood.

As discussed, diffraction on a single path can often be modeled in the frequency domain as

$$H(\omega) = \beta e^{j\varphi} \left(\frac{\omega}{\omega_c} \right)^{\alpha} e^{j\omega\tau}, \tag{2.132}$$

Table 2.3. Discrete channel representation of UWB pulse after passing through common building materials.

Material	Energy in dominant component	Components in the IR
Brick wall	87%	3
Cloth partition	98%	2
Wooden door	98%	2
Concrete block	90%	3
Structure wood	100%	1

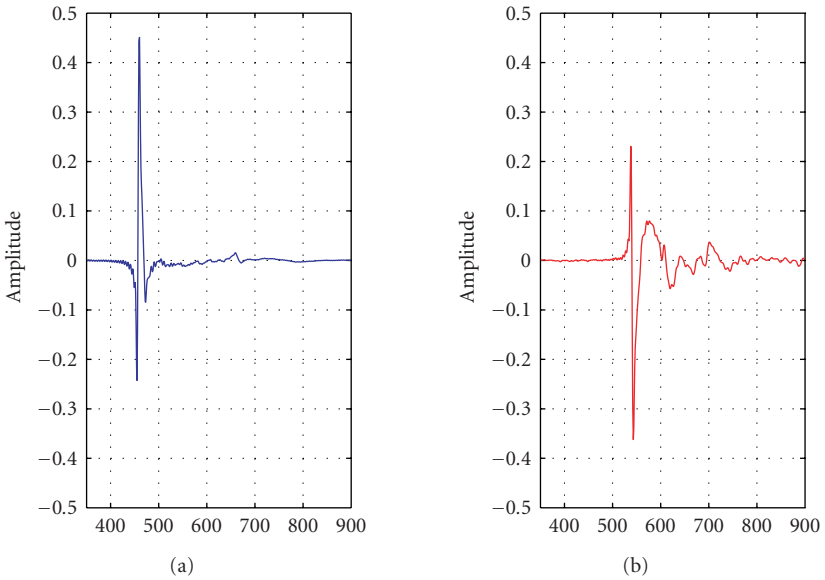

Figure 2.15. (a) Line-of-sight signal; (b) signal reflected from a 6-inch diameter hemisphere.

where ω_c is the center frequency and α depends on the diffraction being modeled. For example, when the pulse experiences single edge diffraction, it can be shown that $\alpha = -0.5$. Consider the pulse shown in Figure 2.17(a) and the resulting pulse from single edge diffraction given in Figure 2.17(b). Again, the frequency-dependent distortion can not be explicity accounted for in the model of (2.114). One approach to include this effect is the GTD approach described in Section 2.3. Alternatively, we can simply use multiple frequency independent "paths" in the discrete-time model to represent the single frequency distorted path. Again using the CLEAN algorithm, we can create a discrete-time impulse-response to represent the distorted pulse. The resulting impulse-response is given in Figure 2.18. In this case, two additional paths are required each of which is 15 dB lower than the main path. However, it should be noted that this is highly dependent on the path and the diffraction experienced as discussed in Section 2.3.

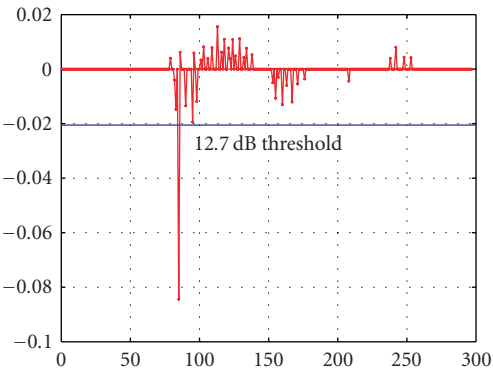

FIGURE 2.16. Impulse-response resulting from the CLEAN algorithm when the received signal is reflected from a hemisphere.

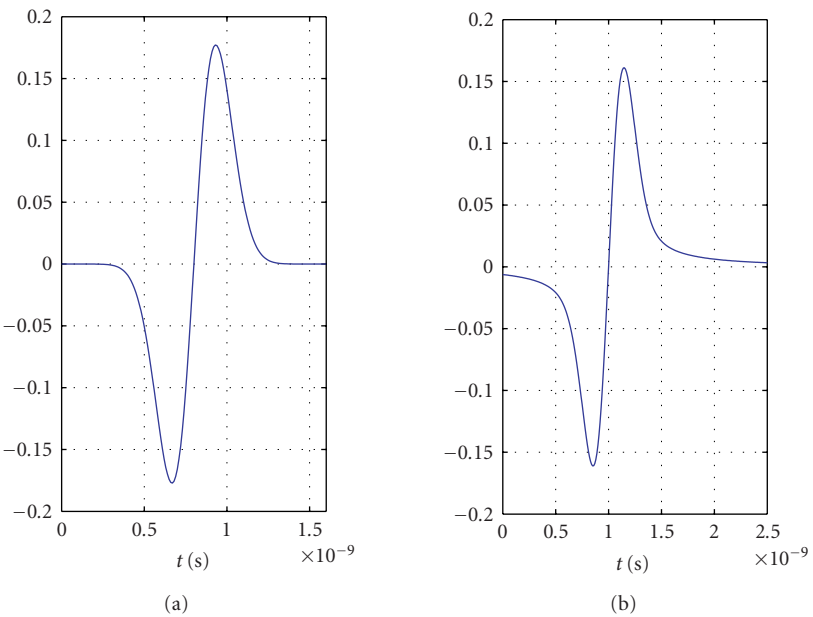

FIGURE 2.17. Received pulse (a) with and (b) without single edge diffraction using values given in [130].

Finally, an additional potential source of pulse distortion in UWB systems comes from the antenna itself. The impulse-response of the antenna can change with angle in both elevation and azimuth. Clearly this is most prevalent with directional antennas such as the Vivaldi or TEM Horn antenna. However, pulse distortion will also occur with omnidirectional antennas such as the bicone. Specifically, the transmitted pulse at different elevation angles will be distorted as compared to the pulse observed at boresight. This can be observed in Figure 2.19, where we

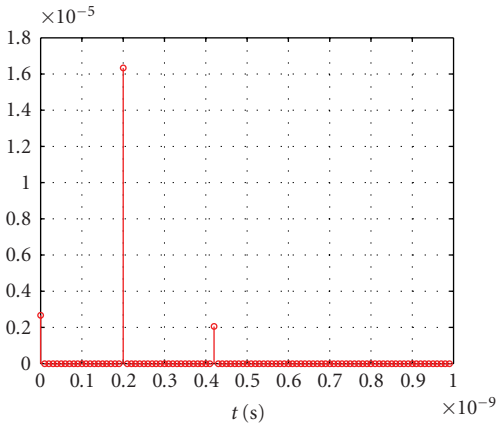

FIGURE 2.18. Discrete-time impulse-response due to a single path experiencing single edge diffraction.

have plotted the received pulse using bicone antennas measured at different elevation angles [126]. For details of the measurements taken by the Virginia Tech Antenna Group please, see [126]. Note that as one would expect, the amplitude of the received pulse amplitude is reduced at larger elevation angles due to less antenna gain. However, the pulse is also slightly distorted as compared to the pulse transmitted (or received) at zero-degree elevation. This brings up a fundamental question about the pulse shape in UWB systems. Since the pulse shape produced by the antenna is different for different angles, the notion of a single pulse shape is problematic. A typical assumption is that the line-of-sight pulse (i.e., the pulse received on boresight) is the transmitted pulse shape. This pulse shape can be used for matched-filter correlation or to create the discrete tap impulse-response channel model from measurement data as discussed above. However, care must be taken when making this assumption. Matched filtering with the incorrect pulse shape will lead to a loss in correlation energy. Using a single pulse shape for channel modeling will lead to the generation of additional multipath components which simply represent the pulse distortion rather than actual paths. This can be clearly seen in Figures 2.20 and 2.21. Figure 2.20 plots an example transmitted pulse from a bicone antenna at elevation angles of (a) zero degrees and (b) 60 degrees. If we assume that the zero degree elevation angle pulse is the nominal pulse shape, the pulse at sixty degrees can be represented using the discrete channel impulse-response shown in Figure 2.21. In other words, if a pulse is received at an elevation angle of sixty degrees, the channel model will account for the resulting pulse distortion by again using additional paths (15 in this case). This can also be demonstrated for pulses arriving (or departing) at other angles. This also indicates that future statistical channel models should include directional information for the multipath components, so that it can be more easily combined with arbitrary antennas.

In conclusion, it is clear that single path frequency distortion can arise from several different mechanisms when UWB signals are employed. This frequency

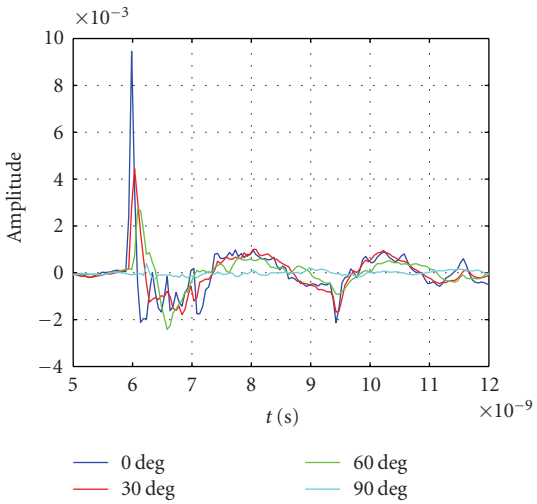

FIGURE 2.19. Received pulse from various elevation angles using biconical antennas.

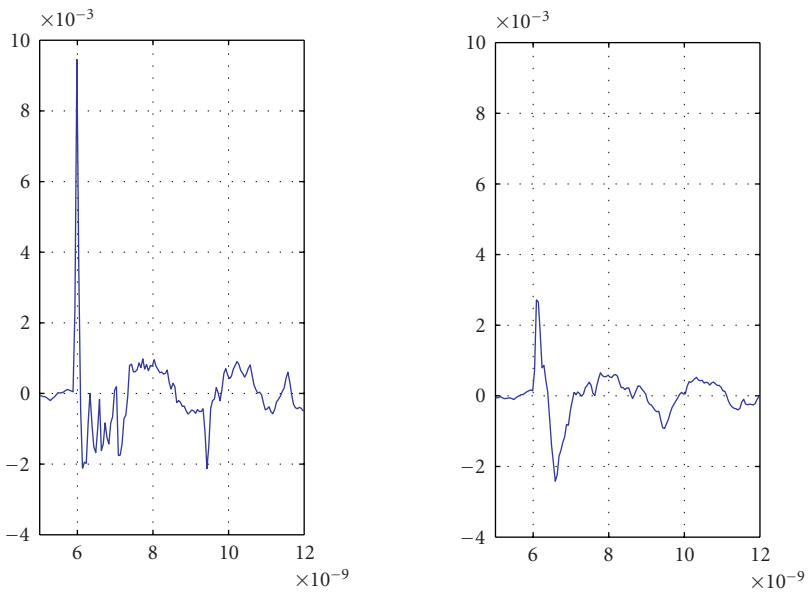

FIGURE 2.20. Received pulse from elevation angles of (a) zero degrees and (b) 60 degrees using biconical antennas.

distortion is not explicitly represented by the discrete-time channel model that is commonly assumed. However, as we have shown, the model can clearly represent this distortion by the inclusion of "phantom paths." Of course, care must be taken

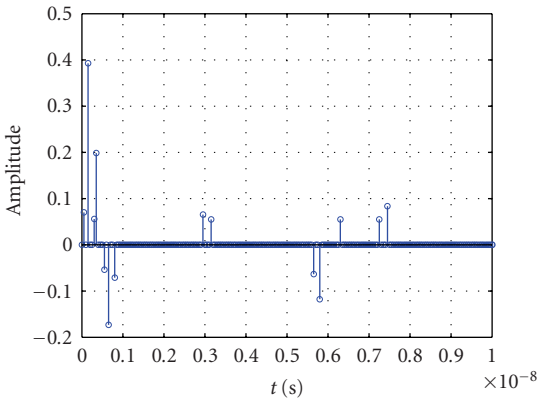

FIGURE 2.21. Resulting impulse-response for pulse at 60° elevation angle assuming boresight pulse was.

when interpreting the model since each path in the model does not necessarily represent a separate independent path.[23] Thus, for UWB systems, we must understand that the channel model is more of a "black box" than in wideband systems where we can generally view each path in the model as a physical transmission path. This places more burden on the researcher to understand what characteristics of the channel are most important to the issue under study. If the receiver is impacted only by the delay spread, temporal correlation, or other statistics of the received signal, the discrete time model is sufficiently accurate. However, if the model is being used as a guide for the number of necessary Rake fingers or physical interpretations of the model, it may not be as useful.

2.6. Standardized channel models

2.6.1. Introduction

In this chapter, we present a channel model for indoor short range ultra-wideband (UWB) radio channels. The model was developed in 2002–2003 through an industrial/academic collaboration under the auspices of the IEEE 802.15.3a standards task group, for the purpose of aiding in the development of a standard for UWB wireless personal area networks (WPANs). The IEEE 802.15.3a solicited contributions from a broad spectrum of experts from industry and academia in the formulation of this channel model. This resulted in a wealth of data, both empirical and theoretical, that was brought before the IEEE 802.15.3a committee. (see [131, 132, 119, 133, 103, 123, 115, 134–136] for more details; these documents, as well as other related materials, are available in the July 2002 through March 2003 online archives of the IEEE 802.15 WPAN, at http://grouper.ieee.org/groups/802/15/pub/

[23]Therefore, the fading of different delay bins need not be independent. However, the one existing investigation [79] of this correlation found the maximum correlation between different delay bins to be less than 0.2.

download.html.) A subgroup of the 802.15.3a examined these data, and formulated a parameterized mathematical channel model that provided a reasonable fit to the empirical data, while maintaining the simplicity and ease of use that is required of a model for use by a standards group. This model was accepted by the full standardization group in early 2003. (The final report of the channel modeling committee is contained in [137]; also, see [102].)

The model is based upon the well-known Saleh-Valenzuela model [94], see also Section 2.5, but with fading statistics modified to more accurately represent the phenomenology associated with ultra-wideband signals. In addition to the general parameterized mathematical model, the IEEE 802.15.3a also specified four particular sets of parameters for the model, intended to represent channel conditions that the committee deemed especially relevant to the UWB WPAN operating space.

In the sections, below we describe the general model, focusing primarily on the mathematical structure of the model, and the distributions of the random quantities that underlie it. We then review the four parameter sets for the model that were defined by the IEEE 802.15.3a committee to represent the specific channel conditions relevant to UWB WPANs, and briefly discuss the fit of the model to a set empirical data measured under those same conditions.

2.6.2. The mathematical model

The mathematical channel model consists of a multipath model based on the work of Saleh and Valenzuela [94], a lognormal shadowing model, and a path loss model of power-law type. All of these aspects have been addressed in Sections 2.4 and 2.5. Here we summarize these considerations (as far as they are relevant to the standard model), and describe the specific parameter choices used in it.

2.6.2.1. Multipath model structure

Mathematically, the multipath model takes the form of a "clustered point process," in which the multipath components (MPCs, also referred to as "rays") are unevenly distributed in time. The physical intuition behind these models is that the high spatial resolution of UWB signals allows the receiver to resolve multiple reflections from each interacting object (IO) in the environment. Thus, the receiver perceives clusters of MPCs, each cluster corresponding to some IO in the environment. The individual MPCs in a cluster arise from the complex scattering process that takes place as the ultra-wideband signal interacts with the structure of the IO.

Thus, the multipath model naturally decomposes into two pieces. First, there is the *cluster arrival process* that describes the times of arrival of clusters at the receiver, as well as their amplitudes. Then, for each cluster, there is a *ray arrival process* describing the times of arrival and amplitudes of individual rays within the cluster. We consider the cluster arrival process first.

Each cluster is associated with a delay time T and an amplitude ξ. Obviously, T is determined by the total distance from transmitter to IO to receiver, and ξ models the overall fading associated with the cluster. Thus, an individual cluster is modeled as

$$c_l(t) = \xi_l \delta(t - T_l), \tag{2.133}$$

where l indexes the clusters, and the cluster arrival process is given by

$$c(t) = \sum_{l=0}^{L} c_l(t) = \sum_{l=0}^{L} \xi_l \delta(t - T_l), \tag{2.134}$$

where L is the total number of clusters. The parameters L, T_l, and ξ_l, $l = 0 \ldots L$, are random variables whose distributions must be specified. Specifics on the distributions of all model parameters will be given in Sections 2.6.2.3 and 2.6.2.4 below.

The arrival of individual MPCs within a cluster is modeled by a ray arrival process. An individual MPC within cluster l is specified by its delay τ relative to the cluster delay, and by its amplitude β relative to the overall cluster fading. We also include a reflection coefficient p, equiprobably ± 1, to account for signal inversions due to reflections. Thus, an individual ray within cluster l is modeled as

$$r_{k,l}(t) = p_{k,l} \beta_{k,l} \delta(t - \tau_{k,l}), \tag{2.135}$$

where k indexes the rays within the cluster, and the ray arrival process for cluster l is given by

$$r_l(t) = \sum_{k=0}^{K(l)} r_{k,l}(t) = \sum_{k=0}^{K(l)} p_{k,l} \beta_{k,l} \delta(t - \tau_{k,l}), \tag{2.136}$$

where $K(l)$ is the total number of rays associated with cluster l.

Putting together the pieces now, cluster l along with its associated rays is modeled as

$$c_l * r_l(t) = \sum_{k=0}^{K(l)} \xi_l p_{k,l} \beta_{k,l} \delta(t - T_l - \tau_{l,k}), \tag{2.137}$$

(the $*$ denotes convolution), and the overall channel impulse-response is given by

$$h(t) = \sum_{l=0}^{L} c_l * r_l(t) = \sum_{l=0}^{L} \sum_{k=0}^{K(l)} \xi_l p_{k,l} \beta_{k,l} \delta(t - T_l - \tau_{l,k}). \tag{2.138}$$

2.6.2.2. Shadowing and path loss models

Shadowing is an overall scaling factor X applied to the channel impulse-response as a whole:

$$h(t) = X \sum_{l=0}^{L} \sum_{k=0}^{K(l)} \xi_l p_{k,l} \beta_{k,l} \delta(t - T_l - \tau_{l,k}). \tag{2.139}$$

The shadowing factor X is of course random.

The path loss model adopted by the IEEE 802.15.3a for the evaluation of standards proposals was the simple free-space model, given by (see Section 2.4)

$$\overline{\mathrm{PL}}(d) = \left(\frac{4\pi d}{\lambda}\right)^2, \tag{2.140}$$

where PL is the path loss, d is the distance, and the wavelength λ is taken to be the geometric mean of the upper and lower 10 dB cutoff frequencies of the signal. While this model provided a sound basis for the relative comparisons of proposals, it is not suitable for system performance modeling, because it does not take into account the variation in path loss that occurs in the diverse environments in which UWB WPANs are expected to operate. A more realistic model that nevertheless preserves much of the simplicity of (2.140) would replace the free-space path loss exponent of 2 by a random path loss exponent η, whose distribution is chosen based on measurement data. This model would be further calibrated by the amount of path loss experienced at a fixed reference distance (say one meter), again determined by measurements. We will return to this issue in Section 2.6.2.4 below.

2.6.2.3. Distributions of the multipath model parameters

The cluster arrival process (2.134) is characterized by the cluster arrival times T_l and the associated cluster fading terms ξ_l, both of which are random. The familiar *homogeneous* Poisson process (see Section 2.5), characterized by a constant cluster arrival rate Λ, was adopted by the IEEE 802.15.3a channel modeling subcommittee. Thus, the cluster *interarrival* times are assumed to be independent identically distributed (i.i.d.) exponential random variables, with mean $1/\Lambda$:

$$P(T_l - T_{l-1} > t) = \exp(-\Lambda t) \tag{2.141}$$

Λ is called the *cluster arrival rate*; its value depends on the RF environment.

As for cluster amplitudes, we generally expect them to decrease as cluster delay increases, on average. The IEEE 802.15.3a model specifies that the conditional expected value of the cluster amplitude should decay exponentially with cluster delay:

$$E[\xi_l^2 \mid T_l] = \Omega_0 e^{-T_l/\Gamma}. \tag{2.142}$$

Here, Ω_0 is a normalization factor, and Γ is the *cluster decay factor*. It was determined that the lognormal distribution (see Section 2.5) provided a good fit to the measurement data available to the 802.15.3a group. Specifically, we have

$$\xi_l^2 = \exp\left(\ln(\Omega_0) - \frac{T_l}{\Gamma} - \frac{1}{2}\sigma_\xi^2 + \sigma_\xi N_{\xi,l}\right), \tag{2.143}$$

where $\{N_{\xi,l} : l = 0 \dots L\}$ are i.i.d. standard normal random variables, and σ_ξ is the lognormal standard deviation of the cluster fading. It is easily verified that ξ_l defined by (2.143) satisfies the exponential decay condition (2.142). Moreover, the cumulative distribution function (CDF) for the cluster amplitudes (2.143) is given by

$$P(\xi_l < b \mid T_l) = \Phi\left(\frac{\ln(b^2/\Omega_0) + T_l/\Gamma + (1/2)\sigma_\xi^2}{\sigma_\xi}\right), \tag{2.144}$$

where Φ is the CDF of the standard normal distribution. In summary, the cluster arrival process consists of a homogeneous Poisson process describing the cluster arrival times, with associated cluster amplitudes that are lognormally distributed and exponentially decaying with the cluster delay.

The ray arrival process (2.136) takes exactly the same form—only the distribution parameters change. Thus, the ray interarrival times are again exponential, this time with *ray arrival rate* λ:

$$P(\tau_{k,l} - \tau_{k,l-1} > t) = \exp(-\lambda t). \tag{2.145}$$

Again, conditional on the ray delay, the ray amplitudes are lognormally distributed, with *ray decay factor* γ,

$$\beta_{k,l}^2 = \exp\left(-\frac{\tau_{k,l}}{\gamma} - \frac{1}{2}\sigma_\beta^2 + \sigma_\beta N_{\beta,k,l}\right), \tag{2.146}$$

implying that

$$E[\beta_{k,l}^2 \mid \tau_{k,l}] = e^{-\tau_{k,l}/\gamma}, \tag{2.147}$$

where again $\{N_{\beta,k,l} : l = 0 \dots L,\ k = 0 \dots K(l)\}$ are i.i.d. standard normal random variables, and σ_β is the lognormal standard deviation of the ray fading. Relative ray arrivals and amplitudes are completely independent of cluster arrivals and amplitudes in this model. It should be noted that the ray decay factor is the same for all clusters in this model.

Finally, we need to specify the distributions of the number of clusters L, and the number of rays $K(l)$ for the lth cluster. Given the exponential decay of the cluster and ray amplitudes, the mathematically convenient choice would be simply to let each of these parameters be infinite. Obviously this is not a satisfactory solution for simulation purposes. A simple remedy in this case is to simply simulate clusters

Table 2.4. Parameters for the multipath model.

Parameter	Symbol
Cluster arrival rate	Λ
Cluster decay factor	Γ
Cluster fading depth	σ_ξ
Ray arrival rate	λ
Ray decay factor	γ
Ray fading depth	σ_β

and rays until the exponential decay of the amplitudes renders them insignificant. This was the approach taken in the reference simulation code presented in [137]. There, cluster arrival times T_l were limited to $T_l < 10\Gamma$, and relative ray arrival times were limited to $\tau_{k,l} < 10\gamma$.

In summary, the parameters describing the multipath model are given in Table 2.4.

2.6.2.4. Distributions of the shadowing and path loss parameters

The standard deviation of the logarithm of the shadowing term X in (2.139) is referred to as the *shadowing depth*. The IEEE 802.15.3a committee adopted a log-normal shadowing model, with a shadowing depth of 3 dB. Thus the shadowing term X in (2.139) would be given by

$$20\log_{10}(X) = 3Z, \tag{2.148}$$

where Z is a standard normal random variable. However, shadowing depth is itself a random quantity that can vary from realization to realization, even in the same environment [82, 74]. This insight can be incorporated into the path loss model by making the shadowing depth a Gaussian random variable, with a prescribed mean and standard deviation (see [102]). Expressed in dB, the shadowing term X would thus be given by

$$20\log_{10}(X) = \sigma_x Z, \tag{2.149}$$

where σ_x is normal. The shadowing depth (in dB) itself is now random, given by

$$\sigma_x^2 = \mathrm{Var}\left(20\log_{10}(X) \mid \sigma_x\right). \tag{2.150}$$

In Section 2.4, we discussed the fact that for system performance modeling the free-space path loss model adopted by the IEEE 802.15.3a committee (for proposal evaluation only) should be modified to take into account the dependence of path loss parameters on the environment. Instead of using a path loss exponent of 2, a random path loss exponent η should be used, whose distribution is dependent on the environment. In addition, the value of the path loss at one meter, denoted by

Table 2.5. Parameters for the shadowing and path loss models.

Parameter	Symbol
Mean shadowing depth	$E\sigma_x$
Variance of shadowing depth	Var σ_x
Mean path loss exponent	$E\eta$
Variance of path loss exponent	Var η
Path loss at one meter	PL_0

Table 2.6. Channel characteristics of the data groups.

Data group	Environment	τ_m (ns)	τ_{rms} (ns)	$N_{10\,\text{dB}}$	N_e
1	LOS, 0 to 4 meters	5.05	5.28	—	24
2	NLOS, 0 to 4 meters	10.38	8.03	—	36.1
3	NLOS, 4 to 10 meters	14.18	14.28	35	61.54
4	Very high multipath	—	25	—	—

PL_0, should also be determined from measurements. Ghassemzadeh et al. in [82, 74] report on an extensive measurement campaign comprising 300 000 frequency responses taken in a variety of residential settings, in both line-of-sight and non-line-of-sight scenarios. These measurements provide a good basis for modeling the path loss as a function of environment. The parameters describing the shadowing and path loss models are given in Table 2.5.

2.6.3. Operational scenarios of interest

The mathematical channel model just presented was formulated in light of several sets of channel measurement data. These measurements encompassed a wide variety of operational scenarios, from residential to office-type environments, in both line-of-sight (LOS) and non-line-of-sight (NLOS) conditions. The IEEE 802.15.3a committee categorized these measurements into four broad groups, representing distinct UWB WPAN operational environments. Measurements representative of each group were analyzed on the basis of four channel characteristics: mean excess delay (τ_l), rms delay (τ_{rms}), mean number of rays within 10 dB of the strongest ray ($K_{10\,\text{dB}}$), and mean number of paths that capture eighty-five percent of the energy in the channel (K_e). The results are summarized in Table 2.6.

The 802.15.3a committee then attempted to fit the mathematical channel model to each of these groups. The resulting channel models, respectively, designated CM1 to CM4, are described in Table 2.7, and the corresponding channel characteristics produced by the model are described in Table 2.8. Comparing Tables 2.7 and 2.8 shows a relatively good fit between the model characteristics and the corresponding characteristics of the measurement data.

Table 2.7. Model parameters values corresponding to data groups 1–4.

Parameter	Symbol	CM1	CM2	CM3	CM4
Cluster arrival rate	Λ (1/ns)	0.0233	0.4	0.0667	0.0667
Cluster decay factor	Γ	7.1	5.5	14.0	24.0
Cluster fading depth	σ_ξ (dB)	3.4	3.4	3.4	3.4
Ray arrival rate	λ (1/ns)	2.5	0.5	2.1	2.1
Ray decay factor	γ	4.3	6.7	7.9	12.0
Ray fading depth	σ_β (dB)	3.4	3.4	3.4	3.4
Mean shadowing depth	$E\sigma_x$ (dB)	1.6	2.7	2.7	2.7
Variance of shadowing depth	Var σ_x (dB)	0.5	0.98	0.98	0.98
Mean path loss exponent	$E\eta$	1.7	3.5	3.5	3.5
Variance of path loss exponent	Var η	0.3	0.97	0.97	0.97
Path loss at one meter	PL_0 (dB)	47	50.5	50.5	50.5

Table 2.8. Channel characteristics of the channel models.

Channel model	Environment	τ_m (ns)	τ_{rms} (ns)	$N_{10\,\mathrm{dB}}$	N_e
CM1	LOS, 0 to 4 meters	5.0	5.0	12.5	20.8
CM2	NLOS, 0 to 4 meters	9.9	8.0	15.3	33.9
CM3	NLOS, 4 to 10 meters	15.9	15.0	24.9	64.7
CM4	Very high multipath	30.1	25.0	41.2	123.3

2.7. Body-area networks

2.7.1. Introduction

Wireless body area networking (WBAN) is an emerging 4 G technological concept for short (1–5 m) and very short (below 1 m) range communication systems with a wide range of potential applications including health-care, surveillance, emergency, entertainment, shopping, and so forth, [138–140]. Figure 2.22 shows the envisioned WBAN and its possible components.

The target characteristics of the devices operating within WBANs are: data rates scalable from low (1–10 kbps) to very high (100–400 Mbps), low-cost, low-power, and small-size. These user devices, operation in the close proximity of the human body, are mainly small body-worn, for example, sensors and tags, however medium-size devices, such as PDA, mobile phone, and so forth, are also envisioned to be part of a typical WBAN.

Due to the specifics of WBAN contrasting with the traditional wireless networks WLAN, GSM, UMTS, several technical challenges remain to be solved for a successful deployment and integration of these systems into future 4 G wireless heterogeneous networks.

The ultra-wideband (UWB) technology is one of the main candidates for noninvasive WBAN due to its potential in fulfilling most of the requirements listed

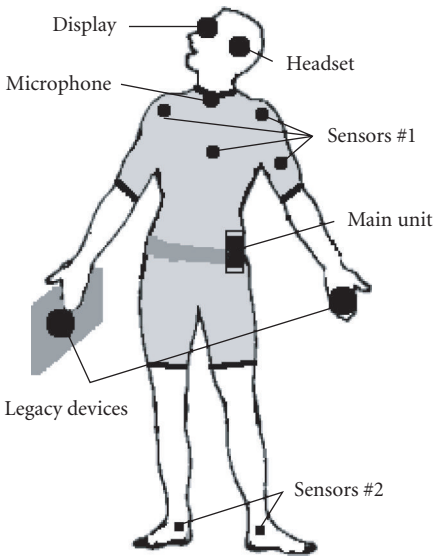

Figure 2.22. Envisioned WBAN and its possible components.

above. The network-level issues for WBAN are strongly dependent on the wide variety and on the specifics of the user scenarios in which the devices operate. The underlying reliable and optimized air-interfaces and adaptive medium access control schemes for WBAN cannot be successfully implemented without a thorough analysis of the specific "around-the-body" radio propagation channels.

In typical WBAN scenarios, for example, for small-size, body-worn, and hand-held devices, the radio propagation channel most likely will exhibit some interesting characteristics such as highly scattered paths and antenna near-field effects especially due to body-proximity conditions. The user proximity effects for handheld devices have been extensively investigated for the GSM/ UMTS frequency bands, for example, [141–144]. For WBAN, some of these aspects have been addressed in UWB propagation investigations presented in [145–148].

Due to the antenna near-field effects and its dynamics, the traditional channel measurement techniques are not directly applicable to the investigation of the radio propagation within the WBAN and new methodologies have to be adopted [145, 146].

Traditionally, the channel sounding measurements have a twofold purpose.

(i) Firstly, a radio channel characterization or model can be obtained for the investigated environments. Traditionally these results are obtained from measurements using antennas with known and close to ideal characteristics. Thus the antenna influence can be easily separated (de-embedded) from the obtained results.

(ii) The second general purpose of radio channel investigations is the study of the antenna efficiency in a given operating scenario and environment.

In this case, the antennas which are under test are the ones envisioned to be used in the actual communication devices.

In the case of WBAN, the clear separation between these two types of radio channel investigations is not possible due to the specifics of the propagation conditions. The de-embedding problem in UWB was discussed in Section 2.2. Ideal UWB antennas are electrically large and are not suitable for on-body scenario investigations. Angle-of-arrival measurements using these large antennas would considerably distort the propagation conditions and yield unrealistic results for WBAN due to the high spatial resolution—10 cm down to 1 cm—possible to obtain with UWB signals. Thus the effects of the body-worn and electrically small antennas can not be separated and have to be part of the radio channel characterization and model. The dynamics in the scenarios with human users make this separation even more complicated than in static scenarios.

The main conclusion from this observations is that the effects of the small-size antennas in realistic user devices have to be included in the developed radio channel model [145, 146].

In the following sections, we will introduce and analyze the most important aspects of radio propagation and antenna measurement techniques for WBAN. The focus here will be on user scenarios with small- and medium-size devices, and two main topics are discussed:

(A) antenna design and analysis for small-size devices,

(B) measurement methodologies required for an appropriate characterization of the WBAN radio propagation channel including body-proximity and antenna effects.

2.7.2. Measurement techniques

2.7.2.1. Antenna designs

In this section, we address the common issues which arise in the design of UWB antennas for WBAN applications. In practice, the WBAN UWB antennas have to share some of the characteristics with the integrated antennas types known from the existing cellular phones such as simplicity, small volume, high total efficiency, and stable radiation characteristics with respect to the body proximity. For sensor networks, where the devices are potentially 3–4 times smaller in volume than a cellular phone, the antenna design is even a more challenge task.

Directional antenna radiation patterns are especially important for body-worn devices where the aim is to minimize the human-body-proximity effects, thus increasing the power efficiency of the device (battery lifetime). Furthermore, in order to minimize the signal distortion, the UWB antenna (transmitter or receiver) must have a flat frequency response and linear phase over the frequency band used. These nondispersive properties are important especially when impulse-radio (IR-) based systems are considered, with fractional bandwidths typically higher than 25% [149]. For any UWB antenna, the flat frequency response requirement cannot be obtained for all spatial directions. Generally, there is only one

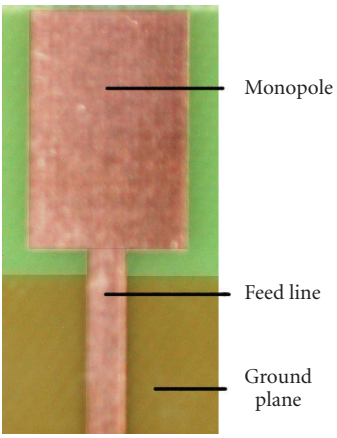

FIGURE 2.23. Example of planar UWB monopole antenna printed on one substrate. Frequency band: 3 GHz to 6 GHz; monopole size: 11 mm × 17 mm; ground plane size: 30 mm × 60 mm.

radiation lobe (direction) in which the nondispersive conditions are well approximated. This is particularly true for directive antennas, for example, the Vivaldi antenna.

Due to their inherent structure, the planar monopole antennas are not directly suited to WBAN applications. The planar monopole design can, however, be further modified to be low-profile. Figure 2.23 shows an example of a simple planar UWB printed monopole antenna for the frequency range of 3 GHz to 6 GHz. Other examples of relatively small-size antennas are the diamond dipole antenna [150] and the folded radiating element, a few millimeters thick [151]. Several other UWB antenna designs are available, which also meet some of the imposed requirements. Main drawbacks of these antennas, from the point of view of commercial WBAN applications, are their size and/or manufacturing cost.

All the antenna designs presented so far present radiation patterns similar to the one of a traditional monopole/dipole antenna. As mentioned earlier, a directional antenna radiation pattern would be desirable for body-worn devices in order to minimize the effects of the human body proximity. To obtain this, the radiation towards the body needs either not to take place or to be reflected by a reflecting antenna part. Promising structures for this are the microstrip patch [152, 153] or slot [154, 155] antennas. Although more complex than the monopole designs, the patch structure can provide low profile geometries and relatively small-volume antennas. Figure 2.24 shows the UWB design for a microstrip antenna [152].

Directional antenna radiation patterns are possible to realize using patch designs or other types with reflectors such as dipole above ground plane. Directivity can be obtained if the antenna is large in the direction of the radiation, such as horn antennas, and so forth. Antennas for WBAN, however, need to be low-profile, therefore only antenna types including a reflector are of practical interest. Research in this area is ongoing.

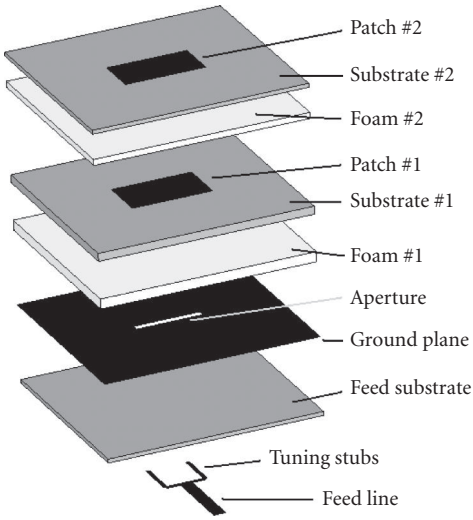

Figure 2.24. Example of aperture-stacked patch antenna for UWB WBAN (copyright Maciej Klemm and Tröster [152]).

2.7.2.2. Antenna analysis

As presented previously, the choice for a specific antenna design has to be based on their main implementation requirements in the WBAN devices: small size in terms of volume, total efficiency, and stable radiation characteristics. The low-cost requirement considered herein is only from the geometrical structure complexity point of view and not necessary the type of materials used.

Electrically small antennas have generally low total efficiency, when matching is included in the analysis. Furthermore, the proximity of human body can significantly modify the impedance bandwidth and radiation characteristics. These main observations lead to the natural conclusion that for an efficient design the antennas used in WBAN devices have to be designed and tested in their normal operating scenarios. Reliable, numerical methods, for example, based on finite-difference time domain (FDTD), need to be employed in order to obtain simulation results. These methods permit modeling of geometrically complex device structures (i.e., not only the antenna element itself) including the nearby antenna surroundings, such as the human body proximity, for example, [156, 157].

The situation is not simple when it comes to the decision on the human body model to be used. Certainly, complex models of the human tissue exist, with or without considering the dispersive effects, for example, [158, 159]. Moreover, full body-phantom models, such as the one presented in [157], for throughout simulations of a WBAN could be used. The precision of the results, but also the complexity, increases proportional to the complexity of the chosen body/tissue model. Thus one has to make an appropriate choice on the body/tissue model, depending on the actual antenna characteristics and operating scenarios. More detailed body models also limit the results to smaller groups of persons.

It is important to distinguish between body/tissue models for internal field and external field analysis. If the internal fields are of interest, a rather accurate and detailed phantom is needed whereas a simple (homogeneous) phantom can be accurate model for the external fields [160].

For example, in the design of antennas for body-worn devices operating in the near-field of each other, the simulation of a multilayered human tissue may be required to correctly obtain the radiation/propagation processes. When only the antennas far-field radiation characteristics are to be optimized the simulation of a complex human tissue is not needed anymore. While in the former case a full body model is needed at least for the area where the devices (antennas) are located, in the later case one can use a truncated model only covering the body part where the device is mounted.

A significant influence of the actual UWB antenna radiation characteristics when used or mounted close to the human body is to be expected. In this respect two important questions arise.

(i) How close to the human body these antennas are located?

(ii) What are the dynamics of the human-body-to-antenna configuration?

The first issue is relevant when optimizing antenna design for operation in the close proximity or on the human body. This leads to a static analysis and optimization of a particular antenna type when mounted close to a dielectric structure.

The second aspect is related to the *changing* near-field effects on the radiation characteristics of the antennas. The geographical dynamics of the human body (or body parts: hands, fingers) relative to the antenna of a body-worn device will reflect in the particular dynamics of the radio propagation conditions (channel), thus influencing the performance of the communication system. The statistical evaluation of these dynamics and variations from user to user is possible with specially design measurement setups, for example, [160].

The small-size, sensor-like devices can be mounted directly in contact with the human skin (e.g., for health-care monitoring systems) thus constant separation distances of maximum 2–3 mm are expected [138, 139]. Another case is that of antennas mounted in clothing (textile antennas) where the separation distance can be larger, in the order of 1–6 mm, and possibly varying up to 10–15 mm due the movements of the user. Headset and similar devices have relatively larger and constant separation distance from the human body of 5–10 mm. The scenario is similar for devices located in pockets. For handheld devices, the situation is similar to scenarios investigated for the GSM/UMTS cellular phones, for example, [143, 144, 160, 161], and the user's hands or fingers were found to be located typically between 5 mm and 40 mm distance from the antenna(s) in the terminal. In such cases, the interaction distance variations are generally large, in the order of 10–30 mm [160].

Regardless of the scenario, the influence of the human body proximity must be analysed and considered when optimizing the antenna design for specific applications. This has further impact on the design of multielement antenna systems, for example, [141, 142, 161], with potential improvement of the throughput and reliability of the communication devices used in the WBAN.

2.7.2.3. The RF antenna connection

The simulations for antenna design presented in Section 2.7.2.1 can be performed using complex or simplified models of the antenna structures and human body tissue. Details such as ground plane and other components of the communication device (housing, PCB, etc.) can be included to obtain even more realistic radiation results. The next step in the antenna investigations is building and testing the actual antennas. Similar to the simulations, the actual communication device can be emulated if necessary for a correct testing (casing, etc.). Experimental radio channel investigations (channel sounding) can then be carried out in typical scenarios envisioned for the WBAN.

Section 2.7.1 presented the argumentation for the need of new measurement methodologies, with the conclusion that the channel characterization for WBAN has to include the influence of the small-size antennas typically used. In traditional radio channel sounding, the antennas used are connected to the measurement equipment with radio frequency (RF) cables. This setup is perfectly suited for electrically large antennas, but not for electrically small antennas, as the radiation characteristics are significantly influenced by the size of the ground plane or any conductive cables acting as large ground planes. Therefore, the length and position of the connecting RF feed cables has a significant influence on the antenna radiation [162].

The ground plane on which the antenna element is mounted can be designed and simulated to fulfill the purpose. Changes in the antenna radiation characteristics due to the size of the ground plane are deterministic and can be accounted for. This is, however, not the case with the RF feed cable connecting the antenna element to the measurement system. The position of the cable is difficult to control during the actual measurements involving test users and can change the radiation significantly, which then lead to unrealistic radiation patterns [147]. Currents running on the cable in the close proximity of the human body can significantly change the signal absorption and signals radiation main direction, level, and so forth. Investigating the radio propagation channel without considering these aspects can lead to unrealistic results in terms of radio channel models and associated performance of different communication systems.

The observations above lead to one natural conclusion: the influence of the connecting RF feed cables or any other conductive cables connected to the device, which does not belong to the final application, ought to be minimized if not completely eliminated. A practical setup was proposed to achieve this, namely, the use of an RF on fiber optic (FO) link instead of the usual conductive cable feed connections [162]. Given the large bandwidth of the used optic fiber (above 10 GHz), a similar setup can be successfully used for UWB radio channel investigations as well.

When the antenna under test is used as transmitter antenna, the proposed setup is relatively simple based on a commercial FO transmitter and receiver pair. The optical receiver is a small detector diode which allows the emulation of small-size devices including the antenna. The optic receiver can be battery powered, thus

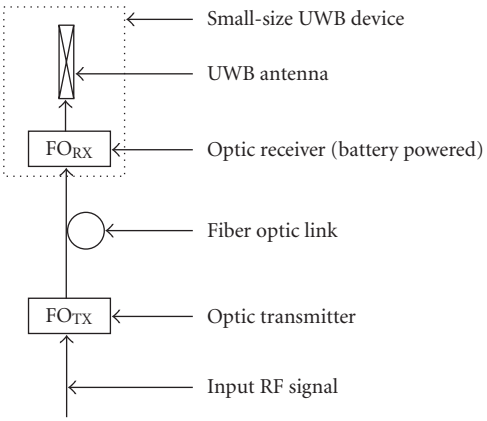

FIGURE 2.25. Fiber optic RF feed for small-size antennas. UWB frequency ranges can be easily accomodated due to the bandwidth of the fiber optic.

no conductive cables are needed to be connected to this side of the measurement chain. For short-range propagation investigations (1–3 m), this solution is good. For longer range investigations, that is, with higher path loss, additional signal amplifiers are required at the output of the optic receiver, which increases the size of the actual emulated device and power consumption of the setup. Figure 2.25 shows the FO setup with the antenna under test connected as radio transmitter. Of course, the antenna under test can be used as receiving antenna and still be connected with FO. In this case, however, the setup requires significantly more hardware components along with a careful design as the optic transmitter (laser) needs to be next to the antenna. The laser is significantly larger than the detector diode used in the optic receiver.

To illustrate the importance of this practical aspect and of the novel RF on FO setup, simulations have been performed for the radiation patterns of a small UWB antenna (folded radiating element) [163] with and without the conductive RF feed cable, respectively. Figures 2.26 and 2.27 show the obtained simulation results in one planar cut in the 3D far-field *total* (power) radiation pattern of the antenna. In all simulations, the antenna ground plane size was 25 mm $\times$ 55 mm. Figure 2.26 shows the result obtained without any conductive RF feed cable. This setup, practically, corresponds to the described RF on FO antenna connection setup. Figure 2.27 shows the different radiation patterns corresponding to different orientations of a 50 mm length and 1.2 mm diameter conductive RF feed cable. Naturally, similar results are obtained for increasing the ground plane size of the antenna in the corresponding direction.

As can be seen, the radiation patterns are not only different, but also the main radiation direction changes significantly when the conductive RF feed cable is connected to the antenna element. Changes in the electrical matching of the small-size antenna element were also disclosed by the simulations.

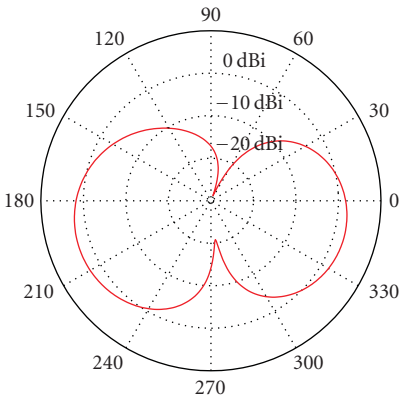

FIGURE 2.26. Simulated far-field antenna radiation pattern at 4.5 GHz for a small-size antenna without the RF feed cable. This setup, practically, corresponds to the described RF on FO antenna connection setup.

An important aspect, not illustrated in Figures 2.26 and 2.27, is related to the changes in the polarisation of the small-size antenna when conductive RF feed cables are used. The simulations showed that the polarisation in the direction of the connecting cable becomes dominant. With a moving cable connection such as in dynamic WBAN scenarios, the polarisation state will be signifcantly "modulated" by the actual position of the RF feed cable. This effect is also considerably minimised by using the RF on FO setup.

The presented results can be generalised for any type of small-size, narrowband, and ultra-wideband antenna. The important parameter is the *electrical* size of the conductive cable and/or ground plane. Due to the frequencies ranges in UWB, the electrical size of practical devices considered in WBAN becomes a factor which cannot be neglected. In the UWB case, the additional changes of the radiation pattern in the frequency domain have to be also considered.

2.7.2.4. On-body measurement setup

In order to highlight the particularities of the required WBAN radio channel measurement setup, as opposed to traditional propagation experiments, we introduce a practical configuration used in [145, 146]. We base our discussions on an emulated WBAN scenario, composed of two body-worn terminals: a portable base station (PBS) and a body-worn device (BWD) [145, 146, 139]. Two small-size, low profile UWB antennas [163] have been selected due to their commercial availability at the time of the experiment. In practice, any suitable small-size antenna type as presented in Section 2.7.2.1 can be considered. The BWD was emulated as a small device (e.g., the size of a sports watch) while the PBS was emulated as a larger device (e.g., the size of a mobile phone). Accordingly, the antennas for PBS and BWD have been used mounted on differently sized ground planes, 50 mm × 110 mm and 25 mm × 55 mm, respectively.

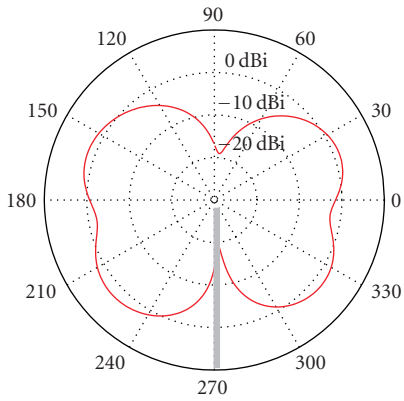

(a)

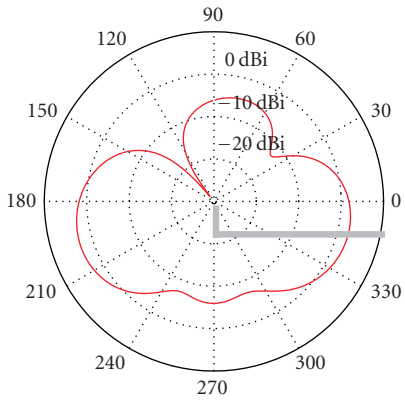

(b)

FIGURE 2.27. Simulated far-field antenna radiation pattern at 4.5 GHz for a small-size antenna with RF feed cable in different positions: (a) vertical and (b) bent to the right. The position of the feed cable is shown schematically.

Figure 2.28 shows the BWD and PBS antennas setups. At the PBS, one antenna element, from the original mount, was used in the measurements. At the BWD side, the RF cable connecting the BWD antenna was replaced by an RF FO link. At the PBS side of the measured link, the larger electrical size of the ground plane allowed the use of simple RF cable connection without a significant radiation pattern distortion. Furthermore, the cable connecting to the receive antenna was always kept vertical.

The investigations were carried out using several adult test persons with different body structures (weight and height). These data can provide initial statistics over different body structures for the investigated radio channel parameters [145, 146]. The PBS was mounted on the left side of the test person at hip height. For the BWD typical, static positions have been investigated on the left arm, right

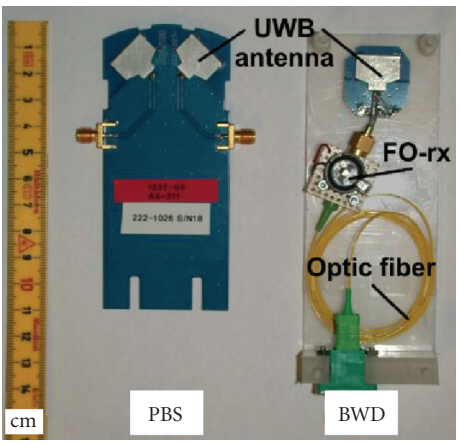

FIGURE 2.28. Example of antenna setup for on-body measurements [145, 146].

arm, and torso. Three different positions of the arms were used. More details can be found in references [145, 146].

Dynamic—thus more realistic—end-user scenarios can be investigated with similar antenna configurations, provided the measuring equipment is capable of capturing the required Doppler spread in the radio channel. A swept time-delay correlation channel sounder with a sufficient flat bandwidth (above 1 GHz) is suitable for these dynamic UWB radio channel measurements [138].

2.7.2.5. Measurements with body phantom

In general, body phantoms (or body-part phantoms) can be used in both antenna radiation investigations and radio channel measurements. The discussion presented in Section 2.7.2.2 on the choice of the type and complexity of body phantom/tissue for simulations is relevant also when considering antenna and channel measurements. For the case of radiation investigation of cellular phones (i.e., relatively narrow band compared to UWB) body phantoms have been successfully designed and analyses, for example, [157, 160, 164, 161]. Further development of these body (or body-part) phantoms has to be performed for the ultra-wide frequency band.

In the on-body UWB radio channel investigations described briefly in Section 2.7.2.4, several test users have been used in order to obtain statistical description of the channel parameters. The larger the number of test users, the better channel statistics can one obtain. Additionally, several types of environments should be investigated to yield geographical statistics as well. These kind of investigations have been carried out successfully for the GSM and UMTS frequency bands, for example, [143, 161]. In the case of the WBAN, the selection of the test users from body structure point of view is also a relevant factor.

FIGURE 2.29. Human torso phantom used for radiation measurements in the GSM and UMTS frequency bands [164].

With these considerations in mind, one can see the high complexity of the measurement campaigns required for throughout UWB WBAN radio channel characterization and modeling.

A method, which possibly can simplify and in the same time complement the methodology presented above, is the use of full body phantoms. Full body phantoms with realistic tissue dielectric properties are expensive and generally they are tuned for narrow frequency bands (GSM, UMTS, etc.) [159]. Simplified body phantom structures are available and described in the literature, for example, [156, 144, 160, 164]. Figure 2.29 shows an example of body torso phantom. These body phantoms can be used in UWB as long as appropriate validity tests are made in the investigated frequency band. The obtained results generally limit the set radio channel parameters which can be correctly evaluated using a specific body phantom structure.

As an example, in the work carried out in [146], body phantom investigations were conducted in order to make an initial assessment on the applicability of such human body models in UWB WBAN radio propagation analysis. The body phantom used consists of two concentric acrylic cylinders, with the gap in-between filled with saline solution conform the ETSI standard [158]. The total height of the body phantom was 1.9 m with an external diameter of 0.3 m. In this configuration, the body phantom had no "arms," "legs," or "head." Thus, from the scenarios described in Section 2.7.2.4, only the "torso" position of the BWD could be replicated with good geometrical approximations; the "right arm" position was possible with the BWD mounted close to the body phantom, on the diagonally opposite side from the PBS position.

The inherent cylindrical symmetry of the body phantom has a potential influence on the propagation mechanism in the around the body area. While for test users the radio waves are highly scattered from the arms and legs, this phenomenon cannot be captured with the simple body phantom. Therefore, a natural extension of this body phantom is the use of two cylindrical "arms" at a certain

distance from the "body." Another observation which has to made is related to the frequency dependency of the dielectric properties of the body phantom. Given the simple model—no explicit tissue model—one can expect a different behavior of the induced currents contributing to the wave propagation along the surface of the body phantom. This in turn leads to the conclusion that the presented body phantom is not suitable for on-body sensor network measurements.

2.7.3. Radio propagation channel

2.7.3.1. Introduction

The network-level design for WBANs strongly depends on the wide variety and specifics of the user scenarios in which the devices are expected to operate. The underlying air-interfaces and adaptive medium access control schemes have to be reliable and optimized. A successful implementation of these communication systems is not possible without a thorough analysis of the specific "around-the-body" radio propagation channels. Traditionally, the radio propagation channel for wireless systems is described in terms of a standard set of parameters: link budget and scattering functions (time-delay versus Doppler spectra). The evaluation of these parameters in typical UWB propagation scenarios has been presented in Sections 2.4, 2.5, and 2.6.

For WBAN UWB systems, it was anticipated in Section 2.7.2 that the radio propagation channel will exhibit some new and interesting characteristics such as antenna near-field and body-proximity effects. All these phenomena are very characteristic to the around-the-body propagation channel, thus a suitable characterization and modeling is required for them. The far-field propagation equations derived in Section 2.2 can be applied under certain conditions with respect to the positions of the transmitter and receiver antennas on the body and antenna types. Nevertheless, the solution for the de-embeding problem combined with double-directional measurements is not practical in typical WBAN scenarios where small devices are used. Similar, the scattering amplitudes in the theoretical expression for the UWB channel presented in Section 2.3 become very difficult to evaluate for the dynamic (nonstationary) around-the-body propagation channel. Furthermore, the dynamic near-field effects due to the body proximity cannot be derived and included analytically. In order to identify and separate the influence of the environment on the measured radio channel, different user and body-phantom positions can be measured. The data can then be analyzed in order to determine the channel impulse-response variability caused by the body phantom or human user only.

These observations lead us to the conclusion that, as opposed to more traditional channel modeling, the radio wave scattering in the around-the-body area is very complex to be described completely in analytical way and the WBAN radio channel has to be characterised and modelled based on empirical results and possibly complex simulations. In this Section, we present the basic principles of the WBAN radio channel characterisation and modeling. For this, we start with a brief

review of the UWB WBAN radio channel measurement results available in the literature. We make a distinction between the models obtained from traditional channel measurements and the new methodology presented in Section 2.7.2. Finally, we present the relevant results from a set of novel WBAN investigations described in references [145, 146].

2.7.3.2. Traditional channel measurement setups

The work presented in [147] is focused on the effects of human body interaction with a close proximity UWB antenna. Antenna performance measurements have been performed in the 1 GHz to 11 GHz frequency band, in the anechoic chamber and various indoor multipath environments. The investigated antenna was a commercially available diamond dipole UWB antenna [150]. For the on-body experiments, the test antenna (transmitter) was belt (waist height) and head mounted, using a cell phone makeup; the 1 GHz to 3 GHz frequency band was measured using a time modulated UWB system from Time Domain Corporation. The receiving antenna was a horn type located at 5 m distance from the antenna under test.

The investigation results in [147] showed a clear antenna interaction with the human body. In light multipath scenarios, this interaction resulted in a 23 dB null in the angular distribution of the power radiated from the "antenna + human body" system in the direction of the human body. In dense multipath scenarios, only a variation of 6.8 dB was noticed, confirming the robustness of the UWB systems in such environments. More realistic WBAN scenarios have been investigated in [148], with both antennas (transmitter and receiver) placed on the body. Two types of scenarios have been considered with antennas positioned on the front side of the body and around the upper torso. Anechoic chamber and an office room environments were used. The antennas used were commercially available small-size, low-profile type [163]. Cable RF feed connections have been used for both antennas but no details on the ground plane size of the antennas and antenna position is given in the publication. Although the accuracy of the results depends on it, the influence of the feed cables on the antenna radiation patterns is not addressed either in [148].

The 3 GHz to 6 GHz frequency band has been measured with a vector network analyzer and the on-body UWB radio channel was described in terms of path loss index and signal mean and rms delay spread. Further results are presented in terms of required Rake receiver fingers and the energy considerations for single- and multihop links. Under the considerations made in Section 2.7.2, it is evident that radio channel results (parameter values and range) are very sensitive to the used measurement setup. Naturally the numerical values for the path loss and time-delay spread strongly depend on the antenna system (antenna element, ground plane, and feed cable) radiation characteristics when located on the body. It has to noted that the results presented in [148] are obtained based on the assumption of ideal, omnidirectional antenna radiation patterns. Furthermore, no analysis of the influence of the feed cable(s) and of the human body proximity on the antenna

radiation characteristics is made, thus the free-space specifications given by the antenna manufacturer are implicitly assumed.

Making one step further, the WBAN investigations presented in [145, 146] address these issues and use improved accuracy of the measurement equipment and antenna setup. The most important remark here is that the extracted radio channel parameters still remain characteristic for the antenna types used and cannot be directly generalized as proposed in [148].

2.7.3.3. Channel measurements with improved accuracy

In the following, we present the main results from investigations carried out following the methodology described in Section 2.7.2. These novel experiments and simulations allow us to disclose the main aspects of the WBAN radio propagation phenomena in terms of

(1) antenna radiation characteristics when operating in the close proximity of a simulated arm phantom,
(2) radio channel characteristics and parameters relevant to the design of a UWB based WBAN communications system.

Similar to the channel measurement in [148], two small-size, low-profile type antennas specified for the 3 GHz to 6 GHz frequency band have been used [163]. The reasoning for the choice of our antenna mount, ground plane size, RF optic fiber feed connection, and user scenarios was presented in Section 2.7.2. The first on-body UWB radio channel measurements using this setup were presented in more details in references [145, 146]. The WBAN was emulated with two body-worn terminals: a portable base station (PBS) and a body-worn device (BWD), similar but not limited to the scenarios considered in [139]. The detailed description of the antennas and the body phantom used in the investigations can be found in Section 2.7.2 and references [145, 146].

For disclosing the effects of the body proximity on the antenna radiation characteristics simulations can be carried out, as described in Section 2.7.2.2. A practical example of antenna analysis results is given in the following. The details of the study can be found in [145, 146].

2.7.3.4. Human body influence on the antenna radiation characteristics

The influence of the arm where the BWD is mounted was modeled as a dielectric brick of 60 mm × 114 mm × 40 mm (width × length × thickness) of muscle tissue with the conductivity $\sigma = 2.22$ S/m and permittivity $\epsilon_r = 41.5$ [159]. Similar for the PBS, the body was modeled as a brick of 145 mm × 155 mm × 30 mm and compared to a much larger part of the body without significant differences in the results. These dimensions for the body models were found after a few iterations aimed to simplify the simulations without introducing significant changes in the obtained results.

The influence of the human body proximity is highlighted in Figures 2.30 and 2.31. The simulated arm and body is located in the right half of the corresponding

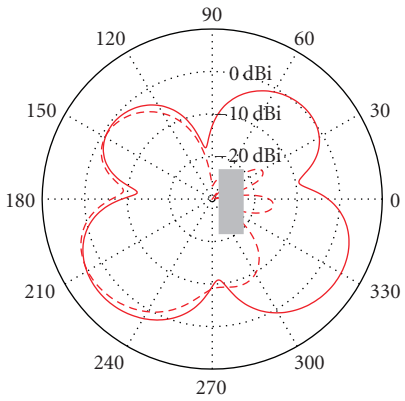

FIGURE 2.30. Simulated BWD, far-field antenna radiation pattern a 4.5 GHz (yz-plane) with and without the proximity of arm. The ground plane size was 25 mm × 55 mm. The simulated arm with dimensions 60 mm × 114 mm × 40 mm is located in the right half of the plot (shaded area).

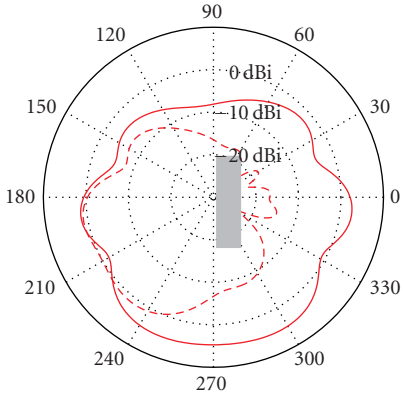

FIGURE 2.31. Simulated PBS, far-field antenna radiation pattern at 4.5 GHz (yz-plane) with and without the proximity of body. The ground plane size was 50 mm × 110 mm. The simulated body with dimensions 145 mm × 155 mm × 30 mm is located in the right half of the plot (shaded area).

radiation pattern plots. Most of the radiation towards the human arm/body disappears due to absorption and reflections. The absorption is largest for the lowest frequencies, some 80% for 3 GHz and some 65% for 6 GHz.

2.7.3.5. Antenna radiation pattern versus frequency

The antenna element used in our previous examples is not radiating in the same way for all frequencies of interest. This is the general case for simple UWB antenna structures orginally designed for operation in free-space conditions.To investigate the change in radiation pattern over frequency, simulations can be performed for

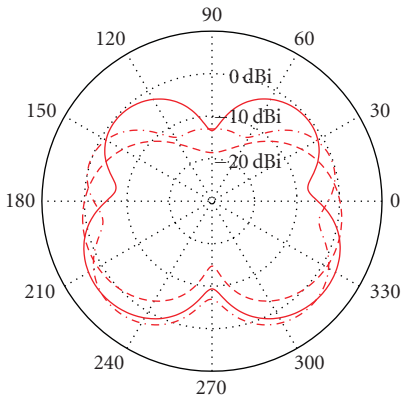

FIGURE 2.32. Simulated antenna radiation (*xz*-plane) versus frequency for the BWD antenna with dimensions as used in the measurements [145, 146].

several frequencies, with and without the human body present. As an example, Figure 2.32 shows the simulation results at 3 GHz, 4.5 GHz, and 6 GHz for the BWD. It is clear that the radiation changes significantly over the frequency band and this influences the channel characterization methodology which has to be applied. Due to this nonstationarity in the frequency domain, the analysis of cross- and autocorrelation properties can yield more correct results if it is performed on several subbands [145, 146].

2.7.3.6. Radio channel parameters

Three main radio channel parameters have been extracted and analyzed from the investigation presented in Sections 2.7.3.2 and 2.7.3.3.

(1) Link budget: wideband power levels can be used for the description of the shadowing effects which occur around-the-body propagation environment [145, 146, 148].
(2) Radio channel frequency transfer function: average slope and autocorrelation properties in consecutive subbands [145, 146]. The frequency-domain analysis is particulary important in UWB systems due to the signal distortion which needs to be analysed, for example, [165, 166].
(3) Signal time-delay dispersion: rms delay spread [145, 146, 148] and delay window length that contains 99% of the total power [145, 146]. These parameters are important for system-level design especially for optimising the performances of low-cost, low-power devices.

Although a more complex description of the radio channel is possible (see Sections 2.4 and 2.5) in typical WBAN scenarios, the above listed parameters were found to be the essential ones. Furthermore, for the time-domain signal statistics analysis, a suitable measurement equipment is required, such as a UWB swept time-delay correlation channel sounder. There were no dynamic WBAN channel investigation results available in the literature at the time of writing this book.

Table 2.9. Main channel parameter results for WBAN presented in [148].

	PL_0 (dB)	γ	Min τ_{rms} (ns)	Max τ_{rms} (ns)
Front side				
Anechoic chamber	82.2	3.3	1.4	2.2
Office	75.8	2.7	2.1	7.5
Around the torso				
Anechoic chamber	—	—	1.4	7.3
Office	109.2	4.1	2.1	9.9

The relevant results from the available radio channel investigation [145, 146, 148] are analyzed in the following sections with focus on their impact on the operation of low-cost, low-power devices.

2.7.3.7. Link budget

The proposed path loss model in [148] is given by the expression:

$$\mathrm{PL}(d) = \mathrm{PL}_0 + 10 \cdot \gamma \cdot \log_{10}(\mathrm{d[m]}/1\mathrm{m}),\ [\mathrm{dB}] \tag{2.151}$$

and Table 2.9 summarizes the main results for the channel parameters in different scenarios [148]. Path loss exponents up to 4.1 were obtained for the office propagation scenarios, with additional possible fluctuations of the received power levels up to 20 dB due to the position of the arms. These results have been further utilised to determine energy levels for single- and multihop links.

From the studies in references [145, 146], Figure 2.33 shows the global statistics obtained in terms of wideband power levels in typical positions of a body-worn device relative to the human body. Five test users have been used in up to four different positions in the same indoor environment. The reference power levels of 0 dB correspond to a free-space (far-field) path loss, assuming 0 dBi antenna gain and a 4.5 GHz carrier and at the same average distances as in the human body measurement scenarios. The averaged cumulative distribution curves over three different cases of positioning the BWD on the body can be well approximated with a linear curve with respect to the power levels expressed in logarithmic units. Nevertheless, significant deviations from these average CDFs are to be expected.

2.7.3.8. Frequency transfer function

The analysis of the frequency-domain data presented in [145, 146] starts with a global characterization, that is, over the whole frequency band which was measured.

Figures 2.34 and 2.35 show as an example the measured frequency transfer function, $H(f)$, for one test person in the four rotated positions, with the BWD in the *left arm* and *right arm* scenarios, respectively. The average and the standard deviations of the $H(f)$ curves (over the 128 measurements) are also plotted to illustrate the measured variability of the channel.

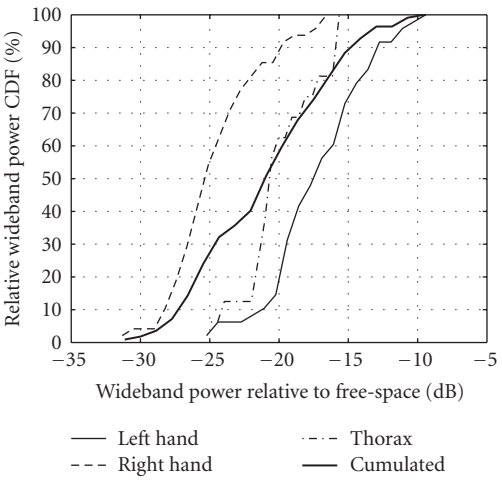

FIGURE 2.33. Statistics calculated for the measured wideband power levels in typical body-area scenarios [145, 146].

Figures 2.34 and 2.35 also show the (average) power delay profiles calculated from the $H(f)$ data. Similar results were obtained for the other WBAN scenarios as presented in [145, 146].

The first remark has to be made here regarding the significantly different frequency-domain behavior of the radio channel for the two scenarios with BWD in the *left arm* and *right arm* scenarios. In the *left arm* scenario, the direct propagation path is very short in the order of 10 cm to 15 cm. This path dominates and does not change significantly if the scenario is static as in our case, that is, the outside environment does not introduce significant changes. Certainly, scattered and attenuated paths from the body and the ground exist, as determined also in [148], and these paths give rise to the variations shown in Figures 2.34 and 2.35. In the *right arm* scenario, the direct propagation path is generally more attenuated than the scattered ones. The outside environment has a strong influence on the overall propagation channel between the transmitter and the receiver. High power multipath components can be observed at relative delays up to 90 nanoseconds from the direct path.

Another remark is that the average $H(f)$ displays generally both small-scale and large-scale fluctuations in frequency domain. This observations is the basis of the analysis of the correlation properties of $H(f)$, presented later in Section 2.7.3.9.

An autoregressive modelling approach as presented in Section 2.5.4 seems possible to achieve. Nevertheless, due the high variability of the frequency transfer function depending on the actual position of the user in the radio environment, a large set of measurements is required. Furthermore, as exemplified in Figures 2.34 and 2.35, a radical change is to be expected when the device is moved to different positions on the body and this effect also has to be introduced in the more general model.

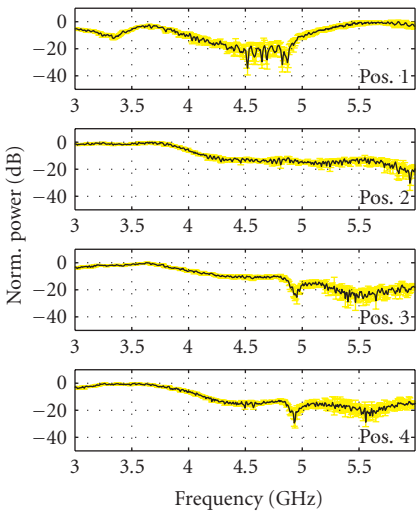

(a)

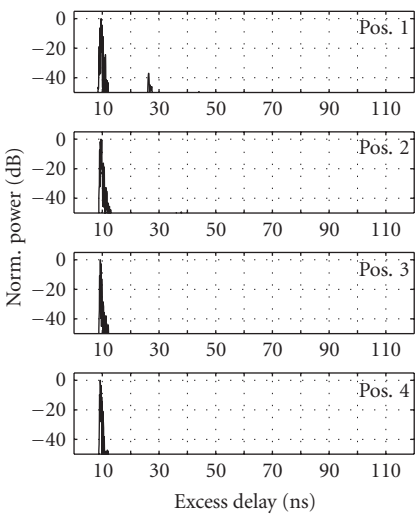

(b)

FIGURE 2.34. Example of (a) measured $H(f)$ and (b) the corresponding power delay profile for one test person in the left arm Pos.V scenario in four different body positions.

In the first step, the slope of each average $H(f)$ was calculated via curve fitting (least mean-square error) and expressed in dB/oct units. In the left arm setups, the $H(f)$ slope values are generally high, in the range -25 dB/oct to -6 dB/oct, while in the torso and right arm setups, the values are lower and range from -7 dB/oct

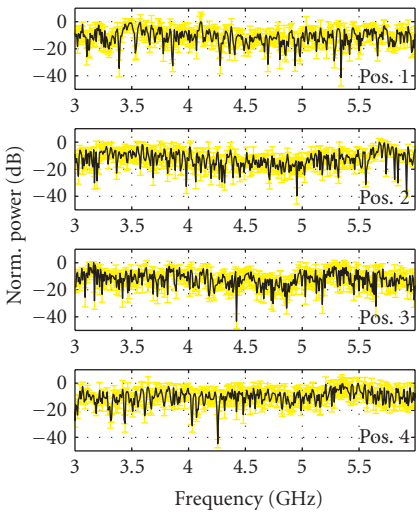

(a)

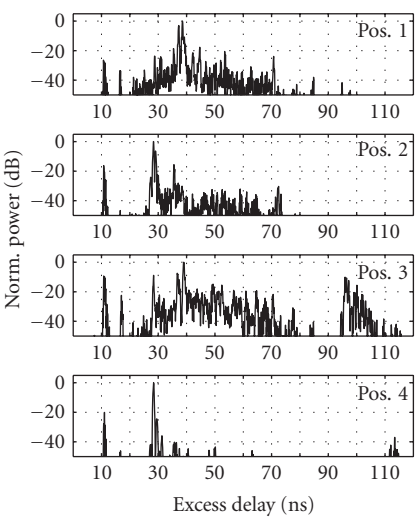

(b)

FIGURE 2.35. Example of (a) measured $H(f)$ and (b) the corresponding power delay profile for one test person in the right arm scenario in all four different body positions.

to +10 dB/oct. For different test persons in similar scenarios, large variations of the $H(f)$ slope values were observed, up to 20 dB/oct. Thus, a clear dependency of the $H(f)$ slope on the human body cannot be disclosed except for the above observations. The range of the possible $H(f)$ slope values can be used, however, when implementing adaptive (pulse shape, template, etc.) receiver structures.

2.7.3.9. Frequency correlation properties

Based on the discussions in Section 2.7.3.8, the correlation properties in the frequency-domain are analyzed on consecutive subbands. The selected subbands are 300 MHz wide, with an overlap factor of 50% (150 MHz). The investigated 3 GHz to 6 GHz band is analyzed with a total of 19 overlapping subbands (300 MHz each) [145, 146]. The width of the subbands can also be chosen based on visual inspection of representative experimental data. Frequency correlation bandwidths, $B_{C0.5}$ and $B_{C0.7}$, can be calculated for the 0.5 and 0.7 frequency correlation levels, respectively. Next, the global cummulative distribution function (CDF) of the $B_{C0.5}$ and $B_{C0.7}$ bandwidths in each subband can be analysed using results from several test users and their positions, in the same indoor environment.

Figure 2.36 shows the obtained CDF for the $B_{C0.5}$ correlation level. Differences can be observed between different frequency subbands in the *left arm* and *torso* scenarios, due to the antenna radiation patterns in combination with the frequency-selective absorption of the human body. In the *right arm* scenario, the frequency autocorrelation function exhibits also significant fluctuations as a result of the scattering in the total environment.

As expected, in the left arm setups (very short range), high average B_C values in the range of 140 MHz were obtained. For the torso setups, slightly lower, in average 120 MHz, average B_C values were determined. In the right arm setups, the influence of the total radio environment is very significant, and low average B_C, in the range of 35 MHz, have been obtained.

The main observation which has to be highlighted here is that in consecutive frequency subbands the frequency correlation properties can be significantly different in certain body-area scenarios (device position relative to the body). Significant variations were observed also between the results for different users, with widely spread CDF curves around the results shown in Figure 2.36. Thus, for an accurate UWB WBAN channel description, a subband analysis is more appropriate rather than considering the entire frequency band. For example, the autoregressive modelling approach can be applied to frequency subbands.

2.7.3.10. Signal time-delay dispersion

In reference [148], rms delay spreads in order of 2 nanoseconds up to 10 nanoseconds have been calculated with the remark that the higher signal spread values in the torso scenarios are possibly due to the echoes present in the measurement environment. From the studies in references [145, 146], Figure 2.37 shows the cumulative distribution curves of the calculated $W99$ parameter (delay window length that contains 99 % of the total power) and rms delay spread values in all investigated body area scenarios.

The first important observation which can be made here is that the $W99$ and the rms delay spread parameters *do not* have similar statistics. While there is a clear separation in two distinct range clusters for the $W99$ parameter values—namely, below 40 nanoseconds and above 80 nanoseconds—this clustering cannot

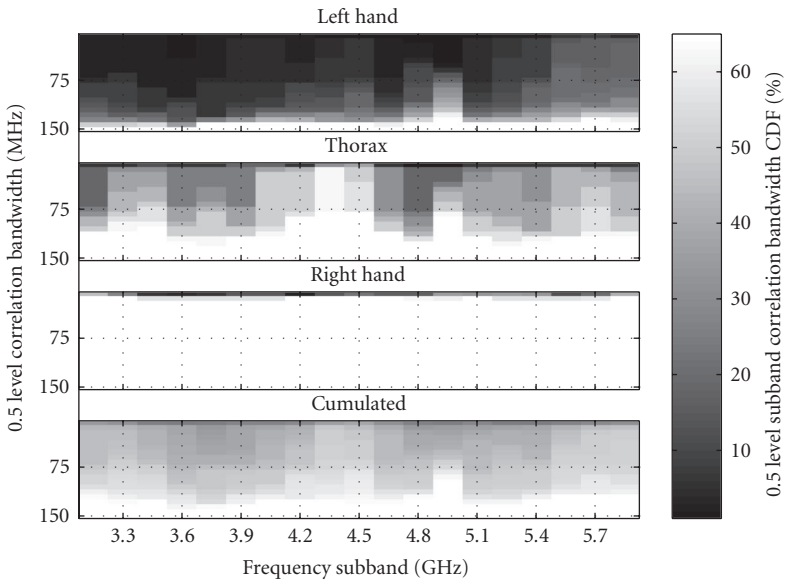

FIGURE 2.36. Example of calculated global cummulative distribution function (CDF) of the $B_{C0.5}$ bandwidths in each subband.

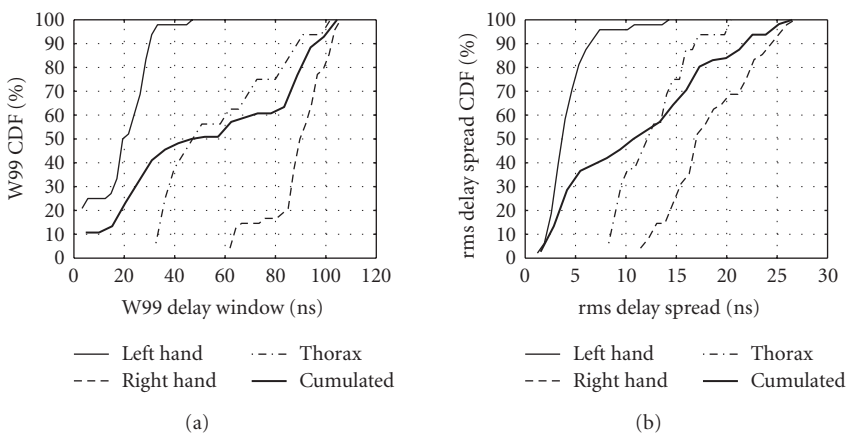

FIGURE 2.37. Statistics calculated for (a) the W99 parameter and (b) rms delay spread in typical body area scenarios.

be observed in the rms delay spread values. Thus, a system performance evaluation based only on the classical delay spread parameter is underestimating the particularities of the WBAN propagation channel.

Furthermore, the curves in Figure 2.37 show significant variation between the results obtained for the different BWD positions.

2.7.4. Conclusions

In this Section, we introduced and analyzed the most important aspects of radio propagation and antenna measurement techniques for WBAN. The focus was on user scenarios with small- and medium-size devices.

Antenna design and analysis for small-size devices is certainly one of the key issues when implementing WBAN. A significant influence of the actual UWB antenna radiation characteristics when used/mounted close to the human body was disclosed [145–148]. Numerical methods, such as FDTD, need to be employed in order to analyze the radiation characteristics of small-size, body-worn UWB antennas. Nevertheless, further investigations are needed in UWB antenna design for small-size, body-worn devices to optimize their radiation patterns and total efficiency when operating in the proximity of the human body.

The presented WBAN scenario measurements and simulations put in evidence the potential influence of the body proximity on the UWB radio propagation channel. The traditional measurement methodologies were shown not to be optimal for an accurate characterization of the WBAN radio propagation channel including body-proximity and antenna effects. In WBAN radio channel measurements with electrically small antennas, the influence of the connecting cables ought to be minimized if not completely eliminated. A practical setup was proposed in References [145, 146] to achieve this: the use of a RF on fiber optic link instead of the usual conductive feed cable. Deriving a radio channel model without considering these aspects can lead to unrealistic characterization of the radio channel and the associated performance of different UWB communication systems.

Body-phantom measurements and simulations can be used to obtain realistic WBAN channel characterization. The use of a simple body phantom specified by ETSI [158] can, however, lead to wrong estimation for parameters such as channel frequency transfer function slope and autocorrelation. Our repeatability tests performed with the body phantom in a realistic but controlled environment showed relatively high uncertainty levels for the estimated frequency and time parameters, except for the wideband power. We believe that more complex-shaped phantoms can be used to improve these results.

The wideband power-level fluctuations up to 20 dB obeserved in static WBAN scenarios [145, 146] have to be taken in consideration as an additional slows-(shadowing) fading margin when designing the communication link. For a proper operation, the receiver input gain control loop has to be able to track relatively slow signal-level variations with this order of magnitude. The frequency correlation properties of the radio channel change significantly over the investigated frequency band of 3 GHz to 6 GHz, mainly due to the changing radiation characteristics of the antennas when operating in close proximity of the human body. An analysis performed on consecutive and partly overlapped frequency subband seems to give a more realistic characterisation of the channel transfer function [145, 146].The influence of the channel frequency transfer function slope and autocorrelation characteristics on the communication link depends very much on

the actual signal bandwidth. Thus the analyzed frequency-domain aspects have to be taken in considerations when designing or optimizing UWB links with different pulse shapes (Gaussian, wavelet, etc.) [145, 146]. The signal energy spread in time(-delay) domain was investigated and significant difference were shown for different body-worn device positions and the total scattering environment in which the user is "immersed" can drastically change the radio propagation between two body-worn devices [145, 146, 148]. Maximising the captured energy, while maintaining a high data rate, requires knowledge about the expected signal spread, even for very short-range communications such as in WBAN.

The presented WBAN radio channel investigations have been only for static scenarios. A natural extension will be to use dynamic and more realistic user scenarios in order to fully describe the associated UWB WBAN radio channels.

2.8. Channel estimation techniques

2.8.1. Introduction

Channel estimation in the UWB regime is of greater significance due to two basic reasons: (i) the transmit power spectral density constraints due to (modified) Part 15 rules that seriously limit the symbol SNR available at the receiver and (ii) the severe multipath due to the ultra-wideband nature of the modulation, implying that the per-path SNR is even lower. There is very little link margin left at the high data rates (480 Mbps) over the more severe multipath channels (such as the CM3 and CM4 [137]), implying that coherent demodulation is desirable so as not to further compromise the link budget; this implies the need for accurate channel estimation at the receiver. Typically, the transmission formats for high-rate link designs incorporate training or pilot symbols for appropriate channel estimation at the cost of some system overhead. However, the choice of the pilot sequences should conform to the choice of the modulation scheme, and the estimator designed accordingly.

In this chapter, we focus on channel estimation techniques for the two main link-layer design approaches presented to IEEE 802.15.3a (high-rate ultra-wideband) Task Group—namely, the multiband OFDM and the direct-sequence-UWB (DS-UWB) based designs, respectively. The MB-OFDM system is based on orthogonal frequency division multiplexing (OFDM) as in 802.11; hence the transmitted pilot is a frequency-domain sequence leading naturally to frequency-domain channel estimation at the receiver. In contrast, DS-UWB is a time-domain modulation scheme, leading to time-domain channel representations and estimation. The complexity and performance of channel estimation in these two cases is then fundamentally determined by (i) N_c, the FFT size chosen for the MB-OFDM implementation and (ii) $\tau \cdot BW_c$, where τ is the maximum delay spread and BW_c is the channel bandwidth for DS-UWB, which represent the parametrization of the channel in the frequency and time domains, respectively.

In the following, the transceiver structures for the two designs including the structure of training symbols are described. Subsequently, the choice of channel estimators and their resulting performance is investigated. Finally, a representative

simulation result is presented that encapsulates the impact of the channel estimator on end-to-end link-layer bit error rates.

2.8.2. Multiband OFDM alliance proposal

2.8.2.1. Description of the MB-OFDM proposal

The MB-OFDM proposal to IEEE 802.15.3a [167] divides the UWB spectrum into several subbands of 528 MHz width each. Within each band, information is transmitted using OFDM modulation. In order to introduce multiple accessing capability and to exploit the inherent frequency diversity, each OFDM symbol is transmitted on a different subband as dictated by a time-frequency code that leads to *band hopping*.

The inherent ability of OFDM to effectively overcome intersymbol interference (ISI) for high-data-rate systems over frequency-selective multipath channels is well known. A brief overview of OFDM is given here; for further details, the reader is referred to [168]. Figure 2.38 shows a block diagrammatic overview of the operations within the MB-OFDM transmitter and receiver implementations.

OFDM effectively converts a (wideband) frequency-selective channel to multiple flat-fading (nonselective) channels by demultiplexing a single high-rate serial data stream onto several lower-rate parallel data streams which are then transmitted independently on the narrowerband subchannels using different carriers that are carefully chosen to maintain mutual orthogonality. MB-OFDM uses $N_c = 128$ subcarriers separated by $\Delta f = 4.125$ MHz that span the 528 MHz width of each subband. In order to ensure orthogonality among subcarriers, the symbol duration is fixed to be $T_{\text{FFT}} = 1/\Delta f = 242.42$ nanoseconds. Each subcarrier is modulated independently with the complex symbol $S_{n,k}$ assumed to be QPSK for our purposes; the subscript denotes the nth OFDM symbol carried on the kth subcarrier. Thus, within the symbol duration T_{FFT}, the transmitted nth OFDM symbol is given by

$$s_n(t) = \frac{1}{\sqrt{N_c}} \sum_{k=0}^{N_c-1} S_{n,k} e^{j2\pi k \Delta f t}, \quad 0 \le t \le T_{\text{FFT}}. \tag{2.152}$$

As is well known, the transmitted (baseband) OFDM symbol is created by a 128-point IFFT operation on $S_{n,k}$.

Because of the multipath nature of the channel, the orthogonality among the subcarriers is lost after passing through the channel. In order to preserve orthogonality during transmission, the MB-OFDM scheme appends 32 zero samples spanning a 60.6-nanoseconds (T_{ZP}) time duration to $s_n(t)$ in (2.152), which is larger than the typical delay spread of UWB channels. To this a 9.5-nanoseconds guard interval is added, thus making the OFDM symbol duration $T_{\text{SYM}} = 312.5$ nanoseconds.

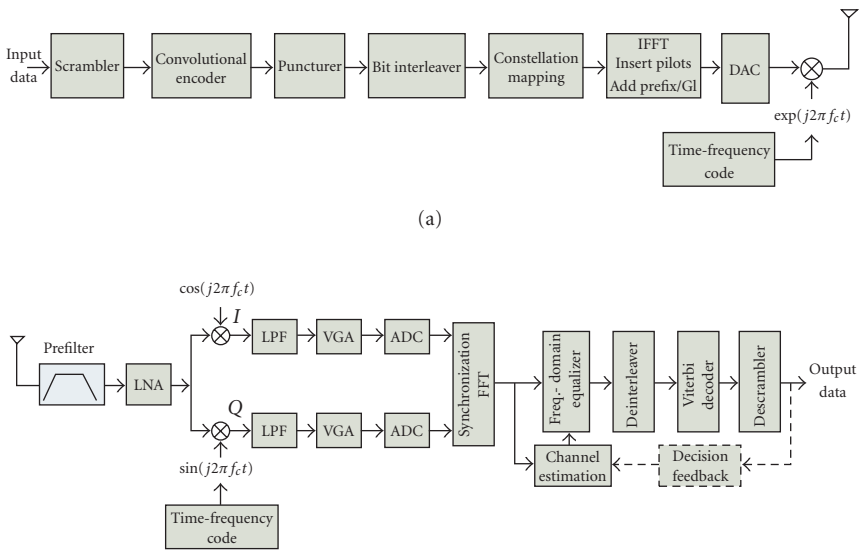

FIGURE 2.38. Structures of the MB-OFDM (a) transmitter and (b) receiver.

At the receiver, orthogonality is restored by adding the last 60.6 nanoseconds of the received signal to the first 60.6 nanoseconds duration of the OFDM symbol. Correlation at the receiver is implemented as a 128-point FFT operation.

A PHY frame is constructed around the MAC payload for transmission whose structure, shown in Figure 2.39, consists of a preamble, header, and the MAC payload. The PLCP preamble portion of the PHY frame is made up of 30 OFDM symbols consisting of the following:

(1) *packet synchronization sequence*: 21 OFDM symbols constructed from a time-domain sequence, which is used for packet detection and acquisition, coarse carrier-frequency estimation and coarse symbol timing,

(2) *frame synchronization sequence*: 3 OFDM symbols constructed from a time-domain sequence, which is used to synchronize the receiver algorithm within the preamble (boundary detection),

(3) *channel estimation sequence*: 6 OFDM symbols constructed from a frequency-domain sequence, which is used for channel estimation, fine carrier frequency estimation and fine symbol timing.

2.8.2.2. Channel estimation and equalization

Availability of an accurate channel transfer function estimate is a prerequisite for coherent symbol detection within an OFDM receiver. Channel estimation in OFDM systems can be classified as frequency-domain- or time-domain-based; each of this can be further divided as being pilot assisted, decision directed, or

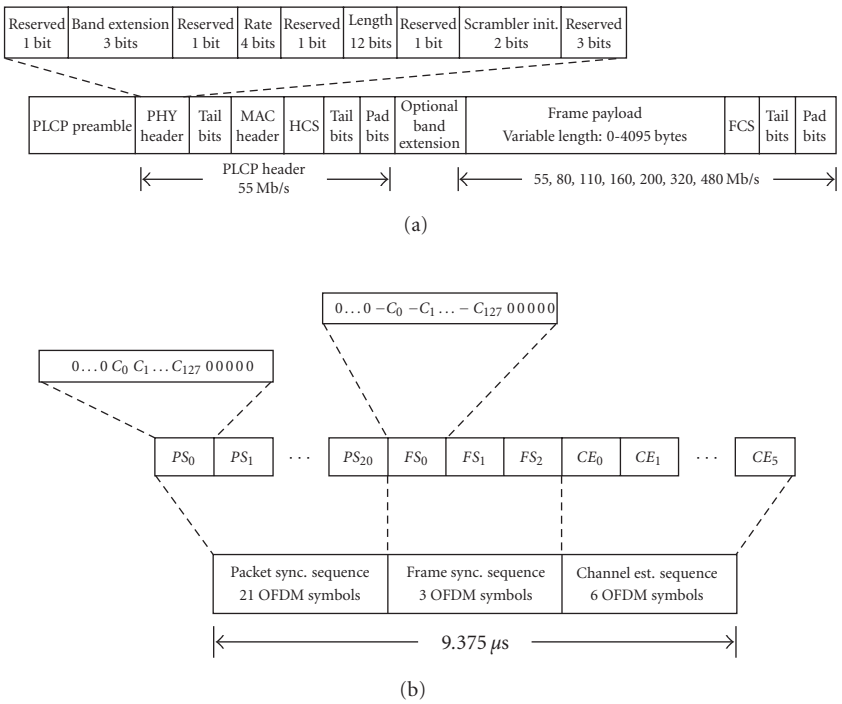

FIGURE 2.39. (a) Structure of the MB-OFDM PHY frame; (b) structure of the preamble (reproduced from [167]).

blind startup. Since the MB-OFDM proposal includes a frequency domain channel estimation sequence transmitted in each PHY frame on all subcarriers, our focus in this section will be on pilot-based frequency-domain (i.e., post-FFT in the receive chain) channel estimation and equalization techniques as indicated in Figure 2.38.

Since the OFDM symbol duration is much larger than the delay spread of typical UWB channels, each subcarrier experiences flat fading. As a result, the effect of the radio channel in the frequency domain is characterized by a multiplicative distortion of the kth subcarrier signal via the (complex) channel response H_k. Thus the received samples post-FFT is given by

$$R_k = H_k S_k + N_k, \quad k = 1, 2, \ldots, N_c, \tag{2.153}$$

where H_k is the channel transfer function sampled at the kth subcarrier location and N_k is the additive white noise of the channel. Equation (2.153) in matrix form can be written as

$$\underline{R} = \mathbf{H}\underline{S} + \underline{N}, \tag{2.154}$$

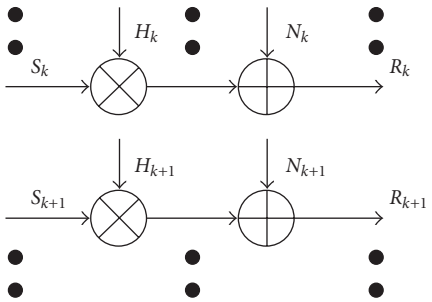

FIGURE 2.40. Effect of channel fading on subcarriers.

where $\mathbf{H}$ is a diagonal matrix with H_k as its diagonal entries and $\underline{S}$, $\underline{R}$, and $\underline{N}$ are the transmitted symbol, received symbol, and the additive noise vectors, respectively, as is shown in Figure 2.40.

The form of (2.153) shows that the least-squares (LS) estimate of the channel coefficients is simply given by

$$\hat{H}_k = \frac{R_k}{S_k} \quad k = 1, 2, \ldots, N_c, \tag{2.155}$$

where the known frequency-domain sequence S_k is sent as part of the preamble in every frame. This sequence is transmitted on all the subbands and done so twice in each subband so as to improve the LS estimates obtained using (2.155). We discuss approaches to enhancing the LS channel estimates more broadly in Section 2.8.2.2. To obtain the (unknown) transmitted symbols, frequency-domain equalization is needed to compensate for the channel based on the channel estimate obtained as above. We consider the topic of equalization separately for uncoded and coded systems.

To estimate the transmitted signal vector $\underline{S}$ from the received signal vector $\underline{R}$, consider the following linear estimator:

$$\hat{\underline{S}} = \mathbf{K}^T \underline{R}. \tag{2.156}$$

The design of the estimator $\mathbf{K}$ could be accomplished based on two different approaches: (a) based on using the estimated channel or (b) using only the statistical properties (and not estimates) of the channel. Typically, two design criteria are usually considered: (i) zero forcing (ZF) which neglects the presence of noise and compensates only for the channel distortion and (ii) minimum mean-square error (MMSE) criterion, in which the channel distortion and noise are simultaneously minimized.

Zero-forcing equalization. Zero-forcing (ZF) equalization attempts to invert the channel transfer function to produce an estimate of the transmitted symbol vector. In other words, the ZF equalizer has to satisfy the condition $\mathbf{K}_{\mathrm{ZF}}^T \mathbf{H} = \mathbf{I}$, where $\mathbf{I}$ is

the $N \times N$ identity matrix, whose solution is $\mathbf{K}_{\mathrm{ZF}}^{T} = \mathbf{H}^{-1}$. Since the channel matrix $\mathbf{H}$ is diagonal, the ZF estimate for the transmitted signal vector $\underline{\hat{S}}_{\mathrm{ZF}} = \mathbf{K}_{\mathrm{ZF}}^{T}\underline{R}$ can be computed independently on a subchannel basis:

$$\hat{S}_{\mathrm{ZF},k} = \frac{1}{H_k} R_k, \quad k = 1, 2, \ldots, N. \tag{2.157}$$

Zero-forcing equalization allows for optimum performance if little or no noise is present. However, since $1/H_k$ takes on very large values for subcarriers in deep fades, ZF equalization causes significant noise enhancement at those (near) spectral nulls and performance suffers as a result.

MMSE equalization. MMSE equalization attempts to minimize the squared norm of the error vector $\|\mathbf{K}_{\mathrm{MMSE}}^{T}\underline{R} - \underline{S}\|^2$ and can be obtained using the orthogonality principle [169, 170]:

$$\mathbf{K}_{\mathrm{MMSE}}^{T} = \mathbf{R}_{\underline{SR}}\mathbf{R}_{\underline{RR}}^{-1}, \tag{2.158}$$

where $\mathbf{R}_{\underline{SR}}$ and $\mathbf{R}_{\underline{RR}}$ are the cross-covariance matrices between $\underline{S}$ and $\underline{R}$ and the autocovariance matrix of $\underline{R}$, respectively,

$$\begin{aligned} \mathbf{R}_{\underline{SR}} &= E(\underline{S}\underline{R}^{H}) = E(\underline{S}(\mathbf{H}\underline{S} + \underline{N})^{H}) = E_s\mathbf{H}^{H}, \\ \mathbf{R}_{\underline{RR}} &= E(\underline{R}\underline{R}^{H}) = E((\mathbf{H}\underline{S} + \underline{N})(\mathbf{H}\underline{S} + \underline{N})^{H}) = E_s\mathbf{H}\mathbf{H}^{H} + \mathbf{R}_{\underline{NN}}, \end{aligned} \tag{2.159}$$

where E_s is the average transmitted signal energy defined as $E_s = E(\underline{S}\underline{S}^{H})$ and $\mathbf{R}_{\underline{NN}}$ is the noise covariance matrix $\mathbf{R}_{\underline{NN}} = \sigma_N^2\mathbf{I}$. Plugging (2.159) in (2.158), the MMSE equalizer is given by

$$\mathbf{K}_{\mathrm{MMSE}}^{T} = \left(\mathbf{H}\mathbf{H}^{H} + \frac{\sigma_N^2}{E_s}\mathbf{I}\right)^{-1}\mathbf{H}^{H}. \tag{2.160}$$

Since $\mathbf{H}$ is a diagonal matrix, equalization can again be done on a subchannel basis, yielding transmitted symbol estimates given by

$$\hat{S}_{\mathrm{MMSE},k} = \frac{H_k^{*}}{\left(|H_k|^2 + \sigma_N^2/E_s\right)} R_k, \quad k = 1, 2, \ldots, N_c. \tag{2.161}$$

Notice that when the noise level is significant, the MMSE solution avoids the noise enhancement problem even when some H_k's are close to zero while at low noise levels, the MMSE solution converges to the ZF solution.

Equalization in the presence of coding. If the receiver decisions are made independently on each subcarrier, symbols sent on subcarriers that have undergone deep fades would be (with high probability) erroneous and would lead to an error floor. Thus, uncoded OFDM is virtually unusable on multipath fading channels with deep notches occurring in the frequency spectrum. Suitable channel coding

with frequency-domain interleaving is thus essential in OFDM to recover symbols lost in subcarriers in deep fades. MB-OFDM uses rate 1/3 convolutional encoding with different puncturing patterns to achieve different code rates (for variable data rates); the coded symbols are interleaved over three subbands.

With Viterbi decoding at the receiver, it is possible to implement an enhanced equalizer for the received sequence based on (estimated) channel. The symbols received on data subcarriers with a higher gain $|H_k|$ are more reliable than those received on subcarriers with smaller channel gains. We can expect to get better performances if the Viterbi decoder is provided with a measure of this reliability, as accomplished by

$$\hat{S}_{\text{weighted},k} = H_k^* R_k, \quad k = 1, 2, \ldots, N_c. \tag{2.162}$$

This equalizer essentially compensates for the phase distortion introduced by the channel on each subcarrier and weights each symbol with $|H_k|^2$ which enables soft Viterbi decoding with performance equivalent to maximum ratio combining. Since the subcarriers have different signal-to-noise ratios after equalization, the above scheme is just a means of feeding the Viterbi decoder with modified metrics. This weighting avoids the noise enhancement inherent to equalized OFDM systems.

Enhancing channel coefficients estimates. The LS channel estimates obtained using (2.155) are unreliable in the presence of noise. While transmitting the channel estimation sequence twice on each band could be used to reduce the effect of additive noise by 3 dB via averaging, this may not suffice to yield estimates of desired accuracy. Typically, the channel estimation sequences are only used to obtain the initial estimates of the channel coefficients which are then updated using decision feedback every OFDM symbol duration. Channel estimation with decision feedback in context of OFDM systems is discussed in [171, 172] and can be described as follows. Initial estimates of the channel coefficients $\hat{H}_k^{(0)}$ are obtained using (2.155) using the frequency-domain pilot symbols in each frame. These estimates are used to demodulate the next OFDM symbol $R_{n+1,k}$ after frequency-domain equalization. The vector of equalized symbols is now soft Viterbi decoded to produce more reliable symbol decisions. The information is reencoded to give $\hat{S}_{n+1,k}$, which is used to update the channel coefficients, $\hat{H}_k^{(1)} = (R_{n+1,k}/\hat{S}_{n+1,k})$, for all k; these estimates are then used to demodulate the next symbol and so on. The idea of decision-feedback is depicted pictorially in Figure 2.41. The decision-feedback scheme has to be modified when applied to MB-OFDM since the interleaving spans 3 OFDM symbols; the channel estimates are updated every 3 OFDM symbols instead of each symbol.

Statistical knowledge of the correlation of the channel frequency response at different subcarriers can also be used to improve the quality of the channel estimates. This can be naturally accomodated within the MMSE framework. Channel estimators that exploit such correlation information are described in [173, 174] and the references therein.

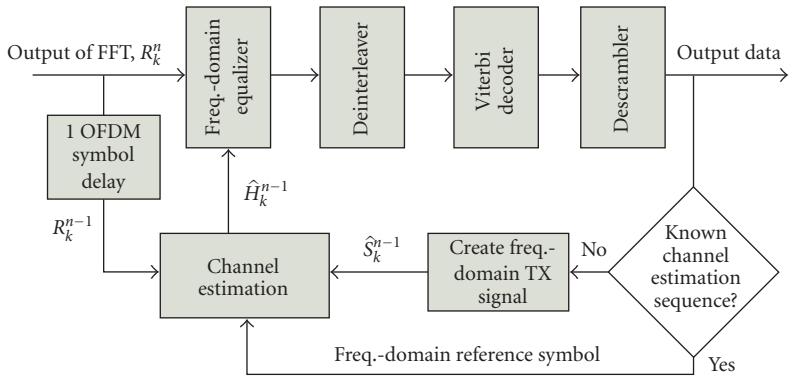

FIGURE 2.41. Decision feedback for updating channel estimates in MB-OFDM proposal.

2.8.2.3. Simulations

The performances of the various channel estimation schemes described above are depicted in Figure 2.42 for a UWB channel model numbered CM1 at 480 Mbps. The UWB channel modeling subcommittee has identified and distinguished four channel models, numbered CM1 to CM4 for baseline testing purposes, based on the severity of the multipath channel [137]. It is clear from the figure that the zero-forcing equalizer has the worst performance owing to the enhancement of noise at subcarriers in deep fades. The MMSE equalizer alleviates the problem of noise enhancement and would be near optimal in the absence of channel coding. However, in the presence of channel coding, when the decoder is provided with the information about the reliability of the subcarriers, it is able to make a more informed decision and thus the BER performance is significantly better in the presence of channel-dependant weighting of the Viterbi decoder metrics.

2.8.3. UWB via impulse radio and direct-sequence spread spectrum

Ultra-wide bandwidth modulations can be achieved either via spreading in time or in frequency domains. Traditionally, UWB has been associated with impulse radio (IR) [175] that transmits information by modulating the amplitude or position of very short (on the order of 100 picoseconds to 2 nanoseconds) pulses. In order to permit multiple accessing, time-hopping IR was proposed [176]; the symbol duration is divided into N_f intervals called frames, each of which contains one pulse. The position of the pulse within the frame is determined by a PN sequence $\{c_k\}$ unique to the kth user of length N_c with elements $c_k \in \{0, N_h\}$ such that $N_h T_c < T_f$. The transmitted signal is thus given by

$$s(t) = \sum_k d_k w(t - kN_c T_f), \tag{2.163}$$

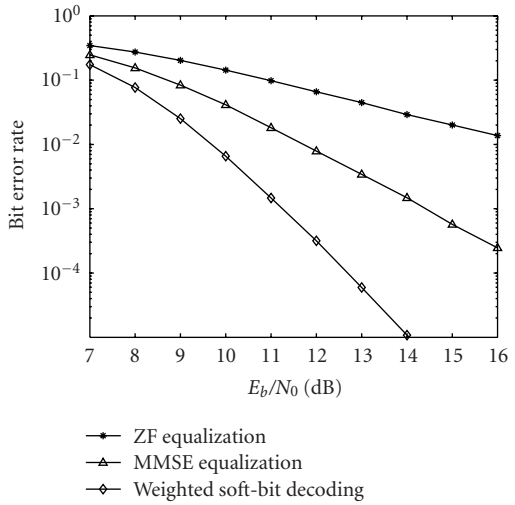

Figure 2.42. Channel estimation performance in MB-OFDM at 480 Mbps in CM1.

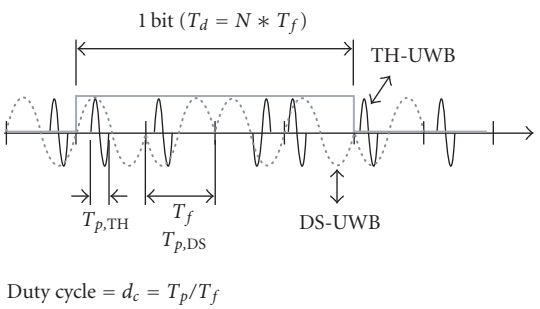

Figure 2.43. Difference between TH-IR and DS-UWB (reproduced from [177]).

where

$$w(t) = \sum_{j=0}^{N_c-1} p(t - jT_f - c_j T_c), \tag{2.164}$$

where $p(t)$ is the UWB pulse with a duration of T_c. In the above expressions, the modulation assumed is binary PAM. An alternative is to use PPM, where the data bit time dithers the UWB pulse to achieve modulation. The data rate for TH-IR is given by $R_s = 1/N_c T_f$.

Alternatively, spreading can be achieved via familar direct-sequence UWB approach, where the pulses are transmitted continuously using a PN sequence of

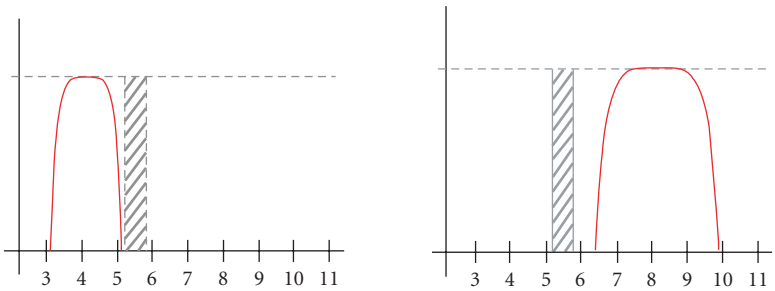

FIGURE 2.44. DS-UWB spectrum (reproduced from [179]).

length N_s with consequent data rate $1/N_c T_c$. A schematic of TH-IR and DS-UWB is shown in Figure 2.43.

For a given pulse width and spreading code length, TH-IR would have a smaller pulse-repetition frequency (PRF) than DS-UWB and thus would be limited to low data rates. For example, assuming $N_h = 10$ and $T_c = 1$ nanoseconds, the frame duration, $T_f = 10$ nanoseconds for the TH-IR systems or a PRF of 100 MHz. On the other hand, DS-UWB uses a T_f equal to the pulse duration and thus the PRF is 1 GHz. Thus DS-UWB systems are potentially capable of accommodating higher data rates than TH-IR, or equivalently more users for a given aggregate link rate [178]. This conclusion extends from the AWGN scenario described above to the realistic case of multipath channels, and is the primary reason why DS-UWB approaches are preferred for higher rates. In either case, the receiver structures for TH-IR and DS-UWB modulation are remarkably similar; hence the sequel just concentrates on DS-UWB.

2.8.3.1. Description of DS-UWB proposal

In contrast to the MB-OFDM scheme that divides the UWB spectrum into several 528 MHz subbands, the DS-UWB [179] scheme uses single-carrier modulation over a much wider bandwidth. Specifically, the UWB spectrum is divided into the low and high bands as shown in Figure 2.44 and depending on the required data rate the transmission occupies one of the two bands or both simultaneously.

Transmission over the wide bandwidth is accomplished by the use of direct-sequence spread-spectrum technique (DS-SS); multiple accessing is achieved using code-division multiple access (CDMA). In CDMA, a binary information sequence at rate R_b is modulo-2 added with a higher-speed binary pseudorandom (PN) code sequence $\{c_n\}$ (often called the chip sequence) producing a high-speed random sequence. The inverse of the chip pulse duration T_c determines the approximate transmission bandwidth and the ratio T_b/T_c (the number of chips transmitted per information bit) is called the processing gain G_p. The transmitted signal is thus

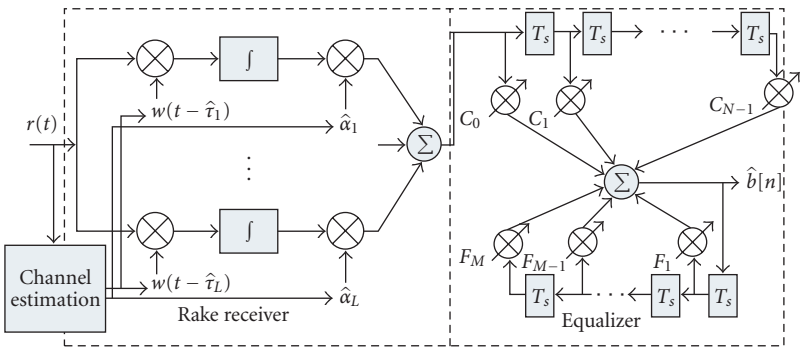

FIGURE 2.45. Structure of a Rake receiver.

given by

$$s(t) = \sum_{k=-\infty}^{\infty} b_k w(t - T_b), \tag{2.165}$$

where

$$w(t) = \sum_{k=0}^{N_c-1} c_k p(t - T_c) \tag{2.166}$$

is the spreading waveform, $\{b_k\}$ is the bit sequence to be transmitted, and $p(t)$ is the UWB pulse.

In DS-UWB proposal, one full length of the chip sequence is sent in each bit interval; such spreading sequences should exhibit the following essential attributes.

(1) they should have favorable periodic autocorrelation properties, that is, low autocorrelation at all nonzero shifts of the sequence;
(2) cross-correlation among different pairs of sequences at all lags should be small to enable multiple access.

Because of the wide bandwidths employed in DS-UWB systems, a very large number of resolved multipath components exist. For example, a multipath channel with maximum delay spread of 100 nanoseconds and signal bandwidth of 1 GHz, will result in 100 resolvable multipath components. Thus, the energy per-path at the receiver is typically very low and several paths must be combined for more reliable data decisions. Typically a Rake receiver (an adaptive correlator with chip-spaced taps) is used for the purpose of combining desired path components; however, this must be tradedoff with greater intersymbol interference (ISI) at Rake output as the length of Rake is increased. The Rake combiner/equalizer constitutes the most significant component complexity-wise in the baseband receive chain of a DS-UWB receiver. Given complexity-induced constraints on the number of

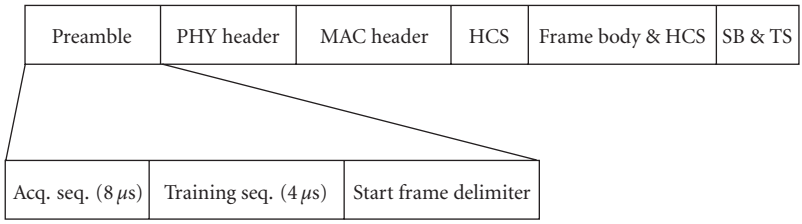

FIGURE 2.46. Structure of the DS-UWB frame.

allowed fingers, it follows that the Rake receiver must employ tracking of the significant multipath components as shown in Figure 2.45.

The code sequence used in the DS-UWB proposal has a basic chip rate of 1.368 Gcps for the low band and consists of a sequence of root-raised-cosine UWB pulses with 30% excess bandwidth. The length of the code sequences and the number of UWB pulses or chips per data symbol are variable from 1 to 24 to support various data rates sent using binary phase-shift keying (BPSK) modulation.

The structure of the PHY frame used in the DS-UWB proposal is shown in Figure 2.46. The preamble, PHY header, and the MAC header are modulated using a length 24 spreading code, while the rest of the frame uses a spreading code of different length as dictated by the data rate. The preamble consists of

(1) an acquisition sequence, which is a random sequence of bits (one bit per code word) and is used for initial symbol time acquisition,
(2) a training sequence, consisting of a fixed sequence of training bits which the receiver uses to estimate the channel and to set the locations of taps and their respective gains for the Rake receiver.

2.8.3.2. Channel estimation

To be able to effectively combine the multipath components, the Rake receiver of Figure 2.45 needs to know the delays and attenuations of the multipath components. Since the DS-UWB proposal incorporates a training sequence to aid the receiver in channel estimation, we confine our discussion to data-aided approaches. Since the acquisition sequence is transmitted ahead of the training sequence, it will be assumed that the receiver has established symbol timing before attempting channel estimation.

Let the impulse-response of the UWB channel be

$$h(t) = \sum_k \alpha_k \delta(t - \tau_k), \tag{2.167}$$

where τ_k and α_k are the delay and real gain of the kth path, respectively. For a detailed discussion on the UWB channel model, refer to [137]. The channel

estimator estimates the tap positions $\{\hat{\tau}_k\}$ and the associated gains $\{\hat{\alpha}_k\}$ using a limited number of L taps (due to complexity reasons) in such a manner that the synthesized channel $\sum_{k=1}^{L} \hat{\alpha}_k \delta(t - \hat{\tau}_k)$ is well matched to the actual channel of (2.167).

In the presence of additive white noise only, the maximum likelihood (ML) criterion is equivalent to the minimum mean-square error estimation. Thus, the delays and channel gains may be obtained by minimizing the mean-squared error, that is,

$$\text{MSE} = E\left(\left(h(t) - \sum_{k=1}^{L} \hat{\alpha}_k \delta(t - \hat{\tau}_k)\right)^2\right). \tag{2.168}$$

Sliding window algorithm. If it is assumed that the delayed versions of the received signal are orthogonal to each other, the sliding window algorithm provides ML estimates of the channel parameters. The sliding window algorithm cross-correlates the received training sequence with the known sequence and uses the positions of correlation peaks as the delays within the Rake receiver. The relative heights of the correlation peaks at these delays provide an estimate of the tap weights [180]. The effect of additive noise can be further alleviated by averaging the estimates over multiple symbols. We note that the assumption of the delayed versions being orthogonal is only approximately valid in DS-UWB for any set of practical spreading codes. Furthermore, typical channel delays may exceed the symbol duration, thereby leading to ISI. Under these conditions, the sliding window algorithm is suboptimal. Also, the complexity of the ML approach to channel estimation is prohibitive in such situations [181–183] and simpler alternatives are desirable.

Successive cancellation algorithm. As mentioned in the previous section, the joint ML estimation of path gains and delays is computationally intensive. Successive channel estimation algorithm [184] provides a more feasible approach to this problem and offers improved performances over the sliding window algorithm by using an iterative algorithm. The algorithm begins by using the sliding window algorithm to find the parameters of the strongest path. The delayed version of the transmitted signal corresponding to the estimated tap is then subtracted from the received sequence and the algorithm is repeated to estimate the parameters of the second strongest path and so on. The number of iterations required is equal to the number of taps to be estimated. In [185], a comparison of the Rake performance using sliding window algorithm and successive cancellation algorithm in context of UWB is provided.

Number of Rake fingers. The number of fingers to be used in the Rake receiver has a significant impact on receiver performance and complexity. Clearly, a good choice of this parameter strongly depends on the channel power-delay profile. In [186], the authors investigate the energy capture as a function of number of Rake fingers in a typical UWB channel. A normalized energy capture metric was defined

as follows:

$$\mathrm{EC}(L) = 1 - \underbrace{\frac{\int_0^T \left| r(t) - \sum_{k=1}^{L} \hat{\alpha}_k s(t - \hat{\tau}_k) \right|^2 dt}{\int_0^T \left| r(t) \right|^2 dt}}_{\text{normalized MSE}}. \tag{2.169}$$

In the absence of any channel estimation errors, the normalized MSE defined in (2.169) decreases as L increases and therefore the EC increases monotonically albeit with diminishing returns. In the presence of channel estimation errors, the EC would start increasing with L after a certain point as described in the next section.

Effect of imperfect channel estimates. Any channel estimate will be imperfect due to the presence of noise, mutual and multiple access interference leading to degradation in Rake performance as compared to the ideal case of perfect channel knowledge. For a fixed total bit energy, as the number of diversity or Rake branches increases, the energy per branch decreases. On the one hand, having more branches enables greater diversity gain; on the other, more imperfect channel estimates leads to decreasing the effective SNR available per branch. This fundamental tradeoff between the diversity order and the channel estimation error is discussed for wideband CDMA in [187]. In [188], the effect of estimation errors and the number of Rake fingers on BER performance is analyzed in a typical UWB channel. In [189], an analytical framework is developed to quantify the effects of channel estimation errors on the performance of UWB systems operating in dense multipath environments.

2.8.3.3. Equalization

The delay spread of typical UWB channels is typically larger than the symbol duration, which causes significant intersymbol interference (ISI). Even with perfect estimation of the tap delays and coefficients for Rake combining, ISI leads to high bit error rates and results in irreducible error floor. This is compounded at higher data rates (i.e., lower processing gains) where the performance approaches that of a narrowband system without equalization. In [190], the authors analyze the detrimental effects of ISI on the performance of DS-CDMA systems with decreasing processing gain. It is therefore essential that a symbol spaced equalizer following Rake combining be incorporated to mitigate ISI as shown in Figure 2.45.

Considering the data rates that the UWB proposals attempt to achieve, and the severity of UWB channels, nonlinear decision-feedback equalizers (DFEs) are a natural choice for DS-UWB systems [191, 192].

Figure 2.47 shows plots of BER for 100 realizations of CM3 channel model with and without decision-feedback equalization. The DF equalizer has 2 feedforward taps and 10 feedback taps [179] and is seen to improve performance considerably.

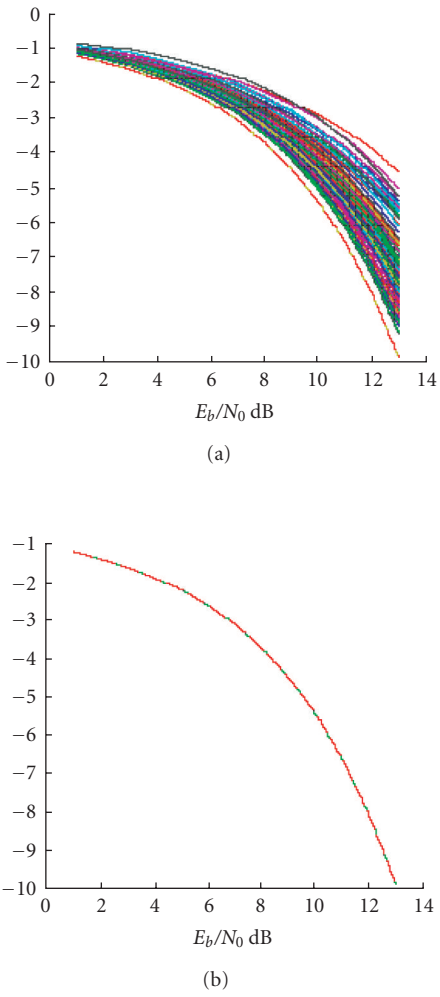

FIGURE 2.47. Effect of ISI on DS-UWB at 57 Mbps in UWB CM3. Each plot shows 100 channel realizations. (a) No equalization; (b) DFE with feedback span of 10 symbols (reproduced from [179]).

Acknowledgments

Part of the work of A. F. Molisch was financed by an INGVAR grant from the Swedish Strategic Research Initiative. Useful discussions with Professor Moe Z. Win, Professor Robert Qiu, and the members of the IEEE 802.15.3a and 802.15.4a are gratefully acknowledged. The work of István Z. Kovács, Gert F. Pedersen, and Patrick C. F. Eggers was supported by the European Power Aware Communications for Wireless Optimised Personal Area Networks (PACWOMAN), IST Contract no. IST-2001-34157, and the Danish Future Adaptive Communication Environment (FACE), AAU, research projects.

Bibliography

[1] J. B. Andersen, T. S. Rappaport, and S. Yoshida, "Propagation measurements and models for wireless communications channels," *IEEE Communications Magazine*, vol. 33, no. 1, pp. 42–49, 1995.

[2] H. L. Bertoni, *Radio Propagation for Modern Wireless Systems*, Prentice-Hall, Upper Saddle River, NJ, USA, 2000.

[3] N. Blaunstein, *Radio Propagation in Cellular Networks*, Artech House, Boston, Mass, USA, 1999.

[4] G. D. Durgin, *Space-Time Wireless Channels*, Prentice-Hall, Upper Saddle River, NJ, USA, 2003.

[5] R. B. Ertel, P. Cardieri, K. W. Sowerby, T. S. Rappaport, and J. H. Reed, "Overview of spatial channel models for antenna array communication systems," *IEEE Personal Communications Magazine*, vol. 5, no. 1, pp. 10–22, 1998.

[6] A. F. Molisch, "Modeling of directional mobile radio channels," *Radio Science Bulletin*, vol. 16, no. 302, pp. 16–26, 2002.

[7] A. F. Molisch and F. Tufvesson, "Multipath propagation models for broadband wireless systems," in *CRC Handbook of Signal Processing for Wireless Commmunications*, M. Ibnkahla, Ed., pp. 2.1–2.43, CRC Press, Boca Raton, Fla, USA, 2004.

[8] J. D. Parsons, *The Mobile Radio Channel*, John Wiley & Sons, New York, NY, USA, 1992.

[9] S. R. Saunders, *Antennas and Propagation for Wireless Communications Systems*, John Wiley & Sons, New York, NY, USA, 2002.

[10] R. Vaughan and J. B. Andersen, *Channels, Propagation and Antennas for Mobile Communications*, IEE Press, London, UK, 2002.

[11] Federal Communications Commission. First report and order 02-48, 2002.

[12] P. Bello, "Characterization of randomly time-variant linear channels," *IEEE Transactions on Communications*, vol. 11, no. 4, pp. 360–393, 1963.

[13] P. Bello, "Time-frequency duality," *IEEE Transactions on Information Theory*, vol. 10, no. 1, pp. 18–33, 1964.

[14] C. Baum, General properties of antennas, *Sensor and Simulation Note 330*, July 1991.

[15] G. A. Deschamps, "I—Le principe de réciprocité en electromagnétisme; II—Application du principe de réciprocité aux antennas et aux guides d'ondes," *Revue du Cethedec*, no. 8, pp. 71–101, 1966.

[16] E. G. Farr and C. Baum, Time domain characterization of antennas with TEM feeds, *Sensor and Simulation Note 426*, October 1998.

[17] M. Kanda, "Time domain sensors for radiated impulsive measurements," *IEEE Transactions on Antennas and Propagation*, vol. 31, no. 3, pp. 438–444, 1983.

[18] Y. T. Lo and S. W. Lee, Eds., *Antenna Handbook*, chapter 2, "Theorems and Formulas", Van Nostrand Reinhold, New York, NY, USA, 1988.

[19] C. Roblin, S. Bories, and A. Sibille, "Characterization tools of antennas in the time domain," in *Proceedings of International Workshop on Ultra Wideband Systems (IWUBS '03)*, Oulu, Finland, June 2003.

[20] A. Shlivinski, E. Heyman, and R. Kastner, "Antenna characterization in the time domain," *IEEE Transactions on Antennas and Propagation*, vol. 45, no. 7, pp. 1140–1149, 1997.

[21] H. J. Schmitt, C. W. Harrison, and C. S. Williams, "Calculated and experimental response of thin cylindrical antennas to pulse excitation," *IEEE Transactions on Antennas and Propagation*, vol. 14, no. 2, pp. 120–127, 1966.

[22] M. Steinbauer, A. F. Molisch, and E. Bonek, "The double-directional radio channel," *IEEE Antennas and Propagation Magazine*, vol. 43, no. 4, pp. 51–63, 2001.

[23] H. T. Friis, "A note on a simple transmission formula," *Proceedings of IRE and Waves and Electrons*, vol. 34, pp. 254–256, May 1946.

[24] A. Sommerfeld, "Theoretisches Uber die Beugung der Roentgenstrahlen," *Zeitschrift für Mathematik und Physik*, vol. 46, pp. 11–97, 1901.

[25] H. Lamb, "The diffraction of a solitary wave," *Proceedings of the London Mathematical Society*, vol. 2, no. 8, pp. 422–437, 1910.

[26] F. G. Friedlander, "The diffraction of sound pulses I. Diffraction by a semi-infinite plane," *Proceedings of the Royal Society of London. Series A, Mathematical and Physical Sciences*, vol. 186, no. 1006, pp. 322–344, 1946.
[27] L. B. Felsen, Ed., *Transient Electromagnetics*, Springer, New York, NY, USA, 1976.
[28] F. G. Friedlander, *Sound Pulses*, Cambridge University Press, Cambridge, Mass, USA, 1st edition, 1958.
[29] L. B. Felsen and N. Marcuvitz, *Radiation and Scattering of Waves*, Prentice-Hall, Upper Saddle River, NJ, USA, 1973.
[30] M. Kline and I. W. Kay, *Electromagnetic Theory and Geometric Optics*, Robert E. Krieger Publishing Company, Melbourne, Fla, USA, 1979.
[31] J. B. Keller, "Geometrical theory of diffraction," *Journal of the Optical Society of America*, vol. 52, pp. 116–130, February 1962.
[32] R. G. Kouyoumjian and P. H. Pathak, "A uniform geometrical theory of diffraction for an edge in a perfectly conducting surface," *Proceedings of the IEEE*, vol. 62, no. 11, pp. 1448–1461, 1974.
[33] L. Y. Atsanin, A. Kostylev, Y. Zinoviev, and A. Pasmurov, *Radar Target Characteristics: Measurements and Applications*, chapter 3, CRC press, Boca Raton, Fla, USA, 1994.
[34] E. M. Kenaugh and D. L. Moffatt, "Transient and impulse response approximation," *Proceedings of the IEEE*, vol. 53, no. 8, pp. 893–901, 1965.
[35] R. C. Qiu, *Digital transmission media: UWB wireless channel, MMIC, and chiral fiber*, Ph.D. thesis, Polytechnic University, Brooklyn, NY, USA, January 1996.
[36] A. Trindade, Q. H. Dang, and A.-J. van der Veen, "Signal processing model for a transmit-reference UWB wireless communication system," in *Proceedings of IEEE Conference on Ultra Wideband Systems and Technologies (UWBST '03)*, pp. 270–274, Blacksburg, Va, USA, November 2003.
[37] R. T. Hoctor, et al., "Delay-hopped transmitted reference UWB—a tutorial," *Special Issue on UWB*, January 2005.
[38] Pulson Communications Corp., "PulsON Communications Corp request for pioneer's preference in the personal communications services," Tech. Rep., GEN Docket 90-314, May 1992.
[39] H. Tomlinson and R. T. Hoctor, "An overview of delay-hopped, transmitted-reference RF communications," Tech. Rep. 2001CRD198, GE Global Research, Niskayuna, NY, USA, January 2002.
[40] R. A. Scholtz, "Multiple access with time-hopping impulse modulation," in *Proceedings of IEEE Military Communications Conference (MILCOM '93)*, vol. 2, pp. 447–450, Boston, Mass, USA, October 1993, invited paper.
[41] M. McClure, R. C. Qiu, and L. Carin, "On the superresolution identification of observables from swept-frequency scattering data," *IEEE Transactions on Antennas and Propagation*, vol. 45, no. 4, pp. 631–641, 1997.
[42] I.-T. Lu, R. C. Qiu, and J. Kwak, "A high-resolution algorithm for complex spectrum search," *Journal of the Acoustical Society of America*, vol. 104, no. 1, pp. 288–299, 1998.
[43] J. G. Proakis, *Digital Communications*, McGraw-Hill, New York, NY, USA, 4th edition, 2000.
[44] R. C. Qiu, "A study of the ultra-wideband wireless propagation channel and optimum UWB receiver design (Part I)," *IEEE Journal on Selected Areas in Communications*, vol. 20, no. 9, pp. 1628–1637, 2002, Special Issue on UWB Radio in Multiple Access Wireless Communications.
[45] R. C. Qiu, "UWB Wireless communications," in *Design and Analysis of Wireless Networks*, Nova Science Publishers, Hauppauge, NY, USA, 2004.
[46] R. C. Qiu, "A generalized time domain multipath channel and its application in ultra-wideband (UWB) wireless optimal receiver design—part II wave-based system analysis," *IEEE Transactions on Wireless Communications*, vol. 3, no. 6, pp. 2312–2324, 2004.
[47] R. C. Qiu, "A generalized time domain multipath channel and its application in ultra-wideband (UWB) wireless optimal receiver design: Part III system performance analysis," to appear in *IEEE Transactions on Wireless Communications*, February 2004.
[48] R. C. Qiu, "A generalized time domain multipath channel and its application in ultra-wideband (UWB) wireless optimal receiver design: system performance analysis," in *Proceedings of IEEE Wireless Communications and Networking Conference (WCNC '04)*, vol. 2, pp. 901–907, Atlanta, Ga, USA, March 2004.

[49] R. C. Qiu, *Image Processing and Jump Regression Analysis*, John Wiley & Sons, New York, NY, USA, 2005.
[50] R. C. Qiu, *UWB pulse propagation—a generalized multipath model*, January 2005.
[51] R. C. Qiu and I. T. Lu, "Multipath resolving with frequency dependence for broadband wireless channel modeling," *IEEE Transransactions on Vehicular Technology*, vol. 48, no. 1, pp. 273–285, 1999.
[52] G. L. Turin, "A statistical model of urban multipath propagation," *IEEE Transransactions on Vehicular Technology*, vol. 21, no. 1, pp. 1–9, 1972.
[53] A. Taha and K. M. Chugg, "On designing the optimal template waveform for UWB impulse radio in the presence of multipath," in *Proceedings of IEEE Conference on Ultra Wideband Systems and Technologies (UWBST '02)*, pp. 41–45, Baltimore, Md, USA, May 2002.
[54] R. M. Burher, "UWB Channel Modeling," in *DARPA NETEX Meeting*, July 2002, Presentations Slides.
[55] F. Sagnard, T. Quiniou, C. Vignat, and G. El Zein, "High resolution algorithms for multipath identification of construction materials: models and characterization for UWB applications," *IEEE Transransactions on Vehicular Technology*, January 2004, submitted for publication.
[56] A. F. Molisch, *Status Report of the Channel Modeling Subgroup*, IEEE, Vancouver, British Columbia, Canada, 2004.
[57] A. F. Molisch, "Models for UWB Propagation Models—a tutorial," *Dynamics of Continuous, Discrete and Impulsive Systems—An International Journal for Theory and Applications*, January 2005, Special issue on UWB.
[58] F. Ramirez-Mireles, "On the performance of ultra-wide-band signals in Gaussian noise and dense multipath," *IEEE Transransactions on Vehicular Technology*, vol. 50, no. 1, pp. 244–249, 2001.
[59] F. Ramirez-Mireles, "Signal design for ultra-wide-band communications in dense multipath," *IEEE Transransactions on Vehicular Technology*, vol. 51, no. 6, pp. 1517–1521, 2002.
[60] W. Zhuang, X. Shen, and Q. Bi, "Ultra-wideband wireless communications—a tutorial," *Wireless Communications and Mobile Computing*, vol. 3, no. 6, pp. 663–685, 2003, special issue on Ultra-Broadband Wireless Communications for the Future.
[61] V. A. Borovikov and B. Y. Kinber, *Geometrical Theory of Diffraction*, IEE Press, London, UK, 1994.
[62] R. Mittra and M. P. Hurst, "Scattering center analysis via Prony's method," *IEEE Transactions on Antennas and Propagation*, vol. 35, no. 8, pp. 986–988, 1987.
[63] S. W. Lee, V. Jamnejad, and R. Mittra, "An asymptotic series for early time response in transient problems," *IEEE Transactions on Antennas and Propagation*, vol. 21, no. 6, pp. 895–899, 1973.
[64] P. H. Pathak and P. R. Rousseau, "Time domain uniform geometrical theory of diffraction for curved wedge," *IEEE Transactions on Antennas and Propagation*, vol. 43, no. 12, pp. 1375–1382, 1995.
[65] T. Veruttipong, "Time domain version of the uniform GTD," *IEEE Transactions on Antennas and Propagation*, vol. 38, no. 11, pp. 1757–1763, 1990.
[66] A. Mohsen and T. B. A. Senior, "The impulse response of a half-plane," *IEEE Transactions on Antennas and Propagation*, vol. 21, no. 3, pp. 254–255, 1973.
[67] B. van der Pol and H. Bremmer, *Operational Calculus Based on the Two-Sided Laplace Integral*, Cambridge University Press, Cambridge, UK, 2nd edition, 1955.
[68] S. M. Scarborough, "Ultrawideband radar imaging and the diagnosis of scattering centers," M.S. thesis, Ohio State University, Columbus, Ohio, USA, 1990.
[69] S. L. Borison and S. Hong, "Short-pulse scattering by a cone—direct and inverse," *IEEE Transactions on Antennas and Propagation*, vol. 16, no. 1, pp. 98–102, 1968.
[70] K. B. Oldham and J. Spanier, *The Fractional Calculus: Theory and Applications, Differentiation and Integration to Arbitrary Order*, Academic Press, New York, NY, USA, 1974.
[71] K. S. Miller and B. Ross, *An Introduction to the Fractional Calculus and Fractional Differential Equations*, John Wiley & Sons, New York, NY, USA, 1993.
[72] R. A. Altes, "Sonar for generalized target description and its similarity to animal echolocation systems," *Journal of the Acoustical Society of America*, vol. 59, no. 1, pp. 97–105, 1976.

[73] N. Engheta, "On fractional calculus and fractional multipoles in electromagnetism," *IEEE Transactions on Antennas and Propagation*, vol. 44, no. 4, pp. 554–566, 1996.

[74] S. S. Ghassemzadeh, R. Jana, C. W. Rice, W. Turin, and V. Tarokh, "A statistical path loss model for in-home UWB channels," in *Proceedings of IEEE Conference on Ultra Wideband Systems and Technologies (UWBST '02)*, pp. 59–64, Baltimore, Md, USA, May 2002.

[75] S. S. Ghassemzadeh, R. Jana, C. W. Rice, W. Turin, and V. Tarokh, "Measurement and modeling of an ultra-wide bandwidth indoor channel," *IEEE Transactions on Communications*, vol. 52, no. 10, pp. 1786–1796, 2004.

[76] A. Alvarez, G. Valera, M. Lobeira, R. Torres, and J. L. Garcia, "New channel impulse response model for UWB indoor system simulations," in *Proceedings of IEEE 57th Semiannual Vehicular Technology Conference (VTC '03)*, vol. 1, pp. 1–5, Jeju, Korea, April 2003.

[77] D. Cassioli and A. Durantini, "A time-domain propagation model of the UWB indoor channel in the FCC-compliant band 3.6 - 6 GHz based on PN-sequence channel measurements," in *Proceedings of IEEE 59th Semiannual Vehicular Technology Conference (VTC '04)*, vol. 1, pp. 213–217, Milan, Italy, May 2004.

[78] D. Cassioli, A. Durantini, and W. Ciccognan, "The role of path loss on the selection of the operating bands of UWB systems," in *Proceedings of 15th IEEE International Symposium on Personal, Indoor, and Mobile Radio Communications (PIMRC '04)*, vol. 4, pp. 2787–2791, Barcelona, Spain, September 2004.

[79] D. Cassioli, M. Z. Win, and A. F. Molisch, "The ultra-wide bandwidth indoor channel: from statistical model to simulations," *IEEE Journal on Selected Areas in Communications*, vol. 20, no. 6, pp. 1247–1257, 2002.

[80] A. Durantini and D. Cassioli, "A multi-wall path loss model for indoor UWB propagation," in *Proceedings of IEEE Semiannual Vehicular Technology Conference (VTC '05)*, Stockholm, Sweden, May 2005.

[81] A. Durantini, W. Ciccognani, and D. Cassioli, "UWB propagation measurements by PN-sequence channel sounding," in *Proceedings of IEEE International Conference on Communications (ICC '04)*, vol. 6, pp. 3414–3418, Paris, France, June 2004.

[82] S. S. Ghassemzadeh, L. J. Greenstein, T. Sveinsson, A. Kavcic, and V. Tarokh, "UWB indoor path loss model for residential and commercial environments," in *Proceedings of IEEE 57th Semiannual Vehicular Technology Conference (VTC '03)*, Orlando, Fla, USA, October 2003.

[83] V. Hovinen, M. Hamalainen, and T. Patsi, "Ultra wideband indoor radio channel models: preliminary results," in *Proceedings of IEEE Conference on Ultra Wideband Systems and Technologies (UWBST '02)*, pp. 75–79, Baltimore, Md, USA, May 2002.

[84] J. Kunisch and J. Pamp, "Measurement results and modeling aspects for the UWB radio channel," in *Proceedings of IEEE Conference on Ultra Wideband Systems and Technologies (UWBST '02)*, pp. 19–23, Baltimore, Md, USA, May 2002.

[85] M. Z. Win, R. A. Scholtz, and M. A. Barnes, "Ultra-wide bandwidth signal propagation for indoor wireless communications," in *Proceedings of IEEE International Conference on Communications (ICC '97)*, pp. 56–60, Montreal, Canada, June 1997.

[86] J. Keignart, J.-B. Pierrot, N. Daniele, et al., "U.C.A.N. Report on UWB Basic Transmission Loss," Tech. Rep. IST-2001-32710, Utility Consumers' Action Network (UCAN), San Diego, Calif, USA, March 2003.

[87] D. Cassioli, W. Ciccognani, and A. Durantini, "D3.1: UWB channel model report," Tech. Rep. IST-2001-35189 ULTRAWAVES, November 2003.

[88] A. Armogida, B. Allen, M. Ghavami, M. Porretta, G. Manara, and H. Aghvami, "Path-loss modelling in short range UWB transmissions," in *Proceedings of International Workshop on Ultra Wideband Systems (IWUWBS '03)*, Oulu, Finland, June 2003.

[89] S. J. Howard and K. Pahlavan, "Measurement and analysis of the indoor radio channel in the frequency domain," *IEEE Transactions on Instrumentation and Measurement*, vol. 39, no. 5, pp. 751–755, 1990.

[90] S. J. Howard and K. Pahlavan, "Autoregressive modeling of wide-band indoor radio propagation," *IEEE Transactions on Communications*, vol. 40, no. 9, pp. 1540–1552, 1992.

[91] D. A. Hawbaker and T. S. Rappaport, "Indoor wideband radiowave propagation measurements at 1.3 GHz and 4.0 GHz," *Electronics Letters*, vol. 26, no. 21, pp. 1800–1802, 1990.
[92] T. S. Rappaport, "Characterization of UHF multipath radio channels in factory buildings," *IEEE Transactions on Antennas and Propagation*, vol. 37, no. 8, pp. 1058–1069, 1989.
[93] T. S. Rappaport, S. Y. Seidel, and K. Takamizawa, "Statistical channel impulse response models for factory an open plan building radio communication system design," *IEEE Transactions on Communications*, vol. 39, no. 5, pp. 794–807, 1991.
[94] A. A. M. Saleh and R. A. Valenzuela, "A statistical model for indoor multipath propagation," *IEEE Journal on Selected Areas in Communications*, vol. 5, no. 2, pp. 128–137, 1987.
[95] S. Mangold, M. Lott, D. Evans, and R. Fifield, "Indoor radio channel modeling-bridging from propagation details to simulation," in *Proceedings of 9th IEEE International Symposium on Personal, Indoor, and Mobile Radio Communications (PIMRC '98)*, vol. 2, pp. 625–629, Boston, Mass, USA, September 1998.
[96] G. Santella and E. Restuccia, "Analysis of frequency domain wide-band measurements of the indoor radio channel at 1, 5.5, 10 and 18 GHz," in *Proceedings of IEEE Global Telecommunications Conference (GLOBECOM '96)*, vol. 2, pp. 1162–1166, London, UK, November 1996.
[97] G. J. M. Janssen, P. A. Stigter, and R. Prasad, "Wideband indoor channel measurements and BER analysis of frequency selective multipath channels at 2.4, 4.75, and 11.5 GHz," *IEEE Transactions on Communications*, vol. 44, no. 10, pp. 1272–1288, 1996.
[98] P. Nobles, D. Ashworth, and F. Halsall, "Indoor radiowave propagation measurements at frequencies up to 20 GHz," in *Proceedings of IEEE 44th Semiannual Vehicular Technology Conference (VTC '94)*, vol. 2, pp. 873–877, Stockholm, Sweden, June 1994.
[99] M. Dohler, B. Allen, A. Armogida, S. McGregor, M. Ghavami, and H. Aghvami, "A new twist on UWB pathloss modelling," in *Proceedings of IEEE 59th Semiannual Vehicular Technology Conference (VTC '04)*, vol. 1, pp. 199–203, Milan, Italy, May 2004.
[100] A. F. Molisch, "Models for UWB propagation channels—a tutorial," *Dynamics of Continuous, Discrete and Impulsive Systems—An International Journal for Theory and Applications*, 2004.
[101] A. S. Y. Poon and M. Ho, "Indoor multiple-antenna channel characterization from 2 to 8 GHz," in *Proceedings of IEEE International Conference on Communications (ICC '03)*, vol. 5, pp. 3519–3523, Anchorage, Alaska, USA, May 2003.
[102] A. F. Molisch, J. R. Foerster, and M. Pendergrass, "Channel models for ultrawideband personal area networks," *IEEE Personal Communications*, vol. 10, no. 6, pp. 14–21, 2003.
[103] S. S. Ghassemzadeh and V. Tarokh, "The ultra-wideband indoor path loss model," Tech. Rep. P802.15 02/277r1SG3a, AT&T Labs, Florham Park, NJ, USA, 2002, IEEE P802.15 SG3a contribution.
[104] A. F. Molisch, Ed., *Wideband Wireless Digital Communications*, Prentice-Hall, New York, NY, USA, 2000.
[105] M. Z. Win and R. A. Scholtz, "On the energy capture of ultrawide bandwidth signals in dense multipath environments," *IEEE Communications Letters*, vol. 2, no. 9, pp. 245–247, 1998.
[106] J. G. Proakis, *Digital Communications*, McGraw Hill, New York, NY, USA, 3rd edition, 1995.
[107] J. Keignart and N. Daniele, "Channel sounding and modelling for indoor UWB communications," in *Proceedings of International Workshop on Ultra Wideband Systems (IWUWBS '03)*, Oulu, Finland, June 2003.
[108] J. D. Choi and W. E. Stark, "Performance of ultra-wideband communications with suboptimal receivers in multipath channels," *IEEE Journal on Selected Areas in Communications*, vol. 20, no. 9, pp. 1754–1766, 2002.
[109] D. Cassioli, M. Z. Win, F. Vatalaro, and A. F. Molisch, "Performance of low-complexity RAKE reception in a realistic UWB channel," in *Proceedings of IEEE International Conference on Communications (ICC '02)*, vol. 2, pp. 763–767, New York, NY, USA, 2002.
[110] R. Hoctor and H. Tomlinson, "Delay-hopped transmitted-reference RF communications," in *Proceedings of IEEE Conference on Ultra Wideband Systems and Technologies (UWBST '02)*, pp. 265–269, Baltimore, Md, USA, May 2002.
[111] A. Batra, et al., Multi-band OFDM physical layer proposal, Document IEEE 802.15-03/267r2, 2003.

[112] D. Helal and P. Rouzet, "Tg3a-stmicro-cfp-document," Tech. Rep. P802.15 03/140r0SG3a, 2003.
[113] G. L. Turin, F. D. Clapp, T. L. Johnston, S. B. Fine, and D. Lavry, "A statistical model of urban multipath propagation," *IEEE Transransactions on Vehicular Technology*, vol. 21, no. 1, pp. 1–9, 1972.
[114] H. Hashemi, "Impulse response modeling of indoor radio propagation channels," *IEEE Journal on Selected Areas in Communications*, vol. 11, no. 7, pp. 967–978, 1993.
[115] M. Pendergrass and W. C. Beeler, "Empirically based statistical ultra-wideband (UWB) channel model," Tech. Rep. P802.15 02/240SG3a, Time-Domain Corporation, Huntsville, Ala, USA, June 2002, IEEE P802.15 SG3a contribution.
[116] F. Zhu, Z. Wu, and C. R. Nassar, "Generalized fading channel model with application to UWB," in *Proceedings of IEEE Conference on Ultra Wideband Systems and Technologies (UWBST '02)*, pp. 13–17, Baltimore, Md, USA, May 2002.
[117] D. Cassioli and A. Durantini, "Measurements, Modeling and Simulations of the UWB Propagation Channel based on Direct-Sequence Channel Sounding," *Wireless Communications and Mobile Computing*, vol. 5, no. 5, August 2005.
[118] R. J.-M. Cramer, R. A. Scholtz, and M. Z. Win, "Evaluation of an ultra-wide-band propagation channel," *IEEE Transactions on Antennas and Propagation*, vol. 50, no. 5, pp. 561–570, 2002.
[119] J. R. Foerster and Q. Li, "UWB channel modeling contribution from Intel," Tech. Rep. P802.15 02/279SG3a, Intel Corporation, Hillboro, Ore, USA, 2002, IEEE P802.15 SG3a contribution.
[120] P. Pagani, P. Pajusco, and S. Voinot, "A study of the ultra-wideband indoor channel: propagation experiment and measurement results," in *COST273 TD(030)060*, Barcelona, Spain, January 2003.
[121] M. Z. Win, F. Ramírez-Mireles, R. A. Scholtz, and M. A. Barnes, "Ultra-wide bandwidth (UWB) signal propagation for outdoor wireless communications," in *IEEE 47th Vehicular Technology Conference (VTC '97)*, vol. 1, pp. 251–255, Phoenix, Ariz, USA, May 1997.
[122] A. Domazetovic, L. J. Greenstein, N. B. Mandayam, and I. Seskar, "A new modeling approach for wireless channels with predictable path geometries," in *IEEE 56th Vehicular Technology Conference (VTC '02)*, vol. 1, pp. 454–458, Vancouver, British Columbia, Canada, September 2002.
[123] J. Kunisch and J. Pamp, "Radio channel model for indoor UWB WPAN environments," presentation P802.15 02/281SG3a, IMST GmbH, June 2002, IEEE P802.15 SG3a contribution.
[124] H. Zhang, T. Udagawa, T. Arita, and M. Nakagawa, "A statistical model for the small-scale multipath fading characteristics of ultra-wideband indoor channel," in *Proceedings of IEEE Conference on Ultra Wideband Systems and Technologies Digest of Technical Papers (UWBST '02)*, pp. 81–85, Baltimore, Md, USA, May 2002.
[125] W. Turin, R. Jana, S. S. Ghassemzadeh, C. W. Rice, and V. Tarokh, "Autoregressive modeling of an indoor UWB channel," in *Proceedings of IEEE Conference on Ultra Wideband Systems and Technologies (UWBST '02)*, pp. 71–74, Baltimore, Md, USA, May 2002.
[126] R. M. Buehrer, W. A. Davis, A. Safaai-Jazi, and D. Sweeney, "Ultra wideband propagation measurements and modeling - final report to darpa netex program," Tech. Rep., Virginia Tech, Blacksburg, Va, USA, 2004, available for download at http://www.mprg.org/people/buehrer/ultra/darpa_netex.shtml.
[127] A. Muqaibel, A. Safaai-Jazi, A. Bayram, and S. M. Riad, "Ultra wideband material characterization for indoor propagation," in *Proceedings of IEEE Antennas and Propagation Society International Symposium (APS '03)*, vol. 4, pp. 623–626, Columbus, Ohio, USA, June 2003.
[128] J. A. Hogbom, "Aperture synthesis with a non-regular distribution of interferometer baselines," *Astronomy and Astrophysics Supplement Series*, vol. 15, pp. 417–426, 1974.
[129] S. M. Yano, "Investigating the ultra-wideband indoor wireless channel," in *IEEE 55th Vehicular Technology Conference (VTC '02)*, vol. 3, pp. 1200–1204, Birmingham, Ala, USA, May 2002.
[130] R. C. Qiu, "A generalized time domain multipath channel and its application in ultra-wideband (uwb) wireless optimal receiver design: Wave-based system ananlysis," *IEEE Transactions on Wireless Communications*, page in press, 2003.
[131] Á. Álvarez, G. Valera, M. Lobeira, R. P. Torres, and J. L. García, "UWB channel model contribution from university of cantabria and ACORDE," presentation P802.15 02/445, University of Cantabria, ACORDE, Santander, Spain, 2002, IEEE P802.15 SG3a contribution.

[132] R. J.-M. Cramer, "An evaluation of indoor ultra-wideband communication channels," presentation P802.15 02/325SG3a, TRW Space & Electronics, Redondo Beach, Calif, USA, June 2002, IEEE P802.15 SG3a contribution.

[133] S. S. Ghassemzadeh, L. J. Greenstein, and V. Tarokh, "The ultra-wideband indoor multipath model," Tech. Rep. P802.15 02/282r1SG3a, AT&T Labs, Florham Park, NJ, USA, 2002, IEEE P802.15 SG3a contribution.

[134] G. Shor, "A proposal for a selection of indoor UWB path loss model," Tech. Rep. IEEE P802.15-02/280-SG3a, Wisair, 2002.

[135] K. Siwiak, "UWB propagation phenomena," Presentation P802.15 02/301SG3a, Time-Domain Corporation, Huntsville, Ala, USA, 2002, IEEE P802.15 SG3a contribution.

[136] M. Z. Win, D. Cassioli, and A. F. Molisch, "The ultra-wide bandwidth indoor channel: from statistical model to simulation," Tech. Rep. P802.18 02/284SG3a, Mitsubishi, 2002, IEEE P802.15 SG3a contribution.

[137] J. R. FoersterEd., "Channel modeling sub-committee report final," Tech. Rep. P802.15 02/490r1, IEEE 802.15 SG3a, February 2003.

[138] My personal Adaptive Global NET (MAGNET), Technical report, European IST FP6 project, IST-2004-507102, (http://www.ist-magnet.org), March 2004.

[139] Universal Remote Signal Acquisition for hEalth (URSAFE), Technical report, European IST FP5 project, Contract No IST-2001-33352, (http://ursafe.tesa.prd.fr), October 2003.

[140] M. A. Uusitalo, Wireless World Research Forum (WWRF), Technical report, general presentation (www.wireless-world-research.org), March 2004.

[141] W. A. Th. Kotterman, G. F. Pedersen, and K. Olesen, "Capacity of the mobile MIMO channel for a small wireless handset and user influence," in *Proceedings of 13th IEEE International Symposium on Personal, Indoor and Mobile Radio Communications (PIMRC '02)*, vol. 4, pp. 1937–1941, Lisbon, Portugal, September 2002.

[142] W. A. Th. Kotterman, G. F. Pedersen, and K. Olesen, "Diversity properties of multi-antenna small handheld terminals," *EURASIP Journal on Applied Signal Processing*, vol. 2004, no. 9, pp. 1340–1353.

[143] J. Ø. Nielsen and G. F. Pedersen, "On the influence of the liquid type on mobile phone measurements using body phantoms," in *Proceedings of 4th International Symposium on Wireless Personal Multimedia Communications (WPMC '01)*, vol. 2, pp. 755–760, Aalborg, Denmark, September 2001.

[144] J. Ø. Nielsen and G. F. Pedersen, "In-network evaluation of body carried mobile terminal performance," in *Proceedings of IEEE International Symposium on Personal, Indoor and Mobile Radio Communications (PIMRC '01)*, vol. 1, pp. D109–D113, San Diego, Calif, USA, September–October 2001.

[145] Future Adaptive Communication Environment (FACE), Technical report, Center For Person-Kommunikation/Center for TeleInFrastruktur, Internal Research project, (http://www.cpk.auc.dk/FACE), Aalborg University, Aalborg, Denmark, October 2003.

[146] Power Aware Communications for Wireless OptiMised personal Area Networks (PACWOMAN), Technical report, European IST FP5 project, Contract No IST-2001-34157, (http://www.imec.be/pacwoman), October 2003.

[147] T. B. Welch, R. L. Musselman, B. A. Emessiene, et al., "The effects of the human body on UWB signal propagation in an indoor environment," *IEEE Journal on Selected Areas in Communications*, vol. 20, no. 9, pp. 1778–1782, 2002.

[148] T. Zasowski, F. Althaus, M. Stäger, A. Wittneben, and G. Tröster, "UWB for non-invasive wireless body area networks: channel measurements and results," in *Proceedings of IEEE Conference on Ultra Wideband Systems and Technologies (UWBST '03)*, pp. 285–289, Reston, Va, USA, November 2003.

[149] Revision of Part 15 of the Commission's Rules Regarding Ultra-Wideband Transmission Systems, First Report and Order, ET Docket 98-153, FCC 02-48. Technical report, Federal Communications Commission, April 2002.

[150] A. Petroff and P. Withington, "PulsON technology overview," Tech. Rep., Time Domain Inc., Huntsville, Ala, USA, July 2001.

[151] 3.1-6.0 GHz Ultra-Wideband Antenna for Commercial UWB Applications, Tech. Rep., SkyCross Inc., Melbourne, Fla, USA, January 2003.

[152] M. Klemm and G. Tröster, "Characterisation of an aperture-stacked patch antenna for ultra-wideband wearable radio systems," in *Proceedings of 15th International Conference on Microwaves, Radar, and Wireless Communications (MIKON '04)*, vol. 2, pp. 395–398, Warsaw, Poland, May 2004.

[153] M. Klemm and G. Tröster, "Small patch antennas for ultra-wideband wireless body area network," in *Proceedings of 7th Ultra-Wideband, Short-Pulse Electromagnetics Conference*, Magdeburg, Germany, July 2004.

[154] N. Behdad and K. Sarabandi, "A multiresonant single-element wideband slot antenna," *IEEE Antennas and Wireless Propagation Letters*, vol. 3, pp. 5–8, 2004.

[155] S. K. Sharma, L. Shafai, and N. Jacob, "Investigation of wide-band microstrip slot antenna," *IEEE Transactions on Antennas and Propagation*, vol. 52, no. 3, pp. 865–872, 2004.

[156] S. C. Hagness, A. Taflove, and J. E. Bridges, "Three-dimensional FDTD analysis of a pulsed microwave confocal system for breast cancer detection: design of an antenna-array element," *IEEE Transactions on Antennas and Propagation*, vol. 47, no. 5, pp. 783–791, 1999.

[157] J. Wang, O. Fujiwara, S. Watanabe, and Y. Yamanaka, "Computation with a parallel FDTD system of human-body effect on electromagnetic absorption for portable telephones," *IEEE Transactions on Microwave Theory and Techniques*, vol. 52, no. 1, pp. 53–58, 2004.

[158] Technical Characteristics and Test Conditions for Radio Equipment Using an Integral Antenna Transmitting Signals to Initiate a Specific Response in the Receiver, ETS 300 341, Technical report, European Telecommunications Standards Institute (ETSI), July 1995.

[159] C. Gabriel, "Compilation of the dielectric properties of body tissues at RF and microwave frequencies, AL/OE-TR-1996-0037," Technical report, US Air Force Armstrong Laboratory, Brooks AFB, Tex, USA, June 1996.

[160] G. F. Pedersen, "Phantoms for radiation measurements of mobile phones," in *Proceedings of IEEE International Symposium on Personal, Indoor and Mobile Radio Communications (PIMRC '01)*, vol. 1, pp. C95–C99, San Diego, Calif, USA, September–October 2001.

[161] G. F. Pedersen, J. Ø. Nielsen, K. Olesen, and I. Z. Kovács, "Antenna diversity on a UMTS handheld phone," in *Proceedings of 10th IEEE International Symposium on Personal, Indoor and Mobile Radio Communications (PIMRC '99)*, vol. 1, pp. 152–156, Osaka, Japan, September 1999.

[162] W. A. Th. Kotterman, G. F. Pedersen, K. Olesen, and P. C. F. Eggers, "Cable-less measurement setup for wireless handheld terminals," in *Proceedings of 12th IEEE International Symposium on Personal, Indoor and Mobile Radio Communications (PIMRC '01)*, vol. 1, pp. B112–B116, San Diego, Calif, USA, September–October 2001.

[163] 3.1-6.0 GHz Ultra-Wideband Antenna for Commercial UWB Applications, Tech. Rep., SkyCross Inc., Melbourne, Fla, USA, November 2002.

[164] G. F. Pedersen and J. Ø. Nielsen, "Radiation pattern measurements of mobile phones next to different head phantoms," in *Proceedings of 13th IEEE International Symposium on Personal, Indoor and Mobile Radio Communications (PIMRC '02)*, vol. 4, pp. 1888–1892, Lisbon, Portugal, September 2002.

[165] I. Z. Kovács and P. C. F. Eggers, "Short-range UWB radio propagation investigations using small terminal antennas," in *Proceedings of International Workshop on Ultra Wideband Systems (IWUWBS '03)*, Oulu, Finland, June 2003.

[166] A. Taha and K. M. Chugg, "On designing the optimal template waveform for UWB impulse radio in the presence of multipath," in *Proceedings of IEEE Conference on Ultra Wideband Systems and Technologies (UWBST '02)*, pp. 41–45, Baltimore, Md, USA, May 2002.

[167] A. Batra, et al., Multi-band OFDM physical layer proposal for IEEE 802.15 task group 3a, www.multibandofdm.org.

[168] R. Van Nee and R. Prasad, *OFDM for Wireless Multimedia Applications*, Artech House Publishers, London, UK, 2000.

[169] L. Scharf, *Statistical Signal Processing*, Addison-Wesley, New York, NY, USA, 1991.

[170] J.-J. van de Beek, O. Edfors, M. Sandell, S. K. Wilson, and P. O. Börjesson, "On channel estimation in OFDM systems," in *IEEE Vehicular Technology Conference (VTC '95)*, vol. 2, pp. 815–819, Chicago, Ill, USA, July 1995.

[171] M. Bossert, A. Donder, and V. Zyablov, "Improved channel estimation with decision feedback for OFDM systems," *Electronics Letters*, vol. 34, no. 11, pp. 1064–1065, 1998.

[172] V. Mignone and A. Morello, "CD3-OFDM: a novel demodulation scheme for fixed and mobile receivers," *IEEE Transactions on Communications*, vol. 44, no. 9, pp. 1144–1151, 1996.

[173] O. Edfors, M. Sandell, J.-J. van de Beek, S. K. Wilson, and P. O. Börjesson, "OFDM channel estimation by singular value decomposition," *IEEE Transactions on Communications*, vol. 46, no. 7, pp. 931–939, 1998.

[174] Y. Li, L. J. Cimini Jr., and N. R. Sollengerger, "Robust channel estimation for OFDM systems with rapid dispersive fading channels," *IEEE Transactions on Communications*, vol. 46, no. 7, pp. 902–915, 1998.

[175] M. Z. Win and R. A. Scholtz, "Impulse radio: how it works," *IEEE Communications Letters*, vol. 2, no. 2, pp. 36–38, 1998.

[176] M. Z. Win and R. A. Scholtz, "Ultra-wide bandwidth time-hopping spread-spectrum impulse radio for wireless multiple-access communications," *IEEE Transactions on Communications*, vol. 48, no. 4, pp. 679–689, 2000.

[177] M. Hämäläinen, V. Hovinen, and J. Iinatti, "Performance comparison between various UWB signals in AWGN channel in presence of multitone interference at the GSM downlink band," in *Proceedings of 4th International Symposium on Wireless Personal Multimedia Communications (WPMC '01)*, pp. 449–453, Aalborg, Denmark, September 2001.

[178] V. S. Somayazulu, "Multiple access performance in UWB systems using time hopping vs. direct sequence spreading," in *Proceedings of IEEE Wireless Communications and Networking Conference (WCNC '02)*, vol. 2, pp. 522–525, Orlando, Fla, USA, March 2002.

[179] R. Roberts, Xtremespectrum CFP document, http://grouper.ieee.org/groups/802/15/pub/2003/Jul03/.

[180] M. Z. Win, *Ultra-wide bandwidth spread-spectrum techniques for wireless multiple access communications*, Ph.D. thesis, Department of Electrical Engineering, University of Southern California, Los Angeles, Calif, USA, 1997.

[181] E. Ertin, U. Mitra, and S. Siwamogsatham, "Maximum-likelihood based multipath channel estimation for code-division multiple-access systems," *IEEE Transactions on Communications*, vol. 49, no. 2, pp. 290–302, 2001.

[182] V. Lotticia, A. D'Andrea, and U. Mengali, "Channel estimation for ultra-wideband communications," *IEEE Journal on Selected Areas in Communications*, vol. 20, no. 9, pp. 1638–1645, 2002.

[183] E. G. Strom and F. Malmsten, "A maximum likelihood approach for estimating DS-CDMA multipath fading channels," *IEEE Journal on Selected Areas in Communications*, vol. 18, no. 1, pp. 132–140, 2000.

[184] A. A. D'Amico, U. Mengali, and M. Morelli, "Multipath channel estimation for the uplink of a DS-CDMA system," in *Proceedings of IEEE International Conference on Communications (ICC '02)*, vol. 1, pp. 16–20, New York, NY, USA, April–May 2002.

[185] B. Mielczarek, M.-O. Wessman, and A. Svensson, "Performance of coherent UWB Rake receivers using different channel estimators," in *Proceedings of International Workshop on Ultra Wideband Systems (IWUWBS '03)*, Oulu, Finland, June 2003.

[186] M. Z. Win and R. A. Scholtz, "On the energy capture of ultrawide bandwidth signals in dense multipath environments," *IEEE Communications Letters*, vol. 2, no. 9, pp. 245–247, 1998.

[187] L. L. Chong, *The effect of channel estimation errors on wideband CDMA systems*, Ph.D. thesis, University of California, San Diego, La Jolla, Calif, USA, 2001.

[188] R. Tesi, M. Hämäläinen, and J. Iinatti, "Impact of the number of fingers of a selective Rake receiver for UWB systems in modified Saleh-Valenzuela channel," in *Proceedings of 4th Finnish Wireless Communication Workshop (FWCW '03)*, Oulu, Finland, October 2003.

[189] H. Niu, J. A. Ritcey, and H. Liu, "Performance of UWB RAKE receivers with imperfect tap weights," in *Proceedings of IEEE Int. Conf. Acoustics, Speech, Signal Processing (ICASSP '03)*, vol. 4, pp. 125–128, Hong Kong, China, April 2003.

[190] K. C. Hwang and K. B. Lee, "Performance analysis of low processing gain DS/CDMA systems with random spreading sequences," *IEEE Communications Letters*, vol. 2, no. 12, pp. 315–317, 1998.

[191] J. G. Proakis, *Digital Communications*, McGraw-Hill, New York, NY, USA, 1986.

[192] T. S. Rappaport, *Wireless Communications: Principles and Practice*, Prentice-Hall, Upper Saddle River, NJ, USA, 1996.

Andreas F. Molisch: Mitsubishi Electric Research Labs, Cambridge, MA, USA;
Department of Electroscience, Lund University, Lund, Sweden

Email: andreas.molisch@ieee.org

Jürgen Kunisch: IMST GmbH, Carl-Friedrich-Gauss-Strasse 2, 47475 Kamp-Lintfort, Germany

Email: kunisch@imst.de

Robert Qiu: Center for Manufacturing Research, Tennessee Technological University,
P.O. Box 5077, Cookeville, TN 38505, USA

Email: rqiu@tntech.edu

Dajana Cassioli: RadioLabs, Dipartimento di Ingegneria Elettronica, Università degli Studi di Roma "Tor Vergata," Via del Politecnico 1, 00133 Roma, Italy

Email: cassioli@ing.uniroma2.it

Michael Buehrer: Department of Electrical and Computer Engineering, Virginia Tech, Blacksburg, VA 24061-0111, USA

Email: buehrer@vt.edu

Marcus Pendergrass: Department of Mathematics and Computer Science, Longwood University,
201 High Street, Farmville, VA 23909, USA

Email: pendergrass@convergentanalysis.com

István Z. Kovács: Department of Communication Technology, Aalborg University, Niels Jernes Vej 12, 9220 Aalborg Ø, Denmark

Gert F. Pedersen: Department of Communication Technology, Aalborg University, Niels Jernes Vej 12, 9220 Aalborg Ø, Denmark

Email: gfp@cpk.auc.dk

Patrick C. F. Eggers: Department of Communication Technology, Aalborg University,
Jernes Vej 12, 9220 Aalborg Ø, Denmark

Email: pe@cpk.auc.dk

Sumit Roy: Department of Electrical Engineering, University of Washington, Seattle,
WA 98195-2500, USA

Email: roy@lagrange.ee.washington.edu

Iyappan Ramachandran: Department of Electrical Engineering, University of Washington,
Seattle, WA 98195-2500, USA

Email: iyappan@ee.washington.edu

3 Signal processing

Ian Oppermann, Matti Hämälainen, Jari Iinatti,
Alberto Rabbachin, Ben Allen, Seyed A. Ghorashi,
Mohammad Ghavami, Olaf Albert,
and Christoph F. Mecklenbräuker

3.1. Introduction

Many different pulse generation techniques may be used to satisfy the requirements of a UWB signal. As discussed in the previous chapters, the FCC requires that the fractional bandwidth is greater than 20%, or that the bandwidth of the transmitted signal is more than 500 MHz, whichever is less. The FCC also stipulates peak power requirements [1]. Many possible solutions may be developed within these restrictions to occupy the available bandwidth.

UWB systems have historically been based on impulse radio concepts. Impulse radio refers to the generation of a series of very short duration pulses, of the order of hundreds of pico seconds. Each pulse has a very wide spectrum that must adhere to the spectral mask requirements. Any given pulse will have very low energy because of the very low power levels permitted for typical UWB transmission. Therefore, many pulses will typically be combined to carry the information for one bit. Continuous pulse transmission introduces a complication in that, without further signal processing at the transmitter, strong spectral lines will be introduced into the spectrum of the transmitted signal. Several techniques are available for minimising these spectral lines, the most common of which are described later in this chapter.

Impulse radio has the significant advantage in that it is essentially a baseband technique. The most common impulse-radio-based UWB concepts are based on pulse position modulation with time hopping (TH-PPM). Time-hopping, direct-sequence techniques, and multicarrier schemes are also described in this chapter. However, the focus will be on impulse radio modulation schemes.

This chapter will address signal processing issues in UWB. The chapter will address both impulse radio techniques and multiband techniques.

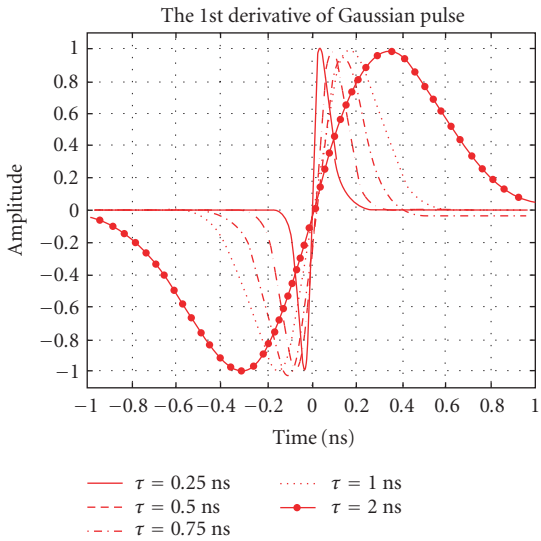

FIGURE 3.1. Gaussian monocycle in time domain.

3.2. Impulse radio schemes

3.2.1. Impulse radio UWB

Time-modulated ultra-wideband (TM-UWB) communication is based on discontinuous transmission of very short pulses or pulsed waveforms (monocycles), examples of which are presented in Figure 3.1. These pulses have the corresponding ultra-wide frequency-domain characteristics presented in Figure 3.2. This type of transmission does not require the use of additional carrier modulation as the pulse will propagate well in the radio channel. The technique is therefore a baseband signal approach. This radio concept is referred to as impulse radio (IR).

One transmitted symbol is spread over N monocycles to achieve a processing gain that may be used to combat noise and interference. This is similar to the approach used for spread spectrum systems. The processing gain derived from this procedure can be defined as

$$\mathrm{PG}_1 = 10\log_{10}(N). \tag{3.1}$$

The monocycle waveform can be any function that satisfies the spectral mask regulatory requirements. Common pulse shapes include Gaussian, Laplacian, or Rayleigh or Hermitean pulses. Data modulation is typically based on pulse position modulation (PPM). In [2], the authors also present pulse amplitude modulation (PAM) in UWB transmission. The UWB receiver is typically a homodyne cross-correlator that is based on an architecture that utilises a direct RF-to-baseband conversion. Intermediate frequency conversion is not needed, which makes the implementation simpler than that in conventional (super-)heterodyne systems.

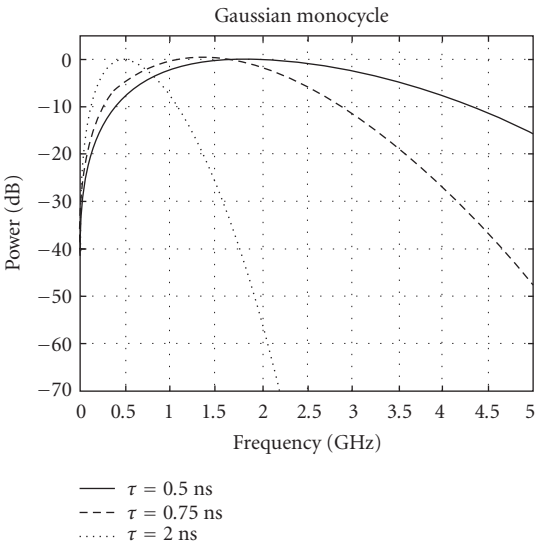

FIGURE 3.2. Gaussian monocycle in frequency domain.

Unlike spread spectrum systems, the UWB pulse does not necessarily occupy the entire chip period. This means that the duty cycle can be extremely low. In a low delay spread channel, the receiver is only required to "listen" to the channel for a small fraction of the period between pulses. The impact of any continuous source of interference is therefore reduced so that it is only relevant when the receiver is attempting to detect a pulse. This leads to processing gain in a similar manner to a spread spectrum system's ability to reduce the impact of interference. Processing gain due to the low duty cycle is given by

$$\mathrm{PG}_2 = 10 \log_{10} \left(\frac{T_p}{\tau_p} \right), \tag{3.2}$$

where

$$\begin{aligned} T_p &= \text{chip period}, \\ \tau_p &= \text{impulse width}. \end{aligned} \tag{3.3}$$

The total processing gain PG is the sum of the two processing gains [3]

$$\mathrm{PG} = \mathrm{PG}_1 + \mathrm{PG}_2 . \tag{3.4}$$

In a discontinuous time-hopped system, consecutive pulses are transmitted according to a pseudorandom (PR) time-hopping code. As the transmitted signal is not continuous, UWB communication is resistant to severe multipath propagation. With a short pulse width and a relative long pulse repetition time (compared to pulse width), the multipath components associated with the transmitted pulse

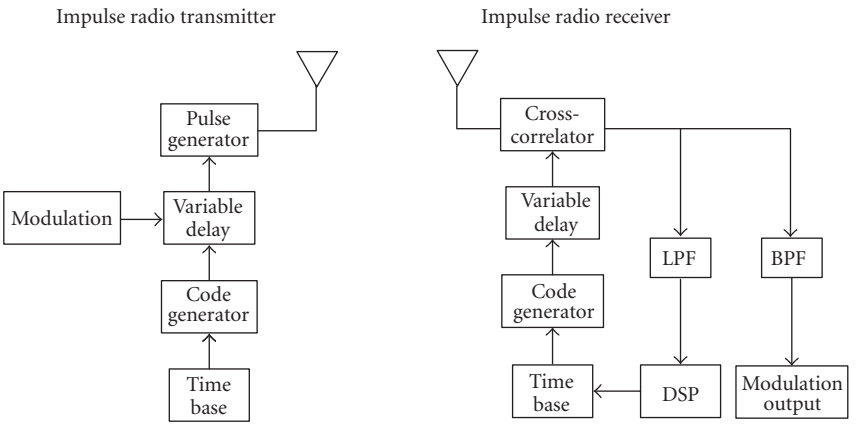

FIGURE 3.3. Block diagram of the TH-PPM UWB impulse radio concept by time domain corporation.

are attenuated before the next pulse is sent, reducing the inter-pulse interference. If the time between pulses is greater than the channel delay spread, there is no ISI between pulses and so no ISI between bits.

In the time domain, the transmitted Gaussian monocycle can be (ideally) approximated by the first derivative of the Gaussian function. Figures 3.1 and 3.2 shows the time and frequency domains of sample monocycles of different duration.

The Gaussian monocycle in the time domain $v(t)$ is given by [3]

$$v(t) = 6A\sqrt{\frac{e\pi}{3}}\frac{t}{\tau_p}e^{-6\pi(t/\tau_p)^2}, \tag{3.5}$$

where A is the pulse amplitude, τ_p is the pulse width, and t is the time.

The corresponding function in the frequency domain is the Fourier transform of $v(t)$, given by

$$F\{v(t)\} = V(f) = -j\frac{Af{\tau_p}^2}{3}\sqrt{\frac{e\pi}{2}}e^{-(\pi/6)f^2\tau_p^2}, \tag{3.6}$$

where f is the frequency.

The nominal centre frequency and the bandwidth of the signal depends on the monocycle's duration in time. The -3 dB bandwidth is approximately 116% of the nominal centre frequency $f_0 = 1/\tau_p$ [3]. Considering an example monocycle duration of 0.75 ns, as shown in Figure 3.1, the nominal centre frequency is 1.33 GHz and the half-power bandwidth is 1.55 GHz. The spectrum of Gaussian monocycle is asymmetrical, as can be seen in Figure 3.2.

Figure 3.3 presents a block diagram of a time-hopping UWB impulse radio concept that utilises pulse position modulation (concept by Time Domain Corporation, USA).

3.2.2. Fast stepped frequency chirps

Both the bandwidth and spectral mask limitations must be satisfied by the UWB signal. There are many means of generating a very wideband signal. One technique is based on fast frequency chirps, which are commonly used in impulse radar applications. It is possible to generate a wideband transmission by sweeping the transmitter's oscillator in the frequency domain. A bandwidth of several hundred MHz can be achieved with a 10 ns sweep time [4]. Wider bandwidths can be achieved using this technique, for example, ground penetrating radar (GPR) systems with 50–1200 MHz bandwidth have been documented in [5].

GPRs based on UWB technology are suitable for object detection in, for example, landmine sweeping and avalanche rescue operations because of the good signal penetration ability and fine space resolution.

3.3. Multicarrier schemes

3.3.1. Multicarrier spread spectrum schemes

Another approach is to extend the techniques utilised for direct-sequence spread spectrum or code-division multiple-access (CDMA) schemes that are used for third generation mobile systems. Wideband CDMA systems with optional multicarrier (MC) techniques can be used to fill the available spectral mask.

There are three main techniques to generate an SS-MC transmission; multicarrier CDMA, multicarrier DS-CDMA, and multitone (MT) CDMA [6]. Each of these techniques relies on, and benefits from, the properties of conventional spread spectrum signals. However, multicarrier systems are reasonably complex to implement. In particular, multicarrier systems require several mixers or digital fast Fourier transform (FFT) techniques to place the different signal components in the required bands.

Figure 3.4 shows a block diagram for an MC-CDMA system. The original data stream is spread over the different subcarriers f_i with each chip of pseudorandom (PR) code C_i. The spectrum spreading is done in the frequency domain [6]. The signal is de-spread at the receiver using corresponding chips g_i of the spreading code C. In UWB applications, the individual modulated carrier needs to fulfil the 500 MHz bandwidth requirements.

Figure 3.5 shows a block diagram for a multicarrier DS-CDMA system. This method involves spreading the original data in the time domain after serial-to-parallel conversion of the data stream [6]. The system needs to obtain the 500 MHz minimum bandwidth requirement to be treated as UWB.

Figure 3.6 shows the block diagram of a multitone-CDMA system. The bandwidth of an MT-CDMA system is smaller than in the previous multicarrier systems because of the small subcarrier spacing. This kind of multicarrier approach is the closest to the original UWB idea. However, it causes the highest self-interference due to the overlapping spectra.

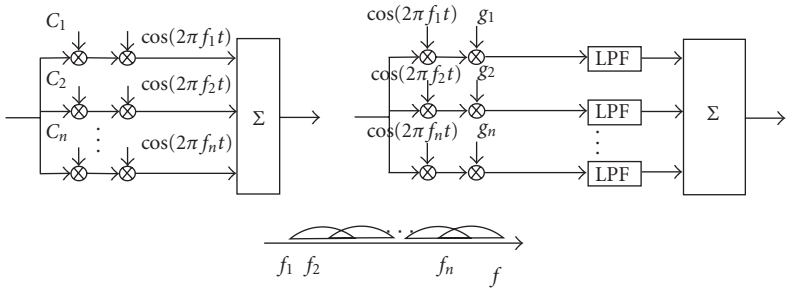

Figure 3.4. Block diagram and spectrum for multicarrier CDMA system.

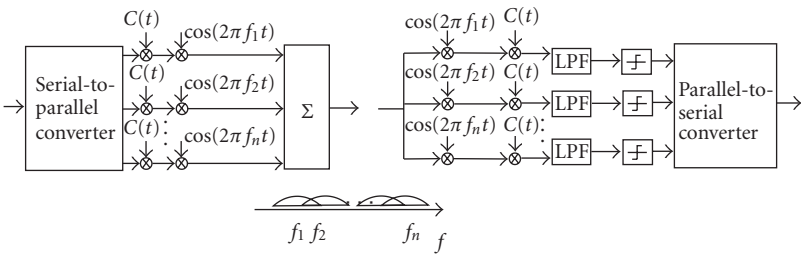

Figure 3.5. Block diagram and spectrum for multicarrier DS-CDMA system.

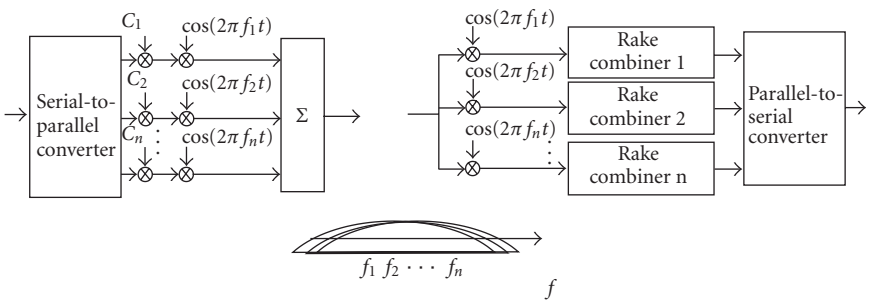

Figure 3.6. Block diagram and spectrum for multitone CDMA system.

Multicarrier technology is used in high data rate applications, for example, in WLAN systems such as Hiperlan2, digital audio or video broadcasting (DAB and DVB, resp.), and in asymmetric digital subscriber line (ADSL).

The advantage of multicarrier technologies over single-carrier systems is that the data rate in each subcarrier is lower than for single-carrier systems. This eases synchronisation of the spreading sequence at the receiver, and helps to avoid ISI. The disadvantage is the increased complexity of the receiver requiring either multiple mixing stages or FFT processing.

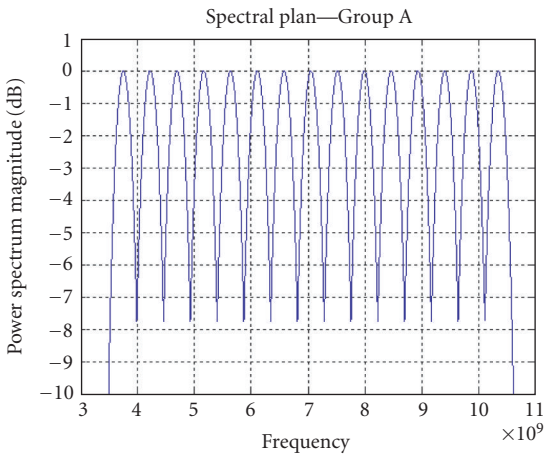

FIGURE 3.7. Multiband frequency plan—Group A.

MC-CDMA schemes spread the signal in the frequency domain. The signal consists of overlapping, relatively narrow carriers that fill the available UWB signal spectrum. MC-DS-CDMA and MT-CDMA schemes apply spreading in the time domain. MT-CDMA has a similar bandwidth to a basic DS-CDMA scheme [6] with relatively small separation of the tones used (f_1 to f_n in Figure 3.6). Consequently, the spreading factor employed for MT-CDMA schemes is much higher than that for the MC schemes. The increased spreading factor increases the processing speed required at the receiver.

The conventional DS-SS technique without multicarrier properties can also be characterised as a UWB technique if the chip rate is high enough. This calls for extremely fast digital signal processing which may be impractical. Issues such as synchronisation will also be a significant challenge.

3.3.2. Multiband UWB

One early proposal within the IEEE 802.15.3 working group for UWB signals [7] utilised overlapping groups of UWB signals each with a bandwidth of 528 MHz. This so-called multiband UWB ensures adherence to the FCC minimum bandwidth requirements and allows for efficient utilisation of the available spectrum.

Figure 3.7 shows the spectrum plan for the first group of UWB signals. The subbands are spaced 470 MHz apart, and multiple 528 MHz signals may be utilised. This allows for flexible coexistence with existing communications systems (such as WLAN systems). Figure 3.8 shows the second group of UWB signals which overlap the first group of UWB signals by 235 MHz. This potentially enhances the system's flexibility with respect to coexistence, interference mitigation, and multiple access.

With this proposal, each group of UWB signals is divided into lower sets (subbands 1–8) and upper sets (subbands 9–15). Only 7 subbands are used in the lower

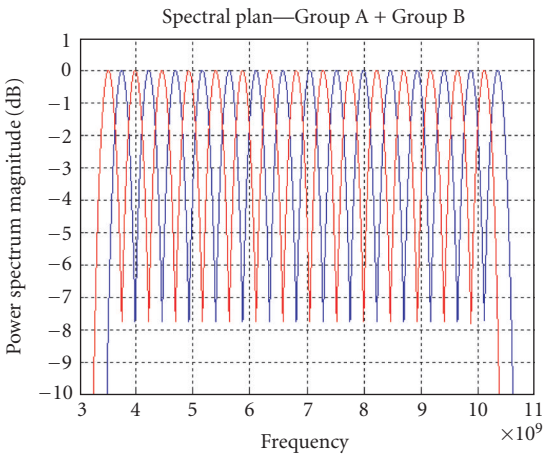

FIGURE 3.8. Multiband frequency plan—Groups A and B.

set, which means one subband can be avoided for coexistence. The upper set is used in parallel to the lower set to increase the bit rate.

3.4. Pulse shapes

This section describes the pulse shapes which may be used with UWB systems. Whilst primarily focused on impulse radio systems, the pulse shapes can also be applied to multiband systems.

3.4.1. Rectangular monocycle

The simplest example of an impulse is a rectangular monocycle which can be represented as follows:

$$P_{\mathrm{Re}}(t) = \sqrt{\frac{1}{T_p}}\Big[U(t) - U\Big(t - T_p\Big)\Big], \tag{3.7}$$

where T_p denotes the pulse width and $U(\cdot)$ represents the unit step function. Thus, by adjusting T_p, the bandwidth of the signal can be controlled. Taking the Fourier transform of P_{Re} yields the familiar $\sin(x)/x$ function with nulls occurring at $1/T_p$ rad/s. The $\sin(x)/x$ function contains a DC term making the wireless transmission of the rectangular monocycle impractical. The time and frequency domains of an example rectangular pulse are shown in Figures 3.9 and 3.10 where the monocycle has been normalised for unit energy.

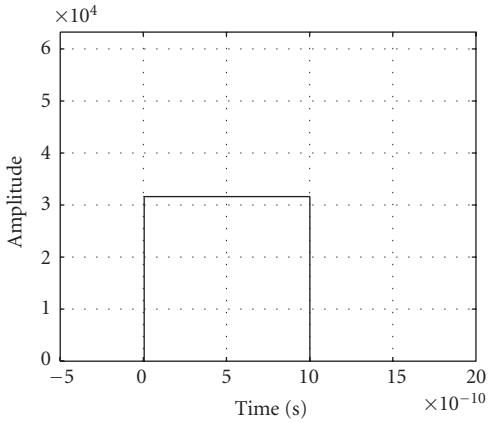

FIGURE 3.9. Rectangular monocycle in time domain.

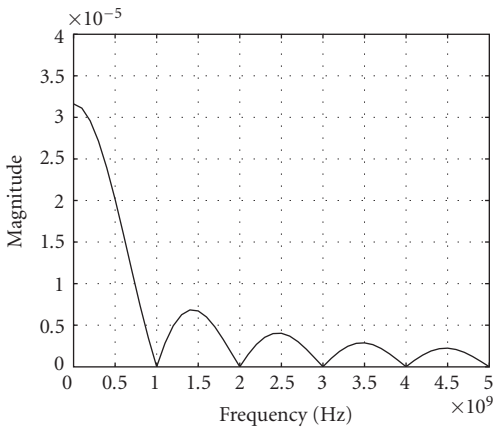

FIGURE 3.10. Rectangular monocycle in frequency domain.

3.4.2. Rayleigh monocycle

The Rayleigh monocycle [8], which is derived from the first derivative of the Gaussian pulse (see below), has the time-domain representation, $P_R(t)$, given by

$$P_R(t) = A_R\left[\frac{t-\mu}{\sigma^2}\right]e^{-(1/2)((t-\mu)/\sigma)^2}, \tag{3.8}$$

where σ is the pulse width and μ is the centre of the pulse. Thus by adjusting σ, the bandwidth can be controlled. The term A_R is a scaling factor which has been introduced such that the total energy in the pulse is normalised to unity.

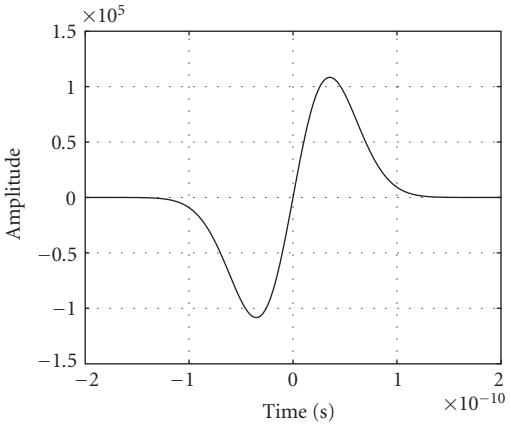

FIGURE 3.11. Rayleigh monocycle in time domain.

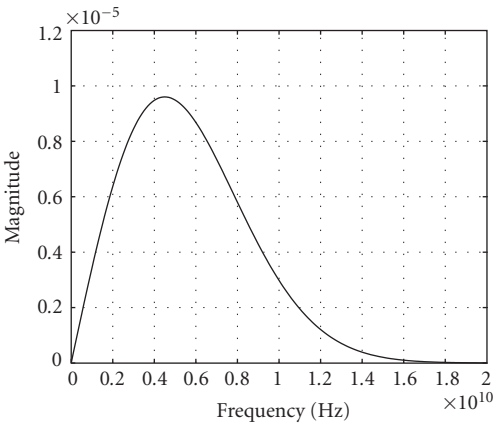

FIGURE 3.12. Rayleigh monocycle in frequency domain.

The frequency spectrum of the Rayleigh monocycle, $P_R(f)$, is

$$P_R(t) = A_R\sqrt{2\pi}(2\pi\sigma f)e^{-(1/2)(2\pi\sigma f)^2}e^{-j(2\pi f\mu+0.5\pi)}. \tag{3.9}$$

The *effective time duration* is defined as the time duration of the waveform that contains 99.99% of the total monocycle energy. Here, 99.99% of the total Rayleigh monocycle energy is in $T_p = 7\sigma$ and centred at $\mu = 3.5\sigma$.

Rayleigh monocycles do not have a DC component enabling them to be used in impulse radio systems. The time and frequency domains of an example Rayleigh monocycle are shown in Figures 3.11 and 3.12 where the monocycle has been normalised for unit energy.

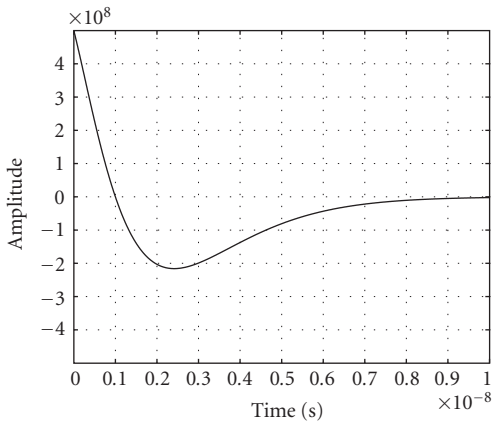

FIGURE 3.13. Laplacian monocycle in time domain.

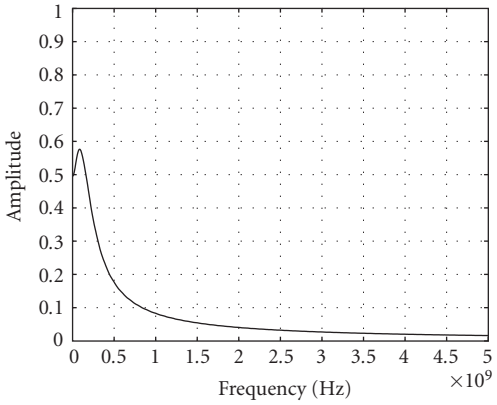

FIGURE 3.14. Laplacian monocycle in frequency domain.

3.4.3. Laplacian monocycle

The time-domain representation of the Laplacian monocycle [8], $P_L(t)$, is given by

$$P_L(t) = \frac{1}{2\sigma}\left[1 - \left(\frac{t}{\sigma}\right)^2\right]e^{-t/\sigma}. \tag{3.10}$$

The time and frequency domains of an example Laplacian monocycle are shown in Figures 3.13 and 3.14 where the monocycle has been normalised for unit energy. It can be seen from the figure that the frequency domain contains a DC term, therefore making the Laplacian monocycle impractical for use in impulse radio applications.

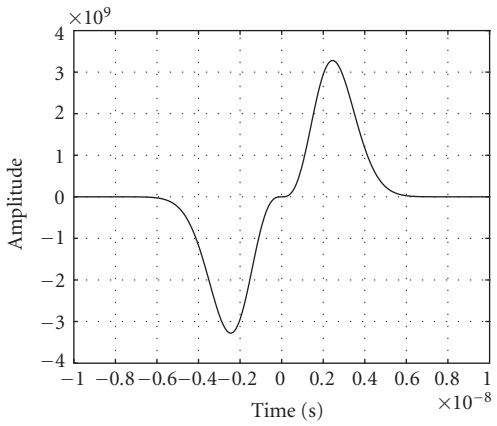

FIGURE 3.15. Cubic monocycle in time domain.

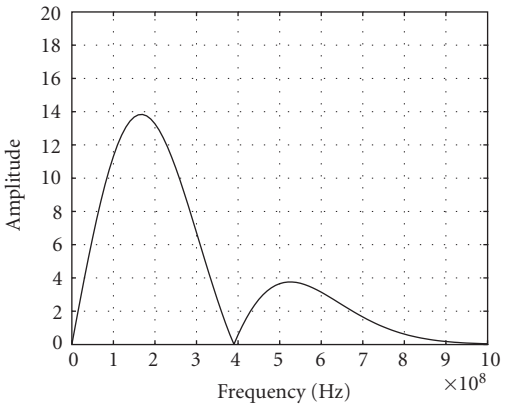

FIGURE 3.16. Cubic monocycle in frequency domain.

3.4.4. Cubic monocycle

The time-domain representation of the cubic monocycle [8], $P_c(t)$, is

$$P_c(t;\sigma) = \frac{t^3}{\sigma^4} e^{-t^2/(2\sigma)^2}. \tag{3.11}$$

The time and frequency domains representations of an example cubic monocycle are shown in Figures 3.15 and 3.16, where the energy is normalised to unity. The cubic monocycle does not contain a cubic term making it possible to be used in impulse radio applications.

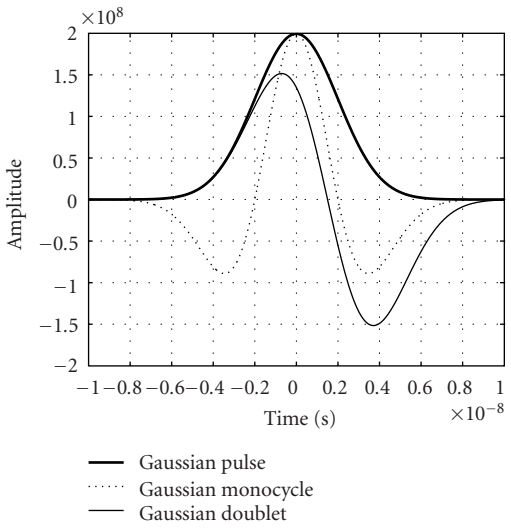

Figure 3.17. Gaussian waveforms in time domain.

3.4.5. Gaussian pulses

This class of pulses derives its name from the Gauss function that frequently occurs in statistical theory and filter design. The familiar Gaussian pulse is a member of this class of monocycles, as are its higher-order derivatives. The derivatives can be generated by filtering the Gaussian pulse since filtering can be modelled by the derivative function. Higher-order derivatives can be generated by successive filtering.

3.4.5.1. The Gaussian pulse

A Gaussian pulse [9] is given by

$$P_{\mathrm{Re}}(t) = \frac{1}{\sqrt{2\pi}\sigma} e^{-(1/2)((t-\mu)/\sigma)^2}, \tag{3.12}$$

where μ is the centre of the pulse and σ relates to the width of the pulse. Note that, like the rectangular pulse, the Gaussian pulse also contains a DC term making it impractical for use in wireless systems. However, higher derivatives do not contain such a term and are therefore applicable. The time and frequency domains of an example Gaussian pulse are shown in Figures 3.17 and 3.18.

3.4.5.2. Gaussian monocycle

The second derivative of the Gaussian pulse is called a Gaussian monocycle and is often used in impulse radio systems. The time domain representation of the

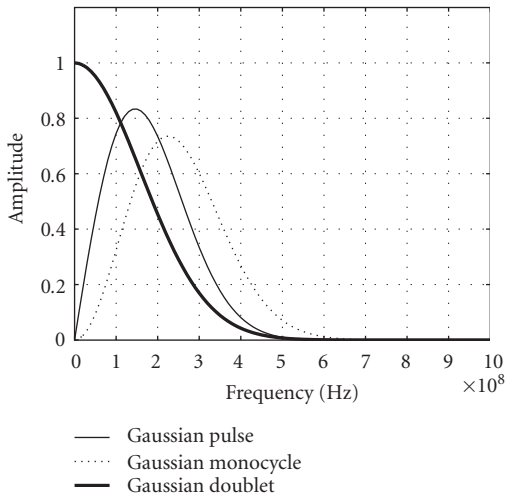

FIGURE 3.18. Gaussian waveforms in frequency domain.

Gaussian monocycle, $P_G(t)$, is

$$P_G(t) = \frac{1}{\sqrt{2\pi}\sigma}\left[1 - \left(\frac{t-\mu}{\sigma}\right)^2\right] e^{-(1/2)((t-\mu)/\sigma)^2}. \tag{3.13}$$

The effective time duration, T_p, for the Gaussian monocycle is $T_p = 7\sigma$ with the centre of $\mu = 3.5\sigma$. The frequency spectrum of a Gaussian monocycle, $P_G(f;\sigma)$, is given by

$$P_G(f) = (2\pi\sigma f)^2 e^{-(1/2)(2\pi\sigma f)^2} e^{-j2\pi f\mu}, \tag{3.14}$$

which does not contain a DC term.

The Gaussian monocycle has a single zero crossing in the time domain, whilst higher-order derivatives have additional zero crossings. Therefore, higher-order Gaussian pulses yield waveforms with lower relative bandwidths and higher centre frequencies. The time and frequency domains of an example Gaussian monocycle are shown in Figures 3.17 and 3.18.

3.4.5.3. Gaussian doublet

The Gaussian doublet [8] consists of two Gaussian pulses (the reversed amplitude of each other) with a time gap of T_w between the maxima of each. The time domain representation of the Gaussian doublet is given by

$$P_{\mathrm{GD}}(t) = \frac{1}{\sqrt{2\pi}\sigma}\left[e^{-(1/2)((t-\mu)/\sigma)^2} - e^{-(1/2)((t-\mu-T_w)/\sigma)^2}\right]. \tag{3.15}$$

Table 3.1. 10 dB bandwidth and the location of the centre frequency for Gaussian signals.

Pulse waveform	f_c	B
Gaussian pulse	$1/T_p$	$2/T_p$
Gaussian doublet	$1/T_p$	$2/T_p$
2nd derivative of Gaussian pulse	$1.73/T_p$	$2.1/T_p$
3rd derivative of Gaussian pulse	$2/T_p$	$2/T_p$

The frequency spectrum of the Gaussian doublet, $P_{\mathrm{GD}}(f)$, is

$$P_{\mathrm{GD}}(f) = 2A_{\mathrm{GD}}\sqrt{2\pi}\sigma \sin(\pi f T_w) e^{-(1/2)(2\pi\sigma f)^2} e^{-j[2\pi f(\mu+0.5T_w)-0.5T_w]}. \tag{3.16}$$

The factor A_G is introduced so that the total energy of the pulse is normalised to unity. The parameters T_w,σ, and μ determine the pulse width. For $T_w = 7\sigma$, the effective time duration would be $T_p = 14\sigma$.

Owing to the similarity of the two basic Gaussian waveforms, the Gaussian pulse and Gaussian doublet have similar spectral envelops. However, the spectral envelope of the Gaussian doublet has regular nulls. The distance between nulls in the frequency domain is inversely proportional to the pulse separation of the doublet (T_w). Note that the bandwidth of the Gaussian doublet is smaller than that of the Gaussian pulse and Gaussian monocycle, however its out-of-band energy is larger. The spectrum for all of the waveform is asymmetric about the centre frequency. The 10 dB bandwidth and the location of the centre frequency for Gaussian signals are given in Table 3.1. Here, the 10 dB bandwidth is defined as $B_{10\,\mathrm{dB}} = f_H - f_L$, where the magnitude spectrum is $1/\sqrt{10}$ of its peak value at frequencies f_H and f_L. The normal centre frequency is defined here as $f_c = (f_H + f_L)/2$. The time and frequency domains of an example Gaussian doublet are shown in Figures 3.17 and 3.18.

3.5. Data modulation

A number of modulation schemes may be used with UWB systems. The potential modulation schemes include both orthogonal and antipodal schemes.

3.5.1. Pulse amplitude modulation

The classic binary pulse amplitude modulation (PAM) can be presented using two antipodal Gaussian pulses as shown in Figure 3.19. The transmitted binary baseband pulse amplitude modulated information signal $s(t)$ can be presented as

$$x(t) = d_j w_{\mathrm{tr}}(t), \tag{3.17}$$

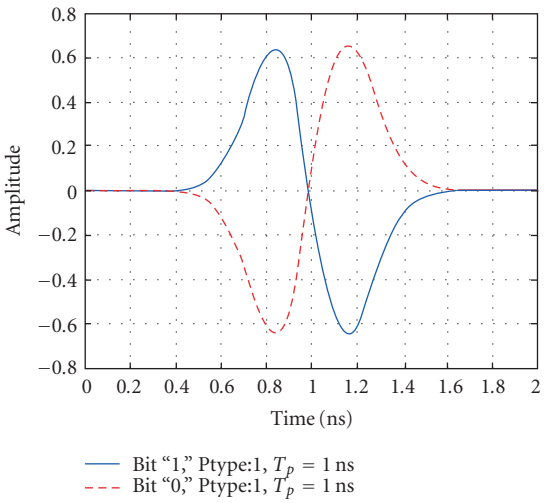

FIGURE 3.19. BPAM pulse shapes for "1" and "0" bits.

where $w_{\text{tr}}(t)$ represents the UWB pulse waveform, j represents the bit transmitted ("0" or "1"), and

$$d_j = \begin{cases} -1, & j = 0, \\ 1, & j = 1. \end{cases} \tag{3.18}$$

In Figure 3.19, the first derivative of the Gaussian pulse is shown, defined as

$$w_{\text{G1}}(t) = -\frac{t}{\sqrt{2\pi}\sigma^3} e^{(-t^2/2\sigma^2)}, \tag{3.19}$$

where σ is directly related with the pulse length T_p by $\sigma = T_p/2\pi$.

3.5.2. On-off keying

The second modulation scheme is binary on-off keying (OOK). Using the following definitions

$$d_j = \begin{cases} 0, & j = 0, \\ 1, & j = 1, \end{cases} \tag{3.20}$$

the waveform used for this modulation can be defined as in (3.19). The major difference between OOK and PAM is that nothing is transmitted in OOK when a "0" bit is chosen.

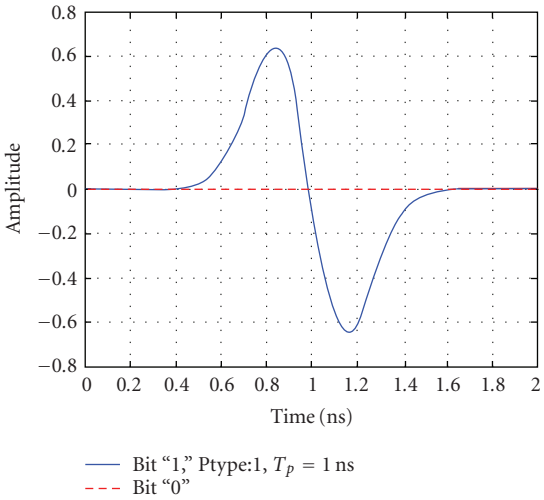

FIGURE 3.20. OOK pulses used for "1" and "0" bits.

3.5.3. Pulse position modulation

With pulse position modulation (PPM), the chosen bit to be transmitted influences the position of the UWB pulse. That means that while bit "0" is represented by a pulse originating at the time instant 0, bit "1" is shifted in time by the amount of δ from 0. The signal can be represented as follows:

$$x(t) = w_{\text{tr}}(t - \delta d_j), \tag{3.21}$$

where d_j assumes the following values, depending on the bit chosen to be transmitted,

$$d_j = \begin{cases} 0, & j = 0, \\ 1, & j = 1, \end{cases} \tag{3.22}$$

and the other variables have been defined previously.

The value of δ may be chosen according to the autocorrelation characteristics of the pulse. The autocorrelation function can be defined as [10]

$$\rho(t) = \int_{-\infty}^{+\infty} w_{\text{tr}}(\tau) w_{\text{tr}}(t + \tau). \tag{3.23}$$

For instance, if we want to implement a standard PPM with orthogonal signals, the optimum value for δ which we call δ_{opt} will be the one which satisfies the

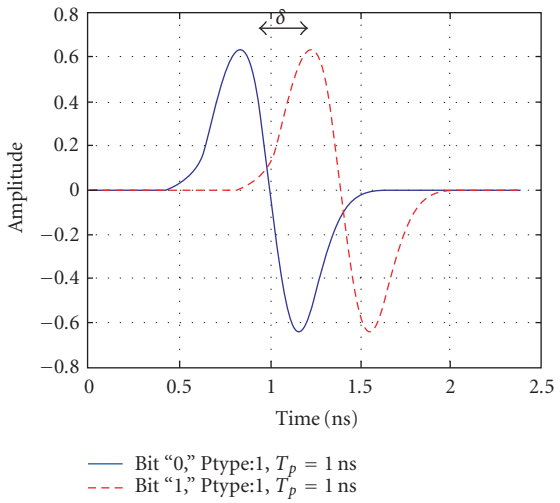

FIGURE 3.21. PPM pulse shapes for "1" and "0" bits.

following equation:

$$\rho(\delta_{\text{opt}}) = \int_{-\infty}^{+\infty} w_{\text{tr}}(\tau) w_{\text{tr}}(\delta_{\text{opt}} + \tau) = 0. \tag{3.24}$$

Figure 3.21 shows a particular case of PPM transmission where data bit "1" is sent delayed by a fractional time interval $\delta < 1$, and data bit "0" is sent at the nominal time.

3.5.4. Pulse shape modulation

Pulse position modulation (PPM) and pulse amplitude modulation (PAM) have been considered for use in UWB impulse radio systems. Pulse shape modulation (PSM) is an alternative where, instead of different pulse positions or pulse amplitudes, different pulse shapes are used to represent information bits. This requires a suitable set of pulses to be used and, like traditional modulation schemes, higher-order modulation is possible by employing a larger pulse set. Modified Hermite polynomial functions (MHPF) [11], wavelets [2], and prolate spheroidal wave functions (PSWF) [12] have been proposed in the literature as pulse sets for PSM systems and all exhibit orthogonal properties. The orthogonality of these pulses is one of the most desirable properties since it enables optimum detection at the receiver. Although other orthogonal pulse sets such as coded monocycles can also be considered, their time and frequency specifications vary for different orders of pulse. MHPF, wavelets, and PSWF wave functions, however, exhibit an almost constant pulse width and frequency bandwidth with increased pulse order.

The application of orthogonal signal sets also enables alternative multiple-access techniques to be considered. This can be attained by assigning groups of orthogonal pulses to each user, where each user then uses the assigned set for pulse

shape modulation. The transmissions will then be mutually orthogonal and not interfering with each other (assuming orthogonality is retained throughout the link to the detector) and can therefore take place simultaneously and in the same frequency band.

3.5.4.1. Modified Hermite polynomial functions

MHPF [11] are derived from Hermite polynomials. Hermite polynomials themselves do not possess orthogonality, however this is achieved by modifying them which leads to the term modified Hermite polynomial functions and are defined as follows:

$$h_n(t) = e^{-t^2/4} h_{en}(t) = (-1)^n e^{t^2/4} \frac{d^n}{dt^n}\left(e^{-t^2/2}\right), \tag{3.25}$$

where $n = 0, 1, 2, \ldots$, and $-\infty < t < \infty$. It can be shown that MHPF satisfy the following differential equations, where the dots refer to the differentiation operation with respect to time:

$$\begin{aligned} \ddot{h}_n + \left(n + \frac{1}{2} - \frac{1}{4}t^2\right) h_n &= 0, \\ \dot{h}_n + \frac{t}{2} h_n &= n h_{n-1}, \\ h_{n+1} &= \frac{t}{2} h_n - \dot{h}_n. \end{aligned} \tag{3.26}$$

The equivalent Fourier transform of the above equations can be written as follows:

$$\begin{aligned} \ddot{H}_n + 16\pi^2 \left(n + \frac{1}{2} - 4\pi^2 f^2\right) H_n &= 0, \\ j8\pi^2 f H_n + j\dot{H}_n &= 4\pi n H_{n-1}, \\ H_{n+1} &= j\frac{1}{4\pi}\dot{H}_n - j2\pi f H_n. \end{aligned} \tag{3.27}$$

The general formula for defining MHPF is given by

$$h_n(t) = k_n e^{-t^2/4\tau^2} n! \sum_{i=0}^{[n/2]} \left(-\frac{1}{2}\right)^i \frac{(t/\tau)^{n-2i}}{(n-2i)!\,i!}, \tag{3.28}$$

where $[n/2]$ denotes the integer part of $n/2$.

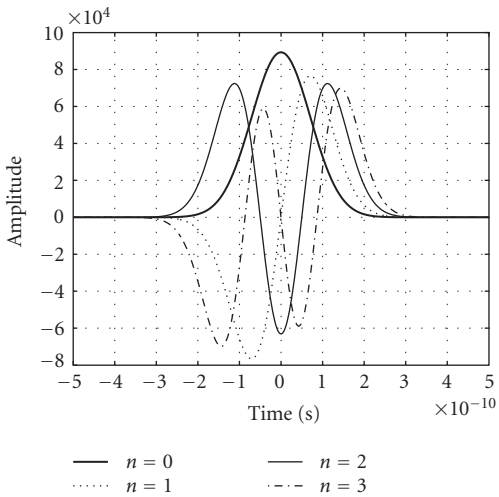

FIGURE 3.22. Modified Hermite wave functions in time domain.

From the above equation, order 0, 1, 2, and 3 MHPF are defined by the following equations:

$$\begin{aligned} h_0(t) &= k_0 e^{-t^2/4\tau^2}, \\ h_1(t) &= k_0 \frac{t}{\tau} e^{-t^2/4\tau^2}, \\ h_2(t) &= k_0 \left[\left(\frac{t}{\tau} \right)^2 - 1 \right] e^{-t^2/4\tau^2}, \\ h_3(t) &= k_0 \left[\left(\frac{t}{\tau} \right)^3 - 3\frac{t}{\tau} \right] e^{-t^2/4\tau^2}. \end{aligned} \tag{3.29}$$

The constants k_n, where $n = 0, 1$, determine the energy, E_n, of the pulse given by

$$k_n = \sqrt{\frac{E_n}{\tau n! \sqrt{2\pi}}}. \tag{3.30}$$

Figures 3.22 and 3.23 show the MHPF in the time and frequency domains for $n = 0, 1, 2, 3$. The functions are normalised for unit energy. The figure shows the pulse durations and bandwidths to be the same for all values of n, and they have a nonzero DC component for $n > 0$. It is also observed that the number of zero crossings in the time domain is equal to the pulse order, n. The increasing centre frequency with pulse order can also be observed and this variable spectral characteristic makes it difficult to apply to UWB impulse radio systems where the transmissions should be within a certain spectral mask.

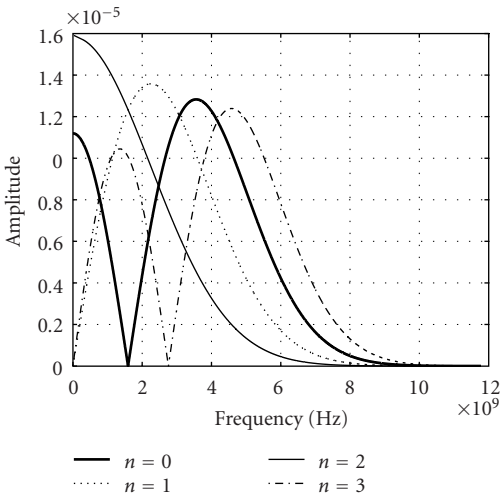

FIGURE 3.23. Modified Hermite wave functions in frequency domain.

A final characteristic of MHPF is the autocorrelation function. The width of the autocorrelation function helps to ascertain the detection performance when subject to jitter. The autocorrelation function of MHPF becomes narrower with increasing pulse order. Thus, higher-order pulses will exhibit a greater sensitivity to jitter.

3.5.4.2. Wavelets

Reference [2] proposes using wavelets as pulse shapes since they exhibit orthogonality and have the same time duration as the order is increased. Using an orthogonal wavelet, wavelet packets can be generated as follows. Consider 2 filters of length $2N$ where $h(n)$ and $g(n)$ are reversed versions of the low and highpass decomposition filter respectively (referred to as *quadrature mirror filters* in filter-bank theory) normalised by $\sqrt{2}$ and N is the length of the wavelet. The following sequence functions can then be used to produce a wavelet packet:

$$W_{2n}(x) = \sqrt{2} \sum_{k=0}^{2N-1} h(k) W_n(2x - k), \tag{3.31}$$

$$W_{2n+1}(x) = \sqrt{2} \sum_{k=0}^{2N-1} g(k) W_n(2x - k), \tag{3.32}$$

where $W_0(x) = \phi(x)$ is the scaling function and $W_1(x) = \varphi(x)$ is the wavelet function. Compared to other types of wavelets, it is shown in reference [2] that the Haar wavelet exhibits a high degree of orthogonality as the order is increased

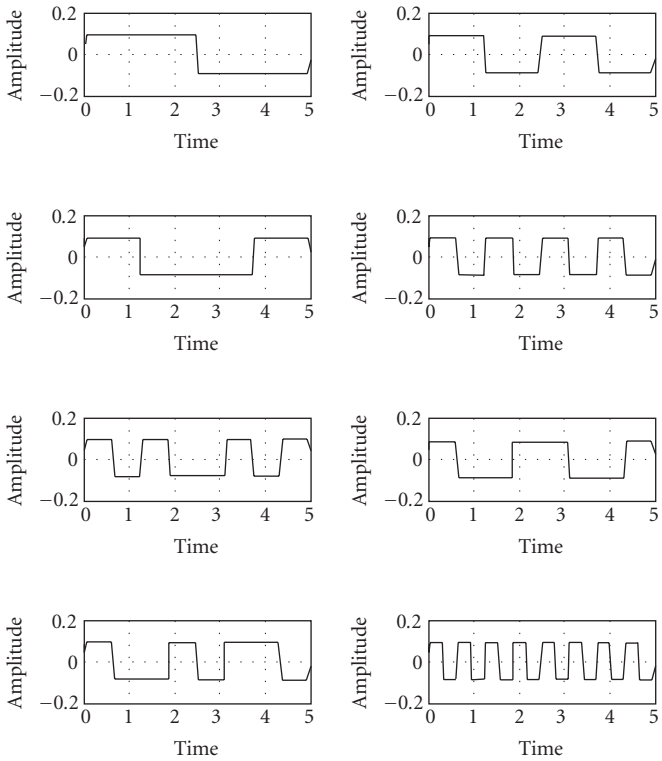

Figure 3.24. The Haar wavelet [2] in time domain.

which can be seen in Figures 3.24 and 3.25. The spectral characteristics are also shown in the figure along with the spectral characteristics of a Gaussian monocycle for comparison. The spectral characteristics show a narrow bandwidth for all orders of packets considered, along with an increased centre frequency as the order is increased. The later characteristic makes it difficult to apply to UWB impulse radio systems. Compared to other wavelets, it also has favourable autocorrelation properties and will therefore be more robust to jitter. However, the construction of this set may be a problem in practice as the Haar wavelets are not regular. Other wavelets do, however, produce a more desirable frequency spectrum due to their smoother time-domain characteristics. Examples of other candidate wavelets are Biorthogonal 6.8 (Bior6.8), Coiflet order 2, Daubechies order 5 (Db5), and Symlet order 5 wavelets.

3.5.4.3. Prolate spheroidal wave functions

In [12] Prolate spheroidal wave functions (PSWF) are used as the set of pulse shapes in a UWB impulse radio system. PSWF's, $\psi(t)$, are defined as the solution

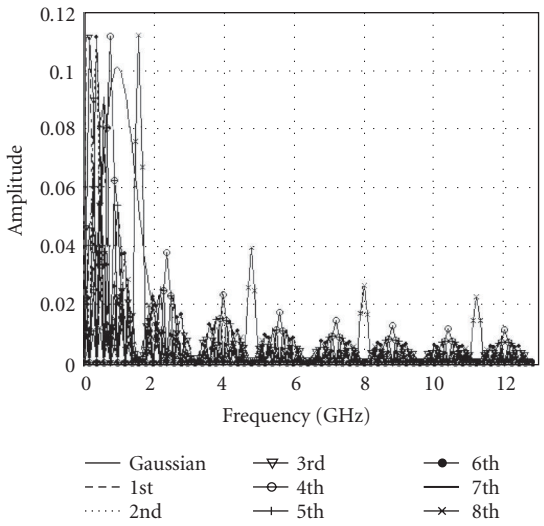

FIGURE 3.25. The Haar wavelet [2] in frequency domain.

of the following equation:

$$\int_{-T/2}^{T/2} \psi(x) \frac{\sin \Omega(t-x)}{\pi(t-x)} dx = \lambda \psi(t). \tag{3.33}$$

PSWF's can also be defined as the solution of the following differential equation:

$$\frac{d}{dt}\left(1-t^2\right)\frac{d\psi}{dt} + \left(\chi - c^2 t^2\right)\psi = 0, \tag{3.34}$$

where λ represents the energy of the part of PSWF that lies in $[-1, 1]$, χ denotes the eigenvalue of $\psi(t)$, Ω, and T are the bandwidth and pulse width of the PSWF, respectively. The constant $c = \Omega T/2$ represents the number of degrees of freedom. The functions produced as solutions to the above are almost time and band limited. They also have a double orthogonality property as shown below:

$$\begin{aligned} \int_{-\infty}^{\infty} \psi_m(t)\psi_n(t)dt &= \delta_{mn}, \\ \int_{-T/2}^{T/2} \psi_m(t)\psi_n(t)dt &= \lambda_m \delta_{mn}, \end{aligned} \tag{3.35}$$

where $\psi_n(t)$ represents a PSWF of order n. This is very useful since guarantees unique demodulation at the receiver and demonstrates one of the strengths of employing PSWF in impulse UWB impulse radio systems.

The computation of PSWF from the above results in a truncated infinite power series, which can be obtained as follows [12].

The expression below is the generalised PSWF equation:

$$\psi_n(t) = \psi_n(\Omega, T, t) = \frac{\left[2\lambda_n(c)/T\right]^{1/2} S_{0n}^1(c, 2t/T)}{\left\{\int_{-1}^{1} \left[S_{0n}^1(c,x)\right]^2 dx\right\}^{1/2}}, \tag{3.36}$$

where the denominator acts as a normalisation factor given by

$$\left\{\int_{-1}^{1} \left[S_{0n}^1(c,x)\right]^2 dx\right\}^{1/2} = \frac{2}{2n+1}. \tag{3.37}$$

For large c, almost all the energy of $\psi(t)$ lies in the interval $[-T/2, T/2]$. The prolate angular function of the first kind is given by

$$S_{0n}^1(c,t) = \begin{cases} \displaystyle\sum_{k=0,2,\ldots}^{\infty} d_k(c) P_k(c,t), & \text{for } n \text{ even}, \\ \displaystyle\sum_{k=1,3,\ldots}^{\infty} d_k(c) P_k(c,t), & \text{for } n \text{ odd}, \end{cases} \tag{3.38}$$

where $P_k(c,t)$ is a Legendre polynomial. The coefficients $d_k(c)$ satisfy the recurrence relation

$$\alpha_k d_{k+2}^n(c) + \left(\beta_k - \chi_n(c)\right) d_k^n(c) + \gamma_k d_{k-2}^n(c) = 0 \tag{3.39}$$

with

$$\begin{aligned} \alpha_k &= \frac{(k+1)(k+2)c^2}{(2k+3)(2k+5)}, \\ \beta_k &= \frac{\left(2k^2+2k-1\right)c^2}{(2k-1)(2k+3)} + k(k+1), \\ \gamma_k &= \frac{k(k-1)c^2}{(2k-3)(2k-1)}. \end{aligned} \tag{3.40}$$

In order to compute $d_k^n(c)$, the infinite series is truncated by setting $d_k^n(c) = 0$ for all $k > 2N + 1$, and the following equation is solved:

$$Od^n = \chi_n d^n. \tag{3.41}$$

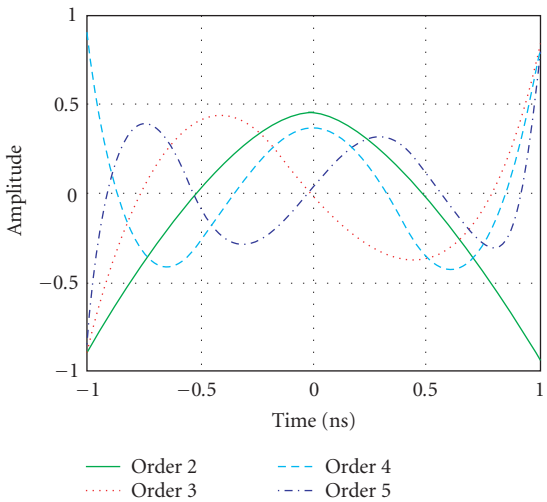

FIGURE 3.26. Prolate spherical wave functions [12] in time domain.

In (3.41), d_n are the eigenvectors and χ_n are the eigenvalues of O. Note that two operators need to be defined to handle the odd and even coefficients. The values of d^n defined by (3.41) should be suitably normalised which can be achieved by using (3.37).

Figures 3.26 and 3.27 show PSWF's for $n = 2, 3, 4, 5$ in both time and frequency domains. It can be seen that all pulses have a zero DC component and that the pulse duration and bandwidth do not change with the value of n. Thus PSWF's are both time and band limited. The centre frequency is also shown to be much less sensitive to pulse order therefore simplifying the control of these functions compared to MHPF and wavelets. Additionally, as the order of pulses is increased, the width of the main lobe of the autocorrelation function stays constant, thus, unlike MHPF, these functions will be less sensitive to jitter.

3.6. Spectrum randomisation and multiple access

Continuous pulse transmission will lead to strong lines in the spectrum of the transmitted signal. The regularity of these energy spikes may interfere with other communication systems over short distances [13]. In order to minimise potential interference from UWB transmissions, a randomising technique is applied to the transmitted signal. This makes the spectrum of the UWB transmission more noise-like. The two main approaches to randomise the pulse train in impulse radio systems are time-hopping (TH) and direct-sequence (DS) techniques. A TH technique randomises the position of the transmitted UWB pulses in time, while the DS approach uses the technique found in spread spectrum systems to produce a sequence of pulses with pseudorandom inversions. Neither the TH nor THE DS techniques leads to further spectrum spreading.

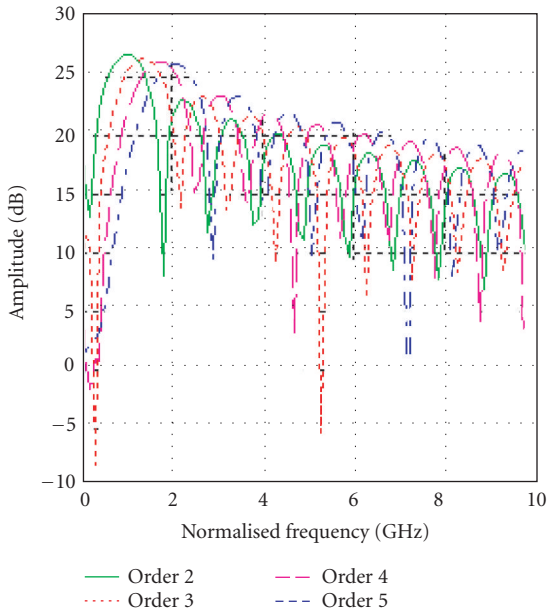

FIGURE 3.27. Prolate spherical wave functions [12] in frequency domain.

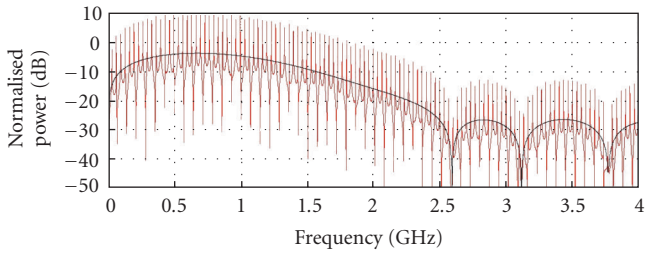

FIGURE 3.28. Spectrum of UWB transmission without randomising techniques.

The spectrum of a modelled UWB transmission with and without a randomising overlay sequence is depicted in Figures 3.28 and 3.29. Figure 3.28 shows the spectrum of a simple pulse train. The spectrum contains strong spectral lines at multiples of the pulse repetition frequency. The envelope of the spectrum is that of a single UWB pulse. Randomising the position in time of the generated pulses using data modulation and other randomising techniques will affect the spectrum in such a way that the energy spikes are spread leading to a smoother spectrum. Figure 3.29 shows the spectrum of a pulse train which includes time-hopping-based randomisation. A number of randomising techniques may be found in the literature [14].

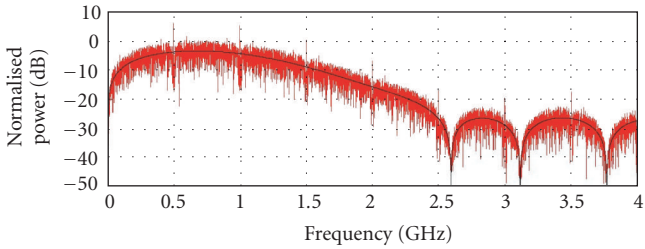

FIGURE 3.29. Spectrum of UWB transmission with randomising techniques.

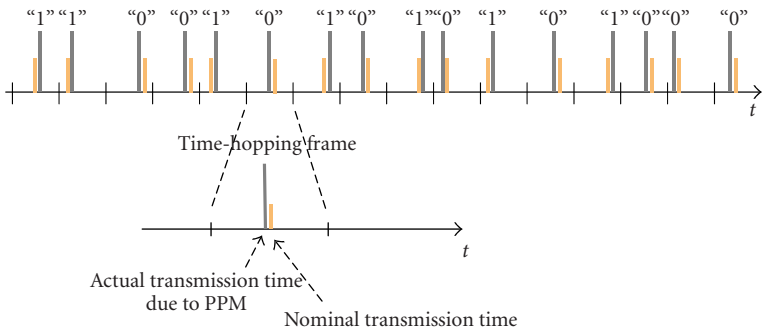

FIGURE 3.30. Time-hopping pulse position modulation technique.

3.6.1. TH-UWB

The data modulation is typically based on PPM using TH-UWB as the basis for a communication system. This approach allows matched filter techniques to be used in the receiver. The optimum time shift depends on the cross-correlation properties of the pulses used. The concept of TH-PPM is presented in Figure 3.30 where only one monocycle per data symbol is used (no processing gain is achieved). Figure 3.30 shows the construction of a single bit for TH-UWB systems.

When a PR code is used to determine the transmission time within a large time frame, the spectra of the transmitted pulses become much more noise-like. The time hopping randomises the signal in both time and frequency domains [14]. Pseudorandom time hopping also minimises collisions between users in multiple-access systems, where each user has a distinct pulse shift pattern [15].

However, a consequence of the PR time modulation is that the receiver needs accurate knowledge of the PR code phase for each user. One can imagine impulse radio systems as time-hopping spread spectrum systems. UWB waveforms are generated without any additional spreading. This simplifies the transceivers relative to conventional SS transceivers [16]. The data rate of the transmission can be selected by modifying the number of pulses used to carry a single data bit. This in turn has an effect on the process gain.

The pulse repetition time (or frame time) typically ranges from a hundred to a thousand times the pulse (monocycle) width. The symbol rate can be defined in terms of the number of monocycles used to modulate one data symbol in fixed frame time as [15]

$$R_s = \frac{1}{T_s} = \frac{1}{N_s T_f}[\text{Hz}], \tag{3.42}$$

where R_s = symbol rate, T_s = symbol time, T_f = time-hopping frame, and N_s = number of monocycles/data bit.

If the data rate in (3.42) is reduced whilst the time-hopping frame remains constant, the number of monocycles per data bit is increased. This leads to an increased processing gain.

3.6.1.1. Data modulation with time hopping

In TH mode, the pulse transmission instant is defined by the pseudorandom code. One data bit is spread over the multiple pulses to achieve a processing gain due to the pulse repetition. The processing gain is also increased by the low-transmission duty cycle.

The TH spreading approach has been studied for PAM, PPM, and PSM. However, OOK cannot take the advantage of TH spreading because of the blank transmission in case of bit "0," and because it would create further problems for synchronisation. The information signal $s(t)$ for the mth user can be analytically described for PAM modulation as

$$s^{(m)}(t) = \sum_{k=-\infty}^{\infty} \sum_{j=1}^{N} w\left(t - kT_d - jT_f - (c_w)_j^{(m)} T_c\right) d_k^{(m)}, \tag{3.43}$$

for PPM modulation as follows:

$$s^{(m)}(t) = \sum_{k=-\infty}^{\infty} \sum_{j=1}^{N} w\left(t - kT_d - jT_f - (c_w)_j^{(m)} T_c - \delta d_k^{(m)}\right), \tag{3.44}$$

and for PSM modulation as follows:

$$s^{(m)}(t) = \sum_{k=-\infty}^{\infty} \sum_{j=1}^{N} w_{d_k^{(m)}}\left(t - kT_d - jT_f - (c_w)_j^{(m)} T_c\right). \tag{3.45}$$

Figures 3.31, 3.32, and 3.33 show a single data bit for PAM, PPM, and PSM,

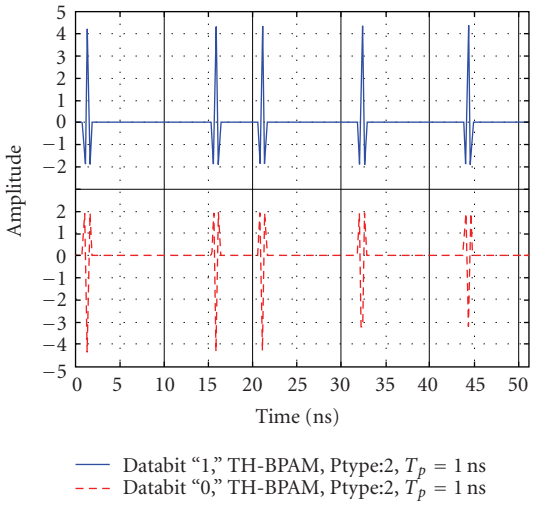

Figure 3.31. Transmitted data bit for BPAM modulation with TH spreading.

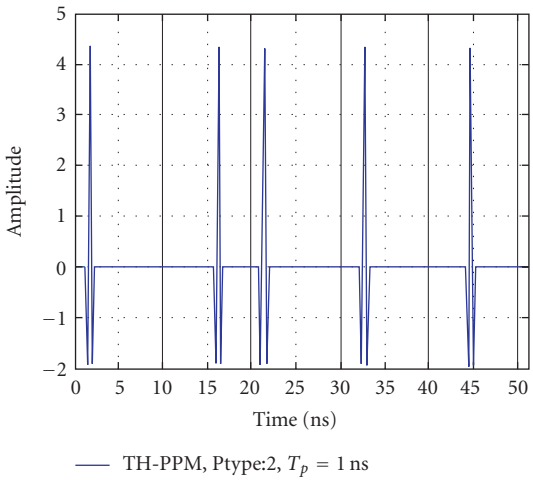

Figure 3.32. Transmitted data bit for PPM modulation with TH spreading.

respectively. Note that in the case of PAM and PPM (Figures 3.31 and 3.32) the same pulse shape has been used to represent either data bit "0" or "1," while in the PSM case (Figure 3.33), two different pulse shapes have been considered. The TH time shift and the PPM time shift combine to determine the transmission instant of the pulse in the case of PPM. The pulse repetition frame is assumed to be 10 ns long in all of these figures.

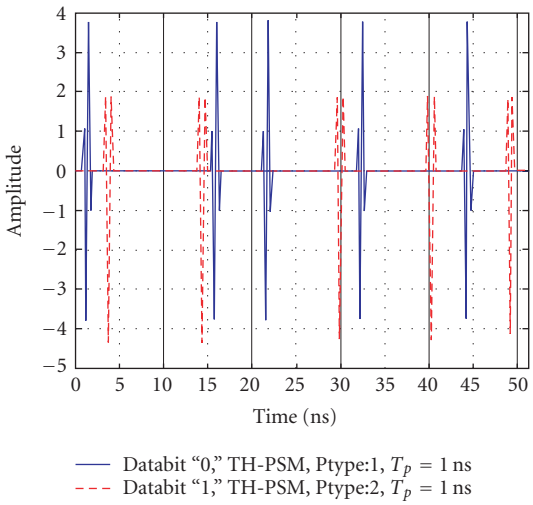

FIGURE 3.33. Transmitted data bit for PSM modulation with TH spreading.

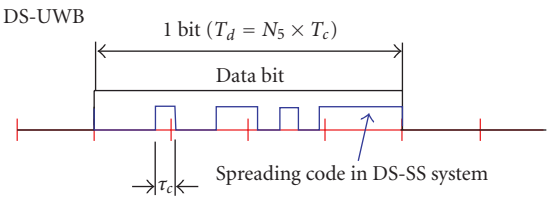

FIGURE 3.34. Direct-sequence signal transmission.

3.6.2. Direct-sequence UWB

Much like the approach taken with spread spectrum techniques [13], DS-UWB employs sequences of UWB pulses (analogous to "chips"). A user in the system is assigned a pseudorandom sequence which controls pseudorandom inversions of the UWB pulse train. A data bit is then used to modulate this sequence of UWB pulses.

In the case of UWB systems, the pulse waveform takes the role of the chip in a spread spectrum system. The DS spreading approach is suitable for PAM, OOK, and PSM modulation schemes. PPM modulation is intrinsically a time-hopping technique since the bit value is given by the position of the pulse in a transmission slot. Figure 3.34 shows the bit structure for a DS-UWB signal. The rectangular waveform is used to indicate the individual sequence elements.

The PAM and OOK data signal $s(t)$ for user m is given by

$$s^{(m)}(t) = \sum_{k=-\infty}^{\infty} \sum_{j=1}^{N} w(t - kT_d - jT_c)\,(c_p)_j^{(m)}\, d_k^{(m)}, \tag{3.46}$$

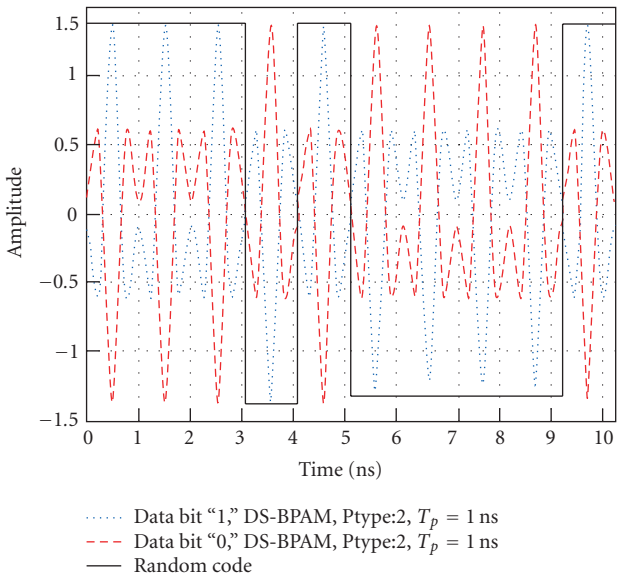

FIGURE 3.35. Time window of a transmitted data bit for BPAM modulation with DS spreading.

where d_k is the kth data bit, $(c_p)_j$ is the jth chip of the PR code, $(c_w)_j$ is the jth code phase defined by the PR code, $w(t)$ is the pulse waveform, T_f is the pulse repetition interval, T_c is the "chip" length, and N is the number of pulses per data bit.

The pseudorandom sequence has values $\{-1, +1\}$ and the bit length is $T_d = NT_c$.

3.6.2.1. Data modulation with DS-UWB

Figure 3.35 shows a single data bit with binary PAM when a data bit "1" or "0" is transmitted. The square wave represents the pseudorandom sequence, which affects the polarity of individual pulses which make up the DS waveform. For clarity, only a small part of the data bit waveform is shown. Pulse type (Ptype in the legend) describes the pulse waveform used. Ptype2 is the second derivative of the Gaussian pulse.

Figure 3.36 shows a single data bit for OOK modulation when data bit "1" or "0" is transmitted. As mentioned above, in the case of data bit "0," the OOK spreading signal is characterised by no transmission.

For PSM modulation, the information signal $s(t)$ for the mth user can be presented as

$$s^{(m)}(t) = \sum_{k=-\infty}^{\infty} \sum_{j=1}^{N} w_{d_k{}^{(m)}}\left(t - kT_d - jT_c(c_p)_j^{(m)}\right), \tag{3.47}$$

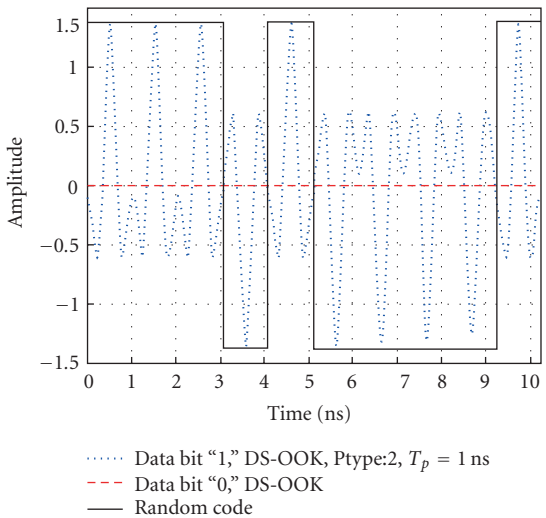

FIGURE 3.36. Time window of a transmitted data bit for OOK modulation with DS spreading.

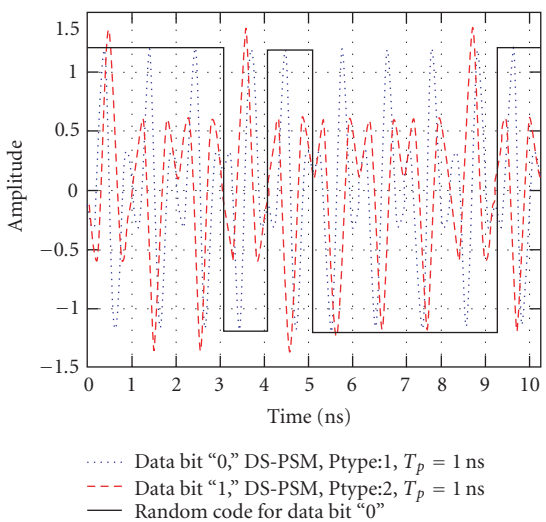

FIGURE 3.37. Time window of a transmitted data bit for PSM modulation with DS spreading.

where the chosen bit d_k for the mth user, defined according to (3.18), determines the choice of the UWB pulse waveform to be transmitted.

Figure 3.37 shows a single data bit using PSM modulation when data bit "1" or "0" is transmitted. Ptype1 and Ptype2 in the legend represent the first and the second derivatives of the Gaussian pulse.

3.6.3. Coexistence and pulse shaping

The problem of choosing a pulse type that will not cause undue interference to other spectrum users is important. The impact that a particular pulse has on other spectrum users will primarily be determined by the amount of energy the pulse has in the pass-band of the victim receiver. Thus by considering the frequency domain characteristics of the candidate pulse, a suitable choice can be made. However, this approach may not be appropriate when the UWB transmitter is operating in close proximity of the victim receiver since energy may be coupled into the receiver by means other than through the receiver front end. Thus, the full spectral characteristics of the pulse should be compared to that of the frequency plan of the victim receiver. Some overlapping narrow bands causing serious interferences may be deliberately avoided, such as 5 GHz in IEEE 802.11a.

In [17], the coexistence of two candidate UWB systems, that is, time-hopped spread spectrum with pulse amplitude modulation (TH-SS PAM) and direct-sequence spread spectrum with pulse amplitude modulation (DS-SS PAM) with GSM900, UMTS/WCDMA, and GPS, was investigated through simulation. The study shows that the proper selection of a UWB pulse type and related pulse width significantly impacts the degree of interference caused to the other spectrum users. It was shown that for short pulses (which is the case for high data rate transmissions), higher-order Gaussian waveforms cause the least interference, whilst for longer pulses (lower data rates), the basic Gaussian monocycle causes the least interference.

The interference environment is dynamic due to user mobility and usage. Thus, it would be advantageous for a UWB system to dynamically adjust its pulse shape according to the prevailing interference environment. Such flexibility would also enable the system to adjust to regional variations in regulation that may be demanded. In order to operate successfully, such a system would be required to sense the interference environment and adjust the pulse shape accordingly, and be programmable with regional regulatory variations as required. An example of such an approach is outlined in [18].

3.7. Synchronisation

3.7.1. Basics

A survey of publications relating to acquisition in direct-sequence spread spectrum systems is given in [19]. Assuming an AWGN channel, the input signal for the receiver in one user case is given by

$$r(t) = \sum_{l=1}^{L} A_l s^{(1)}(t - \tau_l) + n(t), \tag{3.48}$$

where A_l is the amplitude of radio channel path l, τ_l is the delay of radio channel path l, L is the number of resolvable multipath components, and $n(t)$ is the additive white Gaussian noise component.

The path delay term τ_l can be represented as a portion of the chip period, T_c, given as $\tau_l = \xi T_c$. The signal waveform $s(t)$ is dependent on the system concept, that is, TH or DS. In both cases, the signal waveform includes the effect of the spreading code.

The synchronisation stage must provide an estimate ξ_e for the timing offset ξ, that is, τ_e. The maximum likelihood (ML) algorithm generates several values ξ_e to evaluate when the conditional probability density function of the received signal $p(r \mid \tau)$ achieves the maximum value [20]. So,

$$\tau_e = \arg\max_{\tau_e} p(r \mid \tau_e). \tag{3.49}$$

As we assume white Gaussian noise channel, the conditional probability density function is readily evaluated. For the optimal estimation τ_e, we have to maximise

$$\begin{aligned}\lambda(\tau_e) &= \int_0^{T_0} r(t)s(t,\tau_e)dt \\ &= \int_0^{T_0} A_l \sum_{k=0}^{\infty}\sum_{j=1}^{N} w(t-kT_b-jT_f-\tau) \sum_{k=0}^{\infty}\sum_{j=1}^{N} w(t-kT_b-jT_f-\tau_e)dt + n_c(t),\end{aligned} \tag{3.50}$$

where $n_c(t)$ is the additive noise component, and the information signal is in the form of TH-UWB described earlier. In practice, the algorithm is too complex to implement, and some approximations must be used. In the so-called serial search strategy, the phase of the local code τ_e is changed step by step in equal increments. In this way, the correct position within the uncertainty region can be found [20]. Serial search acquisition can be implemented using active correlation measurement technique or passive correlation measurement based on matched filtering (MF).

3.7.1.1. Synchronisation schemes

UWB systems use very large bandwidths, and therefore a dense channel multipath profile with many components can be distinguished from the received signal. The multipath channel then introduces more than one correct synchronisation cell. From the perspective of code synchronisation, this phenomenon causes problems: the energy of the signal is spread over many multipath components, and the energy of each path is very low. Therefore, the paths are difficult to acquire. Depending on the receiver structure (type and length of rake), a number of paths should be acquired.

In DS systems, the uncertainty region corresponds to a multiple of the code length. In TH systems, the uncertainty region is divided into a number of cells (C). The number of cells depends on the number of possible pulse positions combinations in a bit interval. Recently, an algorithm called chip level post detection

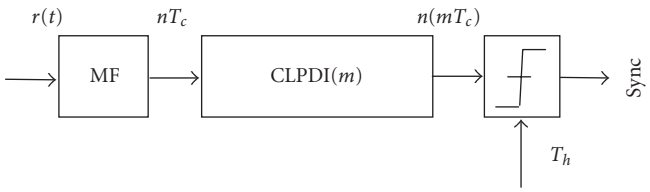

Figure 3.38. MF with CLPDI.

integration (CLPDI) was proposed for code acquisition in direct-sequence CDMA systems [21]. This algorithm is suitable for synchronisation in multipath environments and will be used as a general technique for synchronisation. Other simplified schemes may be adopted from CLPDI.

Once the CLPDI algorithm finds one of the possible synchronisation cells, an additional sweep has to be performed to acquire the necessary number of paths. The aim of this initial code acquisition in multipath channel is to find a starting point to reduce the multipath search time. In this chapter, the method is applied for time-hopping UWB system due to nature of UWB signals.

Figure 3.38 presents the synchronisation algorithm for a multipath environment proposed for DS-CDMA [21]. In DS systems, the impulse response of the matched filter is the time-reversed replica of the spreading code. This means that the impulse response has coefficients given by the spreading code, and the delays between the consecutive coefficients are T_c. The MF output signal is proportional to the autocorrelation function (ACF) of the spreading code. The sampling at the output of the MF is made at least at the chip rate. The MF is followed by a threshold comparison, and if the threshold T_h is crossed, the acquisition process ends. There is detection if the threshold is crossed by the ACF at the zero delay. This occurs with probability of detection, P_d. If the threshold is crossed with some other delay, a false alarm occurs. This happens with the probability of false alarm, P_{fa}. False alarms may be catastrophic, and cause total miss of the correct code phase. Because the MF gives its peak when the code is inside the filter, a multipath channel leads to several peaks.

Chip level post detection integration performs post detection integration at the chip level, that is, a number of consecutive samples at the output of the MF are combined. CLPDI is performed over m samples and CLPDI output is sampled at multiples of $m_T c$ as is presented in Figure 3.38. Because the sampling is done as multiples of $m_T c$, consecutive samples at the output of CLPDI are uncorrelated. In addition, the uncertainty region, that is, the number of cells to be tested in the acquisition, is decreased relative to the pure MF acquisition. The number of cells in the uncertainty region is now reduced to $C_m = C/m$. In addition, the number of potentially correct cells to be tested is reduced, as can be seen comparing Figures 3.39 and 3.40.

In time-hopping systems, the MF collects the samples together according to delays between consecutive chips (pulses as presented in this chapter), that is, the spreading code sets the delays between consecutive "1"s in the impulse response.

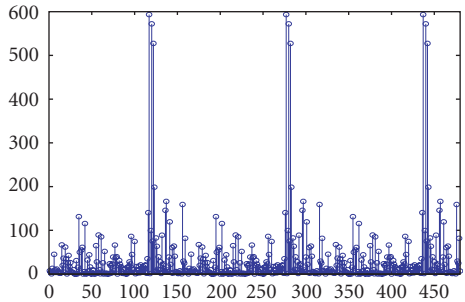

FIGURE 3.39. MF output without noise as function of time in channel model 1, the number of pulses in bit is $N = 10$ and the number of pulse position in frame is $M = 16$.

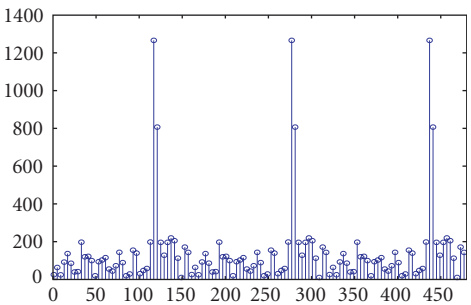

FIGURE 3.40. CLPDI output without noise as function of time in channel model 1, $N = 10$, $M = 16$, and $m = 4$.

Therefore, the MF waits until the chips (pulses) arrive in predetermined timeslots inside frames.

3.7.2. Performance measures

The specifications of satisfactory performance measures for synchronisation will depend on the particular application. The main issue is the time that elapses between the time the synchronisation starts and the time of acquisition. There are two basic scenarios—when there is an absolute time limit and when there is no absolute time limit. If there is no time limit, the most interesting parameter is the mean acquisition time, $T_{\mathrm{MA}} = E\{T_{\mathrm{acq}}\}$ and possibly the variance of the acquisition time $\delta^2_{T_{\mathrm{acq}}}$. This is the case when a data or pilot signal is always present, that is, when the link operates continuously. The mean acquisition time is defined as the expected value of the time which elapses between the initiation of acquisition and the completion of acquisition. If there is a time limit, the parameters are the acquisition time T_{acq} and the time limit T_s. If there is a time limit, a better performance measure is the probability of prompt acquisition $\Pr\{T_{\mathrm{acq}} \leq \mathrm{Ts}\}$, which is

called overall probability of detection P_d^{ov}. The complement of the probability of prompt acquisition is the overall probability of missing the code $P_m^{\text{ov}} = 1 - P_d^{\text{ov}}$. Missing the code occurs in systems where data transmission starts after a certain time interval Ts from the initial system startup, that is, burst communication.

The acquisition time and, therefore, also T_{MA} and P_d^{ov} are functions of several parameters. The most important of these are the probability of detection P_d and the probability of false alarm P_{fa}. The probability of detection is the probability that the decision is the "correct cell" when the correct cell of the uncertainty region is being tested. The probability of false alarm is the probability that the decision is the "correct cell" when a false cell is being tested. If the decision is based on threshold comparison, threshold T_h plays an important role concerning T_{acq} because both P_d and P_{fa} are functions of this threshold. The other parameters are the time spent evaluating one decision variable T_i, the penalty time T_{fa}, and the number of cells in the uncertainty region C.

In this context, mean acquisition time is used as a performance measure. It can be calculated for the DS CLPDI case as [21]

$$\begin{aligned} T_{\text{MA}} = {} & \frac{P_M^{L/m}\left[LT_c + (N-L)\left(T_c + T_{f_a}P_{f_a}\right)\right]}{1 - P_M^{L/m}} \\ & + \frac{\left[NT_c + (N-L)\left(T_c + T_{\text{fa}}P_{\text{fa}}\right)\right]\sum_{i=0}^{L/m-1} iP_M^i}{N\sum_{i=0}^{L/m-1} P_M^i/m} + mT_c \\ & + \frac{(N-L)(N-L+m)\left(T_c + T_{\text{fa}}P_{\text{fa}}\right)}{2N} + NT_c, \end{aligned} \tag{3.51}$$

where the uncertainty region N is the length of the code, no a priori information of the correct code phase exists at the beginning of acquisition, P_{fa} is the probability of false alarm at the output of the CLPDI, $P_M = 1 - P_d$ where P_d is the probability of detection in the correct code phase, $T_{\text{fa}} = K_p T_c$ is the penalty time caused by a false alarm, and T_c is chip interval.

In a multipath propagation environment without the CLPDI block, the T_{MA} is evaluated with a similar equation [22].

3.7.2.1. Performance of CLPDI

Figure 3.41 presents the TH UWB simulation model with matched filter synchronisation. The figure also describes the outputs from different parts of the system.

Chip correlation (point A in Figure 3.41) is performed by correlating the received signal with the template waveform which has the same shape as the received signal (after the antenna).

The pulse waveform in the transmitter in the simulations is an ideal Gaussian pulse. The reference pulse in the receiver is therefore the second derivative of the

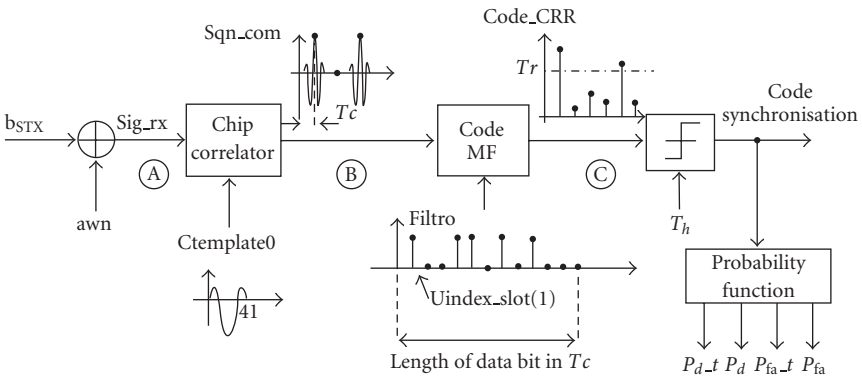

FIGURE 3.41. Simulation model for TH-UWB synchroniser in an AWGN channel.

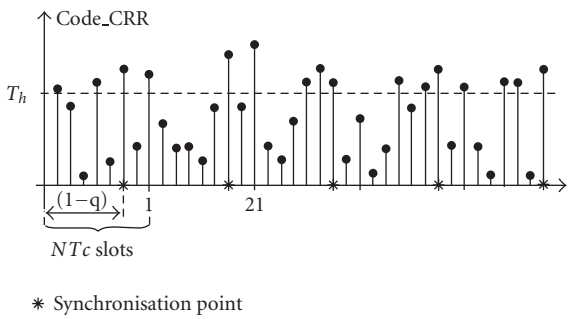

FIGURE 3.42. Output of the code matched filter when six bits are transmitted.

Gaussian pulse because of the effect of the transmitting and receiving antenna [22]. Only one sample per T_c is used to reduce the complexity in the simulations. This is appropriate when the pulse width (T_p) is smaller than the chip length (T_c), and when chip synchronism is assumed. The output of the chip correlator is a sequence that contains the information of the pulse locations within the received sequence in every frame. The chip correlator output is fed into a code-matched filter (CMF). The filter is matched to the whole spreading code (point B in Figure 3.41). In the TH system this means that the delay between consecutive "1"s in the impulse response is not fixed, but depends on the code phase as seen in Figure 3.42. After the filter, a threshold comparison is used (point C in Figure 3.41). The threshold setting is dependent on the desired false alarm rate. Figure 3.42 presents an example of the output of code-matched filter, as well as describing the correct synchronisation points.

In the CLPDI simulations, the CLPDI block is inserted after the code matched filter in the block diagram of the TH-UWB synchroniser (see Figure 3.41).

3.7.2.2. Performance in Saleh-Valenzuela channels

There are a large number of resolvable paths in UWB systems, for example, more than 100, because of the fine path resolution of the UWB channel. The following simulation results only consider the most powerful paths for the code acquisition. The number of cells or chip positions on which the receiver can be considered synchronised is defined by the 20 strongest paths in the MF case. When m-CLPDI is used, we need to make sure that the 20 synchronisation positions defined in the MF case are included in the synchronisation cells for the m-CLPDI algorithm. Since it is possible that the 20 synchronisation cells are nonconsecutive, the number of synchronisation cells in the m-CLPDI case can be bigger than $20/m$. Once one of the synchronisation cells is found, a new acquisition process starts. Verification extra time is added for each false alarm event occurred during the acquisition process.

The simulations consider four modified Saleh-Valenzuela channel models used by the IEEE 802.15.3 working group to measure performance. The pulse width T_p is fixed to 1 ns. The code length is 160, the number of frames per bit is $N = 10$, the number of possible pulse positions in each frame is $M = 16$, the penalty time in the case of false alarm is $T_{\text{fa}} = 100T_b$, and the required $P_{\text{fa}} = 0.01$. The synchronisation process is performed over a data packet of 30 bits and the channel is static over each packet. A new data block is transmitted every time the synchronisation is reached or the data packet has been explored without synchronisation.

Figures 3.43, 3.44, 3.45, and 3.46 present the mean acquisition time of the code MF for $m = 4$, 10, and 20 and the CLPDI block versus SNR for each of the Saleh-Valenzuela channel models. SNR is defined as the E_b/N_0 at the receiver. E_b is the collective bit energy spread over all the paths in the channel. Using CLPDI, the reduced code acquisition time is evident for all the channel models. The mean acquisition time increases in absolute time from both MF and CLPDI passing from the IEEE 802.15.3a channel model 1 (CM1) to the CM4. The reason is the reduced energy borne by the 20 strongest paths whilst moving from CM1 towards CM4. Otherwise, passing from the CM1 to the CM4 relatively increases CLPDI's performance improvement relative to the MF case. As the channel moves from the CM1 to the CM4, the channel gets closer to the situation of having paths with equal average power that gives the best result, as has been shown for data detection using diversity techniques [13]. In CM1, the extra gain achieved using $m = 20$ is not remarkable. This is because of the reduced CM1 delay spread relative to the other channel models.

3.8. Impulse radio demonstrator for 4-PPM

This section discusses an ultra-wideband radio testbed based on pulse position modulation (PPM) for investigating the properties of short-range data communication. PPM was selected because of its low duty cycle which translates to high power efficiency [23]. The testbed is designed to realise data transmission at 6 Msymb/s over a distance of a few meters in indoor office environments. The

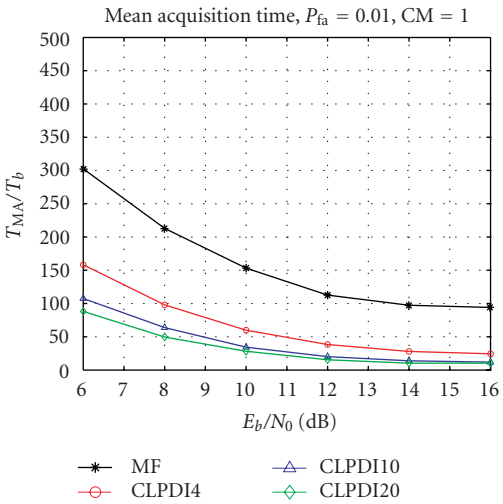

FIGURE 3.43. T_{MA}/T_b as a function of E_b/N_0 in channel model 1.

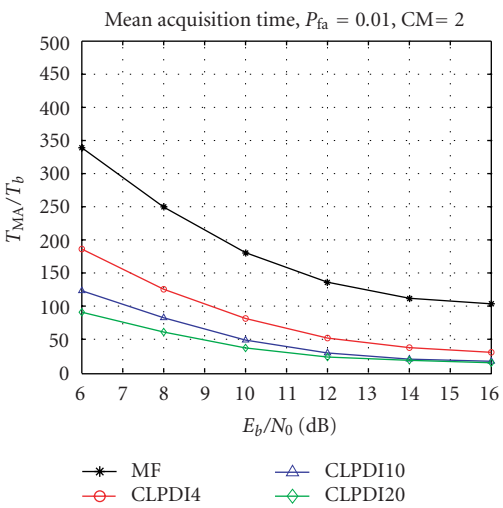

FIGURE 3.44. T_{MA}/T_b as a function of E_b/N_0 in channel model 2.

focus of this effort is on the implementation of commercial-grade microwave circuitry and algorithms for ultra-wideband data transmission, especially concerning mobile battery-driven devices. The testbed hardware is described in detail as well as the two-stage approach used for receiver synchronisation.

The pulse repetition frequency is set to 60 MHz and each PPM symbol is repeated ten times. This gives a symbol rate of 6 Msymb/s. Each PPM symbol carries two bits by means of four possible delays at $\{0, 2\text{ ns}, 4\text{ ns}, 6\text{ ns}\}$. This design results in an uncoded bit rate of 12 Mb/s.

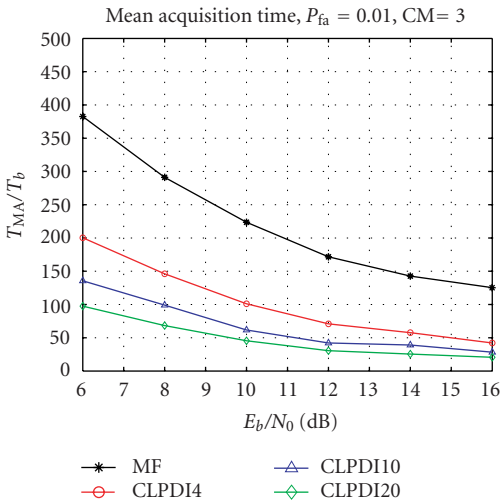

FIGURE 3.45. T_{MA}/T_b as a function of E_b/N_0 in channel model 3.

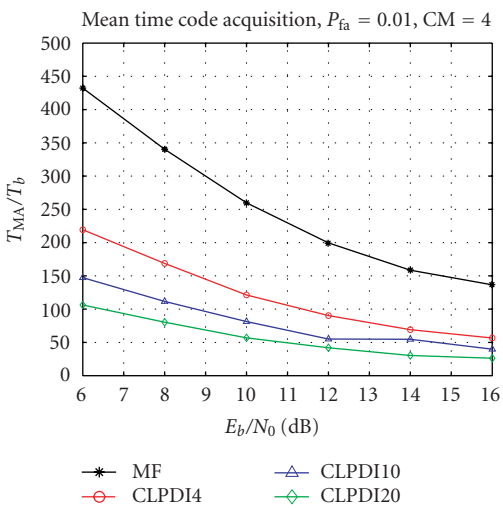

FIGURE 3.46. T_{MA}/T_b as a function of E_b/N_0 in channel model 4.

In an initialisation step, the receiver estimates the pulse repetition frequency of the transmitter and sets the local voltage-controlled crystal oscillator (VCXO) to this estimate. Subsequently, an early-late tracker controls an eight-bit programmable delay shifter with a granularity of 65.1 ps and the local VCXO. The whole synchronisation algorithm is implemented on a low-cost microcontroller (μC) running at a clock of 15 MHz.

Various measurement results obtained from the testbed are discussed and compared to simulations in Matlab. We draw some early conclusions from this work and give some recommendations for future investigations.

3.8.1. Motivation

The pioneering UWB industry has demonstrated that the basic physical layer technology works, but many system-level and operational issues remain that need to be investigated before UWB technology can be integrated into commercial devices [24].

A trial system was designed in hardware which employs a variant of pulse position modulation (PPM) for data transmission. The main purpose of the testbed is a feasibility test for short-range data transmission using commercial *low-power* components, to investigate the behaviour of the microwave circuitry, and to develop new algorithms for the ultra-wideband approach to data transmission.

Currently, there exists just a very small number of methods for generating signals having ultra-wide bandwidth: for example, chirp modulation, direct spreading by high-rate pseudorandom noise sequences [12, 25], fast frequency hopping [26, 27], and transmission via short pulses [28–31]. The latter option was chosen because of its simplicity in circuitry and its inherently low power consumption. It was recently found that such an orthogonal 4-ary PPM outperforms binary offset PPM at all jitter levels in thermal and impulsive noise [32]. For the testbed, a transmission format was chosen which includes a 5th timeslot [31]. The extra timeslot is inserted for aiding in synchronisation and tracking, compare Section 3.8.5.

The testbed is implemented using off-the-shelf electronic components only. The testbed consists of a transmitter part and a receiver part. The data transmission is unidirectional. The testbed can be upgraded for duplex transmission and extended to multiple access in a small network in the future, compare [29].

3.8.2. Transmitter

The testbed uses a PPM format with 4 timeslots of equal duration (2 ns each) and an additional guard interval of longer duration (approx. 8.67 ns) resulting in a pulse repetition frequency (PRF) of $(4 \cdot 2\,\text{ns} + 8.67\,\text{ns})^{-1} = 60\,\text{MHz}$, cf. Figure 3.48. Adopting the naming convention of [23], this modulation format can be called a combination of "x-frame PPM" and "x-pulse PPM." The transmitted PPM signal $s(t)$ can be modelled as

$$s(t) = \sum_{k=-\infty}^{\infty} p\left(t - A_{\lfloor k/10 \rfloor} T - kT_{\text{PRF}} - \tau(t)\right), \tag{3.52}$$

where $p(t)$ denotes the designed pulse shape, $T = 2\,\text{ns}$ is the timeslot duration, and $f_{\text{PRF}} = 1/T_{\text{PRF}} = 60\,\text{MHz}$ is the PRF. The PPM symbols are denoted as $A_k \in \{0, 1, 2, 3\}$ and each symbol is repeated ten times, see (3.52). The slowly varying delay $\tau(t)$ describes fluctuations in the PRF and clock jitter.

The transmitter design is shown in Figure 3.47a. It consists of a clock oscillator which defines the PRF of 60 MHz and generates a stable timebase for the pulse positions within each symbol frame. A divider (denoted by "(: 10)" in Figure 3.47) defines the number of repeated pulses sent per PPM symbol. A data generator produces a pseudorandom noise (PRN) bit stream (binary symmetric source) for measurement purposes. The data bits are mutually uncorrelated and equi-probable which ensures that the pulse positions are uniformly distributed within the 4 timeslots used for data transmission. The delay lines define the pulse positions within a symbol. A symbol switch selects the pulse position to be transmitted during each frame. Finally, a pulse shaping device creates the waveform. The pulse shaping is implemented by two high-frequency transistors (BFP 540F) which shape the rising edge of the delayed 60 MHz signal to the required narrow UWB pulse shape. A discone antenna designed for a center frequency of 5.8 GHz emits the pulses.

In the following, we discuss the transmitter components and measurements in detail.

Clock generator. The clock generator is a crystal oscillator that needs to be well decoupled from the noise emitted by other parts of the transmitter. The overall performance (bit error rate) of PPM is sensitive to the clock jitter variance. To illustrate this, we show the effect of a small ripple (in the range of millivolts) in the power supply of the crystal oscillator which can cause significant clock jitter. Figure 3.49 shows oscillograms of the observed signal at the receiver side with and without the supply voltage ripple.

Frequency divider. The divider is set to 10 and every PPM symbol is repeated ten times. This enables the receiver to average received symbols over ten realisations. This can be interpreted as a spreading gain of 10. In a future testbed enhancement, this simple repetition code can be replaced by a time-hopping spreading sequence to identify the user of interest in multiple-access scenarios.

Pseudorandom noise data generator. For the experiments, a two-bit wide pseudorandom noise (PRN) data generator is implemented. The data are generated for measuring the link performance by counting bit errors for bit error rate (BER) measurements. In a future implementation step, this data generator will be replaced by an external source providing, for example, encoded multimedia data streams.

Delay lines. The demonstrator uses an integrated circuit 3D3215 (Data Delay Devices Inc.). This component implements five equally spaced taps of $T = 2$ ns delay each. In the testbed, it is driven at almost its maximum usable frequency and some delay tolerances have been observed. Delay variations are also due to differences in the capacitive loads due to the circuit layout. These load differences have been eliminated by introducing small parallel capacitors.

Symbol switch. The symbol switch consists of a symbol latch and a 4 to 1 multiplexer. The two data bits are latched first and then control the address of the

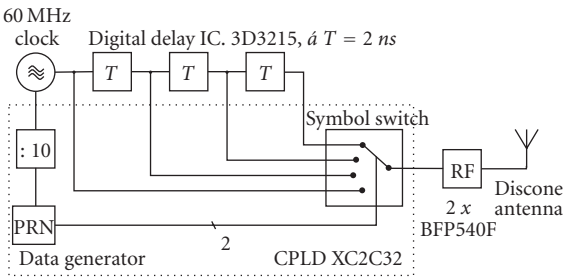

(a)

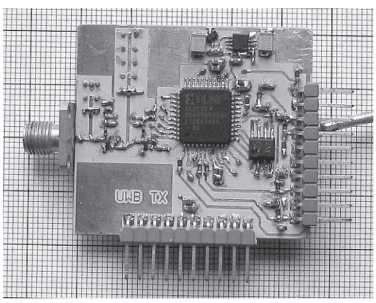

(b)

FIGURE 3.47. (a) Block diagram of the transmitter; (b) Realisation.

multiplexer. The outputs of the 3D3215 delay taps are connected to the data inputs of the multiplexer. It proves to be important to switch among the inputs when *all* input signals have high state. If this condition is violated, an additional rising edge is generated resulting in spurious pulses.

Figure 3.48 shows the measured 4-ary symbol pulses after the first pulse shaper transistor stage. In this figure, we also observe a small spurious pulse. This is caused by switching the multiplexer from an input with a low signal to one with a high signal. In the testbed, these spurious pulses occur only once every $10T_{\text{PRF}} \approx 166.7$ ns when the transmitter modulates a new pair of data bits which is distinct from the previous bits.

The digital part of the PPM transmitter is integrated into a complex programmable logic device (CPLD, CoolRunner II, XILINX Inc.) which generates very fast rising edges. The subsequent pulse shaper steepens the rising edges using a high-pass filter.

Pulse shaper. For the pulse shaper, two stages of high-frequency transistors (BFP 540F) with grounded emitters are used. Every stage has a highpass RC filter at its input and a shorted microstrip line at the output for shortening the amplified pulse. The shorted microstrip line in the first stage is much longer than in the

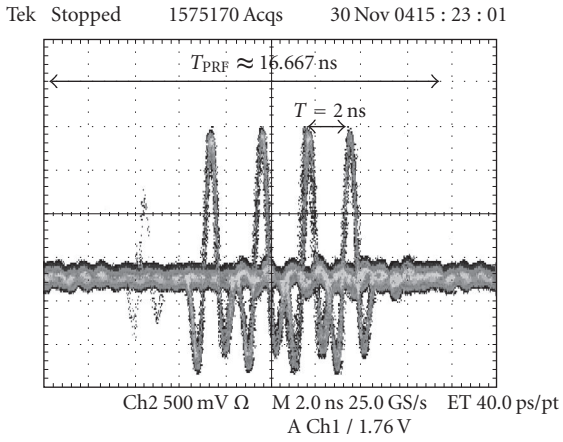

(a)

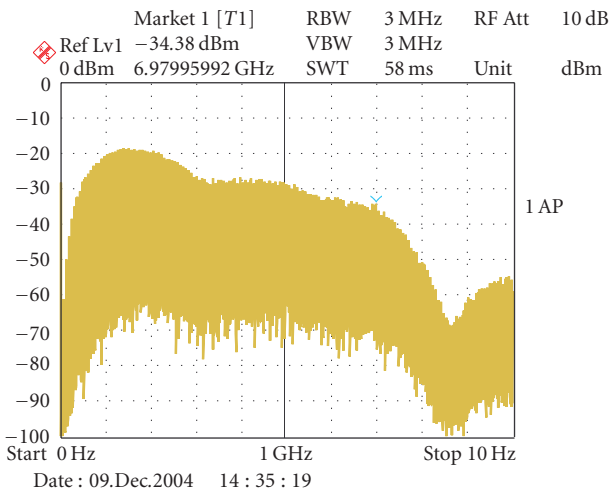

(b)

FIGURE 3.48. (a) Modulated symbol pulses after the first pulse shaper stage. (b) Spectral power density of the PPM signal.

second otherwise the amplitude of the pulse would decrease significantly. The collector resistance is chosen to produce a low output resistance and to allow a high PRF. The UWB transmitter generates pulse peak voltages of nearly 3 V at 50 Ω with a pulse width well below 100 ps (measured at half amplitude).

Antenna. Traditional broadband antennas are designed with multiple resonant structures which cause excessive ringing and group delay distortion (e.g., log-periodic Yagi-Uda antenna). Several antenna types were designed and evaluated

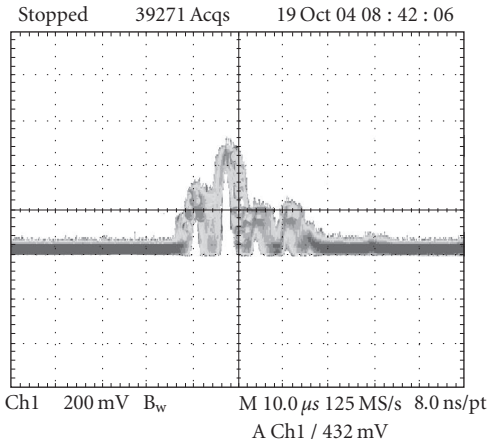

FIGURE 3.49. Influence of transmitter clock jitter on the received signal: (a) with; (b) without jitter. This is an oscillogram with vertical histogram function.

by measurements to find a practical UWB antenna solution. Such an antenna solution should result in a narrow pulse response without ringing or introducing additional echoes. Such echoes occur due to imperfect matching between the transmitter output and the antenna input. Antenna mismatch causes part of the pulse power to be reflected repeatedly between antenna connector and the second transmitter's collector. A 6 dB attenuator is included between the second transistor and the antenna connector for reducing such echoes.

UWB impulse radio transmitters need to be placed near (or even inside) the antenna to cope with mismatch problems and the resulting echoes.

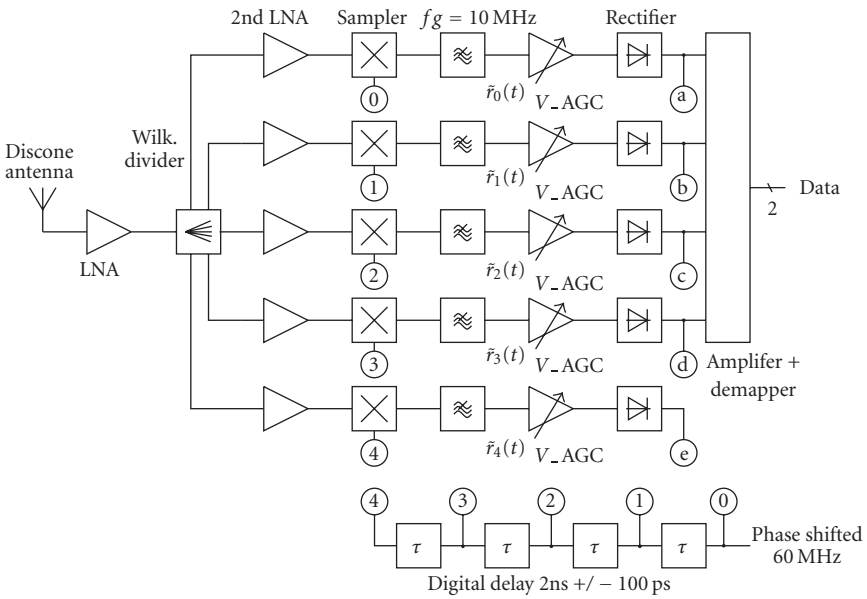

FIGURE 3.50. Block diagram of the data path of the receiver.

Power supply. Not shown in the block diagram is the power supply. Its quality defines the clock precision and the accuracy of the pulse position amplitude. Noise (Ripple) on the power supply causes clock jitter. Only a low impedance of the power supply guarantees a constant supply voltage for the pulse shaper. This is a stringent requirement for generating equally shaped narrow pulses with low jitter.

If switched power supply units are used, it is best to synchronise them. Otherwise mixing resulting from non-linearities causes low frequency noise on the power supply lines which are hard to filter out.

3.8.3. Receiver

The receiver architecture is shown in Figures 3.50 and 3.51. The antenna is the same type of discone antenna as that used by the transmitter. The average received power level is expected to be the transmitted power decreased by approximately 60 dB [33]. Low-noise amplifiers (LNA) are used in the front end for increasing the signal amplitude and to ensure sufficient signal-to-noise ratio for the down conversion. The LNAs consist of InGaP/GaAs MMIC (NBB-300, RF Micro Devices Inc.). A Wilkinson power divider splits the received signal into five branches of equal strength. Five sampling mixers sample the input signal at different delays. Each of the five branches has one sampling mixer. The fifth branch of the receiver aids the synchronisation, see Section 3.8.5. The sampling mixers contain dual Schottky diodes and pulse shapers for generating the narrow LO (local oscillator) pulses. Low-pass filters are used for averaging the pulse energy coherently and

filtering out additive interference. Five equal voltage-controlled amplifiers amplify the signal after down conversion. Five full-wave rectifiers are used for noncoherent symbol reception. Included in the amplifier and decoder block is a circuit made of several operational amplifiers realising the mapping of PPM symbols to bit pairs.

Another set of five low-pass filters is used for the synchronisation part of the receiver (see Figure 3.51). It averages the energy of a high number of symbols and suppresses interference. A five-channel analogue-to-digital converter (ADC) samples all inputs simultaneously. A μC is used for executing the synchronisation algorithm and fulfills several other tasks in the testbed. A clock generator delivers the timebase of the receiver: it is frequency controlled by the μC.

Antenna and first LNA. The LNA performs a filtering together with the antenna as well as a signal amplification. The gain has been set to a rather high value because of the high-noise factor of the sampling mixer.

The same echo problem as in the transmitter exists in the receiver between the antenna and the LNA. Here also an attenuator has been included to reduce the echo generated in the antenna line. This attenuator could be omitted by a shorter distance between receiver front end and antenna. This would only be possible by a higher degree of integration of the front end.

Power divider. The power divider is a Wilkinson type with three stages and five paths. Because of the high number of paths, the input impedance is chosen to be $25\,\Omega$. That causes the need for an impedance match between the output of the first LNA stage and the input of the Wilkinson power divider. The transfomer is a tapered microstrip line several wavelengths long.

The mutual layout coupling is a big part of the disparity of the practical realisation of the five output paths of the power divider. Nevertheless this power divider was chosen due to its additional isolation between the outputs and lower insertion loss between the input and each of the outputs. The isolation between the outputs is required because of the limited LO to RF isolation of the sampling mixer circuitry. This part will be much easier to realise if it is integrated onto a chip. Then the isolation of the different arms can be realised by buffer amplifiers.

Second LNA. The second LNAs together with the Wilkinson power divider help to isolate the five sampling mixers from each other. Every sampling mixer generates at its input the so-called kick-back pulses especially if the IF output voltage is nonzero.

Sampling mixer. Each of the five parallel sampling mixers consists mainly of a pair of fast Schottky diodes (BAT15, Infineon Technologies) and a pulse transformer/shortener made up of a microstrip slotline connection. The slotline ends in a short on one side and by the diodes and charge capacitors at the other. This type of sampling mixer is well described in the literature and our design is adapted from [34, 35]. A photograph of a single sampling mixer is shown in Figure 3.53.

The bank of sampling mixers is not required to be very amplitude linear because the outputs are evaluated relative to each other only. Therefore, the circuitry for discharging the charge capacitors and biasing can be omitted in principle.

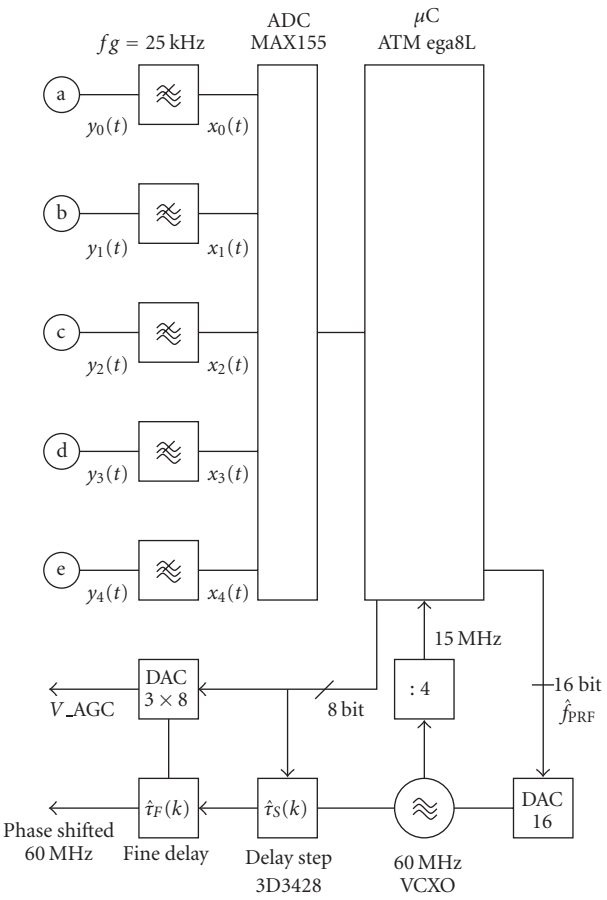

FIGURE 3.51. Synchronisation and control components of the receiver. The inputs $a, b, \ldots, e$ are connected to the corresponding points in Figure 3.50.

The received PPM signal $r(t)$ at the front end of the receiver can be modelled as a linearly filtered version of (3.52) in additive noise,

$$r(t) = \sum_{k=-\infty}^{\infty} q\left(t - A_{\lfloor k/10 \rfloor} T - kT_{\text{PRF}} - \tau(t)\right) + n(t), \tag{3.53}$$

where $q(t)$ denotes the overall pulse shape, $T = 2\,\text{ns}$ is the timeslot duration, $f_{\text{PRF}} = 1/T_{\text{PRF}} = 60\,\text{MHz}$ is the PRF, and $n(t)$ denotes the noise. The pulse shape $q(t)$ results from the linear distortions between the antenna connectors at the transmitter and the receiver.

The sampling mixers are clocked synchronously at the receiver's estimate of the PRF which is denoted by $\hat{f}_{\text{PRF}} = (\hat{T}_{\text{PRF}})^{-1}$.

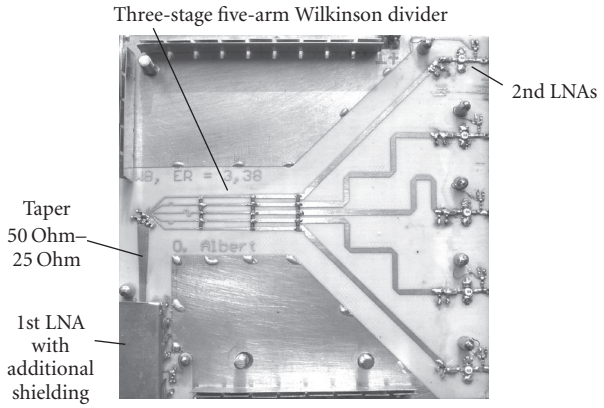

FIGURE 3.52. Front-end PCB of the UWB receiver.

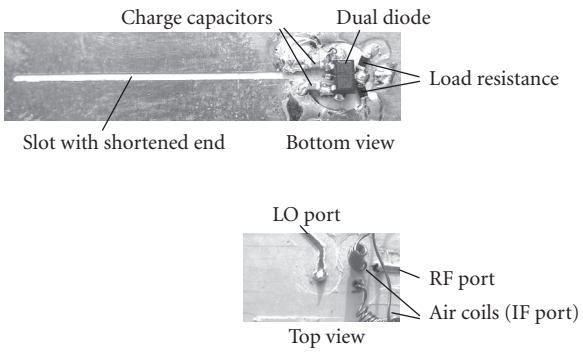

FIGURE 3.53. Detailed photographic images of the sampling mixer PCB.

The ℓth sampling mixer ($\ell = 0, 1, \ldots, 4$) is triggered at the delay $\ell T + \epsilon_\ell + \hat{\Delta}(t)$ where $\hat{\Delta}(t)$ is adjusted by the μC using the *delay step* and *fine delay*, and $|\epsilon_\ell| \ll T$ describes small constant delay deviations from the PPM symbol delay slots at ℓT, that is, we designed an early-late sampler with $\epsilon_0 \approx \epsilon_3 \approx -100$ ps and $\epsilon_1 \approx \epsilon_2 \approx 100$ ps.

After the sampling mixer in the ℓth signal path of the receiver, we obtain

$$\tilde{r}_\ell(t) = \sum_{n=-\infty}^{\infty} r(t)\delta\left(t - n\hat{T}_{\mathrm{PRF}} - \ell T - \epsilon_\ell - \hat{\Delta}(t)\right), \quad \ell = 0, 1, \ldots, 4. \tag{3.54}$$

The oscillogram shown in Figure 3.54 is measured at the sampling mixer output. The horizontal scaling is 200 ns/division and the symbol duration is $10T_{\mathrm{PRF}} \approx 166.7$ ns. In this figure, we see approximately 12 spikes per division. The spikes mark the LO feedthrough.

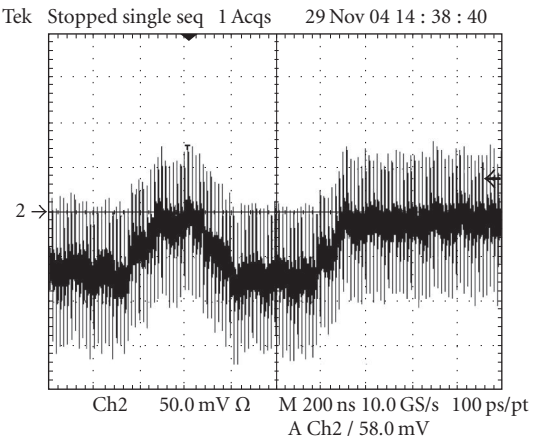

FIGURE 3.54. Oscillogram of the sampling mixer output, 10 pulses per symbol, approx. 12 pulses per 200 ns division.

3.8.4. Local oscillator pulse generation

The only difference between the five receiver paths is the position of the local oscillator pulses which control the diodes in the sampler circuit.

The main receiver clock of 60 MHz is the source of the local oscillator pulses. The same digital delay line as the one used in the transmitter is also applied in the receiver. The distance is adjusted to equidistance plus or minus a small fraction. So two early and two late LO signals are generated. This is used to detect the exact position in the time frame of the incoming signal. Further details can be found in Section 3.8.5.

A CPLD generates the rising edges used in the pulse sharpening circuit. In a later stage, it is foreseen to implement a time hopping sequence generator in the CPLD for mitigating multiple-access interference.

In contrast to the transmitter, only one transistor stage is necessary in the pulse shaper of the receiver because the amplitude and impedance requirements are less stringent than in the transmitter.

Signal low-pass filter. High-input impedance and low-noise operational amplifiers augment the signal amplitude of the now down-sampled signal. In front of them LC low-pass filters are included. For low ringing, Bessel characteristic has been chosen.

The large coils of the filters can pick up noise easily so care must be taken to ensure proper shielding, especially at this low-amplitude stage.

Low-frequency amplifiers. The variable gain amplifiers (VGA) following the first low-frequency stage amplify the received pulses to constant amplitude. The low-frequency amplifier stages consist of three parallel dual channel VGA (AD604, Analog Devices Inc.). One problem arising from this discrete realisation is to

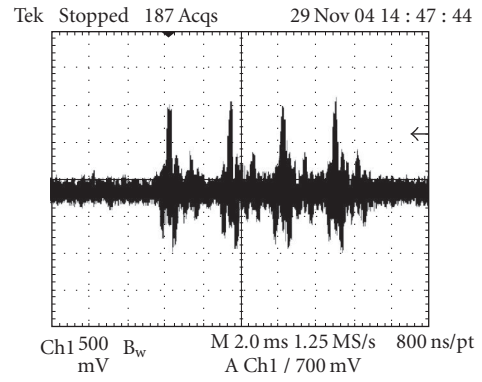

(a)

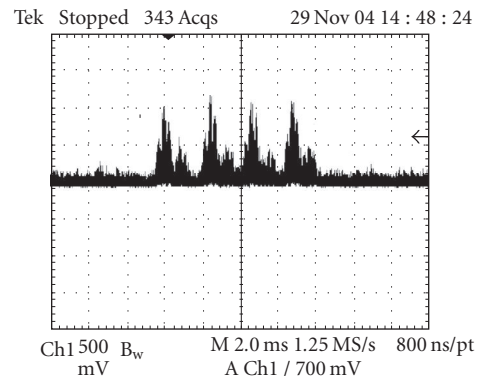

(b)

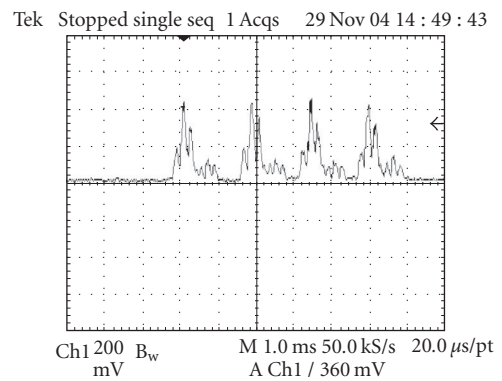

(c)

FIGURE 3.55. Oscillograms of the receiver baseband signals, not frequency locked. (a) Output of the VGA, (b) output of the full-wave rectifier, (c) output of the synchronisation low-pass filter.

ensure equal gain of all five paths used for every gain setting. This is controlled by the μC by means of an 8 bit DAC channel. An oscillogram of one channel is given in Figure 3.55a. This kind of oscillogram—with all four transmitted pulses in one receiver path—can only be observed when transmitter and receiver work with a frequency offset.

Full-wave rectifier. Before this stage the signal has both polarities. So depending on the environment and antenna position, the bigger part of the pulse oscillation can be either positive or negative. A clamp amplifier (AD8036, Analog Devices Inc.) operates as a precision full-wave rectifier. It is used to flip all pulses to positive voltage values (Figure 3.55b).

De-mapper. The PPM de-mapper compares the levels on all four signal paths and selects the pair of bits that best represents the PPM symbol. It consists of operational amplifiers.

Synchronisation low-pass filter. For synchronisation, all five signal paths are low-pass filtered by 3rd-order RC filters. The cut-off frequency is approximately 25 kHz. This value is a trade-off between averaging over a large number of PPM symbols and a low group delay. Low group delay is important for the delay tracking range of the synchronisation algorithm. A lower cutoff frequency results in a filter which averages over more PPM symbols. The improved signal to noise ratio eases the detection of delay offsets by the μC (Figure 3.55c). For further improvement of the signal to noise ratio, a peak-value rectifier is placed before the input of the synchronisation low-pass filter.

Analogue-to-digital converter (ADC). The low-pass filtered signal gets injected into the analogue-to-digital converter. This ADC must sample all five input signals simultaneously. Therefore the MAX155 was selected.[1]

The ADC is entirely controlled by the μC and works with an input clock of 3.75 MHz. It outputs 8- bit samples to be proccessed by the synchronisation algorithm executed by the μC.

Microcontroller. The 8-bit μC is an ATMega8L (ATMEL Inc.). This μC is powerful enough for delay tracking with update cycles below 60 μs. In the testbed, it operates on a 15 MHz clock derived from the VCXO.

The main task of the algorithm implemented in the μC is the delay tracking. The synchronisation algorithm itself is described and discussed in Section 3.8.5. Other tasks of the μC include hardware initialisation during power-up, offset voltage compensation of the ADCs, initial PRF acquisition (for details see page 61), automatic gain control by setting the gain in the VGA (see page 56), and debugging support by tracing of key quantities via a serial output port and otherwise unused DACs.

Digital-to-analogue converter (DAC). An eight-channel DAC is integrated into the receiver circuitry for three different tasks. The first task is to set the gain of the variable gain amplifier. In this way, the automatic gain control (AGC) loop is

[1] Can be replaced by the newer and faster MAX1304, MAXIM Inc.

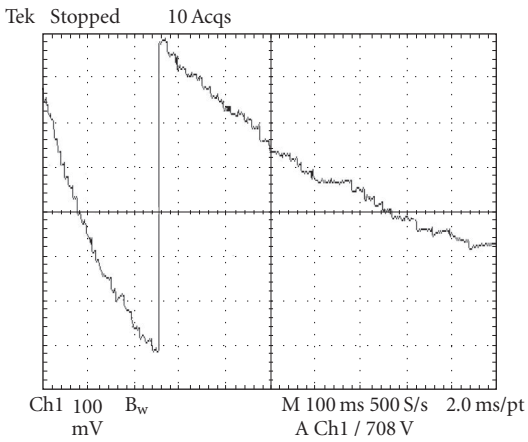

(a)

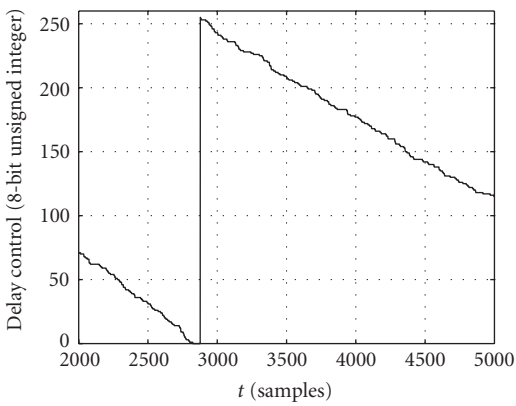

(b)

FIGURE 3.56. (a) Oscillogram of the DAC output showing the delay shift control trajectory versus time. (b) Simulation trace of 8-bit quantised delay shifter control values.

closed. The second task is to control the fine delay circuitry shown in Figure 3.51. In this way, the receiver's clock timing can be delayed in steps of $T_{\text{PRF}}/256$. The third DAC channel is used as a debug output. With that output the 8-bit address of the phase delay table can be displayed on an oscilloscope easily (Figure 3.56).

The receiver phase is locked if a sawtooth is displayed. The period of the sawtooth gives the period of the offset frequency between transmitter and receiver.

Delay shifter. The receiver synchronisation subsystem uses a digitally controlled delay shifter, comprising the *delay step* and *fine delay* blocks in Figure 3.50. The delay shifter is controlled by an 8-bit input $d \in \{0, 1, \ldots, 255\}$ and is designed to

realise the delay $d\Delta$ with a granularity of $\Delta = 65.1$ ps. This results in delays up to $(255/256)T_{\text{PRF}} \approx 16.60$ ns.

The controlled delay shifter is implemented in two stages, *delay step* and *fine delay*, respectively. The *delay step* is based on an 8-bit controllable delay circuit (3D3428-0.25 from Data Delay Devices Inc.) having delay steps of 0.25 ns. This granularity is too coarse for timing adjustment of the receiver. Therefore, a second stage, *fine delay*, is serially concatenated with a range of delay shifts of approximately 1 ns. The *fine delay* is controlled by one output of the 8-bit DAC. This combination realises a very fine delay adjustment in 256 quantised steps with a stepsize of approximately 65.1 ps.

3.8.5. Receiver synchronisation

The guard interval in the symbol frame (see Figure 3.48) is introduced to aid synchronisation. In this design, it induces approximately 108% excess bandwidth into the system. As a result, a discrete frequency component at the PRF is introduced in the spectrum [23, 31]. This component can be extracted to derive the symbol frame timing.

In (3.53), the PPM symbols $A_k \in \{0, 1, 2, 3\}$ are assumed mutually independent, identically, and uniformly distributed, and $\tau(t)$ denotes a slowly varying delay for which the first-order probability density is uniform in $[0, T_{\text{PRF}}]$. The synchronisation algorithm first estimates $f_{\text{PRF}}(0)$ and subsequently tracks $\tau(t)$ and $f_{\text{PRF}}(t)$ for $t > 0$ by means of an early-late discriminator.

As shown in Figure 3.50, the receiver front-end splits $r(t)$ using the Wilkinson power divider into five parallel signal paths. The signal on each path is amplified by a factor of g, sampled at the receiver's estimate $(\widehat{T}_{\text{PRF}})^{-1}$ of the PRF (see page 55), low-pass-filtered with $f_{g1} = 10$ MHz and rectified. This low-pass filter serves as an integrator for summing the energy of 10 consecutive pulses. The resulting $y_\ell(t)$ is passed on to the PPM symbol decoder by selecting the signal path having maximum magnitude. The synchronisation part of the receiver shown in Figure 3.51 passes $y_\ell(t)$ through a second low-pass filter with $f_{g2} = 25$ kHz. The resulting $x_\ell(t)$ serves as input to the ADC:

$$\begin{aligned} y_\ell(t) &= \left| g \int_0^t h_{\text{LP1}}(t - t')\tilde{r}_\ell(t')\, dt' \right|, \\ x_\ell(t) &= \int_0^t h_{\text{LP2}}(t - t')\, y_\ell(t')\, dt'. \end{aligned} \tag{3.55}$$

The third-order low-pass filter characterised by $h_{\text{LP2}}(t)$ is designed such that it effectively averages over a large number of pulses (approx. 3000 pulses are averaged). Finally, the ADC quantises $x_\ell(kT_S)$ to 8 bits and delivers the values $x_\ell[k]$ to the μC.

Pulse repetition frequency acquisition. Let $x_\ell[k]$ be the 8-bit quantised ADC input value of the ℓth ADC at sample instant k where $\ell \in \{0, 1, \ldots, 4\}$, see Figure 3.51. Note that the ADC input signals are low-pass-filtered with 25 kHz cutoff and the sampling interval is approximatly $T_S = 58\,\mu$s. Further, let $x_{(\ell)}[k]$ be the *sorted* ADC

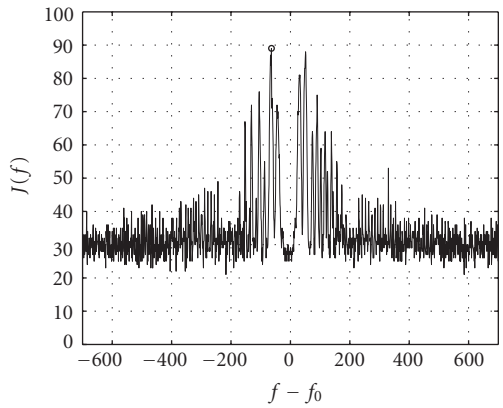

FIGURE 3.57. Simulated goal function $J(f)$ realisation versus frequency deviation.

input values at sample instant k such that

$$0 \le x_{(0)}[k] \le x_{(1)}[k] \le \cdots \le x_{(4)}[k] \le 255. \tag{3.56}$$

The following goal function $J(f)$ is maximised for coarse frequency estimation for the initial acquisition of the PRF:

$$J(f) = \frac{1}{n}\sum_{k=1}^{n}\left(\frac{x_{(1)}[k] + x_{(2)}[k] + x_{(3)}[k] + x_{(4)}[k]}{4} - x_{(0)}[k]\right). \tag{3.57}$$

This goal function estimates the depth of the PPM symbol guard interval as the difference between the arithmetic mean of the four largest ADC input values and the smallest one.

This goal function can be reformulated as

$$J(f) = \frac{1}{4n}\sum_{k=1}^{n}\left(x_0[k] + x_1[k] + x_2[k] + x_3[k] + x_4[k] - 5x_{(0)}[k]\right), \tag{3.58}$$

which shows that we do not need to sort the input ADC values. It suffices to find the index $\widehat{\ell}[k] \in \{0, 1, \ldots, 4\}$ of the minimum magnitude ADC value

$$x_{(0)}[k] = \min_{0\le\ell\le 4} x_\ell[k] = x_{\widehat{\ell}[k]}[k] \tag{3.59}$$

for each sample k.

In the testbed implementation, we chose to average over $n = 64$ ADC samples. The μC sweeps through the range of frequencies $\{f_{\min}, f_{\min} + 1, \ldots, f_{\max}\}$ represented by 16-bit integers. At each frequency f, the goal function (3.58) is evaluated. In simulations, the properties of this goal function were evaluated numerically. A typical realisation of $J(f)$ obtained from simulations is shown in

Figure 3.57 versus frequency deviation from the true PRF. The goal function is not smooth, but shows a large number of local extrema. We observe that the global maximum value of $J(f)$ in this realisation is located very *near* the true PRF.

It turns out that $J(f)$ becomes small and insensitive to τ in (3.52) for frequencies f far from the true PRF. For frequencies f near to the true PRF, the local maxima of $J(f)$ become larger and larger. In the immediate neighbourhood around the true PRF, the goal function value becomes sensitive to the delay τ in (3.53).

In the testbed, this scheme achieves significantly less than 100 Hz deviation on average from the transmitter's PRF of 60 MHz. This corresponds to an accuracy better than $1.7 \cdot 10^{-6}$.

Finally, the μC sets the VCXO to the frequency $\hat{f}$ achieving the maximum $J(\hat{f})$.

Delay lag estimator/corrector. The delay lag between transmitter and receiver is defined as $\Delta(t) := \tau(t) - \hat{\tau}(t)$ where $\tau(t)$ is defined in (3.52) and $\hat{\tau}(t)$ is introduced in (3.53).

The delay lag estimator receives the ADC samples $x_\ell[k]$ for $\ell = 0, \ldots, 4$ at $t = kT_S$. First, it finds the index $\hat{\ell}[k]$ of the signal path with minimum observed magnitude,

$$\hat{\ell}[k] = \underset{\ell \in \{0,1,\ldots,4\}}{\arg\min}\, x_\ell[k]. \tag{3.60}$$

If $\hat{\ell}[k] \neq 4$, we conclude that the receiver has lost the symbol frame timing because the signal path for $\ell = 4$ should always take samples from the guard intervals. In this case, the delay lag estimator uses a parabola interpolation for the ADC values,

$$p_k(m) = a_k + b_k m + c_k m^2 \stackrel{!}{=} x_{\hat{\ell}[k]+m}[k], \quad \text{for } m \in \{-1, 0, +1\}, \tag{3.61}$$

for estimating

$$\hat{\Delta}[k] = \hat{\Delta}(kT_S) \mod T_{\text{PRF}}. \tag{3.62}$$

The algorithm first determines the parabola coefficients and calculates

$$\hat{\Delta}[k] := 4 - \hat{\ell}[k] + \frac{a_k b_k}{c_k}. \tag{3.63}$$

On the other hand, if $\hat{\ell}[k] = 4$, we conclude that the receiver is in a synchronised state because the guard interval is correctly located with respect to the receiver timing. Now, we only need to track small delay errors. In this case, we use a variant of an early-late discriminator for estimating $\Delta(kT_S)$. Remember that the signal paths for $\ell = 0$ and 3 are sampled *early* whereas those for $\ell = 1$ and 2 are sampled

late, see page 55:

$$\widehat{\Delta}[k] := Q\left(\frac{x_1[k] - x_0[k]}{x_1[k] + x_0[k] + 1}\right) + Q\left(\frac{x_2[k] - x_3[k]}{x_2[k] + x_3[k] + 1}\right), \tag{3.64}$$

where $Q(\cdot)$ is a suitable quantiser function.

Finally, the obtained estimate $\widehat{\Delta}[k]$ is programmed via the control interface of the two-stage delay shifter described on page 60. A lookup table is used for mapping each desired $\widehat{\Delta}[k]$ onto a pair of control bytes for the *delay step* and *fine delay*, such that $\widehat{\Delta}[k] \approx \hat{\tau}_S[k] + \hat{\tau}_F[k]$ as shown in Figure 3.51. A typical trajectory of $\widehat{\Delta}[k]$ from a simulation in noise is shown in Figure 3.56b and a corresponding trace from the testbed is shown in Figure 3.56a. The testbed trace is obtained with an oscilloscope by monitoring the values of $\widehat{\Delta}[k]$ which are regularly output on an additional DAC.

3.8.6. Complexity of UWB impulse radio systems

From today's viewpoint, the promise of low-complexity implementations of IR-UWB systems can only be met by noncoherent receivers. These suboptimal implementations will have a far lower bit rate than the envisioned 480 Mb/s because the ISI can not be equalised in time domain with current state of the art systems.

The low-complexity promise was stated by assuming that the complexity bottleneck is the frequency synthesiser with phase locked loops and narrowband filtering. For coherent IR-UWB systems, the counterparts are fine-granularity delay shifters and low-jitter oscillators.

However, the use of IQ-demodulators or IF-digitalisation is not required for IR-UWB systems. Here, sampling mixers are employed which do not consume much DC power.

Concerning the synchronisation tasks in the testbed, we observe that the acquisition of the pulse repetition frequency is fairly easy and can be accomplished at low computational cost. The early-late discriminator for fine delay tracking is rather susceptible to disparities of the gains on different symbol paths in the receiver. Therefore, the μC needs to calibrate the gains on all symbol paths during power-up.

3.9. Conclusions

UWB systems may be primarily divided into impulse radio (IR) systems and multiband systems. Multiband systems offer the advantage of potentially efficient utilisation of spectrum.

However, IR systems however have the significant advantage of simplicity, and so are potentially lower cost. In addition, IR is essentially a baseband technique. The IR UWB concepts investigated support many modulation schemes including orthogonal and antipodal schemes. However, the basic modulation must also include some form of spectrum randomisation techniques to limit the interference

caused by the transmitted pulse train. Both TH and DS randomisation techniques were examined. Which modulation scheme to use depends on the expected operating conditions and the desired system complexity.

This chapter has introduced the application of impulses to UWB wireless transmissions. A number of candidate pulse waveforms have been characterised in the time and frequency domains. The application of orthogonal pulse waveforms has then been introduced where these waveforms enable advanced modulation and multiple-access schemes to be implemented. However, the success of these schemes is determined by the extent of pulse distortion caused by the transmitter and receiver circuitry and the propagation channel. Thus, distortion mitigation techniques are required. Finally, the issue of coexistence of impulse radio with other spectrum users has been discussed.

Acknowledgments

This work was funded by Siemens AG Austria PSE PRO RCD, all member companies of ftw., and **K***plus* within ftw. Project I0. The authors would like to thank Holger Arthaber at EMST, Vienna University of Technology, for measurement support and reviewing the text.

Bibliography

[1] FCC press release, February 2002, http://www.fcc.gov/Bureaus/Engineering_Technology/News_Releases/2002/nret0203.html.

[2] J. T. Conroy, J. L. LoCicero, and D. R. Ucci, "Communication techniques using monopulse waveforms," in *Proceedings of IEEE Military Communications Conference (MILCOM '99)*, vol. 2, pp. 1181–1185, Atlantic City, NJ, USA, October–November 1999.

[3] Time Domain Corporation, Comments of Time Domain Corporation, Docket 98-154. In the Matter of Revision of Part 15 of the FCC's rules regarding ultra wideband transmission systems, 1998.

[4] G. F. Stickley, D. A. Noon, M. Chernlakov, and I. D. Longstaff, "Preliminary field results of an ultra-wideband (10-620 MHz) stepped-frequency ground penetrating radar," in *Proceedings of IEEE International Geoscience and Remote Sensing (IGARSS '97)*, vol. 3, pp. 1282–1284, Singapore, Republic of Singapore, August 1997.

[5] L. Carin and L. B. Felsen, Eds., *Ultra-Wideband, Short-Pulse Electromagnetics 2*, Conference Proceedings, Kluwer Academic/Plenum Press, New York, NY, USA, 1995, 605 pages.

[6] R. Prasad and S. Hara, "An overview of multi-carrier CDMA," in *Proceedings of IEEE 4th International Symposium on Spread Spectrum Techniques and Applications (ISSSTA '96)*, vol. 1, pp. 107–114, Mainz, Germany, September 1996.

[7] IEEE, "Draft Standard for Telecommunications and Information Exchange Between Systems—LAN/MAN Specific Requirements—Part 15.3: Wireless Medium Access Control (MAC) and Physical Layer (PHY) Specifications for High Rate Wireless Personal Area Networks (WPAN)," Draft P802.15.3/D17, February 2003.

[8] C. J. Le Martret and G. B. Giannakis, "All-digital PAM impulse radio for multiple-access through frequency-selective multipath," in *Proceedings of IEEE Global Telecommunications Conference (GLOBECOM '00)*, vol. 1, pp. 77–81, San Francisco, Calif, USA, November–December 2000.

[9] Y.-P. Nakache and A. F. Molisch, "Spectral shape of UWB signals-influence of modulation format, multiple access scheme and pulse shape," TR-2003-40, May 2003.

[10] J. G. Proakis and M. Salehi, *Communication System Engineering*, Prentice-Hall, Englewood Cliffs, NJ, USA, 1994.

[11] B. Allen, M. Ghavami, A. Armogida, and H. Aghvami, "UWB—A ubiquitous wire replacement technology?"

[12] W. Zhuang, X. Shen, and Q. Bi, "Ultra-wideband wireless communications," *Wireless Communications and Mobile Computing*, vol. 3, no. 6, pp. 663–685, 2003.

[13] J. G. Proakis, *Digital Communications*, McGraw-Hill, New York, NY, USA, 1995.

[14] P. Withington, R. Reinhardt, and R. Stanley, "Preliminary results of an ultra-wideband (impulse) scanning receiver," in *Proceedings of IEEE Military Communications Conference (MILCOM '99)*, vol. 2, pp. 1186–1190, Atlantic City, NJ, USA, October–November 1999.

[15] M. Z. Win and R. A. Scholtz, "Comparisons of analog and digital impulse radio for wireless multiple-access communications," in *Proceedings of IEEE International Conference on Communications (ICC '97)*, vol. 1, pp. 91–95, Montreal, Quebec, Canada, June 1997.

[16] R. J. Fontana, J. F. Larrick, and J. E. Cade, "An ultra wideband communications link for unmanned vehicle applications," in *Proceedings of Association for Unmanned Vehicle Systems International 1997 Conference (AUVSI '97)*, Multispectral Solutions, Baltimore, Md, USA, June 1997.

[17] M. Hämäläinen, V. Hovinen, R. Tesi, J. H. J. Iinatti, and M. Latva-aho, "On the UWB system coexistence with GSM900, UMTS/WCDMA, and GPS," *IEEE Journal on Selected Areas in Communications*, vol. 20, no. 9, pp. 1712–1721, 2002.

[18] R. Zetik, J. Sachs, and R. Thomä, "From UWB radar to UWB radio," in *Proceedings of International Workshop on Ultra-Wideband Systems (IWUWBS '03)*, Oulu, Finland, June 2003, Center of Wireless Communications (CWC), IEEE.

[19] M. Katz, *Code acquisition in advanced CDMA networks*, Ph.D. thesis, Acta Universitatis Ouluensis C175, University of Oulu, Oulu, Finland, 2002.

[20] J. Iinatti, "Performance of DS code acquisition in static and fading multipath channels," *IEE Proceedings on Communications*, vol. 147, no. 6, pp. 355–360, 2000.

[21] J. Iinatti and M. Latva-aho, "A modified CLPDI for code acquisition in multipath channel," in *Proceedings of IEEE Symposium on Personal, Indoor and Mobile Radio Communications (PIMRC '01)*, pp. 6–10, San Diego, Calif, USA, September–October 2001.

[22] F. Ramirez-Mireles and R. A. Scholtz, "System performance analysis of impulse radio modulation," in *Proceedings of Radio and Wireless Conference (RAWCON '98)*, pp. 67–70, Colorado Springs, Colo, USA, August 1998.

[23] R. Otte, L. P. de Jong, and A. H. M. van Roermund, *Low-Power Wireless Infrared Communications*, Kluwer Academic, New York, NY, USA, 1999.

[24] W. Hirt and D. L. Moeller, "UWB radio technology—the global view of a wireless system integrator," in *Proceedings of International Symposium on Advanced Radio Technologies (ISART '02)*, Boulder, Colo, USA, March 2002.

[25] L. Qinghua and L. A. Rusch, "Multiuser detection for DS-CDMA UWB in the home environment," *IEEE Journal on Selected Areas in Communications*, vol. 20, no. 9, pp. 1701–1711, 2002.

[26] J. Foerster, V. Somayazulu, S. Roy, et al., "Intel CFP presentation for a UWB PHY, Intel's multiband UWB PHY proposal for IEEE 802.15.3a," Technical Report IEEE 802.15-03/109r1, Intel Corporation, Santa Clara, Calif, USA, 2003.

[27] C. Sandner, A. Wiesbauer, C. Grewing, et al., "A 3 GHz to 7 GHz fast-hopping frequency synthesizer for UWB," in *Proceedings of International Workshop on Ultra-Wideband Systems (IWUWBS '04)*, pp. 405–409, Kyoto, Japan, May 2004.

[28] V. Vilnrotter, M. K. Simon, and T.-Y. Yan, "The power spectrum of pulse position modulation with dead time and pulse jitter," Technical Report 42–133, Telecommunications and Mission Operations, Jet Propulsion Laboratory, Pasadena, Calif, USA, 1998.

[29] M. Z. Win and R. A. Scholtz, "Ultra-wide bandwidth time-hopping spread-spectrum impulse radio for wireless multiple-access communications," *IEEE Transactions on Communications*, vol. 48, no. 4, pp. 679–689, 2000.

[30] A. F. Molisch, Y.-P. Nakache, P. Orlik, et al., "Time hopping impulse radio," Technical Report IEEE 802.15-03/109r1, Mitsubishi Electric, Princeton University, Georgia Institute of Technology, and New Jersey Institute of Technology, Princeton, NJ, USA, 2003.

[31] O. Albert and C. F. Mecklenbräuker, "Low-power ultra-wideband radio testbed for short-range data transmission," in *Proceedings of International Workshop on Ultra-Wideband Systems (IWUWBS '03)*, Oulu, Finland, June 2003, Center of Wireless Communications (CWC), IEEE.

[32] W. M. Lovelace and J. K. Townsend, "The effects of timing jitter and tracking on the performance of impulse radio," *IEEE Journal on Selected Areas in Communications*, vol. 20, no. 9, pp. 1646–1651, 2002.

[33] B. Kull and S. Zeisberg, "UWB receiver performance comparison," in *Proceedings of International Workshop on Ultra-Wideband Systems (IWUWBS '04)*, pp. 21–25, Kyoto, Japan, May 2004.

[34] B. Schiek, *Meßsysteme der Hochfrequenztechnik*, Hüthig, Heidelberg, Germany, 1984.

[35] D. Kress and R. Irmer, *Angewandte Systemtheorie*, VEB Verlag Technik, Berlin, Germany, 1989.

Ian Oppermann: Department of Electrical and Information Engineering, University of Oulu, 90014, Finland

Email: ian@ee.oulu.fi

Matti Hämälainen: The Centre for Wireless Communications (CWC), University of Oulu, Oulu, Finland

Email: matti.hamalainen@ee.oulu.fi

Jari Iinatti: The Centre for Wireless Communications (CWC), University of Oulu, Oulu, Finland

Email: jari.iinatti@ee.oulu.fi

Alberto Rabbachin: The Centre for Wireless Communications (CWC), University of Oulu, Oulu, Finland

Email: alberto.rabbachin@ee.oulu.fi

Ben Allen: Centre for Telecommunications, King's College London, UK

Email: ben.allen@kcl.ac.uk

Seyed A. Ghorashi: Centre for Telecommunications, King's College London, UK

Email: seyed.ghorashi@kcl.ac.uk

Mohammad Ghavami: Centre for Telecommunications, King's College London, UK

Email: mohammad.ghavami@kcl.ac.uk

Olaf Albert: Siemens AG Austria, PSE PRO Radio Communication Devices, Erdberger Lände 26–28, 1030 Vienna, Austria

Email: olaf.albert@siemens.com

Christoph F. Mecklenbräuker: Das Forschungszentrum Telekommunikation Wien (ftw.), Donau City Strasse 1/3, 1220 Wien, Austria

Email: cfm@ftw.at

A print edition of this book can be purchased at
http://www.hindawi.com/spc.5.html
http://www.amazon.com/dp/9775945100

4 Higher-layer issues: ad hoc and sensor networks

Maria-Gabriella Di Benedetto, Luca De Nardis, and Salvatore Falco

4.1. Introduction

Ultra-wide-band (UWB) radio has the potential of allowing simultaneous communication of a large number of users at high bit rates [1–3]. In addition, the high temporal resolution inherent to UWB provides robustness against multipath fading and is particularly attractive for indoor local area network (LAN) applications. UWB is also capable of recovering distance information with great precision. As we will show later in this chapter, distance and position data can lead to better organization of wireless networks, for instance, through better resource management and routing [4]. UWB signals spread, however, over very large bandwidths and overlap with narrowband services. As a consequence, regulatory bodies impose severe limitations on UWB power density in order to avoid interference provoked by UWB onto coexisting narrowband systems [5]. It is therefore necessary to take into account power considerations when designing UWB systems. Throughout this chapter we will show how the distance information made available by the UWB technology can be exploited to achieve low power levels and increase network lifetime in the long term, while providing an adequate network performance (in terms of data throughput) in the short term.

In the last few years, the increasing interest in applications based on the deployment of ad hoc networks triggered significant research efforts regarding the introduction of the energy-awareness concept in the design of medium access control (MAC) and routing protocols. Ad hoc networks are in fact considered as a viable solution for scenarios in which fixed infrastructure, and consequently unlimited power sources, are not available. In such scenarios, an efficient management of the limited power supply available in each terminal is a key element for achieving acceptable network lifetimes. This is particularly true for sensor networks, for which long battery duration is one of the basic requirements, given the typical size of such networks (up to thousands of terminals), as will be analyzed in Section 4.2.

Location information is another valuable way of achieving energy-awareness in ad hoc networks. In Section 4.3 we first review location-aware routing protocols

with focus on power efficiency. We then address the problem of information exchange through the network by means of specifically designed protocols.

Next, we introduce in Section 4.4 a MAC protocol which foresees a dedicated procedure for the acquisition of distance information and which is tailored on UWB features.

The last section of the chapter, Section 4.5, analyzes the effect of mobility on the behavior of the proposed MAC and routing strategies.

4.2. Power-efficient UWB networks

4.2.1. Introduction

This section briefly illustrates the current research trends regarding power-efficient MAC, and power-efficient routing strategies.

4.2.2. Power-efficient MAC

As far as power-aware MAC design is concerned, most of the research activity took the moves from existing solutions for medium access in wireless networks, and in particular carrier sensing multiple access (CSMA), and out-of-band signaling.

CSMA is based on a channel sensing period performed by each terminal before starting transmission. The performance obtained by CSMA is however heavily affected by two phenomena, the well-known "hidden terminal" and "exposed terminal" problems. In order to solve the hidden and exposed terminal problems, solutions that substitute CSMA have been proposed. The multiple access with collision avoidance (MACA) protocol [6], for example, replaces the carrier sensing procedure with a three-way handshake between transmitter and receiver. Following this approach, further modifications of the MACA protocol have been developed, such as MACAW [7] and MACA-by invitation (MACA-BI) [8].

Practical implementations of MAC protocols combine handshake and carrier sensing, as proposed in the floor acquisition multiple access (FAMA) protocol [9]. These protocols are commonly referred to as CSMA with collision avoidance (CSMA-CA). An example of CSMA-CA is the distributed foundation wireless MAC (DFWMAC), which has been adopted for the MAC layer of the 802.11 IEEE standard [10].

An alternative solution to CSMA-CA is offered by the out-of-band signaling protocol [11]. This solution splits the available bandwidth into two channels: a data channel used for data packet exchange, and a narrowband signaling channel on which sinusoidal signals (referred to as busy tones) are asserted by terminals that are transmitting and/or receiving, in order to avoid interference produced by hidden terminals. In order to reduce the number of exposed terminals, the use of two different *busy tones* for transmitting and receiving terminals was proposed in [12].

CSMA-CA is by far the most common approach adopted in narrowband wireless LANs. This family of protocols suffers, however, from several drawbacks in

terms of power consumption: packet collisions, which cause a waste of power due to re-transmission, terminals blocked in idle state by active transmissions, and overhearing, that is, power consumption in the reception of packets by non-intended destinations. Several protocols aiming at solving these drawbacks were proposed. Among all, it is worth mentioning the power-aware multiple access protocol with signaling for ad hoc networks (PAMAS) [13]. This protocol combines the CSMA approach with the out-of-band principle, in order to minimize the time a terminal spends in the idle state without neither transmitting nor receiving. The protocol foresees, in fact, a control channel on which the handshake between transmitter and receiver takes place, and a data channel on which data packets are exchanged. The control channel allows terminals to determine when they may safely switch to sleep mode, saving thus power, without affecting data throughput or end-to-end delay. The main idea behind PAMAS is that if a node detects the channel as busy, it goes in sleep mode rather than waste power in idle mode without being able to exchange data packets. The protocol defines dedicated handshakes, which allow terminals to determine for how long they can keep the radio interface switched off. Simulations show that this approach leads to a power save of up to 70% compared to the standard MACA protocol. It should be noted, however, that part of the dramatic advantage shown by PAMAS over MACA is intrinsically due to the assumption of adopting a CSMA-CA approach at the MAC level. PAMAS exploits, in fact, the presence of "pause" periods in the terminal lifetime, due to busy channel or lost contention, to save energy without affecting delay and throughput. If a different solution, for example, Aloha without carrier sensing, is adopted, the PAMAS-like approach is no longer a suitable option.

4.2.3. Power-efficient routing

Power-efficient routing is another topic which is of great interest in relation to distributed ad hoc and sensor networks. Most of the power-aware protocols proposed in the literature are based either on the definition of power-effective routing metrics or on the exploitation of additional information, such as location of terminals in the network. In both cases, the final aim is to find source-destination paths that minimize power consumption.

Regarding the definition of power-aware routing metrics, [14] provides a thorough analysis of the effect of power-aware metrics on network lifetime and fairness in energy consumption between different terminals in the network. The metrics taken into account in the analysis include transmission power, cumulative transmitted and received power, residual power in each node, and their combinations. Interestingly, simulation results presented in [14] show that a straightforward minimization of transmitted power does not necessarily lead to a longer lifetime for each terminal in the network. The adoption of a power-aware routing metric may in fact give rise to paths composed of a high number of hops, involving thus a higher number of terminals in each communication. This strategy provides however fair power consumption between different terminals, increasing thus the

network operation time before the first terminal runs out of power with the consequence of potentially causing a network partition.

For the specific case of UWB, a method for setting up connections by optimizing a power-dependent cost function is described in [15], and further refined in [16, 17]. In [15], a communication cost is attached to each path, and the cost of a path is the sum of the costs related to the links it comprises. The cost function is expressed as the sum of two components as follows:

$$C(x, y) = \delta \cdot C_0 \cdot d^{\alpha} + C_1 \cdot R \cdot d^{\alpha}. \tag{4.1}$$

The first component takes into account the synchronization cost for setting-up a new link. If two nodes already share an active link, $\delta = 0$ and there is no synchronization cost. If two nodes do not share an active link, $\delta = 1$ and a synchronization cost is added. The second component takes into account the cost for transmitting data, and depends upon the requested data rate R. Both terms are related to power consumption, and therefore depend upon the distance d between two nodes. Note that the evaluation of such a distance relies on the precise ranging capabilities offered by the UWB technique. The parameter α is related to channel propagation characteristics and has commonly a value between 2 and 4. Constants C_0 and C_1 are used to weight the synchronization and transmission components.

In [16] the proposed strategy is compared against traditional routing in a scenario characterized by fixed terminals and full network connectivity. Results show that the power-saving strategy, as expected, leads to multihop communication paths between terminals within reach of each other (physical visibility) and by this way increases network performance by reducing average emitted power and thus interference levels [16]. In [17] an improved version of the cost function was proposed, in order to introduce additional parameters in the route selection metrics. The general form of this cost function is given by

$$C(x, y) = C(\text{power}) + C(\text{sync}) + C(\text{interference}) + C(\text{quality}) + C(\text{delay}), \tag{4.2}$$

where the first two terms, related to power and synchronization, respectively, resemble the two terms defined in (4.1).

The UWB ranging capability is the basis for the definition of the above power aware cost function; ranging information, however, can be even more efficiently exploited to build a network map through a distributed protocol, providing thus the input for a location-based routing algorithm. This topic will be addressed in Section 4.3, which deals with both distributed positioning and location-based routing protocols.

4.3. Location-aware UWB networks

4.3.1. Introduction

As anticipated in Section 4.2, location information is valuable for achieving power-efficiency in ad hoc networks. In this section we investigate how location information can be exploited in UWB networks, thanks to the accurate ranging capability offered by this technique. First, we review location-aware routing protocols available in literature, with focus on power-efficient protocols. Next, we address the topic of how location information can be gathered and exchanged in a UWB network, by providing an example of a GPS-free positioning protocol suitable for a UWB network, and finally we analyze the effect of UWB-based positioning on the location-aware routing protocols originally designed for GPS-enabled terminals.

4.3.2. Location-aware routing protocols

As a general concept, all location-aware routing protocols pursue an improvement of network performance by taking into account location information in the route selection process. Depending on how this information is used, different aspects of the routing performance can be optimized. Section 4.3.2.2, for example, shows how location information can be used for increasing route stability. The main focus being here on power efficiency, however, the remaining part of this section addresses routing protocols that exploit location information for reducing routing overhead, and thus power consumption.

4.3.2.1. Greedy perimeter stateless routing

The greedy perimeter stateless routing (GPSR) [18] protocol uses location information to reduce protocol overhead and obtain a good scalability when both terminal mobility and network size increase. GPSR adopts positional information as the key metric in packet forwarding, and uses the following simple "greedy" forwarding strategy.

(1) Each packet is marked by the source terminal with the latest information about the location of the destination.
(2) Each intermediate node forwards the packet to the neighboring visible node, that is, closest to the location of the destination stored in the packet itself.

Note that greedy forwarding does not guarantee that a path between source and destination is always detected, even if it exists. An example of greedy forwarding failure is presented in Figure 4.1. Node x, after receiving a packet from source S intended for destination D, cannot find a neighbor which satisfies the greedy forwarding rule, since both neighbors y and z are further than x from the destination D.

When greedy forwarding fails, the GPSR protocol switches from greedy forwarding to perimeter forwarding, in which a terminal is allowed to forward the

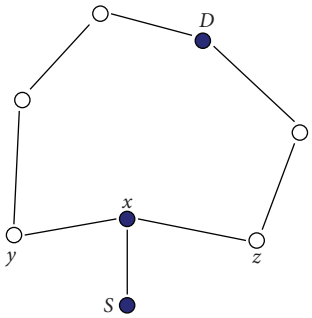

FIGURE 4.1. Example of greedy forwarding failure. Arcs in the figure represent physical visibility between nodes. The greedy forwarding rule fails at node x since both neighbors y and z are further than x from the destination D.

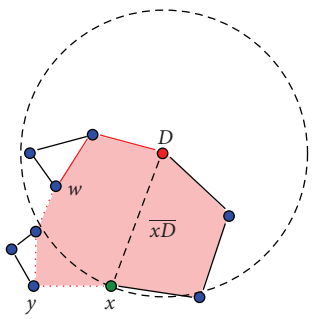

FIGURE 4.2. Combination of perimeter forwarding and greedy forwarding. Arcs in the figure represent physical visibility between nodes. The selected path is represented by a thick line (dotted links: perimeter forwarding, filled links: greedy forwarding).

packet to a neighbor which is further than itself from destination, in order to solve the stall caused by greedy forwarding. The perimeter forwarding strategy uses the so-called right-hand rule to forward packets around the area in which the greedy approach fails, and can be described as follows (see Figure 4.2).

Suppose that x is the first terminal in which greedy forwarding fails.

(1) Terminal x records its position in the apposite L_f field in the packet.
(2) Terminal x uses the information on its location and the location of destination D recorded in the packet to determine the $\overline{xD}$ line.
(3) Terminal x, based on the position of its neighbors, determines which is the first edge in counterclockwise direction from the $\overline{xD}$ line (edge $\overline{xy}$ in Figure 4.2).
(4) Terminal x forwards the packet to terminal y.
(5) Terminal y checks if it is closer to destination D than the position recorded in the L_f field. If this is the case, y switches back to greedy forwarding, otherwise repeats the procedure from step 2.

In the example in Figure 4.2, x enters the perimeter forwarding, and w switches back to the greedy forwarding. The grey area defines the perimeter over which the algorithm switches from greedy forwarding to perimeter forwarding.

4.3.2.2. Location-aware long-lived route selection in wireless ad hoc network

The location-aware long-lived routing (LLR) protocol [19] belongs to the family of source-initiated, on-demand routing protocols. The protocol exploits location information aiming at the minimization of route failures and, as a consequence, of route reconstruction procedures. As in traditional source routing protocols, a source terminal S in need of a route to a destination broadcasts route discovery packets to its neighbors, and the latter will forward packets until the destination is reached.

In LLR, the source S includes two additional information fields in each generated packet: its own position (X_S, Y_S) and radio transmission range R_s. Each terminal A in physical connectivity with S that receives the packet uses such information and its own position (X_A, Y_A) and transmission range R_A to evaluate two figures.

(1) Forward movement limit (FML), that measures the maximum relative movement between A and S which can be tolerated before the distance between A and S is larger than the transmission range of A, defined as

$$\text{FML} = R_A - \text{distance}(A,S) = R_A - \sqrt{(X_S - X_A)^2 + (Y_S - Y_A)^2}. \tag{4.3}$$

(2) Backward movement limit (BML), that measures the maximum relative movement between A and S which can be tolerated before the distance between A and S is larger than the transmission range of S, defined as

$$\text{BML} = R_S - \text{distance}\,(A,S) = R_S - \sqrt{(X_S - X_A)^2 + (Y_S - Y_A)^2}. \tag{4.4}$$

FML and BML are then used to evaluate the normalized movement limit (NML), which provides a single figure averaging FML and BML (note that FML $\neq$ BML when $R_S \neq R_A$):

$$\text{NML} = \frac{\text{FML} \cdot \text{BML}}{\text{FML} + \text{BML}}. \tag{4.5}$$

Terminal A updates the packet by including the NML and substituting (X_A, Y_A) and R_A to (X_S, Y_S) and R_S, respectively, and forwards it to its neighbors.

The NML is an indicator of link stability: the higher the NML value, the lower the probability of link failure due to terminal mobility. When the destination D

receives several route discovery packets originated from the source S, it selects the route characterized by the highest NML, in order to minimize the probability of a route failure. In [19] two alternative ways are foreseen to evaluate the end-to-end reliability of each route, depending on the way a route discovery packet is updated.

Additive NML. Each terminal adds the NML value relative to the last hop to the value carried by the packet, and the best path is characterized by the maximum overall NML.

Min-max NML. Each terminal compares the NML just evaluated with the value recorded in the packet: if the current value is lower than the old one, the packet is updated by overwriting the NML field, otherwise the field is left unchanged. In this case the best route is determined by the worst link in each route (which determines the NML value in the route discovery packet).

4.3.2.3. Distance routing effect algorithm for mobility (DREAM)

The DREAM algorithm [20] proposes the idea of using location information to reduce the amount of routing overhead. The protocol combines both proactive and reactive approaches, by relying on both periodic updates by each terminal for the dissemination of location information and a flooding-like procedure for sending a packet to the targeted destination.

When a source terminal S starts the procedure at $t = t_1$ it is supposed to have the following information:

(i) its own position (X_S, Y_S),
(ii) the positions of its one-hop neighbors,
(iii) the position of the destination D, (X_D, Y_D), at a given time $t_0 < t_1$,
(iv) the maximum speed v of the destination, or at least a probability density function of the speed, $p(v)$.

The source, based on this information, defines a geographical region in which the routing packets should be forwarded, and determines the subset of neighbors that are positioned inside this region, as shown in Figure 4.3. The forwarding region is determined by the angle α.

Depending on the information on destination speed, two cases are possible.

(1) v is known: in this case the distance x traveled by the destination in the period $t_1 - t_0$ is given by $x = v * (t_1 - t_0)$, and, given a distance r between S and D, one has

$$\alpha = \arcsin \frac{x}{r}. \tag{4.6}$$

(2) $p(v)$ is known: in this case in order to determine a forwarding region including D with probability p, the corresponding value of α can be derived from [20]:

$$\int_{r \cdot \sin \alpha/(t_1 - t_0)}^{+\infty} p(v)dv \geq p. \tag{4.7}$$

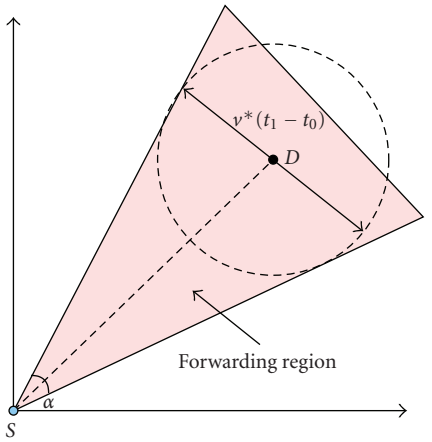

FIGURE 4.3. Definition of the forwarding region in the DREAM protocol.

Once α has been determined, the terminal sends the packet indicating the neighbors lying within the forwarding region. Each intermediate terminal, when receiving a packet, evaluates if the packet should be forwarded by defining its own forwarding region, and by checking if any neighbor lies within it. If no neighbor lies within the forwarding region, the packet is not forwarded, reducing thus the overhead by avoiding packet retransmissions in wrong directions.

As stated before, the procedure requires positional information regarding not only the source, but also its neighbors and destination. This information is exchanged through a distributed dissemination algorithm, which constitutes the proactive routing protocol part.

Each terminal A periodically broadcasts update packets containing its own position; two types of update packets are defined in DREAM:

(i) *short-lived packets*, for updating the location tables in A's neighbors,

(ii) *long-lived packets*, for updating the location tables in terminals that are not in direct connectivity with A.

Note that the lifetime of each packet is defined in terms of physical distance reached from the terminal originating the packet: each terminal B receiving an update packet generated by terminal A checks both A's position (recorded in the packet) and its own position: if the distance between A and B is higher than the packet lifetime, the packet is discarded, otherwise, it is forwarded. Short-lived and long-lived packets are emitted by each terminal with different frequencies, taking into account the so-called distance effect, which is represented in Figure 4.4 and can be described as follows.

Given a terminal A moving at speed v, and two terminals B and C that at $t = t_0$ are positioned at distances D_{AB} and $D_{AC} \gg D_{AB}$ from A, respectively, terminal B will experience a faster variation of the forwarding region to destination A than terminal C, due to A's movement in the time interval $t_1 - t_0$ (i.e., the angle α_B will increase faster than the angle α_C to keep A in the forwarding region). As a

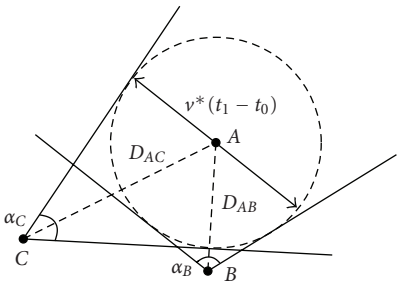

FIGURE 4.4. Example of distance effect. Given two nodes B and C at distances D_{AB} and D_{AC}, with $D_{AC} > D_{AB}$, the angles α_B and α_C as derived either from (4.6) or (4.7) are such that $\alpha_B > \alpha_C$, and B needs thus more frequent updates than C on the position of A, in order to keep A within the forwarding region.

consequence, B will need much more frequent updates than C regarding A's position: such updates will be provided by means of short-lived packets that will reach B without increasing the routing overhead all over the network. C will receive updates at lower frequency by means of long-lived packets.

Each terminal is thus expected to adapt the emission frequencies of both long-lived and short-lived packets to its own speed: fixed terminals will use the lowest frequencies, while highly mobile terminals will send frequent updates.

4.3.2.4. Location-aided routing (LAR)

The LAR protocol [21, 22] is a typical on-demand routing protocol. In order to find a route between source and destination terminal, it relies on a flooding-based route discovery procedure originated by the source by means of a broadcast route request (RRQ) packet. The packet is forwarded by other nodes all over the network until either it reaches the destination (in which case the connection enters in the *found* status) or a timeout expires leading to a route discovery failure. When the destination receives an RRQ packet from the source, it replies with a route reply (RRP) packet which proceeds backward on the selected path, until it reaches the source, that can then start the transmission of data (DATA) packets. A node which detects a connection failure while sending or receiving RRP or DATA packets starts an alarm procedure based on the transmission of broadcast route reconstruction (RRC) packets. When an RRC packet reaches the source of the connection, the transmission of DATA packets is stopped, and the source decides either to drop the connection or to start searching for a new path to destination.

The major drawback of a flooding-based on-demand protocol is the huge amount of routing overhead generated during path search procedures. The location-aided routing exploits location information in order to reduce the amount of routing overhead, although in a different way from the DREAM algorithm described in Section 4.3.2.3. The LAR protocol uses in fact the location information during connection set-up in order to reduce the number of control

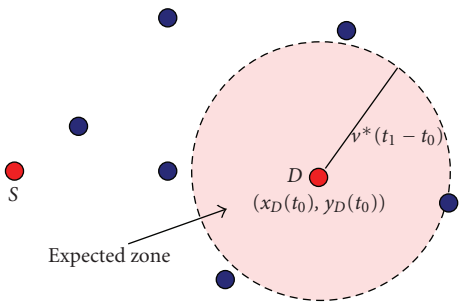

FIGURE 4.5. Definition of *expected zone* in the LAR protocol. If source S knows the position of destination D in $t = t_0$, $(x_D(t_0), y_D(t_0))$, and the maximum speed v of D, it can define the region in which D can lie within in $t = t_1$ (*expected zone*) as a circle of radius $d_{\text{MAX}} = v \cdot (t_1 - t_0)$ centered in the position of D in $t = t_0$.

packets, while no position information is used during DATA packets transmission, since they are sent along the path found during the set-up phase. The basic location information required by LAR consists in

(i) source position,
(ii) destination position,
(iii) maximum terminal speed.

Such information is exploited during the route discovery procedure as follows. Suppose that a terminal S starts a route discovery procedure to destination D at time $t = t_1$, and that the last information update regarding D's location was received by S at $t = t_0$. Based on the estimation of the maximum speed v of terminal D, S can evaluate the maximum distance traveled by D since the last location update. Such a distance is given by $d_{\text{MAX}} = v \cdot (t_1 - t_0)$. As a consequence, the current position occupied by D lies in a circular region of radius d_{MAX} centered on $(x_D(t_0), y_D(t_0))$, referred to as the *expected zone*, represented in Figure 4.5.

The expected zone indicates which zone of the network should be reached by RRQ packets. The key idea in LAR is to exploit this information to reduce the amount of RRQ packets flooding through the network, by allowing forwarding of packets generated by the source only in the direction of the expected zone containing the destination. The region of the network in which forwarding is allowed is referred to as *request zone*. An intermediate terminal is allowed to forward an RRQ packet only if it lies within the request zone defined by the source of the connection request.

Note that the request zone may be defined in several ways, the only constraint being that such zone must include both the position of the source S and the expected zone. A smaller request zone leads to a stronger reduction of the routing overhead, and can thus achieve a higher power efficiency; on the other hand, it leads to a lower number of neighbors involved in the route discovery procedure, and may cause a lower percentage of successful connections. Figures 4.6 and 4.7 show two different definitions of the request zone, and the effect on the number of neighbors involved in the route discovery procedure. In Figure 4.6 a conic request

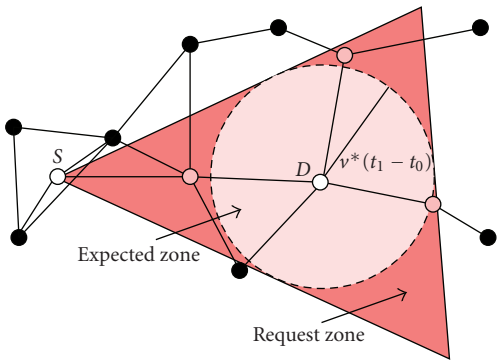

FIGURE 4.6. Definition of conic request zone in the LAR protocol. The nodes that fall within the request zone defined by source S and destination D are represented in grey, while the nodes that are not involved are represented in black.

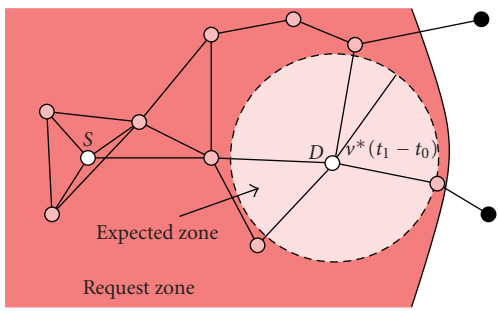

FIGURE 4.7. Definition of spherical request zone in the LAR protocol. The nodes that fall within the request zone defined by source S and destination D are represented in grey, while the nodes that are not involved are represented in black.

zone is considered, similar to the forwarding region defined in the DREAM protocol, while a spherical request zone is presented in Figure 4.7.

In both figures nodes that are involved in the route discovery procedure are represented in grey, while the nodes which are not involved are black. It is evident that the conic request zone reduces the overhead much more effectively than the spherical one, since a lower number of nodes forwards the RRQ packets. On the other hand, for particular topologies the conic request zone may lead to connection set-up failures which could be avoided with a larger request zone. An example of route discovery failure is shown in Figure 4.8, which shows a situation in which no intermediate nodes in physical connectivity with the source fall within the request zone.

The choice of size and shape of the request zone is thus the result of a trade-off between effectiveness in overhead reduction and probability of successful connection set-up.

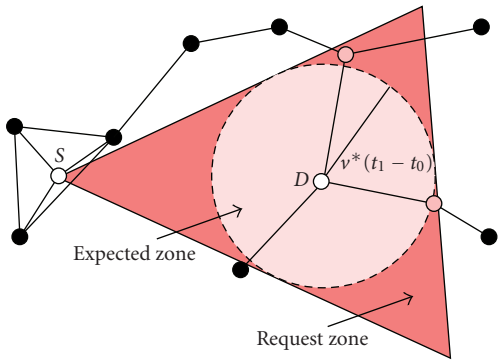

FIGURE 4.8. Route discovery failure due to a conic request zone in the LAR protocol. The nodes that fall within the request zone defined by source S and destination D are represented in grey, while the nodes that are not involved are represented in black. Note that a route discovery procedure generated in S and directed to destination D fails, since none of the grey nodes is in physical connectivity with the source S. A larger request Zone, involving black nodes, would instead lead to a success.

A more advanced trade-off can be obtained by allowing the source node to perform several attempts of route discovery to a given destination and adopting in each attempt an increasingly larger request zone: the result would be a higher percentage of successful connection set-ups, at the price of a higher overhead, obtained as the sum of the routing packets transmitted in each attempt.

This approach neglects, however, the effect on the latency in connection set-up: since each attempt would require a significant amount of time, the interval between connection request and set-up may turn out to be unacceptable in case of delay-sensitive applications.

As in the case of the DREAM protocol, information about the position of the destination is required at the source in order to reduce routing overhead, and thus location information must be disseminated through the network. Oppositely to DREAM, however, in LAR such dissemination is performed by piggybacking location information in all routing packets, without any additional control packet. At the beginning of network operations, terminals will be thus forced to find routes in the absence of location information. In such a situation basic flooding is adopted.

4.3.3. From GPS to UWB positioning

The protocols described in Section 4.3.2 share the common assumption that each terminal retrieves its own location information from GPS. As a consequence, protocols focus on how to disseminate location information, assuming the problem of retrieving it as solved.

The adoption of the UWB technology in place of GPS as the basis for retrieving position information opens new doors to location-based applications (such as indoor deployment), but also poses new challenges.

Since UWB can only provide ranging information, in fact, distributed processing of ranging measurements is required in order to build a network map. The problem of how to build such a map is not trivial, in particular in the case of a pure ad hoc network, where no fixed reference points are available. The self-positioning algorithm (SPA) [23], proposes a solution to this problem. The SPA is composed of two steps. First, each node in the network attempts to build a coordinate system centered on itself, and to determine the position of its neighbors in this system. Second, the node-centered coordinate systems converge to a global network-wide coordinate system.

In the first phase, each node N_i tries to build a coordinate system by

(1) detecting the set of its one-hop neighbors K_{N_i}, by using beacons,
(2) evaluating the set of distances from its neighbors D_{N_i},
(3) broadcasting D_{N_i} and K_{N_i} to its one-hop neighbors.

Since all nodes perform the above procedure, node N_i knows the distance from all its one-hop neighbors, the IDs of its two-hop neighbors, and a subset of the distances between the one-hop neighbors and the two-hop neighbors. This information is used by N_i to build its own coordinate system.

In the second phase, all coordinate systems evolve into a network-wide coordinate system by choosing the same orientation of the x and y axes. Iteratively, pairs of nodes rotate and align their coordinate systems. Using this distributed approach, a network-wide coordinate system is eventually achieved. Note that nodes that are not able to build their own node-centered coordinate system can obtain their position in the network-wide coordinate system if they are in range with three nodes that already received the coordinate system.

UWB-based positioning poses thus additional requirements, with respect to GPS, to location-aided routing protocols.

(i) Determination of a network-wide coordinate system may require a long time. Furthermore, occasional large errors in position information due to lack of connectivity or unfavorable topology may occur. The routing algorithm must be then capable to find routes and establish connection even for incomplete or lacking positioning information.
(ii) Estimation of absolute terminal speeds is in general not available.

The GPSR protocol requires a location service in order to provide the position of the destination to the source, in order to mark the packet with such information. When this location service is not available from start, as in UWB-based positioning, each data packet must be forwarded by means of flooding, with a high routing overhead.

LLR can be adapted to a UWB-based positioning system with minor changes, but the protocol is inherently tailored for scenarios characterized by terminal mobility (in which route stability is the main concern), and does not offer major advantages in terms of power efficiency in networks composed of still or slowly mobile terminals.

In the DREAM protocol, both selection of routes and dissemination of information rely on positioning to work properly: in particular, the proactive dissemination algorithm exploits the capability of a terminal to determine its physical

distance from terminals which are not reachable, to evaluate the validity of an update packet. If location information is not available or subject to errors, both the proactive and reactive parts of the protocol are affected. Furthermore, lack of speed information poses an additional issue to the correct behavior of the protocol.

Oppositely, LAR protocol inherently offers a backup solution when no positioning information is available. In fact, in the case of absence of information regarding the position of the destination, the protocol switches to a basic flooding scheme, resembling a dynamic source routing [24] protocol. In this case the lack of positioning information results in a reduced efficiency of the protocol.

The above considerations led to the choice of adopting LAR as the routing protocol for the integrated power-efficient and location-aware solution presented in the next section.

4.4. Power-efficient and location-aware medium access control design

4.4.1. Introduction

The analysis carried out in Sections 4.2 and 4.3 showed that both distance and position information can be exploited in order to optimize network performance by reducing power consumption and enabling location-aware path selection strategies. In the case of UWB networks, in particular, it was highlighted in Section 4.3 that position information must be derived by means of a dedicated protocol from distance information. The design of a medium access control protocol capable of providing accurate distance information is thus a fundamental step for the development of advanced location-aware strategies in UWB networks.

In this section we will introduce a MAC protocol which foresees a dedicated procedure for the acquisition of distance information, and is furthermore tailored for the characteristics of UWB in a low data rate application scenario: the so-called uncoordinated, wireless, baseborn medium access for UWB communication networks $(\text{UWB})^2$.

4.4.2. The $(\text{UWB})^2$ MAC protocol

As already mentioned in Section 4.2, CSMA is almost universally adopted in MAC for narrowband wireless networks, since it overcomes the drawback of frequent packet collisions experienced in the case of plain Aloha [25]. The CSMA approach, however, shows significant advantages over the Aloha approach under the two following key hypotheses:

(1) simultaneous transmissions of multiple packets result in destructive collisions because of multiuser interference,
(2) high traffic is offered to the network.

Although the above hypotheses are reasonable in a traditional narrowband wireless LAN, we will discuss in the following why this may not longer be the case for a UWB network, in particular when low data rate applications, such as those typical of sensor networks, are considered.

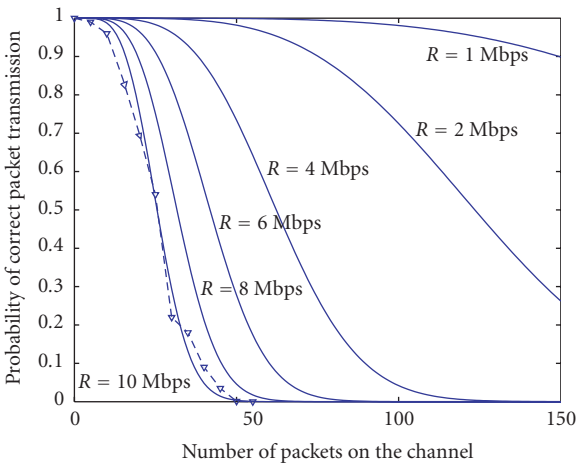

FIGURE 4.9. Probability of successful packet transmission as a function of the number of packets on the channel. Different solid lines correspond to different data rates from 1–10 Mbps. The dashed line shows simulation results in the specific case of $R = 10$ Mbps. Drawn from [26].

We will refer throughout this analysis to the specific case of time-hopping impulse radio UWB (TH-IR-UWB), for which the $(\text{UWB})^2$ was originally designed. The applicability of the ideas exposed here to other UWB variants, such as direct sequence UWB or multiband OFDM UWB remains to be analyzed.

As explained in previous chapters, UWB in its impulse radio version is based on the emission of very short pulses which are modulated in position (pulse position modulation (PPM)) or amplitude (pulse amplitude modulation (PAM)) by the information bits. The duty cycle of emitted signals depends thus on the ratio between the pulse repetition period (PRP), that is, the average interval between two consecutive pulses, and the duration of a pulse. In the case of low data rate transmissions, where bit rates in the order of 100 kbps, or below, can be considered as an acceptable target, this corresponds to signal duty cycles as low as 10^{-6}: the adoption of short pulses offers thus an intrinsic protection from MUI.

Simulation results presented in [26] suggest in fact that in the case of LDR scenarios, the huge bandwidth adopted for transmissions translates in very short, rare pulses, and thus in a low probability of collisions between pulses emitted by different terminals. Under this condition the probability of packet error is negligible even in presence of 100 simultaneous packet transmissions (see Figure 4.9, drawn from [26]).

In the case of PPM, the UWB signal is quasiperiodic due to the rather small PPM shift value which is usually adopted. In order to mitigate energy peaks at multiples of the average pulse repetition frequency, time intervals between UWB pulses must be randomized. This is achieved by adopting TH codes, which introduce additional pseudorandom delays in pulse transmissions. The adoption of the TH principle also offers an additional degree of freedom for multiple access, which

can be obtained by assigning different TH codes to different users, thus adopting a TH code division multiple access (TH-CDMA) scheme.

The above considerations led to the definition of the $(UWB)^2$ protocol.

$(UWB)^2$ is a multichannel MAC protocol. Multichannel CDMA MAC algorithms, commonly referred to as multicode, have been intensively investigated for direct sequence (DS) CDMA networks [27–29]. Note, however, that although in the last years most of the research efforts were focused on DS CDMA, frequency hopping (FH) CDMA and TH-CDMA also provide viable solutions.

The $(UWB)^2$ protocol applies indeed the multicode concept to the specific case of a TH-IR UWB system. $(UWB)^2$ adopts a hybrid scheme based on the combination of a common control channel, provided by a common TH code, with dedicated data channels associated to transmitter TH codes. The adoption of a hybrid scheme can be motivated as follows:

(1) it simplifies the receiver structure, since data transmissions (and corresponding TH codes) are first communicated on the control channel;
(2) it provides a common channel for broadcasting. This is a key property for the operation of protocols in higher layers. Broadcast messages are, for example, required for routing and distributed positioning protocols.

As regards code assignment, a unique association between MAC ID and Transmitter Code can be obtained by adopting the algorithm described in [30] which avoids implementing a distributed code assignment protocol.

The multiple access capability warranted by the TH codes is used by the $(UWB)^2$ protocol in data transmission. The protocol relies for the access to the common channel on the high MUI robustness provided by the processing gain of UWB.

$(UWB)^2$ is designed for distributed networks dedicated to low data rate applications. As a consequence, it does not assume that synchronization between transmitter and receiver is available at the beginning of packet transmission, because of clock drifts in each terminal during inactivity periods. As a consequence, a synchronization trailer long enough to guarantee the requested synchronization probability is added to each packet. The length of the trailer depends on current network conditions, and is provided to the MAC by the synchronization logic.

In the view of allowing the introduction of the location-related functions presented in the previous sections, in particular distributed positioning and location-aware routing, $(UWB)^2$ also exploits the ranging capability offered by UWB. Distance information between transmitter and receiver is in fact collected during control packets exchange.

The procedures adopted in $(UWB)^2$ for transmitting and receiving packets, described in [26], have in fact two main objectives:

(i) to exchange information such as the adopted synchronization trailer, that is, hopping sequence and length,
(ii) to perform ranging. Since no common time reference is available, a two-way handshake is required to collect distance information by estimating the round-trip time of signals in the air.

An example of such procedure is shown in Figure 4.10, where a transmitter Tx and

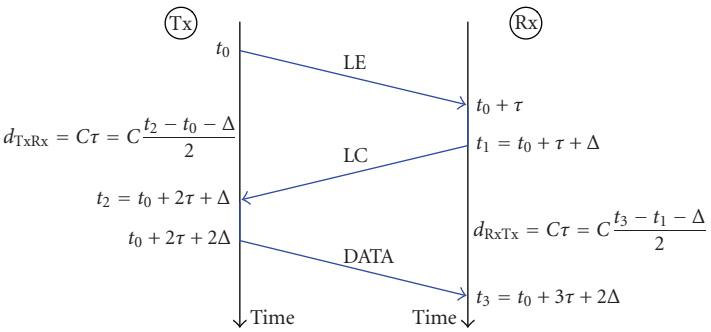

Figure 4.10. Example of two-way ranging procedure.

receiver Rx set up a DATA packet transmission by exchanging a link establishment (LE) packet transmitted on the common code, followed by a link confirm (LC) packet transmitted on the transmitter code of the receiver Rx, and finally by the DATA packet on the transmitter code of transmitter Tx. Thanks to the adoption of a delay Δ known to both Tx and Rx, this handshake allows the determination of the propagation delay τ and thus of the distance Tx–Rx to both the devices involved in the communication.

The ranging procedure made available by $(UWB)^2$ provides the information that is required by the positioning and routing algorithms, and thus enables the adoption of a location-aware, power-efficient path selection strategy, based on the combination of three key components: the $(UWB)^2$ MAC protocol [26], the self-positioning algorithm [23], and the location-aided routing protocol [21].

Performance analysis of such strategy in specific test cases, characterized by different degrees of mobility and different mobility models, will be the subject of the next section.

4.5. Performance analysis in specific test cases

4.5.1. Introduction

In this section we will analyze the performance of the solution presented in the three previous sections of this chapter, composed of the $(UWB)^2$ MAC protocol, of a distributed positioning protocol, and of the LAR routing protocol, combined with a power-aware routing metric. The analysis will focus on two main aspects:

(i) effectiveness of the proposed solution in terms of network lifetime and throughput,

(ii) effect of mobility on system performance.

To this aim, we first address the problem of mobility modeling, by comparing several mobility models and determining their effect on network topology. Next, we define three test cases, each of them with different node mobility characteristics. The behavior of the proposed MAC and routing strategy within each test case is finally studied.

4.5.2. Mobility models

Introducing mobility within the simulated scenarios allows to test the proposed protocols under more realistic conditions. This is particularly true for routing protocols, where performance greatly varies with the topology of the network. Since different mobility models lead to different topologies, however, it is important to select the mobility model that best fits the reference scenario, that is, the typical mobile user that each node in the network represents.

Different mobility models are presented in literature. An interesting subclass is composed by *group* mobility models. This class of models was introduced to emulate particular node behaviors, such as crowds moving towards a common destination or rescue (and similar) squads, where each node is bound to show some degree of mobility similarity with other nodes belonging to the same group.

4.5.2.1. Mobility models in literature

Several mobility models for ad hoc network are proposed in the literature: (1) the Random Mobility or Brownian model [31], with no relation between speed and direction of the node in two subsequent timeslots; (2) the Random Direction model [32], with nodes keeping the same velocity during the whole simulation; (3) the Ko mobility model used for evaluating the LAR protocol [21], according to which the path walked by the node is formed by sections with exponentially distributed length and random direction; (4) the Markovian model [33], which has many moving states and a transit matrix used to determine whether the node should keep or change the current motion direction; (5) the Random Waypoints [24], whose movement paths are composed of segments with random speed, direction, and duration, separated by stand-still periods, simulating pausing intervals; (6) the Inertia [34], in which the node moves along a random direction, with random speed, for a random time, and then decides whether to keep the same movement characteristic for the next movement segment (the node's inertia), or to select a new direction, speed, and duration.

All the previous models are, clearly, inadequate to simulate a group movement, since each node has its own movement pattern, which has no relationship with those exhibited by other nodes; in fact, these models were mainly developed with the aim of testing traffic loads offered to the system, rather than reproducing realistic behaviors.

The need for group mobility models, showing correlated movements among the nodes and offering flexibility for the implementation of particular behaviors, has lead to the design of other models; among these, the exponential correlated random (ECR) model [35]. Other approaches are proposed in literature, in order to bypass the limitation of ECR; those reviewed here are the Reference Point Group Mobility model [36], and the Reference Velocity Group Mobility model [37]; besides these models, a new proposal, the Kerberos mobility model, has been designed and is presented in this section.

An important note on the choice of the mobility model is that, besides models designed with other aims, there exist no "good" or "bad" mobility models: each

model is different. Each mobility model may or may not show a global, mobility-related property, that could in turn be exploited by the system. The capability of taking into account the characteristics of the mobility model during the design phase marks, therefore, the difference among a general/unoptimized system, and a well-designed one.

4.5.2.2. Nongroup mobility models

In order to make a comparison between group and nongroup mobility models, simulations were performed, which adopt two nongroup mobility models: the Random Waypoints [24], and the Inertia [34] models.

In the Random Waypoints model, each node selects a random direction, speed, and movement duration; at the end of the movement, the node stands still for a random time; after the pause time, the node selects a new random direction, speed, and movement duration, and starts walking along the new path. The Random Waypoints model shares a particular mobility pattern with other models adopting the random direction approach: the "density wave" effect, with a greater concentration of the nodes in the central area.

According to the Inertia model, after the end of its movement segment, a node must choose the direction for the next segment. The two alternative choices for the next segment are: (1) the node keeps the current direction, with probability ρ, or (2) the node selects randomly a new direction, with probability $1 - \rho$; the weight of the two alternatives can be different, with a higher probability of keeping the current direction ($\rho > 1/2$). The name Inertia refers indeed to the node property of seldomly changing its direction.

4.5.2.3. Group mobility models

Group mobility models, as previously stated, require that nodes movements are, somehow, related. In particular, two kinds of relations can be imposed on the nodes: (1) the nodes must show some relationship in their directions and/or velocities, or (2) the nodes must be somehow close to each other. Models of the first kind are better suited to simulate the movement of a crowd heading towards a given direction; such models show the *network partition* property, with nodes of a given group emerging by the compound of all network nodes and forming, in vast areas, distinguishable subnetworks of nodes with similar velocities and directions. When, on the contrary, the relationship among group nodes is a distance one, the resulting geographical distribution is characterized by the concentration of the nodes in a limited area; in this case, the nodes usually do not show any relationship in velocity or direction.

Reference point group mobility. The Reference Point Group Mobility (RPGM) model was developed by Hong et al. in [36]. To represent the group mobility behavior of the mobile nodes, the model defines, for each group, a logical *reference point*, whose movement is followed by all nodes in the group. The path the reference point moves along defines the entire group mobility behavior, including

location, speed, direction, acceleration, and so forth. Thus the group trajectory is determined by providing a path for the reference point, with any node in the group randomly placed in the neighborhood of its reference point.

Once next position (x, y) of the reference point is determined (the path of the reference point can be selected with any nongroup-oriented mobility model), each other node position is calculated adding a random motion vector $\overrightarrow{\mathrm{RM}}$ to (x, y). The length and direction of this module can be determined through any policy; the authors of the model suggest a uniform distribution within a given range from the reference point for the length, and a uniform distribution between 0° and 360° for the direction.

Main RPGM characteristic is that the groups are characterized by *physical proximity*, that is, all the nodes are close to the reference point. Obviously, the way this physical proximity translates itself into actual distribution of the nodes within deployment area depends on the values actually used for the distribution of the length of the $\overrightarrow{\mathrm{RM}}$ random motion vector.

One drawback of the direct implementation of such a mobility model is that it does not implement a check on the maximum/minimum node velocity, because of the position-based approach. Since the resulting position of a node is calculated as the sum of two vectors, the reference point position (x, y) and the random motion vector $\overrightarrow{\mathrm{RM}}$, it is possible, for given values of these two parameters, that the node should have a speed higher than its maximum; a similar case holds for the minimum velocity.

About the resultant distribution of the nodes, the adoption of this approach typically distributes the nodes inside a circular area centered around the reference point: the wider the distance from the reference point, the more vast the area in which the nodes are distributed, the looser the bonds between the nodes in the group.

Reference velocity group mobility. The Reference Velocity Group Mobility (RVGM) model has been presented in [37] as an evolution of RPGM. The fundamental concept proposed is that movement similarity is a more fundamental characteristic for group mobility than physical proximity; thus nodes being part of the same group should show close velocities and directions, rather than physical proximity.

Each group, therefore, is characterized by a *group velocity*. The nodes that are members of the group have velocities close to the characteristic group velocity, with slight deviations. Hence, the characteristic group velocity is also the mean group velocity. The distributions of both the group velocity and the velocity deviation can be of any type, in order to model the various possible mobility patterns.

Main characteristic for RVGM is that, in a scenario with infinite dimensions area, the network will eventually incur a complete partition, with each subnetwork corresponding to a group; in a finite-dimensions area this behavior is not fully developed, because of the presence of area boundaries, but is latently present in the movement patterns.

The main reason why RVGM was evolved from RPGM is that the former model is better suited when dealing with mobility or partition prediction purposes; representing the nodes by their physical coordinates, RPGM does not allow to easily detect group movement patterns and the trend in network topology changes.

About the resultant distribution of the nodes, the adoption of this approach typically distributes the nodes to cover the whole area with nodes with similar velocities and directions.

Kerberos mobility model. The basic concept in Kerberos mobility model is that each node in a group is allowed to move around freely, provided it keeps contact with the other nodes in its group.

This basic concept can be translated into the adoption of a condition of physical proximity between the given node and the other nodes of its group: when this condition is met, the node moves according to a nongroup mobility model (e.g., Inertia), while, when the node is far from its fellows, it is obliged to move closer to them.

The difference between *Kerberos* and RPGM models is that, in the latter, each node follows the reference point and, for this reason, is close to its fellows; this is how physical proximity arises in RPGM. In the *Kerberos* model, on the contrary, it is explicitly required for each node to monitor its distance from its fellows, and to stay close to them.

Kerberos requires that, after each mobility update, each node checks how many nodes of its own group it is connected to: this set of nodes forms the *fellowship* of the node. Two nodes in the same fellowship can be connected through a direct link when the destination node is within range, or through relaying of intermediate nodes, all belonging to the group, which are at the same time, members of the fellowship. If the number of nodes in the fellowship is greater than half the number of nodes forming the group, the node is allowed to move freely; otherwise, the node is separated by the main chunk of group (if any exists), and is compelled to move towards the closest group node not belonging to its fellowship.

Notes on group mobility models. The different approaches adopted by RPGM, RVGM, and *Kerberos*, are characterized by different and characterizing patterns in the disposition of the nodes belonging to a single group. In the case of RPGM, since the nodes are bound to stay within a given range from the same point, each group forms a globular pattern, centered around the reference point; this usually means a high level of connectivity between the nodes in the group. On the other hand, in the case of Kerberos, there are higher probabilities for patterns in which the nodes form a chain or a line; this happens because, once connectivity requirements are verified, each node is allowed to move freely, and therefore even further from the group itself.

However, *Kerberos* mobility model is closer to RPGM than to RVGM; it is possible, changing the connectivity requirement into a maximum distance from a chosen node (the "group leader"), to obtain mobility patterns very similar to RPGM.

4.5.2.4. Mobility model metrics and test scenario

In order to analyze the impact of different mobility models on the performance of a routing protocol, it is appropriate to simulate the mobile network and to test the protocol. It is also possible, however, to analyze the topological characteristics of networks adopting the different mobile models. These topological properties have, obviously, a deep impact on routing performance: for example, the average number of nodes within range will affect the route availability between any two given nodes, so that those mobility models that scatter the nodes over the whole simulation area are expected to have a lower route availability than those mobility models which concentrate the nodes in smaller areas.

In [38], the authors provide a number of mobility model metrics, to be applied to the evaluation of mobility models impact on routing performance.

(i) *Number of link changes*: the number of transitions from the state "connected" to the state "disconnected" and vice versa, for the link between any pair of nodes in the network. Its average over the number of links in the network is the *average number of link changes*, and is calculated separately for links between nodes of the same group and for links between nodes of different groups.

(ii) *Link duration*: the average duration of the link between two nodes, that is, the average time that two nodes remain continuously within range. Its average over the number of links in the network is the *average link duration*, and is calculated separately for links between nodes of the same group and for links between nodes of different groups.

(iii) *Path availability*: the fraction of time during which a path of links within transmission range is present between two nodes in the network. Its average over the number of links in the network is the *average path availability*, and is calculated separately for paths between nodes of the same group and for paths between nodes of different groups.

We propose an additional metric, in order to evaluate the probability that any two given nodes are within range.

(iv) *Link availability*: the percentage of time during which link between two given nodes is active, that is, the two links are within transmission range. Its average over the number of links in the network is the *average link availability*, and is calculated separately for links between nodes of the same group and for links between nodes of different groups.

The simulation scenario consisted in a network of 16 nodes, divided into 4 groups of 4 nodes each. The deployment area was a square with 100 m sides, with transmission range equal to 20 m. The simulations have been performed with different values for node maximum velocity, from 1 m/s to 10 m/s, and lasted 2 hours. As regards the mobility model parameters, RPGM $\overrightarrow{\text{RM}}$ maximum length has been set to 30 m; *Kerberos* simulations were performed adopting Inertia as mobility model when a node is free to move.

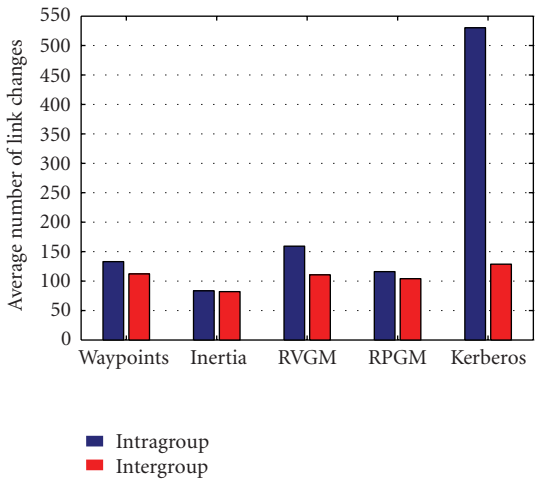

FIGURE 4.11. Average number of link changes for different mobility models.

4.5.2.5. Mobility models simulation results

Number of link changes. Figure 4.11 shows the average number of link changes for all the mobility models investigated, and for both intergroup and intragroup cases; the values are expressed in average number of changes per minute.

Kerberos shows a high number of changes in links between nodes belonging to the same group. This is the result of two behaviors:

(i) when a node is connected to the group, it is allowed to move freely, without any constraint based on the positions of the other nodes of its group. This means that nodes in the same, connected, group may be headed along different directions; the result is a high number of link breaks or set-ups;

(ii) when a node detects that its group is disconnected, it is compelled to move towards the other nodes in its group: the result is the set-up of one or more links with group nodes.

The second most notable result in Figure 4.11 is that the difference between intra and intergroup links is higher in group mobility models than in nongroup ones: a foreseeable effect of the group bound observed by the former models, since the latter do not make distinction between group and nongroup mobility models.

In the evaluation of a routing protocol, this mobility model metrics can give an estimation of the control traffic that the protocol produces each time a link is established or is broken: this includes control traffic to update network topology knowledge, alternative route checking, and so forth.

Link duration. The average link duration of each mobility model is shown in Figure 4.12, for intra and intergroup links; the values are expressed in seconds.

This mobility model metrics tells apart the group by the nongroup mobility models: the former show a high difference in average link duration between intra

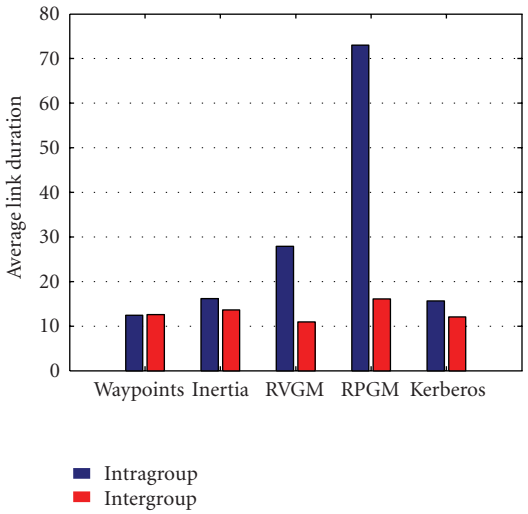

FIGURE 4.12. Average link duration, in seconds, for different mobility models.

and intergroup links. In the case of RVGM, the higher duration for intragroup links is derived from the circumstance that, if two nodes form an intragroup link, they have a large probability to have similar velocities and directions. In the case of *Kerberos* and, above all, RPGM, the *physical proximity* property is what make the link more stable: the nodes forming the intragroup link are very likely to remain close in the future. *Kerberos* shows the lowest average link duration among group mobility models, because group nodes neither share similar velocities and directions (as in RVGM), nor are compelled to stay within a maximum distance from a common point; however, the constraint on group connectivity allows a node to break its intragroup link only if it has, at least, another intragroup link, otherwise it will depart from its group. Between the nongroup mobility models, Inertia has a slightly higher average link duration than Random Waypoints. This is due to the fact that the two nodes composing the link will be more likely to keep on moving in the same direction if they are modeled with Inertia, rather than with Random Waypoints.

This metric shows different information, with respect to the *number of link changes*, because it measures the length of a connection *after* it has been established, while the other metric measures the frequency of link establishment. Taking RPGM and Random Waypoints as examples, these models have *average number of link changes* values that are very close, but their values for *average link duration* are far apart: this happens because both establish links with the same frequency, but those exhibited by RPGM are built by nodes that are compelled to stay close for a long time, while in Random Waypoints the nodes usually break the link shortly after they build it.

Regarding routing, this metric gives an estimation of the average reliability of a link. This parameter impacts the procedures that must select the most reliable

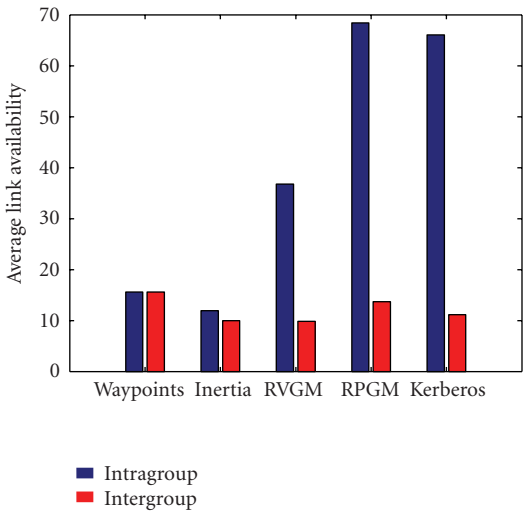

FIGURE 4.13. Average link availability, in percentage of time, for different mobility models.

route among several possible: it is clear that a route mainly composed of intragroup links will be much more reliable than another mainly composed of intergroup links—under the hypothesis of the adoption of a group mobility model.

Link availability. Figure 4.13 shows the results for the *average link availability* metric, expressed in percentage of time in which a given link is established.

It is clear how group and nongroup mobility models greatly differentiate themselves, as regards the availability of a link. Nongroup mobility models do not distinguish between intra and intergroup links; also, the percentage of availability of a link is quite low, since the link is formed by nodes that move in a completely independent fashion. Group mobility models, on the contrary, highly privilege intragroup links over the others: the similarity in the movement of the RVGM, the physical proximity requirement of the RPGM, and the group connectivity constraint of Kerberos, all result in a more probable presence of a link between nodes of the same group; on the other side, nodes from different groups are compelled to have different movement behaviors, ending in less frequent links.

Through the average link availability mobility model metrics, it is possible to determine the expected number of links a node has. The connectivity of a node is an important parameter for a routing protocol: it can be used to calculate the expected load on each link, to estimate the capability of performing relaying for other nodes traffic.

Path availability. Simulation results for the average path availability are shown in Figure 4.14. For each possible pair of nodes in the network, simulations have been performed to determine the probability of existence of a path, composed of one or more links. The intragroup paths are those in which the starting and the ending nodes of the path are members of the same group.

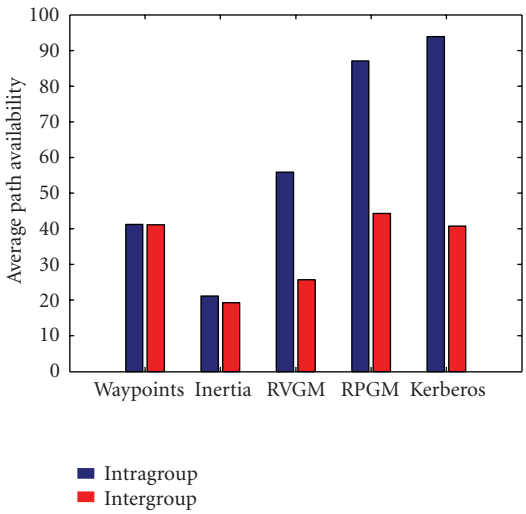

FIGURE 4.14. Average path availability, in percentage of paths, for different mobility models.

Once again, it is possible to tell apart the group from the nongroup mobility models, because of the difference between inter and intragroup values, and of the value of the latter case. As expected, nongroup mobility models show no difference between intra and intergroup paths, since all the nodes are moved independently from their group fellows. The difference between Random Waypoints and Inertia is given by the fact that Random Waypoints scatters the nodes all over the simulation area: the probability of network partition (which implies a dramatic decrease in average path availability values) is therefore high, but is lower than in Inertia, where some nodes tend to be separated by the remaining network for long times. As regards the group mobility models, note that

(i) *Kerberos* shows the highest average path availability for intragroup paths. With the adoption of this mobility model, the network shows highly connected groups that span over wide areas. intragroup links are less frequent, but they allow a large number of paths to exist;

(ii) RPGM shows a lower *average path availability* for intragroup paths, but higher than *Kerberos* for intergroup ones. Physical proximity requirement allows for a few group partitions, but the groups cover wider areas than *Kerberos*, thus increasing the probability of an intergroup link, which sustains a number of intergroup paths;

(iii) RVGM results are due to the aforementioned property of similarity in movements, rather than in physical proximity, for the nodes of a group. The resulting values are similar to an average between the nongroup and the remaining group mobility models.

As one could expect, the *path availability* mobility model metrics is the one with the most direct impact on routing performance. It, in fact, directly translates in the probability of existence of a path between any two given nodes. Low path

probabilities could require routing strategies that invest few resources in path discovery, since there is a higher possibility that this procedure ends in a failure.

Simulation results show that different mobility models have quite different properties, as regards the *path availability*: comparing, for example, the Random Waypoints and the RVGM, the latter shows a higher availability for intragroup path than the former, while the opposite holds for intergroup paths. The actual answer on the global path availability depends on the ratio between intra and intergroup links in the actual network, that is, on the ratio between group and network cardinality. It is important to underline, however, that in those scenarios in which group mobility models are more suited, there is, typically, also a traffic relationship between group nodes; that is to say, a node will be more likely to communicate with nodes of the same group, rather than nodes of other groups: the effect of this property is that the actual percentage of routes found depends also on the ratio between intra and intergroup path, weighted with the ratio between intra and intergroup communications.

4.5.3. Test cases

We will investigate three different test cases which are characterized by the following common scenario: a network of N terminals deployed in initial random positions. Each terminal periodically generates a connection request to a random destination, following a Poisson distribution with average time λ between two subsequent requests. Each connection request is characterized by a constant bit rate R_c and a total number of bits to be transferred which is randomly selected in the interval [1, MaxDimBit]. Each terminal is furthermore characterized by a total amount of energy E_{TOT}, which is reduced after each packet transmission or reception based on the following energy model [39]:

$$\begin{aligned} E_{\text{TX}} &= E_{\text{start}} + L \cdot \left(E_{\text{Tx-bit-rate}}(R_b) + E_{\text{Tx-bit-prop}}(R_b) \cdot d^{\alpha}\right), \\ E_{\text{RX}} &= E - \text{start} + L \cdot \left(E_{\text{Rx-bit-fixed}} + E_{\text{Rx-bit-rate}}(R_b)\right), \end{aligned} \tag{4.8}$$

where L is the length of the packet.

Note that, although this model is not specific for UWB, it addresses a class of devices which is close, in terms of achieved bit rate and complexity, to the UWB devices foreseen for low bit rate networks.

All test cases share furthermore the settings adopted for positioning and routing protocols, in particular data and control packet sizes. Finally, the initial amount of energy E_{TOT} for each node is the same in all the three test cases, although its actual value depends on the transmission range.

The three test cases differ however in the mobility pattern of the terminals.

(i) Test case 1: network of still terminals in random positions.

(ii) Test case 2: network of mobile terminals in initial random positions, following the *inertia* mobility model.

(iii) Test case 3: network of mobile terminals in initial random positions, following the *Kerberos* mobility model.

The initial selection of terminal positions can heavily influence the network performance, in particular in the scenario considered in test case 1: as a consequence, in order to determine the average performance of the strategies, N_{runs} simulation runs were executed, with terminals deployed in random positions in an area of A_{side}xA_{side} m^2. Given a set of terminals in random coordinates, however, network topology is also determined by the transmission range, which influences the network connectivity. For this reason, tests were executed for three different transmission ranges, $R_{\text{TX-low}}$, $R_{\text{TX-med}}$, and $R_{\text{TX-high}}$, leading to low, medium, and high network connectivity, respectively. The common settings to all tests cases are presented in Table 4.1, while Table 4.2 presents the initial energy per node for each transmission range.

In each test case four different strategies were compared, which combine in different ways the two key components of the proposed solution: location-aided routing algorithm and power-aware routing metric. The distinction between the routing protocol and the routing metric allows in fact to evaluate the effect of each of the two components on system performance.

The four strategies are as follows:

(i) dynamic source routing with hop minimization (DSR + hop),
(ii) dynamic source routing with cost function minimization (DSR + cost),
(iii) location-aided routing with hop minimization (LAR + hop),
(iv) location-aided routing with cost minimization (LAR + cost).

As previously stated, the performance of each strategy was analyzed under conditions of limited available energy taking into account two aspects: long-term system performance, that is, how long the network is alive and thus capable of transferring data, and short-term system performance, that is, how network behaves during its life. The following routing strategy metrics were selected to measure long-term and short-term performance.

(i) Number of found connections.
(ii) Number of DATA packets delivered to destination.
(iii) Percentage of found connections.
(iv) End-to-end throughput for DATA packets.

A found connection is defined as a connection in which the destination terminal, following the reception of a routerequest (RRQ) packet, is able to send back to the source terminal a routereply (RRP) packet. The total number of found connections is a good indicator of the long-term behavior of the network since, given the constant rate λ of connection requests generation, a longer network lifetime will lead to a higher number of requested Connections and, eventually, of found connections. Since each connection, however, is set up in order to transfer DATA packets, we also consider the total number of DATA packets transferred during network lifetime, in order to determine which is the impact of each strategy at packet level.

The percentage of found connections, oppositely, allows to measure the network behavior in the short-term, by measuring how good each connection is served

Table 4.1. Simulation settings common to all test cases.

Parameter	Value
R_b	1 Mbps
R_c	50 kbps
λ	50 s
MaxDimBit	1 Mbit
N	20
α	4
E_{start}	$2.76 \cdot 10^{-5}$ J
$E_{\text{Tx-bit-rate}}$	$3.25 \cdot 10^{-7}$ J
$E_{\text{Tx-bit-prop}}$	$1.25 \cdot 10^{-11}$ J
$E_{\text{Rx-bit-fixed}}$	$1.13 \cdot 10^{-7}$ J
$E_{\text{Rx-bit-rate}}$	$2.79 \cdot 10^{-7}$ J
A_{dim}	80 m
$R_{\text{TX-low}}$	20 m
$R_{\text{TX-med}}$	40 m
$R_{\text{TX-high}}$	60 m
RRQ size	760 bit
RRP size	760 bit
DATA size	5000 bit
ACKDATA size	250 bit
RRC size	250 bit

by the network. The end-to-end throughput for DATA packets provides the same kind of short-term information at the packet level.

Note that the evaluation of the short-term performance behavior is fundamental in the comparison of the different strategies since, from a theoretical viewpoint, a strategy could lead to an overall high number of found connections, thanks to a long lifetime which allows for a high number of requested connections, but at the price of a low percentage of found connections.

4.5.3.1. Test case 1

This test case analyzed a scenario with terminals in fixed locations, which are unknown at start of operations.

Since terminals could not move, network topology only changed when a terminal ran out of energy: as a consequence, in this scenario, performance was significantly affected by the transmission range. Furthermore, as we will see, different strategies were affected in a different way by variations in network connectivity.

Figure 4.15 presents the number of found connections under conditions of low network connectivity. The LAR + hops strategy achieves the highest number of found connections, but the performance of the four strategies is quite similar, since the main factor in determining network behavior is the degree of network connectivity. This conclusion is also supported by the other indicators, that is, the

Table 4.2. Initial energy amount per node for each of the three transmission ranges considered in simulations.

Range	Energy E_{TOT}
$R_{\text{TX-low}}$	25 J
$R_{\text{TX-med}}$	250 J
$R_{\text{TX-high}}$	800 J

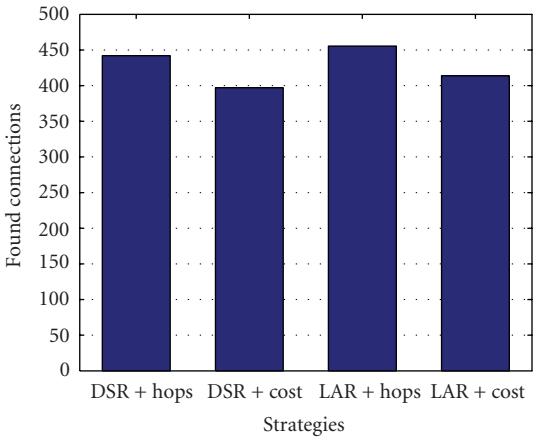

Figure 4.15. Found connections for test case 1 with $R_{\text{TX-low}}$.

number of DATA packets, the percentage of found connections, and the DATA throughput, presented in Figures 4.16, 4.17, and 4.18.

Interestingly, the adoption of the power-aware cost function in place of number of hops leads to slightly worse performance in terms of number of found connections and of delivered DATA packets, indicating a shorter network lifetime. This can be explained by observing that when the transmission range is low, the energy costs in transmission and reception which are not related to propagation are more relevant in the overall energy consumption, thus eliminating the advantage of increasing the number of hops per connection. As an example, let us consider the case of the transmission of a DATA packet over a distance $d = 10$ m. The overall energy cost of the transmission $(E_{\text{TX}} + E_{\text{RX}})$, based on the model in (4.8) is given by

$$\begin{aligned} E &= 2 \cdot E_{\text{start}} + L \cdot \left(E_{\text{Rx-bit-fixed}} + E_{\text{Rx-bit-rate}}(R_b) + E_{\text{Tx-bit-rate}}(R_b)\right) \\ &\quad + L \cdot \left(E_{\text{Tx-bit-prop}}(R_b) \cdot d^{\alpha}\right) \\ &= 5.52 \cdot 10^{-5} + 5000 \cdot \left(7.17 \cdot 10^{-7}\right) + 5000 \cdot \left(1.25 \cdot 10^{-7}\right) \\ &= 4.27 \cdot 10^{-3}\ \text{J}. \end{aligned} \tag{4.9}$$

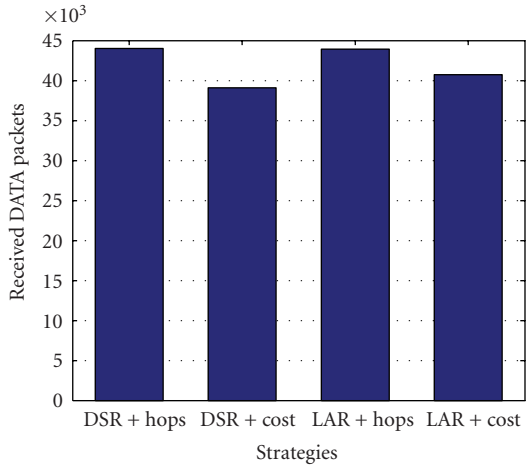

FIGURE 4.16. Received DATA packets for test case 1 with $R_{\text{TX-low}}$.

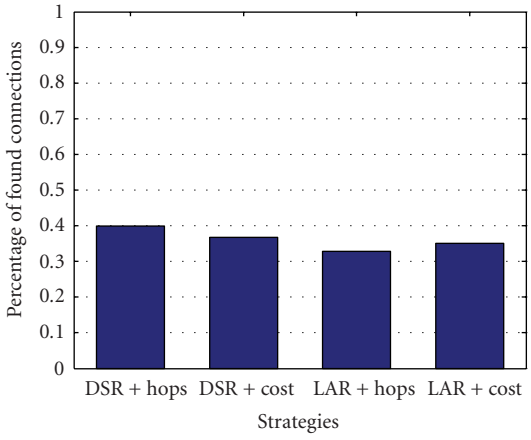

FIGURE 4.17. Percentage of found connections for test case 1 with $R_{\text{TX-low}}$.

If two hops over $d = 5$ m are used in place of the single hop, we get the overall cost:

$$\begin{aligned} E &= 4 \cdot E_{\text{start}} + 2 \cdot L \cdot \left(E_{\text{Rx-bit-fixed}} + E_{\text{Rx-bit-rate}}(R_b) + E_{\text{Tx-bit-rate}}(R_b)\right) \\ &\quad + 2 \cdot L \cdot \left(E_{\text{Tx-bit-prop}}(R_b) \cdot d^{\alpha}\right) \\ &= 1.104 \cdot 10^{-4} + 2 \cdot 5000 \cdot \left(7.17 \cdot 10^{-7}\right) + 2 \cdot 5000 \cdot \left(7.8125 \cdot 10^{-9}\right) \\ &= 7.35 \cdot 10^{-3}\,\text{J}, \end{aligned} \tag{4.10}$$

which is higher than the cost of the single hop at longer distance.

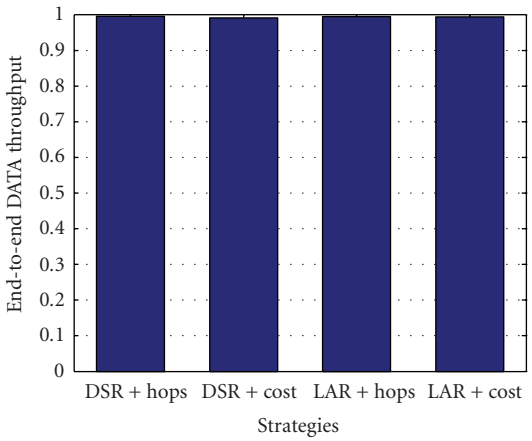

FIGURE 4.18. End-to-end DATA throughput for test case 1 with $R_{\text{TX-low}}$.

As far as routing algorithms are concerned, results show that, independently of the selected routing metric, the performance increase guaranteed by the adoption of LAR is far from dramatic. This can be explained by observing that the main advantage of LAR is the reduction of overhead by avoiding broadcast packets being forwarded in wrong directions. Under the condition of low connectivity, the number of broadcast packets is inherently limited by the low number of links available in the network, thus achieving the same effect pursued by LAR, at the price of a low percentage of found connections.

If we consider a higher transmission range, on the other hand, the above considerations are no longer valid, and we would thus expect an advantage in terms of network lifetime by adopting the power-aware cost function and the LAR protocol.

The results for transmission range set to $R_{\text{TX-med}}$ are presented in Figures 4.19 and 4.20 for found connections and delivered number of DATA packets, respectively. Results show that in both cases the LAR + cost strategy leads to the best performance, increasing by a factor of 2 both the number of found connections and the number of DATA packets. Furthermore, the adoption of the power-aware cost function leads to better performance independently of the selected routing algorithm.

Noticeably, also the short-term performance indicators, presented in Figures 4.21 and 4.22, are improved by the adoption of LAR routing and power-aware cost function.

The advantage of the LAR + cost solution is confirmed when the $R_{\text{TX-high}}$ transmission range is considered: Figure 4.23 shows that the number of found connections is increased by a factor of 2 by adopting the LAR + cost strategy.

The increase in found connections obtained by adopting the cost function is around 10%, as it was in the case of transmission range set to $R_{\text{TX-med}}$. This is coherent with the fact that, given the number of terminals and the size adopted in the

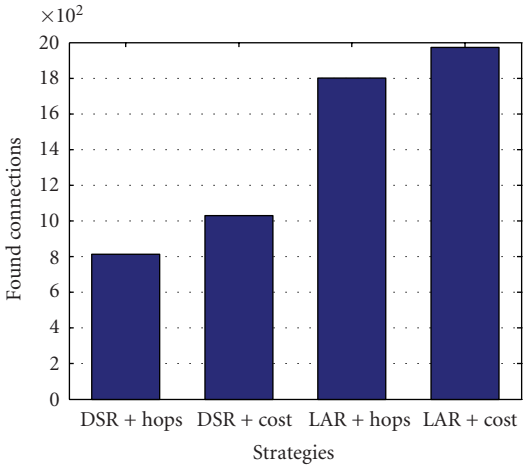

FIGURE 4.19. Found connections for test case 1 with $R_{\text{TX-med}}$.

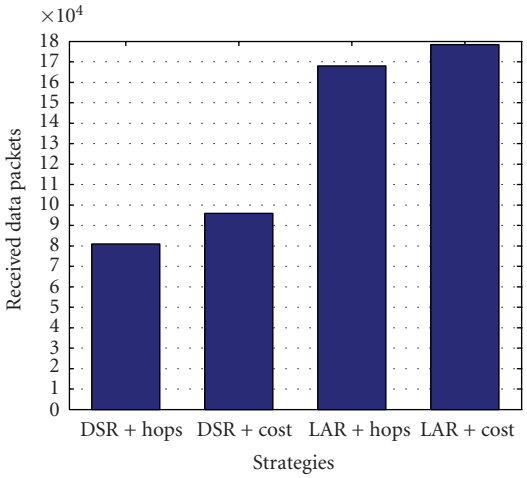

FIGURE 4.20. Received DATA packets for test case 1 with $R_{\text{TX-med}}$.

test cases, the average distance between two terminals is 40 m. As a consequence, the maximum advantage from the cost function is obtained when the transmission range reaches 40 m, that is, for $R_{\text{TX-med}}$. Further increases of the transmission range do not lead to any additional gain, since the energy saving obtained with the cost function is not related to the maximum transmission distance reachable by a terminal, but to the actual distance between terminals.

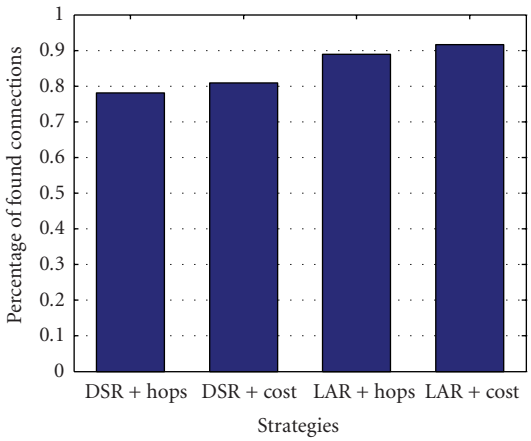

FIGURE 4.21. Percentage of found connections for test case 1 with $R_{\text{TX-med}}$.

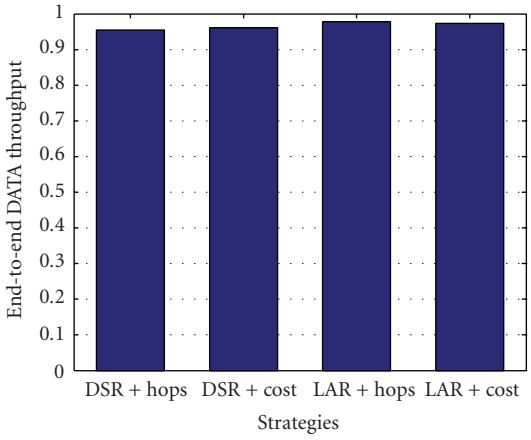

FIGURE 4.22. End-to-end DATA throughput for test case 1 with $R_{\text{TX-med}}$.

TABLE 4.3. Inertia mobility settings for test case 2.

Parameter	Value
V_{MAX}	6 m/s
ρ	0.5

4.5.3.2. Test case 2

This test case analyzed a scenario in which terminals were randomly deployed, and then moved following the *Inertia* mobility model, with mobility settings presented in Table 4.3.

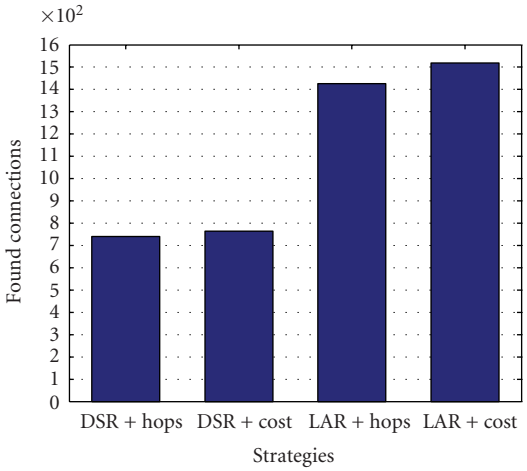

FIGURE 4.23. Found connections for test case 1 with $R_{\text{TX-high}}$.

The movement capability of terminals had a strong impact on network behavior, in particular in scenarios where network connectivity was more affected by mobility. This is the case when low transmission range $R_{\text{TX-low}}$ is considered: the introduction of mobility led indeed to results which are completely different from those obtained in test case 1 with still terminals.

Figure 4.24 shows the number of found connections in this scenario. It is evident that in this case, the introduction of the LAR algorithm increases network performance also with transmission range set to $R_{\text{TX-low}}$: in particular, the comparison between DSR + hops and LAR + hops shows an increase of about 20% in the number of found connections.

Note that in conditions of low connectivity and mobility, the adoption of cost instead of hops does not bring any advantage. As already observed for test case 1, in fact, the low transmission range leads in most cases to a higher energy consumption when moving from a single hop to two or more hops. In presence of mobility, furthermore, the cost-based strategies suffer from an additional increase of energy spent in signaling connection failures due to mobility by means of broadcast RRC packets. In fact, since the cost function leads to a higher average number of hops, as shown in Figure 4.25, the paths selected with this metric are more subject to failures caused by terminal mobility.

If we consider a transmission range set to $R_{\text{TX-med}}$, we observe, on the contrary, that the adoption of the cost function significantly increases the number of found connections. In this condition the best solution is thus the LAR + cost strategy, as shown in Figure 4.26.

This conclusion is also confirmed by the other long-term parameter, that is, the number of received DATA packets, shown in Figure 4.27.

The short-term parameters confirm that LAR + cost is overall the best choice: the throughput, presented in Figure 4.28, is almost identical for both LAR-based

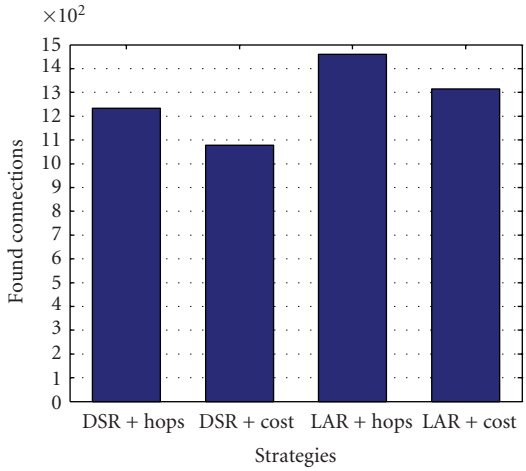

FIGURE 4.24. Found connections for test case 2 with $R_{\text{TX-low}}$.

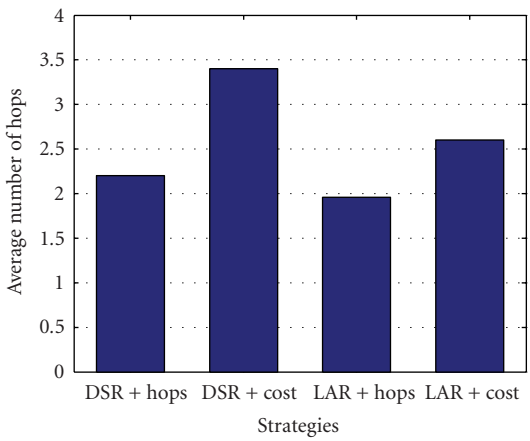

FIGURE 4.25. Average number of hops for test case 2 with $R_{\text{TX-low}}$.

strategies, and the same is true for the percentage of found connections, in Figure 4.29.

The advantage obtained by the LAR-based strategies on the short-term parameters is also influenced by the longer network lifetime. As an example, Figure 4.30 shows the evolution of the percentage of found connections over time for a single simulation run. The plot shows that the difference in the average value (Figure 4.29) is due to the capability of LAR-based strategies to keep the network in steady state for a longer period of time.

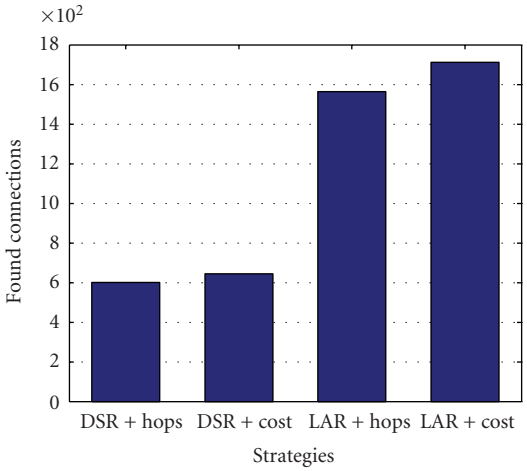

FIGURE 4.26. Found connections for test case 2 with $R_{\text{TX-med}}$.

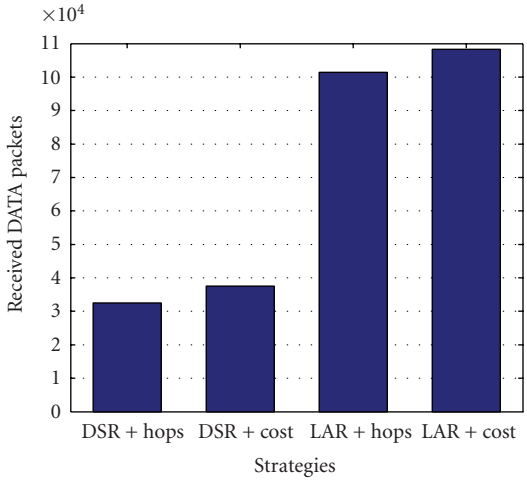

FIGURE 4.27. Received DATA packets for test case 2 with $R_{\text{TX-med}}$.

The case of high network connectivity confirms LAR-based strategies as the most efficient ones (see Figure 4.31), but in this case the performance gain achieved with the cost function is not significant.

This can be explained by considering that, as already observed for test case 1, an increase of transmission range over the average distance between two terminals does not bring any additional advantage for cost-based strategies. At the same time, the negative effect of connection failures due to mobility increases with transmission range, since RRC packets are transmitted at maximum power; this means that each RRC packet will consume higher energy, and that each packet will

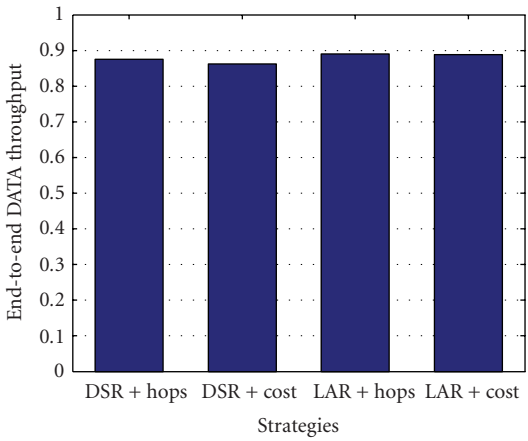

FIGURE 4.28. End-to-end DATA throughput for test case 2 with $R_{\text{TX-med}}$.

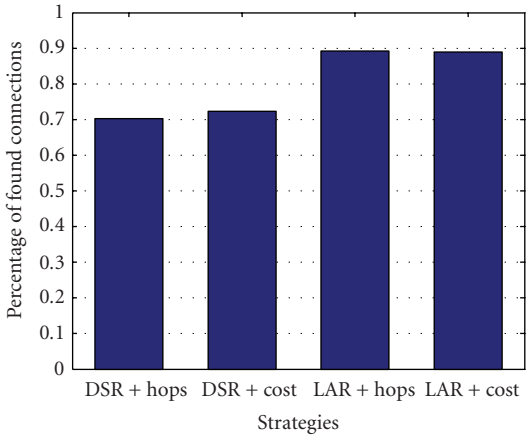

FIGURE 4.29. Percentage of found connections for test case 2 with $R_{\text{TX-med}}$.

be forwarded for a higher number of times, thanks to the higher network connectivity. As a consequence, the efficiency of cost-based strategies is reduced.

4.5.3.3. Test case 3

This test case analyzed a scenario in which terminals were randomly deployed, and then moved following the Kerberos mobility model, with mobility settings presented in Table 4.4.

The analysis of the performance of the four strategies in the case of the *Kerberos* mobility model is somewhat more difficult than in the other cases; the peculiar spatial distribution of terminals generated by this group mobility model must

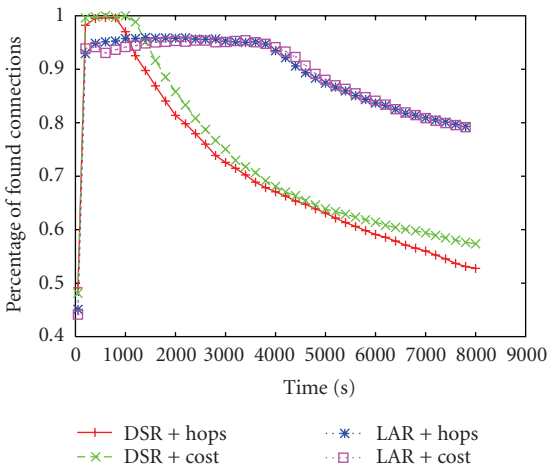

FIGURE 4.30. Percentage of found connections for test case 2 with $R_{\text{TX-med}}$ (single run).

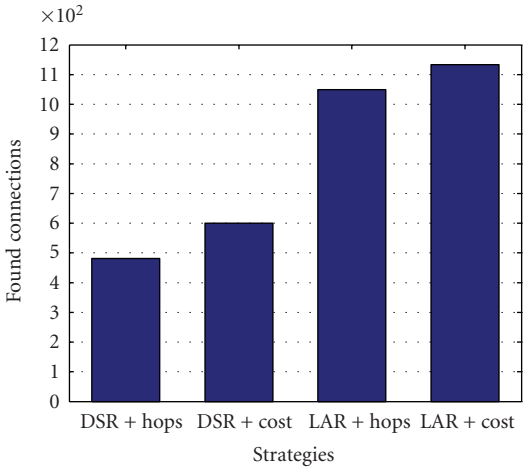

FIGURE 4.31. Found connections for test case 2 with $R_{\text{TX-high}}$.

be taken into account for a correct evaluation of the simulation results, and the distinction between intra and intergroup network topology properties must be considered.

The global number of found connections in the case of low transmission range is presented in Figure 4.32. The figure shows that, as much as in the case of test case 2, the presence of mobility allows for a higher network connectivity and thus leads to better results than in the case of still terminals. For all the four strategies, however, performance is significantly worse than in the case of the *Inertia* mobility model, as confirmed by the number of received DATA packets, presented in Figure 4.33.

Table 4.4. Kerberos mobility settings for test case 3.

Parameter	Value
V_{MAX}	6 m/s
Kerberos range	$R_{TX} - V_{MAX}/3$ m
N_{neigh}	4

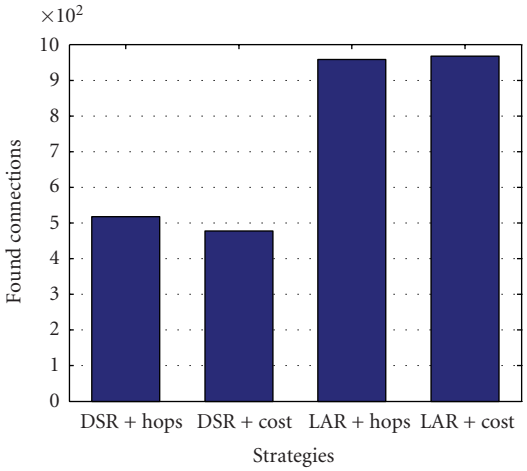

Figure 4.32. Found connections for test case 3 with $R_{TX\text{-}low}$.

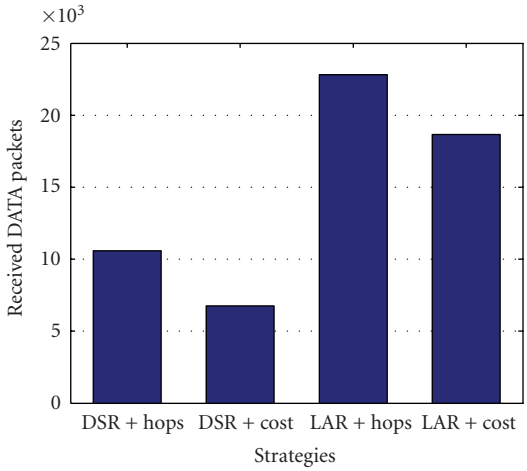

Figure 4.33. Received DATA packets for test case 3 with $R_{TX\text{-}low}$.

This is due to the fact that the *Kerberos* model does not lead to a uniform distribution of nodes, but creates groups of nodes. Figure 4.34 shows in fact the

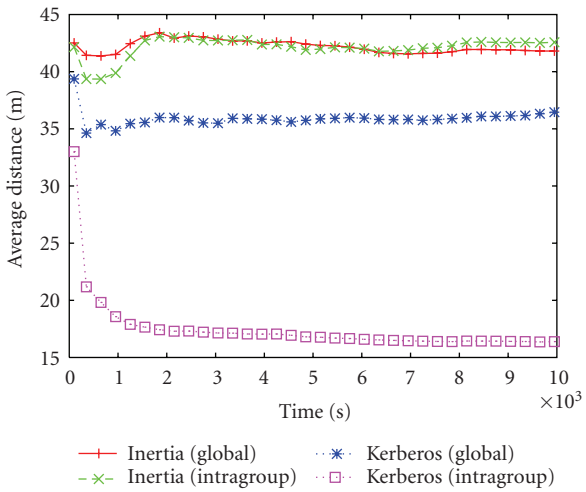

FIGURE 4.34. Average distances between two nodes in the network (global) and between two nodes in the same group (intragroup) for Inertia and Kerberos, the latter with Kerberos range = $R_{\text{TX-low}} - V_{\text{MAX}}/3$ m.

average distance between two nodes in the network and the average distance between two nodes in the same group for both *Inertia* and *Kerberos*. As one could expect, the two distances are similar in the case of *Inertia*, since no special group behavior is defined in the model. Oppositely, in the case of *Kerberos* a large difference between the two values can be observed.

The lower performance observed for all strategies in test case 3 is due to the higher connectivity which characterizes the *Kerberos* model. Results in Section 4.5.2.5 show in fact that this mobility model guarantees a higher average connectivity than the *Inertia* model; this translates in a higher number of forwarded RRQ packets, and thus a shorter network lifetime. The higher connectivity, on the other hand, leads to a better performance the short term, as presented in Figure 4.35, showing the percentage of found connections for the first 5000 seconds of a simulation run for the same strategy (DSR + hops) with the two mobility models.

The higher network connectivity also determines in this test case a larger performance gap between DSR and LAR-based strategies. The average increase in number of found connections obtained by switching to LAR is in fact in the order of 100% for test case 3, whereas it was only around 20% in test case 2 with the same settings (see Figure 4.24).

Note that the cost-based strategies are penalized by both the short transmission range and the negative effect of mobility on route duration, and achieve thus lower performance than the hop-based strategies, similarly to what was observed in test cases 1 and 2.

The results with medium transmission range $R_{\text{TX-med}}$, presented in Figures 4.36 and 4.37, confirm that the adoption of the LAR strategies increases the network lifetime. In this case too, the adoption of the cost-based metric has a negative

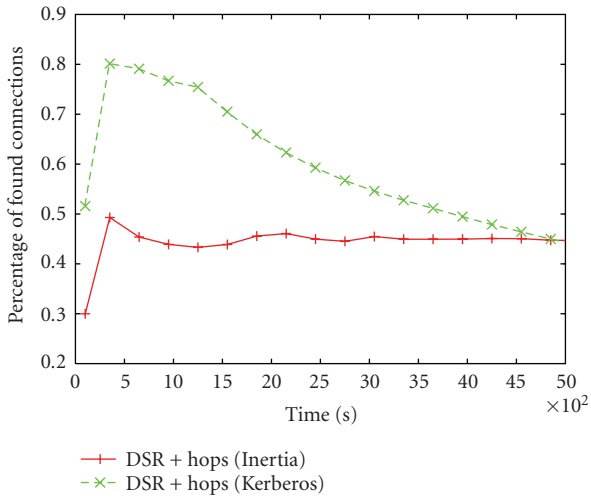

FIGURE 4.35. Percentage of found connections in a single simulation run for the DSR + hops strategy with Inertia and Kerberos mobility models.

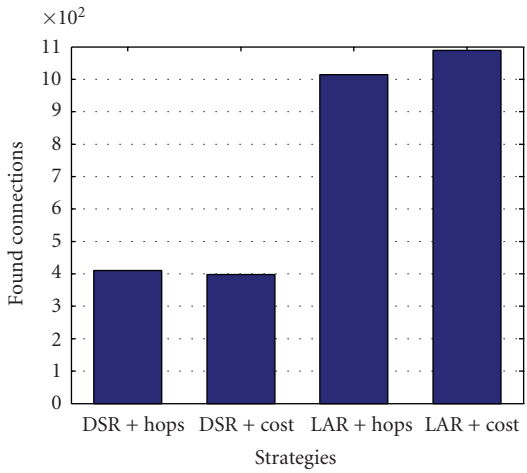

FIGURE 4.36. Found connections for test case 3 with $R_{\text{TX-med}}$.

effect on network performance, so that the LAR + hops strategy is still the overall best solution in this scenario. Note that this conclusion differs from what was obtained for the same transmission range in test cases 1 and 2. In particular, in test case 2 the negative effect of mobility was compensated by the energy saving achieved with a higher number of hops, so that for the transmission range $R_{\text{TX-med}}$, the LAR + cost led to the best performance (Figure 4.26). This is no longer true in test case 3, due the peculiar mobility pattern characterizing the *Kerberos* model. In

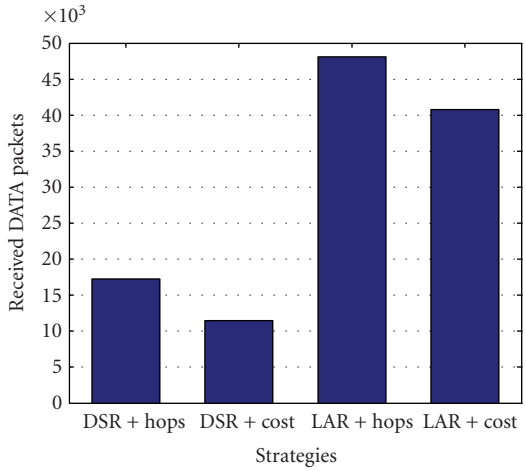

FIGURE 4.37. Received DATA packets for test case 3 with $R_{\text{TX-med}}$.

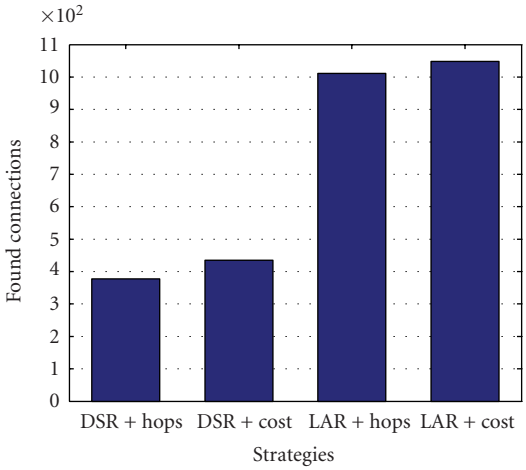

FIGURE 4.38. Found connections for test case 3 with $R_{\text{TX-high}}$.

Section 4.5.2.5 it was show in fact that the *Kerberos* mobility model is characterized by a shorter intergroup link duration if compared to *Inertia*: as a consequence, the adoption of intergroup links in a connection has a stronger negative effect on route stability. The cost-based strategies are more sensible to this effect, since the selected routes are characterized by a high number of hops, and there is thus a significant probability for a route to include one or more intergroup links. The lower route stability is clearly indicated by the fact that, despite the highest number of found connections, the LAR + cost strategy is capable of delivering a lower number of DATA packets than the LAR + Hops strategy: this is due to the fact that

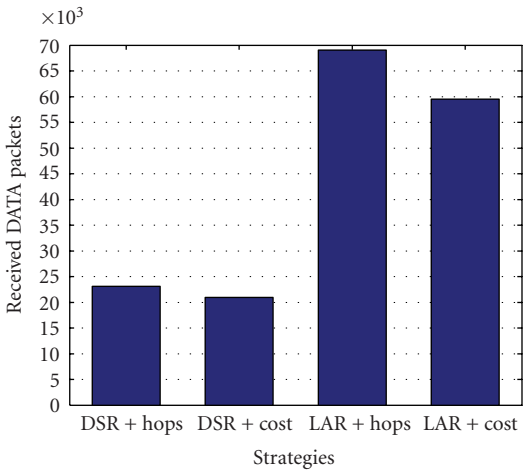

FIGURE 4.39. Received DATA packets for test case 3 with $R_{\text{TX-high}}$.

routes selected with the LAR + cost strategy have a shorter duration and thus the corresponding connections are able to deliver a lower number of packets before being broken for a lack of connectivity.

Results with high transmission range $R_{\text{TX-high}}$ (Figures 4.38 and 4.39) further confirm that cost-based strategies are heavily affected by the mobility pattern of the *Kerberos* model. Although in fact the higher network connectivity allows a higher average number of packets to be delivered in each connection for all the four strategies, yet a significant gap can be observed between hop-based and cost-based strategies.

Quite interestingly, as the transmission range (and consequently the *Kerberos Range*) increases, the results in test case 3 approach those obtained in test case 2; this is coherent with the fact that, as the Kerberos range increases, there is a lower and lower probability for a node to remain isolated from its own group and thus to be forced to modify its mobility pattern. As a consequence, the *Kerberos* mobility model will fall back more and more to the standard *Inertia* mobility model.

4.5.4. Conclusions

The analysis carried out throughout this section had the objective of testing the effectiveness of the location-based, power-aware approach for MAC and routing in low bit rate UWB networks introduced in the previous sections of this chapter.

The results of such analysis highlight that the exploitation of ranging and locationing information provided by the UWB physical layer may effectively extend network lifetime without significant effects on short-term network performance.

The analysis also pointed out the direct relation between the scenario in which the network is deployed and the performance of the selected routing strategy. In particular, network connectivity, transmission range, and mobility pattern of the

nodes are all factors which can influence the performance of a routing strategy and, most important, may have a different effect on different strategies.

Results showed in fact that, depending on the scenario, the best network performance can be obtained by means of either a full exploitation of the positional information provided by UWB in both routing algorithm and metric (as in test cases 1 and 2), or a partial one, limited to the adoption of the location information in the routing algorithm (as in test case 3).

The flexibility guaranteed by the cost function defined in Section 4.1, however, enables a smooth transition from a fully power-aware metric to a traditional hop-based metric, and thus allows for a fine adaptation of the MAC and routing strategy to any network scenario, ranging between the two extreme cases of sparse networks of fixed nodes and dense networks of highly mobile nodes.

Bibliography

[1] M.-G. Di Benedetto and G. Giancola, *Understanding Ultra Wide Band Radio Fundamentals*, Prentice Hall, Upper Saddle River, NJ, USA, 2004.

[2] M.-G. Di Benedetto and B. Vojcic, "Ultra wide band wireless communications : a tutorial," *Journal of Communications and Networks*, vol. 5, no. 4, pp. 290–302, 2003.

[3] M. Z. Win and R. A. Scholtz, "Ultra-wide bandwidth time-hopping spread-spectrum impulse radio for wireless multiple-access communications," *IEEE Transactions on Communications*, vol. 48, no. 4, pp. 679–689, 2000.

[4] L. De Nardis and M.-G. Di Benedetto, "Medium access control design for UWB communication systems: review and trends," *Journal of Communications and Networks*, vol. 5, no. 4, pp. 386–393, 2003.

[5] Federal Communications Commission, "Revision of Part 15 of the Commission's rules regarding ultra-wideband transmission systems," Report 98–153, Federal Communications Commission, Washington D.C., USA, 2002.

[6] P. Karn, "MACA—A new channel access protocol for packet radio," in *Proceedings of ARRL/CRRL Amateur Radio Ninth Computer Networking Conference*, pp. 134–140, Ontario, Canada, September 1990.

[7] V. Bharghavan, A. Demers, S. Shenker, and L. Zhang, "MACAW: A media access protocol for wireless LANs," in *Proceedings of Conference on Applications, Technologies, Architectures and Protocols for Computer Communication (SIGCOMM '94)*, pp. 212–225, London, UK, August–September 1994.

[8] F. Talucci and M. Gerla, "MACA-BI (MACA by invitation). A wireless MAC protocol for high speed ad hoc networking," in *Proceedings of 6th IEEE International Conference on Universal Personal Communications Record*, vol. 2, pp. 913–917, San Diego, Calif, USA, 1997.

[9] C. L. Fullmer and J. J. Garcia-Luna-Aceves, "Floor acquisition multiple access (FAMA) for packet radio networks," in *Proceedings of Conference on Applications, Technologies, Architectures and Protocols for Computer Communication (SIGCOMM '95)*, pp. 262–273, Cambridge, Mass, USA, August–September 1995.

[10] B. P. Crow, I. Widjaja, J. G. Kim, and P. T. Sakai, "IEEE 802.11 wireless local area networks," *IEEE Communications Magazine*, vol. 35, no. 9, pp. 116–126, 1997.

[11] F. A. Tobagi and L. Kleinrock, "Packet switching in radio channels: part II—The hidden terminal problem in carrier sense multiple access and the busy tone solution," *IEEE Transactions on Communications*, vol. 23, no. 12, pp. 1417–1433, 1975.

[12] J. Deng and Z. J. Haas, "Dual busy tones multiple access (DBTMA): a new medium access control for packet radio networks," in *Proceedings of IEEE International Conference on Universal Personal Communications (ICUPC '98)*, vol. 2, pp. 973–977, Florence, Italy, October 1998.

[13] S. Singh and C. S. Raghavendra, "PAMAS: Power aware multiaccess protocol with signalling for ad hoc networks," *ACM Computer Communication Review*, vol. 28, no. 3, pp. 5–26, 1998.

[14] C.-K. Toh, "Maximum battery life routing to support ubiquitous mobile computing in wireless ad hoc networks," *IEEE Communications Magazine*, vol. 39, no. 6, pp. 138–147, 2001.

[15] M.-G. Di Benedetto and P. Baldi, "A model for self-organizing large-scale wireless networks," in *Proceedings of International Workshop on 3G Infrastructure and Services*, pp. 210–213, Athens, Greece, July 2001.

[16] L. De Nardis, P. Baldi, and M.-G. Di Benedetto, "UWB ad-hoc networks," in *Proceedings of IEEE Conference on Ultra Wideband Systems and Technologies (UWBST '02)*, pp. 219–223, Baltimore, Md, USA, May 2002.

[17] P. Baldi, L. De Nardis, and M.-G. Di Benedetto, "Modeling and optimization of UWB communication networks through a flexible cost function," *IEEE Journal on Selected Areas in Communications*, vol. 20, no. 9, pp. 1733–1744, 2002.

[18] B. Karp and H. T. Kung, "Gpsr: greedy perimeter stateless routing for wireless networks," in *Proceedings of 6th ACM/IEEE International Conference on Mobile Computing and Networking (ACM MOBICOM '00)*, pp. 243–254, Boston, Mass, USA, August 2000.

[19] D. Kim, Y. Choi, and C. K. Toh, "Location-aware long lived-route selection in wireless ad hoc network," in *IEEE 52nd Vehicular Technology Conference (VTC '00)*, vol. 4, pp. 1914–1919, Boston, Mass, USA, September 2000.

[20] S. Basagni, I. Chlamtac, V. R. Syrotiuk, and B. A. Woodward, "A distance routing effect algorithm for mobility (DREAM)," in *Proceedings of ACM/IEEE International Conference on Mobile Computing and Networking (ACM MOBICOM '98)*, pp. 76–84, Dallas, Tex, USA, 1998.

[21] Y.-B. Ko and N. H. Vaidya, "Location-aided routing (LAR) in mobile ad hoc networks," in *Proceedings of 4th Annual ACM/IEEE International Conference on Mobile Computing and Networking (MOBICOM '98)*, pp. 66–75, Dallas, Tex, USA, October 1998.

[22] Y.-B. Ko and N. H. Vaidya, "Optimizations for location-aided routing (LAR) in mobile ad hoc networks," Tech. Rep. 98-023, CS Department, Texas A & M University, Dallas, Tex, USA, 1998.

[23] S. Capkun, M. Hamdi, and J. P. Hubaux, "GPS-free positioning in mobile Ad-Hoc networks," in *Proceedings of 34th Annual Hawaii International Conference On System Sciences*, pp. 3481–3490, Maui, Hawaii, USA, January 2001.

[24] D. B. Johnson and D. A. Maltz, "Dynamic source routing in ad hoc wireless networks," in *Mobile Computing*, vol. 353, pp. 153–181, Kluwer Academic Publishers, Dordrecht, The Netherlands, 1996.

[25] D. P. Bertsekas and R. Gallager, *Data Networks*, Prentice Hall, Englewood Cliffs, NJ, USA, 2nd edition, 1992.

[26] M.-G. Di Benedetto, L. De Nardis, M. Junk, and G. Giancola, "$(\text{UWB})^2$: uncoordinated, wireless, baseborn medium access for UWB communication networks," *Springer Mobile Networks and Applications*, vol. 10, no. 5, pp. 663–674, 2005.

[27] D. Raychaudhuri, "Performance analysis of random access packet-switched code division multiple access systems," *IEEE Transactions on Communications*, vol. 29, no. 6, pp. 895–901, 1981.

[28] S. Dastangoo, B. R. Vojcic, and J. N. Daigle, "Performance analysis of multi-code spread slotted ALOHA (MCSSA) system," in *Proceedings of IEEE Global Telecommunications Conference (GLOBECOM '98)*, vol. 3, pp. 1839–1847, Sydney, NSW, Australia, November 1998.

[29] E. S. Sousa and J. A. Silvester, "Spreading code protocols for distributed spread-spectrum packet radio networks," *IEEE Transactions on Communications*, vol. 36, no. 3, pp. 272–281, 1988.

[30] M. S. Iacobucci and M.-G. Di Benedetto, "Computer method for pseudo-random codes generation," National Italian patent, RM2001A000592.

[31] Y.-C. Hu and D. B. Johnson, "Caching strategies in on-demand routing protocols for wireless ad hoc networks," in *Proceedings of 6th Annual International Conference on Mobile Computing and Networking (MOBICOM '00)*, pp. 231–242, Boston, Mass, USA, August 2000.

[32] E. M. Royer, P. M. Melliar-Smith, and L. E. Moser, "An analysis of the optimum node density for ad hoc mobile networks," in *Proceedings of IEEE International Conference on Communications (ICC '01)*, vol. 3, pp. 857–861, Helsinki, Finland, June 2001.

[33] B. Liang and Z. J. Haas, "Predictive distance-based mobility management for multidimensional PCS networks," *IEEE/ACM Transactions on Networking*, vol. 11, no. 5, pp. 718–732, 2003.

[34] S. Basagni, I. Chlamtac, and V. R. Syrotiuk, "Dynamic source routing for ad hoc networks using the global positioning system," in *Proceedings of IEEE Wireless Communications and Networking Conference (WCNC '99)*, vol. 1, pp. 301–305, New Orleans, La, USA, September 1999.

[35] M. Bergamo, R. Hain, K. Kasera, D. Li, R. Ramanathan, and M. Steenstrup, "System design specification for mobile multimedia wireless network (MMWN) (draft)," Tech. Rep., DARPA project DAAB07-95C -D156, October 1996.

[36] X. Hong, M. Gerla, G. Pei, and C.-C. Chiang, "A group mobility model for ad hoc wireless networks," in *Proceedings of 2nd ACM International Workshop on Modeling and Simulation of Wireless and Mobile Systems (MSWiM '99)*, pp. 53–60, Seattle, Wash, USA, August 1999.

[37] K. H. Wang and B. Li, "Group mobility and partition prediction in wireless ad-hoc networks," in *Proceedings of IEEE International Conference on Communications (ICC '02)*, vol. 2, pp. 1017–1021, New York, NY, USA, April–May 2002.

[38] F. Bai, N. Sadagopan, and A. Helmy, "Important: a framework to systematically analyze the impact of mobility on performance of routing protocols for adhoc networks," in *Proceedings of 22nd Annual Joint Conference of the IEEE Computer and Communications Societies (INFOCOM '03)*, vol. 2, pp. 825–835, San Francisco, Calif, USA, March–April 2003.

[39] R. Min and A. Chandrakasan, "A framework for energy-scalable communication in high-density wireless networks," in *Proceedings of International Symposium on Low Power Electronics and Design (ISLPED '02)*, pp. 36–41, Monterey, Calif, USA, August 2002.

Maria-Gabriella Di Benedetto: INFOCOM Department, School of Engineering, University of Rome La Sapienza, 00184 Rome, Italy

Email: gaby@infocom.ing.uniroma1.it

Luca De Nardis: INFOCOM Department, School of Engineering, University of Rome La Sapienza, 00184 Rome, Italy

Email: lucadn@newyork.ing.uniroma.it

Salvatore Falco: INFOCOM Department, School of Engineering, University of Rome La Sapienza, 00184 Rome, Italy

Email: sfalco@newyork.ing.uniroma1.it

5 Spatial aspects of UWB

Thomas Kaiser, Jürgen Kunisch, Werner Sörgel, Christian Waldschmidt, Werner Wiesbeck, F. Argenti, T. Bianchi, L. Mucchi, L. S. Ronga, Alain Sibille, Sigmar Ries, Christiane Senger, W. Pam Siriwongpairat, Masoud Olfat, Weifeng Su, K. J. Ray Liu, and Feng Zheng

5.1. Introduction

The aim of this part is to discuss the spatial aspects of the UWB radio channel from various perspectives. First, in Section 5.2, *a model for the UWB radio channel* by J. Kunisch, a spatial model is presented based on measurement data that were obtained in office environments with line-of-sight, non-line-of-sight, and intermediate conditions. Basically, the goal was to arrive at expressions for the space-variant impulse response or, equivalently, for its space-variant transfer function such that impulse responses or transfer functions belonging to adjacent locations could be correlated properly. The distinguishing feature of the ultra-wideband indoor radio channel is that certain individual paths are recognizable and resolvable in the measurements. This is adequately reflected by the proposed spatial model. Moreover, the model covers also movements of the receiving or transmitting antennas on a small scale (several wavelengths). At the end, the relevant model equations are presented in a compact, algorithmic-like form.

Section 5.3, *UWB antenna arrays* by W. Sörgel et al., introduces state-of-the-art UWB antenna array concepts and their applications. Then, the transient radiation behaviors of UWB antenna arrays in the frequency and in the time domain are discussed by deriving the antenna arrays, transient responses and their quality measurements such as dispersion and ringing. The theoretical modeling is substantiated by experimental results, and then this section finishes with simulation results for a linear exponentially tapered slot antenna array (Vivaldi antennas) for time-domain beam steering.

In Section 5.4, *UWB polarization diversity* by F. Argenti et al., two transmitting antennas with orthogonal polarization are proposed in order to uniformly cover an indoor area. A single-antenna receiver results into a 2×1 MISO (multiple-input single-output) system so that space-time coding becomes applicable. The goal is to employ the polarization diversity in order to obtain a quality constant symbol detection while the receiver moves around within the covered area.

Section 5.5, *spatial diversity* by A. Sibille, addresses several basic issues pertaining to spatial diversity in UWB systems. It mainly concentrates on impulse-based radio, but it also evokes effects concerning frequency-domain modulation schemes such as OFDM. The main subjects are the impacts of electromagnetic coupling between sensors and of channel properties (like fading and angular variance) on spatial diversity.

Beside the two main pillars of MIMO signal processing, namely, spatial multiplexing and space-time coding, the third and most classical one is *beamforming*, which is revisited in Section 5.6, *UWB beamforming and DOA estimation* by S. Ries et al. Beamforming for UWB signals has some special properties that are different from the narrowband case. For instance, because of the absence of grating lobes in the beampattern, the spacing of the array elements is not limited by half of the wavelength, so that high resolution can be achieved with only a few array elements. Interestingly, the short duration of UWB pulses is also beneficial for digital beamforming. This means that despite enormous sampling rate requirements, digital beamforming of UWB signals is not too far away to become reality. At the end of this section, the principal feasibility of direction-of-arrival (DOA) estimation is shown by an illustrative example.

In Section 5.7, *performance analysis of multiantenna UWB wireless communications* by W. P. Siriwongpairat et al., the performance of UWB-MIMO systems using different models for the wireless channels and different modulation schemes is presented. In particular, the performance merits of UWB-ST-coded systems employing various modulation and multiple-access techniques, including time-hopping (TH) M-ary pulse-position modulation (MPPM), TH binary phase-shift keying (BPSK), and direct-sequence (DS) BPSK are pointed out. At the end, the application of multiple transmit and/or receive antennas in an UWB-OFDM system is discussed.

Section 5.8, *channel capacity of MIMO UWB indoor wireless channels* by F. Zheng and T. Kaiser, concludes this part. Therein the channel capacity will be evaluated in terms of ergodic capacity and outage probability for UWB indoor wireless systems with multiple transmit and receive antennas (multiple-input multiple-output, MIMO). For some special cases, analytic closed-form expressions for the capacity of UWB wireless communication systems are given, while for other cases the capacity is obtained by Monte Carlo simulation approach. Several conclusions can be drawn from these results. For instance, the UWB-MIMO communication rate supportable by the channel increases linearly with the number of transmit or receive antennas for a given outage probability, which reminds on the significant data rate increase of MIMO narrowband fading channels.

5.2. A model for the ultra-wideband space-variant indoor multipath radio channel

5.2.1. Introduction

The foundation of all wireless systems is the radio channel. Consequently, a component which is of paramount importance for the design of any wireless system

is a channel model that reproduces the radio propagation aspects relevant to this particular system. In this section, we will construct, in a step-by-step fashion, such a model of the ultra-wideband radio channel. The model is based on measurement data (cf. [1]) that were obtained in office environments with line-of-sight, non-line-of-sight, and intermediate conditions. We will also give site-specific parameter profiles that have been derived from these measured data.

In particular, the model will apply to the indoor multipath channel in the FCC frequency band [2] and it will cover, to some amount, space-variant properties of the channel. The typical application focuses on inter- or intraoffice communication with distances between transmitter (Tx) and receiver (Rx) below approximately 10 m, for example, WPAN[1] systems.

Basically, the aim is to arrive at expressions for the space-variant impulse response or, equivalently, its space-variant transfer function such that impulse responses or transfer functions belonging to adjacent locations will be correlated properly. From such a basic description, more specialized models may be derived easily, for example, a discrete channel model that incorporates effects of modulation and demodulation.

A distinguishing feature of the ultra-wideband indoor radio channel is that certain individual paths are recognizable and resolvable[2] in the measurements. In contrast to dense multipath contributions, the corresponding echoes exist individually over distances larger than a wavelength. Consequently, an important requirement for our model is that it will incorporate this property: the delay and amplitude changes of individual paths corresponding to changing positions of the transmitter or receiver will be accounted for to produce a realistic Doppler behavior (e.g., delay-Doppler spectrum).

Another important aspect of the model which again is related to space variance is that it is focused on small-scale rather than large-scale behavior. Our model will be suited to describe movements of the receiving or transmitting terminal antenna within certain areas measuring several wavelengths in diameter, but it will not be suited to derive, for example, power laws for movements on a larger scale, say, across a large building. This limitation is a consequence of the limitations of the underlying measured data.

The model is of a hybrid nature. By that we mean that it combines a statistical approach (to model dense multipath) and a simple quasideterministic method (to model strong individual echoes). Therefore, the model is basically a statistical model—in the sense that for a model realization certain values are drawn from prescribed distributions with prescribed parameters—, but it also has a minor deterministic component—in the sense that for a model realization certain values are derived from a fixed algorithm that does not depend on statistical distributions but

[1]WPAN stands for wireless personal area networks.

[2]The notion of resolvability is somewhat fuzzy here because the capability to resolve a path is mostly an attribute of the "superresolution" algorithm used to estimate echo positions, rather than an attribute of the path itself. A path may be considered resolvable, for example, if it can be resolved by an optimal estimator. This in turn poses the question of what is meant by an "optimal" estimator (e.g., in terms of resolution and accuracy).

on a description of the environment. In our case, however, we do not use a description of the real environment (like it would be the case with ray tracing/launching models), rather a trivial surrogate environment will be used—hence the designation "quasideterministic."

We will start out by reviewing some important properties of the ultra-wideband radio channel in the next section. The following Section 5.2.3 will elaborate on how these properties influence the design of the model. Finally, the model equations will be presented compactly in an algorithm-like form.

5.2.2. The ultra-wideband radio channel

What, then, are those properties specific to ultra-wideband channels that necessitate the design of dedicated ultra-wideband channel models beyond reparameterizing standard models that are applicable to plain wideband conditions?

The indoor ultra-wideband radio channel differs from the plain wideband channel in at least two respects.

Spatial resolution. For indoor environments, the ratio of the spatial resolution (proportional to the inverse bandwidth) and the characteristic geometric dimensions of a room are such that echoes caused by certain paths may be appreciably distinguishable from each other.[3] This applies in particular to early echoes corresponding to paths with small excess delays. For example, in LOS conditions, the direct path may be shorter by more than the spatial resolution than the second shortest path, causing a gap in between the corresponding two echoes. With increasing delay, the arrival probability for paths increases because the corresponding path distances get longer, which in turn increases the probability of interactions with the environment. Consequently, the onset of the inevitable dense multipath regime is shifted towards larger delays. For medium to large excess delays, the power delay profile (PDP) fits quite well into the exponential decay scheme that has been observed for wideband channels (cf., e.g., [3]). For small excess delays, however, ultra-wideband channel PDPs tend to have a more spiky appearance caused by individual echoes. Yet the first path corresponding to LOS conditions may be followed by some trailing multipath contributions caused, for example, by the mechanical antenna support.

Depending on the environment and Tx-Rx distance, the direct path, floor, ceiling, and wall reflections may be recognizable. An example for an LOS ultra-wideband channel PDP illustrating these points is given in Figure 5.1. Furthermore, Figure 5.2 shows 150 adjacent power delay profiles for the same channel obtained by displacing one antenna over a linear distance of 150 cm. The individual

[3]The term "path" is used here to denote a trajectory along which energy travels, that is, paths are related to the physical process of wave propagation. In contrast, the term "echo" is used here to denote certain features observable in an impulse response. An echo may be caused by superposition of several contributions arriving via different paths—unresolved superposition shows as fading. An echo can also result as an artifact of signal processing (countermeasures: e.g., windowing, superresolution algorithms, etc.). In this sense, echoes are related to the observation of the wave propagation process.

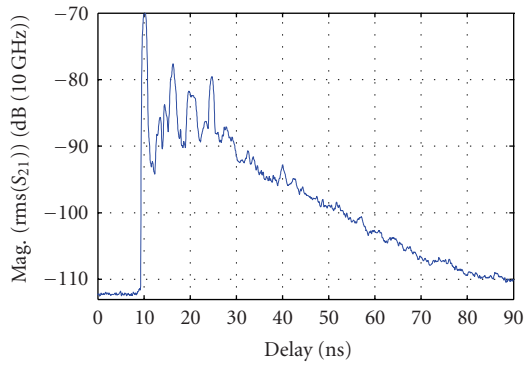

(a)

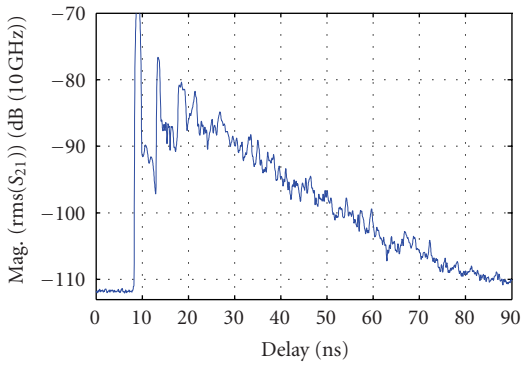

(b)

FIGURE 5.1. Power delay profile derived from 30 × 30 impulse responses on a 30 cm × 30 cm grid for LOS conditions: (a) measurement; (b) model.

echoes and the dependence of the corresponding delays from the spatial position (including a slight curvature of the LOS trace due to an appreciable change of the Tx-Rx distance over the 150 cm of antenna displacement) are clearly visible. The trace slanted to the right (beginning approximately at 16 nanoseconds for displacement = 0 m) corresponds to a strong wall reflection. Figures 5.3, 5.4, 5.5, and 5.6 show the response of the channel to an impulse with a waveform that corresponds to a Kaiser-Bessel frequency-domain window. All figures show a comparison of measurement and model results, which, due to the hybrid model nature, are expected to be "similar," but not identical.

Frequency behavior. For ideal constant gain antennas, the free-space channel power gain as a function of the frequency f follows an f^{-2} law which may be neglected for small fractional bandwidths. For an ultra-wideband channel extending from 3 to 11 GHz, however, the f^{-2} law amounts to a difference of approximately

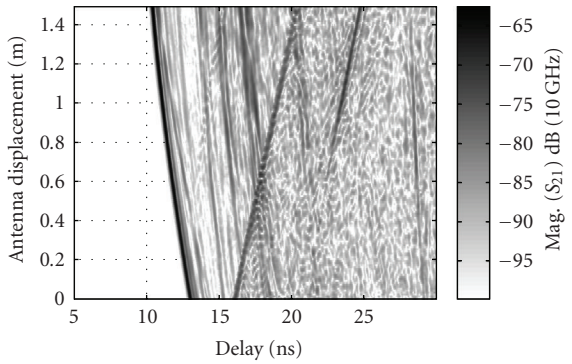

(a)

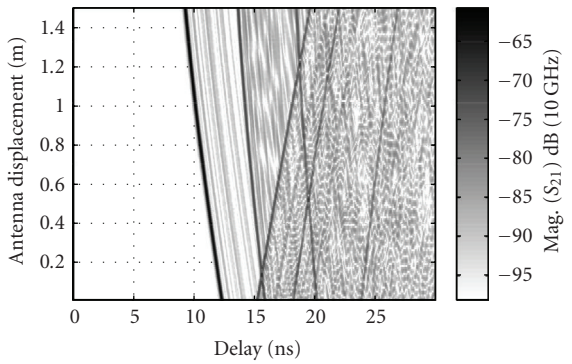

(b)

FIGURE 5.2. Power delay profiles for 150 cm displacement of one antenna almost perpendicular to the line of sight: (a) measurement; (b) model.

11 dB between the lower and upper bandlimits—the corresponding figure for W(ideband)CDMA[4] is in the order of 0.02 dB. Strongly depending on the considered environment and the employed antennas, different exponents or other frequency dependencies may occur (cf. [1, 4]). A gain decay with increasing frequency may be expected to cause a reduction of the "effective" bandwidth as the larger part of the received signal energy concentrates towards lower frequencies. To take full advantage of the radio channel, this property has to be considered in both antenna and signal design, and consequently by the channel model (cf., e.g., [5]).

5.2.3. Model description

This section gives an overview of the model elements.

[4]UTRA: 5 MHz bandwidth centered around approximately 2 GHz.

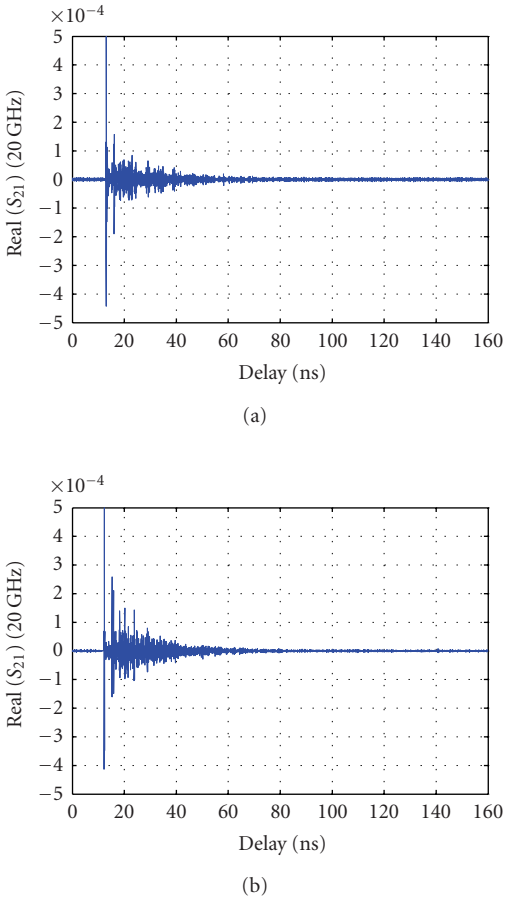

FIGURE 5.3. Example for a single impulse response (LOS): (a) measurement; (b) model.

5.2.3.1. Modeled quantity

The primary quantity to be modeled is the space-variant transfer function $H(f, \mathbf{r}_t, \mathbf{r}_r)$, where f, $\mathbf{r}_t$, and $\mathbf{r}_r$ denote frequency, transmitter, and receiver positions, respectively. From H other relevant quantities may be derived easily, including the space-variant impulse response $h(\tau, \mathbf{r}_t, \mathbf{r}_r)$ and the baseband impulse response $h_B(\tau, \mathbf{r}_t, \mathbf{r}_r)$, and so forth.

By assuming trajectories $\mathbf{r}_t(t)$ or $\mathbf{r}_r(t)$, space variance may be converted to time variance caused by motion of terminals.

5.2.3.2. Modeling approach

In the last section, it was pointed out that the power delay profile roughly follows an exponential decay rule. Furthermore, in a dense multipath region, the samples

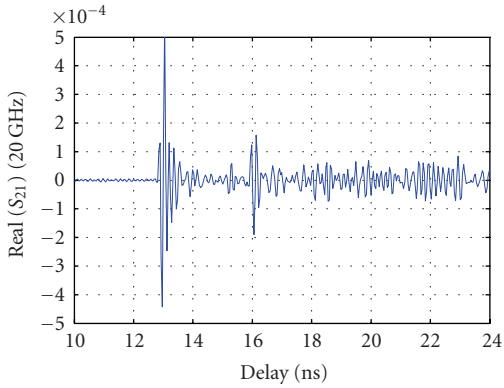

(a)

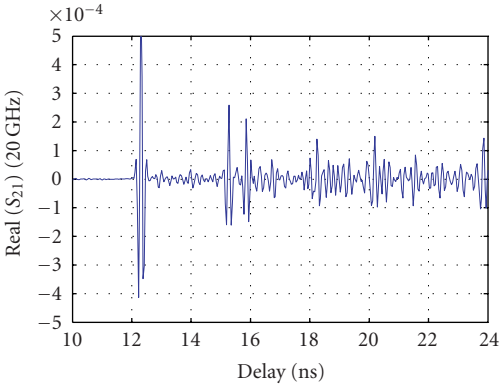

(b)

FIGURE 5.4. Example for a single impulse response (LOS, detail): (a) measurement; (b) model.

of the baseband impulse response reasonably follow a Rayleigh amplitude statistic [1]. Therefore, the approach from [3] is adopted as a starting point. To account for the ultra-wideband specific channel behavior, the model proposed here is based on the following rules.

Rule 1. For given $\mathbf{r}_t$ and $\mathbf{r}_r$, a number of individual echoes (arrival times and complex amplitudes) are generated according to a certain algorithm described below.

Rule 2. With each individual echo, a diffuse multipath cluster is associated with Rayleigh amplitude echoes generated in every bin, an exponential echo power decay law, and uniformly distributed phase.

Rule 3. For any $\mathbf{r}_t$ and $\mathbf{r}_r$, the arrival times of an individual echo and its associated multipath cluster are equal.

Rule 4. The cluster height (the maximum ray power expectation value within the given cluster) is set to be a certain amount (which is a model parameter) below the power of the associated individual echo.

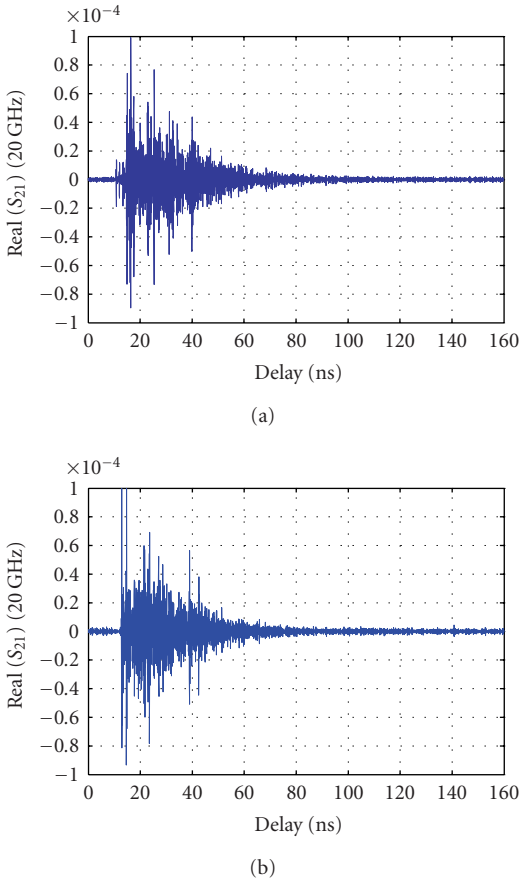

FIGURE 5.5. Example for a single impulse response (NLOS): (a) measurement; (b) model.

Rule 5. The cluster decay parameter is unique for all clusters and is chosen to have a similar value as the decay parameter of the overall resulting single cluster.

Rule 6. All of these clusters are generated according to the same parameters.

Rule 7. For each individual echo, only a single multipath cluster realization is generated, which is to be used for all transmitter and receiver positions $\mathbf{r}_t$ and $\mathbf{r}_r$.

Rule 8. The individual echoes and their associated clusters are coherently superimposed.

Rule 9. A frequency-dependent power decay corresponding to the bandwidth is enforced.

From the above rules, it is obvious that the model uses some important elements of the well-known Saleh-Valenzuela (SV) model [3], among these the multiple clusters approach. Unlike SV, however, cluster arrival times are not drawn

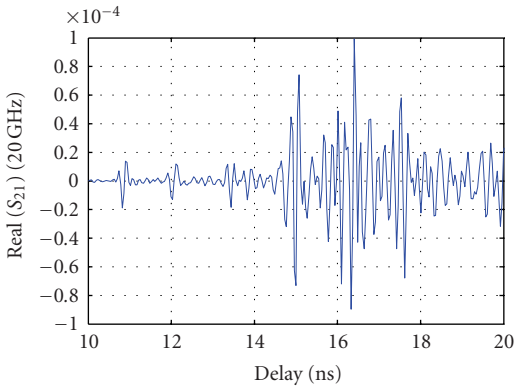

(a)

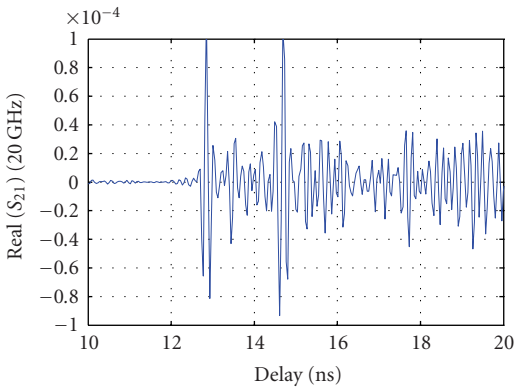

(b)

FIGURE 5.6. Example for a single impulse response (NLOS, detail): (a) measurement; (b) model.

from a Poisson distribution, rather (cf. Rules 1–3) they are to be determined by a dedicated algorithm that also produces the arrival times of individual echoes—this algorithm is essential to ensure proper space-variant properties of the model. Rule 4 is required to make the individual echoes "stand out" over their associated multipath clusters; an individual echo plus its associated cluster may be considered the impulse response of that path that corresponds to the individual echo. Rules 5 and 6 then follow from the simple (but also weak) assumption that impulse responses along different paths are similar regarding power decay as a function of delay. Rule 7 again is related to the interpretation of each cluster as per-path impulse response: changing transmitter or receiver position on a *small* scale will mainly affect each cluster's delay and phases, with only minor disturbance of its shape.

Using a tailored algorithm to generate the arrival times and amplitudes of individual echoes and their clusters (instead of SV's homogeneous Poisson process with exponential power decay of cluster amplitudes) offers several advantages;

in particular, the positions of the individual echoes and the associated multipath clusters may be adjusted to render a realistic Doppler spectrum (in wave number domain, corresponding to angle-of-arrival domain) which is consistent with measurement data.

5.2.3.3. Generation of individual echoes

Viewed from the receiver position, and assuming that each individual echo corresponds to a wavefront arriving from a certain direction, each of the individual echoes may be thought of as being caused by a wave emitted from a virtual source situated at a certain distance in that direction from the receiver, assuming free-space propagation. In other words, the transmitter may be replaced by an equivalent ensemble of virtual sources.

In contrast, in the transmitter perspective, only signals departing into certain directions will eventually arrive at the receiver. In this view, each of these directions may be thought of as corresponding to a virtual sink such that all signals absorbed in virtual sinks are summed up to form the total signal arriving at the receiver—the receiver may be replaced by an equivalent ensemble of virtual sinks.

Both pictures, and especially directions of departure and arrival, are linked by the fact that both virtual sources and sinks are determined by interactions with the enviroment along paths that connect transmitter and receiver.

The proposed model employs this approach and generates a set of virtual sources from which the individual echoes are derived self-consistently for different terminal positions. It is reasonable to assume that many of the strong low excess delay individual echoes correspond to important low-order interactions, for example, direct transmission and single floor, ceiling, and wall reflections. Therefore, as a first-order approximation, positions of potential virtual sources are generated as *image* positions of the transmitter position $\mathbf{r}_t$ up to a certain order in a generic room with respect to given mirror positions.[5] Each wall is assumed to act as a mirror, and no other mirrors are considered. Only a subset of all such virtual sources is actually used.

Essentially, this approach represents a trivial ray-tracing type of method applied to an extremely simplistic environment model. Although this is far from a rigorous deterministic treatment, this approach is justified by its ability to introduce reasonable spatial correlation of the modeled impulse responses.

Adaptation of the model to a specific environment requires a proper selection scheme. While general selection schemes are still subject to investigations, the subsets for the measurement-derived scenarios under consideration here are given in Table 5.1. Obviously, more general schemes to generate virtual source positions beyond using images can be devised.

[5]This is not to say that all important interactions are specular reflections. The image approach is used because it captures basic characteristic dimensions of generic rooms, and for its algorithmic simplicity.

Table 5.1. Model parameters.

Parameter	Unit	Office LOS	Office NLOS	Office-office	
N		2048	2048	2048	Number of samples of h_B, H
R	ns^{-1}	12.8	12.8	12.8	Sampling rate in delay domain
B	GHz	10	10	10	Bandwidth of h_B
F	GHz	6	6	6	Center frequency
d_0	m	0.8	1.0	3.5	Reference distance for individual echo power law
α_0		3.0	2.0	3.0	Path loss exponent for individual echo power law
G_{MP}	dB	−20.0	−16.0	−19.0	Cluster gain with respect to associated individual echo
$G_{\text{MP,LOS}}$	dB	−13.0	N/A	0.0	Additional cluster gain for LOS individual echo
G	dB	−5.0	−20.0	−21.0	Basic gain
γ	ns	10.0	9.5	12.5	Multipath cluster exponential decay parameter
β		1.1	1.01	1.3	Frequency-domain decay exponent
σ_N^2	dB	−118	−123	−121	Normalized measurement I/Q noise variance
x_t	m	1.78	0.91	−1.32	Nominal transmitter coordinates
y_t	m	4	4.39	1.8	
z_t	m	1.5	1.5	1.5	
x_r	m	3.0, . . . ,4.5	0.15, . . . , 1.65	3.9, . . . , 4.2	Range of receiver coordinates
y_r	m	1.5, . . . , 1.8	1.5, . . . , 1.8	2.5, . . . , 4.0	Covered by measurement
z_r	m	1.5	1.5	1.5	
X_0, X_1	m	0, 5.06	0, 5.06	−5.06, 5.06	Mirror positions
Y_0, Y_1	m	0, 5.00	0, 5.12	0, 5.12	
Z_0, Z_1	m	0, 2.75	0, 2.75	0, 2.75	
Q		3	3	3	Maximum image order per space dimension
$K = (k)$		172, 123,173, 130, 124, 215	171, 179, 164, 115, 173, 177	172, 221, 123, 179, 228, 130, 173, 32, 312, 110, 174, 170	Set of selected virtual source indices

It should be noted that despite the apparent asymmetry with respect to transmitter and receiver positions (virtual source coordinates are determined from transmitter coordinates), a virtual source determined as transmitter image just represents an environment interaction: a reflection, which in itself is a symmetric process with respect to receiver and transmitter positions. Virtual sources just aid in geometric calculations and could be replaced by virtual sinks (obtained from images of the receiver position $\mathbf{r}_r$). In particular, this implies that transmission from various transmitter positions (in a vicinity of the original transmitter position) to a given fixed receiver position can be modeled by using the same set K (see below for a definition of K) of virtual source indices, applied to a set of virtual sinks determined from the receiver position. If both variations of transmitter and receiver positions are to be modeled, either virtual sources or sinks can be used equally well.

5.2.4. Model summary

This section details all of the model equations. A complete list of all model parameters used below is given in Table 5.1, including measurement-based values for these scenarios.

Office LOS. Transmission within an office of approximately 5 m × 5 m × 2.75 m, line-of-sight condition between Tx and Rx.

Office NLOS. Transmission within an office of approximately 5 m × 5 m × 2.75 m, line of sight between Tx and Rx obstructed by metal cabinet of approximately 0.6 m × 1.8 m × 2 m.

Office-office. Transmission through light plasterboard wall between two adjacent offices of approximately 5 m × 5 m × 2.75 m.

The following steps are used to generate samples $h_d(n, \mathbf{r}_t, \mathbf{r}_r) \triangleq h_B(n/R, \mathbf{r}_t, \mathbf{r}_r)$, for $n = 0, \ldots, N-1$, of the baseband impulse response h_B.

5.2.4.1. Definition of virtual sources

Let $\mathbf{r}_t \triangleq (x_t, y_t, z_t)$. A grid of virtual source coordinates is defined by

$$\begin{aligned} x_q(m,n,p) &\triangleq \mu(x_t, X_0, X_1, m), \\ y_q(m,n,p) &\triangleq \mu(y_t, Y_0, Y_1, n), \\ z_q(m,n,p) &\triangleq \mu(z_t, Z_0, Z_1, p), \end{aligned} \tag{5.1}$$

for $m, n, p = -Q \ldots Q$, where

$$\mu(x,a,b,q) \triangleq x + q(b-a) + \left(1 - (-1)^q\right)\frac{a+b-2x}{2}. \tag{5.2}$$

This defines a total of $(2Q+1)^3$ virtual sources, which may be numbered from

1 to $(2Q+1)^3$ by a scalar index k according to the correspondence

$$(m,n,p) \longleftrightarrow k = 1 + m + Q + (n+Q)(2Q+1) + (p+Q)(2Q+1)^2. \tag{5.3}$$

The point

$$(m,n,p) = (0,0,0) \longleftrightarrow k_{\mathrm{LOS}} \triangleq \frac{(2Q+1)^3+1}{2} \tag{5.4}$$

corresponds to the line-of-sight path. In the following, the single index k is used instead of m,n,p.

5.2.4.2. Generation of individual echo parameters

From the $(2Q+1)^3$ virtual sources generated above, only a subset K is selected to generate individual echoes. For

$$\mathbf{r}_r \triangleq (x_r, y_r, z_r), \tag{5.5}$$

the arrival time (delay) of individual echo $k \in K$ is given by

$$\tau(k, \mathbf{r}_t, \mathbf{r}_r) \triangleq \frac{d(k, \mathbf{r}_t, \mathbf{r}_r)}{c_0}, \tag{5.6}$$

where

$$d(k, \mathbf{r}_t, \mathbf{r}_r) = \sqrt{(x_q(k) - x_r)^2 + (y_q(k) - y_r)^2 + (z_q(k) - z_r)^2} \tag{5.7}$$

is the distance between virtual source k and position $\mathbf{r}_r$, and c_0 is the free-space propagation velocity.

If k does not correspond to the direct (LOS) path, that is, $k \neq k_{\mathrm{LOS}}$, the power gain $G(k, \mathbf{r}_t, \mathbf{r}_r)$ is given by[6]

$$G(k, \mathbf{r}_t, \mathbf{r}_r) = \left(\frac{c_0}{4\pi d_0 F}\right)^2 \left(\frac{d(k, \mathbf{r}_t, \mathbf{r}_r)}{d_0}\right)^{-\alpha}, \tag{5.8}$$

where α is a model parameter. Otherwise,

$$G(k, \mathbf{r}_t, \mathbf{r}_r) = \left(\frac{c_0}{4\pi d(k, \mathbf{r}_t, \mathbf{r}_r) F}\right)^2. \tag{5.9}$$

The amplitude gain is then given by

$$A(k, \mathbf{r}_t, \mathbf{r}_r) \triangleq G(k, \mathbf{r}_t, \mathbf{r}_r)^{1/2}. \tag{5.10}$$

[6]Conceptually, the power law is attributed partly to the strength of the virtual source rather than solely to attenuation due to (free-space) propagation between the virtual source and the observation point. Assuming a certain power law is equivalent to adopting a certain dependence between virtual source strength and distance to the observation point.

5.2.4.3. Generation of associated multipath clusters

For individual echo k, multipath power values

$$|b(k,n)|^2, \quad \text{for } n = 1,\ldots,N-1, \tag{5.11}$$

are drawn from an exponential distribution with parameter

$$\mathrm{E}\left\{|b(k,n)|^2\right\} = 10^{G_{\mathrm{MP}}/10\,\mathrm{dB}} \exp\left(-\frac{n}{R\gamma}\right), \tag{5.12}$$

where the delay index n corresponds to delay $\tau = n/R$.

If $k = k_{\mathrm{LOS}}$, then $G_{\mathrm{MP}} + G_{\mathrm{MP,LOS}}$ is used instead of G_{MP} in (5.12). From $|b(k,n)|^2$, the complex multipath amplitudes (normalized to the amplitude of the associated individual echo) are

$$\begin{aligned} b(k,0) &\triangleq 1 \quad \text{(associated individual echo)},\\ b(k,n) &\triangleq \sqrt{|b(k,n)|^2}\exp(j\phi_{k,n}), \quad n = 1,\ldots,N-1, \end{aligned} \tag{5.13}$$

with uniform i.i.d. phases $\phi_{k,n}$. By applying a DFT to $b(k,n)$, samples $B(k,l)$ of the normalized and delay-less transfer function of the kth cluster are obtained:

$$B(k,l) = \sum_{n=0}^{N-1} b(k,n)\exp\left(-\frac{j2\pi nl}{N}\right), \quad l = 0,\ldots,N-1, \tag{5.14}$$

where the frequency index l corresponds to the frequency

$$f(l) \triangleq F + \frac{R}{N}\left(\mathrm{mod}\left(l+\frac{N}{2},N\right) - \frac{N}{2}\right). \tag{5.15}$$

5.2.4.4. Superposition of individual echoes and associated multipath clusters

Samples of the overall transfer function are obtained by denormalizing, shifting, and summing over all clusters:

$$\begin{aligned} H_d(l,\mathbf{r}_t,\mathbf{r}_r) &\triangleq H(f(l),\mathbf{r}_t,\mathbf{r}_r) = 10^{G/20\,\mathrm{dB}}\\ &\quad\times \sum_{k\in K} A(k,\mathbf{r}_t,\mathbf{r}_r)B(k,l)\exp\left(-j2\pi f(l)\tau(k,\mathbf{r}_t,\mathbf{r}_r)\right). \end{aligned} \tag{5.16}$$

Note that in the sum on the right-hand side of (5.16) the term $B(k,l)$ does not depend on $\mathbf{r}_t$ and $\mathbf{r}_r$, in accordance with Rule 7 formulated above.

5.2.4.5. Filtering and frequency-dependent power decay

A frequency-dependent gain decay and bandwidth limitation is applied by the substitution

$$\begin{aligned} H_d(l) &\longleftarrow H_d(l)\left(\frac{f(l)}{F}\right)^{-\beta} \quad \text{for } |f(l)-F| \le \frac{B}{2}, \\ H_d(l) &\longleftarrow 0 \quad \text{otherwise.} \end{aligned} \tag{5.17}$$

Optionally, at this stage another filter may be applied which corresponds to a different frequency-domain window or a prescribed transmitted impulse form.

5.2.4.6. Noise addition

An inverse DFT of $H_d(l, \mathbf{r}_t, \mathbf{r}_r)$ yields samples

$$h_d(n, \mathbf{r}_t, \mathbf{r}_r) = \frac{1}{N}\sum_{l=0}^{N-1} H_d(l, \mathbf{r}_t, \mathbf{r}_r)\exp\left(\frac{j2\pi nl}{N}\right), \quad n = 0, \ldots, N-1, \tag{5.18}$$

of the normalized bandlimited baseband impulse response which may be subjected to *observation* noise

$$h_d(n, \mathbf{r}_t, \mathbf{r}_r) \longleftarrow h_d(n, \mathbf{r}_t, \mathbf{r}_r) + s_r(n, \mathbf{r}_t, \mathbf{r}_r) + js_i(n, \mathbf{r}_t, \mathbf{r}_r), \tag{5.19}$$

where $s_r(n, \mathbf{r}_t, \mathbf{r}_r)$ and $s_i(n, \mathbf{r}_t, \mathbf{r}_r)$ are i.i.d. zero-mean Gaussian random variables with variance σ_N^2.[7]

5.2.4.7. Normalization

Finally, samples of the baseband impulse response h_B are obtained by

$$h_B\left(\frac{n}{R}, \mathbf{r}_t, \mathbf{r}_r\right) = Rh_d(n, \mathbf{r}_t, \mathbf{r}_r), \quad n = 0, \ldots, N-1. \tag{5.20}$$

Equation (5.20) assumes h_B is nonzero only in an interval which is shorter than N/R (no aliasing in delay domain), which implies a constraint for N and R. Note that h_B has dimension s^{-1}.

5.2.5. Summary

We have constructed a model of certain ultra-wideband indoor radio channels. The model is based upon Saleh-Valenzuela multipath clusters. Unlike Saleh-Valenzuela, cluster arrival times are modeled in a quasideterministic fashion;

[7] Note that the values specified in Table 5.1 have been determined such as to reproduce the measurement noise of the underlying measurement data.

furthermore clusters are augmented by adding strong individually recognizable paths. An essential new element is the use of a simple geometric model of a generic environment to provide consistent space-variant behavior of such strong individual paths and their associated multipath clusters for small-scale movements of the terminals. The model explicitly includes a global frequency decay of the resulting transfer functions.

5.3. UWB antenna arrays

5.3.1. Introduction

Since the United States FCC has opened the spectrum from 3.1 GHz to 10.6 GHz, that is, a bandwidth of 7.5 GHz, for unlicensed use [6] with up to −41.25 dBm/MHz effective isotropic radiated power (EIRP), numerous applications in communications and sensor areas are showing up. All these applications have in common that they spread the necessary energy over a wide frequency range in this unlicensed band in order to radiate below the limit. The resulting ultra-wideband (UWB) systems are mainly limited by the strict power regulations, which protect the wireless systems assigned to frequencies within the UWB band. The usage of highly efficient UWB antennas and antenna systems with multiple antennas is an important option in order to cope with the challenging power restriction and enables features like exploitation of spatial diversity, beamforming, and direction estimation. The basis for this is the understanding of the characteristics and specialties of UWB antenna arrays. The theory of wideband antenna arrays is the subject of many textbooks, which trade this problem usually from a frequency-domain point of view.

However, frequency-domain theory alone is not sufficient for assessing the influence of UWB antenna arrays on the system performance. Therefore, the treatment of the transient radiation behavior of UWB antenna arrays in time domain is given by deriving the antenna arrays transient response and analyzing its quality measures like dispersion and ringing. The influence of the single element's transient response, the geometry of the array, the coupling between neighboring elements, and the feeding network are discussed in the context of a typical array geometry: the linear array. The theoretical modeling is illustrated by experimental results. The section finishes with simulation results for the application of a linear array of Vivaldi antennas, exponentially tapered slot antennas (TSA), for time-domain beam steering.

5.3.2. Modeling UWB antenna arrays

5.3.2.1. Transfer function and impulse response

In general, the electrical properties of antennas are characterized by input impedance, efficiency, gain, effective area, radiation pattern, and polarization properties [7]. For narrowband applications, it is possible to analyze these at the center

frequency of the system. For larger bandwidths, all of them become more or less frequency dependent, but the straightforward evaluation of the named parameters as functions of frequency is not sufficient for the characterization of the transient radiation behavior. One proper approach to take transient phenomena into account is to model the antenna as a linear time-invariant transmission system that translates the exciting voltage u_{tx} at the terminal into the radiated electrical far field e_{rad}. This system can be fully characterized by its transient response $\mathbf{h}(\theta,\psi)$. Assuming free-space propagation, this can be written according to (5.22) as shown in [8]. The dimension of the antenna's normalized transient response $\mathbf{h}$ is m/s. Together with the time-integrating convolution $*\mathbf{h}$, this relates to the meaning of a normalized[8] effective height:

$$\frac{u_{rx}}{\sqrt{Z_{L0}}} = \mathbf{h}(\theta,\psi) * \frac{\mathbf{e}_{\mathrm{inc}}}{\sqrt{Z_{F0}}}, \tag{5.21}$$

$$\begin{aligned}\frac{\mathbf{e}_{\mathrm{rad}}(\theta,\psi)}{\sqrt{Z_{F0}}} &= \frac{1}{r}\delta\left(t-\frac{r}{c_0}\right) * \mathbf{a}(\theta,\psi) * \frac{u_{tx}}{\sqrt{Z_{L0}}} \\ &= \frac{1}{r}\delta\left(t-\frac{r}{c_0}\right) * \frac{\partial}{\partial t}\mathbf{h}(\theta,\psi) * \frac{u_{tx}}{\sqrt{Z_{L0}}}.\end{aligned} \tag{5.22}$$

The effective antenna gain G_{eff} can be readily calculated from the antenna's response in frequency domain $\mathbf{H}$:

$$\begin{aligned}G_{\mathrm{eff}}(f,\theta,\psi) &= \frac{\omega^2}{\pi c_0}\left|\mathbf{H}(f,\theta,\psi)\right|^2, \\ \mathbf{e}_{\mathrm{tot}} &= \sum_i \mathbf{e}_i \\ &= \sum_i \frac{1}{r_i}\delta\left(t-\frac{r_i}{c_0}\right) * \frac{\partial}{\partial t}\mathbf{h}_{\mathbf{i}}(\theta,\psi) * \sqrt{\frac{Z_{F0}}{Z_{L0}}}u_{tx,i}.\end{aligned} \tag{5.23}$$

The voltages $u_{tx,i}$ at the port of each radiator are determined by the properties of the signal source, the feed network (signal distribution and matching), and the mutual coupling between the single radiators. The presence of electromagnetic coupling of the single radiators can be modeled using the self and mutual coupling impedance matrix $\mathbf{Z}_c$ [9]. It can be transformed into a scattering parameter matrix $\mathbf{S}_c$, which describes the N element array as a linear N-port, see (5.24). If a single source signal is assumed, which is distributed by a linear feed network on the N single radiators, the array together with the feed network behaves as single antenna with a transfer function for the radiated electric field. This transfer function can be obtained by analyzing the linear network consisting of feed network, mutual coupling network, and coupling to the radiated far-field. The latter is modeled as a directional and polarized far-field port of the array [10]. This model includes

[8]Normalized means that the regarded voltages are normalized to the square root of the antennas characteristic impedance $\sqrt{Z_{L0}}$ and the electric field is normalized to the square root of the free-space characteristic impedance $\sqrt{Z_{F0}}$.

all relevant effects due to mismatch and mutual coupling [11]. The impedance matrix can be obtained from measurements or numerical simulations. Analytic expressions are available for some special array geometries of narrowband radiators like linear arrays of dipole antennas [9]. Applying multiple sources, this type of model has been used with great success in order to describe the properties of multiple-input multiple-output (MIMO) antenna arrays [11]:

$$\mathbf{S}_c = \mathbf{Z}_{L0}^{1/2}\left(\mathbf{Z}_c + \mathbf{Z}_{L0}\right)^{-1}\left(\mathbf{Z}_c - \mathbf{Z}_{L0}\right)\mathbf{Z}_{L0}^{-1/2}. \tag{5.24}$$

In (5.24) $\mathbf{Z}_{L0}$ denotes the diagonal matrix of the port impedances to which the scattering parameters are normalized. Assuming a single source signal u_{tx} and identical single elements that are identically oriented, the transfer function $\mathbf{h}_{\mathrm{ar}}$ of the antenna array can be written as a convolution of the single elements transient responses $\mathbf{h}$ and the time-domain array factor f_{ar}:

$$\mathbf{h}_{\mathrm{ar}} = \mathbf{h} * f_{\mathrm{ar}}. \tag{5.25}$$

The time-domain array factor (5.25) f_{ar} is determined by the array topology, the feeding network, and the mutual coupling of the elements. For the synthesis of ultra-wideband arrays, the combination of the time-domain array factor and the transient response of the single element is of high importance. Therefore, (5.25) is analyzed for different parameters. It is mandatory to introduce realistic transient responses for the single elements in order to get realistic results for the dispersive behavior of the whole array. In order to separate the influences of the different phenomena, possible simplifications and the related assumptions are shown. The distortions that the mutual coupling introduces due to reflections and reradiation can be neglected if the distance between the elements is large enough. The amount of coupling also depends on the type of the single radiators: omnidirectional radiators are more likely to couple than more directive ones.

It is assumed that the mutual coupling and the antenna mismatch can be neglected in the bandwidth of interest. Then the array factor can be written as the scalar sum of the path transfer functions $W_i(t)$ of the feeding network for each element i:

$$f_{\mathrm{ar}} = \sum_{i=1}^{N} W_i(t) * \delta\left(t - \tau_{\hat{r},i}\right). \tag{5.26}$$

The time delay $\tau_{\hat{r},i}$ refers to the relative delay for the signal propagating from the single element i to an observation point in the array's far-field zone in direction $\hat{r}$. The delay $\tau_{\hat{r},i}$ is the difference between the time of arrival (TOA) to the same observation point for radiation from element i and radiation from a reference point in the array structure, which is usually the center of the array. The weighting functions $W_i(t)$ are the transfer functions of the active or passive feeding network of the array. In the case of a passive power divider network, the weighting functions

$W_i(t)$ are bound to

$$\sum_{i=1}^{N} \left|\left| W_i(t) \right|\right|^2 \leq 1. \tag{5.27}$$

In the case of an ideal dispersion free feeding network, they reduce to $W_i(t) = w_i \delta(t - \tau_{\text{feed},i})$. This leads to a simplified formulation for the time-domain array factor:

$$f_{\text{ar}} = \sum_{i=1}^{N} w_i \, \delta\left(t - \tau_{\hat{r},i} - \tau_{\text{feed},i}\right). \tag{5.28}$$

As well as a tapered amplitude distribution is used in frequency domain in order to lower the sidelobes, the w_i can be used in time domain in order to lower the ringing for the off-boresight directions. In the following calculations for an ideal feeding network, a uniform amplitude distribution with

$$w_i = \frac{1}{\sqrt{N}} \tag{5.29}$$

is assumed.

5.3.2.2. Evaluation

The transient response of the antenna array can be evaluated with respect to the peak value p and the full width at half maximum (FWHM) $w_{0.5}$ of its analytic[9] envelope $|\mathbf{h}_{\text{ar}}^{+}|$ [12]. The peak value indicates what maximum output voltage of the array might be expected for a given incident field. The FWHM is a measure in which time interval the main energy of the radiated signal is concentrated for a given direction:

$$\begin{aligned} p(\theta,\psi) &= \max_{t} \left| \mathbf{h}_{\text{ar}}^{+}(t,\theta,\psi) \right|, \\ \text{FWHM}(\theta,\psi) &= \max_{|\mathbf{h}_{\text{ar}}^{+}(t,\theta,\psi)| = p(\theta,\psi)/2} t - \min_{|\mathbf{h}_{\text{ar}}^{+}(t,\theta,\psi)| = p(\theta,\psi)/2} t. \end{aligned} \tag{5.30}$$

For a more detailed analysis of the antenna's transient response, see [13, 12]. The FWHM can also be used to define a time-domain far-field criterion [14]. In the far-field region, it is assumed that for the boresight direction the propagation delays are equal for all elements. The maximum error at a given distance r is the difference in propagation delay between the center of the array and the outmost element at $D/2 = (1/2)(N-1)d$ is

$$\Delta t = \frac{r}{c_0}\left(\sqrt{1 + \frac{D^2}{4r^2}} - 1\right). \tag{5.31}$$

[9] $(\cdot)^{+}$ denotes the complex analytical signal in time domain.

The requirement that this error will be less than a fraction of the duration of the impulse response αFWHM results in

$$r_{\mathrm{FF}} > \frac{D^2}{8c_0\alpha\mathrm{FWHM}}. \tag{5.32}$$

There is up to now no standardized value for α. Practical values range from $\alpha = 1/8, \ldots, 1/3$ depending on the required accuracy. For an array with $N = 4$ elements, spacing $d = 40\,\mathrm{mm}$, and single elements for the FCC frequency range with a typical FWHM = 115 picoseconds, this range of α yields an $r_{\mathrm{FF}} = 4.6, \ldots, 1.8\,\mathrm{m}$. In frequency domain, the well-known far-field criterion for harmonic excitation with $f = 10.6\,\mathrm{GHz}$ yields for the same array $r_{\mathrm{FF}} > 2D^2/\lambda = 1.8\,\mathrm{m}$. For smaller r, the transient response becomes more and more dependent on the distance $\mathbf{h}_{\mathrm{ar}} = \mathbf{h}_{\mathrm{ar}}(r, \theta, \psi)$.

5.3.3. Uniform spaced linear array

In Figure 5.7, the orientation of a single Vivaldi element is shown together with the employed spherical coordinate system. The xy-plane coincides with the H-plane and the xz-plane coincides with the E-plane[10] of the antenna. The single-element Vivaldi antenna consists of an exponentially tapered slot, etched onto the metallic layer on a Duroid 5880 substrate. The narrow side of the slot is used for feeding the antenna, the opening of the taper points to the direction of the main radiation. The Vivaldi is designed with a Marchand balun feeding network, which has been developed for the frequency range of 3.1–10.6 GHz with a return loss better than 10 dB. The size of this antenna is $78 \times 75 \times 1.5\,\mathrm{mm}^3$. The radiation is supported by the travelling wave structure. The propagation velocity on the structure varies only slightly with frequency. The CW gain is calculated from the measured directional transient response $h(\theta, \psi)$ according to (5.23). The maximum gain of the single element is 7.9 dB at 5.0 GHz [15].

In Figure 5.8, the geometry of the linear array is shown. The single elements are arranged along the y-axis and are separated with equal spacing d. An observation point in the far-field region is visible with the same direction ψ for each element. The propagation paths are parallel rays emerging from the single elements as shown in Figure 5.8. In (5.33) the delay for element i is given relative to the center of the array dependent on the angle ψ:

$$\tau_{r,i} = \frac{r_i - r_1}{c_0} = \frac{1}{c_0}\left(\frac{N-1}{2} - i\right) d \sin\psi. \tag{5.33}$$

Similar expressions like (5.33) are readily obtained for other geometries like a circular array or a rectangular array following similar geometrical considerations.

[10]The H-plane contains the magnetic field vector $\mathbf{H}$ and the direction of maximum radiation. Accordingly, the E-plane contains the electric field vector $\mathbf{E}$ and the direction of maximum radiation.

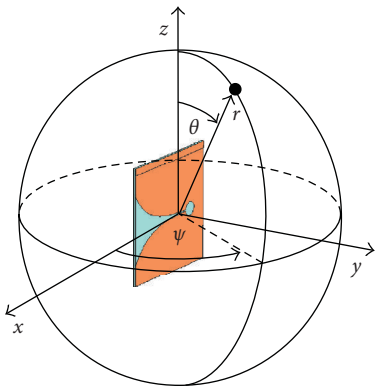

FIGURE 5.7. Coordinate system with a single Vivaldi element.

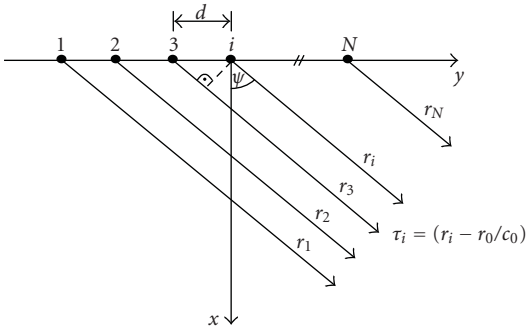

FIGURE 5.8. Geometry of a uniform linear array.

5.3.3.1. Results for the uniform linear array

For the uniform linear array (ULA), the main parameters are the number of elements N, the spacing of the elements d, the distribution of the excitation, especially a time delay between neighboring elements $\Delta\tau$.

In Figure 5.9, the measured magnitude of the transient response analytic envelope is shown for the single Vivaldi element in H-plane. Its high peak value ($p_{\max} = 0.35$ m/nanosecond) and the short FWHM = 115 picoseconds of the transient responses envelope stand for very low dispersion and ringing. For off-boresight directions $|\psi| > 30°$, the antenna exhibits no unique center of radiation. Also the amplitude decreases in these directions. For $\psi = 180°$, an appreciable backward radiation occurs with $p(\psi = 180°) = 0.08$ m/nanosecond. The transient response for this direction is more dispersive and shows a width of FWHM = 807 picoseconds. The measured transient response of one single Vivaldi element is taken for the simulations of the arrays transient response according to (5.25). The measurement bandwidth was 20 GHz. For details on the measurement procedure, see [13, 12]. Assuming a uniform amplitude distribution and negligible coupling,

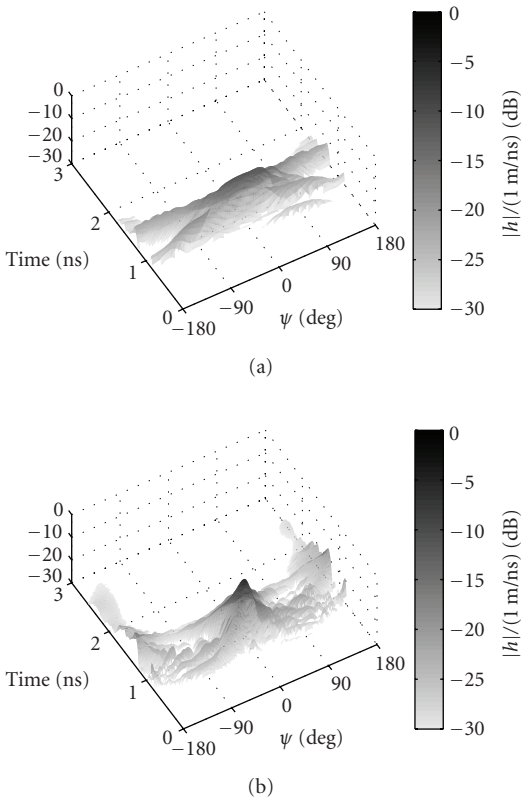

FIGURE 5.9. (a) Measured transient response of single Vivaldi element. (b) Simulated transient response of linear array with $N = 4$ Vivaldi elements with spacing $d = 4$ cm. The simulation is based on the measurement of the single element.

the maximum peak value of the arrays transient response

$$p_{\max,\mathrm{ar}} = \max_{\theta,\psi} p_{\mathrm{ar}}(\theta,\psi) = \sqrt{N} p_{\max,i} \tag{5.34}$$

increases $\sim \sqrt{N}$. In the same manner as the main peak increases, the peak amplitude for the off-boresight directions is decreased $\sim 1/\sqrt{N}$ because for these directions the impulse responses of the single elements are resolved in time and the single element i is excited with $\sim 1/\sqrt{N}$ according to (5.29) as can be seen in Figure 5.11. Depending on the duration and the spectral properties of the excitation, this ringing can cause significant sidelobes.

Neglecting the mutual coupling, the array gain increases linearly with the number of elements $G_{\mathrm{array}} = NG_i$. The spacing d of the array elements has a significant impact on the transient response: the maximum dimension of the array determines the maximum ringing for the off-boresight directions in terms of FWHM as can be seen from Figure 5.12. Larger element spacing narrows the beam

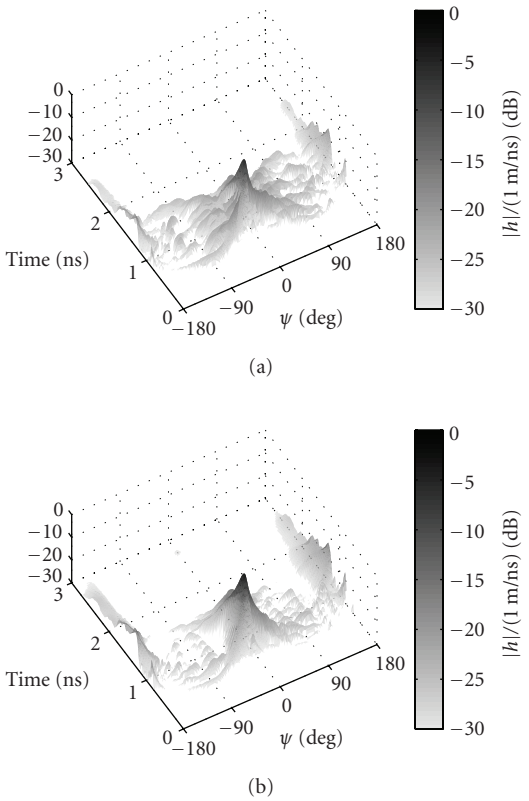

FIGURE 5.10. (a) Simulated transient response of a linear array with $N = 4$ Vivaldi elements with spacing $d = 8$ cm. (b) $N = 7$ Vivaldi elements with spacing $d = 4$ cm. The simulations are based on the measurement of the single element.

with constructive interference of the single-element signals whereas the peak value $p(\psi)$ for the off-boresight directions depends on the number of elements. The antenna gain in the frequency domain is strongly affected by the element spacing (see Figure 5.13). For element spacings with $d > \lambda$, frequency-selective grating lobes emerge. Therefore, an element spacing $d < 28$ mm is required for a grating-lobe-free operation below 10.6 GHz. As seen before for short pulses, these grating lobes transform into a ringing behavior.

5.3.4. Beam steering

The application of phased arrays is an established technology for steering the antenna beam electronically. For ultra-wideband applications, the steering of the antenna main beam direction is an interesting option for location aware devices in order to scan sequentially the surrounding space and to cancel interference from other devices. This can be achieved by introducing a mutual delay $\Delta\tau$ between

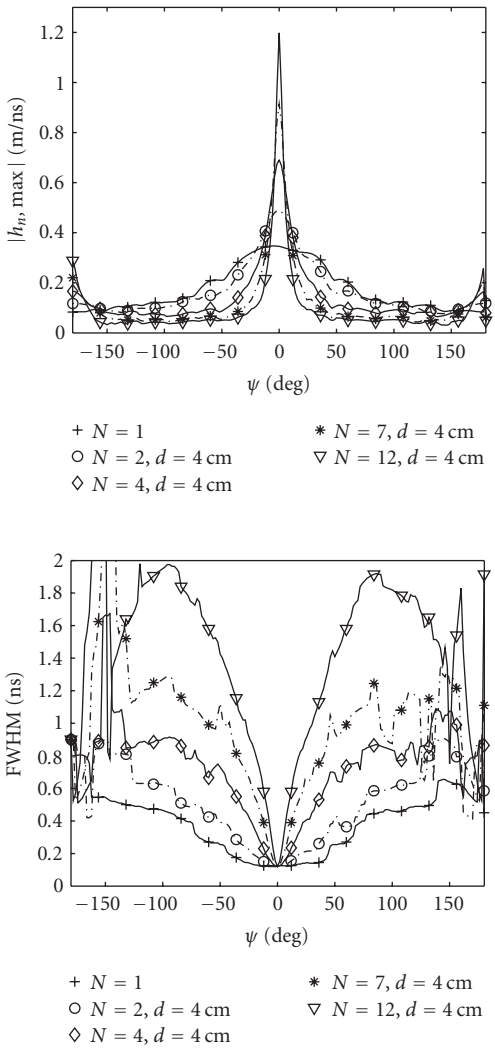

FIGURE 5.11. Pattern for the peak value $p(\psi)$ and FWHM $w_{0.5}(\psi)$ of the array impulse response for varying number of elements N; $d = 4$.

neighboring elements. The effect can be visualized best by looking at the time-domain array factor f_{ar} according to (5.28). On Figure 5.14(a) it is shown for $\Delta\tau = 0$ picosecond. Each line in the diagram represents the angle-dependent delay $\delta(t - \tau_{\hat{r},i} - \tau_{\text{feed},i})$. The directions where the lines cross yield the maximum radiation. Now let $\tau_{\text{feed},i} = i\Delta\tau$, then the lines are shifted in time with a fixed mutual delay $\Delta\tau$. Due to this shift, the crossing points of the single-element radiation curves shift too. For small shifts, the crossing in backward direction will be attenuated by the convolution with the single-element response. For increasing $\Delta\tau$, the

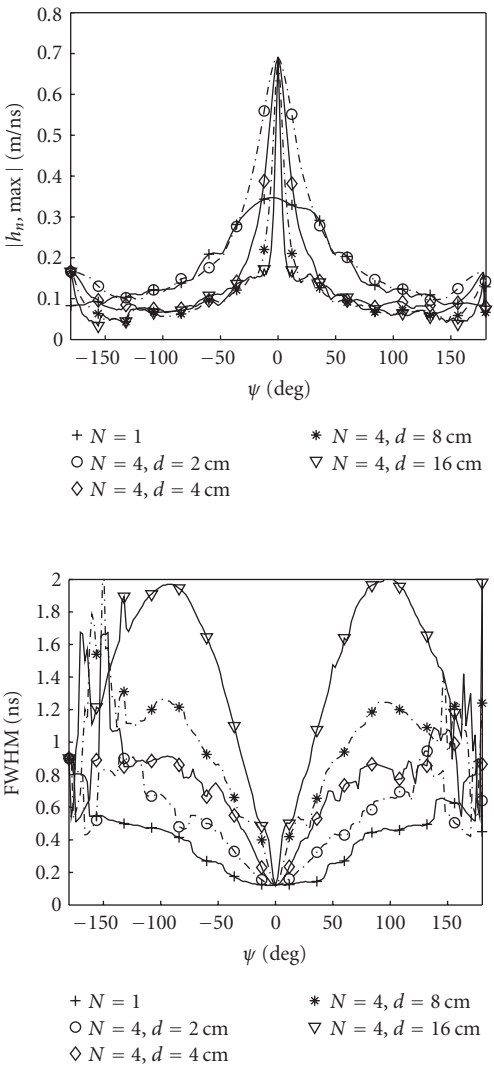

FIGURE 5.12. Pattern for the peak value $p(\psi)$ and FWHM $w_{0.5}(\psi)$ of the array impulse response for varying d; $N = 4$.

two crossing points move towards each other until they coincide for $\Delta\tau = d/c_0$ at $\psi = 90°$. This is the special case of an end-fire array (see Figure 5.15(a)). If the mutual delay is larger, no crossing occurs anymore (see Figure 5.15(b)). The directions for maximum radiation are calculated by

$$\psi_{\max} = \arcsin\left(\frac{\Delta\tau c_0}{d}\right). \tag{5.35}$$

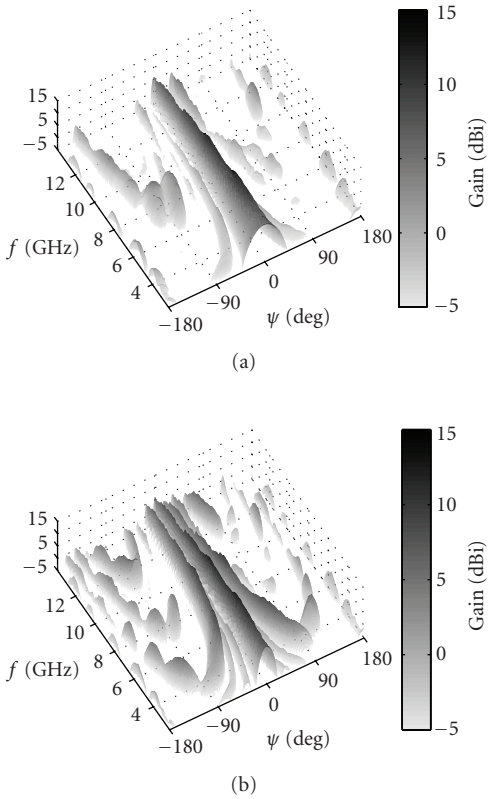

FIGURE 5.13. (a) Simulated gain of a linear array with $N = 4$ Vivaldi elements with spacing $d = 4$ cm. (b) $N = 4$ Vivaldi elements with spacing $d = 8$ cm. The simulations are based on the measurement of the single element.

The sensitivity to changes of $\Delta\tau$ is obtained as

$$\frac{\partial \psi_{\max}}{\partial \Delta\tau} = \frac{180^\circ}{\pi} \frac{c_0}{d} \frac{1}{\sqrt{1 - (\Delta\tau c_0/d)^2}}. \tag{5.36}$$

For example, a linear array with spacings $d = 4$ cm exhibits in the main beam direction a sensitivity to a variation of $\Delta\tau$ of 0.43°/picosecond. This determines the requirements on the timing accuracy of an active, true-time delay beam-steered array. As expected from the time-domain array factor, the dispersive behavior of the scanning array cannot be better than that of the single element for the scanning direction $\psi_{\max}$. It is worsening for the directions aside $\psi_{\max}$. This is due to the effect that the resolved transient responses of the array factor begin to lie within the mainlobe of the single element. Therefore, they may encounter an appreciable amplification.

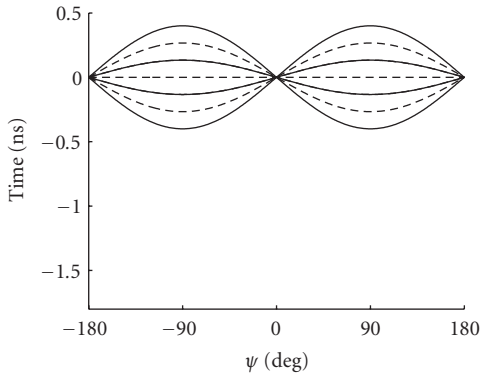

(a)

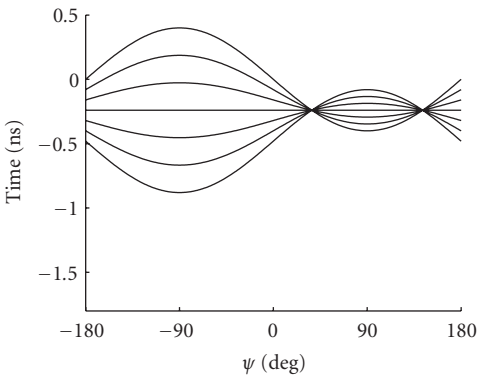

(b)

FIGURE 5.14. (a) Time-domain array factor f_{ar} of a linear array with $N = 7$ elements, spacing $d = 4$ cm (solid and dashed lines). The solid lines hold for an array with $N = 4$ elements and spacing $d = 8$ cm; $\Delta\tau = 0$ picosecond. (b) $N = 7$ elements with spacing $d = 4$ cm and a delay between neighboring elements of $\Delta\tau = 80$ picoseconds.

5.3.5. Summary

The application of UWB antenna arrays has been analyzed on the basis of the arrays transient response, which provides all relevant information about their transient radiation and reception behavior. With respect to a given array topology, simplified expressions for the time-domain array factor have been introduced. Together with measurements of the transient response of a single element, the parameters of linear arrays are analyzed. It can be concluded that the appearance of grating lobes for sparse arrays in narrowband applications translates into additional dispersiveness for off-boresight directions. In time domain, this means additional ringing and therefore a higher FWHM than within the main beam. The maximum of the FWHM depends on the size of the array. The dispersive properties of a UWB array has to be taken into account for beam-steering purposes. Also

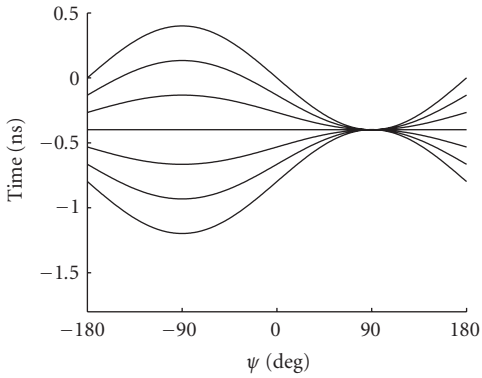

(a)

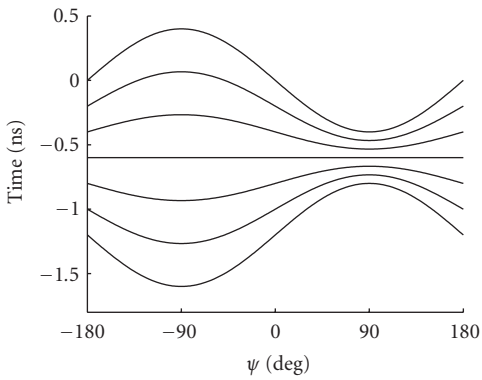

(b)

FIGURE 5.15. (a) Time-domain array factor f_{ar} of a linear array with $N = 7$ elements, spacing $d = 4$ cm and a delay between neighboring elements of $\Delta\tau = 133$ picoseconds. (b) $N = 7$ elements with spacing $d = 4$ cm and a delay between neighboring elements of $\Delta\tau = 200$ picoseconds.

the timing accuracy of the delay network single elements has to be considered. The presented analysis is independent of the signal that might be applied to the array. The spatio-dispersive properties of the array and their impact on a given signal can be tested in a simulative design study with the presented tools.

5.4. UWB polarization diversity

5.4.1. Introduction

In the early days of radio communication systems, baseband transmission has been the first form of delivering information between remote locations by means of electromagnetic waves. Several problems related to these first systems were overcome by the invention of heterodyning and superheterodyning methods, which introduced the modulation concept [16]. Nowadays, the advances in the field of

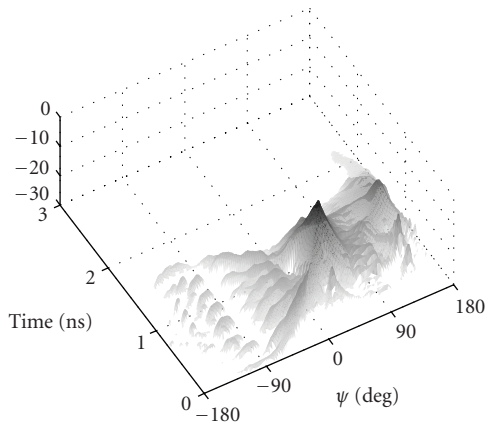

(a)

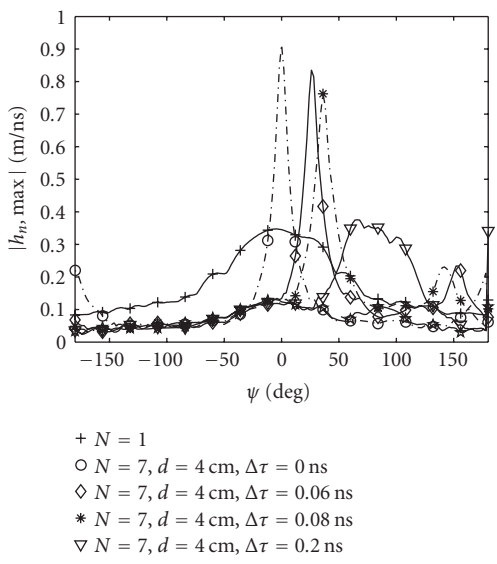

(b)

FIGURE 5.16. (a) Simulated transient response of a linear array with $N = 7$ Vivaldi elements with spacing $d = 4$ cm and delay between neighboring elements of $\Delta\tau = 80$ picoseconds. (b) Pattern for the peak value $p(\psi)$ of the array impulse response for varying $\Delta\tau$.

transmitter and receiver technology give to impulse radio a new important role in the scenario of communication systems [17].

Ultra-wideband (UWB) signals are characterized by a band of several hundreds of MHz up to several GHz. The Federal Communications Commission (FCC) issued in February 2002 a Report and Order (R&O) [6] in which defines as UWB any signal that occupies, on an unlicensed basis, more than 500 MHz in

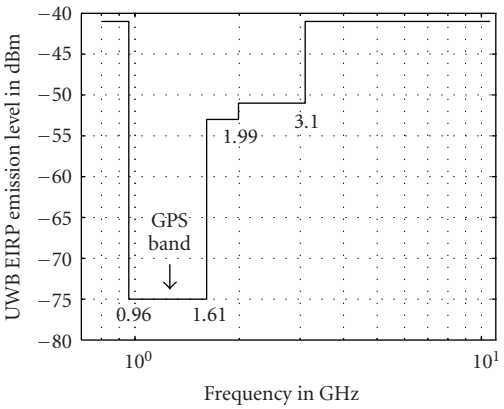

FIGURE 5.17. Mask of the allowed PDS.

the band between 3.1 and 10.6 GHz and whose power spectrum density (PSD) meets a given mask designed to introduce no interference to already deployed services, such as global positioning system (GPS) and personal communication services (PCS) digital cellular systems. The mask is shown in Figure 5.17. Early UWB systems used the available band to transmit baseband impulses characterized by a very narrow time duration [18]. In such systems, particular research effort has been devoted to a proper design of the impulse shaping filter such that to concentrate as much energy as possible in the allowable bandwidth with a tolerable PSD. An advantage of this technique is that fine resolution of multipath is feasible, resulting in a reduced fading. This fact, along with the limited allowed transmission power due to the imposed emission constraint, makes the UWB technology a valid candidate for indoor short-range transmission, typical of wireless personal area network (WPAN). Preliminary and simple computations of capacity demonstrate that data rates greater than 100 Mbps at 10-meter distance—thus, much higher than already standardized short-range techniques, such as Bluetooth and IEEE 802.11b—will be accomplished.

Recently, a different concept of UWB signal has emerged [19–21]. Instead of transmitting single impulses occupying a large bandwidth, the available spectrum is divided into several bands that can be accessed separately by a single or multiple users. Due to FCC definition, each band must be at least 500 MHz. Usually, a number of bands between 3 and 10 are taken into consideration. This method, referred to as *multiband UWB*, has several advantages with respect to *impulse radio UWB*. A flat PSD can be accomplished in each band, so that higher power can be conveyed into the channel with respect to impulse-based UWB. Choosing proper positions of the bands allows regional regulation constraint on spectrum occupancy to be met. Also from an implementation point of view, the multiband approach is attracting since less stringent requirements can be imposed on the ADC sampling rate and dynamic range, so that a software-defined receiver becomes feasible. Different combinations of CDMA and OFDM have been proposed for fully exploiting

the 500 MHz band and several band-hopping methods have been foreseen to allow several users to access the channel as well several piconets to coexist.

Another important aspect of UWB systems is antenna technology and design related to minimum space occupancy and portability as well as space diversity exploitation [22, 23]. Critical points in antenna design are the required huge bandwidth and the tradeoff between antenna gain, antenna dimensions, and flatness of the antenna-to-antenna response [24]. More attention must be paid to the position of the transmitting and receiving antennas and their relative orientation since this influences the antenna-to-antenna frequency response. For transmission between several devices and a base station, more than one antenna can be foreseen at the base station, but only one, for dimension containment, at the portable devices. Exploiting such diversity is an important issue of UWB systems.

In this study, a UWB transmission system able to provide a fast, local-range, wireless connection on an unlicensed basis by using the same frequency spectrum assigned to other narrowband communication standards is considered. Several channel models have been presented in the literature [25–27], but only a few consider the distortion effect caused by a real UWB antenna.

Based on the observation that the antenna-to-antenna frequency response strongly depends on the mutual orientation, a technique using two transmitting antennas with orthogonal orientation to create diversity in the received UWB signal is proposed. The receiver is equipped with a single antenna whose orientation and position are arbitrary within the coverage area, thus resulting in a special case of a $2:1$ MIMO system. Space-time[11] encoding is used at the transmitter to exploit polarization diversity without increasing the signal bandwidth [28]. The performance of different multiple-access schemes for the downlink is investigated. It will be demonstrated that the proposed system allows reliable detection independently of the receiving antenna orientation and a uniform coverage of the indoor area.

This section is organized as follows. Section 5.4.2 introduces the system of antennas used in the transmit/receive devices and reviews Alamouti's method to exploit polarization diversity. Section 5.4.3 presents the model of the proposed multiband UWB system, the methods for multiple access to the channel, and the model of the transmitted signal. Section 5.4.4 describes the UWB channel model that will be used in the simulations. Section 5.4.5 presents a derivation of the conditional probability of error of the proposed system given the knowledge of the channel status, whereas in Section 5.4.6 a semianalytical approach is used to derive the average probability of error. Implementation issues are discussed in Section 5.4.7. Concluding remarks are given in Section 5.4.8.

5.4.2. Antenna issues and polarization diversity

The study and design of UWB antennas has a key role in assessing the overall performance of a communication system. In this section, the specific antenna

[11]The term polarization time would be more appropriate in this context. Here, we use the term space time since it is customary in multiple antenna systems.

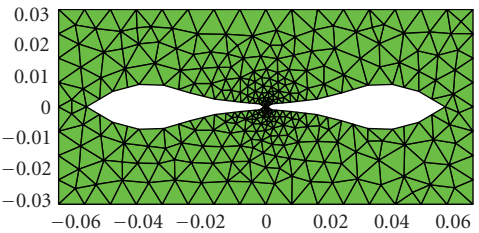

FIGURE 5.18. Shape of the slot antenna designed for UWB communications (the dimensions are in meters).

considered for our analysis is described. The antenna has been designed for impulse radio UWB systems, but can be used also for our multiband UWB system.

The complete antenna design and analysis is described in [24]. It is a slot antenna, having a length of approximately six inches. The shape of the antenna is shown in Figure 5.18. Although a particular type of antenna is considered, the proposed method can be applied to any antenna shape. In [24], a tool for achieving the three-dimensional radiation pattern of the antenna is presented. Once the relative positions and orientations of the receiving and transmitting antennas are given, the antenna-to-antenna transfer function, computed on a preassigned frequency grid, can be evaluated. As it will be shown, these transfer functions are strongly dependent on the relative orientations of the antennas.

To avoid performance loss due to the orientation-variant radiation pattern, two antennas with orthogonal orientation at the transmission side are used. It will be demonstrated that such a system is able to deliver a sufficiently high level of signal *independently of the orientation of the receiving antenna*.

In Figure 5.19, the specific indoor environment used to simulate the proposed system is shown. It sketches a quite large environment ($16 \times 16 \times 7$ meters), with a staircase leading to an intermediate floor. The two base-station antennas, with orthogonal orientation, are placed on the ceiling of the room. Seven different possible locations and orientations of the portable UWB device are shown. In Figure 5.20, the amplitude antenna-to-antenna transfer functions evaluated for each position and for each transmitting antenna (denoted as H and V polarizations) are given. As can be seen, a common trend for all polarizations and all locations is that the amplitude response decreases with frequency, so that the highest frequency bands are expected to yield the main contribution to the total bit error rate.

Diversity can be created in the time, frequency, or space domain to combat negative effects of the channel due to fading [29]. Also cross-polarized antennas can be used to increase the diversity order at the receiver [30–33]. In a space diversity scheme, that is, based on an antenna separation equal to ten times the wavelength, a uniform coverage is not guaranteed with real antennas due to the frequency distortion induced by orientation. With polarization diversity, this problem can be avoided.

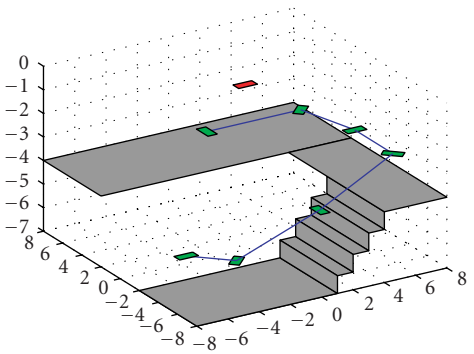

FIGURE 5.19. Scheme of the indoor environment. The position of the base-station antennas and seven different possible locations and orientations of the UWB device are shown.

But, diversity may decrease the resources available for user data transmission. Recently, space-time coding methods have been proposed to exploit diversity without wasting system resources. In this study, Alamouti's scheme [34], a well-known two-branch space-time block-coding (STBC) method, is considered. It allows two coded symbols to be transmitted in two consecutive time intervals over two channels that, in this case, are related to the orthogonally oriented antennas. Alamouti's method is now briefly reviewed. Let s_0 and s_1 be the complex symbols to be transmitted in the consecutive time intervals $(0, T)$ and $(T, 2T)$. The symbols transmitted over the antennas in the time intervals $\{(0, T), (T, 2T), \dots\}$ are

$$\begin{aligned} &\text{Antenna } V : \{c_{V1}, c_{V2}, \dots\} = \{s_0, -s_1^*, \dots\}, \\ &\text{Antenna } H : \{c_{H1}, c_{H2}, \dots\} = \{s_1, s_0^*, \dots\}. \end{aligned} \tag{5.37}$$

Let h_H and h_V be the complex gains introduced by the channel in the links from the H and V antennas to the receiver. In this scheme, it is assumed that the channel coefficients do not vary within the period $(0, 2T)$. Hence, the received signal sequence $\{r_0, r_1, \dots\}$ is

$$\{r_0, r_1, \dots\} = \{s_0 h_V + s_1 h_H + n_0, -s_1^* h_V + s_0^* h_H + n_1, \dots\}, \tag{5.38}$$

where n_0 and n_1 are the AWGN contributions. The space-time decoder, which has knowledge of the channel status, builds two decision variables by combining the received symbols as follows:

$$\begin{aligned} \{\hat{s}_0, \hat{s}_1, \dots\} &= \{r_0 h_V^* + r_1^* h_H,\ r_0 h_H^* - r_1^* h_V, \dots\} \\ &= \Big\{ s_0 \Big(|h_V|^2 + |h_H|^2 \Big) + n_0 h_V^* + n_1^* h_H, \\ &\qquad s_1 \Big(|h_V|^2 + |h_H|^2 \Big) + n_0 h_H^* - n_1^* h_V, \dots \Big\}. \end{aligned} \tag{5.39}$$

As can be seen, a factor two of diversity gain is achieved.

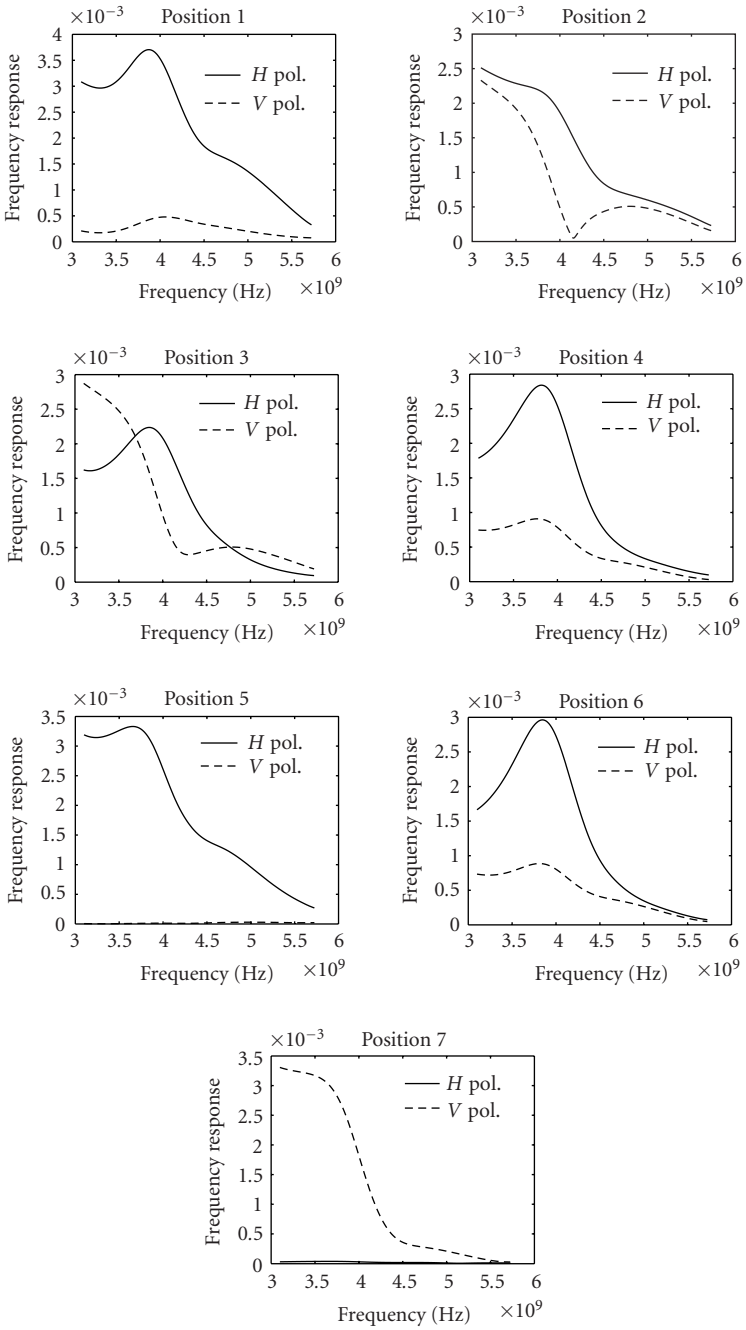

FIGURE 5.20. Amplitude transfer functions in the different positions of the UWB device within the room.

Table 5.2. Boundary and center frequencies (GHz) of the proposed UWB system.

Band	Low	Center	High
1	3.1	3.35	3.6
2	3.725	3.975	4.225
3	4.35	4.6	4.85
4	5.225	5.475	5.725

In the following section, the proposed multiband UWB system with polarization diversity is described.

5.4.3. System model: multiband UWB

The proposed system uses a multiband approach to generate the UWB signal. It will be assumed that M bands can be accessed by the users or the devices connected to the system. According to the FCC recommendations, each band must be at least W Hz wide, where $W > 500$ MHz. The boundary and center frequencies of the proposed UWB system, for which we have chosen $M = 4$, are shown in Table 5.2.

The multiband approach allows the channel to be shared by the different users by means of frequency-division multiplex (FDM). Each band is divided into temporal slots and accessed by means of time-division multiplex (TDM). Note that a user device can access contemporarily more than one band only if it disposes of a multicarrier demodulator.

Due to the large frequency width, multipath propagation affects the reception of signals in each band. Orthogonal frequency-division multiplex (OFDM) has been proposed to combat channel degradation due to a frequency-selective channel [35, 36]. The transmitted symbol in each time/frequency tile, created by the mixed FDM/TDM multiple access, is obtained by applying OFDM to a set of user information bits. Since OFDM creates a further splitting of the available spectrum, several choices for assigning frequency bins (belonging, eventually, to different bands) to active users can be considered. The different strategies will be discussed in the following subsection.

5.4.3.1. Multiple access in multiband UWB

Assume that each band is divided into N subcarriers. In the proposed system, $N = 128$ has been assumed. Hence, MN subcarriers are available to be assigned to the total number, say K, of active users. For the sake of simplicity, a progressive index spanning all the subcarriers, even if they belong to different bands, is used. Hence, the nth subcarrier, $n = 0, 1, \ldots, MN - 1$, has the frequency

$$f_n = f_{q,\text{low}} + \Delta f\, p, \tag{5.40}$$

where $n = qN + p$, $f_{q,\text{low}}$ is the lower bound frequency assigned to the qth band, and $\Delta f = W/N$ is the subcarrier spacing.

It is assumed that each subcarrier is exclusively assigned to each user, that is, it cannot be shared between two, or more, users. Let

$$I(k,l) = \{i_{k,l,m},\ m = 0,1,\ldots,M_I - 1\}, \quad k = 0,1,\ldots,K-1,\ l = 0,1,2,\ldots, \tag{5.41}$$

be the subset of carriers assigned to the kth user in the lth symbol time. The number of carriers M_I assigned to each user in each symbol time depends on the type of multiple access that is used. Some simple methods of accessing the channel are now illustrated.

In a purely FDM access, all users transmit contemporarily using different subcarriers. Assuming that evenly spaced subcarriers are assigned to different users, the set of assigned subcarriers can be expressed as

$$I_{\mathrm{FDM}}(k,l) = \left\{k + mK,\ m = 0,1,\ldots,\left\lfloor \frac{MN}{K} \right\rfloor - 1\right\}. \tag{5.42}$$

In a purely TDM access, time slots are assigned cyclically to different users, but, in a slot, all subcarriers are assigned to a user, that is,

$$I_{\mathrm{TDM}}(k,l) = \begin{cases} m, & m = 0,1,\ldots,MN-1,\ l = k,\ k+K,\ k+2K,\ldots, \\ \varnothing, & l \neq k,\ k+K,\ k+2K,\ldots. \end{cases} \tag{5.43}$$

In a mixed FDM/TDM access, a set of adjacent subcarriers is assigned to a user at each slot time, but the set of assigned subcarriers changes at each time interval. We have

$$I_{\mathrm{FDM-TDM}}(k,l) = \left\{m + \mathrm{rem}(k+l,K)\left\lfloor \frac{MN}{K} \right\rfloor,\ m = 0,1,\ldots,\left\lfloor \frac{MN}{K} \right\rfloor - 1\right\}, \tag{5.44}$$

where $\mathrm{rem}(p,q)$ is the remainder of the division between the integers p and q. With a suitable choice of system parameters, the subcarriers assigned to a user do not span more than one band at each time interval, and, as a particular case, all subcarriers within a band may be assigned to the same user.

A graphical representation of the three access methods used in this study is shown in Figure 5.21.

5.4.3.2. Signal model

In this section, the model of the transmitted signal is presented. Let $d_{k,n}^{(l)}$ be the data symbol transmitted by the kth user in the lth symbol time over the nth subcarrier. In the following, it will be assumed that $d_{k,n}^{(l)}$ belongs to a given constellation of symbols. After Alamouti's STBC, two sequences, $\{c_{H,k,n}^{(l)}\}$ and $\{c_{V,k,n}^{(l)}\}$, are created

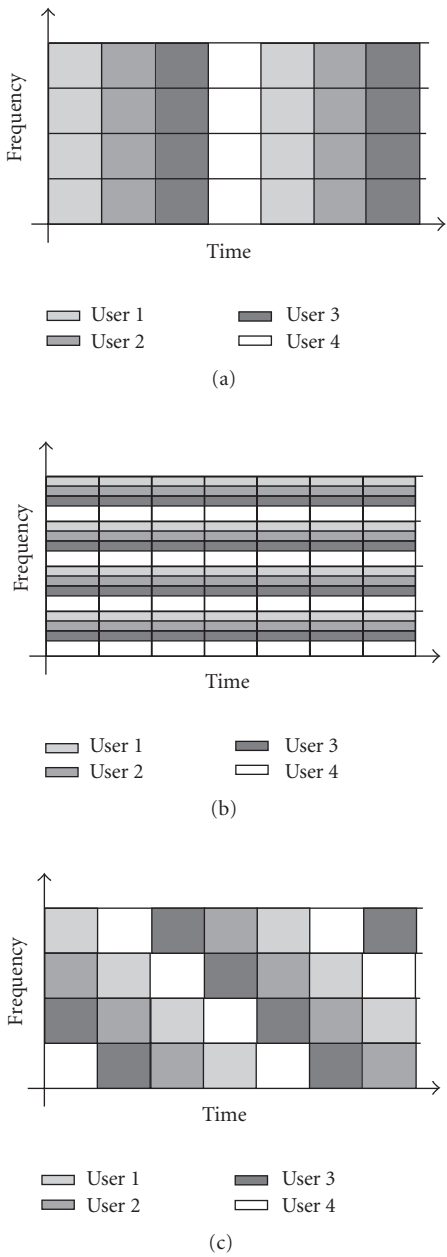

FIGURE 5.21. Assignments of the time-frequency tilings with the different access methods: (a) TDM, (b) FDM, and (c) mixed TDM/FDM.

and transmitted over the H and V polarizations of the antenna. By using the definitions given in the previous section, we have

$$s_{X,k,n}^{(l)}(t) = c_{X,k,n}^{(l)} e^{j2\pi f_n t} \tag{5.45}$$

for $t \in [lT, (l+1)T]$, where T is the symbol duration time and X denotes either the H or the V antenna. Hence, the signal transmitted over the qth band by the X antenna is

$$S_{X,q}^{(l)}(t) = \sum_{k=0}^{K-1} \sum_{n \in I(k,l),\, n=qN}^{(q+1)N-1} c_{X,k,n}^{(l)} e^{j2\pi f_n t}. \tag{5.46}$$

Consider now the effect of the channel on the transmitted signal. It can be modeled as the convolution of the antenna-to-antenna transfer function with a random process taking into account different channel characteristics (multipath, fading, time variability, etc.). The slicing of the spectrum into several narrow subbands makes the channel in each subcarrier flat. Assuming a slow motion of the mobile user, the effect of the channel on the nth subcarrier within the lth time interval is modeled as a complex constant that will be denoted as

$$h_{X,n}^{(l)} = \alpha_{X,n}^{(l)} e^{j\phi_{X,n}^{(l)}}. \tag{5.47}$$

A description of the channel model and of the statistics assumed to derive the variable $h_{X,n}^{(l)}$ is given in the next section.

The signal received by the user, equipped with a single antenna, in the nth band and in the lth symbol time interval is given by

$$\begin{aligned} R^{(l)}(t) &= \sum_{q=0}^{M-1} S_{H,q}^{(l)}(t) + S_{V,q}^{(l)}(t) \\ &= \sum_{k=0}^{K-1} \sum_{n \in I(k,l)} \alpha_{H,n}^{(l)} e^{j\phi_{H,n}^{(l)}} c_{H,k,n}^{(l)} e^{j2\pi f_n t} \\ &\quad + \sum_{k=0}^{K-1} \sum_{n \in I(k,l)} \alpha_{V,n}^{(l)} e^{j\phi_{V,n}^{(l)}} c_{V,k,n}^{(l)} e^{j2\pi f_n t} + w(t), \end{aligned} \tag{5.48}$$

where $w(t)$ is AWGN.

To extract the information delivered by the nth subcarrier, the receiver performs the correlation with $e^{-j2\pi f_n t}$, that is,

$$\begin{aligned} r_{k,n}^{(l)} &= \int_{lT}^{(l+1)T} R_m^{(l)}(t) e^{-j2\pi f_n t} dt \\ &= \alpha_{H,n}^{(l)} e^{j\phi_{H,n}^{(l)}} c_{H,k,n}^{(l)} + \alpha_{V,n}^{(l)} e^{j\phi_{V,n}^{(l)}} c_{V,k,n}^{(l)} + w_{k,n}^{(l)}. \end{aligned} \tag{5.49}$$

By applying Alamouti's decoder to two consecutive received symbols, we have

$$\begin{aligned}\widehat{d}_{k,n}^{(l)} &= r_{k,n}^{(l)}\alpha_{V,n}^{(l)}e^{-j\phi_{V,n}^{(l)}} + \left(r_{k,n}^{(l+1)}\right)^{*}\alpha_{H,n}^{(l)}e^{j\phi_{H,n}^{(l)}},\\ \widehat{d}_{k,n}^{(l+1)} &= r_{k,n}^{(l)}\alpha_{H,n}^{(l)}e^{-j\phi_{H,n}^{(l)}} - \left(r_{k,n}^{(l+1)}\right)^{*}\alpha_{V,n}^{(l)}e^{j\phi_{V,n}^{(l)}}\end{aligned} \tag{5.50}$$

and by using (5.49) in (5.50) we have

$$\begin{aligned}\widehat{d}_{k,n}^{(l)} &= \left(\left(\alpha_{V,n}^{(l)}\right)^2 + \left(\alpha_{H,n}^{(l)}\right)^2\right)d_{k,n}^{(l)} + w_{k,n}^{(l)}\alpha_{V,n}^{(l)}e^{-j\phi_{V,n}^{(l)}} + \left(w_{k,n}^{(l+1)}\right)^{*}\alpha_{H,n}^{(l)}e^{j\phi_{H,n}^{(l)}},\\ \widehat{d}_{k,n}^{(l+1)} &= \left(\left(\alpha_{V,n}^{(l)}\right)^2 + \left(\alpha_{H,n}^{(l)}\right)^2\right)d_{k,n}^{(l+1)} + w_{k,n}^{(l)}\alpha_{H,n}^{(l)}e^{-j\phi_{H,n}^{(l)}} - \left(w_{k,n}^{(l+1)}\right)^{*}\alpha_{V,n}^{(l)}e^{j\phi_{V,n}^{(l)}}.\end{aligned} \tag{5.51}$$

In the next section, the model used to derive the coefficients $h_{X,n}^{(l)}$ is presented, whereas in the following section the probability of error of the system is derived.

5.4.4. The UWB channel

Models for describing the effect of the channel are usually extracted from sets of measurements conducted in different indoor/outdoor environments [25–27, 37]. The set of measurement should be sufficiently large so that a general model, able to capture the main characteristics of the channel, can be derived.

In a wireless connection, the received signal is characterized by the superposition of replicas of the transmitted signal due to the reflections and diffraction of the EM wave around the objects (walls, furniture, persons, etc.) that are present in the environment. Hence, the received signal may be either attenuated or amplified according to destructive or constructive arrival of different echoes. The different replicas can be discriminated with a time resolution approximately equal to the inverse of the bandwidth of the system. In narrowband systems, a high number of replicas fall into the bin representing the time resolution of the system. Hence, for the central limit theorem, the received signal is assumed multiplied by a complex gain distributed as a Gaussian random variable, that is, its amplitude is Rayleigh distributed. Given the transmission environment, the model could be derived not only on a statistical basis but also from geometrical considerations. For example, if it is known that the transmitter and the receiver are in line of sight (LOS), then the direct path is assumed to prevail over the others paths and the global received signal becomes Ricean distributed.

The model used for narrowband signals is not valid for UWB signals. The time resolution of the system is so high that the number of paths impinging the receiver antenna in a time-resolution bin is not so large to justify the use of the central limit theorem. The IEEE 802.15.3a task group [38], aiming at defining a standard for a wireless interface based on UWB, has evaluated how a certain number of indoor wireless channel models fitted the set of UWB channel measurements. Among available models, that of Saleh and Valenzuela [37] has been found particularly

suitable to describe the behavior of the UWB channel. In such a model, the rays of the transmitted signal are characterized by arriving at the receiver grouped in clusters. A power delay profile of clusters and of rays within a cluster must be defined as well as statistics for interarrival times between clusters and interarrival time of rays within a cluster.

Based on this model and on a set of propagation measurements, Foerster et al. [26] introduced a modified model for UWB signals. The impulse response of the channel is assumed equal to

$$h(t) = Y \sum_{j=0}^{J} \sum_{p=0}^{P} \alpha_{j,p} \delta(t - T_j - \tau_{j,p}), \tag{5.52}$$

where T_j is the arrival time of the first ray of the jth cluster, $\tau_{j,p}$ is the arrival time of the pth path within the jth cluster (measured starting from the arrival of the first ray), $\alpha_{j,p}$ is the complex gain of each path, Y models the shadowing of the link. The interarrival times between clusters $(T_j - T_{j-1})$ and the interarrival times between rays within a cluster $(\tau_{j,p} - \tau_{j,p-1})$ are exponentially distributed with arrival rates Λ and λ, respectively. The power delay profiles of clusters and of rays within a cluster are exponentially distributed with decay factors Γ and γ, respectively. The path complex gain can be written as $\alpha_{j,p} = \xi_j \beta_{j,p}$, where ξ_j and $\beta_{j,p}$ are distributed as log-normal random variables, that is, $20 \log_{10} \xi_j$ and $20 \log_{10} \beta_{j,p}$ are normal random variables, that is, $\mathcal{N}(0, \sigma_1^2)$ and $\mathcal{N}(0, \sigma_2^2)$, respectively. Hence, also $\alpha_{j,p}$ is log-normally distributed, that is, $20 \log_{10} \alpha_{j,p}$ is $\mathcal{N}(\mu_{j,p}, \sigma_1^2 + \sigma_2^2)$, where $\mu_{j,p}$ is computed by normalizing the path energy with respect to the first arrived path energy. This normalization takes into account the power delay profiles with decay factors Γ and γ and the values of the realization of the interarrival times (see [26] for more details). Finally, Y is a log-normal distributed shadowing, that is, $20 \log_{10} Y$ is $\mathcal{N}(0, \sigma_Y^2)$.

In the present study, a mixed deterministic/statistic modeling of the channel is used.

It is assumed that an LOS link between the transmitter and the receiver exists. This link is modeled as a deterministic transfer function depending on the frequency as well as on the relative orientation of the transmitting and receiving antennas. The seven positions and orientations sketched in Figure 5.19, whose transfer functions are plotted in Figure 5.20, have been taken into consideration in the simulations.

This deterministic model, however, does not include the several echoes received after reflections and diffraction around objects in the room, that is, the non-LOS (NLOS) part of the received signal. Dealing with such echoes in a deterministic way affects the generality of the environment and its modeling. Hence, a statistic modeling for this NLOS component has been considered. For this purpose, the model described in [26] and previously reviewed has been used. The values of the parameters of the models that have been used in the simulations are taken from [26] and are reported in Table 5.3 It should be noted that, due to the

Table 5.3. Parameters of the channel model.

Λ	0.0667	(1/ns)
λ	2.1	(1/ns)
Γ	14	
γ	7.9	
σ_1	3.4	(dB)
σ_2	3.4	(dB)
σ_Y	3	(dB)

nature of the UWB transmission, the parameters of this model do not refer to a baseband representation.

The LOS and the NLOS components are linearly combined according to a parameter θ that allows us to vary the percentage of energy deriving from the LOS component. Let $a_{X,n}$ be the transfer function of the LOS link from the X (either H or V) to the receiving antenna, measured at the nth subcarrier frequency. This function depends on the positions of the receiver and on the relative orientation of the transmitting/receiving antennas but does not depend on time. Samples of this function are plotted in Figure 5.20. Moreover, let $g_{X,n}^{(l)}$ be a realization of the coefficients obtained from the NLOS model at the nth subcarrier frequency, valid for the X antenna link and at the lth symbol time. The coefficients $h_{X,n}^{(l)}$ used in Section 5.4.3.2 are given by

$$h_{X,n}^{(l)} = \sqrt{\theta}\, a_{X,n} + \sqrt{1-\theta}\, g_{X,n}^{(l)} b_n. \tag{5.53}$$

The function b_n is the antenna-to-antenna transfer function when the transmitting and receiving antennas are favorably coupled and at a distance of three meters (the minimum distance in the walk depicted in Figure 5.19). This function has been introduced to simulate the reception of the NLOS component by our specific antenna system. In fact, it yields a frequency shaping to the NLOS component dependent on the antenna characteristics and similar to that encountered by the LOS component.

A feature that must also be considered for a realistic simulation of our system is the correlation between the signals transmitted from the two orthogonally disposed antennas. Since the correlation coefficient between the two channels depends on several factors, quite difficult to be modeled, in this study the two extreme cases, in which the channels, that is, the variables $g_{H,n}^{(l)}$ and $g_{V,n}^{(l)}$, are either completely correlated or completely uncorrelated, are considered. The experimental results will demonstrate that the proposed system yields a gain with respect to a single antenna system in both cases.

5.4.5. Probability of error

The probability of error of the UWB communication system depends on the signalling used and on the status of the channel. Since the multiband UWB

communication link provides M macrobands, each one divided into N OFDM subcarriers, the probability of error for a single subcarrier is first analyzed. By assuming that a single antenna is used, either H or V, and that the modulation is binary antipodal, the expression for the error rate as a function of the received SNR $\gamma_{b,n}$ at the nth subcarrier is given by

$$P_2\left(\gamma_{b,n}^{(l)}\right) = Q\left(\sqrt{2\gamma_{b,n}^{(l)}}\right), \tag{5.54}$$

where

$$\gamma_{b,n}^{(l)} = \left|h_{X,n}^{(l)}\right|^2 \frac{E_b}{N_0} \tag{5.55}$$

and $h_{X,n}^{(l)}$ is the channel coefficient seen from the X antenna to the receiver at the generic nth subcarrier frequency, given in (5.53). This channel coefficient takes into account both the antenna orientation effect as well as the multipath nature of the UWB channel.

In the case of space-time transmit diversity with order two at the receiver, the probability of error measured at a single OFDM subcarrier is again given by $P_2(\gamma_{b,n}^{(l)})$ in (5.54), where now, however, $\gamma_{b,n}^{(l)}$ is given by

$$\gamma_{b,n}^{(l)} = \left(\left|h_{H,n}^{(l)}\right|^2 + \left|h_{V,n}^{(l)}\right|^2\right)\frac{E_b}{N_0}. \tag{5.56}$$

This result is true if the channel coefficients from the two antennas are independent of each other and if they do not vary during two consecutive bit intervals.

The probability of error seen by the kth user of interest is the average over all the subcarriers. Let

$$\mathbf{\Omega}_k^{(l)} = \left[\gamma_{b,n_1}^{(l)}, \ldots, \gamma_{b,n_{M_I}}^{(l)}\right]^T, \quad n_1, \ldots, n_{M_I} \in I(k,l), \tag{5.57}$$

be the vector of SNRs over the M_I subcarriers assigned to the kth user at the lth time interval. M_I and $I(k,l)$ are defined in Section 5.4.3.1.

The desired probability of error is then given by

$$P_2\left(\mathbf{\Omega}_k^{(l)}\right) = \frac{1}{M_I}\sum_{n\in I(k,l)} P_2\left(\gamma_{b,n}^{(l)}\right). \tag{5.58}$$

In order to obtain the unconditional error probability, $P_2(\mathbf{\Omega}_k^{(l)})$ has to be averaged over the joint probability density function of $\mathbf{\Omega}_k^{(l)}$, that is, the following integral has to be calculated:[12]

$$P_2 = \int P_2\left(\mathbf{\Omega}_k^{(l)}\right) p\left(\mathbf{\Omega}_k^{(l)}\right) d\mathbf{\Omega}_k^{(l)}. \tag{5.59}$$

[12]The dependence on the time index l is here dropped, because the probability of error is assumed not to be dependent on the instant of observation.

Unfortunately, a closed form of the integral in (5.59) is not easy to achieve due to the complex formulation of the random variables $\gamma_{b,n}^{(l)}$ that depend instantaneously on the channel complex value $h_{X,n}^{(l)}$ seen between the transmitter and the receiver.

Due to the problems related to solving (5.59), a semianalytical approach, based on Monte Carlo simulations, has been used to evaluate the total average probability of error. A set of channel coefficients $\{h_{X,n}^{(l)}\}$ for each antenna was generated, so that (5.58) could be computed. Then, the total average probability of error P_2 is approximated by

$$\overline{P}_2 = \frac{1}{N_r} \sum_{z=1}^{N_r} P_2\left(\mathbf{\Omega}_{k,z}^{(l)}\right), \tag{5.60}$$

where $\mathbf{\Omega}_{k,z}^{(l)}$ is the zth realization of the vector $\mathbf{\Omega}_k^{(l)}$ and N_r is the number of Monte Carlo trials.

The numerical results are reported in the next Section 5.4.6.

5.4.6. Results

The performance of the proposed system has been evaluated by means of a semianalytical approach. $N_r = 100$ independent realizations of the UWB channel model described in Section 5.4.4 have been generated, considering all the seven positions and orientations reported in Section 5.4.2. Hence, the conditional probability of error relative to each channel realization relying on the SNR expressed in (5.55) for the single-antenna case and on (5.56) for the polarization diversity case, respectively, was evaluated. Finally, the overall performance of the different systems by averaging the probability of error over the N_r channel realizations was obtained.

Four systems based on different antenna configurations and channel hypotheses are considered. The first two systems, denoted as H pol. and V pol., refer to the cases in which only one of either the H or V antenna is employed at the transmitter. The name HV corr. denotes the system using two antennas with orthogonal orientations and Alamouti's coding, assuming that the NLOS components of the two channels, that is, $g_{H,n}^{(l)}$ and $g_{V,n}^{(l)}$, are completely correlated. Conversely, with HV ind., an analogous two-antenna system, where $g_{H,n}^{(l)}$ and $g_{V,n}^{(l)}$ are completely uncorrelated, is denoted.

The results of simulations considering the TDM access scheme, described in Section 5.4.3.1, are shown in Figure 5.22. In this case, we suppose that LOS path carries the 80% of total transmitted power, that is, $\theta = 0.8$. The error probability relative to each receiver position and orientation as well as the error probability obtained by averaging over all the seven positions are shown. As can be seen, the proposed system gains almost 5 dB in the average.

As can be seen, the performance of the single-antenna systems varies widely for the different receiver positions and antenna orientations as well as considering either the H or V antenna at the transmitter. The proposed polarization-diversity schemes allow us to achieve a performance very close to that of the "best"

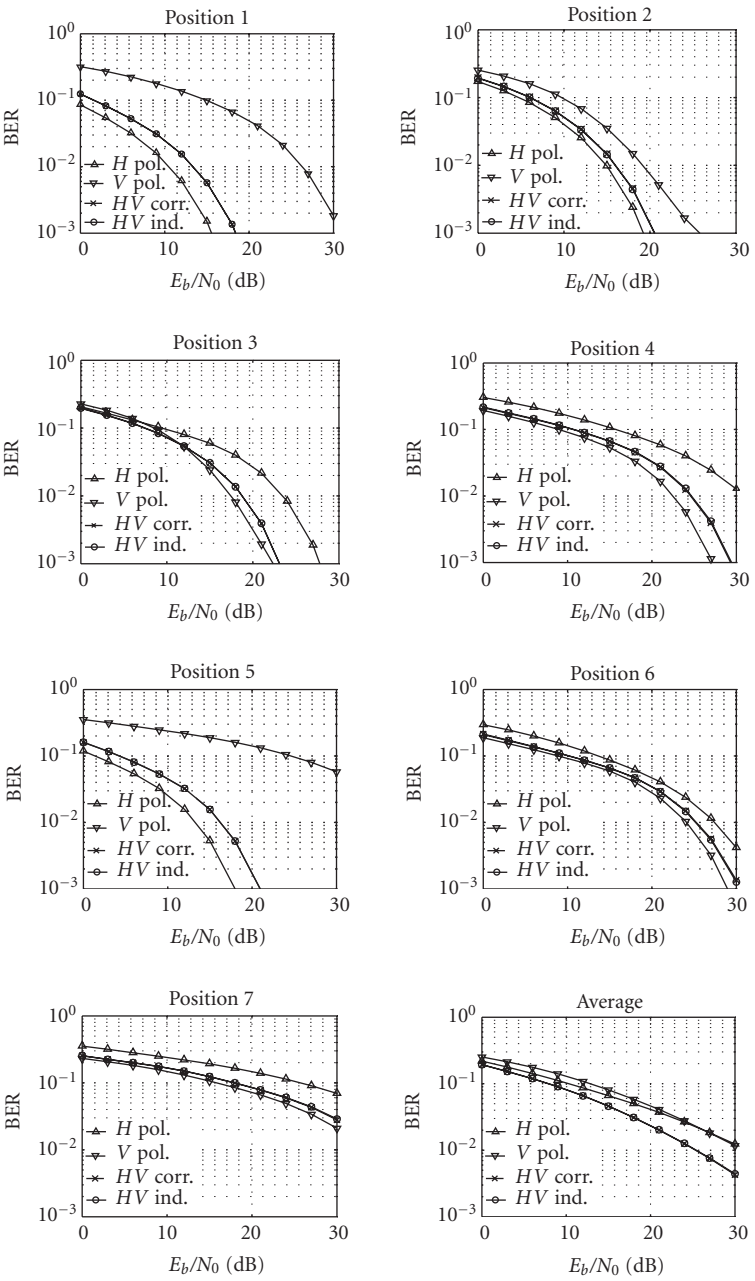

FIGURE 5.22. Performance of single-antenna (H pol. and V pol.) and polarization-diversity (HV corr. and HV ind.) systems. The different positions/orientations described in Section 5.4.2 are considered. The right bottommost figure plots the average of the other curves. TDM access scheme with LOS carrying 80% of the total transmitted power has been used.

transmit antenna, that is, the antenna showing the most favorable amplitude response with respect to the current receiver position and orientation. As a result, the average error probability of the polarization-diversity schemes outperforms that of both the H pol. and the V pol. schemes. Moreover, the behavior of the polarization-diversity scheme appears to be independent of the correlation between the NLOS components of the two channels. The diversity gain showed in the average performance is to be ascribed mainly to the different frequency responses due to the orthogonal orientations of the two transmit antennas. It is worth noting that this fact allows us to avoid any space separation between the two antennas.

The independence of the polarization diversity gain from channel correlation as well as the overall system performance appear to be strictly related to the percentage of power carried by the LOS path. In Figure 5.24, the average error probability curves of the four proposed systems using the TDM access scheme are compared considering two different LOS conditions. In particular, the cases in which LOS path carries either 20% or 80% of total transmitted power are taken into consideration.

The benefits of polarization diversity with respect to the single-antenna system are evident for both LOS conditions. Moreover, it is remarkable that even for the 20%-LOS case the performance gain obtained with polarization diversity seems to be independent of the correlation of channel multipath components. On the other hand, by comparing Figures 5.23(a) and 5.23(b), it is apparent that the overall system performance depends on the LOS power, that is, there is a slight performance improvement when LOS power increases.

The last issue that has been considered is the effect of the access scheme on the overall performance of the system. In Figure 5.24, the error probability obtained with the TDM, FDM, and FDM-TDM access schemes are compared, considering the HV ind. system and the 80%-LOS case. As can be seen, the performance of the proposed system is independent of the access scheme. This result can be ascribed to the fact that we have tested an uncoded system. The effect of the different access methods is to distribute the errors in different ways over a group of symbols and this has a small impact on the average bit error rate of the system, unless some channel coding is used to protect information from channel errors.

5.4.7. Implementation issues

This section mainly focuses on the dependence of the frequency response of a practical UWB antenna from the mutual orientation of the transmitter and the receiver. However, the real communication environment and the terminal design present several open problems and technological challenges.

5.4.7.1. Signal processing

The first and most important issue is related to the implementation of ultra-wideband signal processing stages in the terminals. The impulse radio [18] approach

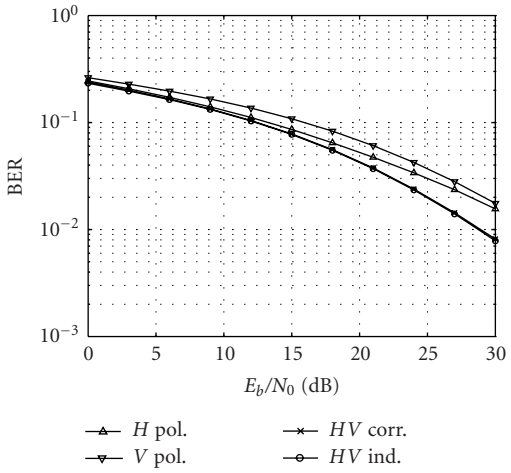

(a)

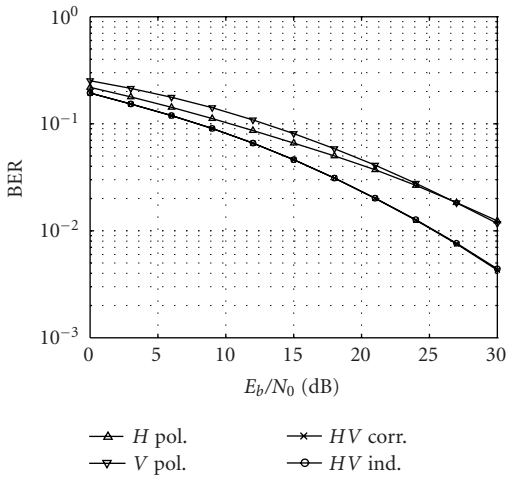

(b)

FIGURE 5.23. Performance comparison between different LOS conditions. LOS path carries (a) 80% and (b) 20% of the total power.

provides a simple way to implement UWB transmission but it provides a limited control over the spectral content of the transmitted signal, giving rise to coexistence problems with other services. The UWB multiband paradigm offers a good spectrum utilization and sophisticated reception schemes, but requires very complex RF analog stages.

To obtain a good control over the UWB radio signal, digital signal processing techniques are envisaged. The analog-to-digital conversion can be performed in

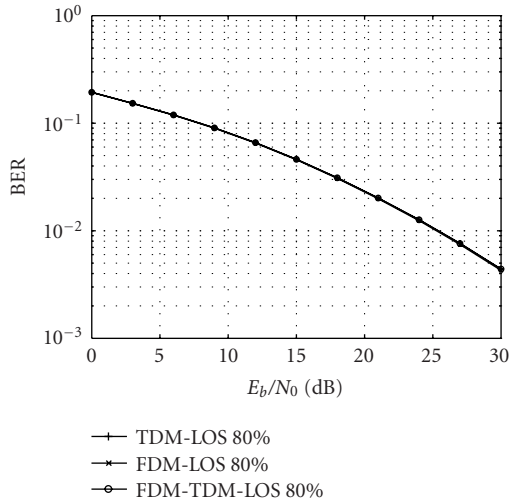

FIGURE 5.24. Performance comparison among different multiple access methods. The *HV* ind. system with the LOS carrying the 80% of the total power is considered.

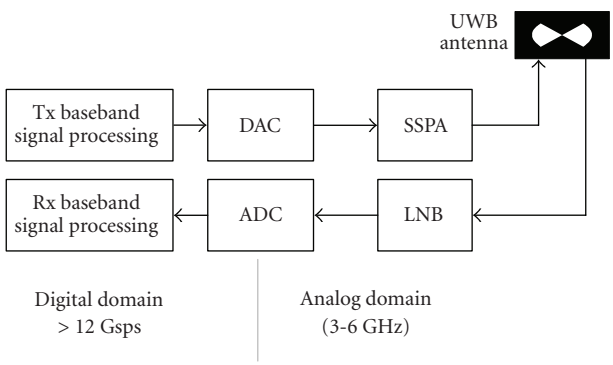

FIGURE 5.25. Single-band UWB conversion stages.

two ways for the multiband approach:

(i) single-branch conversion stages;

(ii) multibranch conversion stages.

The first case, represented in the Figure 5.25, employs a single ultra-wideband direct conversion from the digital domain to the analog one and vice versa. The approach is subject to the availability of fast conversion devices and presents the advantage of a perfectly coherent signal synthesis in the UWB frequency bands (3–6 GHz).

In the second case, shown in Figure 5.26, the RF section is subdivided into 4 branches of 500 MHz each. The requirements for ADC and DAC devices are less stringent in this case but the up-down conversion sections of the branches need to

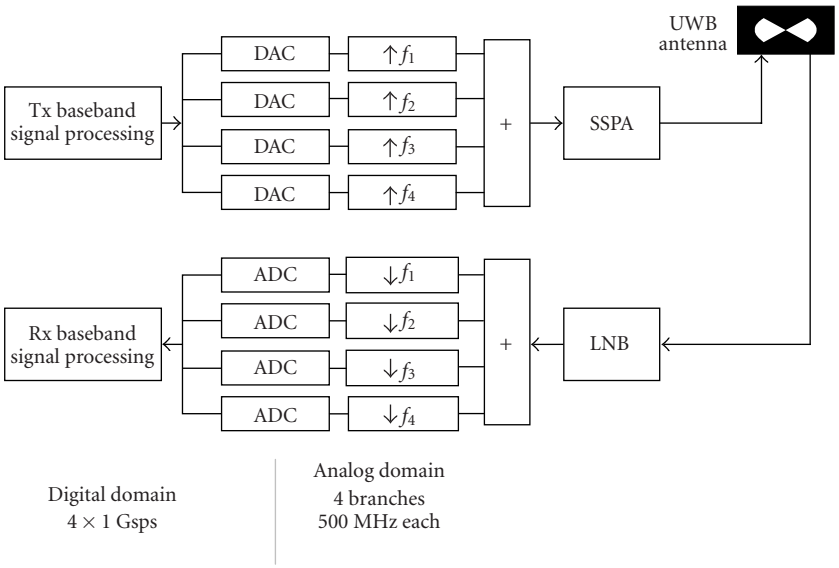

Figure 5.26. Multiband UWB conversion stages.

be properly synchronized in order to obtain a coherent synthesis of the transmitted UWB signal.

5.4.7.2. Antennas location

Another important implementation issue is related to the positioning of antennas on the communication environment. As stated in the previous sections of this chapter, a polarization diversity is introduced to mitigate the frequency-variant radiation pattern. This approach eliminates to need of a minimum separation of the antennas involved in the space-time coding scheme, thus allowing a colocation of orthogonally polarized sensors.

5.4.7.3. Power management

The main target of the orientation diversity scheme is to provide a quasiconstant quality of UWB radio coverage in an indoor environment. The transmitted power is balanced between the two orthogonally oriented transmitting antennas in order to provide a constant RF transmitted power.

As in many other wireless systems, a closed-loop power control must be implemented, in order to compensate the fading effect induced by mobility of the terminals and the scatterers and to limit the interference to other services in the same bandwidth. It is worth noting that such a power control is not able to mitigate the frequency distortive effect described in the previous sections and does not interfere with the proposed diversity schemes since it does not modify the power

balance between the two antennas. For stability reasons, it should be realized with a slow time-constant power measurement scheme, averaging the fast variation of the combined received power.

5.4.8. Summary

The performance of a multiband UWB system with polarization diversity is investigated. The scope of the present work is to avoid the degradation of the frequency response between the transmit and receive antennas due to their mutual orientation. A mixed deterministic and statistic UWB channel model is proposed, which includes both LOS and NLOS components. Polarization transmit diversity is used to guarantee high performance at the receiver independently of the antenna-to-antenna orientation. Three different multiple-access schemes are considered, FDM, TDM, and hybrid FDM-TDM. An improvement with respect to a single-antenna system is obtained for all access schemes without the need of a minimum separation of the transmit antennas. Some implementation aspects are analyzed showing the advantages of the multiband approach which reduces signal processing complexity and makes the software radio concept feasible also for UWB applications. Finally, it is worth noting that the methodology used in this work can be applied to different environments and antenna shapes.

5.5. Spatial diversity

This work investigates spatial diversity in the context of ultra-wideband (UWB) communication systems. For this purpose, several spatial correlation functions are defined, which may help predict the performance of a diversity-based multisensor receiver in a given space-variant channel, and for a given pulsed or multiband modulation scheme. According to the results, full correlation of output signals, or of the contrary very fast decorrelation, can be obtained, depending on the nature of the receiver operating principle. Maps of spatially variant signals without or with diversity combining schemes are shown for simulated discrete multipath channels, and also for measured channels in a few environments. Finally electromagnetic issues relative to the coupling between close UWB sensors are considered.

5.5.1. Introduction

5.5.1.1. Context of the work

Spatial diversity is a well-known method to combat fading, which has been pioneered as early as the late twenties [39, 40]. The word diversity itself first suggests that radio systems employing such a technique intend to take advantage of the signal variability from one sensor to another, in order to improve the link robustness. A second simple idea is that by using several antennas at reception, we

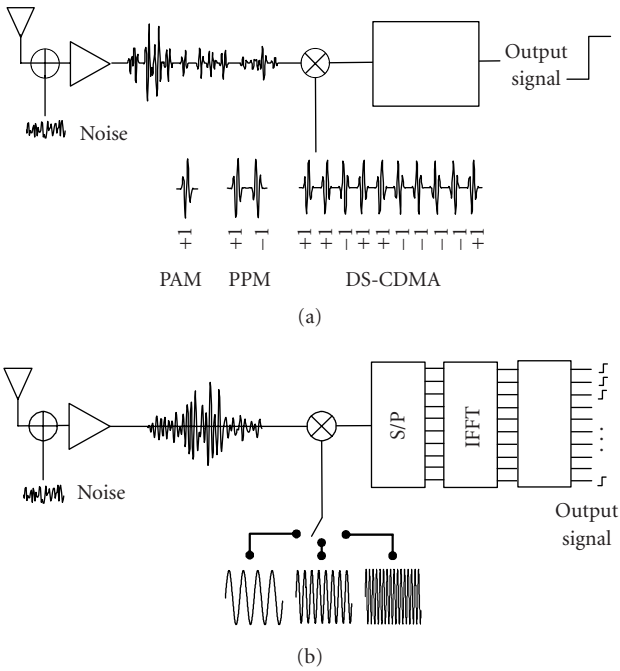

FIGURE 5.27. Matched-filter correlation and detection for (a) pulse-based and (b) MBOFDM physical-layer schemes.

may try to "capture" more energy from the ambient medium, thereby improving the signal-to-noise (SNR) or signal-to-interference (SIR) ratio. Both contribute to performance improvement, let it be through the range, the throughput, or more generally speaking through network capacity. However, since the early days of diversity, it has been appreciated how far smart antenna approaches could go, well beyond such simple ideas as expressed above, and could concern all sorts of radio signal processing issues involving multiple antennas. In the present work, we will address the as yet little investigated issue of diversity in ultra-wideband systems, and will limit ourselves to the two time-honoured effects mentioned above. The paper attempts to define spatial diversity "descriptors" which are suited to the way the received signals are processed in a specific receiver. For this purpose, some of the main candidate modulation schemes for standardization are considered, operating either in the time domain (pulsed schemes) or in the frequency domain (OFDM schemes).

We consider the linear system model depicted in Figure 5.27, where a single-antenna transmitter communicates with a multiple-antenna receiver through the radio environment. After going through antenna and front-end filters, the signal is correlated with a reference template or FFT processed at baseband, resulting in an analog output signal. Spatial diversity descriptors are built from this signal, which *de facto* is template dependent. In a digital architecture, this signal is the decision variable, but digital quantization issues are here irrelevant. Such a model

is quite general, and is suited to various UWB physical-layer schemes as will be seen below.

5.5.1.2. System model

The output signals can very generally be written as the result of a correlation operation between the received signal and a reference waveform (template):

$$S(\tau) = \int F(r(t))\,\mathrm{ref}(t-\tau)dt, \tag{5.61}$$

where the τ dependence expresses the clock synchronisation dependence, and $F(\cdot)$ is a linear operator applied to the received signal. According to the choice of the template waveform, a wide selection of basic UWB physical-layer schemes can be covered:

(i) pulse-amplitude modulation (PAM), where $F(\cdot) = I_d(\cdot)$, and where the template is a single pulse, for example, reproducing the temporal shape of the received signal for an ideal dispersionless channel (matched filtering);

(ii) binary pulse-position modulation (BPPM), where $F(\cdot) = I_d(\cdot)$, and where the template is composed of two pulses of opposite polarities, separated by a (small) time delay;

(iii) direct-sequence code-division multiplexing access (DSCDMA), where $F(\cdot) = I_d(\cdot)$, and where the template is composed of a repetition of a single pulse, multiplied by a PN sequence of ± 1;

(iv) switched multiband (SMB), where $F(\cdot) = I_d(\cdot)$, and where there are now as many template waveforms as the number of bands, each template being chosen in order to comply with the spectral requirements of its own band;

(v) multiband-OFDM (MBOFDM), where $F(\cdot) = \mathrm{FFT}(\cdot)$, which is equivalent to a many-tone filter bank per band, with a template vector of samplers associated to each band at the frequency-domain FFT output.

The signals can be either complex (baseband) or real (true signals) without restriction to generality. In what follows, complex signals will be used for multiband schemes, and real signals for pulse-based schemes.

5.5.1.3. Definition of spatial diversity descriptors

Since spatial diversity may be a useful approach to improve radio systems performance, it appears necessary to define "descriptors" which might be helpful to predict the potential improvement expected from spatial diversity. In the following, we will make a substantial use of normalized intersensor correlations, which relate the output signal on one antenna to its value on another antenna as follows:

$$\rho = \frac{E(S_1 S_n^*)}{E\left(|S_1|^2\right)}, \tag{5.62}$$

where $E(\cdot)$ stands for the expectation operator, and S_1 and S_n are output signals upstream of the decision stage, for sensors 1 and n, respectively.

From a practical point of view, ρ_{1n} gives us an indication about what we can expect for the signal output issued from another sensor, in comparison to what it is on a given sensor, in a statistical sense for a given statistical set (environment, scenario). From the definition quoted above, we define several ways to compute intersensor correlations, depending on the way the receiver is operated.

(i) In the case of ρ_{SR} (synchronized reference), it is assumed that optimum synchronisation is achieved on the reference sensor (sensor 1), resulting in the maximal value of the correlator output for this sensor. For sensor n, it is assumed that the clocking times are the same as sensor 1:

$$\rho_{SR} = \frac{E(S_1(\tau_{\max 1})S_n^*(\tau_{\max 1}))}{E\left(|S_1|^2\right)} \tag{5.63}$$

with $S_k(\tau) = \int r_k(t)\mathrm{ref}(t-\tau)dt$ and $\tau_{\max 1} = \arg(\max S_1(\tau))$.

(ii) The case of ρ_{SS} (synchronized sensors) is similar to ρ_{SR}, except that the clocking times on sensor n are adjusted in order to maximize the correlator outputs also on this sensor:

$$\rho_{SS} = \frac{E(S_1(\tau_{\max 1})S_n^*(\tau_{\max n}))}{E\left(|S_1|^2\right)} \tag{5.64}$$

with $\tau_{\max 1} = \arg(\max S_1(\tau))$, $\tau_{\max n} = \arg(\max S_n(\tau))$.

(iii) ρ_{RD} (RAKE decorrelation) assumes perfect (total) RAKE combining on the reference sensor 1, achieved by filtering with the conjugate transpose of the channel transfer function. Signals from other sensors are subjected to the same filter, which is expected to decorrelate signals very effectively [41]. Using (5.61), we have $F_{\mathrm{RD},1}(r_k(t)) = h^*(\mathbf{r}_1, -\tau) \otimes r_k(t)$, where $\otimes$ stands for the convolution, and

$$\rho_{RD} = \frac{E(S_1(\tau_{\max 1})S_n^*(\tau_{\max 1}))}{E\left(|S_1|^2\right)} \tag{5.65}$$

with $S_k(\tau) = \int F_{\mathrm{RD},1}(r_k(t))\mathrm{ref}(t-\tau)dt$, $\tau_{\max k} = \arg(\max S_k(\tau))$.

(iv) ρ_{RC} (RAKE combining) assumes perfect (total) RAKE combining on each individual sensor. We now have

$$\rho_{RC} = \frac{E(S_1(\tau_{\max 1})S_n^*(\tau_{\max n}))}{E\left(|S_1|^2\right)} \tag{5.66}$$

with $S_k(\tau) = \int F_{\mathrm{RD},k}(r_k(t))\mathrm{ref}(t-\tau)dt$, $\tau_{\max k} = \arg(\max S_k(\tau))$.

(v) In the case of MBOFDM, the FFT stage output is a vector of complex signals. We thus naturally define the single-band correlation as

$$\rho_{\mathrm{SBO}} = \frac{E(\mathbf{S}_1\mathbf{S}_n^*)}{E\left(|\mathbf{S}_1|^2\right)}, \tag{5.67}$$

which is subsequently averaged over all subbands to give ρ_{MBO}.

(vi) Switched multibands do not differ from pulsed-based modulations, except through the pulse duration which is longer. Since the mean frequency is switched at regular times in order to cover the whole bandwidth, however, a specific intersensor correlation ρ_{SMB} is defined by averaging the correlation over all subbands.

(vii) In addition, a narrowband correlation $\rho_{\mathrm{NB}} = E(H_1(\overline{F})H_n^*(\overline{F}))/E(|H_1(\overline{F})|^2)$ has been used, for the sake of comparison. $\overline{F}$ is the mean received signal frequency, and H_k is the frequency-domain transfer function between transmitter and receiver sensor k, including the channel.

5.5.2. Signal waveforms and channel model

5.5.2.1. Signal waveforms

In the present work, we assume ideal antennas at both transmitter and receiver, which means here that these antennas are frequency independent when operated in transmission with no gain (isotropic antennas). It is well known however that any antenna obeys the relation $A_{\mathrm{em}} = \lambda^2 G/4\pi$ between the gain G and the effective area in reception, for an impedance-matched load and a wavelength λ. This implies such an ideal antenna to act as an integrator in the time domain, and also that the transmitted and received signals differ [42]. As a representative example, a pulsed waveform whose 3 dB bandwidth is close to 3 GHz is shown in Figure 5.28, and has been chosen to respect the FCC mask. In a noise-limited receiver with a perfect channel, the optimal template for the correlator is the received signal itself, therefore we choose this same signal for the template in the computation of correlator outputs for intersensor correlations.

5.5.2.2. Channel model

We assume a space-variant discrete channel model. For a given position of the receiving and transmitting antennas, the channel is described as a discrete sum of plane wave multipaths, each characterized by its delay, its amplitude, and its direction of arrival (DOA). The channel impulse response (CIR) can be written as a function of delay and receiver antenna position $\mathbf{r}$ as follows:

$$h(\mathbf{r},\tau) = \sum_i A_i \delta\left(\tau - \tau_i(\mathbf{r})\right) \quad \text{with } \tau_i(\mathbf{r}) = \tau_{i0} - \frac{\mathbf{r}\mathbf{u}_i}{c}, \tag{5.68}$$

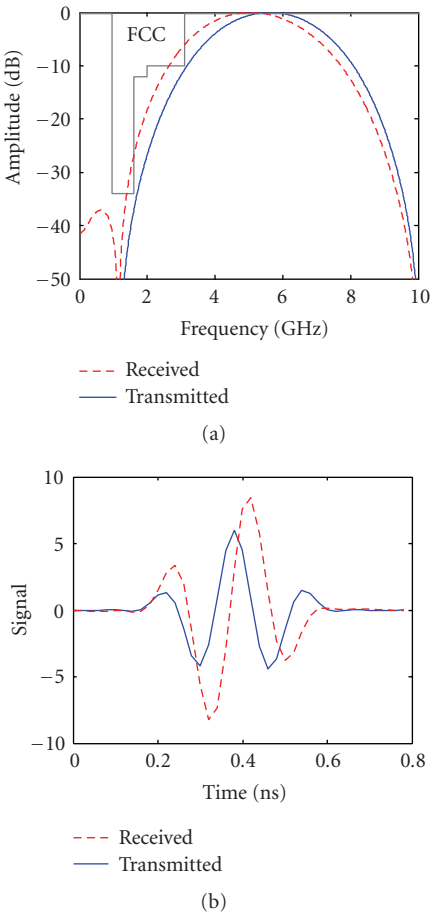

FIGURE 5.28. (a) Spectra of the transmitted and received signals for ideal antennas, in comparison with the FCC mask; (b) temporal waveforms.

where τ_{i0} is a fixed path delay, $\mathbf{u}_i$ is a unitary vector along the DOA at the receiver, and c is the velocity of light.

As compared to usual wideband channel models, the present model has the following differences.

(i) When we deal with *real* and not complex signals, the CIR has to be real as well and not complex. This means in particular that the path amplitudes are real, positive or negative. According to physical intuition, the signs and amplitudes of the received paths are related to the elementary events experienced by the pulsed waves, that is, specular metallic reflections, diffraction, transmission, and so forth.

(ii) We expect a much greater number of paths, due to the extremely large bandwidth. The multipath density has been experimentally ascertained [43–50].

The statistics and related parameters of path amplitudes, delays, and DOAs are obviously a crucial issue for the pertinence of the channel model. For the purpose of the present work, we make simplifying assumptions, which should not dramatically affect our conclusions.

(i) We specify fixed-delay bin durations, in which the number of occurrences of path times of arrival (TOA) is distributed according to a Poisson law. The TOAs in each bin are randomly distributed.

(ii) Path amplitudes are governed by a Ricean distribution, whose K factor is randomly generated within certain limits (uniform law); the signs of path amplitudes are also randomly chosen (uniform law). In addition, the decay of amplitudes with delay (i.e., path length) is governed by an attenuation exponent.

(iii) Path DOAs are governed by a Gaussian distribution in azimuth and elevation.

In the practical simulation examples below, elevations will be systematically nil. The major changes in the parameters will fall on the azimuth spread, and on the multipath density. Most simulations will make use of omnidirectional scenario, that is, for which the azimuth distribution function will be flat over 360°. In some cases, we will make use of clustered channels, that is, for which several multipath distributions with differing statistical parameters are superimposed. Here we have selected 3 representative channels.

Channel 1. It has a dominant multipath cluster concentrated in a small delay range and in a small angle range, followed by a trailing multipath cluster of lesser amplitude, and scattered in angle. This channel may describe an indoor line-of-sight (LOS) situation.

Channel 2. It has an exponential-like power delay profile over a fairly large range of delays, with a moderately dense multipath structure. This channel may describe a relatively "gentle" indoor LOS or NLOS (non-LOS) case.

Channel 3. It is similar to channel 2, except that the multipath density is much higher ("bad" NLOS channel).

Typical realisations of these channels are shown in Figure 5.29.

5.5.3. Spatial correlations in the extreme UWB regime

Assuming a discrete channel model, it is possible to evaluate the various spatial diversity descriptors considered in Section 5.5.1.2. According to the discussion of Section 5.5.2.1, we can take the received pulse $p_r(t)$ of an ideal channel itself as the reference template. Then in the absence of receiver filtering and for a single pulse transmitted at time 0 and received at sensor position $\mathbf{r}_k$, the received signal writes

$$\mathrm{rec}\,(\mathbf{r}_k, t) = \sum_i A_i p_r\left(t - \tau_i(\mathbf{r}_k)\right). \tag{5.69}$$

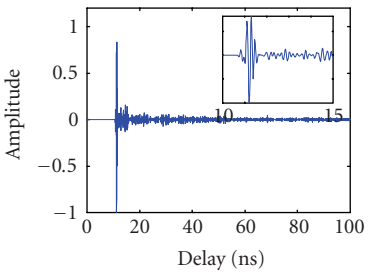

(a)

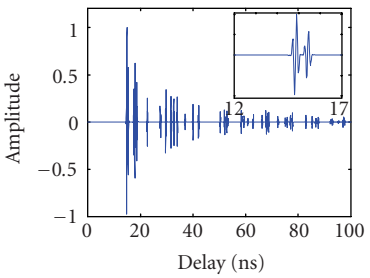

(b)

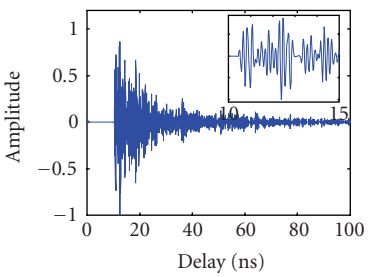

(c)

FIGURE 5.29. Impulse response of (a) channel 1, (b) channel 2, and (c) channel 3.

Therefore,

$$S_k(\tau) = \int \sum_i A_i p_r(t - \tau_i(\mathbf{r}_k)) p_r(t - \tau) dt = \sum_i A_i \widetilde{p}_r(\tau - \tau_i(\mathbf{r}_k)), \tag{5.70}$$

with

$$\widetilde{p}_r(\tau) = \int p_r(t) p_r(t - \tau) dt \quad \text{(pulse autocorrelation)}. \tag{5.71}$$

The intersensor correlation makes an extensive use of the quantity

$$E(S_1(\tau_a)S_n^*(\tau_b)) = E\left(\sum_{i,j} A_i A_j^* \widetilde{p}_r(\tau_a - \tau_i(\mathbf{r}_1))\widetilde{p}_r^*(\tau_b - \tau_j(\mathbf{r}_n))\right), \tag{5.72}$$

where the values of τ_a, τ_b differ for the various intersensor correlations. In the next five subsections, we will restrict computations to the "extreme UWB regime," for which all interpath delay lags are well larger than the total pulse autocorrelation duration.

5.5.3.1. Synchronized reference

In the case of ρ_{SR}, we have $\tau_a = \tau_b = \tau_{i_M}(\mathbf{r}_1)$, where $i_M = \arg(\max|A_i|)$. Then

$$\begin{aligned} E(S_1(\tau_{\max 1})S_n^*(\tau_{\max 1})) &= E\left(\sum_{i,j} A_i A_j^* \widetilde{p}_r\left(\tau_{i_M}(\mathbf{r}_1) - \tau_i(\mathbf{r}_1)\right)\widetilde{p}_r^*\left(\tau_{i_M}(\mathbf{r}_1) - \tau_j(\mathbf{r}_n)\right)\right) \\ &= E\left(|A_{i_M}|^2 \widetilde{p}_r(0)\widetilde{p}_r^*\left(\tau_{i_M}(\mathbf{r}_1) - \tau_{i_M}(\mathbf{r}_n)\right)\right) \\ &= E\left(|A_{i_M}|^2 \widetilde{p}_r(0)\widetilde{p}_r^*\left(\frac{(\mathbf{r}_n - \mathbf{r}_1)\mathbf{u}_{i_M}}{c}\right)\right) \\ &= E\left(|A_{i_M}|^2 \widetilde{p}_r(0)\widetilde{p}_r^*\left(\frac{d_{1n}\cos(\alpha_{1n,i_M})}{c}\right)\right), \end{aligned} \tag{5.73}$$

where α_{1n,i_M} is the angle between $(\mathbf{r}_n - \mathbf{r}_1)$ and $\mathbf{u}_{i_M}$ and $d_{1n} = |\mathbf{r}_n - \mathbf{r}_1|$. Finally,

$$\rho_{\text{SR}} = \frac{E\left(|A_{i_M}|^2 \widetilde{p}_r(0)\widetilde{p}_r^*(d_{1n}\cos(\alpha_{1n,i_M})/c)\right)}{|\widetilde{p}_r(0)|^2 E\left(|A_{i_M}|^2\right)}. \tag{5.74}$$

The statistical set will affect the value of ρ_{SR} through the distribution of DOA angles and the distribution of wave amplitudes. Assuming that the angular and amplitude stochastic variables are independently distributed yields

$$\rho_{\text{SR}} = \frac{E(\widetilde{p}_r^*(d_{1n}\cos(\alpha_{1n,i_M})/c))}{\widetilde{p}_r^*(0)}. \tag{5.75}$$

When the statistical set describes a single location where the receiving antenna positions occupy a small-scale space area or volume, we can assume that the angles of arrival do not change over this volume, in which case the expectation operator $E(\cdot)$ above disappears. According to the cosine between this angle and the vector joining two spatial diversity antenna positions, we find for the synchronized

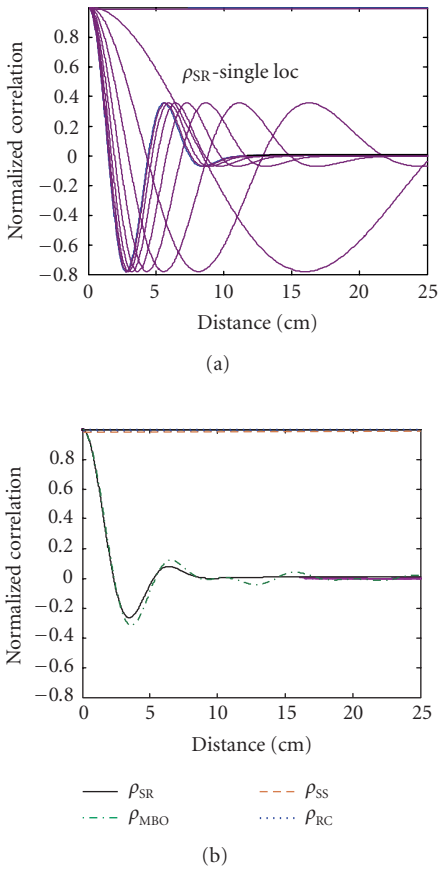

FIGURE 5.30. Intersensor correlations in the extreme UWB regime: (a) single-location averaging; (b) multiple-location averaging.

reference intersensor correlations a series of pulse autocorrelation functions that are identical except for a dilation factor on the distance axis. Such functions are shown on Figure 5.30 for the pulse waveform of Figure 5.28.

When the statistical set describes several locations with a similar path loss (in order to guarantee the angular and amplitude stochastic variables independence), we have to take into account the angular distribution function. Assuming the statistical set is very large, we can approximate the discrete sums by integrals, yielding the expression

$$\rho_{SR} = \frac{\int P_\alpha(\alpha)\widetilde{p}_r^*(d_{1n}\cos(\alpha)/c)\,d\alpha}{\widetilde{p}_r^*(0)}, \tag{5.76}$$

where P_α is the distribution function of the angles of arrival.

In the case of a uniform distribution (the locations cover equally all possible orientations with respect to the Tx-Rx LOS direction), we have $\rho_{SR} = \int \tilde{p}_r^*(d_{1n}\cos(\alpha)/c)d\alpha/2\pi\tilde{p}_r^*(0)$. Again this expression is shown on Figure 5.30.

5.5.3.2. Synchronized sensors

In the case of ρ_{SS}, we have $\tau_a = \tau_{i_M}(\mathbf{r}_1)$, $\tau_b = \tau_{i_M}(\mathbf{r}_n)$, where $i_M = \arg(\max|A_i|)$. Then

$$\begin{aligned} E\left(S_1(\tau_{\max 1})S_n^*(\tau_{\max n})\right) &= E\left(\sum_{i,j} A_i A_j^* \tilde{p}_r(\tau_{i_M}(\mathbf{r}_1) - \tau_i(\mathbf{r}_1))\tilde{p}_r^*(\tau_{i_M}(\mathbf{r}_n) - \tau_j(\mathbf{r}_n))\right) \\ &= E\left(|A_{i_M}|^2 |\tilde{p}_r(0)|^2\right) \end{aligned} \tag{5.77}$$

resulting in $\rho_{SS} = 1$. Therefore, whatever the statistical set, the receiver correlator outputs are fully correlated. This can be very simply explained by saying that if the pulses are synchronised on each receiver branch, the output signals are equal.

5.5.3.3. RAKE decorrelation

In the case of ρ_{RD}, the computation of intersensor correlations first requires expressing the combined effects of channel and RAKE filtering. Let us specialize to the case where the total RAKE filter is derived from the channel for the reference sensor position $\mathbf{r}_1$, but is nevertheless applied to a different antenna position $\mathbf{r}$:

$$\begin{aligned} h^*(\mathbf{r}_1, -\tau) \otimes h(\mathbf{r}, \tau) &= \sum_{i,j} A_i^* A_j \delta(-\tau - \tau_i(\mathbf{r}_1)) \otimes \delta(\tau - \tau_j(\mathbf{r})) \\ &= \sum_{i,j} A_i^* A_j \delta(\tau + \tau_i(\mathbf{r}_1) - \tau_j(\mathbf{r})). \end{aligned} \tag{5.78}$$

Therefore, the received signal writes, for any receiving antenna position $\mathbf{r}_k$,

$$\begin{aligned} \mathrm{rec}(\mathbf{r}_k, t) &= \sum_{i,j} A_i^* A_j p_r(t + \tau_i(\mathbf{r}_1) - \tau_j(\mathbf{r}_k)), \\ S_k(\tau) &= \int \sum_{i,j} A_i^* A_j p_r(t + \tau_i(\mathbf{r}_1) - \tau_j(\mathbf{r}_k)) p_r(t - \tau) dt \\ &= \sum_{i,j} A_i^* A_j \tilde{p}_r(\tau + \tau_i(\mathbf{r}_1) - \tau_j(\mathbf{r}_k)). \end{aligned} \tag{5.79}$$

Let us write the quantity

$$\begin{aligned} &E(S_1(\tau_a)S_n^*(\tau_b)) \\ &\quad = E\left(\sum_{i,j,k,l} A_i^* A_j A_k A_l^* \tilde{p}_r(\tau_a + \tau_i(\mathbf{r}_1) - \tau_j(\mathbf{r}_1))\tilde{p}_r^*(\tau_b + \tau_k(\mathbf{r}_1) - \tau_l(\mathbf{r}_n))\right). \end{aligned} \tag{5.80}$$

In the case of ρ_{RD}, $\tau_a = \arg(\max(S_1(\tau))) = 0$, since the effect of the time reversed RAKE filtering is to combine constructively all multipaths at this delay. In practice, there would be a true unique delay allowing for the respect of the causality principle. Furthermore, in the case of ρ_{RD}, we also have $\tau_b = 0$. Thus

$$\begin{aligned} &E(S_1(0)S_n^*(0)) \\ &\quad = E\left(\sum_{i,j,k,l} A_i^* A_j A_k A_l^* \, \widetilde{p}_r(\tau_i(\mathbf{r}_1) - \tau_j(\mathbf{r}_1)) \widetilde{p}_r^*(\tau_k(\mathbf{r}_1) - \tau_l(\mathbf{r}_n)) \right) \\ &\quad = E\left(\sum_{i,j,k,l} A_i^* A_j A_k A_l^* \, \widetilde{p}_r\left(\tau_{i0} - \tau_{j0} - \frac{\mathbf{r}_1(\mathbf{u}_i - \mathbf{u}_j)}{c} \right) \right. \\ &\qquad \left. \times \widetilde{p}_r^*\left(\tau_{k0} - \tau_{l0} - \frac{\mathbf{r}_1 \mathbf{u}_k}{c} + \frac{\mathbf{r}_n \mathbf{u}_l}{c} \right) \right). \end{aligned} \tag{5.81}$$

In the extreme UWB regime where multipaths are so much separated in delay that the pulse autocorrelations attached to each multipaths never overlap whatever the receiving sensor position, only terms for which $i = j$ and $k = l$ do not cancel. Therefore,

$$\begin{aligned} E(S_1(0)S_n^*(0)) &= \widetilde{p}_r(0) E\left(\sum_i |A_i|^2 \sum_k |A_k|^2 \widetilde{p}_r^*\left(\frac{\mathbf{u}_k(\mathbf{r}_n - \mathbf{r}_1)}{c} \right) \right) \\ &= \widetilde{p}_r(0) E\left(\sum_i |A_i|^2 \sum_k |A_k|^2 \widetilde{p}_r^*\left(\frac{d_{1n} \cos(\alpha_{1n,k})}{c} \right) \right), \end{aligned} \tag{5.82}$$

where $\alpha_{1n,k}$ is the angle between $\mathbf{u}_k$ and $\mathbf{r}_n - \mathbf{r}_1$. The term $\sum_i |A_i|^2$ is the total energy in the impulse response, which can be considered constant whatever the sensor position in a small-scale volume, and also constant for a statistical set of several locations having the same path loss. Therefore, it can be factored from the expectation, and disappears after normalization:

$$\rho_{\mathrm{RD}} = \frac{E\left(\sum_k |A_k|^2 \widetilde{p}_r^*(d_{1n} \cos(\alpha_{1n,k})/c) \right)}{E\left(\sum_k |A_k|^2 \widetilde{p}_r^*(0) \right)}. \tag{5.83}$$

Assuming a continuous distribution and the independence between amplitude and angular stochastic variables yields

$$\rho_{\mathrm{RD}} = \frac{\int |A(\alpha)|^2 P_\alpha(\alpha) \widetilde{p}_r^*(d_{1n} \cos(\alpha)/c) d\alpha}{\widetilde{p}_r^*(0) \int |A(\alpha)|^2 P_\alpha(\alpha) d\alpha}. \tag{5.84}$$

These expressions differ slightly from the equivalent ones for ρ_{SR} by the fact that

all multipaths come into play in ρ_{RD}. For this reason, it may be predicted that there will be less difference between a single location and multiple locations, stemming from the fact that even for a single location there are already many DOAs involved.

Assuming a Clarke's scenario where $|A(\alpha)|^2 P_\alpha(\alpha)$ does not depend on α will again lead to the expression

$$\rho_{\mathrm{RD}} = \frac{\int \widetilde{p}_r^*\left(d_{1n}\cos(\alpha)/c\right)d\alpha}{2\pi\widetilde{p}_r^*(0)} = \rho_{\mathrm{SR}}. \tag{5.85}$$

5.5.3.4. RAKE combining

In the case of ρ_{RC}, we have adaptive RAKE filtering for each sensor location, resulting in moderate changes in the above expressions:

$$\begin{aligned} &E(S_1(0)S_n^*(0)) \\ &\quad = E\left(\sum_{i,j,k,l} A_i^* A_j A_k A_l^* \widetilde{p}_r\left(\tau_i(\mathbf{r}_1) - \tau_j(\mathbf{r}_1)\right)\widetilde{p}_r^*\left(\tau_k(\mathbf{r}_n) - \tau_l(\mathbf{r}_n)\right)\right) \\ &\quad = E\left(\sum_{i,j,k,l} A_i^* A_j A_k A_l^* \widetilde{p}_r\left(\tau_{i0} - \tau_{j0} - \frac{\mathbf{r}_1\left(\mathbf{u}_i - \mathbf{u}_j\right)}{c}\right)\right. \\ &\qquad \left.\times \widetilde{p}_r^*\left(\tau_{k0} - \tau_{l0} - \frac{\mathbf{r}_n\left(\mathbf{u}_k - \mathbf{u}_l\right)}{c}\right)\right). \end{aligned} \tag{5.86}$$

In the extreme UWB case,

$$E(S_1(0)S_n^*(0)) = \left|\widetilde{p}_r(0)\right|^2 E\left(\sum_i \left|A_i\right|^2 \sum_k \left|A_k\right|^2\right), \tag{5.87}$$

and finally

$$\rho_{\mathrm{RC}} = 1. \tag{5.88}$$

We again arrive at the simple and intuitive conclusion that if total RAKE combining is applied on each receiver branch, the correlator outputs are equal and consequently totally correlated.

5.5.3.5. Multiband OFDM

In the case of ρ_{SBO}, we have, for a given sensor position $\mathbf{r}$,

$$\mathbf{S} = \sum_i A_i \exp\left(j\omega\tau_i(\mathbf{r})\right), \tag{5.89}$$

where $\omega/2\pi$ is the vector of frequencies. Thus for two positions $\mathbf{r}_1$ and $\mathbf{r}_n$ of the

sensor we have

$$E(\mathbf{S}_1\mathbf{S}_n^*) = E\left(\sum_{i,j} A_i A_j^* \exp\left(j\omega\tau_i(\mathbf{r}_1)\right)\exp\left(-j\omega\tau_j(\mathbf{r}_n)\right)\right)$$
$$= E\left(\sum_{i,j} A_i A_j^* \sum_k \exp\left(j\omega_k\left(\tau_i(\mathbf{r}_1) - \tau_j(\mathbf{r}_n)\right)\right)\right) \tag{5.90}$$
$$= E\left(\sum_{i,j} A_i A_j^* \sum_k \exp\left(j\omega_k\left(\tau_{i0} - \tau_{j0} - \frac{\mathbf{r}_1\mathbf{u}_i - \mathbf{r}_n\mathbf{u}_j}{c}\right)\right)\right).$$

In the extreme UWB case again we have $i = j$ otherwise the enormous frequency diversity achieved by the ultra-wideband will average the exponential to zero. Thus

$$E(\mathbf{S}_1\mathbf{S}_n^*) = E\left(\sum_i |A_i|^2 \sum_k \exp\left(j\omega_k\left(\frac{(\mathbf{r}_n - \mathbf{r}_1)\mathbf{u}_i}{c}\right)\right)\right). \tag{5.91}$$

If we assume independence between amplitude and angular variables, this writes

$$E(\mathbf{S}_1\mathbf{S}_n^*) = E\left(\sum_i |A_i|^2\right) E\left(\sum_k \exp\left(j\omega_k\left(\frac{(\mathbf{r}_n - \mathbf{r}_1)\mathbf{u}_i}{c}\right)\right)\right),$$

that is, (5.92)

$$\rho_{\text{SBO}} = \frac{1}{N_F} E\left(\sum_k \exp\left(\frac{j\omega_k d_{1n}\cos(\alpha_{1n,k})}{c}\right)\right),$$

where N_F is the number of frequency tones. With a continuous approximation of the angular scenario,

$$\rho_{\text{SBO}} = \frac{\sum_k \int P_\alpha(\alpha)\exp\left(j\omega_k d_{1n}\cos(\alpha)/c\right)d\alpha}{N_F \int P_\alpha(\alpha)d\alpha}. \tag{5.93}$$

In the case of a uniform angular distribution, this yields

$$\rho_{\text{MBO}} = \frac{1}{N_F}\sum_k \rho_{\text{NBC}}(\omega_k, d_{1n}), \tag{5.94}$$

with

$$\rho_{\text{NBC}}(\omega, d) = \frac{1}{2\pi}\int_{-\pi}^{\pi} \exp\left(\frac{j\omega d\cos(\alpha)}{c}\right)d\alpha = J_0\left(\frac{\omega d}{c}\right) \tag{5.95}$$

J_0 being a Bessel function of the first kind.

Finally, we arrive at ρ_{MBO} by averaging the correlations over all subbands:

$$\rho_{\text{MBO}} = \sum_{m=1}^{N_B} \frac{\rho_{\text{SBO},m}}{N_B}, \tag{5.96}$$

where N_B is the number of subbands. This expression is nothing else than the narrowband intersensor correlation, averaged over all frequency tones. Because of this averaging, the oscillating dependence of the Bessel function will tend to washout, as the peak positions scale with the inverse of the frequency. This explains why beyond about 10 cm distance in the graph of Figure 5.30 the correlation is virtually flat and equal to zero. Basically the same kind of mechanism operates to explain the fast decorrelation seen on ρ_{SR} or ρ_{RD}. Those quantities involve the pulse autocorrelation, which is the Fourier transform of the power spectral density, and therefore exhibits small and evanescent time-domain sidelobes in the UWB case for the used waveform.

When the extreme UWB regime is not realized, it is no longer possible to separate distinct multipaths by a duration greater than the pulse autocorrelation and greater than the time of flight between the distant sensors. Therefore, there is in the data a superposition between signals originating from several distinct multipaths. Since analytical expressions would be tedious to obtain, the following section presents results of simulations in this intermediate UWB regime, allowing to assess the differences with the extreme UWB regime.

5.5.4. Spatial correlation functions results

5.5.4.1. Pulse-based modulation schemes

According to Section 5.5.1.2, we present below simulation results for the 5 kinds of intersensor correlations ρ_{SR}, ρ_{SS}, ρ_{RD}, ρ_{RC}, and ρ_{MBO}. In addition, we have plotted two narrowband correlations at the center frequency: the first one is the Clarke scenario ρ_{NBC} correlation [40], the second one (ρ_{NB}) has been simulated in the same way as the other correlations with the same set of channels. In all these simulations, the sensors are perfectly uncoupled (virtual array), and the intersensor distance has been varied from 0 to 25 cm by steps of 0.5 cm.

The curves of Figure 5.31 have been computed over a statistical set of 100 realisations of CIRs, corresponding to 100 different locations with randomly chosen orientations. Thus they express the location variability of the channel. A few observations can already be drawn from these data.

(i) The correlations do not significantly depend on the channel, at least in the conditions of the simulations (signal BW of Figure 5.28, 3 GHz).

(ii) There are only moderate differences with ideal channel results of the previous section (Figure 5.30). In particular ρ_{SS} and ρ_{RC} are very close to 1, while ρ_{SR}, ρ_{RD}, and ρ_{MBO} exhibit a fast decorrelation. ρ_{SR} exhibits the smallest and least oscillating values versus intersensor distance.

(iii) Narrowband correlations exhibit sustained oscillations versus intersensor distance, in close agreement with an ideal Clarke scenario.

It may seem surprising that, given the high multipath density of channel 3, the plots of Figure 5.31 closely resemble those of the extreme UWB regime (Figure 5.30). The first reason for that is that all output signals have similar spectral contents whatever the channel, determined by the pulse shape. The second reason

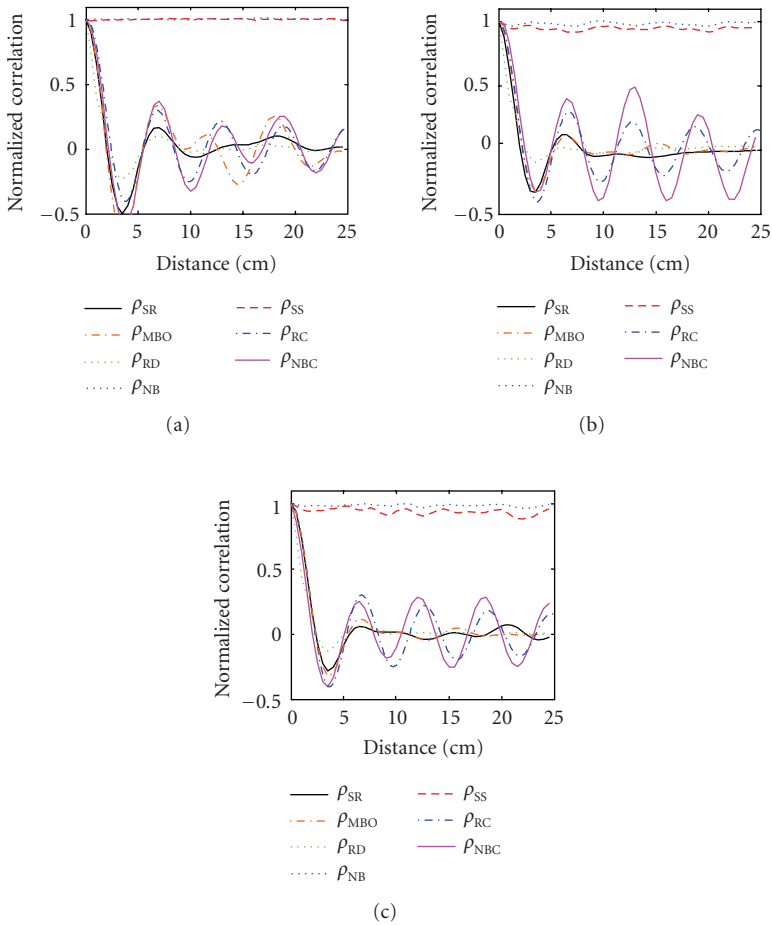

FIGURE 5.31. Intersensor correlations with multiple-location averaging for (a) channel 1, (b) channel 2, and (c) channel 3.

is better understood by first looking at simulation results for *single locations*, that is, for which the statistical set only expresses the small-scale spatial variance for a unique set of DOAs-DODs. It can be seen, for example, for channel 2 (Figure 5.32) that there is a large variability from one location to another, and ρ_{SR}, ρ_{RD}, and ρ_{MBO} do not behave quite identically. In particular, ρ_{RD} exhibits by far the fastest decorrelation with increasing distance, and its behaviour is significantly different from the extreme UWB regime of Figure 5.30. The survival of the decorrelation for ρ_{RD} on a single location is due to the great path diversity inherent to RAKE decorrelation, and is an interesting feature since this case corresponds to the practical situation of a receiver in a given position. This efficient decorrelation also applies to a lesser extent to ρ_{MBO}, since OFDM signal outputs contain all multipaths and again exhibit path diversity. When multiple locations define the statistical set, the angular

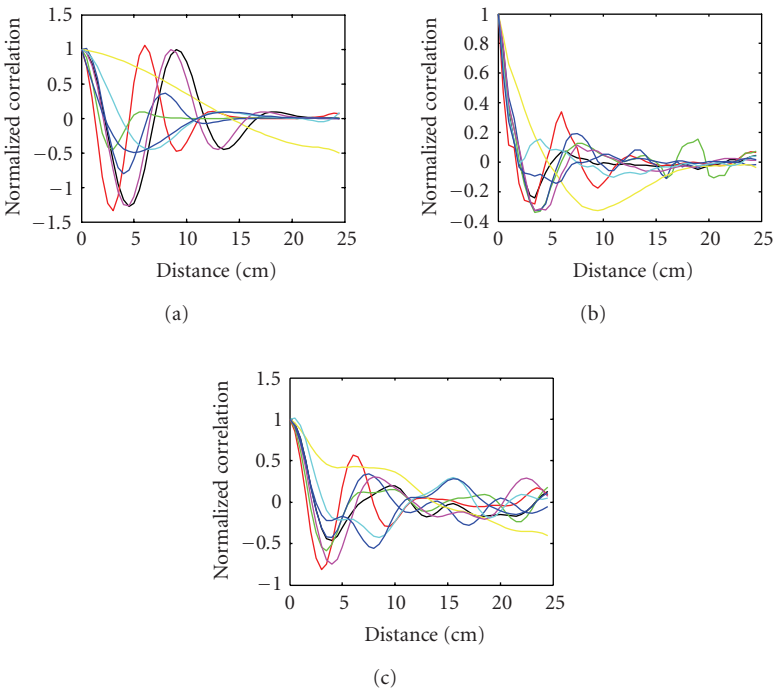

FIGURE 5.32. Intersensor correlations with single-location averaging for channel 2; (a) ρ_{SR}, (b) ρ_{RD}, and (c) ρ_{MBO}.

variability is sufficient to randomize the intersensor correlations, which explains why all three channels have near similar behaviours (Figure 5.31).

It is possible to evaluate the BW sensitivity of these results by modifying the pulse waveform, keeping it spectrally centred around 5 GHz. It can be seen on Figure 5.34 that we recover a narrowband behaviour for ρ_{SR} by reducing the bandwidth below about 400 MHz, at least on the explored range of distances. The bandwidth is indeed directly related to the coherence distance of the pulse waveform. The long coherence distance in narrowband is thus responsible for the oscillating character of ρ_{NBC}, while in the UWB case the very short coherence distance is responsible for the near-zero correlation at relatively short distances. When the bandwidth is reduced, ρ_{SS} and ρ_{RC} tend to become less than 1, which is the result of the onset of small-scale fading.

5.5.5. Space-variant channels

5.5.5.1. Modeled channels

In the narrowband case, the spatial variance of the signals is the Fourier transform of the complex amplitude of incoming waves in wavevector space. In ultrawideband, this spatial variance results from such Fourier transforms, weighted by

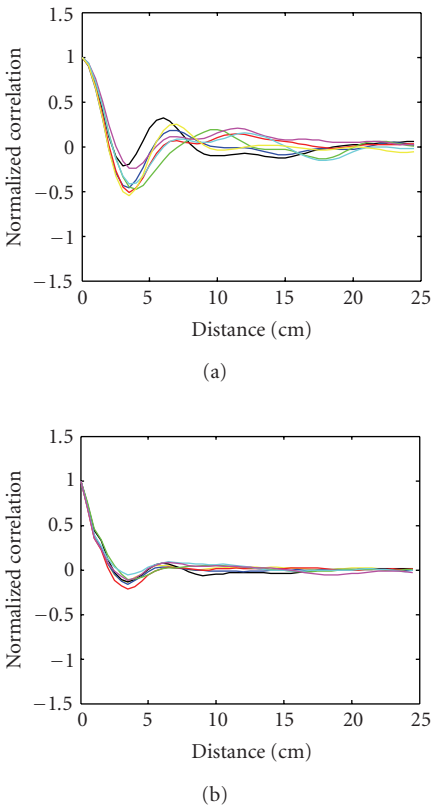

FIGURE 5.33. Intersensor correlations with single-location averaging for channel 3: (a) ρ_{SR}; (b) ρ_{RD}.

the frequency-dependent complex gain of the waves. This introduces extra spatial features with respect to the narrowband case. Such features can be seen very clearly by plotting maps of the receiver signal outputs versus the sensor position. In Figure 5.35 can be seen such a map of the maximum correlation output in the narrowband case (centre frequency) plotted in linear scale, and in the UWB single pulse case for channel 3 (the spatial increment in x, y directions is 2 cm). The former is characterized by Rayleigh fading and a visually quasirandom appearance, due to the large number of interacting waves which destroy coherence. The latter exhibits visible structures and an amplitude distribution close to Rice. Such structures can be expected in a dense channel on the basis that the received pulses may overlap each other, and this overlap changes with the sensor position through the wave directions. When the overlap favours a constructing interference of the pulses, the signal amplitude at the correlator output is enhanced, which corresponds to the dark squares. This is the UWB equivalent of narrowband fading.

In the case of channel 1 (LOS-like), the structures are linear and larger, which directly stems from the smaller angular spread of the main paths (Figure 5.36).

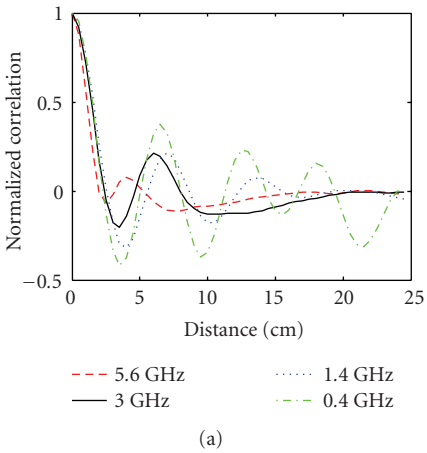

(a)

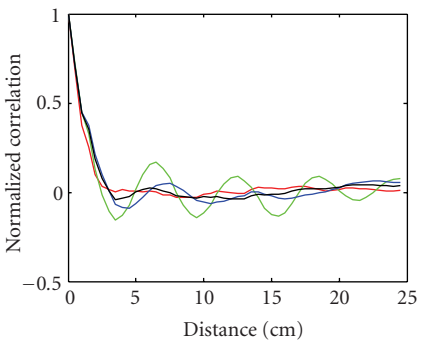

(b)

FIGURE 5.34. Intersensor correlations with multiple-location averaging for channel 2 as a function of the received signal bandwidth (inset): (a) ρ_{SR}; (b) ρ_{RD}.

5.5.5.2. Measured channels

Several UWB channel measurements have been carried out in recent years in order to assess various characteristics of the channel such as multipath statistics [43, 45, 46], DOA-DOD [47, 48], and spatial structure [49]. Here we show a few results which have been obtained at ENSTA and by RadioLabs researchers [46, 50]. The former made use of specially designed shaped monocones [51], with a measuring bandwidth from 2 to 10 GHz (vector network analyser). The latter made use of commercial biconical antennas, and measurements were carried out with a bandwidth of 2.4 GHz around 4.78 GHz using a pulse generator and a digital sampling oscilloscope. Depending on the scenario, it can be seen that a variety of small-scale spatial structures can be seen, with little or very little fading in the LOS one, and stronger fading in NLOS scenarios.

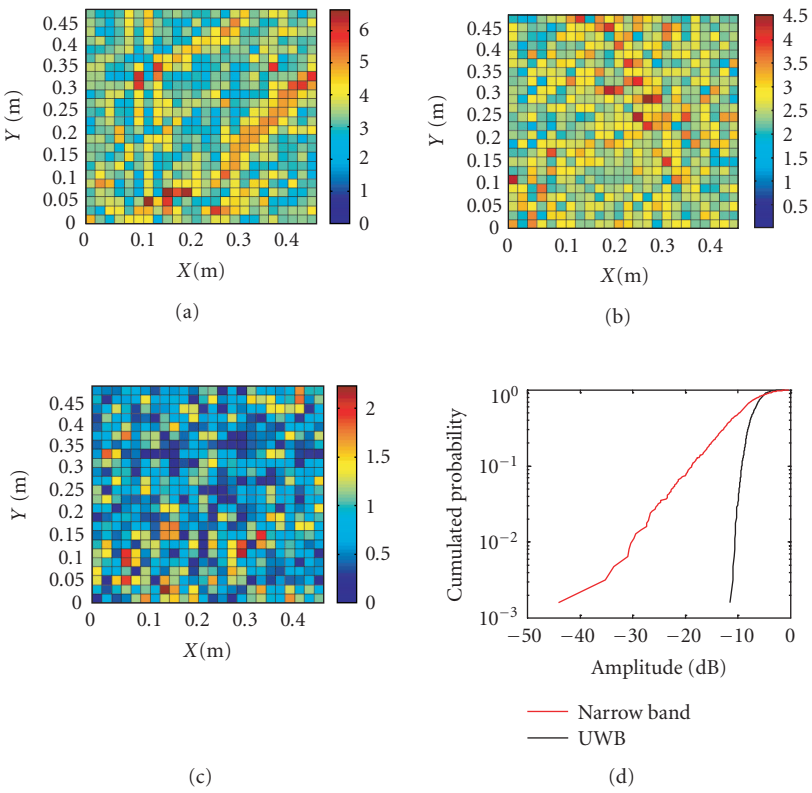

FIGURE 5.35. Channel 3 small-scale structures of the received signal in the UWB (a)-(b) and in the narrowband (c) case, and (d) amplitude distribution.

5.5.6. Diversity combining

5.5.6.1. Combining in the time domain

According to the above results, it appears that the channel spatial variance may be quite rich especially in NLOS and dense multipath scenarios. This richness can be exploited through adequate receiver and even transmitter or MIMO architectures [52, 53]. A simple approach is to combine received signals with maximum ratio combining (MRC) weights, subsequent to proper synchronization in each output branch. The results of Section 5.5.4 show that the correlation between synchronized signals even on close sensors approaches 1, meaning that we can expect efficiently gaining energy and SNR from this combining approach. In the simulations below, a circular array of 5 cm radius with 9 sensors (including a central one) was scanned on the square area of 50×50 cm. Several evaluations of the average combining capability were carried out for subarrays of two sensors (including the central one), extracted from the 9-sensor array (5 cm intersensor distance). The

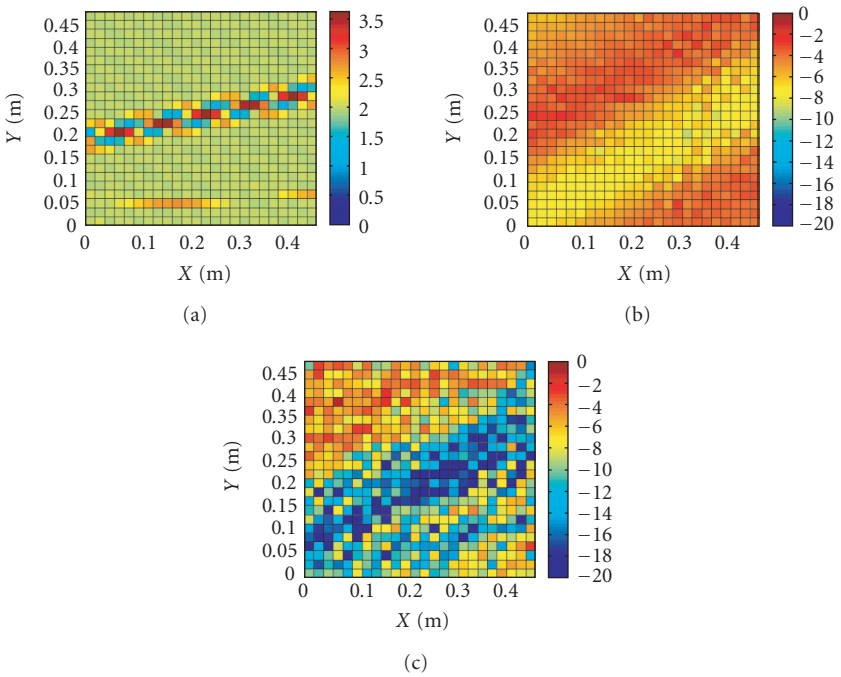

FIGURE 5.36. UWB small-scale structure of the received signal for (a) channel 2 and (b) channel 1 (single sensor-UWB), and narrowband small-scale structure for (c) channel 1 (single sensor-narrowband), in linear scale.

interest of these 8 subarrays is that they cover all possible orientations in the plane.

(i) MRC combining without resynchronization (same clocking for the two sensors). The combining performance is averaged on the 8 subarrays for each array position.

(ii) MRC combining after optimal synchronization of each sensor. The combining performance is averaged on the 8 subarrays for each array position.

(iii) MRC combining without resynchronization, but after selection of the best subarray among the 8 ones per array position.

The first approach is very ineffective, which stems from the near-zero correlation for ρ_{SR} (average output signal on sensor 2 is close to zero if synchronization performed on sensor 1). The second approach is much more effective, with a net gain typically 3–5 dB for 2 sensors, resulting from the near-1 correlation for ρ_{SS}. The third approach, although suboptimal, is nearly as performant as the latter.

5.5.7. Electromagnetic coupling issues for close sensors

In all spatial diversity considerations above, the sensors were electromagnetically uncoupled, either a simulation assumption or an experimental fact when measurements involved a virtual array. However, in practical applications, it is likely that

sensors will be at short distances, because they will have to be integrated on a small terminal or on a limited size access point. We can expect significant electromagnetic coupling in such a situation, and it is necessary to assess the importance of such an effect, especially in the case of UWB which is not as well known as narrowband. According to the previous sections, it appears that in many practical cases of interest spatial diversity will bring extra energy to the useful signal. Therefore, we will focus on the influence of coupling on extra energy capture by diversity. Replacing a single electrical generator (the receiving antenna) by, for example, an array of two radiators intuitively seems to imply a doubling of the received power (3 dB gain as seen in the last section), provided suitable impedance matching by a network was achieved. This assumption is only true under the condition of electromagnetically uncoupled sensors. Otherwise electromagnetic short-circuiting reduces the useable power delivered to the loads. While two far away sensors deliver at most $2 \times |E|^2/8R_a$, where $R_a = \mathrm{Re}(Z_a)$ is the antenna radiation resistance, in the extreme case of very strong coupling, for instance, two short circuited sensors will deliver at most $|E|^2/8R_a$, that is, there will be no power gain (Figure 5.40). Thus electromagnetic coupling appears to be the true limitation to the spatial diversity advantage in UWB systems, rather than intersensor correlation which does not have the meaning it has in narrowband systems as discussed above.

Obviously coupling will very much depend on the geometry and radiation characteristics of the radiators. Nevertheless, it is interesting to consider the case of canonical radiators, and of radiators arranged in an array where the coupling may be expected to be large. A good example might be an array of dipoles, since dipoles are probably the most emblematic and most employed radiators, and since when arranged parallel to each other they are expected to be strongly coupled as the result of their direction of radiation. Unfortunately, ordinary dipoles (or monopoles) are resonant (narrowband) radiators, typically of length $\lambda/2$. Shaped monocones on a ground plane have been designed, optimized, fabricated, and successfully tested, whose bandwidth starts at 3 GHz up to 10 GHz and beyond [51]. They are derived from conventional monopoles, but are much less resonant. Assemblies of two such monopoles in an array of varying intersensor distance (12 cm, 8 cm, and 4 cm) allow to investigate the importance of coupling, through electromagnetic simulations (method of moments, WIPL commercial software). A fairly large ground plane of constant size 30×16 cm was used, in order to avoid any detrimental influence of its finiteness on the antenna impedance and for a fair comparison between arrays with varying intersensor distances. The smallest investigated distance should be appreciated in comparison with the monopole diameter of 2.3 cm (Figure 5.41). Each radiator is fed through an exponentially shaped transition region, between a feeding coaxial line and the monopole itself. The feeder, together with the monopole shape, is indeed a critical issue for the proper impedance matching of the antenna to 50 Ω [54]. This array electrically behaves as a linear two-port device, characterized by a scattering S matrix, or equivalently by an impedance or admittance matrix. In all cases, the presence of electromagnetic coupling between sensors is characterized by off-diagonal entries. The matrices are

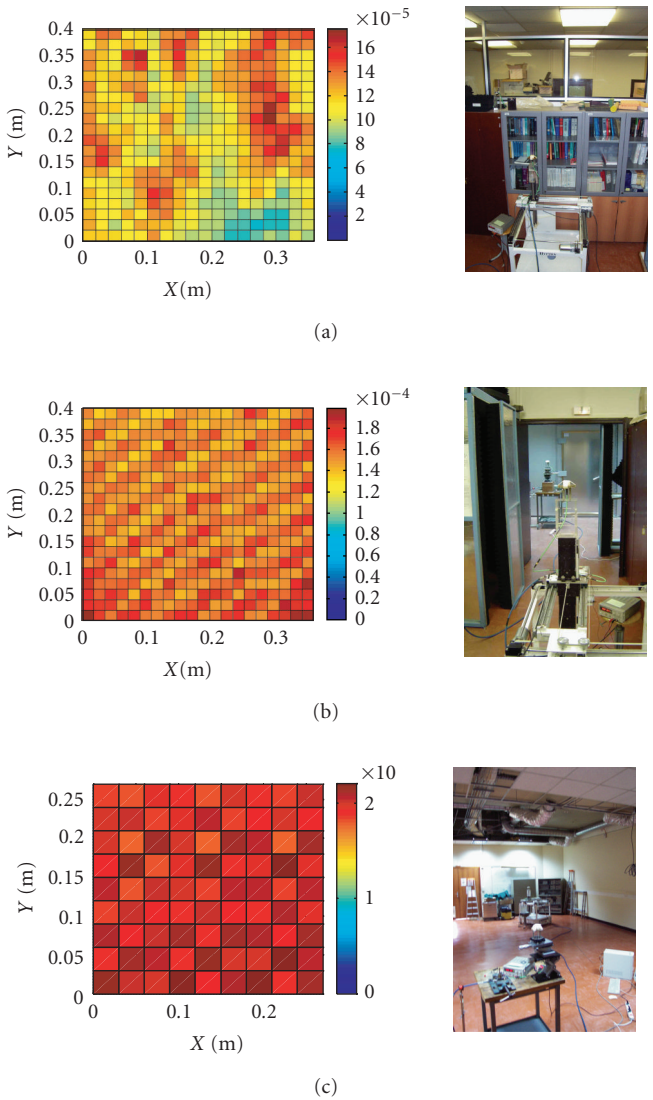

FIGURE 5.37. Small-scale fading structure in three ENSTA environments ((a) NLOS and (c) two LOS ones, linear scale). Spatial steps are 2 and 3 cm, respectively. The scenario in (b) contains two large reflectors forming a "corridor," which results in a regular interference structure.

also symmetric by virtue of reciprocity, and in addition the diagonal elements are here equal because of the presence of a symmetry plane between the radiators.

Several features can be seen in Figure 5.42.

(i) The return loss is basically below −15 dB in the 3–6 GHz band, which is traditionally considered to be a good impedance matching for an antenna.

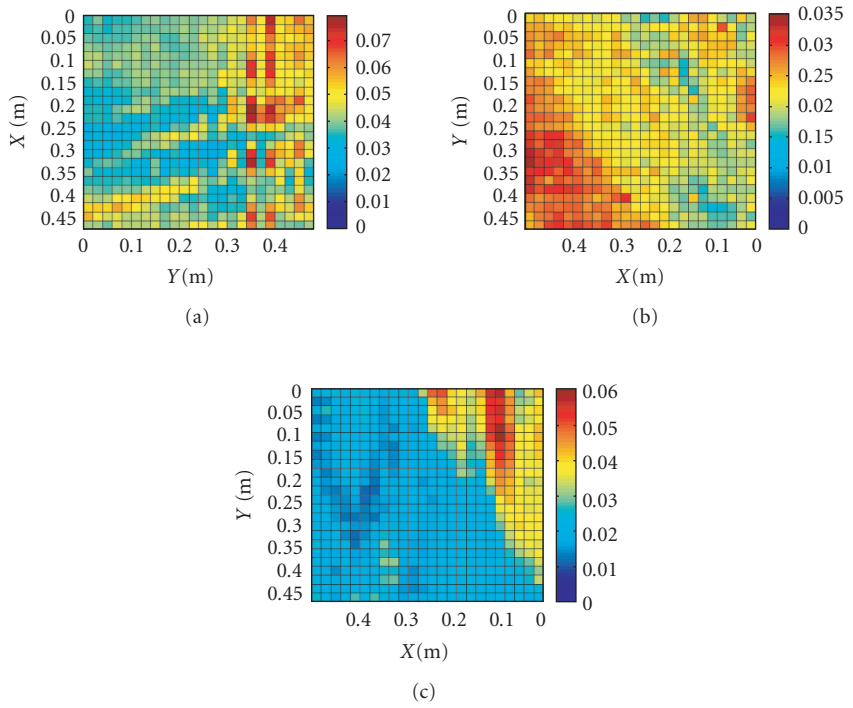

FIGURE 5.38. Small-scale fading structure in three Radiolabs laboratory environments (a) LOS (b) NLOS, and (c) NLOS (linear scale, spatial step: 2 cm).

(ii) The transmission coefficient from one radiator to the other by electromagnetic coupling is below −20 dB for the most distant array, and rises to below −10 dB for the shortest distance at the smallest frequency.

(iii) The transmission coefficient decreases with increasing frequency, for example, from −11 dB to −24 dB between 3 and 8 GHz for the smallest array.

The first remark shows that even in the smallest array, electromagnetic coupling remains moderate. This is of course a favourable feature for spatial diversity applications. Nevertheless, it is useful to analyse the effect of this residual coupling in a quantitative manner. For this purpose, we have computed the power loss in two ways.

(i) *The array is operated in transmission*, that is, one radiator is excited by a generator while the other behaves as a parasitic element delivering some loss power into its 50 Ω matched load. An efficiency can therefore be defined, equal to the ratio of the radiated power to the total power supplied to the excited radiator. It can be seen that even in the worst case of the smallest array, the efficiency is better than −0.4 dB at 3 GHz, rapidly growing to better than −0.1 dB at 6 GHz. This means that a very small power is lost to the load of the parasitic radiator (Figure 5.43).

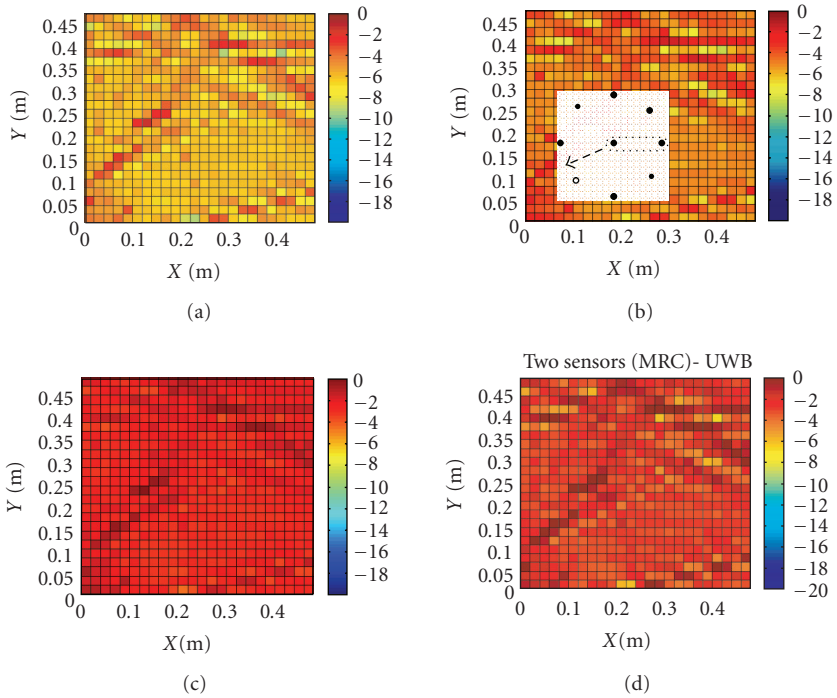

FIGURE 5.39. Small-scale fading structure of two sensor subarrays (channel 3); inset: array geometry showing one subarray; (a) single sensor reference (single sensor-UWB); (b) combining without resynchronization (two sensors (MRC)-UWB); (c) combining after optimal synchronization (two sensors (MRC)-UWB); (d) selection, no resynchronization (two sensors (MRC)-UWB) (all scales in dB, spatial steps 2 cm).

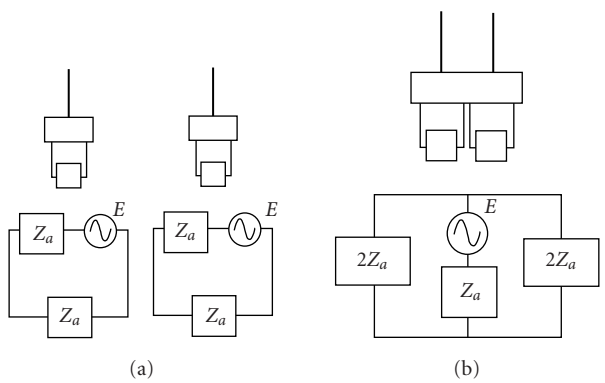

FIGURE 5.40. (a) Two isolated sensors versus (b) two extremly coupled sensors.

(ii) *The array is operated in reception.* An arbitrary scenario was here considered, in which waves of constant amplitude 1 V/m are incident on the array

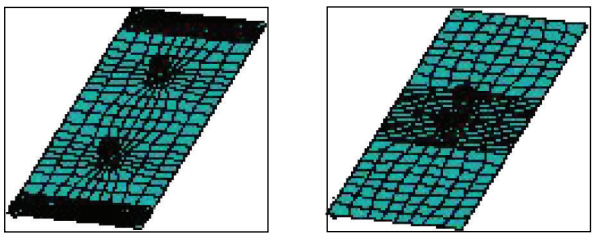

FIGURE 5.41. Schematic view of the dual UWB arrays, with intersensor distances of 12 cm and 4 cm.

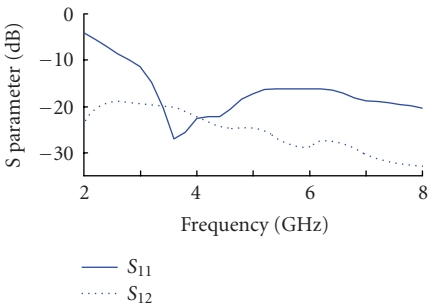

(a)

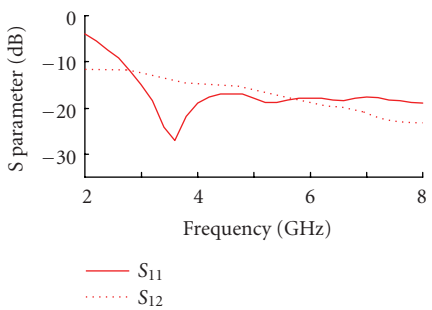

(b)

FIGURE 5.42. S parameters of the arrays: (a) 12 cm distance; (b) 4 cm distance.

between 0° and 90° elevation and 0° to 360° azimuth. The total received power delivered to the loads can be seen on Figure 5.44. There is virtually no difference between both arrays, meaning that the total received power is not affected by sensors proximity. Actually when comparing the average received powers for intersensor distances of 12 and 4 cm, the difference is less than 2%. As a matter of comparison, two $\lambda/4$ monopoles distant from $\lambda/10$ lose 45% of received power.

It is interesting to remark the decrease in frequency of the received power. This feature is typical of UWB, and is due to the frequency dependence of the antenna effective area for a constant gain antenna, scaling as λ^2 as recalled in

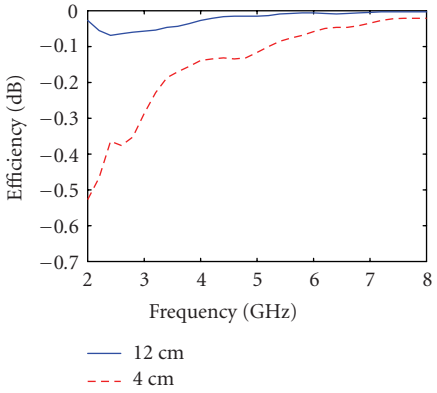

Figure 5.43. Efficiency of the dual sensor array operated in transmission, as defined in the text.

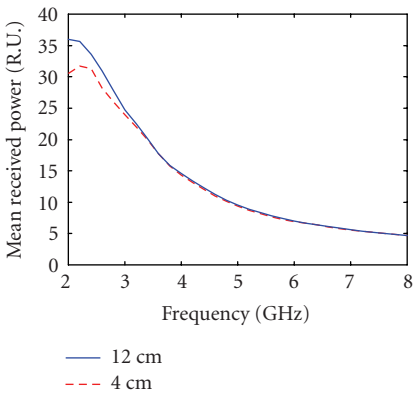

Figure 5.44. Mean received power for a hypothetical omnidirectional scenario of incident waves.

Section 5.5.2.1. Obviously low frequencies are more favourable to the link budget. This characteristic explains why the transmission coefficient between the two sensors decreases with increasing frequency, since in the case of power fed to one radiator, the second behaves as a very close receiver.

In order to conclude this section, let us mention that the radiation patterns have also been investigated in detail. It turns out that the "shadowing effect" of one loaded UWB monopole on the other, although not negligible, is basically minor and does not change the general characteristics of the elementary radiators radiation patterns (Figure 5.45).

5.5.8. Summary and conclusion

This work has attempted to address spatial diversity in UWB systems by taking into account the way this diversity could be exploited in a practical receiver. This has

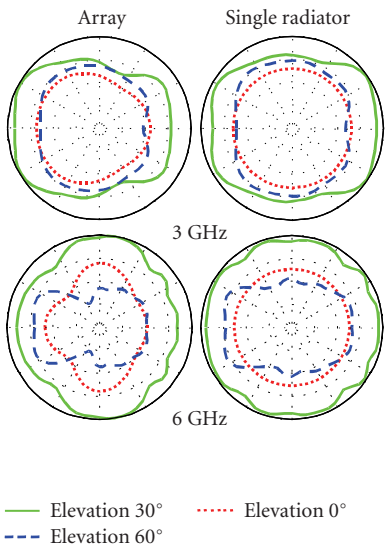

FIGURE 5.45. Copolarized radiation pattern showing the moderate modification due to the presence of the nearby radiator at 4 cm (dotted line: elavation 0°, full line: elevation 30°, dashed line: elavation 60°).

led to the definition of various spatial diversity "descriptors," which are intersensor correlations between the output signals of the various diversity branches of the receiver. According to the way the synchronisation is carried out on these signals, or on the modulation scheme, full correlation or full decorrelation is found. The former is useful in order to gather as much energy as possible and improve SNR. The latter is useful in, for example, MIMO approaches where such a decorrelation can allow spatial multiplexing of data flows [41]. The distant-dependent intersensor correlations depend on the channel multipath density and angular scenario, especially when they are computed on single locations (small-scale averaging). The signal bandwidth is also an important parameter, narrowband correlations being recovered below a frequency which depends on the multipath density, and on the intersensor distance. Maps of the spatial variability of receiver output signals have been presented, both for simulated channels using a discrete mutipath model, and for a few experimental measurements carried out by ENSTA and by RadioLabs [46, 50]. Although fading is much less prominent than in narrowband Rayleigh fading conditions, significant variations of the signal are seen, especially in NLOS case where multipath dense and angularly spread scenarios lead to irregularly structured maps of output signal amplitude. Improvement towards less spatial variance is seen when diversity combining is carried out, through adequate combining schemes. The influence of electromagnetic coupling between sensors has also been evaluated, through electromagnetic simulations of UWB shaped monocones for which copolarized radiative coupling is a priori the greatest. Such coupling phenomena may act as a short-circuiting mechanism between the sensors, annihilating the benefit of diversity combining. It appears that coupling has a

rather small detrimental effect on, for example, the transmission efficiency of dual sensors arrays made of such monocones, or on the total received power, or on the radiation patterns of each monocone. Distances down to 4 cm appear acceptable, for the FCC band 3.1–10.6 GHz.

5.6. UWB beamforming and DOA estimation

5.6.1. Introduction

This section is split into three parts. First, we briefly introduce the general properties of UWB beamforming, which differ from the narrow- and broadband cases. The results are basically also valid for broadband pulses as long as the wavefront travel time across the array is greater than the pulse duration. Second, the major part of this section is devoted to digital UWB beamforming through investigating the impact of sampling on the beamformers' performance. At the end, we demonstrate by real data that DOA estimation could be principally feasible even in typical dense multipath environments if *clusters* are in focus and not paths.

5.6.2. Ideal beamforming for UWB signals

In this section, we will focus on special properties of the beampattern for short UWB pulses that are different from the well-known narrowband beampattern.

To start, we consider the case of a linear equispaced array, consisting of N equidistant omnidirectional antennas. If c is the propagation speed, Φ is the angle of incidence of an impulse signal $s(t)$ measured with respect to broadside direction and d is the distance between two sensors, then the signal recorded at the nth sensor is given by

$$y_n(t) = s\left(t + n\frac{d}{c}\sin(\Phi)\right) = s\left(t + n\tau_\Phi\right), \quad n = 0(1)N-1, \tag{5.97}$$

where $\tau_\Phi = (d/c)\sin(\Phi)$. Note that in this investigation we omit the influence of a real UWB channel characterized by multipath propagation.

The ideal "delay-and-sum" or time-delay beamformer produces

$$y(\Phi,\Theta,t) = \frac{1}{\sum h_n}\sum_{n=0}^{N-1} h_n y_n\left(t - n\tau_\Theta\right), \tag{5.98}$$

where $\tau_\Theta = (d/c)\sin(\Theta)$ are the *steering delays*, Θ is the *steering angle*, and h_n are the weighting coefficients. In order to achieve a *time-independent* beampattern,[13] the total energy of the beamformer output is often used,

$$\mathrm{BP}(\Theta,\Phi) = \left(\int_{-\infty}^{\infty} \left| y(\Phi,\Theta,t)\right|^2 dt\right)^{1/2}, \tag{5.99}$$

[13]A very similar looking alternative beampattern is defined as [55] $\mathrm{BP}(\Theta,\Phi) = \max_t |y(\Phi,\Theta,t)|$.

which reduces to the conventional narrowband beampattern if $s(t)$ is of narrowband type. The problem is that for short UWB pulses, an exact analytical evaluation of (5.99) is in general not possible. For some special UWB pulses, approximate formulas for the beampattern have been developed [56].

Some insight can be gained by computing the spectrum of the beamformer output. It is given by

$$Y(\Phi,\Theta,f) = S(f)\frac{1}{\sum h_n}\sum_{n=0}^{N-1} h_n\, \mathrm{e}^{-\mathrm{j}\,2\pi n f(d/c)(\sin(\Phi)-\sin(\Theta))}, \tag{5.100}$$

where the sum is recognized as the weighted discrete aperture function or the Fourier transform of a window sequence h_n. Such functions have been investigated extensively for fixed frequency f, and their properties are well known, see [57].

Introducing the directivity function di defined by

$$\mathrm{di}(x) = \frac{1}{\sum h_n}\sum_{n=0}^{N-1} h_n\, \mathrm{e}^{\mathrm{j}\,2\pi n x} \tag{5.101}$$

for convenience, (5.100) can be expressed as

$$Y(\Phi,\Theta,f) = S(f)\,\mathrm{di}\left(f\frac{d}{c}(\sin(\Phi)-\sin(\Theta))\right). \tag{5.102}$$

Note that $\mathrm{di}(x)$ is periodic with period 1.

Now, by using Parseval's relation

$$\int_{-\infty}^{\infty} |\, y(\Phi,\Theta,t)\,|^2 dt = \int_{-\infty}^{\infty} |\, Y(\Phi,\Theta,f)\,|^2 df, \tag{5.103}$$

it is obvious that the UWB beampattern can also be analysed in the frequency domain. Under the assumption that $s(t)$ is a real-valued bandlimited energy signal with frequencies in the band from B_1 to B_2, the beampattern is expressed as

$$\begin{aligned}\mathrm{BP}(\Theta,\Phi)^2 &= \int_{-\infty}^{\infty} |\, Y(\Phi,\Theta,f)\,|^2 df \\ &= 2\int_{B_1}^{B_2} |\, S(f)\,|^2 \left|\,\mathrm{di}\left(f\frac{d}{c}(\sin(\Phi)-\sin(\Theta))\right)\right|^2 df.\end{aligned} \tag{5.104}$$

Splitting the frequency band into a number of M nonoverlapping adjacent narrow frequency bands B_i from B_{i_1} to B_{i_2} with bandwidth ΔB_i, we obtain by the

generalised mean value theorem for integrals

$$\begin{aligned} \mathrm{BP}(\Theta,\Phi)^2 &= 2\sum_{i=1}^{M}\int_{B_{i_1}}^{B_{i_2}} |S(f)|^2 \left|\,\mathrm{di}\left(f\frac{d}{c}(\sin(\Phi)-\sin(\Theta))\right)\right|^2 df \\ &\approx 2\sum_{i=1}^{M}\left(\int_{B_{i_1}}^{B_{i_2}} |S(f)|^2 df\right)\left|\,\mathrm{di}\left(f_i\frac{d}{c}(\sin(\Phi)-\sin(\Theta))\right)\right|^2, \end{aligned} \tag{5.105}$$

where the frequency f_i lies in the frequency band B_i. Hence, the UWB beampattern is approximately a weighted superposition of narrowband beampatterns for different frequencies f_i.

This property can be exploited to obtain a rough estimate for the mainlobe width of the UWB beampattern.

The mainlobe width or beamwidth in the $u = \sin(\Theta)$ variable of the classical narrowband beampattern with uniform array weighting for a wavelength λ is usually given by [58]

$$u = \frac{\lambda}{Nd}, \tag{5.106}$$

where N is the number of array elements and d is the distance between two elements. Since the mainlobes are averaged from λ_1 to λ_2 with corresponding mainlobe widths from

$$u_1 = \frac{\lambda_1}{Nd} \longrightarrow u_2 = \frac{\lambda_2}{Nd}, \tag{5.107}$$

it is reasonable to assume that the average resulting mainlobe has a width given by

$$u = \frac{(\lambda_1+\lambda_2)/2}{Nd}, \tag{5.108}$$

corresponding to the virtual center frequency $(B_1 + B_2)/2$ of the band from B_1 to B_2. This is also reported in [55]. It is not possible to give a more precise general estimate, since the averaging is weighted with the specific pulse energy spectrum. Hence, for concrete cases, simulations are the tool for more precise mainlobe estimates; sometimes, for special pulse shapes, it is possible to obtain analytical approximations, and this is certainly an interesting field for future investigations.

Regarding the grating lobes, which are well known in the narrowband case, there is also an averaging effect for the UWB beampattern that mitigates them [56, 55]. A simple explanation of this phenomenon is that the grating lobes occur at different angles for different signal frequencies in contrast to the mainlobe, which is always located at the same angle. Hence, for a UWB signal, the grating lobes are averaged out to some extent, whereas the mainlobes are added coherently. However, it seems difficult to extract more precise information from (5.105).

In order to still gain more insight, a time-domain discussion seems to be more suitable. If $s(t)$ is a real-valued energy signal, we can write

$$\begin{aligned}
&\int_{-\infty}^{\infty} |\, y(\Phi,\Theta,t)\,|^2 dt \\
&\quad= \int_{-\infty}^{\infty} \left(\frac{1}{\sum h_n} \sum_{n=0}^{N-1} h_n y_n(t - n\tau_{\Theta,n}) \right)^2 dt \\
&\quad= \int_{-\infty}^{\infty} \frac{1}{\sum h_n} \sum_{n=0}^{N-1} \frac{1}{\sum h_l} \sum_{l=0}^{N-1} s(t + n\tau_\Phi - n\tau_\Theta) s(t + l\tau_\Phi - l\tau_\Theta)\, dt \\
&\quad= \frac{1}{\left(\sum h_n\right)^2} \sum_{n=0}^{N-1} \sum_{l=0}^{N-1} h_n h_l \int_{-\infty}^{\infty} s(t + n\tau_\Phi - n\tau_\Theta) s(t + l\tau_\Phi - l\tau_\Theta)\, dt,
\end{aligned} \tag{5.109}$$

or by introducing the usual definition of the autocorrelation function

$$\mathrm{ACF}_s(\tau) = \int_{-\infty}^{\infty} s(t) s(t+\tau)\, dt, \tag{5.110}$$

we obtain

$$\int_{-\infty}^{\infty} |\, y(\Phi,\Theta,t)\,|^2 dt = \frac{1}{\left(\sum h_n\right)^2} \sum_{n=0}^{N-1} \sum_{l=0}^{N-1} h_n h_l \,\mathrm{ACF}_s\left((l-n)(\tau_\Phi - \tau_\Theta)\right) \tag{5.111}$$

for the UWB beampattern. Since $\mathrm{ACF}_s(\tau)$ has its maximum for $\tau = 0$, the beampattern has as maximum value

$$\mathrm{BP}(\Theta,\Theta)^2 = \mathrm{ACF}_s(0). \tag{5.112}$$

Further, since the modulus $|\mathrm{ACF}_s(\tau)|$ of an autocorrelation function is majorized by a decreasing function in τ, no true grating lobes can appear in the beampattern. Of course, this property is of great importance for UWB array design, since it allows one to choose the antenna distance without the $\lambda/2$ limitation, *enabling the achievement high resolution with only a few array elements*.

More precisely, we can express the beampattern as

$$\mathrm{BP}(\Theta,\Phi)^2 = \frac{1}{\left(\sum h_n\right)^2} \left(\sum_{n=0}^{N-1} h_n^2 \right) \mathrm{ACF}_s(0) \tag{5.113}$$

$$+ \frac{1}{\left(\sum h_n\right)^2} \sum_{n=0}^{N-1} \sum_{\substack{l=0 \\ l\neq n}}^{N-1} h_n h_l \mathrm{ACF}_s\left((l-n)(\tau_\Phi - \tau_\Theta)\right). \tag{5.114}$$

Now, for pulses with duration T, which means that $\mathrm{ACF}_s(\tau)$ is negligible for $|\tau| > T$, if

$$T < \tau_\Phi - \tau_\Theta, \tag{5.115}$$

then all terms in the second sum (5.114) disappear, and a *fixed sidelobe level*

$$\frac{\sum h_n^2}{\left(\sum h_n\right)^2}\,\mathrm{ACF}_s(0) \tag{5.116}$$

remains. As an example, in the case of an angle of incidence of 90°, the fixed sidelobe level is reached at the steering angle of −90° if

$$T < \frac{2d}{c}. \tag{5.117}$$

If the pulse has a shorter duration, the fixed level is already reached at a smaller stearing angle, which can be computed from (5.115).

An additional important property of UWB beamforming can be derived as follows. By Cauchy's inequality for sums [59], the ratio

$$\frac{\sum h_n^2}{\left(\sum h_n\right)^2} \tag{5.118}$$

is always $\geq 1/N$ and takes its minimum value $1/N$ if and only if all the weighting coefficients h_n are equal. This is an important result, because it means that

(i) for impulse beamforming, an unequal weighting of the array elements is not only useless, but detrimental since it increases the sidelobe level;

(ii) the maximum ratio of mainlobe to sidelobe level is $\sqrt{N}$.

Furthermore, this result can be extended to the more general case where h_n is substituted by a linear time-invariant system with impulse response $h_n(t)$, see [60].

In order to gain more insight for typical UWB signals, we will evaluate the beampattern by numerical simulations. Most often found in the literature is the twice differentiated Gaussian impulse

$$g(t) = \left(1 - 16\pi\left(\frac{t}{\triangle T}\right)^2\right) \mathrm{e}^{-8\pi(t/\triangle T)^2}, \tag{5.119}$$

where the nominal duration $\triangle T$ is set to $2 \cdot 10^{-10}$ second, leading to a -3 dB bandwidth from 5 GHz to 11.5 GHz. An alternate UWB waveform is a pulse form adapted to the FCC (Federal Communications Commission) mask. The FCC pulse is a combination of 6 rect functions in frequency domain multiplied by a Hamming window, which leads to the following pulse in the time domain:

$$g_{\mathrm{FCC}}(t) = 2\sum_{i=1}^{6} a_i b_i \mathrm{sinc}(b_i t)\cos(2\pi f_i t)\, w(t), \tag{5.120}$$

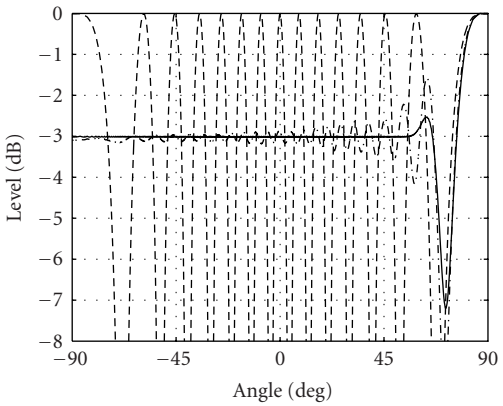

FIGURE 5.46. Beampattern of $g(t)$ (solid line) and $g_{\mathrm{FCC}}(t)$ (dash-dotted line) impulses arriving at 90° on array 1 with 2 elements at distance $14\lambda/2$ and of narrowband signal with wavelength λ (dashed line).

where

$$\begin{aligned} w(t) &= 0.54 + 0.46\cos\left(\frac{2\pi t}{10\,\mathrm{ns}}\right) \text{ (Hamming window)},\\ (a_1,\ldots,a_6) &= [0.43, 0.02, 0.22, 0.27, 0.86, 0.27]\cdot 10^{-2},\\ (b_1,\ldots,b_6) &= [1.5666, 0.983, 0.369, 1.146, 7.144, 1.575](\mathrm{GHz}),\\ (f_1,\ldots,f_6) &= [0, 1.27, 1.95, 2.71, 6.85, 11.21](\mathrm{GHz}). \end{aligned} \tag{5.121}$$

In the simulations, the first derivative of this transmit pulse will be used, since the receive antenna is approximated in first order as a differentiator. The wavelength of the corresponding sinewave is chosen according to a nominal center frequency of 6.85 GHz. Two typical array configurations are considered throughout this section:

(i) array 1 has 2 elements at distance 7λ,

(ii) array 2 has 8 elements at distance λ,

so that both arrays use the same aperture. Note that in the narrowband case, grating lobes will appear in the beampattern. In Figures 5.46, 5.47, 5.48, and 5.49, $\mathrm{BP}(\Theta,\Phi)$ is evaluated for signals arriving at 0° or 90°, and the beampatterns corresponding to $g(t)$, $g_{\mathrm{FCC}}(t)$ and a sinewave of frequency 6.85 GHz are plotted in the same figure for comparision.

Figures 5.46, 5.47, 5.48, and 5.49 show the striking feature of impulse beamforming, namely, the mitigation of grating lobes [56, 55].

A further interesting property that can be observed in Figures 5.46, 5.47, 5.48, and 5.49 is the dependence of the beampattern and especially its sidelobes on the pulse shape, which can also be expected from (5.111). This is the object of further research and may have influence on pulse shaping in future UWB systems.

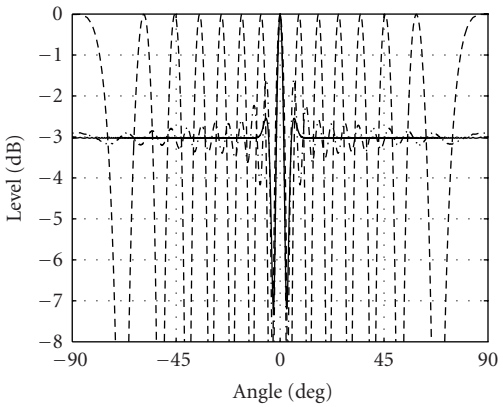

FIGURE 5.47. Beampattern of $g(t)$ (solid line) and $g_{\mathrm{FCC}}(t)$ (dash-dotted line) impulses arriving at 0° on array 1 with 2 elements at distance $14\lambda/2$ and of narrowband signal with wavelength λ (dashed line).

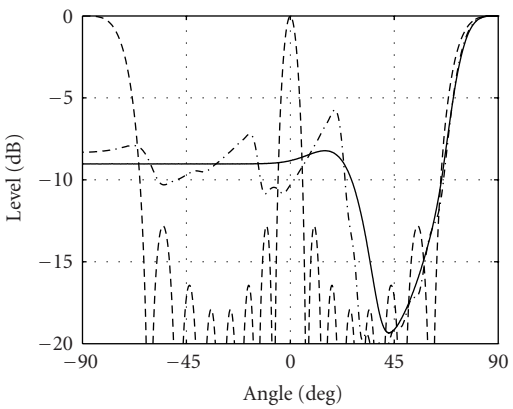

FIGURE 5.48. Beampattern of $g(t)$ (solid line) and $g_{\mathrm{FCC}}(t)$ (dash-dotted line) impulses arriving at 90° on array 2 with 8 elements at distance λ and of narrowband signal with wavelength λ (dashed line).

5.6.3. Digital UWB beamforming

Even if the sampling of UWB signals with a bandwidth of several GHz is far away from mass-market applications, it can be realized for a short duration even today with sophisticated storage oscilloscopes. Hence, at least for research purposes, it is possible to realize UWB beamforming based on sampled signals—so *digital* beamforming becomes of relevance. The intuitive first approach is the rather simplistic digital time-delay beamforming. Of course, numerous other methods for UWB beamforming are known and are worth being considered as well, see, for example, [61–63, 55] and the literature cited therein. Since the computational requirements of such sophisticated approaches are often much higher, digital time-delay beamforming (with interpolated signals) is an attractive and a feasible method for

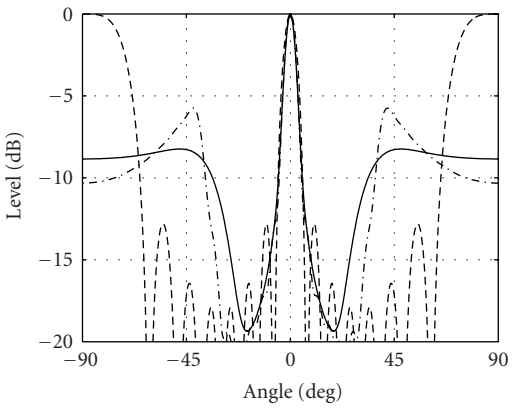

FIGURE 5.49. Beampattern of $g(t)$ (solid line) and $g_{\mathrm{FCC}}(t)$ (dash-dotted line) impulses arriving at 0° on array 2 with 8 elements at distance λ and of narrowband signal with wavelength λ (dashed line).

systems with a large number of antennas and/or with very high sampling frequencies. However, there is one critical point: for steering a beam to arbitrary directions, which is desirable for many reasons (direction estimation, adaptive beamforming), signal values are needed between the sample points. To cope with this problem, all digital time-delay beamformers apply some kind of interpolation.

The simplest method is to use nearest-neigbour interpolation (NN interpolation), thus replacing the signal value at the desired steering delay with the signal value at the nearest sampling point. For narrowband beamforming, nearest-neighbor interpolation is known to produce large errors. This detrimental effect can be reduced by heavily oversampling the input signals [64]. However, due to the immense bandwidth of UWB signals, this seems to be unrealistic in the near future. A better method is to use linear interpolation between the two nearest sampling points, which requires two multiplications for each desired signal value. This approach still produces large errors in the narrowband case without adequate oversampling [65]. It should be mentioned that these two interpolation methods are the optimum methods for the case that only one or two signal samples can be used to approximate a time-shifted signal value [66]. In the next section, a precise treatment of this topic will be presented, and it will be shown that UWB impulses give better results than in the narrowband case.

5.6.3.1. The digital interpolation beamformer

A thorough investigation of digital time-delay beamforming using interpolation of signal samples will now be given. Recall that ideal time-delay beamforming means appropriately delaying and summing sensor signals. The ideal time-delay beamformer produces

$$y(\Phi,\Theta,t) = \frac{1}{N}\sum_{n=0}^{N-1} s\left(t + n\tau_{\Phi} - n\tau_{\Theta}\right). \tag{5.122}$$

No weighting, that is, $h_n = 1$, for all n, will be applied, since the derivation in the last section has shown that it is detrimental for the beamforming of short pulses.

Now, in a digital realization, the signals at each antenna are sampled at a rate $f_s > 2f_c$, where f_c is the cutoff frequency resulting in signal samples of the form

$$s\left(\frac{k}{f_s} + n\tau_\Phi\right). \tag{5.123}$$

Based on these sample values, the ideal beamformer output (5.122) has to be approximated.

Note that in general the desired time instants for beamsteering at angle Θ,

$$t + n\tau_\Phi - n\tau_\Theta, \tag{5.124}$$

do not coincide with the discrete sampling instants

$$\frac{k}{f_s} + n\tau_\Phi. \tag{5.125}$$

There is a time difference $\tau_{\epsilon n}$ between the ideal steering delay $n\tau_\Theta$ and its preceding sample point $k_n(\Theta)/f_s$.

We will therefore interpolate the original signals in each channel by the sample values. This has to be developed with some care. The easiest way is to start with perfect reconstruction using the sinc-kernel, hence to use Shannons sampling theorem (see Appendix 5.6.A), and finally replacing the sinc-kernel with a short time-limited interpolation kernel.

It follows from (5.155) that

$$s(t + n\tau_\Phi) = \sum_{k=-\infty}^{\infty} s\left(\frac{k}{f_s} + n\tau_\Phi\right)\mathrm{sinc}(f_s t - k) \tag{5.126}$$

if the sampling frequency f_s is higher than $2f_c$. Now, since the time origin is arbitrary, we can replace t by $t - n\tau_\Theta$, which results in

$$s(t + n\tau_\Phi - n\tau_\Theta) = \sum_{k=-\infty}^{\infty} s\left(\frac{k}{f_s} + n\tau_\Phi\right)\mathrm{sinc}\left(f_s(t - n\tau_\Theta) - k\right). \tag{5.127}$$

Applying this procedure for each channel, the ideal time-delay beamformer can be implemented using signal samples

$$y(\Phi, \Theta, t) = \frac{1}{N}\sum_{n=0}^{N-1}\sum_{k=-\infty}^{\infty} s\left(\frac{k}{f_s} + n\tau_\Phi\right)\mathrm{sinc}\left(f_s(t - n\tau_\Theta) - k\right). \tag{5.128}$$

Replacing now "sinc" by a timelimited kernel "ker" with finite duration T the complete expression of the sample approximation of the ideal time-delay beamformer, or, in other words, *the digital time-delay interpolation beamformer* (DTDIBF) is given by

$$y_d(\Phi,\Theta,t) := \frac{1}{N}\sum_{n=0}^{N-1}\sum_{k=\lfloor f_s(t-n\tau_\Theta)-T\rfloor+1}^{k=\lfloor f_s(t-n\tau_\Theta)+T\rfloor} s\left(\frac{k}{f_s}+n\tau_\Phi\right)\ker\left(f_s(t-n\tau_\Theta)-k\right), \tag{5.129}$$

where the summation limits for the finite-time kernel are used.

The quality of the DTDIBF in relation to the ideal beamformer is given by the following theorem (for the proof, see Appendix 5.6.B).

Theorem 5.6.1. *Let ker be a time-limited reconstruction kernel, and let m be an integer ≥ 1. Then the conditions*

$$\left.\frac{d^i\,\mathrm{KER}(f)}{df^i}\right|_{f=k} = \delta_i\delta_k \quad (k\in\mathbb{Z};\ i=0,\dots m-1) \tag{5.130}$$

on the kernel's Fourier transform $\mathrm{KER}(f)$ *imply the following error bound for the difference between the ideal time-delay beamformer output and the DTDIBF output:*

$$\left|\left|y(\Phi,\Theta,t)-y_d(\Phi,\Theta,t)\right|\right|_C \leq \frac{M_m(\ker)}{m!}\left(\frac{f_s}{\pi 2 f_c}\right)^{-m}\left|\left|s(t)\right|\right|_C, \tag{5.131}$$

if $s(t)$ is bandlimited with cutoff frequency f_c, or in a version more appropriate for the UWB case

$$\left|\left|y(\Phi,\Theta,t)-y_d(\Phi,\Theta,t)\right|\right|_C \leq \frac{M_m(\ker)}{m!}(f_s)^{-m}\left|\left|\frac{d^m s(t)}{dt^m}\right|\right|_C, \quad \text{for } s(t)\in C^{(m)}(\mathbb{R}). \tag{5.132}$$

$M_m(\ker)$ is the mth absolute moment of a kernel ker, which is defined by

$$M_m(\ker) = \sup_{t\in\mathbb{R}}\sum_{k=-\infty}^{\infty}\left|(t-k)^m\ker(t-k)\right|. \tag{5.133}$$

Note also the other notations given in Appendix 5.6.A.

As can be expected from the results of single channel interpolation [67], the maximum deviation of the digital from the ideal beamformer output depends on the *cutoff frequency versus sampling rate*, the order m and $M_m(\ker)/m!$, which depends on the specific kernel, and can therefore be predicted using the curves given in Figure 5.50. For more details, see (5.139) below.

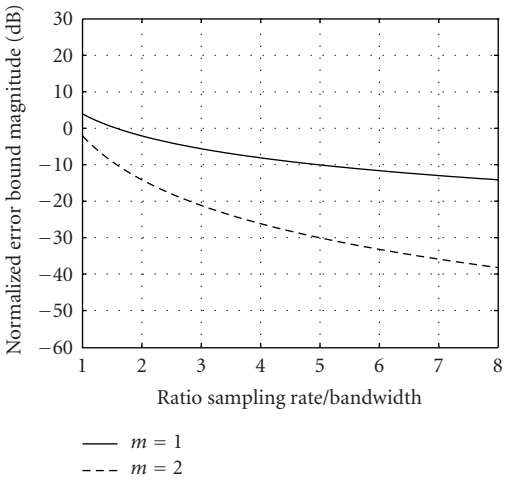

FIGURE 5.50. Normalized error bound in dB for $\ker_m$, $m = 1$ and 2.

A second remark is that the use of the error bound from (5.132) should be preferred in the UWB case, because the estimate in (5.131) is based on the Bernstein inequality [68], which is saturated (worst case) for narrowband signals with cutoff frequency f_c. To give a concrete example, for $m = 2$, a complex exponental signal with amplitude 1 and cutoff frequency 0.5, the evaluation of $(\pi 2 f_c/f_s)^m \|s\|_C$ results in $\pi^2(f_s)^{-2}$, while for the UWB pulse $s(t) = \operatorname{sinc}(t)$ with the same cutoff frequency, $(f_s)^{-m}\|d^m s(t)/dt^m\|_C$ can be shown to have the value $(\pi^2/3)(f_s)^{-2}$, hence the value is only 1/3 of the value for the (worst) narrowband case. A similar result is valid if the $\|\,\|_C$-norm is replaced by the $L^2(\mathbb{R})$-norm.

A further consequence is as follows. Since matched filtering reduces the effective bandwidth, it should in view of (5.131) be carried out before the digital beamforming process.

We will mention here as concrete examples of kernels with finite duration only the unique optimum solutions for $m = 1$ and $m = 2$, since the number of samples for computing an interpolated value should be kept to a minimum for UWB beamforming. For higher m, which might be interesting in the future, see [66, 67].

For $m = 1$, the corresponding kernel is the rect-function

$$\ker_1(t) = \operatorname{rect}(t) = \begin{cases} 1, & |t| \le 0.5, \\ 0, & |t| > 0.5, \end{cases} \tag{5.134}$$

with Fourier transform

$$\mathrm{KER}_1(f) = \operatorname{sinc}(f), \tag{5.135}$$

and for $m = 2$, the corresponding kernel is the $\triangle(t)$-function

$$\ker_2(t) = \triangle(t) = \begin{cases} 1 - |t|, & |t| \le 1, \\ 0, & |t| > 1, \end{cases} \tag{5.136}$$

with Fourier transform

$$\mathrm{KER}_2(f) = \mathrm{sinc}^2(f). \tag{5.137}$$

Further, the moments of these kernels are given by

$$M_1(\ker_1) = 0.5, \qquad M_2(\ker_2) = 0.25. \tag{5.138}$$

It is observed that for $m = 1$ and $m = 2$, these optimum methods are well known, as $\ker_1$ reconstruction is *sample and hold* and $\ker_2$ reconstruction *is linear interpolation* [67].

The performance of these kernels for bandlimited signals can be compared by plotting the normalized error bound, for $\|s\|_C = 1$ in dB,

$$20 \log \left| \frac{M_m(\ker)}{m!} (\pi)^m \left(\frac{f_s}{B} \right)^{-m} \right| \tag{5.139}$$

as a function of the ratio sampling rate versus bandwidth (Figure 5.50). The tradeoff between the sampling rate and the number of samples used for signal interpolation is clearly observed. However, Figure 5.50 allows one to choose the corresponding sampling rate and kernel to fulfill a specified normalized interpolation error.

As a final remark, it should be mentioned that the new modified linear interpolation with recursive 1-pole multiplier requires less preprocessing as described in [69] and the revitalized linear interpolation gives better results than using $\ker_2$ as expected with only slightly more processing load.

5.6.3.2. The beampattern of the digital time-delay interpolation beamformer in the narrowband case

In many situations, time-delay beamforming is applied to narrowband signals with unknown frequencies in a certain frequency band of interest. Even for impulse beamforming, this case is important, because it applies to the presence of narrowband interference. Therefore, digital beamforming will be investigated for this specific case, and the serious phenomenon denoted as "pseudograting lobes" will be analysed. We will use the complex signal representation to make the derivations less intricate; as usual, the results can be applied for real signals too.

Following the derivation of the digital time-delay beamformer in the general case, if the input signal at antenna n is a complex exponential arriving at an angle Θ

with an unknown frequency f, where $|f| < f_c$, with f_c as the maximum frequency of the beamformers target frequency band

$$s\left(t + n\frac{d}{c}\sin(\Phi)\right) = \mathrm{e}^{\mathrm{j}2\pi f(t+n(d/c)\sin(\Phi))}, \tag{5.140}$$

then the digital beamformer produces

$$y_d(\Phi,\Theta,t) = \frac{1}{N}\sum_{n=0}^{N-1}\sum_{k=-\infty}^{\infty} \mathrm{e}^{\mathrm{j}2\pi f((k/f_s)+n\tau_\Phi)}\ker\left(f_s(t-n\tau_\Theta)-k\right). \tag{5.141}$$

A better understanding of this relation can be obtained by rewriting it (the detailed derivation can be found in Appendix 5.6.C) as

$$y_d(\Phi,\Theta,t) = \frac{1}{N}\sum_{n=0}^{N-1} \mathrm{e}^{\mathrm{j}2\pi f(t+n\tau_\Phi-n\tau_\Theta)} \sum_{k=-\infty}^{\infty} \mathrm{e}^{\mathrm{j}2\pi k f_s(t-n\tau_\Theta)}\mathrm{KER}\left(k+\frac{f}{f_s}\right). \tag{5.142}$$

Hence, the squared magnitude of the digital beamformers output using the "di" abbreviation can be written as

$$\begin{aligned}&\left|y_d(\Phi,\Theta,t)\right|^2\\ &\quad= \left|\sum_{k=-\infty}^{\infty} \mathrm{e}^{\mathrm{j}2\pi t k f_s}\mathrm{KER}\left(k+\frac{f}{f_s}\right)\mathrm{di}\left(f\frac{d}{c}\sin(\Phi)-(f+kf_s)\frac{d}{c}\sin(\Theta)\right)\right|^2.\end{aligned} \tag{5.143}$$

This is the narrowband digital interpolation beampattern. The spectrum repetition due to the sampling operation is clearly observed, and it is also presented in the directivity function. For a closer analysis, it is useful to express (5.143) in the following way:

$$\begin{aligned}&\left|y_d(\Phi,\Theta,t)\right|^2\\ &\quad= \Bigg|\underbrace{\mathrm{KER}\left(\frac{f}{f_s}\right)}_{\text{weight}}\underbrace{\mathrm{di}\left(f\frac{d}{c}\sin(\Phi)-(f)\frac{d}{c}\sin(\Theta)\right)}_{\text{ideal narrowband di function}}\\ &\qquad+\sum_{k\neq 0}\mathrm{e}^{\mathrm{j}2\pi t k f_s}\underbrace{\mathrm{KER}\left(k+\frac{f}{f_s}\right)}_{\text{weights}}\underbrace{\mathrm{di}\left(f\frac{d}{c}\sin(\Phi)-(f+kf_s)\frac{d}{c}\sin(\Theta)\right)}_{\text{undesired di functions}}\Bigg|^2,\end{aligned} \tag{5.144}$$

or, by neglecting cross-terms,

$$|\, y_d(\Phi,\Theta,t)\,|^2 \approx \left|\underbrace{\mathrm{KER}\left(\frac{f}{f_s}\right)}_{\text{weight}}\right|^2 \left|\underbrace{\mathrm{di}\left(f\frac{d}{c}\sin(\Phi)-(f)\frac{d}{c}\sin(\Theta)\right)}_{\text{ideal narrowband di function}}\right|^2 + \sum_{k\neq 0}\left|\underbrace{\mathrm{KER}\left(k+\frac{f}{f_s}\right)}_{\text{weights}}\right|^2 \left|\underbrace{\mathrm{di}\left(f\frac{d}{c}\sin(\Phi)-(f+kf_s)\frac{d}{c}\sin(\Theta)\right)}_{\text{undesired di functions}}\right|^2. \tag{5.145}$$

Note that if $\mathrm{KER}(f) = \mathrm{rect}(f)$, which means that Shannon's sampling series (5.155) is used for the reconstruction, then all the terms except the one for $k = 0$ in the sum vanish, and the ideal narrowband beampattern is recovered.

If this is not the case, (5.145) reveals that the digital interpolation beampattern consists of the ideal narrowband beampattern and a sum of undesired terms due to imperfect interpolation. These terms take their maximum values if the argument of the di functions is an integer (under the assumption of an equispaced array). Hence, the equation

$$M = \frac{d}{c}\left(f\sin(\Phi)-(f+kf_s)\sin(\Theta)\right) \tag{5.146}$$

with integer M describes the angular distribution of the peaks in the digital beampattern, since for the solutions of this equation in M, k, Φ, and Θ, the 1-periodic function di takes its maximum. Except for $k = 0$ and $M = 0$, this means that there is a peak in the beampattern at an undesired angle, weighted relative to the mainlobe by

$$\left|\mathrm{KER}\left(k+\frac{f}{f_s}\right)/\mathrm{KER}\left(\frac{f}{f_s}\right)\right|^2. \tag{5.147}$$

This disturbing phenomenon has been called "pseudograting lobes" (PGLs), and formula (5.145) shows that it is inherent in any reconstruction procedure by time-limited kernels. The angle Θ related to the undesired peaks can be predicted exactly by solving (5.146) for a given angle of incidence Φ for all $k \neq 0$. Also, since $\mathrm{KER}(f)$ decays with frequency, the main contributions will come from the first small values of k, especially from $k \pm 1$.

However, the term "pseudograting lobes" from [65], where it is discussed in detail for linear lowpass interpolation, is misleading, since the solution of (5.146) for $M = 0$ and $k \neq 0$ is in fact an *undesired mainlobe*. The position of these

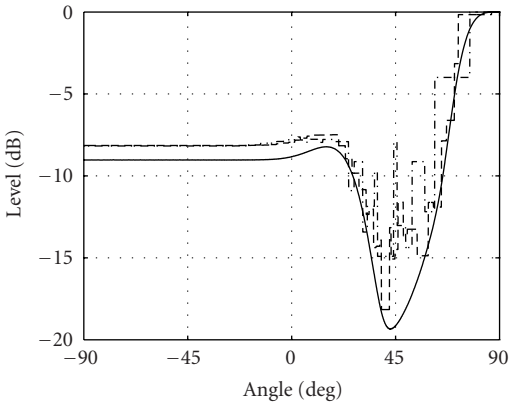

FIGURE 5.51. Ideal beampattern of $g(t)$ arriving at 90° on array 2 (solid line) and its digital beampattern using NN interpolation with $f_s = 20\,\text{GHz}$ (dash-dotted line) and $f_s = 40\,\text{GHz}$ (dashed line).

undesired mainlobes is calculated from (5.146) solving for $M = 0$ as

$$\Theta_{k,f} = \arcsin\left(\sin(\Phi)\frac{1}{1+k(f_s/f)}\right). \tag{5.148}$$

This effect is important since it means that the use of a random array or an aperiodic array, which has no grating lobes [58], does not help eliminate the errors in the "digital" beampattern due to the undesired mainlobes.

Hence, in the narrowband case, these undesired mainlobe errors can only be reduced by improving upon the interpolation by choosing good reconstruction kernels with high spectral damping around the integers, or choosing a higher sampling frequency, as can be predicted from (5.132).

Again, for a UWB signal, the situation improves: (5.148) shows that the positions of the undesired mainlobes are frequency dependent, and therefore an averaging effect over frequency occurs, which reduces the undesired mainlobes. However, it seems difficult to extract precise information from (5.148) so that it is better to rely on the results concerning interpolation.

5.6.3.3. Simulation results

In Figures 5.51, 5.52, 5.53, 5.54, 5.55, 5.56, and 5.57, the digital beampatterns for the two UWB pulses are compared to the ideal analog beampattern. The simulations are preliminarily restricted to the case of array 2. In Figures 5.51 and 5.52, nearest-neigbour interpolation is used in order to approximate the true-time delays at sampling frequencies $f_s = 20\,\text{GHz}$ and $f_s = 40\,\text{GHz}$. In Figures 5.53 and 5.54, linear interpolation is used at sampling frequencies $f_s = 20\,\text{GHz}$ and $f_s = 40\,\text{GHz}$. Figures 5.55 and 5.56 show linear interpolation and the revitalized linear interpolation [69] is compared at sampling frequency $f_s = 30\,\text{GHz}$.

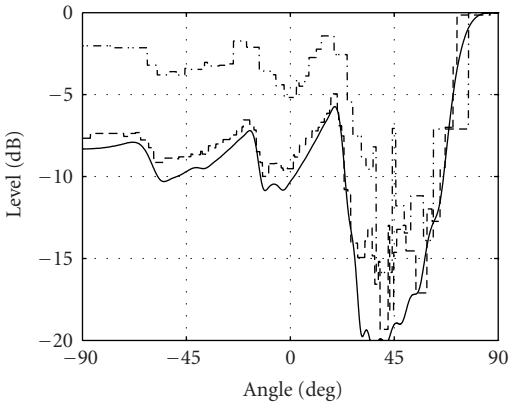

FIGURE 5.52. Ideal beampattern of $g_{\mathrm{FCC}}(t)$ arriving at 90° on array 2 (solid line) and its digital beampattern using NN interpolation with $f_s = 20\,\mathrm{GHz}$ (dash-dotted line) and $f_s = 40\,\mathrm{GHz}$ (dashed line).

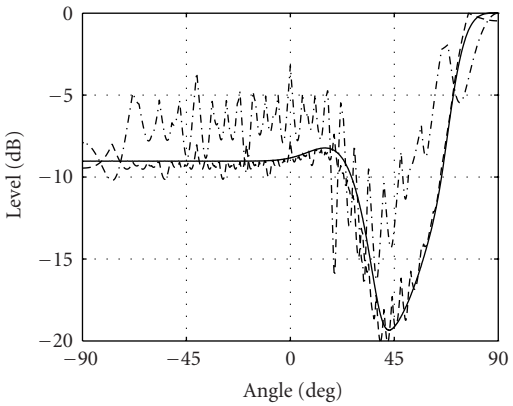

FIGURE 5.53. Ideal beampattern of $g(t)$ arriving at 90° on array 2 (solid line) and its digital beampattern using linear interpolation with $f_s = 20\,\mathrm{GHz}$ (dash-dotted line) and $f_s = 40\,\mathrm{GHz}$ (dashed line).

In Figure 5.57, the digital beampattern of a narrowband signal with frequency $f = 10\,\mathrm{GHz}$ arriving at 90° on an array designed for $\lambda/2$ and its digital beampattern using NN interpolation with $f_s = 20\,\mathrm{GHz}$ and linear interpolation with $f_s = 20\,\mathrm{GHz}$ are shown. Here, two fully developed undesired mainlobes are visible at −90° and 19.4°, corresponding to $k = \pm 1$ in (5.148), clearly demonstrating this phenomenon in the narrowband case.

The use of UWB signals reduces the errors significantly in comparision to the narrowband case, and the digital beampattern of the UWB pulses are quite close to the ideal pattern, at least in the case of $f_s = 40\,\mathrm{GHz}$. This is due to the fact that in the narrowband case, the interpolation errors from different antenna signals can add constructively, while in the UWB case, the averaging effect reduces the interpolation errors. In fact, at $f_s = 40\,\mathrm{GHz}$, the cheapest method, namely,

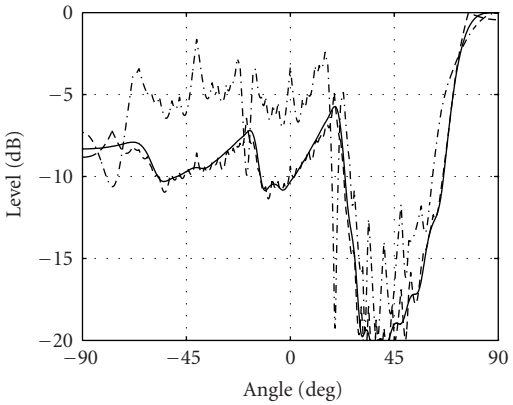

FIGURE 5.54. Ideal beampattern of $g_{\mathrm{FCC}}(t)$ arriving at 90° on array 2 (solid line) and its digital beampattern using linear interpolation with $f_s = 20$ GHz (dash-dotted line) and $f_s = 40$ GHz (dashed line).

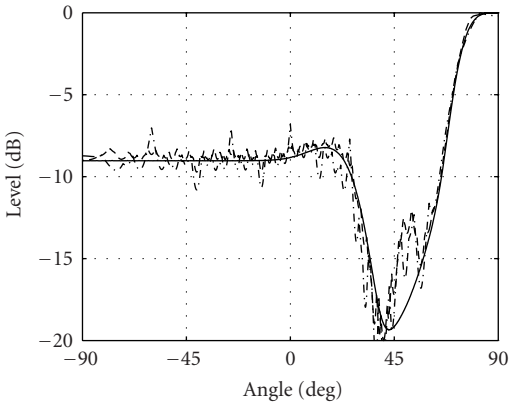

FIGURE 5.55. Ideal beampattern of $g(t)$ arriving at 90° on array 2 (solid line) and its digital beampattern using linear interpolation with $f_s = 30$ GHz (dash-dotted line) and revitalized linear interpolation with $f_s = 30$ GHz (dashed line).

nearest-neigbour interpolation, which needs no multiplications, leads to an acceptable beampattern. This means that fortunately digital delay-and-sum beamforming of UWB signals is not complicated from the viewpoint of pure digital signal processing complexity.

5.6.4. Direction-of-arrival estimation in UWB environments

After discussing UWB beamforming in a rather ideal environment, that is, no multipath propagation, we will now focus on estimating the relevant DOAs in *realistic UWB scenarios*. Note that indoor environments for high-data-rate UWB communication systems are characterized by significant multipath propagation. Referred to UWB beamforming, this means that several wavefronts coming from

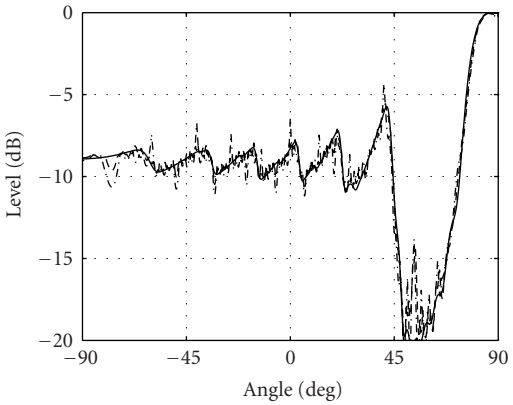

FIGURE 5.56. Ideal beampattern of $g_{\mathrm{FCC}}(t)$ arriving at 90° on array 2 (solid line) and its digital beampattern using linear interpolation with $f_s = 30\,\mathrm{GHz}$ (dash-dotted line) and revitalized linear interpolation with $f_s = 30\,\mathrm{GHz}$ (dashed line).

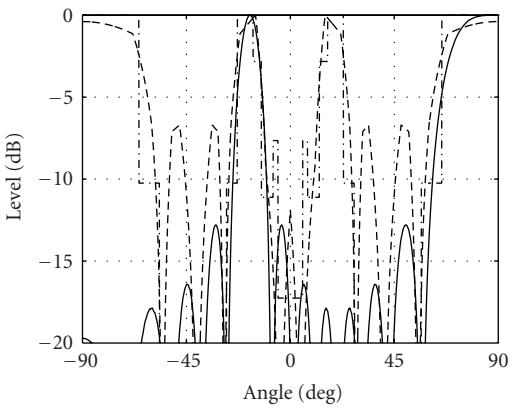

FIGURE 5.57. Ideal beampattern of narrowband signal with frequency $f = 10\,\mathrm{GHz}$ arriving at 90° on array designed for $\lambda/2$ (solid line) and its digital beampattern using NN interpolation with $f_s = 20\,\mathrm{GHz}$ (dash-dotted line) and linear interpolation with $f_s = 20\,\mathrm{GHz}$ (dashed line).

different directions will simultaneously impinge on the antenna array. Hence, the beamformer should either suppress these additional directions or better, if possible, should efficiently combine them. For that reason, a crucial question before entering the subject of *multipath-capable UWB beamformers* is whether the most relevant DOAs could be prinicipally determined in typical UWB environments. The aim of this section is to highlight this issue in an exemplary way in order to introduce it into this quite open field of UWB DOA estimation.

Despite the huge UWB bandwidth, the dense multipath propagation makes it impossible to resolve any path in an indoor environment. For that reason, estimating the DOA of each path is impossible too. Fortunately, the UWB propagation is

marked by distinct *clustering* meaning that a couple of paths coming from one major direction are grouped into a cluster so that a DOA could be assigned to cluster (on behalf of a path). As a special case in LOS (line-of-sight) conditions, the major goal should be to estimate the DOA of the LOS path and in NLOS (without a dominant LOS) scenarios the rough DOA of a cluster (see [70]) is sufficient.

A simple but not optimal way to estimate the DOA is by utilizing a beamformer scanning in a circle and selecting the arrival angles associated with the largest magnitudes as the relevant DOAs. Therefore, for this task the digital beamformer introduced in the previous section is applied. The weights of the different branches are set to one and the delays $\tau_n = n\tau_\Theta = (nd/c)\sin(\Theta)$ are varied continuously in order to steer the mainlobe in the desired direction Θ. The beamformer output is given by

$$\mathrm{BP}\,(t_0, \Delta t, \Theta) := \left(\int_{t_0}^{t_0+\Delta t} |\, y(\Phi, \Theta, t)\,|^2 dt \right)^{1/2}, \tag{5.149}$$

where t_0 is the starting point, Δt is the length of the observation interval, and Φ is the variable representing the DOAs and picked by

$$\hat{\Phi}(t_0, \Delta t) = \max_{\Theta} \left(\mathrm{BP}\,(t_0, \Delta t, \Theta) \right). \tag{5.150}$$

First we consider a two-path channel

$$h(t, \theta) = \alpha_1 \delta(t, \theta - \theta_1) + \alpha_2 \delta(t, \theta - \theta_2) \tag{5.151}$$

with the same path delay but different attenuations $\alpha_1 = \alpha_2 = 1$, and different impinging directions $\theta_1 = -45^\circ$ and $\theta_2 = 22.5^\circ$. This transmit pulse is of Gaussian shape (5.119) so as to gain a first impression of close to ideal DOA estimation and the antenna spacing is $d = \lambda = 4.4$ cm. Figure 5.58 shows the resulting normalized (scaled by its maximum) beampattern. Observe that not only the magnitude deviation (meaning more robustness against additional noise) but also the accuracy of the DOA estimation is improved with increasing number of antennas. Next, we consider a more realistic UWB impulse response, which is generated according to the IEEE standard channel model for UWB NLOS indoor environments [71]. This NLOS impulse response consists of more than 100 paths and has a length of 80 nanoseconds with 10-nanosecond delay spread. The resulting beampattern is shown in Figure 5.59 with $\Delta t = 50$ nanoseconds. Every circle at the ground surface marks time and angle of arrival for a ray with *positive* amplitude of the impulse response whereas every cross represents a negative one. The six significant regions with large magnitudes correspond to the six major clusters, so it can be seen that the DOA of a cluster could be satisfactorily resolved in angle and also in time.

In the last example a real LOS scenario is under investigation. The channel impulse responses were measured in labaratories of the IMST GmbH (Germany, Kamp-Lintfort) with $f_s = 10$ GHz and $d = 5$ cm. The true DOA of the LOS component is indicated by a black vertical line in Figure 5.60, and for $N = 4$ and

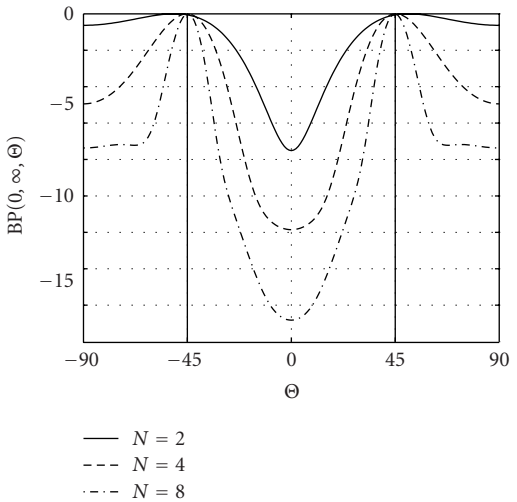

FIGURE 5.58. Normalized beampattern for $N = 2$ (solid line), $N = 4$ (dashed line), and $N = 8$ (dash-dotted line).

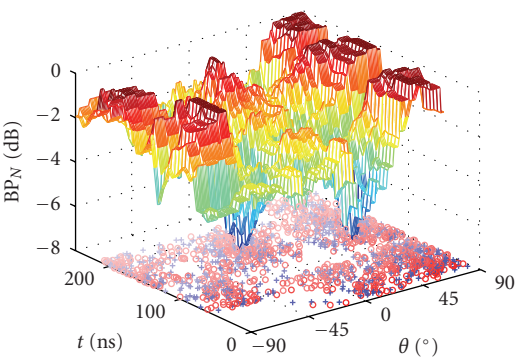

FIGURE 5.59. Normalized beampattern for IEEE standard model CM3 impulse response, $N = 4$.

$\Delta t = 10$ nanoseconds the estimated DOA is again the maximum of the normalized beampattern. It can be seen that both are in good agreement.

5.6.5. Conclusions

The aim of this section was to introduce UWB beamforming with special focus on *digital* UWB beamforming, which is today and will be in the future a critical task because of the enormous UWB bandwidth and the associated extremly high sampling frequency. Digital beamforming was investigated for rather ideal channels, that is, neither noise nor multipath propagation has been yet considered; however,

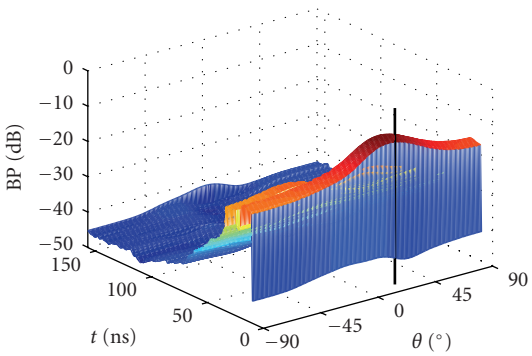

FIGURE 5.60. BP for $N = 4$, $\Delta t = 10$ nanoseconds, $d = 5$ cm in an LOS scenario.

it seems that increasing the bandwidth is beneficial for mitigating errors caused by sampled data. Measurements have shown that despite the huge bandwidth, each single path cannot be resolved in the channel impulse response meaning that beamforming towards a single path is principally not successful. For that reason, at the end of the section, the estimation of the direction of arrivals is exemplary investigated by common models and real data. The obtained figures indicate that DOA estimation could be achieved by considering clusters—so a *group of paths*—on behalf of paths. Nevertheless, much more research is required to substantiate these first qualitative observations by quantitative ones. Future research will therefore concern UWB DOA estimation and in particular UWB (digital) beamforming in noisy multipath environments.

Appendices

5.6.A. Mathematical notations and preliminary results

In the following, a real- or complex-valued signal $s(t)$ defined on the real line $\mathbb{R}$ is of finite duration T, if it vanishes outside the interval $[-T, T]$. The Fourier transform (spectrum) of a function $s(t) \in L^1(\mathbb{R})$, the set of absolutely integrable functions, will be denoted by

$$S(f) = \int_{-\infty}^{\infty} s(t) \mathrm{e}^{-\mathrm{j}2\pi f t} dt \quad (f \in \mathbb{R}). \tag{5.152}$$

The same notation will be used for the Fourier transform if $s(t) \in L^2(\mathbb{R})$, the set of square-integrable functions on the real line. $s(t)$ will be called bandlimited with bandlimit (or cutoff frequency) f_c if $S(f)$ vanishes outside the interval $[-f_c, +f_c]$.

A function $g(t)$ is an entire function of exponential type σ if it is analytic in the complex plane together with

$$\left|g(z)\right| \leq A e^{\sigma |z|} \tag{5.153}$$

for a constant A and any complex z.

The Paley-Wiener theorem [68] states that $g(t)$ is an entire function of exponential type πB and belongs to $L^2(\mathbb{R})$ if and only if $g(t)$ is bandlimited with bandlimit $B/2$ and $G(f) \in L^2(\mathbb{R})$, and the following applies:

$$g(z) = \int_{-B/2}^{B/2} G(f) e^{j2\pi f z} df. \tag{5.154}$$

$C(\mathbb{R})$ denotes the set of all functions $g(t)$, uniformly continuous and bounded on the real line, endowed with the supremum norm $\|g(t)\|_C = \sup_{t\in\mathbb{R}} |g(t)|$ and $C^r(\mathbb{R})$ is the set of functions $g(t)$ such that $d^i g(t)/dt^i \in C(\mathbb{R})$, $0 \le i \le r$, where $d^i g(t)/dt^i$ is the ith derivative of $g(t)$. Square brackets $\lfloor x \rfloor$ mean the greatest integer less than or equal to x, and the Kronecker symbol δ_i is defined as $\delta_i = 1$ for $i = 0$, $\delta_i = 0$ for $i \neq 0$. The sinc function is given by $\operatorname{sinc}(t) = \sin(\pi t)/(\pi t)$ with the usual continuous completion.

We will use the space of entire signals of exponential type πB bounded on the real line and denote this space by $\mathrm{BL}(B)$. This signal space is very convenient, since it contains all important signal types occuring in the applications, namely, the bandlimited absolutely integrable or square-integrable signals with highest frequency $f_c = B/2$. This includes bandwidth B, as well as the CW signals $e^{j2\pi f t}$ for all frequencies $f \le f_c$; for further properties, see [68, 72] (where this space is denoted by $B^\infty_{\pi B}$). We will use this signal space to formulate error bounds in the supremum norm.

Using this notation, one version of the famous Shannon sampling theorem states that if a signal $s(t)$ is in $\mathrm{BL}(B)$, then it can be reconstructed without error by the Shannon sampling series

$$s(t) = \sum_{k=-\infty}^{\infty} s\left(\frac{k}{f_s}\right) \operatorname{sinc}(f_s t - k), \tag{5.155}$$

if the sampling frequency f_s is higher than B. The condition $f_s > B$ is necessary since $\mathrm{BL}(B)$ contains signals that are not absolutely integrable [68].

5.6.B. Proof of Theorem 5.6.1

For all $t \in \mathbb{R}$, we have

$$\begin{aligned} &|\, y(\Phi,\Theta,t) - y_d(\Phi,\Theta,t) \,| \\ &\quad = \frac{1}{N} \left| \sum_{n=0}^{N-1} s(t - n\tau_\Theta + n\tau_\Phi) - \sum_{n=0}^{N-1} \sum_{k=-\infty}^{\infty} s\left(\frac{k}{f_s} + n\tau_\Phi\right) \ker(f_s(t - n\tau_\Theta) - k) \right| \\ &\quad \le \frac{1}{N} \sum_{n=0}^{N-1} \left| s(t - n\tau_\Theta + n\tau_\Phi) - \sum_{k=-\infty}^{\infty} s\left(\frac{k}{f_s} + n\tau_\Phi\right) \ker(f_s(t - n\tau_\Theta) - k) \right|. \end{aligned} \tag{5.156}$$

Now, setting $t' = t - n\tau_\Theta$ and observing that $\|s\|_C = \|s(\cdot + n\tau_\Phi)\|_C$, the inner terms can be estimated using [67, Theorem 2], and (5.132) follows. Equation (5.131) is a version of (5.132) for bandlimited signals, because if the signal $s(t)$ is in BL(B), then the Bernstein inequality [68] states that

$$\left\| \frac{d^m s(t)}{dt^m} \right\|_C \leq (B\pi)^m \|s\|_C, \quad m \geq 0. \tag{5.157}$$

Using this in (5.132) yields (5.131).

5.6.C. Proof of equation (5.143)

Applying Poisson's summation formula [73], it holds that

$$\sum_{k=-\infty}^{\infty} \ker(x-k) = \sum_{k=-\infty}^{\infty} \mathrm{KER}(k) \mathrm{e}^{\mathrm{j}2\pi kx}, \tag{5.158}$$

where the summation limits on the left-hand side are formally extended to infinite values and uniform convergence of the series on the left-hand side is assumed to be true. The next step

$$\sum_{k=-\infty}^{\infty} \mathrm{e}^{-\mathrm{j}2\pi(f/f_s)(x-k)} \ker(x-k) = \sum_{k=-\infty}^{\infty} \mathrm{KER}\left(k + \frac{f}{f_s}\right) \mathrm{e}^{\mathrm{j}2\pi kx} \tag{5.159}$$

follows by the modulation theorem for Fourier transforms. Setting $x = f_s t$ and multiplying by $\mathrm{e}^{\mathrm{j}2\pi ft}$ gives the identity

$$\sum_{k=-\infty}^{\infty} \mathrm{e}^{\mathrm{j}2\pi f(k/f_s)} \ker(f_s t - k) = \mathrm{e}^{\mathrm{j}2\pi ft} \sum_{k=-\infty}^{\infty} \mathrm{KER}\left(k + \frac{f}{f_s}\right) \mathrm{e}^{\mathrm{j}2\pi k f_s t}. \tag{5.160}$$

Setting $t - n\tau_\Theta$ for t in (5.160), we obtain

$$\sum_{k=-\infty}^{\infty} \mathrm{e}^{\mathrm{j}2\pi f(k/f_s)} \ker(f_s(t - n\tau_\Theta) - k) = \mathrm{e}^{\mathrm{j}2\pi f(t-n\tau_\Theta)} \sum_{k=-\infty}^{\infty} \mathrm{KER}\left(k + \frac{f}{f_s}\right) \mathrm{e}^{\mathrm{j}2\pi k f_s (t-n\tau_\Theta)}. \tag{5.161}$$

Using this equation in (5.141) gives (5.142) and combining the exponentials and changing the summation order yields

$$y_d(\Phi, \Theta, t) = \mathrm{e}^{\mathrm{j}2\pi ft} \sum_{k=-\infty}^{\infty} \mathrm{e}^{\mathrm{j}2\pi k f_s t} \mathrm{KER}\left(k + \frac{f}{f_s}\right) \frac{1}{N} \sum_{n=0}^{N-1} \mathrm{e}^{\mathrm{j}2\pi(f(n\tau_\Phi - n\tau_\Theta) - k f_s n\tau_\Theta)}, \tag{5.162}$$

so that evaluation of the inner sum results in (5.143).

5.7. Performance analysis of multiantenna UWB wireless communications

5.7.1. Introduction

The idea of employing multiple-input multiple-output (MIMO) technology in ultra-wideband (UWB) system has gained considerable interest recently. By the use of space-time (ST) coding [74–78], MIMO systems exploit both spatial and temporal diversities, and hence promise to improve the system performance significantly. In this section, we present a performance evaluation for UWB-MIMO multiuser systems in case of Nakagami frequency-selective fading environment. First, we quantify the performance merits of single-carrier UWB ST-coded systems regardless of specific coding schemes. We consider various modulation and multiple-access techniques, including time-hopping (TH) binary pulse-position modulation (BPPM), TH binary phase-shift keying (BPSK), and direct-sequence (DS) BPSK. Second, we show that the combination of ST coding and RAKE receiver is able to exploit spatial diversity as well as multipath diversity, richly inherent in UWB environments. Utilizing the real orthogonal design (ROD) [77] as the engine code for UWB-ST codes, DS-UWB-MIMO transmission is shown to be a promising scheme that provides superior performance for both single- and multiple-user scenarios.

Another approach for combating the detrimental effects of multipath fading in UWB systems is to use orthogonal frequency-division multiplexing (OFDM). With OFDM modulation, the duration of each symbol is much longer than the delay spread, so the channel response at each subcarrier could be considered almost flat. Recently, in [79–83], space-frequency (SF) coded MIMO-OFDM has been proposed to exploit spatial as well as frequency diversities in multipath environment. It has been shown in [84–86] that UWB-OFDM is able to make benefit of the multipath diversity. Here, we will discuss the application of SF coding in UWB-OFDM systems to gain both spatial and frequency diversities.

5.7.2. UWB communications

According to the Federal Communications Commission (FCC) definition, UWB technology is a transmission scheme that occupies a bandwidth of more than 20% of its center frequency, or nominally more than 500 MHz. The ultra-wideband nature offers several advantages over narrowband technology including high data rate, low power consumption, extensive multipath diversities, and support for multiple access. These unique characteristics of UWB make it a viable candidate for future short-range wireless communications. Recently, the two leading proposals for IEEE 802.15.3a wireless personal area networking (WPAN) standard [87] have been based on single-carrier (SC) UWB and multicarrier (MC) multiband (MB) OFDM. The signal model for both SC-UWB and MC-UWB systems will be given in the subsequent subsections.

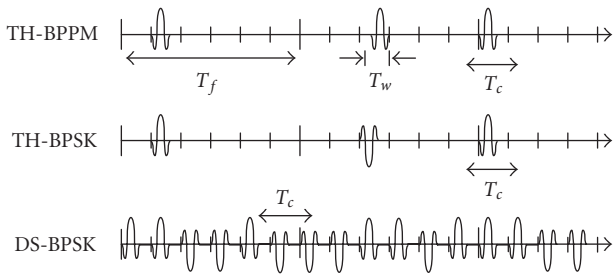

FIGURE 5.61. UWB signals with various modulation and multiple-access techniques.

5.7.2.1. Single-carrier UWB

SC-UWB, also referred to as carrier-free and impulse communications, is implemented by directly modulating a sequence of impulse-like waveforms that occupies several GHz bandwidth. In order to allow multiuser transmission without catastrophic collisions, the multiple-access approaches such as TH and DS spreading have been exploited. Figure 5.61 illustrates an example of TH-UWB and DS-UWB signals.

The TH-UWB utilizes low duty-cycle pulses, where the time spreading between the pulses is used to provide time multiplexing of users. The uth user's transmitted waveform at the kth frame can be described as [88–90]

$$\widetilde{x}_u(k;t) = \sqrt{E_u}\, a_u(k)\widetilde{w}(t - kT_f - c_u(k)T_c - b_u(k)T_d), \tag{5.163}$$

where $\widetilde{w}(t)$ is the transmitted monocycle of duration T_w, and T_f is the frame interval with $T_f \gg T_w$. The monocycle is normalized to have unit energy, and each frame is transmitted with energy E_u. To accommodate the TH sequences in multiple-access environments, T_f is further divided into N_c segments of T_c seconds, where $N_c T_c \leq T_f$. The TH sequence of the uth user is denoted by $\{c_u(k)\}$, $0 \leq c_u(k) \leq N_c - 1$. The modulation delay is represented by T_d and the data sequence is either $\{a_u(k)\}$ or $\{b_u(k)\}$, depending on the modulation techniques. In BPPM, the data are conveyed by the positions of the pulses, whence $a_u(k) = 1$ for all k and $b_u(k) \in \{0, 1\}$. BPSK, on the other hand, alternates the polarities of the pulses in response to the information. Accordingly, the data sequence is $a_u(k) \in \{-1, 1\}$ whereas $b_u(k) = 0$ for all k.

In contrast to TH approach, DS-UWB employs a train of high duty-cycle pulses whose polarities follow pseudorandom code sequences. The transmitted DS-BPSK signal model can be described as [91, 92]

$$\widetilde{x}_u(k;t) = \sqrt{\frac{E_u}{N_c}}\, d_u(k) \sum_{n_c=0}^{N_c-1} c_u(n_c)\, \widetilde{w}(t - kT_f - n_c T_c), \tag{5.164}$$

where $d_u(k) \in \{-1, 1\}$ is the data, $\{c_u(n_c)\}_{n_c=0}^{N_c-1} \in \{-1, 1\}$ represents the spreading

sequence, and $T_c \geq T_w$ denotes the hop period. The factor $\sqrt{1/N_c}$ is introduced such that the sequence of N_c monocycles has unit energy, and hence the transmitted energy per frame is E_u.

5.7.2.2. Multicarrier UWB

As opposed to the conventional SC-UWB in which a single bandwidth is used for all data transmission, MC-UWB system uses multiple-carrier frequencies to transmit the information. Since utilizing the whole available UWB spectrum (from 3.1 GHz to 10.6 GHz) leads to several disadvantages, such as high transceiver complexity, requirement on high-speed analog-to-digital converters, and high power consumption, MC MB-UWB approach [87] has been introduced.

In MB-UWB system, the available bandwidth is divided into several subbands with smaller bandwidth. Each subband occupies a bandwidth of at least 500 MHz in compliance with the FCC regulations. In order to efficiently capture the multipath energy, which is richly inherent in UWB environment, OFDM technique has been used to modulate the information in each subband. The major difference between MB-OFDM and traditional OFDM scheme is that the MB-OFDM transmission is not performed continually on every subband. Instead, the modulated OFDM signal is transmitted over different subbands at staggered time in order to enable full frequency diversity and accommodate multiuser communication. Specifically, consider an MB-OFDM system with N subcarriers and the subband bandwidth of B_{sb}. The uth user's transmitted complex continuous MB-OFDM signal at the sth symbol period can be modeled as

$$x_u^s(t) = \sum_{k=0}^{N-1} d_u^s(k) p_u^s(k; t - sT), \tag{5.165}$$

in which T represents OFDM symbol duration, $d_u^s(k)$ denotes the complex symbol to be sent over the kth subcarrier, and $\{p_u^s(k;t)\}_{k=0}^{N-1}$ is a set of N-orthogonal waveforms. Typically, $p_u^s(k;t)$ is given by

$$p_u^s(k;t) = w(t) \exp\left(j2\pi\left(f_u^s + k\Delta f\right)t\right), \tag{5.166}$$

where $w(t)$ is a lowpass pulse of duration T, and $\Delta f = 1/T = B_{\text{sb}}/N$ is the frequency spacing between the adjacent subcarreirs. The carrier frequency, f_u^s, specifies subband, in which the signal is transmitted during the sth OFDM symbol duration. These carrier frequency sequences are based on time-frequency codes, which are uniquely assigned to different users so as to minimize the multiple-access interference.

5.7.3. MIMO communications

In a point-to-point MIMO system, multiple antennas are deployed at both transmitter and receiver, as shown in Figure 5.62. At the transmitter, the data sequence

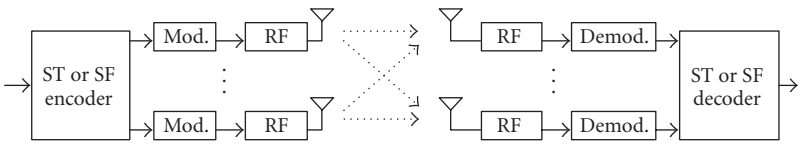

FIGURE 5.62. A point-to-point MIMO communication system.

is divided into blocks. Each block is encoded into a codeword matrix **D**. Each column of **D** contains a sequence of symbols that will be sent from each transmit antenna over a series of time slot or frequency tones (depending on the underlined modulation scheme, e.g., single carrier or multicarrier). These symbol streams are modulated with a pulse-shaping function, translated to the passband via parallel radio frequency (RF) chains, and then simultaneously transmitted over all transmit antennas. After down conversion, matched-filtering and demodulation processes, the receiver jointly decodes the received signals across all receive antennas.

The design of matrix **D** is originally studied for flat-fading channels. In this case, the row and column indices of **D** indicate the dimensions of space and time, and hence **D** is termed space-time (ST) code. For a MIMO system with N_t transmit and N_r receive antennas, **D** is an $K \times N_t$ matrix whose (k, i)th element, denoted by $d^i(k)$, represents the symbol transmitted at transmit antenna i over time slot k. Here, K represents the number of time slots for one codeword transmission. The MIMO channel is described by an $N_t \times N_r$ matrix **A**. The (i, j)th component of **A**, denoted by α^{ij}, is the channel fading coefficient from the ith transmit to the jth receive antenna. The received signal at each receive antenna is a noisy superposition of the N_t transmitted signals degraded by the channel fading. Consider the case when the channels are quasistatic, that is, they remain constant during the transmission of an entire codeword. The received signal can be described as an $K \times N_r$ matrix

$$\mathbf{Y} = \sqrt{\frac{E}{N_t}}\mathbf{DA} + \mathbf{N}, \tag{5.167}$$

where **N** is the matrix of additive complex Gaussian noises, each with zero mean and variance $N_0/2$ per dimension. For normalization purposes, the fading coefficient for each transmit-receive link is assumed to have unit variance, and the ST code satisfies the energy constraint $\mathrm{E}[\|\mathbf{D}\|^2] = KN_t$. Here, $\mathrm{E}[\mathbf{X}]$ and $\|\mathbf{X}\|$ denote the expectation and Frobenius norm[14] of **X**, respectively. The factor $\sqrt{1/N_t}$ ensures transmit energy identical to single-antenna transmission. Assuming that the channel state information (CSI) is perfectly known at the receiver, the receiver performs maximum likelihood (ML) decoding by choosing the codeword $\hat{\mathbf{D}}$ that minimizes

[14]The Frobenius norm of an $M \times N$ matrix $\mathbf{X} = (x_{mn})$ is defined as [93]

$$\|\mathbf{X}\|^2 = \mathrm{tr}\,(\mathbf{X}^{\mathcal{H}}\mathbf{X}) = \mathrm{tr}\,(\mathbf{X}\mathbf{X}^{\mathcal{H}}) = \left(\sum_{m=0}^{M-1}\sum_{n=0}^{N-1}|x_{mn}|^2\right).$$

the square Euclidean distance between the hypothesized and actual received signal matrices, that is,

$$\hat{\mathbf{D}} = \arg\min_{\mathbf{D}} \left\| \mathbf{Y} - \sqrt{\frac{E}{N_t}}\mathbf{D}\mathbf{A} \right\|^2. \tag{5.168}$$

The upper bound of the average pairwise error probability (PEP) between $\mathbf{D}$ and $\hat{\mathbf{D}}$ is of the form [74, 75]

$$P(\mathbf{D} \longrightarrow \hat{\mathbf{D}}) \leq \left[G_c \frac{\rho}{4N_t} \right]^{-G_d}, \tag{5.169}$$

where $\rho = E/N_0$ is the average signal-to-noise ratio (SNR) at each receive antenna. The quantities G_d and G_c depend on the distribution of channel fading coefficients and the structure of $\mathbf{D}$. They characterize the performance of ST-coded MIMO system as follows. The exponent G_d determines the slope of the error probability curve plotted as a function of SNR (measured in dB). The factor G_c displaces the performance curve rather than alternating its slope. The minimum values of G_d and G_c over all pairs of distinct codewords are called diversity gain and coding gain, respectively.

In wideband system, the channel fading is frequency selective. To exploit the additional frequency diversity in wideband MIMO communications, SF code incorporating with OFDM modulation has been introduced. The strategy of SF coding is to distribute the symbols across space (transmit antenna) and frequency (OFDM tones). The codeword $\mathbf{D}$ in this case represents SF codeword of size $N \times N_t$, where N is the number of OFDM tones. Note that the design of SF code is restricted to one OFDM symbol duration (T seconds), and the MIMO channel is normally assumed constant over a period of T. The performance criteria for SF coded MIMO-OFDM can be characterized in a similar fashion as that of ST system.

5.7.4. Single-carrier UWB-MIMO system

The application of ST coding in SC-UWB communication was first proposed in [94], where a specific ST code is used for 2-transmit-antenna system. In this section, we will introduce a general SC-UWB-MIMO system model, in which all ST coding schemes can be used directly. Under this model, we will provide the analysis of the receiver processing and system performances.

5.7.4.1. Transceiver design

We consider an SC-UWB-MIMO multiuser system with N_u users, each equipped with N_t transmit antennas, and a receiver with N_r receive antennas as shown in Figure 5.63.

For each user, the sequence of binary symbols is divided into blocks of N_b symbols. Each block is encoded into an ST codeword to be simultaneously sent

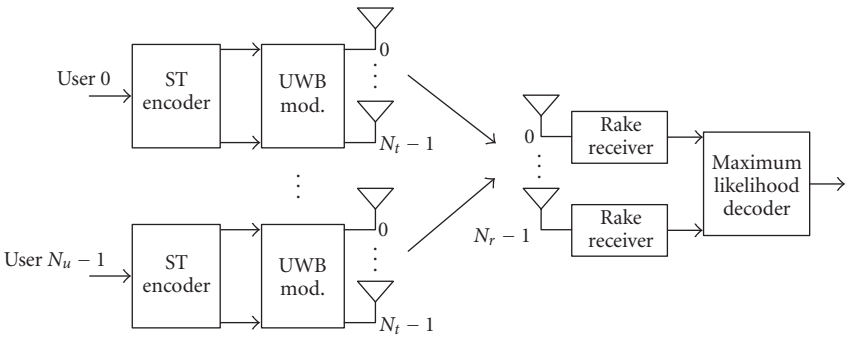

FIGURE 5.63. A SC-UWB-MIMO multiuser communication system.

over all transmit antennas. The ST codeword matrix can be expressed as a $K \times N_t$ matrix

$$\mathbf{D}_u = \begin{pmatrix} d_u^0(0) & d_u^1(0) & \cdots & d_u^{N_t-1}(0) \\ d_u^0(1) & d_u^1(1) & \cdots & d_u^{N_t-1}(1) \\ \vdots & \vdots & \ddots & \vdots \\ d_u^0(K-1) & d_u^1(K-1) & \cdots & d_u^{N_t-1}(K-1) \end{pmatrix}, \tag{5.170}$$

where $d_u^i(k) \in \{-1, 1\}$ represents the binary symbol transmitted by the uth user at transmit antenna i over time slot k. Since K time slots are required for N_b symbols transmission, the code rate is $R = N_b/K$. The transmitter converts the ST codeword matrix into a $K \times N_t$ UWB ST signal matrix $\widetilde{\mathbf{X}}_u(t) = [\widetilde{x}_u^i(k;t)]$ by modulating the symbol $d_u^i(k)$ into UWB signal $\widetilde{x}_u^i(k;t)$. The UWB signal depends on particular multiple-access and modulation techniques. With TH approach, $\widetilde{x}_u^i(k;t)$ is modeled as (see (5.163))

$$\widetilde{x}_u^i(k;t) = \sqrt{\frac{E_u}{N_t}}\,\widetilde{w}\left(t - kT_f - c_u(k)T_c - \frac{1 - d_u^i(k)}{2}T_d\right) \tag{5.171}$$

for BPPM, and

$$\widetilde{x}_u^i(k;t) = \sqrt{\frac{E_u}{N_t}}\,d_u^i(k)\,\widetilde{w}(t - kT_f - c_u(k)T_c) \tag{5.172}$$

for BPSK. With DS-BPSK technique (see (5.164)), the UWB signal becomes

$$\widetilde{x}_u^i(k;t) = \sqrt{\frac{E_u}{N_t N_c}}\,d_u^i(k)\sum_{n_c=0}^{N_c-1} c_u(n_c)\,\widetilde{w}(t - kT_f - n_c T_c). \tag{5.173}$$

Note that the factor $\sqrt{1/N_t}$ is introduced to ensure that the total transmitted energy of the uth user is E_u during each frame interval, independent of the number of transmit antennas.

The MIMO channel coefficients are assumed to be real, mutually independent, and quasistatic. Ignoring the Doppler effect, the channel impulse response from transmit antenna i of user u to receive antenna j can be modeled as

$$h_u^{ij}(t) = \sum_{l=0}^{L_u-1} \alpha_u^{ij}(l)\delta(t-\tau_u(l)), \tag{5.174}$$

where $\alpha_u^{ij}(l)$ is the multipath gain coefficients, L_u denotes the number of resolvable paths, and $\tau_u(l)$ represents the path delays relative to the delay of the desired user's first arrival path. Without loss of generality, we let the first user be the desired user, and assume $\tau_0(0) = 0$. In order to simplify the analysis, we assume that the minimum resolvable delay is equal to the pulse width. The amplitude of the lth path, $|\alpha_u^{ij}(l)|$, is modeled as a Nakagami-m random variable with average power $\Omega_u(l)$, that is, [95]

$$p_{|\alpha_u^{ij}(l)|}(x) = \frac{2}{\Gamma(m)}\left(\frac{m}{\Omega_u(l)}\right)^m x^{2m-1}\exp\left(-\frac{m}{\Omega_u(l)}x^2\right), \tag{5.175}$$

where $\Gamma(\cdot)$ denotes the Gamma function, m is the fading parameter ($m \geq 1/2$), and $\Omega_u(l) = \mathrm{E}[|\alpha_u^{ij}(l)|^2]$. For each user, the time delay $\tau_u(l)$ and the average power $\Omega_u(l)$ are assumed identical for every transmit-receive link.

Due to the effect of propagation channel and the variation of antenna characteristics caused by large bandwidth, the shape of transmitted monocycle $\widetilde{w}(t)$ is modified to its second derivative at the receive antenna output [96]. Denote the received monocycle waveform by $w(t)$ and let $x_u^i(k;t)$ be of the form similar to the transmitted waveform $\widetilde{x}_u^i(k;t)$ by replacing $\widetilde{w}(t)$ with $w(t)$.

The signal received at each receive antenna consists of mulitpath signals from all active users and thermal noise. With the first user being the desired user, the received signal at receive antenna j can be expressed as

$$r^j(t) = y_0^j(t) + n_{\mathrm{MU}}^j(t) + n^j(t), \tag{5.176}$$

where $n_{\mathrm{MU}}^j(t) = \sum_{u=1}^{N_u-1} y_u^j(t)$ is the multiuser interference, and

$$y_u^j(t) = \sum_{i=0}^{N_t-1}\sum_{k=0}^{K-1}\sum_{l=0}^{L_u-1} \alpha_u^{ij}(l)x_u^i(k;t-\tau_u(l)) \tag{5.177}$$

represents the signal from the uth user. The real additive white Gaussian noise process, $n^j(t)$, is assumed to have zero mean and two-sided power spectral density $N_0/2$. By choosing the signal parameters such that $N_cT_c + \max_u\{\tau_u(L_u-1)\} \leq T_f$, we can guarantee that there is no intersymbol interference (ISI).

As depicted in Figure 5.63, an SC-UWB-MIMO receiver comprises N_r RAKE receivers and an ML decoder where the decoding process is performed jointly

across all N_r receive antennas. The RAKE receiver employs L ($L \le \max_u\{L_u\}$) correlators, each using the delayed versions of the received monocycle as the reference waveform. Denote the reference signal by $v_{k'}(t)$. The output of the l'th correlator at receive antenna j is given by

$$y^j_{k'}(l') = \int_{-\infty}^{\infty} v_{k'}\left(t - \tau_0(l')\right) r^j(t)dt \triangleq y^j_{d,k'}(l') + n^j_{\text{tot},k'}(l'), \tag{5.178}$$

where $y^j_{d,k'}(l')$ denotes the correlator output corresponding to the desired transmitted information, and $n^j_{\text{tot},k'}(l') \triangleq n^j_{\text{MU},k'}(l') + n^j_{k'}(l')$ is the combination of multiuser interference and sample noise. In what follows, we analyze the receiver assuming different modulation and multiple-access techniques employed. For notation convenience, we denote the autocorrelation function of $w(t)$ as $\gamma(s) = \int_{-\infty}^{\infty} w(t-s)w(t)ds$.

TH-BPPM. The design of TH-BPPM receiver depends on the choice of the modulation delay, T_d. With $T_d = \arg\min_{T_d} \gamma(T_d)$, the correlation waveform adopted at each RAKE receiver is modeled as

$$v_{k'}(t) = w\left(t - k'T_f - c_0(k')T_c\right) - w\left(t - k'T_f - c_0(k')T_c - T_d\right). \tag{5.179}$$

Substituting (5.171) and (5.179) into (5.178), after some manipulations, the correlator output is given by

$$y^j_{k'}(l') = \left[1 - \gamma(T_d)\right]\sqrt{\frac{E_0}{N_t}} \sum_{i=0}^{N_t-1} d^i_0(k')\alpha^{ij}_0(l') + n^j_{\text{tot},k'}(l'). \tag{5.180}$$

Next we arrange the correlator outputs in the matrix form

$$\mathbf{Y}^j = \left[1 - \gamma(T_d)\right]\sqrt{\frac{E_0}{N_t}}\mathbf{D}_0\mathbf{A}^j_0 + \mathbf{N}^j_{\text{tot}}, \tag{5.181}$$

where $\mathbf{D}_0$ is the desired user's ST symbol defined in (5.170). Both matrices $\mathbf{Y}^j$ and $\mathbf{N}^j_{\text{tot}}$ are of size $K \times L$ whose (k,l)th elements are $y^j_k(l)$ and $n^j_{\text{tot},k}(l)$, respectively. The multipath gain coefficient matrix $\mathbf{A}^j_0$ of size $N_t \times L$ is formatted as

$$\mathbf{A}^j_0 = \begin{pmatrix} \alpha_0^{0j}(0) & \alpha_0^{0j}(1) & \cdots & \alpha_0^{0j}(L-1) \\ \alpha_0^{1j}(0) & \alpha_0^{1j}(1) & \cdots & \alpha_0^{1j}(L-1) \\ \vdots & \vdots & \ddots & \vdots \\ \alpha_0^{(N_t-1)j}(0) & \alpha_0^{(N_t-1)j}(1) & \cdots & \alpha_0^{(N_t-1)j}(L-1) \end{pmatrix}. \tag{5.182}$$

Given the CSI on MIMO channels, the output of ML decoder is

$$\hat{\mathbf{D}}_0 = \arg\min_{\mathbf{D}_0} \sum_{j=0}^{N_r-1} \left\| \mathbf{Y}^j - \left[1 - \gamma(T_d)\right]\sqrt{\frac{E_0}{N_t}}\mathbf{D}_0\mathbf{A}^j_0 \right\|^2. \tag{5.183}$$

TH-BPSK. The reference waveform used at the TH-BPSK receiver is the delay version of the received monocycle, that is,

$$v_{k'}(t) = w(t - k'T_f - c_0(k')T_c). \tag{5.184}$$

Substituting (5.172) and (5.184) into (5.178), we obtain

$$y^j_{k'}(l') = \sqrt{\frac{E_0}{N_t}} \sum_{i=0}^{N_t-1} d^i_0(k')\alpha^{ij}_0(l') + n^j_{\text{tot},k'}(l'). \tag{5.185}$$

The correlator outputs can be written in the matrix form as

$$\mathbf{Y}^j = \sqrt{\frac{E_0}{N_t}}\mathbf{D}_0\mathbf{A}^j_0 + \mathbf{N}^j_{\text{tot}}, \tag{5.186}$$

in which $\mathbf{Y}^j$, $\mathbf{A}^j_0$, and $\mathbf{N}^j_{\text{tot}}$ are in the same forms as the ones stated in (5.181). The decision rule for the ML decoder can be written similar to (5.183) as

$$\widehat{\mathbf{D}}_0 = \arg\min_{\mathbf{D}_0} \sum_{j=0}^{N_r-1} \left\| \mathbf{Y}^j - \sqrt{\frac{E_0}{N_t}}\mathbf{D}_0\mathbf{A}^j_0 \right\|^2. \tag{5.187}$$

DS-BPSK. The DS-BPSK receiver adopts the monocycle sequence

$$v_{k'}(t) = \sqrt{\frac{1}{N_c}} \sum_{n'_c=0}^{N_c-1} c_0(n'_c)w(t - k'T_f - n'_cT_c) \tag{5.188}$$

as the reference waveform. From (5.173), (5.188), and (5.178), we have

$$y^j_{k'}(l') = \sqrt{\frac{E_0}{N_t}} \sum_{i=0}^{N_t-1} d^i_0(k') \sum_{l=0}^{L_0-1} \alpha^{ij}_0(l) f(l, l') + n^j_{\text{tot},k'}(l'), \tag{5.189}$$

where

$$f(l, l') \triangleq \frac{1}{N_c} \sum_{n_c{}'=0}^{N_c-1} c_0(n_c{}') \sum_{n_c=0}^{N_c-1} c_0(n_c)\gamma[(n_c - n_c{}')T_c + \tau_0(l) - \tau_0(l')]. \tag{5.190}$$

We rewrite the correlator outputs in the matrix form as

$$\mathbf{Y}^j = \sqrt{\frac{E_0}{N_t}}\mathbf{D}_0\mathbf{A}^j_0\mathbf{F} + \mathbf{N}^j_{\text{tot}}, \tag{5.191}$$

in which $\mathbf{F}$ is an $L_0 \times L$ matrix whose (l, l')th element is $f(l, l')$. The multipath gain coefficient matrix $\mathbf{A}_0^j$ of size $N_t \times L_0$ is of a form similar to (5.182). Subsequently, the decision rule can be stated as

$$\hat{\mathbf{D}}_0 = \arg\min_{\mathbf{D}_0} \sum_{j=0}^{N_r-1} \left\| \mathbf{Y}^j - \sqrt{\frac{E_0}{N_t}} \mathbf{D}_0 \mathbf{A}_0^j \mathbf{F} \right\|^2. \tag{5.192}$$

5.7.4.2. Performance analysis

To evaluate the performance of SC-UWB MIMO systems, we first calculate the statistics of noise and interference. According to (5.178), the noise sample $n_{k'}^j(l')$ is Gaussian distributed with zero mean and variance $\sigma_n^2 \triangleq (N_0/2) \int_{-\infty}^{\infty} v_{k'}^2(l')dt$. To investigate the distribution of multiuser interference, we express $n_{\mathrm{MU},k'}^j(l')$ (see (5.176) and (5.178)) as

$$n_{\mathrm{MU},k'}^j(l') = \sum_{u=1}^{N_u-1} \sum_{i=0}^{N_t-1} \sum_{l=0}^{L-1} \alpha_u^{ij}(l) n_{u,k'}^i(l, l'), \tag{5.193}$$

where $n_{u,k'}^i(l, l') \triangleq \int_{-\infty}^{\infty} v_{k'}(l') x_u^i(t - \tau_u(l))dt$. Using the same approach as in [96], one can show that $n_{u,k'}^i(l, l')$ is approximately Gaussian random variable with zero mean and variance

$$\mathrm{E}\left[\left| n_{u,m}^j(k) \right|^2 \right] = \frac{E_u}{N_t} \frac{1}{T_f} \int_{-\infty}^{\infty} \left[\int_{-\infty}^{\infty} w(t - s) v(t) dt \right]^2 ds \triangleq \frac{E_u}{N_t} \sigma_a^2. \tag{5.194}$$

Assuming Nakagami-m fading coefficients, independent of the transmitted signals, and using central limit theorem, we can show that for sufficiently large L, N_t and N_u, $n_{\mathrm{MU},k'}^j(l')$ is approximately Gaussian random variable with zero mean and variance $\sigma_a^2 \sum_{u=1}^{N_u-1} E_u \sum_{l=0}^{L-1} \Omega_u(l)$. Hence, $n_{\mathrm{tot},k'}^j(l')$ is zero-mean Gaussian random variable with variance

$$\sigma_{n_{\mathrm{tot}}}^2 = \sigma_a^2 \sum_{u=1}^{N_u-1} E_u \sum_{l=0}^{L-1} \Omega_u(l) + \sigma_n^2. \tag{5.195}$$

Since the total noise and interference can be approximated with Gaussian distribution, PEP can be evaluated in a similar fashion as in the conventional narrowband MIMO system. The values of σ_n^2, σ_a^2, and PEP depend on particular modulation and multiple-access techniques, and will be given in the following subsections.

TH-BPPM. From (5.179), we have

$$\int_{-\infty}^{\infty} \left[v_{k'}(t - \tau_0(l')) \right]^2 dt = 2[1 - \gamma(T_d)]. \tag{5.196}$$

The noise variance becomes $\sigma_n^2 = [1-\gamma(T_d)]N_0$, and σ_a^2 is obtained from (5.194) as $\sigma_a^2 = 2(\bar{\sigma}_a^2 - \sigma_d^2)$, in which $\bar{\sigma}_a^2 \triangleq (1/T_f)\int_{-\infty}^{\infty}\gamma^2(s)ds$ and $\sigma_d^2 \triangleq (1/T_f)\int_{-\infty}^{\infty}\gamma(s)\gamma(s-T_d)ds$.

Suppose that $\mathbf{D}_0$ and $\hat{\mathbf{D}}_0$ are two distinct transmitted ST codewords, following similar calculation steps as in [97], the PEP conditioned on the channel coefficient matrix $\mathbf{A}_0^j$ is given by

$$P\left(\mathbf{D}_0 \longrightarrow \hat{\mathbf{D}}_0 \mid \mathbf{A}_0^j\right) = \mathrm{Q}\left(\sqrt{\frac{\rho}{2N_t}\sum_{j=0}^{N_r-1}\left\|(\mathbf{D}_0-\hat{\mathbf{D}}_0)\mathbf{A}_0^j\right\|^2}\right), \tag{5.197}$$

where $\mathrm{Q}(x)$ is the Gaussian error function,[15] and $\rho = [1-\gamma(T_d)]^2E_0/(2\sigma_{n_{\mathrm{tot}}}^2)$, which can be expressed as

$$\rho = \left[4\frac{\bar{\sigma}_a^2-\sigma_d^2}{[1-\gamma(T_d)]^2}\sum_{u=1}^{N_u-1}\frac{E_u}{E_0}\sum_{l=0}^{L-1}\Omega_u(l) + \frac{2N_0/E_0}{[1-\gamma(T_d)]}\right]^{-1}. \tag{5.198}$$

Applying the inequality $\mathrm{Q}(x) \le (1/2)\exp(-x^2/2)$, for $x > 0$, the conditional PEP in (5.197) can be upper-bounded by

$$P\left(\mathbf{D}_0 \longrightarrow \hat{\mathbf{D}}_0 \mid \mathbf{A}_0^j\right) \le \frac{1}{2}\exp\left(-\frac{\rho}{4N_t}\sum_{j=0}^{N_r-1}\left\|(\mathbf{D}_0-\hat{\mathbf{D}}_0)\mathbf{A}_0^j\right\|^2\right). \tag{5.199}$$

For convenience, let us define $\mathbf{Z} = (\mathbf{D}_0-\hat{\mathbf{D}}_0)^T(\mathbf{D}_0-\hat{\mathbf{D}}_0)$, where $(\cdot)^T$ denotes transpose operation. Notice that

$$\left\|(\mathbf{D}_0-\hat{\mathbf{D}})\mathbf{A}_0^j\right\|^2 = \sum_{l=0}^{L-1}\left(\mathbf{a}_0^j(l)\right)^T\mathbf{Z}\mathbf{a}_0^j(l), \tag{5.200}$$

where $\mathbf{a}_0^j(l)$ represents the lth column of $\mathbf{A}_0^j$. Since $\mathbf{Z}$ is a real symmetric matrix, there exists a set of nonnegative eigenvalues $\{\lambda_i\}_{i=0}^{N_t-1}$ and the corresponding normalized eigenvectors $\{\mathbf{v}_i\}_{i=0}^{N_t-1}$ such that

$$\mathbf{Z} = \mathbf{V}\mathbf{\Lambda}\mathbf{V}^T, \tag{5.201}$$

where $\mathbf{V} \triangleq [\mathbf{v}_0\mathbf{v}_1\cdots\mathbf{v}_{N_t-1}]$ is an orthonormal matrix, and $\mathbf{\Lambda}$ is a diagonal matrix whose diagonal elements are the eigenvalues of $\mathbf{Z}$. Substituting (5.201) into (5.200), we have

$$\left\|(\mathbf{D}_0-\hat{\mathbf{D}}_0)\mathbf{A}_0^j\right\|^2 = \sum_{l=0}^{L-1}\sum_{i=0}^{N_t-1}\lambda_i\left|\beta^{ij}(l)\right|^2, \tag{5.202}$$

[15] The Gaussian error function is defined as $\mathrm{Q}(x) = (1/\sqrt{2\pi})\int_x^{\infty}\exp(-s^2/2)ds$.

in which $\beta^{ij}(l) \triangleq (\mathbf{a}_0^j(l))^T \mathbf{v}_i$. Since $\{\alpha_0^{ij}(l)\}_{i=0}^{N_t-1}$ are independent identically distributed (i.i.d.) and $\mathbf{V}$ is orthonormal, $\{\beta^{ij}(l)\}_{i=0}^{N_t-1}$ are i.i.d. random variables whose magnitudes are approximately Nakagami-m distributed with parameter $\widetilde{m} = N_t m/(N_t m - m + 1)$ and average power $\Omega_0(l)$ (see [95, page 25]). By the use of characteristic functions, $|\beta^{ij}(l)|^2$ is approximately Gamma distributed, that is, [98]

$$p_{|\beta^{ij}(l)|^2}(x) = \frac{1}{\Gamma(\widetilde{m})}\left(\frac{\widetilde{m}}{\Omega_0(l)}\right)^{\widetilde{m}} x^{\widetilde{m}-1}\exp\left(-\frac{\widetilde{m}}{\Omega_0(l)}x\right). \tag{5.203}$$

Substituting (5.202) into (5.199) and averaging (5.199) with respect to the distribution of $|\beta^{ij}(l)|^2$, the resultant PEP upper bound is given by

$$P\left(\mathbf{D}_0 \longrightarrow \hat{\mathbf{D}}_0\right) \le \left[\prod_{l=0}^{L-1}\prod_{i=0}^{N_t-1}\left(1+\frac{\rho}{4N_t}\frac{\Omega_0(l)}{\widetilde{m}}\lambda_i\right)\right]^{-\widetilde{m}N_r}. \tag{5.204}$$

For high SNR environments, the bound can be further simplified to

$$P\left(\mathbf{D}_0 \longrightarrow \hat{\mathbf{D}}_0\right) \le \left[G_0(\widetilde{m})\frac{\rho}{4N_t}\right]^{-\widetilde{m}rN_rL}, \tag{5.205}$$

where $G_0(\widetilde{m}) \triangleq (\widetilde{m})^{-1}(\prod_{l=0}^{L-1}\Omega_0(l))^{1/L}(\prod_{i=0}^{r-1}\lambda_i)^{1/r}$, r is the rank, and $\{\lambda_i\}_{i=0}^{r-1}$ represent nonzero eigenvalues of matrix $\mathbf{Z}$. For a single-user system, since there is no effect of multiple-access interference, ρ reduces to $[1-\gamma(T_d)]E_0/2N_0$. Consequently, the minimum values of $\widetilde{m}rN_rL$ and $G_0(\widetilde{m})$ over all pairs of distinct codewords define diversity gain and coding gain of TH-BPPM MIMO system.

TH-BPSK. Since the reference signal for TH-BPSK system is the shifted monocycle whose energy is unity, $\sigma_n^2 = N_0/2$ and $\sigma_a^2 = \bar{\sigma}_a^2$. Following the similar calculations as in BPPM, the upper bound of the PEP can be expressed as

$$P\left(\mathbf{D}_0 \longrightarrow \hat{\mathbf{D}}_0\right) \le \left[G_0(\widetilde{m})\frac{\rho}{4N_t}\right]^{-\widetilde{m}rN_rL}, \tag{5.206}$$

where $G_0(\widetilde{m})$ is of the same form as the one defined in (5.205), and

$$\rho = \frac{E_0}{2\sigma_{n_{\text{tot}}}^2} = \left[2\bar{\sigma}_a^2\sum_{u=1}^{N_u-1}\frac{E_u}{E_0}\sum_{l=0}^{L-1}\Omega_u(l) + \left(\frac{E_0}{N_0}\right)^{-1}\right]^{-1}, \tag{5.207}$$

which becomes E_0/N_0 for the single-user system.

DS-BPSK. From (5.188), we can show that $\sigma_n^2 = N_0/2$ and $\sigma_a^2 = \bar{\sigma}_a^2$. As in TH-UWB, the upper bound of the PEP conditioned on the channel matrix is given by

$$P\left(\mathbf{D}_0 \longrightarrow \hat{\mathbf{D}}_0 \mid \mathbf{A}_0^j\right) \le \frac{1}{2}\exp\left(-\frac{\rho}{4N_t}\sum_{j=0}^{N_r-1}\left\|(\mathbf{D}_0-\hat{\mathbf{D}}_0)\mathbf{A}_0^j\mathbf{F}\right\|^2\right), \tag{5.208}$$

where $\rho = E_0/(2\sigma^2_{n_{\text{tot}}})$ is in the same form as (5.207). By the use of eigenvalue decomposition as in (5.201), we obtain

$$\left\|(\mathbf{D}_0 - \hat{\mathbf{D}}_0)\mathbf{A}_0^j\mathbf{F}\right\|^2 = \text{tr}\left(\mathbf{F}^T(\mathbf{A}_0^j)^T\mathbf{Z}\mathbf{A}_0^j\mathbf{F}\right) = \text{tr}\left((\mathbf{B}^j)^T\boldsymbol{\Lambda}\mathbf{B}^j\right), \tag{5.209}$$

where $\text{tr}(\cdot)$ stands for the trace operation, and $\mathbf{B}^j \triangleq \mathbf{V}^T\mathbf{A}_0^j\mathbf{F}$ is an $N_t \times L$ matrix. Let $\mathbf{I}_x$ denote an $x \times x$ identity matrix, $\otimes$ represent the tensor product, and $\text{v}(\mathbf{X})$ stack the columns of $\mathbf{X}$ in a single column vector. Then, we have

$$\sum_{j=0}^{N_r-1}\left\|(\mathbf{D}_0 - \hat{\mathbf{D}}_0)\mathbf{A}_0^j\mathbf{F}\right\|^2 = \sum_{j=0}^{N_r-1}\text{tr}\left((\mathbf{B}^j)^T\boldsymbol{\Lambda}\mathbf{B}^j\right) = \mathbf{b}^T\Delta\mathbf{b}, \tag{5.210}$$

where

$$\Delta \triangleq \mathbf{I}_{N_rL} \otimes \boldsymbol{\Lambda}, \qquad \mathbf{b} \triangleq \left[\text{v}^T(\mathbf{B}^0)\cdots\text{v}^T(\mathbf{B}^{N_r-1})\right]^T. \tag{5.211}$$

Denote the correlation matrix of $\mathbf{b}$ by $\mathbf{R} = \text{E}[\mathbf{b}\mathbf{b}^T]$. Since $\mathbf{R}$ is nonnegative definite, it has a symmetric square root $\mathbf{U}$ such that $\mathbf{R} = \mathbf{U}^T\mathbf{U}$ [93]. Let $\mathbf{q} = (\mathbf{U}^T)^{-1}\mathbf{b}$. Observe that $\text{E}[\mathbf{q}\mathbf{q}^T] = \mathbf{I}_{N_tN_rL}$, and hence the components of $\mathbf{q}$ are uncorrelated. Now, the upper bound of the conditioned PEP in (5.208) can be reexpressed as

$$P(\mathbf{D}_0 \longrightarrow \hat{\mathbf{D}}_0 \mid \mathbf{A}_0^j) \le \exp\left(-\frac{\rho}{4N_t}\mathbf{q}^T\mathbf{U}\Delta\mathbf{U}^T\mathbf{q}\right). \tag{5.212}$$

Assuming that $\mathbf{R}$ is full rank, $\mathbf{U}$ is also full rank [93]. Therefore, maximum diversity gain can be achieved by maximizing the rank of Δ. Note that

$$\text{rank}(\Delta) = N_rL\text{rank}(\boldsymbol{\Lambda}) = N_rL\text{rank}(\mathbf{Z}), \tag{5.213}$$

where $\text{rank}(\mathbf{X})$ stands for the rank of $\mathbf{X}$. Hence, the rank criterion for DS-UWB ST system is identical to that of TH-UWB ST system. In order to quantify the coding gain, it might be necessary to evaluate the statistics of $\mathbf{q}$ which is difficult to obtain for Nakagami fading distribution. The performance of DS-UWB ST system can be further investigated by computer simulations.

5.7.4.3. SC-UWB using ROD ST code

In this section, we consider two-transmit-antenna system employing ROD ST coding scheme [77]. Generalization to UWB ST systems with higher number of transmit antennas is straightforward. The user subscript u is omitted for notation simplicity. Based on ROD structure, the ST code is modeled as

$$\mathbf{D} = \begin{pmatrix} d^0 & d^1 \\ -d^1 & d^0 \end{pmatrix}. \tag{5.214}$$

Since two time slots are used for the transmission of two symbols (d^0 and d^1), the code is of full rate $R = 1$. The corresponding matrix $\mathbf{Z}$ is given by

$$\mathbf{Z} = \sum_{i=0}^{1} (d^i - \widehat{d}^{\,i})^2 \mathbf{I}_2 = 4 \sum_{i=0}^{1} \delta (d^i - \widehat{d}^{\,i}) \mathbf{I}_2. \tag{5.215}$$

For ROD code with rate $1/K$, where $K \geq 2$ is an even integer, the codeword $\mathbf{D}$ of size $K \times 2$ is modeled as

$$\mathbf{D} = d \begin{pmatrix} \begin{pmatrix} 1 & 1 \\ -1 & 1 \end{pmatrix}^T \cdots \begin{pmatrix} 1 & 1 \\ -1 & 1 \end{pmatrix}^T \end{pmatrix}^T_{K \times 2}. \tag{5.216}$$

In this case, the data symbol d is transmitted repeatedly over K frames from both transmit antennas. The matrix $\mathbf{Z}$ becomes

$$\mathbf{Z} = (d - \widehat{d}\,)^2 K \mathbf{I}_2 = 4K\delta (d - \widehat{d}\,) \mathbf{I}_2. \tag{5.217}$$

Observe that both full- and reduced-rate codes result in two equal eigenvalues $\lambda_0 = \lambda_1 \triangleq \lambda$ and the matrix $\mathbf{Z} = \lambda \mathbf{I}_2$ of full rank ($r = 2$). Substituting the eigenvalues into (5.205), we arrive at

$$P(\mathbf{D} \longrightarrow \hat{\mathbf{D}}) \leq \left[\prod_{l=0}^{L-1} \left(\frac{\Omega(l)}{\widetilde{m}} \frac{\rho\lambda}{8} \right) \right]^{-2\widetilde{m}N_r}, \tag{5.218}$$

where $\widetilde{m} = 2m/(m+1)$. With channel parameters and N_r being fixed, (5.218) depends only on the value of $\rho\lambda$. The higher the $\rho\lambda$, the better the performance.

To compare the performance of various systems, we assume that the energy per bit E_b is fixed. For simplicity, we also assume that all users have equal transmitted energy per frame (E). Expressing E in term of E_b, we have $E = E_b$ for full-rate and $E = E_b/K$ for $1/K$-rate codes. Assuming one erroneous symbol, the eigenvalues for $1/K$ rate are K times larger than those for full-rate code. We denote the eigenvalue of full-rate code as $\bar{\lambda}$.

In single-user case, $\rho\lambda$ is $[1 - \gamma(T_d)](E_b/2N_0)\bar{\lambda}$ for BPPM and $(E_b/N_0)\bar{\lambda}$ for BPSK, regardless of the code rate. As a result, reducing the code rate does not improve the performance of single-user systems. In addition, $\rho\lambda$ of TH/DS-BPSK systems are $2[1 - \gamma(T_d)]^{-1}$ times that of TH-BPPM system. Since $[1 - \gamma(T_d)] < 2$, TH/DS-BPSK systems tend to outperform TH-BPPM system for every code rate. On the other hand, we show in [99] that the multiuser system with reduced rate provides higher value of $\rho\lambda$, and hence likely to performs better than that with full rate.

Figures 5.64 and 5.65 show the BER performance of TH and DS UWB systems in single-user and asynchronous multiuser environments. We employ UWB signals with $T_f = 100$ nanoseconds, $T_w = 0.8$ nanosecond, and random TH or

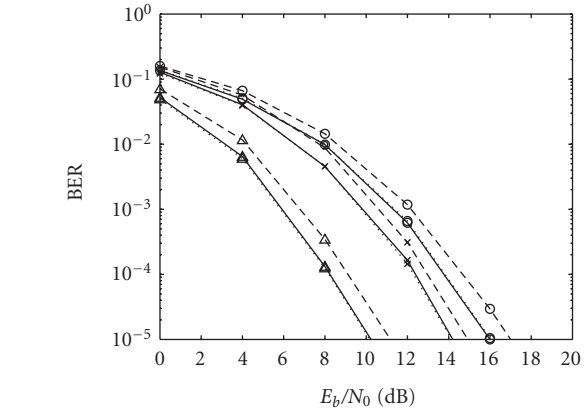

(a)

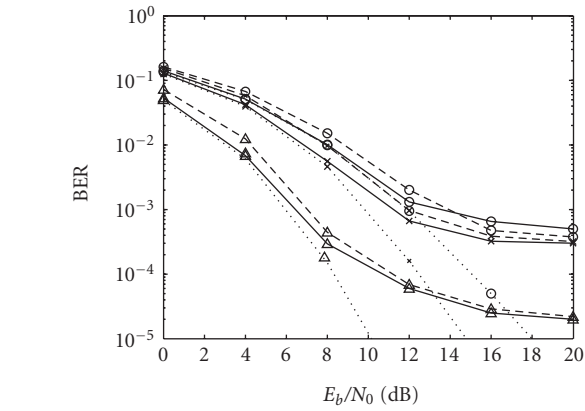

(b)

FIGURE 5.64. TH and DS UWB systems: (a) single user; (b) multiuser ($N_u = 5$).

spreading sequence. The received monocycle is modeled as the second derivative of the Gaussian pulse [96]. The channel parameters are $m = 2$ and $\sum_{l=0}^{L_u-1} \Omega_u(l) = 1$, with delay profile following [100]. The number of fingers for the RAKE receiver is chosen to be $L = 4$.

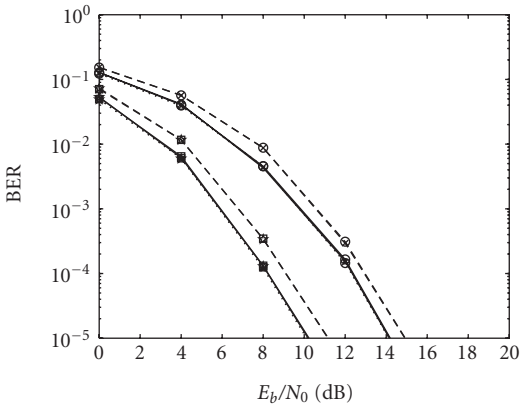

- TH-BPPM, $N_r = 1$, $R = 1$
- TH-BPPM, $N_r = 1$, $R = 1/2$
- TH-BPPM, $N_r = 2$, $R = 1$
- TH-BPPM, $N_r = 2$, $R = 1/2$
- TH-BPSK, $N_r = 1$, $R = 1$
- TH-BPSK, $N_r = 1$, $R = 1/2$
- TH-BPSK, $N_r = 2$, $R = 1$
- TH-BPSK, $N_r = 2$, $R = 1/2$
- DS-BPSK, $N_r = 1$, $R = 1$
- DS-BPSK, $N_r = 1$, $R = 1/2$
- DS-BPSK, $N_r = 2$, $R = 1$
- DS-BPSK, $N_r = 2$, $R = 1/2$

(a)

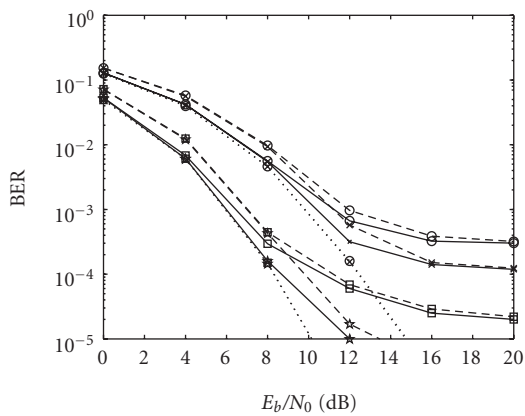

- TH-BPPM, $N_r = 1$, $R = 1$
- TH-BPPM, $N_r = 1$, $R = 1/2$
- TH-BPPM, $N_r = 2$, $R = 1$
- TH-BPPM, $N_r = 2$, $R = 1/2$
- TH-BPSK,$N_r = 1$, $R = 1$
- TH-BPSK, $N_r = 1$, $R = 1/2$
- TH-BPSK, $N_r = 2$, $R = 1$
- TH-BPSK, $N_r = 2$, $R = 1/2$
- DS-BPSK, $N_r = 1$, $R = 1$
- DS-BPSK, $N_r = 1$, $R = 1/2$
- DS-BPSK, $N_r = 2$, $R = 1$
- DS-BPSK, $N_r = 2$, $R = 1/2$

(b)

FIGURE 5.65. TH and DS UWB-MIMO systems with ROD ST codes of different rates: (a) single user; (b) multiuser ($N_u = 5$).

We can see from Figure 5.64 that MIMO systems outperform SISO systems, regardless of the modulation and multiple-access techniques. Consider the single-user case illustrated in Figure 5.64(a). At any fixed SNR, the performances of TH-BPSK and DS-BPSK systems are close to each other, and both BPSK systems yield superior performances to TH-BPPM. In Figure 5.64(b), we show the performances when 5 asynchronous users are active. In low SNR regime, TH/DS-BPSK systems outperform TH-BPPM scheme, and both BPSK systems yield close performances. However, due to the multiple-access interference, the BER of TH multiuser systems slightly drop with increasing E_b/N_0, and a high error floor can be noticed at high SNR. On the other hand, even in multiple-access scenarios, we can still see considerable improvement of DS-BPSK ST system.

In Figure 5.65, we compare the performance UWB systems employing ROD ST codes with full and half rates. Both figures illustrate that BPSK provides lower BER than BPPM scheme, regardless of the code rate. From Figure 5.65(a), we can see that the performances of full- and half-rate ROD codes are close to each other for every modulation schemes. This supports the theoretical results that for single user system, decreasing the rate of ROD ST code does not improve the performance. Unlike the single-user case, the results in Figure 5.65(b) confirm our expectation that when the code rate is lower, both TH-BPSK and TH-BPPM multiuser systems achieve better performances, especially in high SNR regime. However, for DS-BPSK multiple-access systems, the BER improvement obtained from reducing the code rate is insignificant. This is because for $N_u = 5$, the effect of multiuser interference to DS system is considerably small, and ROD ST code provides close to maximum achievable performance without decreasing the code rate.

5.7.5. Multicarrier UWB-MIMO system

In this section, multiantenna UWB-OFDM system model, including transceiver structure and SF coding, will be described. Based on this model, we will quantify the performance criteria in terms of diversity order and coding gain. Finally, some simulation results will be shown for the SF-coded UWB-OFDM systems.

5.7.5.1. Transceiver design

We consider a scenario that has been proposed for IEEE 802.15.3a WPAN standard. The available UWB spectrum of 7.5 GHz is divided into several subbands, each with bandwidth $B_{\text{sb}} = 528$ MHz (multiband (MB) OFDM). Each user uses one subband per transmission. At each user, the signals from all transmit antennas share the same subband. Within this subband, the OFDM modulation with $N = 128$ subcarriers is used at every transmit antenna. Denoting the OFDM block period by T, the frequency separation between two adjacent subcarriers is $\Delta f = B_{\text{sb}}/N = 1/T$. In what follows, we will investigate a peer-to-peer MB-UWB MIMO-OFDM communication system with N_t transmit and N_r receive antennas, as shown in Figure 5.66.

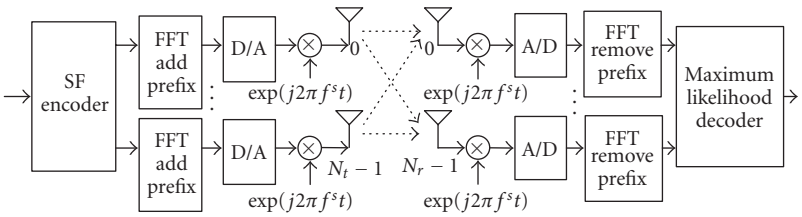

FIGURE 5.66. A peer-to-peer MB-UWB MIMO-OFDM communication system.

First, the transmitter partitions the input bit sequence into blocks of N_b bits. Each block is mapped onto an $N \times N_t$ SF codeword matrix

$$\mathbf{D} = \begin{pmatrix} d^0(0) & d^1(0) & \cdots & d^{N_t-1}(0) \\ d^0(1) & d^1(1) & \cdots & d^{N_t-1}(1) \\ \vdots & \vdots & \ddots & \vdots \\ d^0(N-1) & d^1(N-1) & \cdots & d^{N_t-1}(N-1) \end{pmatrix}, \tag{5.219}$$

where $d^i(k)$ represents the complex symbol to be transmitted over subcarrier k by transmit antenna i. Next, the transmitter applies N-point IFFT over each column of $\mathbf{D}$. In order to avoid the ISI, a cyclic prefix is added to the output of the IFFT processing before passing the discrete OFDM signal through a digital-to-analog converter. The analog baseband OFDM signal is then modulated by the subband carrier frequency. As depicted in Figure 5.66, f^s denotes the subband carrier frequency of the sth OFDM symbol. Finally, the modulated MB-OFDM signals are simultaneously sent from all N_t transmit antennas. Since N_b information bits are transmitted in T seconds, the transmission rate is $R = N_b/T = N_b B_{\text{sb}}/N$.

The receiver performs down conversion, matched filtering, discards the cyclic prefix, and applies the FFT. In this way, OFDM converts a frequency-selective fading channel into N parallel flat-fading channels whose fading coefficients are equal to the channel frequency response at the subcarriers center frequency. Recall the channel impulse response in (5.174). Its corresponding frequency response is given by

$$H^{ij}(f) = \sum_{l=0}^{L-1} \alpha^{ij}(l) \exp\left(-\mathrm{j}\, 2\pi f \tau(l)\right), \quad \mathrm{j} \triangleq \sqrt{-1}. \tag{5.220}$$

Consequently, the received signal at the kth subcarrier at receive antenna j is

$$y^j(k) = \sqrt{\frac{E}{N_t}} \sum_{i=0}^{N_t-1} d^i(k) H^{ij}(k) + n^j(k), \tag{5.221}$$

where $n^j(k)$ is complex additive white Gaussian noise with zero mean and power spectral density $N_0/2$ per dimension, and

$$H^{ij}(k) = \sum_{l=0}^{L-1} \alpha^{ij}(l) \exp\left[-\mathrm{j}\, 2\pi k \Delta f \tau(l)\right] \tag{5.222}$$

is the frequency response of the channel at subcarrier k. The SF codeword matrix is normalized to have energy $\mathrm{E}[\|\mathbf{D}\|^2] = NN_t$, and the factor $\sqrt{E/N_t}$ guarantees that the average transmitted energy is E, independent of the number of transmit antennas.

For subsequent performance evaluation, we provide the matrix representation of (5.221) as follows. Based on the formulation in [82], we rewrite the received signal at receive antenna j in the matrix form as

$$\mathbf{Y}^j = \sqrt{\frac{E}{N_t}}\mathbf{S}_D\mathbf{H}^j + \mathbf{N}^j, \tag{5.223}$$

where $\mathbf{S}_D$ is the data matrix of a form

$$\mathbf{S}_D = \left[\mathbf{S}^0 \quad \mathbf{S}^1 \quad \cdots \quad \mathbf{S}^{N_t-1}\right], \tag{5.224}$$

in which

$$\mathbf{S}^i = \mathrm{diag}\left(d^i(0), d^i(1), \ldots, d^i(N-1)\right), \tag{5.225}$$

and $\mathrm{diag}(\cdot)$ forms a diagonal matrix from its arguments. The channel vector $\mathbf{H}^j$ of size $NN_t \times 1$ is given by

$$\mathbf{H}^j = \left[\left(\mathbf{H}^{0j}\right)^T \quad \left(\mathbf{H}^{1j}\right)^T \quad \cdots \quad \left(\mathbf{H}^{(N_t-1)j}\right)^T\right]^T, \tag{5.226}$$

where

$$\mathbf{H}^{ij} = \left[H^{ij}(0) \quad H^{ij}(1) \quad \cdots \quad H^{ij}(N-1)\right]^T. \tag{5.227}$$

The received signal vector $\mathbf{Y}^j$ and the noise vector $\mathbf{N}^j$ are of size $N \times 1$ whose kth elements are $y^j(k)$ and $n^j(k)$, respectively. From (5.223), the decision rule at the ML decoder can be stated as

$$\hat{\mathbf{D}} = \arg\min_{\mathbf{D}} \sum_{j=0}^{N_r-1} \left\| \mathbf{Y} - \sqrt{\frac{E}{N_t}}\left(\mathbf{I}_{N_r} \otimes \mathbf{S}_D\right)\mathbf{H}^j \right\|^2. \tag{5.228}$$

5.7.5.2. Performance analysis

Following the computation steps as in [97], the PEP conditioned on the channel matrix is given by

$$\begin{aligned} P(\mathbf{D} \longrightarrow \hat{\mathbf{D}} \mid \mathbf{H}^j) &= \mathrm{Q}\left(\sqrt{\frac{\rho}{2N_t}\sum_{j=0}^{N_r-1}\left|\left|\Delta_S \mathbf{H}^j\right|\right|^2}\right) \\ &\leq \frac{1}{2}\exp\left(-\frac{\rho}{4N_t}\sum_{j=0}^{N_r-1}\left|\left|\Delta_S \mathbf{H}^j\right|\right|^2\right), \end{aligned} \tag{5.229}$$

where $\rho = E/N_0$ is the average SNR at each receive antenna, and $\Delta_S = \mathbf{S}_D - \mathbf{S}_{\hat{D}}$ represents the difference of codeword matrices. For convenience, let us denote an $N_t L \times 1$ channel vector $\mathbf{a}^j = [(\mathbf{a}^{0j})^T \cdots (\mathbf{a}^{(N_t-1)j})^T]^T$, in which $\mathbf{a}^{ij} = [\alpha^{ij}(0)\ \alpha^{ij}(1) \cdots \alpha^{ij}(L-1)]^T$. According to (5.222), we can express (5.226) as

$$\mathbf{H}^j = (\mathbf{I}_{N_t} \otimes \mathbf{W})\mathbf{a}^j, \tag{5.230}$$

where $\mathbf{W}$ is an $N \times L$ Fourier matrix, defined as

$$\mathbf{W} = \begin{pmatrix} 1 & 1 & \cdots & 1 \\ \omega^{\tau(0)} & \omega^{\tau(1)} & \cdots & \omega^{\tau(L-1)} \\ \vdots & \vdots & \ddots & \vdots \\ \omega^{(N-1)\tau(0)} & \omega^{(N-1)\tau(1)} & \cdots & \omega^{(N-1)\tau(L-1)} \end{pmatrix}, \tag{5.231}$$

in which $\omega = \exp(-\mathrm{j}\,2\pi\Delta f)$. As a consequence, the term $\|\Delta_S \mathbf{H}^j\|^2$ in (5.229) can be expressed as

$$\begin{aligned} \left|\left|\Delta_S \mathbf{H}^j\right|\right|^2 &= \left|\left|\Delta_S (\mathbf{I}_{N_t} \otimes \mathbf{W})\mathbf{a}^j\right|\right|^2 \\ &= (\mathbf{a}^j)^{\mathcal{H}}\left((\mathbf{I}_{N_t} \otimes \mathbf{W}^{\mathcal{H}})\Delta_S^{\mathcal{H}}\Delta_S(\mathbf{I}_{N_t} \otimes \mathbf{W})\right)\mathbf{a}^j. \end{aligned} \tag{5.232}$$

Assume that the MIMO channel is spatially uncorrelated, that is, the channel taps $\alpha^{ij}(l)$ are independent for different i and j. Also, let each link have the same power delay profile, that is, $\mathrm{E}[|\alpha^{ij}(l)|^2] = \Omega(l)$. Denote $\mathbf{R}^{1/2} = \mathbf{I}_{N_t} \otimes \mathrm{diag}(\sqrt{\Omega_0}\sqrt{\Omega_1} \cdots \sqrt{\Omega_{L-1}})$, and let $\mathbf{q}^j = (\mathbf{R}^{1/2})^{-1}\mathbf{a}^j$. We can show that the elements of $\mathbf{q}$ are uncorrelated Nakagami-m distributed with normalized power $\Omega = 1$. Substituting $\mathbf{a}^j = \mathbf{R}^{1/2}\mathbf{q}^j$ into (5.232), we have

$$\left|\left|\Delta_S \mathbf{H}^j\right|\right|^2 = (\mathbf{q}^j)^{\mathcal{H}} \underbrace{(\mathbf{I}_{N_t} \otimes \mathbf{U}^{\mathcal{H}})\Delta_S^{\mathcal{H}}\Delta_S(\mathbf{I}_{N_t} \otimes \mathbf{U})}_{\triangleq \mathbf{Z}} \mathbf{q}^j, \tag{5.233}$$

where

$$\mathbf{U} \triangleq \mathbf{W}\,\mathrm{diag}\left(\sqrt{\Omega_0}, \sqrt{\Omega_1}, \ldots, \sqrt{\Omega_{L-1}}\right). \tag{5.234}$$

Since $\mathbf{Z}$ is a symmetric matrix of size $N_tL \times N_tL$, it can be decomposed into $\mathbf{Z} = \mathbf{V}\mathbf{\Lambda}\mathbf{V}^{\mathcal{H}}$, where $\mathbf{V} \triangleq [\mathbf{v}_0\mathbf{v}_1 \cdots \mathbf{v}_{N_tL-1}]$ is a unitary matrix, and $\mathbf{\Lambda} = \text{diag}\{\lambda_0, \lambda_1, \ldots, \lambda_{N_tL-1}\}$ is a diagonal matrix whose diagonal elements are the eigenvalues of $\mathbf{Z}$. After some manipulations, we arrive at

$$||\Delta_S \mathbf{H}^j||^2 = \sum_{n=0}^{N_tL-1} \lambda_n |\beta_n^j|^2, \tag{5.235}$$

where $\beta_n^j \triangleq \mathbf{v}_n^{\mathcal{H}}\mathbf{q}^j$. Since $\mathbf{V}$ is unitary and the components of $\mathbf{q}^j$ are i.i.d., $\{\beta_n^j\}$ are independent random variables whose magnitudes are approximately Nakagami-$\widetilde{m}$ distributed with parameter $\widetilde{m} = N_tLm/(N_tLm - m + 1)$ and average power $\Omega = 1$ (see [95, page 25]). Note that when N_tL or m is large, $\widetilde{m}$ is approximately one. Substituting (5.235) into (5.229) and averaging (5.229) with respect to the distribution of $|\beta_n^j|^2$ (see (5.203)), the resultant upper bound of the PEP is given by

$$P(\mathbf{D} \longrightarrow \hat{\mathbf{D}}) \leq \left[\prod_{n=0}^{N_tL-1} \left(1 + \frac{\rho}{4N_t}\frac{1}{\widetilde{m}}\lambda_n\right)\right]^{-\widetilde{m}N_r}. \tag{5.236}$$

Assume the rank and nonzero eigenvalues of matrix $\mathbf{Z}$ to be r and $\{\lambda_n\}_{n=0}^{r-1}$, respectively. For high SNR environments, the bound can be simplified to

$$P(\mathbf{D} \longrightarrow \hat{\mathbf{D}}) \leq \left[G_c \frac{\rho}{4N_t}\right]^{-G_d}, \tag{5.237}$$

in which

$$G_c = (\widetilde{m})^{-1}\left(\prod_{n=0}^{r-1} \lambda_i\right)^{1/r} \tag{5.238}$$

defines the coding gain, and

$$G_d = \widetilde{m}rN_r \tag{5.239}$$

defines the diversity gain of UWB MIMO-OFDM system. From (5.233), we observe that

$$\text{rank}(\mathbf{Z}) = \text{rank}\Big(\big[\Delta_S(\mathbf{I}_{N_t} \otimes \mathbf{U})\big]^{\mathcal{H}}\Delta_S(\mathbf{I}_{N_t} \otimes \mathbf{U})\Big) = \text{rank}(\Delta_S(\mathbf{I}_{N_t} \otimes \mathbf{U})). \tag{5.240}$$

Since Δ_S is of size $N \times NN_t$ whereas $\mathbf{U}$ is of size $N \times L$, $\text{rank}(\Delta_S(\mathbf{I}_{N_t} \otimes \mathbf{U})) \leq \min\{N, N_tL\}$. Therefore, we can quantify the maximum achievable diversity gain as

$$G_d = \min\{\widetilde{m}N_tN_rL, \widetilde{m}N_rN\}. \tag{5.241}$$

5.7.5.3. MC-UWB using SF codes

In this section, we compare the performance of UWB MB-OFDM systems employing various SF codes. Each SF code has a form

$$\mathbf{D} = \begin{bmatrix} \mathbf{G}_0^T & \mathbf{G}_1^T & \cdots & \mathbf{G}_{P-1}^T & \mathbf{0}_{(N-P\Upsilon N_t)\times N_t}^T \end{bmatrix}, \tag{5.242}$$

where $\Upsilon \in \{1, 2, \ldots, L\}$ denotes the frequency diversity order, and $\mathbf{0}_{m\times n}$ stands for all-zero matrix of size $m \times n$. The matrix $\mathbf{G}_p$ is of size $\Upsilon N_t \times N_t$ whose structure depends on particular SF code. Let us consider a system with two transmit antennas. Based on the SF code in [82], $\mathbf{G}_p$ is given by

$$\mathbf{G}_p = (\mathbf{I}_{N_t} \otimes \mathbf{1}_{\Upsilon\times 1}) \begin{pmatrix} x_{p,0} & x_{p,1} \\ -x_{p,1}^* & x_{p,0}^* \end{pmatrix}, \tag{5.243}$$

in which $\mathbf{1}_{\Upsilon\times 1}$ is an all-one matrix of size $\Upsilon \times 1$, and $x_{p,i}$ is selected from BPSK or QPSK constellations. We also exploit a full-rate SF code [83] whose $\mathbf{G}_p$ is specified as

$$\mathbf{G}_p = \sqrt{N_t} \begin{pmatrix} \mathbf{x}_{p,0} & \mathbf{0}_{\Upsilon\times 1} \\ \mathbf{0}_{\Upsilon\times 1} & \mathbf{x}_{p,1} \end{pmatrix}, \tag{5.244}$$

where $\Upsilon \times 1$ matrix $\mathbf{x}_{p,i}$ is defined as follows. For simplicity, we omit the subscript p and denote $K = \Upsilon N_t$. Let $\mathbf{s} = [s_1\ s_2 \cdots s_K]$ be a vector of BPSK or QPSK symbols. The $1 \times \Upsilon K$ matrix $\mathbf{x} \triangleq [\mathbf{x}_0^T\ \mathbf{x}_1^T]$ is specified as

$$\mathbf{x} = \frac{1}{\sqrt{K}} \mathbf{s}\mathbf{V}(\theta_1, \theta_2, \ldots, \theta_K), \tag{5.245}$$

in which $\mathbf{V}$ is a Vandermonde matrix[16] with $\theta_k = \exp(\mathrm{j}(4k-3)\pi/(2K))$ for $K = 2^s$ $(s \geq 1)$ and $\theta_k = \exp(\mathrm{j}(6k-1)\pi/(3K))$ for $K = 3 \cdot 2^s$ $(s \geq 0)$ [83].

Based on the same channel model as in Section 5.7.4, the performances of MB-OFDM system with spectral efficiency of 1 bit/s/Hz are illustrated in Figures 5.67(a) and 5.67(b). In Figure 5.67(a), we show the performance of the SF codes with a frequency diversity of order $\Upsilon = 2$. We observe that regardless of particular SF coding scheme, the spatial diversity gained from UWB-MIMO architecture does improve the system performance significantly. In addition, the performance can be further improved with the choice of SF code and permutation scheme.

In Figure 5.67(b), we compare the performance of MB-OFDM system with different frequency diversity orders. Here, we utilize the full-rate SF code [83] with $\Upsilon = 2, 3$, and 4. We can see that by increasing the frequency-diversity order, the system performance can be improved. This observation is in accordance with our theoretical result in (5.237). Therefore, with a properly designed SF code, we can effectively exploit both spatial and frequency diversities in UWB environment.

[16] A Vandermonde matrix with variables $\theta_1, \theta_2, \ldots, \theta_K$ is a $K \times K$ matrix whose kth $(k = 1, 2, \ldots, K)$ row is defined as $[\theta_1^{k-1}\ \theta_2^{k-1} \cdots \theta_K^{k-1}]$.

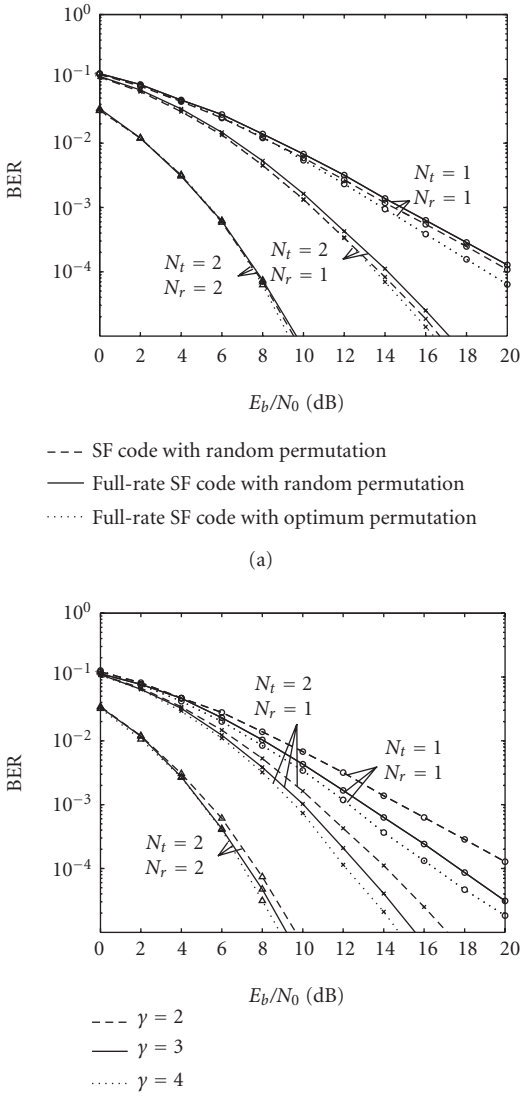

FIGURE 5.67. Performance of MB-OFDM: (a) with different SF codes; (b) with different diversity orders.

5.7.6. Summary

In this section, we provide performance analysis for multiantenna UWB communication systems with various transmission schemes. Based on Nakagami-m frequency-selective fading channels, the performance metrics (diversity and coding gains) of UWB-MIMO systems are quantified regardless of specific coding

schemes. For SC-UWB, we show that the use of ST coding in combination with RAKE receiver architecture is able to exploit spatial as well as multipath diversity, inherent in UWB environments. Comparing various modulation techniques, DS-UWB MIMO scheme is shown to achieve superior performance in both single-user and multiuser scenarios. For MC-UWB, we show that SF codes in addition to OFDM modulations are able to provide spatial as well as frequency diversities, thereby significantly improving the system performance.

5.8. Channel capacity of MIMO UWB indoor wireless systems

5.8.1. Introduction

In this section, we will investigate the problem of channel capacity calculation for UWB indoor wireless systems. In [101–103], the channel capacity of M-ary PPM UWB systems is discussed. However, the random fading property of UWB channel gains is not taken into account there. To the best of the authors' knowledge, there are no other reports appeared in the literature to address this problem up to now. We aim to make further development towards this problem in the sense of information theory. Our concern will be focused on the systems having multiple transmit and receive antennas (MIMO). The work by Foschini and Gans [104] and Telatar [105, 106] has shown that for a conventional narrowband fading channel, a MIMO system can achieve capacity of approximately $\min(N_T, N_R)$ times that of a separate channel, where N_T and N_R are the numbers of transmit and receive antennas, respectively. The measured data rates are found to be about 30% smaller than that being anticipated from an idealized model [107–109], showing that the capacity gains over single-antenna systems are still promising. Therefore, it is of importance to investigate how the capacity of MIMO UWB channels behaves.

As channel capacity depends on the statistical properties of the channel, we need first to investigate the statistics for the multipath fading of UWB indoor wireless system, which is our starting point.

In Sections 5.8.3, 5.8.4, 5.8.5, and 5.8.6, we discuss the frequency-flat case, while in Sections 5.8.7, 5.8.8, and 5.8.9, we consider the frequency-selective case. In Section 5.8.10, we investigate the effect of line-of-sight transmission on UWB channel capacity. Note that in the frequency-flat case, a UWB communication channel differs from a classic narrowband frequency-flat communication channel in that the statistics of the amplitude fading for both cases is different. Note also that the frequency-flat case is rather unrealistic but serves as a good "starting point."

This section gives a summary of our researching results on this topic. The details will be provided elsewhere.

Notation 1. Throughout this section, $\mathbf{I}$ is an identity matrix whose dimension is implied by context, Pr denotes the probability of an event, $P_A(x)$ and $p_A(x)$ represent the cumulative distribution function (cdf) and probability density function (pdf), respectively, of random variable A, $\mathcal{E}_A(f(A))$ stands for the expectation of

a function of random variable A, taking expectation over the statistics of A, and tr represents the trace of a square matrix. The log function is understood as the natural logarithm of its argument. Hence, the unit of the channel capacity is in nats.

5.8.2. A statistical model for the multipath fading of ultra-wideband indoor wireless systems

For UWB indoor wireless communication systems, its propagation model can be often described by the real impulse response [110]:

$$h(t,\tau) = \sum_{l=1}^{N_{\text{path}}(t)} a_l(t)\delta\big(\tau - \tau_l(t)\big), \tag{5.246}$$

where t and τ are the observation time and delay time of the impulse response, respectively, $N_{\text{path}}(t)$ is the number of multipath components at time t, $a_l(t)$ and $\tau_l(t)$ stand for the random time-varying amplitude and arrival-time of the received signal via the lth path at time t, respectively, and δ denotes the Dirac delta function. It is clear that a UWB wireless channel can be characterized by the statistics of the random variables (or processes) $N_{\text{path}}(t)$, $\tau_l(t)$, and $a_l(t)$. The statistical models for the narrowband indoor wireless channels have been well studied and some models have been widely accepted, see, for example, the survey paper [111]. However, these models cannot be applied directly to UWB wireless channels, since a UWB signal with its GHz bandwidth can resolve paths with a path delay difference on the order of one nanosecond. Hence, the number of scatterers within one resolvable path is in the order of 2 or 3 (when considering a typical office environment and employing a ray-tracing model) [112]. With this phenomenon being considered, several models for UWB channels have been proposed recently, for example, see [110, 113]. In [113], the so-called POCA-NAZU model is presented to describe the small-scale multipath amplitude fading for the received UWB signals. In [110], a stochastic tapped-delay-line (STDL) propagation model for the UWB indoor channel was proposed, as shown in (5.246). The parameters of the STDL model are extracted from the measured impulse responses. It is shown there that the best-fit distribution of the small-scale magnitude statistics is Nakagami distribution, differing from a Rayleigh distribution. Since the model in [110] is extracted based on experimental data, we will adopt this model as the basis of our analysis in this section. Note that now a standard channel model for UWB indoor communication systems is drafting [114].

Let $X(t)$ denote the transmitted UWB signal, which is propagated through an indoor multipath fading channel, and let $Y(t)$ denote the received signal. Then the relationship between $X(t)$ and $Y(t)$ can be modeled by

$$Y(t) = \sum_{l=1}^{N_{\text{path}}(t)} a_l(t)X\big(t - \tau_l(t)\big) + N(t). \tag{5.247}$$

Let us denote a_l as

$$a_l = v_l \zeta_l, \tag{5.248}$$

where $v_l := \text{sign}(a_l)$, the sign of a_l, and $\zeta_l := |a_l|$, the magnitude of a_l. It has been shown in [110] that the statistics of ζ_l in (5.247) can be approximated by a Nakagami distribution, the general form of whose pdf is as follows:

$$p_{\zeta_l}(x) = \begin{cases} \dfrac{2m^m x^{2m-1}}{\Gamma(m)\Omega_l^m} \mathrm{e}^{-mx^2/\Omega_l} & \text{when } x \geq 0, \\ 0 & \text{when } x < 0, \end{cases} \qquad m \geq \frac{1}{2}, \tag{5.249}$$

where Γ denotes the Gamma function, $\Omega_l = \mathcal{E}(a_l^2)$, and $m = [\mathcal{E}(a_l^2)]^2 / \text{Var}[a_l^2]$. In general, m should be a function of l. For example, in [110], m is modeled as a random variable, whose pdf is not specified. For that reason, we assume a constant m (see also the comment on page 16). In this section, we substitute m with another parameter κ by simply defining $\kappa = 2\,\text{m}$. Hence, it is clear that $\kappa \geq 1$. By so doing the pdf of $|a_l|$ in (5.249) can be rewritten as

$$p_{\zeta_l}(x) = \begin{cases} 2\left(\dfrac{\kappa}{2\Omega_l}\right)^{\kappa/2} \dfrac{1}{\Gamma(\kappa/2)} x^{\kappa-1} \mathrm{e}^{-(\kappa x^2/2\Omega_l)} & \text{when } x \geq 0, \\ 0 & \text{when } x < 0. \end{cases} \tag{5.250}$$

It is also known that the power of the amplitude fading is exponentially decreasing with the excess delay. Therefore, it is reasonable to assume that Ω_l varies with l according to the following model:

$$\Omega_l = r\Omega_{l-1}, \tag{5.251}$$

where $r < 1$ is a constant. According to the data reported in [110], r takes value between 0.93 and 0.97. Of course, the value of r is determined by the scenario of the communications.

For the model regarding v_l, no discussion has been addressed in the literature, to the best of the authors' knowledge. It seems justifiable to assume that

$$p_{v_l}(x) = \frac{1}{2}\delta(x-1) + \frac{1}{2}\delta(x+1), \tag{5.252}$$

that is, v_l takes the signs $+1$ and -1 with equal probability.

It is shown in [110] that the excess delay of lth delay bin, τ_l, is lognormally distributed. However, we will assume that τ_l is deterministic in this section to make our analysis tractable, which is also reasonable based on the following argument.

Recalling the exposition in [115] on the characterization of a wideband frequency-selective fading channels, a tapped-delay-line channel is also obtained as follows:

$$Y(t) = \sum_{l=1}^{L} a_l(t) X\big(t - (l-1)\tau\big) + N(t), \tag{5.253}$$

where $\tau = 1/W_X$, with W_X being the bandwidth of the transmitted signal X, and $L = \lfloor T_m W_X \rfloor + 1 \approx \lfloor W_X/\Delta f_c \rfloor + 1$, with T_m and Δf_c being the multipath spread and the coherence bandwidth of the channel, respectively. In channel capacity calculation, we can assume that the transmitted signal will occupy the whole bandwidth of the channel frequency band. Hence, we will also use W_X to denote the bandwidth of the channel. In [115], model (5.253) is derived from frequency domain. It has a direct interpretation in time domain, that is, the output of the receiver consists of the signals coming from several delay bins. Denote the resolution of the path delay for each delay bin as τ'. Then it is easy to see from this interpretation that $L = \lfloor T_m/\tau' \rfloor + 1$. Thus we can see that $\tau' \approx 1/W_X = \tau$.

Even though model (5.253) is derived from wideband channels, it applies to UWB channels as well if the random nature in the excess delay is ignored. On the other hand, if the fingers of UWB RAKE receiver are large enough, it is reasonable to take τ_l in model (5.247) as deterministic since we can simply choose τ_l as $(l-1)$ times of the width of one delay bin.

Notice that another important difference between models (5.247) and (5.253) is that the statistics of $a_l(t)$ for the two cases is different in general. In UWB case, since the bandwidth of a UWB signal is very large (up to several GHz), a UWB receiver can resolve paths with a path delay difference on the order of one nanosecond or even less than that. Thus the central limit theorem cannot apply to UWB case and a_l for UWB channels will have its own distribution. Therefore, *we will adopt* (5.253) *with* a_l *having the distribution composed by* (5.250) *and* (5.252) *as the basic model of our study*.

We presume that the communication is carried out using bursts. The burst duration is assumed to be short enough so that the channel can be regarded as essentially fixed during a burst, but long enough that the standard information-theoretic assumption of infinitely long code block lengths is a reasonable idealization. In this quasistatic scenario, it is meaningful to associate a channel capacity with a given realization of the channel fading.

We further assume that the receiver possesses a complete knowledge of the instantaneous channel parameters, that is, the realizations of $a_l(t)$ and their statistics. However, we assume that the transmitter is not aware of the information about channel parameters. Thus no power control can be applied to the transmitted signals.

Now we are ready to discuss the channel capacity.

5.8.3. The case of single-transmit and single-receive antenna (SISO)—frequency-flat channels

First we study the case of single-transmit and single-receive antenna and for frequency flat channels. Some simplification procedures are needed to make the analysis tractable. Our main assumptions are as follows.

Assumption 1. The channel is frequency flat, that is, $L = 1$.

Assumption 2. The number κ is assumed to be constant.

Assumption 3. The noise $N(t)$ is zero-mean Gaussian and white with variance σ_N^2.

Assumption 4. The power of the transmitted signal is bounded by $\mathrm{P_X}$, that is, $\mathcal{E}(X^2(t)) \leq \mathrm{P_X}$ for all t.

Based on Assumption 1, (5.253) is simplified to

$$Y(t) = a(t)X(t) + N(t). \tag{5.254}$$

For notational convenience, we define $\Omega = \Omega_1$ since only Ω_1 is of concern.

In Sections 5.7.3 and 5.7.4, we will discuss ergodic capacity and hence assume that the fading process is ergodic.

Based on Assumption 2 and the result presented in the preceding subsection, the random variable $|a(t)|$ will be of distribution defined by pdf (5.250).

The channel capacity for an AWGN channel with a given fading amplitude a is given by

$$C|_a = W_X \log\left(1 + \frac{a^2\,\mathrm{P_X}}{\sigma_N^2}\right). \tag{5.255}$$

So the ergodic channel capacity, denoted as C_e, turns out to be

$$C_e = \mathcal{E}_a(C|_a) = \frac{W_X}{\Gamma(\kappa/2)} \int_0^\infty \log\left(1 + \frac{u}{\beta}\right) u^{\kappa/2-1}\,\mathrm{e}^{-u}\,du, \tag{5.256}$$

where

$$\beta := \frac{\kappa\sigma_N^2}{2\Omega\,\mathrm{P_X}} = \frac{\kappa}{2\,\mathrm{SNR}}, \quad \mathrm{SNR} := \frac{\Omega\,\mathrm{P_X}}{\sigma_N^2}. \tag{5.257}$$

SNR defined in (5.257) can be considered as the ratio of signal power (at the receiver side) to noise power. Let us define

$$J(\kappa;\beta) := \int_0^\infty \log\left(1 + \frac{u}{\beta}\right) u^{\kappa/2-1}\,\mathrm{e}^{-u}\,du. \tag{5.258}$$

Then we have

$$C_e = \frac{W_X}{\Gamma(\kappa/2)} J(\kappa;\beta). \tag{5.259}$$

The function $J(\kappa;\beta)$ can be calculated recursively in terms of the following

equations:

$$J(\kappa;\beta) = \mathrm{e}^{\beta}\,\beta^{(\kappa-2)/2}\Gamma\left(\frac{\kappa}{2}\right)\Gamma\left(1-\frac{\kappa}{2},\beta\right) + \left(\frac{\kappa}{2}-1\right)J(\kappa-2;\beta),$$
$$J(1;\beta) = \sqrt{\pi}\left[\pi\,\mathrm{erfi}\left(\sqrt{\beta}\right) - \gamma_E - 2\log 2 - \log\beta - 2\beta\cdot\ {}_2F_2\left([1,1],\left[2,\frac{3}{2}\right],\beta\right)\right],$$
$$J(2;\beta) = \mathrm{e}^{\beta}\,\Gamma(0,\beta), \tag{5.260}$$

where $\gamma_E \approx 0.5772$ is Euler constant, and ${}_2F_2([\alpha_1,\alpha_2],[\alpha_3,\alpha_4],z)$, $\Gamma(\alpha,z)$, and $\mathrm{erfi}(z)$ denote the generalized hypergeometric function, incomplete Gamma function, and imaginary error function, respectively, whose definition can be seen in [116].

5.8.4. The case of multiple-transmit and multiple-receive antennas (MIMO)—frequency-flat channels

In this case, the input-output relation (channel model) can be described by

$$\mathbf{Y}(t) = \mathbf{A}(t)\mathbf{X}(t) + \mathbf{N}(t), \tag{5.261}$$

where $\mathbf{A}(t) = [a_{nm}(t)]_{m_Y\times m_X}$ is a random matrix characterizing the amplitude fading of the channel, $\mathbf{X}(t) \in R^{m_X}$ and $\mathbf{Y}(t) \in R^{m_Y}$ are the vectors of transmitted signals and received signals, respectively, m_X and m_Y denote the numbers of transmit and receive antennas, respectively, and $\mathbf{N}(t) \in R^{m_Y}$ is the noise vector.

Assumption 5. It is assumed that all a_{nm}, $n = 1,\ldots,m_Y$, $m = 1,\ldots,m_X$, are independent.

Assumption 6. The noise $\mathbf{N}$ is zero-mean Gaussian with covariance matrix $\sigma_{\mathbf{N}}^2\mathbf{I}_{m_Y}$.

Assumption 7. The power of the transmitted signal is bounded by $\mathrm{P_X}$, that is, $\mathcal{E}(\mathbf{X}^T(t)\mathbf{X}(t)) \le \mathrm{P_X}$ for all t.

Assumption 8. The receiver possesses a complete knowledge of the instantaneous channel parameters, while the transmitter is not aware of the information about the channel parameters.

According to the discussion in Section 5.7.2, the magnitude of each element of matrix $\mathbf{A}$, say $|a_{nm}|$, has the following pdf:

$$p_{|a_{nm}|}(x) = \begin{cases} \dfrac{2}{(2\Omega/\kappa)^{\kappa/2}\Gamma(\kappa/2)}x^{\kappa-1}\,\mathrm{e}^{-\kappa x^2/2\Omega} & \text{when } x \ge 0, \\ 0 & \text{when } x < 0. \end{cases} \tag{5.262}$$

The mutual information between $\mathbf{X}$ and $\mathbf{Y}$ for a given $\mathbf{A}$ is

$$\mathcal{I}(\mathbf{X};\mathbf{Y} \mid \mathbf{A}) = \mathcal{H}(\mathbf{Y} \mid \mathbf{A}) - \mathcal{H}(\mathbf{Y} \mid \mathbf{X},\mathbf{A}) = \mathcal{H}(\mathbf{Y} \mid \mathbf{A}) - \mathcal{H}(\mathbf{N}). \tag{5.263}$$

It is well known that if $\mathbf{X}$ is constrained to have covariance $\mathbf{Q}$, the choice of $\mathbf{X}$ that maximizes $\mathcal{I}(\mathbf{X};\mathbf{Y} \mid \mathbf{A})$ is Gaussian variable with covariance $\mathbf{Q}$. Thus the channel capacity for a given fading matrix $\mathbf{A}$ turns out to be [117, 105, 106]

$$C|_{\mathbf{A}} = W_X \log\det\left(\mathbf{I}_{m_Y} + \frac{1}{\sigma_{\mathbf{N}}^2}\mathbf{A}\mathbf{Q}\mathbf{A}^T\right), \tag{5.264}$$

where $\mathbf{A}^T$ represents the transpose of matrix $\mathbf{A}$. Let us define $\Psi(\mathbf{Q}) = \mathcal{E}_{\mathbf{A}}[\log\det(\mathbf{I}_{m_Y} + (1/\sigma_{\mathbf{N}}^2)\mathbf{A}\mathbf{Q}\mathbf{A}^T)]$. Then the ergodic channel capacity is given by

$$C_e = W_X \max_{\mathrm{tr}(\mathbf{Q}) \le \mathrm{P_X}} \Psi(\mathbf{Q}). \tag{5.265}$$

Similar to the argument as that in [105, 106], we can show (for the details, see [118]) that the optimal $\mathbf{Q}$ should be $\mathbf{Q}_{\mathrm{opt}} = (\mathrm{P_X}/m_X)\mathbf{I}$ even for the distribution of $\mathbf{A}$ defined in (5.262). Thus we have

$$C_e = W_X \mathcal{E}_{\mathbf{A}}\left[\log\det\left(\mathbf{I}_{m_Y} + \frac{\mathrm{P_X}}{m_X\sigma_{\mathbf{N}}^2}\mathbf{A}\mathbf{A}^T\right)\right]. \tag{5.266}$$

To use (5.266) to calculate the channel capacity, we need to know the distribution of the matrix $\mathbf{A}\mathbf{A}^T$. Unfortunately, this distribution is known only when $\mathbf{A}$ possesses some special distribution (typically normal distribution) if both $m_X > 1$ and $m_Y > 1$, see, for example, [119]. Therefore, we will consider some special cases in the following.

(i) *Single-transmit and multiple-receive antennas (SIMO).* In this case, $m_X = 1$ and $m_Y > 1$. By using the property of matrix determinant, we can obtain the analytic expression for the ergodic channel capacity as follows:

$$C_e = \frac{W_X}{\Gamma((\kappa/2)m_Y)} J(m_Y\kappa;\beta). \tag{5.267}$$

(ii) *Multiple-transmit and single-receive antennas (MISO).* In this case, $m_X > 1$ and $m_Y = 1$. The ergodic channel capacity is given by

$$C_e = \frac{W_X}{\Gamma((\kappa/2)m_X)} J(m_X\kappa;m_X\beta). \tag{5.268}$$

Remark 5.8.1. Notice that when $\kappa = 2$, the fading model for each elements of $\mathbf{A}$ reduces to Rayleigh distribution, which corresponds to the classic narrowband wireless communication channel. So we expect that the results obtained for this specific κ also recover the results obtained in [105, 106]. This is indeed the case. Substituting $\kappa = 2$ into (5.267) and (5.268), respectively, readily reveals that (5.267) and (5.268) indeed reduce to [106, equations (9) and (10)].

(iii) *Limiting case: infinitely many transmit and receive antennas.* In this case, we suppose that $m_X \to \infty$, $m_Y \to \infty$, and at the same time $\max\{m_X, m_Y\}/\min\{m_X, m_Y\} \to \xi$, which is a constant. Following the similar development of [106, equation (13)], we can show that

$$\lim_{m_{\min}\to\infty} \frac{C_e}{m_{\min}} = \frac{W_X}{2\pi\sigma_{\mathbf{A}}^2} \int_{\eta_-}^{\eta_+} \log\left(1 + \zeta \frac{\mathrm{P_X}}{\sigma_{\mathbf{N}}^2} v\right) \sqrt{\left(\frac{\eta_+}{v} - 1\right)\left(1 - \frac{\eta_-}{v}\right)}\, dv, \quad (5.269)$$

where $m_{\min} = \min\{m_X, m_Y\}$, $\eta_\pm = \sigma_{\mathbf{A}}^2 \xi_\pm$, $\xi_\pm = (\sqrt{\xi} \pm 1)^2$, and

$$\sigma_{\mathbf{A}}^2 := \mathcal{E}\left(\mathbf{A}_{ij} - \mathcal{E}\left(\mathbf{A}_{ij}\right)\right)^2 = \Omega\left[1 - \frac{2}{\kappa} \frac{\Gamma^2((\kappa+1)/2)}{\Gamma^2(\kappa/2)}\right],$$
$$\zeta = \begin{cases} \xi^{-1} & \text{if } m_X \geq m_Y, \\ 1 & \text{if } m_X < m_Y. \end{cases} \quad (5.270)$$

Specifically, if $m_X = m_Y$, the above formula gives (cf. [105, 106])

$$\lim_{m_X\to\infty} \frac{C_e}{W_X m_X} = \log(\mathrm{SNR}_1) - 1 + \frac{\sqrt{1 + 4\,\mathrm{SNR}_1} - 1}{2\,\mathrm{SNR}_1} + 2\tanh^{-1} \frac{1}{\sqrt{1 + 4\,\mathrm{SNR}_1}}, \quad (5.271)$$

where SNR_1 is defined as $\mathrm{SNR}_1 := \sigma_{\mathbf{A}}^2\, \mathrm{P_X}/\sigma_{\mathbf{N}}^2$.

Equations (5.269) and (5.271) show that when both the numbers of transmit and receive antennas are large and they are in the same order, the *ergodic channel capacity of the MIMO UWB wireless systems is proportional to the numbers of either transmit or receive antennas.*

The detailed derivations for (5.267), (5.268), and (5.269) can be found in [118].

5.8.5. Capacity versus outage probability— frequency-flat channels

The results that we have obtained in the previous subsections apply to the case where the fading matrix is ergodic and there are no constraints on the decoding delay on the receiver. In practical communication systems, we often run into the case where the fading matrix is generated or chosen randomly at the beginning of the transmission, while no significant channel variability occurs during the whole transmission. In this case, the fading matrix is clearly not ergodic. We suppose that the fading matrix still has the distribution defined in the previous subsections. In this case, it is more important to investigate the channel capacity in the sense of outage probability. An outage is defined as the event that the communication channel does not support a target data rate. Thus, according to [120], outage probability, denoted by $P_{\mathrm{out}}(R)$, is defined as follows. With a given rate R, we associate a set Θ_R in the space of fading matrix $\mathbf{A}$. The set is the largest possible set for which C_Θ, the capacity of the compound channel with parameter $\mathbf{A} \in \Theta_R$, satisfies $C_\Theta \geq R$. The outage probability is then defined as $P_{\mathrm{out}}(R) = \Pr\{\mathbf{A} \notin \Theta_R\}$. Thus it

is clear that

$$P_{\text{out}}(R) = \Pr\{\mathbf{A} \notin \Theta_R\} = \Pr\{C|_{\mathbf{A}} < R\} = \Pr\{C|_{\mathbf{A}} \leq R\}, \tag{5.272}$$

that is, the outage probability can be actually viewed as the cumulative distribution function of the conditional Shannon capacity. Notice that the last equality of the above equation follows from the fact that $C(\mathbf{X}; \mathbf{Y} \mid \mathbf{A})$ is a continuous function of continuous random variable $\mathbf{A}$.

Based on the above discussion, we can evaluate the outage probability for frequency-flat UWB channels for the following three cases.

(i) *SISO case.* In this case, we suppose that Assumptions 1, 2, 3, and 4 hold. Let us define $\eta = a^2$. It is easy to obtain the cdf of η as follows:

$$P_\eta(x) = \Pr\{\eta \leq x\} = \int_0^x \left(\frac{\kappa}{2\Omega}\right)^{\kappa/2} \frac{1}{\Gamma(\kappa/2)} x^{\kappa/2-1} \, \mathrm{e}^{-\kappa x/2\Omega} \, dx = \frac{1}{\Gamma(\kappa/2)} \gamma\left(\frac{\kappa}{2}, \frac{\kappa}{2\Omega} x\right), \tag{5.273}$$

where $\gamma(\alpha, z)$ is the incomplete Gamma function, whose definition can be seen in [116]. Therefore, from (5.255), it follows that

$$P_{\text{out}}(R) = \Pr\left\{\eta \leq \frac{\sigma_N^2}{\mathrm{P_X}} (\, \mathrm{e}^{R/W_X} - 1)\right\} = \frac{1}{\Gamma(\kappa/2)} \gamma\left(\frac{\kappa}{2}, \beta(\, \mathrm{e}^{R/W_X} - 1)\right). \tag{5.274}$$

(ii) *SIMO case.* In this case, we suppose that Assumptions 1, 2, 4, 5, and 6 hold. Similarly we can obtain the outage probability as

$$P_{\text{out}}(R) = \frac{1}{\Gamma((\kappa/2)m_Y)} \gamma\left(\frac{\kappa}{2} m_Y, \beta(\, \mathrm{e}^{R/W_X} - 1)\right). \tag{5.275}$$

(iii) *MISO case.* In this case, we suppose that Assumptions 1, 2, 3, 5, 7, and 8 hold. We have

$$P_{\text{out}}(R) = \frac{1}{\Gamma((\kappa/2)m_X)} \gamma\left(\frac{\kappa}{2} m_X, m_X \beta(\, \mathrm{e}^{R/W_X} - 1)\right). \tag{5.276}$$

5.8.6. Numerical results—frequency-flat channels

In this subsection, we will investigate the variation of channel capacity with respect to various kinds of parameters. Suppose $W_X = 1$. So the unit of the channel capacity is nats/s/Hz.

Figure 5.68 depicts the variation of channel capacity C_e with respect to the number κ for SISO case. We can see from this figure that even though the channel capacity increases with κ, the quantities increased is not large compared to the base case ($\kappa = 1$), especially when $\kappa \geq 10$. For example, for the case of SNR = 0 dB, when κ is increased from 1 to 10, C_e increases $(0.6695 - 0.5335)/0.5335 = 25.5\%$, while

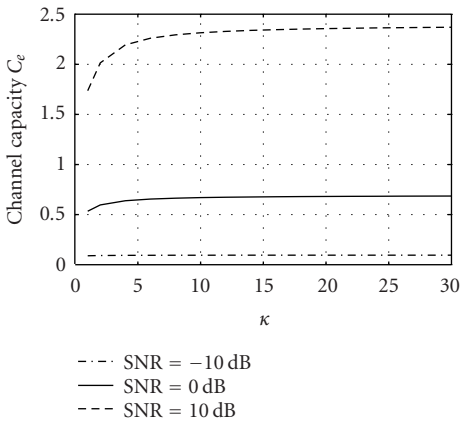

FIGURE 5.68. Variation of ergodic channel capacity C_e (in nats/s/Hz) with κ for SISO case.

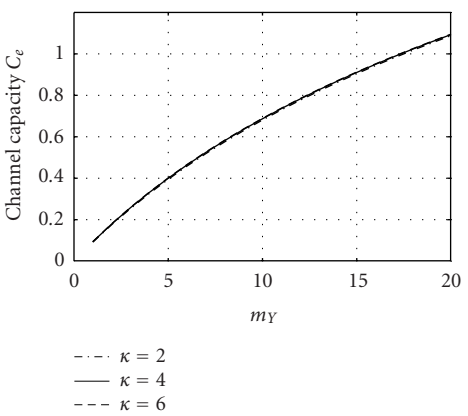

FIGURE 5.69. Variation of ergodic channel capacity C_e (in nats/s/Hz) with the number of receive antennas m_Y for SIMO case (SNR = −10 dB).

when κ is increased from 10 to 30, C_e increases only $(0.6850 - 0.6695)/0.5335 = 2.31\%$.

Figure 5.69 shows the relationship between channel capacity and the number of receive antennas for SIMO case. It can be seen from this figure that the capacity increases with m_Y almost logarithmically. This phenomenon is similar to the corresponding one in the case of narrowband Rayleigh fading channels (cf. [105, 106, Example 3]).

Figure 5.70 shows the relationship between channel capacity and the number of transmit antennas for MISO case. It is interesting to observe from this figure that in the case of large SNR the capacity increases with m_X rapidly when m_X is small ($m_X \leq 6$), however, the increase is very slow when m_X becomes large ($m_X > 6$). This phenomenon is different from the one in the case of narrowband Rayleigh fading channel, see [105, 106, Example 4], where it is found that C_e does

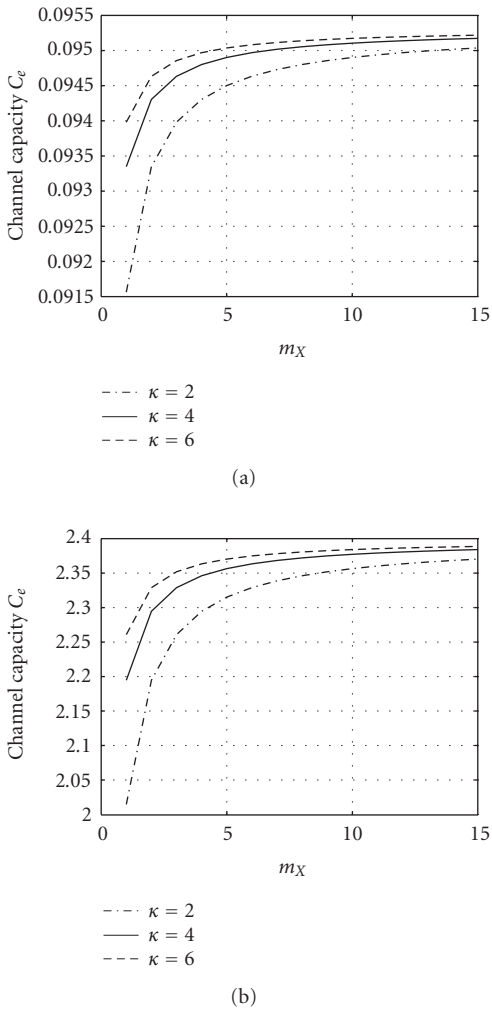

FIGURE 5.70. Variation of ergodic channel capacity C_e (in nats/s/Hz) with the number of transmit antennas m_X for MISO case. (a) SNR $= -10$ dB. (b) SNR $= +10$ dB.

not change with m_X when $m_X \geq 2$. An important phenomenon can also be observed by comparing Figures 5.70(a) and 5.70(b), that is, when the signal-to-noise ratio is low, the benefit obtained by distributing the available power to different transmit antennas is very limited as far as average capacity is concerned.

From Figures 5.69 and 5.70, we can see that increasing the number of receiver antennas can obtain more benefit in channel capacity than increasing the number of transmit antennas. Principally, the channel capacity could be increased indefinitely by employing a large number of receive antennas, but it appears to increase only logarithmically in this number; while employing $3 \sim 5$ transmit antennas

can approach the best advantage of the multiple transmit antenna systems (for the case of single receive antenna and under the assumption of frequency nonselectiveness). The reason for this phenomenon is twofold. First, the power is constrained to be a constant, for different m_X, among all the transmit antennas, while no such constraint is applied to receive antennas. Second, it is assumed that the receiver possesses the full knowledge about the channel state.

5.8.7. SISO case—frequency-selective channels

Now we begin to investigate frequency-selective UWB channels. We first study SISO case. Equation (5.253) is the model we will consider in this subsection. Let $S_X(f)$ stand for the power spectral density (PSD) functions of the process $X(t)$. Again we need some simplifying assumptions, which are as follows.

Assumption 9. The number κ is assumed to be constant and the same for all delay bins.

Assumption 10. The amplitude fading $a_l(t)$, $l = 1, \ldots, L$, are assumed to be independent to each other and has the same distribution, as described by (5.250) and (5.252).

Assumption 11. The noise $N(t)$ is zero-mean white Gaussian with double-sided PSD being N_0.

Assumption 12. The power of the transmitted signal is bounded by $\mathrm{P_X}$, that is,

$$\mathcal{E}\left(X^2(t)\right) = 2\pi \int_{-W_X/2}^{W_X/2} S_X(f)df \leq \mathrm{P_X}\,. \tag{5.277}$$

Based on the assumption made in the end of Section 5.7.2, the dependence of the fading $a_l(t)$ on time can be neglected for our analysis. Hence, we will simply denote $a_l(t)$ as a_l. For notational convenience, we use the variable $\mathbf{F}$ to denote the L-tuple $(a_1, \ldots, a_L)$, that is, $\mathbf{F} = (a_1, \ldots, a_L)$. Define

$$\Phi(t) = \sum_{l=1}^{L} a_l X\left(t - (l-1)\tau\right) \tag{5.278}$$

and denote the PSD of Φ as $S_\Phi(f)$. Now (5.253) can be written as

$$Y(t) = \Phi(t) + N(t). \tag{5.279}$$

To apply the classical Shannon capacity formula to model (5.279), we can divide the whole frequency band $[-W_X/2,\ +W_X/2]$ of $S_\Phi(f)$ to many small bands with bandwidth Δf. From frequency f to $f + \Delta f$, the spectrum of Φ can be considered

as flat with its value being approximated by $S_\Phi(f)$. Therefore, for this subchannel, the mutual information $\Delta\mathcal{I}|_F$, conditioned upon F, is

$$\Delta\mathcal{I}|_F = \Delta f \log\left(1 + \frac{S_\Phi(f)\Delta f}{N_0 \Delta f}\right) = \Delta f \log\left(1 + \frac{S_\Phi(f)}{N_0}\right). \tag{5.280}$$

Thus, taking the limit $\Delta f \to df$ in (5.280), we obtain the conditional mutual information, denoted as $\mathcal{I}|_F$, between X and Y as follows:

$$\mathcal{I}|_F = \int_{-W_X/2}^{W_X/2} \log\left(1 + \frac{S_\Phi(f)}{N_0}\right) df. \tag{5.281}$$

So the conditional channel capacity $C|_F$ is given by the maximization of $\mathcal{I}|_F$ subject to the power constraint (5.277), that is,

$$C|_F = \max_{\int_{-W_X/2}^{W_X/2} S_X(f)df \le \mathrm{P}_X/2\pi} \int_{-W_X/2}^{W_X/2} \log\left(1 + \frac{S_\Phi(f)}{N_0}\right) df. \tag{5.282}$$

Define $H(f) = \sum_{l=1}^{L} a_l \, \mathrm{e}^{-\mathrm{j}2\pi f(l-1)\tau}$. Then we have

$$S_\Phi(f) = S_X(f)\left|H(f)\right|^2. \tag{5.283}$$

From (5.282) and (5.283), it is clear that the capacity is achieved when $X(t)$ is such that, among other conditions, the equality for power constraint holds.

If the information about F, and hence about $H(f)$, is available to the transmitter, the result of [117, Section 8.3] can be used to obtain the optimal $S_X(f)$ to achieve $C|_F$, which is as follows:

$$S_X(f) = \begin{cases} \Theta - \dfrac{N_0}{\left|H(f)\right|^2} & \text{when } f \in F_\Theta, \\ 0 & \text{when } f \notin F_\Theta, \end{cases} \tag{5.284}$$

where F_Θ is the range of f for which $N_0/|H(f)|^2 \le \Theta$ and Θ is a constant which satisfies the following equation:

$$\int_{f \in F_\Theta \cap [-W_X/2,\, +W_X/2]} \left(\Theta - \frac{N_0}{\left|H(f)\right|^2}\right) df = \frac{\mathrm{P}_X}{2\pi}. \tag{5.285}$$

The above solution for the optimal $S_X(f)$ is actually the frequency-domain version of "water-filling" algorithm.

In our case, since the transmitter is unaware of the fading information F, the above algorithm does not apply. Now let us consider the design for optimal $S_X(f)$ which should maximize $\int_{-W_X/2}^{W_X/2} \log(1+S_X(f)|H(f)|^2/N_0)df$. Since no information on $|H(f)|$ is available to the transmitter, it is reasonable to assume, at the transmitter side, that $|H(f)|$ is a constant. Then applying formula (5.284) to the case of the *presumed* $|H(f)|$ and noticing the power constraint yield that the optimal

$S_X(f)$ is uniform:

$$S_X(f) = \begin{cases} \dfrac{\mathrm{P_X}}{2\pi W_X} & \text{when } f \in \left[-\dfrac{W_X}{2}, \dfrac{W_X}{2} \right], \\ 0 & \text{otherwise.} \end{cases} \tag{5.286}$$

Substituting (5.286) into (5.282) gives

$$C|_F = \int_{-W_X/2}^{W_X/2} \log\left(1 + \frac{\mathrm{P_X}\,|H(f)|^2}{2\pi W_X N_0}\right) df. \tag{5.287}$$

Define $\rho = \mathrm{P_X}/2\pi W_X N_0$. Simple manipulation will yield

$$C|_F = \frac{W_X}{\pi} \int_0^{\pi} \log\left(1 + \rho\left[\sum_{l=1}^{L} a_l \cos\left((l-1)u\right)\right]^2 + \rho\left[\sum_{l=1}^{L} a_l \sin\left((l-1)u\right)\right]^2\right) du. \tag{5.288}$$

For the general model of frequency-selective channel (5.278)-(5.279), it seems difficult to obtain the closed-form expression for $C|_F$. In the following, we will consider the case of $L = 2$. When $L > 2$, we can use Monte Carlo method to evaluate $C|_F$.

The case of $L = 2$. To simplify notation, let us define $\bar{C}|_F = C|_F/W_X$. To obtain the analytical expression for the capacity, we need further assume that $r = 1$ here, that is, $\Omega_1 = \Omega_2 := \Omega$. Since only two clusters are involved, the errors in the capacity introduced by this simplification can be neglected for the moment. Applying $L = 2$ to (5.288), we have

$$\bar{C}|_F = \log \frac{1 + \rho(\eta_1 + \eta_2) + \sqrt{\left[1 + \rho(\eta_1 + \eta_2)\right]^2 - 4\rho^2\eta_1\eta_2}}{2}, \tag{5.289}$$

where η_1 and η_2 are defined as $\eta_1 = a_1^2$ and $\eta_2 = a_2^2$, respectively.

By a long and tedious computation, we can show that

$$\begin{aligned} P_{\bar{C}|_F}(x) = {} & \frac{(\kappa-1)!\sqrt{\pi}}{2^{\kappa-1}\Gamma(\kappa/2)\Gamma\left((\kappa+1)/2\right)} \left[1 - \mathrm{e}^{-\kappa\mu_1(x)/2\Omega} \sum_{l=0}^{\kappa-1} \left(\frac{\kappa}{2\Omega}\right)^l \frac{\mu_1^l(x)}{l!}\right] \\ & - \frac{4}{\kappa}\left(\frac{\kappa}{2\Omega}\right)^{\kappa} \frac{1}{\Gamma^2(\kappa/2)} \int_{\mu_0(x)}^{\mu_1(x)} \mathrm{e}^{-\kappa\mu/2\Omega} \frac{\left[\rho^{-1}\,\mathrm{e}^x\mu - \rho^{-2}\,\mathrm{e}^x\left(\mathrm{e}^x - 1\right)\right]^{\kappa/2}}{\mu} \\ & \cdot F\left(\frac{1}{2}, \frac{\kappa}{2}; \frac{\kappa}{2} + 1; \frac{4\left[\rho^{-1}\,\mathrm{e}^x\mu - \rho^{-2}\,\mathrm{e}^x\left(\mathrm{e}^x - 1\right)\right]}{\mu^2}\right) d\mu, \end{aligned} \tag{5.290}$$

where $\mu_0(x) = (e^x - 1)/\rho$, $\mu_1(x) := 2(e^x - e^{x/2})/\rho$, and $F(\alpha_1, \alpha_2; \alpha_3; z)$ denotes the hypergeometric function, whose definition can be found in [116].

The detailed derivation for (5.290) can be found in [118].

Having the expression for $P_{\bar{C}|_{\bar{F}}}(x)$ at hand, the outage probability is simply given by

$$P_{\text{out}}(R) = P_{C|_{\bar{F}}}(R) = P_{\bar{C}|_{\bar{F}}}\left(\frac{R}{W_X}\right), \tag{5.291}$$

where R is the communication rate supportable by the channel with a probability of $1 - P_{\text{out}}(R)$, or in other words, with an outage probability of $P_{\text{out}}(R)$.

5.8.8. MIMO case—frequency-selective channels

In this case, the input-output relation can be generally described by the following equation:

$$\mathbf{Y}(t) = \sum_{l=1}^{L} \mathbf{A}_l \mathbf{X}\big(t - (l-1)\tau\big) + \mathbf{N}(t), \tag{5.292}$$

where $\mathbf{X}(t)$ and $\mathbf{Y}(t)$ are m_X- and m_Y-dimensional vectors, respectively. Let $\mathbf{S}_{\mathbf{X}}(f)$ denote the power spectral density matrix of the process $\mathbf{X}(t)$.

In addition to Assumption 6, we further need the following assumptions.

Assumption 13. The amplitude fading matrices $\mathbf{A}_l, l = 1, \ldots, L$, are assumed to be independent, and all the entries of $\mathbf{A}_l, l = 1, \ldots, L$, are also assumed to be independent. Suppose $\mathbf{A}_l = [a_{l,mn}]_{m_Y \times m_X}$ with $a_{l,mn} = v_{l,mn}\zeta_{l,mn}$, $l = 1, \ldots, L$, $m = 1, \ldots, m_Y$, $n = 1, \ldots, m_X$. Then $v_{l,mn}$ and $\zeta_{l,mn}$ assume distributions as specified by (5.252) and (5.250), respectively, with Ω_l being governed by the model (5.251).

Assumption 14. The power of the transmitted signal is bounded by $\mathrm{P_X}$, that is,

$$\mathcal{E}\left(\mathbf{X}^T(t)\mathbf{X}(t)\right) = 2\pi \int_{-W_{\mathbf{X}}/2}^{W_{\mathbf{X}}/2} \operatorname{tr}\left(\mathbf{S}_{\mathbf{X}}(f)\right) df \le \mathrm{P_X}, \tag{5.293}$$

where $W_{\mathbf{X}}$ is the bandwidth of the transmitted signal $\mathbf{X}$.

Define $\bar{F} = (\mathbf{A}_1, \ldots, \mathbf{A}_L)$. Based on the same idea as that in the derivation of (5.288), we can show that the channel capacity conditioned upon $\bar{F}$, denoted as $C|_{\bar{F}}$, is given by

$$C|_{\bar{F}} = \frac{W_{\mathbf{X}}}{\pi} \int_0^{\pi} \log\det\left\{\mathbf{I}_{m_Y} + \frac{\rho}{m_X}\left[\sum_{l=1}^{L} \mathbf{A}_l\, e^{-j(l-1)u}\right]\left[\sum_{l=1}^{L} \mathbf{A}_l^T\, e^{j(l-1)u}\right]\right\} du. \tag{5.294}$$

The details for the derivation of (5.294) are given in [118].

Since it is extremely difficult, if possible, to obtain the closed-form expression for the integral in (5.294), we use Monte Carlo method instead to evaluate the distribution of $C|_{\bar{f}}$, denoted as $P_{C|_{\bar{f}}}(x)$. In the simulation, it is preferable to first find the distribution of $\bar{C}|_{\bar{f}} := C|_{\bar{f}}/W_{\mathbf{X}}$.

Having $P_{\bar{C}|_{\bar{f}}}(x)$, the outage probability of the channel capacity can be obtained through the equation

$$P_{\text{out}}(R) = P_{C|_{\bar{f}}}(R) = P_{\bar{C}|_{\bar{f}}}\left(\frac{R}{W_{\mathbf{X}}}\right). \tag{5.295}$$

5.8.9. Numerical results—frequency-selective channels

In this subsection, we will investigate the capacity results for different system configurations, which depend on several factors such as the number of transmit and receive antennas (m_X and m_Y, respectively), frequency-selectivity (characterized by L), and the ratio between signal power and noise power (ρ), and so forth.

In all the simulations except for the case stated otherwise, it is assumed that $\kappa = 4$, $\Omega_1 = 1$, and $r = 0.95$. In Monte Carlo method, we first generate 20 000 random channel realizations, then use formula (5.294) to calculate the channel capacity for a given realization of the channel, and finally find the cdf of the channel capacity. As aforementioned, the parameter κ is chosen to be a constant in this section. Of course, the case for the dependence of κ on l can be also included in the simulation if its exact model is given.

All results, except those for the case of SISO and $L = 2$, will be obtained based on Monte Carlo simulations, while for the case of SISO and $L = 2$, we calculate the capacity via two approaches, one is analytic method where parameter r is approximated by 1, and another is Monte Carlo method where r equals 0.95.

We first compare the results obtained by Monte Carlo method to those obtained through analytic method for the case of SISO and $L = 2$. The result is plotted in Figure 5.71, which shows that the difference between these two methods is negligible.

Figure 5.72 shows the effect of frequency-selectivity on the channel capacity, where the case of $m_X = m_Y = 1$ is investigated. The curve labelled with $L = 1$ corresponds to the case of frequency-flat channel. It can be observed from this figure that the channel capacity for a given outage probability increases with L and the fluctuation (or variance) of the channel capacity decreases with L. Comparing Figures 5.72(a) and 5.72(b), we can see that this phenomenon is displayed more clearly in the scenario of high signal-to-noise ratio. The reason that the channel capacity increases with L is very simple: the power of the received signal is increased with the increase of L, while the reason that the fluctuation of the channel capacity decreases with L could be understood in such a way: due to more and more echoes received, the channel behaves more and more deterministically.

In Figure 5.72, we have used uniform power spectrum distribution (PSD) for the transmitted signal since it is assumed that the transmitter is not aware of the information about channel parameters. On the other hand, if the transmitter has

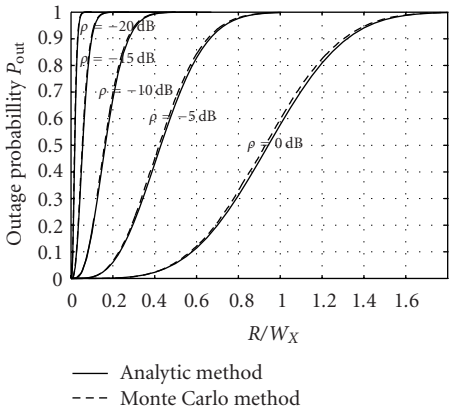

(a)

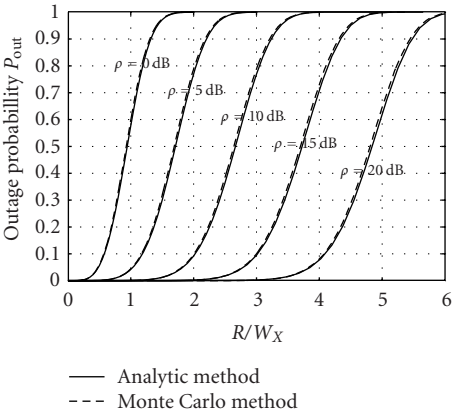

(b)

FIGURE 5.71. Outage probability P_{out} versus transmission rate R/W_X (in nats/s/Hz) for different ρ. Comparison between analytic method and Monte Carlo method ($L = 2$, $m_X = m_Y = 1$). (a) For the case of low SNR. (b) For the case of high SNR.

the knowledge about channel parameters, optimal PSD can be employed. It is interesting to compare the capacity for the two cases: uniform and optimal PSD schemes. The result is plotted in Figure 5.73. From this figure we can see that when the signal-to-noise ratio is low, optimal PSD scheme can increase the channel capacity considerably compared to uniform PSD scheme, while when the ratio is high, the benefit of optimal PSD scheme can be hardly seen compared to uniform one. This phenomenon is demonstrated more clearly in Figure 5.74, where the ergodic capacity is used for illustration. Let C_{uni} and C_{opt} denote the ergodic capacity of the system for uniform and optimal PSD schemes respectively. We use $C_{\text{uni}}/C_{\text{opt}}$ as an index for the efficiency of uniform PSD scheme relative to optimal one. We can see from this figure that the efficiency of uniform PSD scheme is

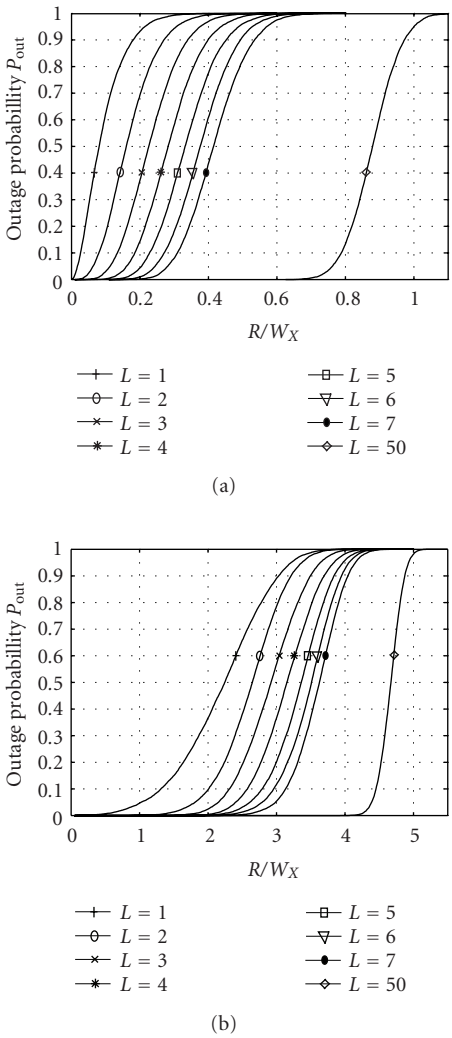

FIGURE 5.72. Outage probability P_{out} versus transmission rate R/W_X (in nats/s/Hz) for different L. Effect of frequency-selectivity on the channel capacity ($m_X = m_Y = 1$). (a) $\rho = -10$ dB. (b) $\rho = +10$ dB.

lower than 0.61 when the signal-to-noise ratio is low ($\rho \leq -20$ dB). This says that the transmission rate can be increased roughly more than 1.6 times if the optimal PSD scheme instead of the uniform one is adopted for the aforementioned case. But when $\rho \geq +10$ dB, $C_{\text{uni}}/C_{\text{opt}}$ almost approaches one.

From the results shown in Figures 5.73 and 5.74, we can say that one should consider measures, such as frequency domain water-filling algorithm, to take full advantage of frequency-selectivity if the signal-to-noise ratio of the UWB systems is low.

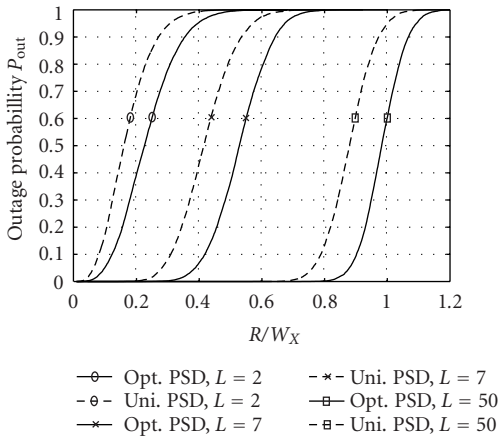

(a)

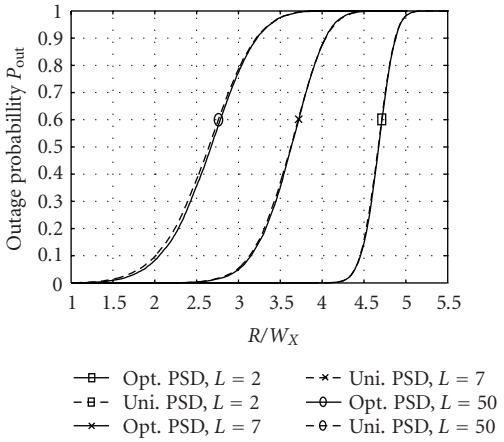

(b)

FIGURE 5.73. Outage probability P_{out} versus transmission rate R/W_X (in nats/s/Hz) for different L. Comparison between optimal PSD and uniform PSD ($m_X = m_Y = 1$). (a) $\rho = -10$ dB. (b) $\rho = +10$ dB.

To investigate the effect of the two numbers m_X and m_Y on the capacity, we study three cases: case (i)—$m_Y = 1$, but m_X is a variable larger than one (MISO); case (ii)—$m_X = 1$, but m_Y is a variable larger than one (SIMO); and case (iii)—both m_X and m_Y are variables larger than one, but we fix $m_X = m_Y$.

The results for MISO case are depicted in Figure 5.75. From this figure, it can be seen that for a given ρ, the outage probability decreases with the increase of the number of transmit antennas when R/W_X is lower than some value, but increases instead when R/W_X is higher than this value. Notice that the corresponding outage probability is so high when R/W_X is larger than this value that to transfer information at this rate is of little practical interest.

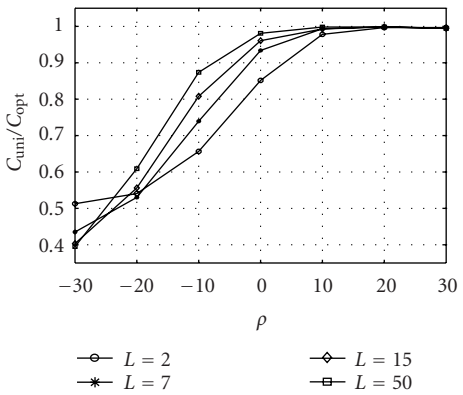

FIGURE 5.74. Efficiency of uniform PSD relative to optimal PSD ($m_X = m_Y = 1$).

The results for SIMO case are demonstrated in Figure 5.76, which shows that, for a given outage probability P_{out}, the transmission rate R increases with $\log m_Y$ almost linearly.

Figure 5.77 shows the results for MIMO case, from which we can observe that, for a given outage probability P_{out}, the transmission rate R increases with m_X (or m_Y) almost linearly.

5.8.10. LOS effect on UWB channel capacity

In a recent paper [121], Gesbert investigated the problem that whether or not multipaths for MIMO wireless communication systems are beneficial as channel capacity and coverage are concerned. This concern is motivated by the observation: for a MIMO systems, multipaths can increase the diversity but degrade SNR, while the line-of-sight (LOS) transmission, corresponding to an extreme case for a lower multipaths, can strengthen SNR but provide no diversity. Therefore, it seems that a compromising region for the benefit of multipaths should exist. This is indeed the case for narrowband communications, as shown in [121]. In this subsection, we aim to investigate if it is also true for UWB communications.

We will consider model (5.292) for two extreme cases: LOS and non-LOS (NLOS) case. For NLOS case, we will assume that all $\mathbf{A}_l$ $(l = 1, 2, \ldots, L)$ are of the distribution as specified in Assumption 14. For LOS case, we will assume that all $\mathbf{A}_l$ $(l = 2, \ldots, L)$ are of the distribution as specified in Assumption 14, but $\mathbf{A}_1$ is of the following form $\mathbf{A}_1 = \mathbf{v}_r \mathbf{v}_t^T$, where $\mathbf{v}_r$ and $\mathbf{v}_t$ are m_X- and m_Y-dimensional vectors, respectively, each entry is $+1$ or -1 with equal probability, and all the elements in $\mathbf{v}_r$ and $\mathbf{v}_t$ are independent. The above model for $\mathbf{A}_1$ is borrowed from narrowband LOS channel model, see [121]. Note that the value of each entry in the above chosen $\mathbf{A}_1$ will satisfy $\mathcal{E}([\mathbf{A}_1]_{ij}^2) = 1$ for all i and j, which makes the comparison between LOS and NLOS be justfiable.

The numerical results are depicted in Figures 5.78, 5.79, 5.80, 5.81, 5.82, and 5.83. It can be seen from Figures 5.78, 5.79, and 5.80 that for a moderate L ($L = 15$),

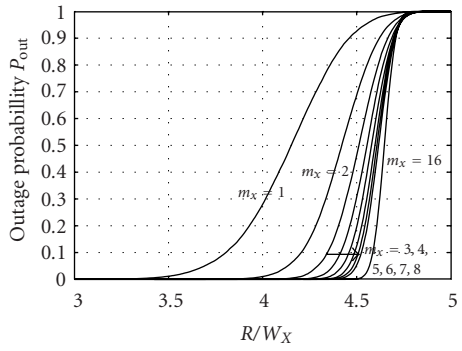

(a)

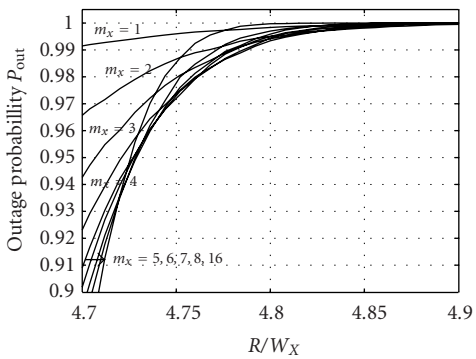

(b)

FIGURE 5.75. Outage probability P_{out} versus transmission rate R/W_X (in nats/s/Hz) for different m_X. Effect of the number of transmit antennas on the channel capacity ($\rho = +10$ dB, $L = 15$, $m_Y = 1$, MISO). (a) Panorama. (b) Detail.

the difference in capacity between LOS and NLOS cases can be perceived only when both the numbers of the transmit and receive antennas are high. From Figures 5.81, 5.82, and 5.83, it can be observed that when L is small, NLOS scenario is always favorable for MIMO, but LOS scenario is favorable for SIMO and MISO when communication rate is low. When the communication rate is high, NLOS scenario is favorable for SIMO and MISO, but notice that the outage probability for communication in this region of the rate is so high that communication at this rate is almost discarded.

5.8.11. Summary

In this section, we have investigated the channel capacity for UWB wireless systems. The results can be roughly summarized for two cases: frequency-flat channels and frequency-selective channels.

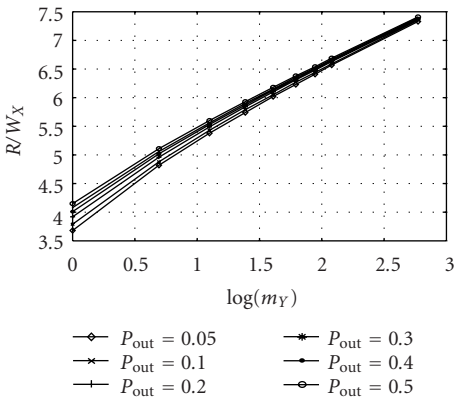

FIGURE 5.76. The transmission rate R/W_X (in nats/s/Hz) versus m_Y for different outage probability P_{out} ($\rho = +10\,\text{dB}$, $L = 15$, $m_X = 1$, SIMO).

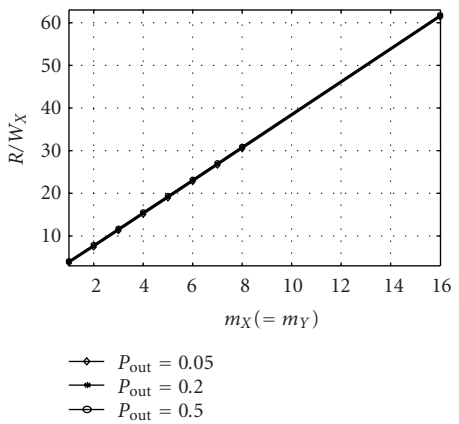

FIGURE 5.77. The transmission rate R/W_X (in nats/s/Hz) versus m_X (or m_Y) for different outage probability P_{out} ($\rho = +10\,\text{dB}$, $L = 15$, $m_X = m_Y$).

For frequency-flat UWB channels, the analytic expression for the ergodic channel capacity of UWB wireless communication systems is presented for four special cases: SISO, SIMO, MISO, and MIMO (in the situation of infinitely many transmit and receive antennas). Formulae on the outage probability about the channel capacity are also presented for cases SISO, SIMO, and MISO. It is shown that increasing the number of receive antennas can obtain more benefit in channel capacity than increasing the number of transmit antennas. Principally, the channel capacity could be increased indefinitely by employing a large number of receive antennas, but it appears to increase only logarithmically in this number for SIMO case; while employing $3 \sim 5$ transmit antennas can approach the best advantage

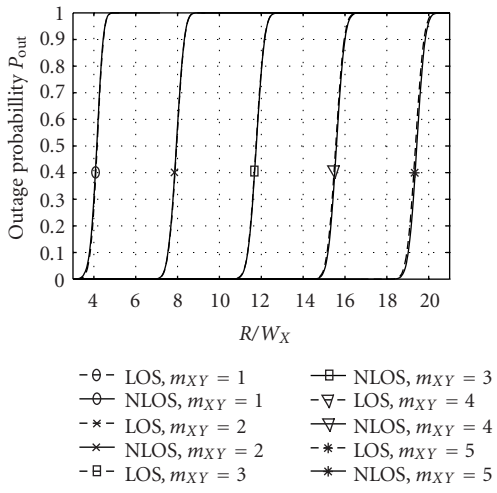

(a)

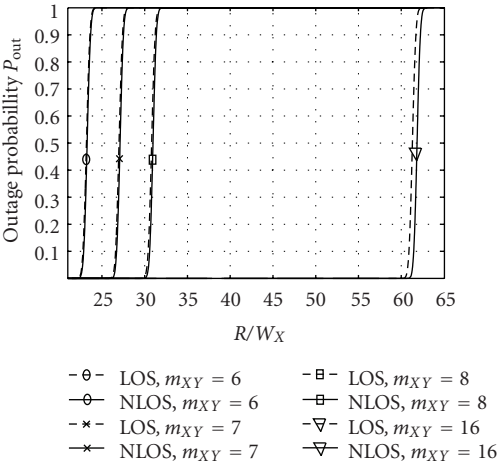

(b)

FIGURE 5.78. Outage probability P_{out} versus transmission rate R/W_X (in nats/s/Hz) for different number of antennas. Comparison between LOS and NLOS (MIMO, $\rho = +10$ dB, $L = 15$).

of the multiple transmit antenna systems (irrespective of all other parameters considered herein) as far as channel capacity is concerned for MISO case. We have also observed that when the signal-to-noise ratio is low, the benefit in average capacity obtained by distributing the available power to different transmit antennas is very limited.

For frequency-selective UWB channels, an analytic expression for the capacity of UWB wireless communication systems for SISO case and when STDL consists

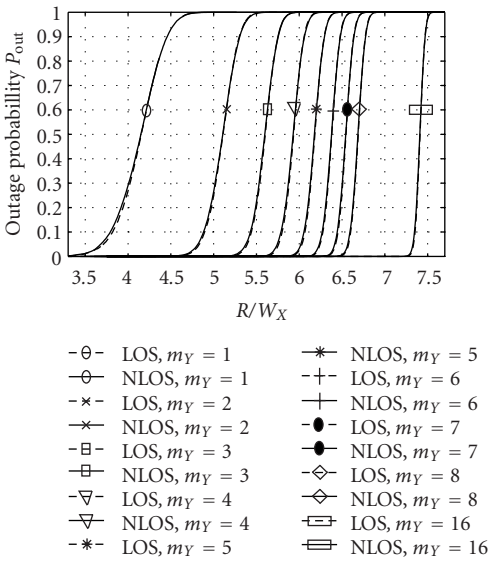

FIGURE 5.79. Outage probability P_{out} versus transmission rate R/W_X (in nats/s/Hz) for different number of antennas. Comparison between LOS and NLOS (SIMO, $\rho = +10$ dB, $L = 15$).

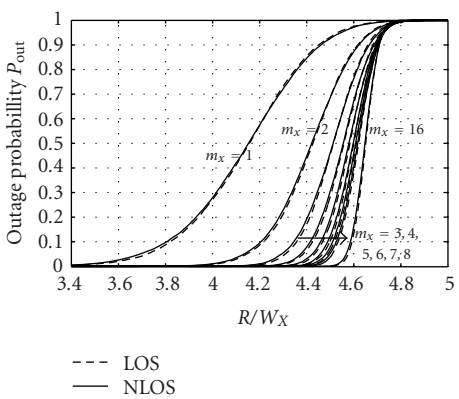

FIGURE 5.80. Outage probability P_{out} versus transmission rate R/W_X (in nats/s/Hz) for different number of antennas. Comparison between LOS and NLOS (MISO, $\rho = +10$ dB, $L = 15$).

of only two taps and the fading power ratio is approximated by one has been obtained, while the closed form for the channel capacity for other cases seems to be extremely difficult to obtain. Therefore, Monte Carlo simulation method is resorted to obtain the capacity for these cases. The numerical results show that the difference between the results obtained by the analytic method and the Monte Carlo method for the case of SISO and $L = 2$ is negligible. The following observations can be drawn from our results.

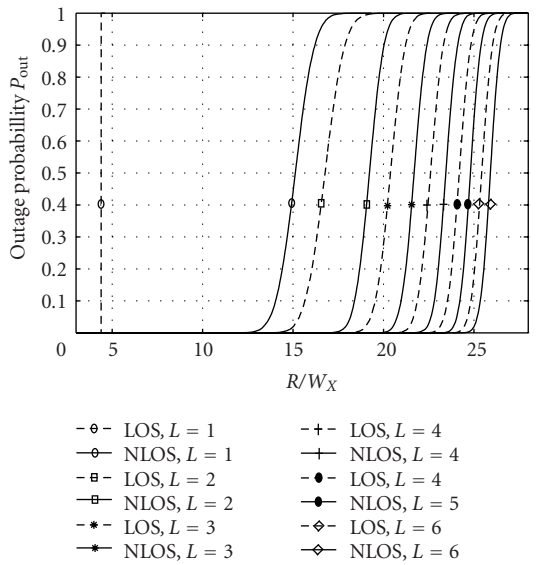

(a)

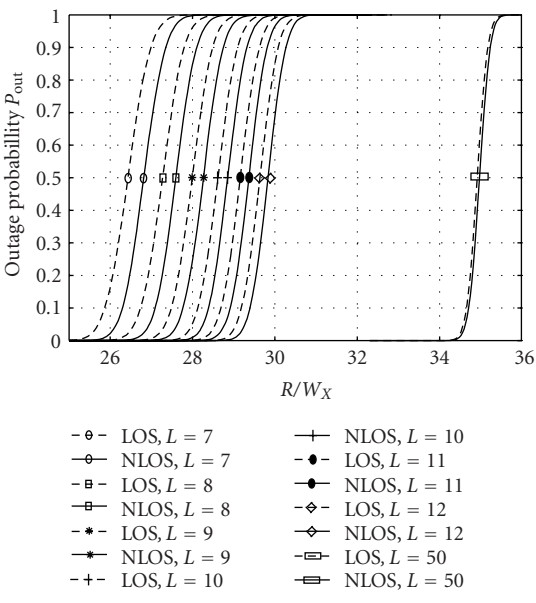

(b)

FIGURE 5.81. Outage probability P_{out} versus transmission rate R/W_X (in nats/s/Hz) for different L. Comparison between LOS and NLOS (MIMO, $\rho = +10$ dB, $m_X = m_Y = 8$).

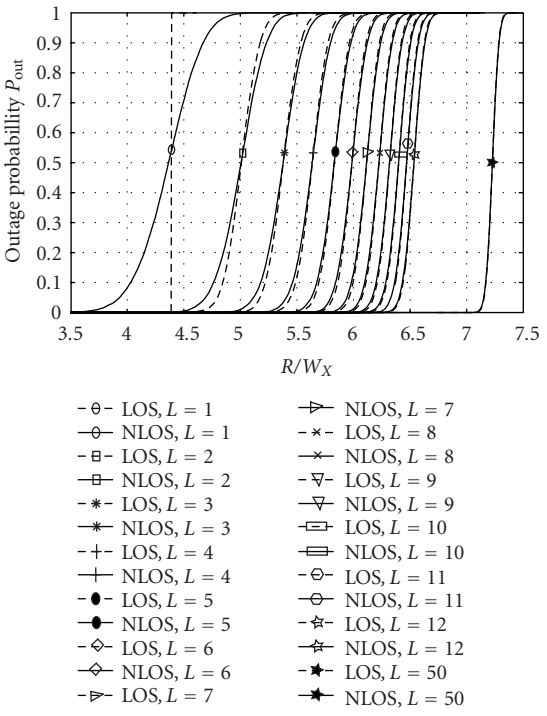

FIGURE 5.82. Outage probability P_{out} versus transmission rate R/W_X (in nats/s/Hz) for different L. Comparison between LOS and NLOS (SIMO, $\rho = +10$ dB, $m_Y = 8$).

(i) When the signal-to-noise ratio is low, the outage probability decreases remarkably with L.

(ii) When the signal-to-noise ratio is lower than some value, say -20 dB, using optimal power spectrum distribution at the transmitter side can increase the reliable transmission rate considerably, compared to the uniform power spectrum distribution scheme, while when the signal-to-noise ratio is higher than some value, say 10 dB, the benefit of optimal power spectrum distribution is very limited. Therefore, one should consider measures, such as frequency-domain waterfilling algorithm, to take full advantage of frequency selectivity if the signal-to-noise ratio of the UWB systems is low.

(iii) In MISO case, the outage probability decreases with the increase of the number of transmit antennas when the communication rate is lower than some value, but increases when the rate is higher than this value (but communication at a rate higher than this value is often inadmissible due to too high outage probability). Therefore, if the required transmission rate is indeed too high and the available power is limited, it is better to concentrate all power in one antenna, rather than to distribute the power in multiple antennas, to transmit information signals.

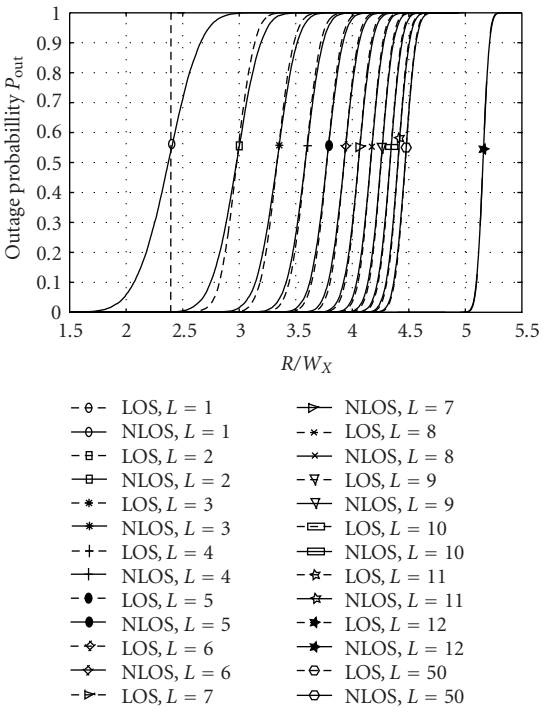

FIGURE 5.83. Outage probability P_{out} versus transmission rate R/W_X (in nats/s/Hz) for different L. Comparison between LOS and NLOS (MISO, $\rho = +10$ dB, $m_X = 8$).

(iv) In SIMO case, the communication rate supportable by the channel with a given outage probability increases approximately *logarithmically* with the number of receive antennas.

(v) In MIMO case with equal number of transmit and receive antennas, the communication rate supportable by the channel with a given outage probability increases approximately *linearly* with the number of transmit or receive antennas.

(vi) The effect of LOS transmission on UWB systems are also investigated. It is shown that

(1) for a moderate number of received pulses, the difference in capacity between LOS and NLOS cases can be perceived only when both the numbers of the transmit and receive antennas are high;
(2) when L is small, NLOS scenario is always favorable for MIMO, but LOS scenario is favorable for SIMO and MISO when the communication rate is low.

Acknowledgments

The author thanks S. Bories and X. Niffle for carrying out the channel measurements at ENSTA, and A. Durantini and D. Cassioli for providing channel measurements carried out by RadioLabs and authorising their publication in this book.

This work has been partly funded by the European Commission within IST project "ULTRAWAVES" (FP5).

Bibliography

[1] J. Kunisch and J. Pamp, "Measurement results and modeling aspects for the UWB radio channel," in *Proceedings of IEEE Conference on Ultra Wideband Systems and Technologies (UWBST '02)*, pp. 19–23, Baltimore, Md, USA, May 2002.

[2] Federal Communications Commission (FCC), First Report and Order 02-48, February 2002.

[3] A. Saleh and R. Valenzuela, "A statistical model for indoor multipath propagation," *IEEE Journal on Selected Areas in Communications*, vol. 5, no. 2, pp. 128–137, 1987.

[4] J. Kunisch and J. Pamp, "UWB radio channel modeling considerations," in *Proceedings of International Conference on Electromagnetics in Advanced Applications (ICEAA '03)*, Torino, Italy, September 2003.

[5] J. Romme and B. Kull, "On the relation between bandwidth and robustness of indoor UWB communication," in *Proceedings of IEEE Conference on Ultra Wideband Systems and Technologies (UWBST '03)*, pp. 255–259, Reston, Va, USA, November 2003.

[6] Federal Communications Commission (FCC), "First report and order revision of part 15 of the commission's rules regarding ultra-wideband transmission systems," Washington, DC, USA, ET Docket 98-153, 2002.

[7] C. A. Balanis, *Antenna Theory: Analysis and Design*, John Wiley & Sons, New York, NY, USA, 1997.

[8] C. E. Baum, "General Properties of Antennas," *Sensor and Simulation Notes*, Note 330, Air Force Research Laboratory, Directed Energy Directorate, Kirtland, New Mexico, 1991.

[9] J. D. Kraus, *Antennas*, Electrical Engineering Series, McGraw-Hill, New York, NY, USA, 2nd edition, 1988.

[10] W. Wiesbeck and E. Heidrich, "Wide-band multiport antenna characterization by polarimetric RCS measurements," *IEEE Transactions on Antennas and Propagation*, vol. 46, no. 3, pp. 341–350, 1998.

[11] C. Waldschmidt, W. Sörgel, and W. Wiesbeck, "Technology: Antenna Design," to appear in JASP Book on Smart Antennas.

[12] W. Sörgel and W. Wiesbeck, "Influence of the antennas on the ultra-wideband transmission," *EURASIP Journal on Applied Signal Processing*, vol. 2005, no. 3, pp. 296–305, 2005.

[13] W. Sörgel, F. Pivit, and W. Wiesbeck, "Comparison of time domain and frequency domain measurement procedures for ultra wideband antennas domain measurement procedures for ultra wideband antennas," in *Proceedings of 25th Annual Meeting & Symposium on Antenna Measurement Techniques Association (AMTA '03)*, Irvine, Calif, USA, October 2003.

[14] L. Bowen, E. Farr, and W. Prather, "A collapsible impulse radiating antenna," in *Proceedings of Ultra-Wideband, Short-Pulse Electromagnetics Conference*, Edinburgh, Scotland, UK, June 2000.

[15] W. Sörgel, C. Waldschmidt, and W. Wiesbeck, "Transient responses of a Vivaldi antenna and a logarithmic periodic dipole array for ultra wideband communication," in *Proceedings of IEEE Antennas and Propagation Society International Symposium*, vol. 3, pp. 592–595, Columbus, Ohio, USA, June 2003.

[16] R. S. Carson, *Radio Communications Concepts: Analog*, John Wiley & Sons, New York, NY, USA, 1990.

[17] S. G. Glisic, *Advanced Wireless Communications: 4G Technologies*, John Wiley & Sons, New York, NY, USA, 2004.

[18] M. Z. Win and R. A. Scholtz, "Impulse radio: how it works," *IEEE Communications Letters*, vol. 2, no. 2, pp. 36–38, 1998.

[19] *The UWB Multiband Coalition*, available at: http://www.multibandofdm.org/.

[20] G. R. Aiello and G. D. Rogerson, "Ultra-wideband wireless systems," *IEEE Microwave*, vol. 4, no. 2, pp. 36–47, 2003.

[21] S. Roy, J. R. Foerster, V. S. Somayazulu, and D. G. Leeper, "Ultrawideband radio design: the promise of high-speed, short-range wireless connectivity," *Proceedings of IEEE*, vol. 92, no. 2, pp. 295–311, 2004.

[22] A. Sibille and S. Bories, "Spatial diversity for UWB communications," in *Proceedings of 5th European Personal Mobile Communications Conference (EPMCC '03)*, pp. 367–370, Glasgow, Scotland, UK, April 2003.

[23] IEEE, "IEEE standard for information technology—telecommunications and information exchange between systems—local and metropolitan area networks—specific requirements part 15.3: wireless Medium Access Control (MAC) and Physical Layer (PHY) specifications for high rate Wireless Personal Area Networks (WPANs)," IEEE 802.15.3-2003, 2003, pp. 1–315.

[24] S. N. Makarov, *Antenna and EM Modeling with MATLAB*, John Wiley & Sons, New York, NY, USA, 2002.

[25] D. Cassioli, M. Z. Win, and A. F. Molisch, "The ultra-wide bandwidth indoor channel: from statistical model to simulations," *IEEE Journal on Selected Areas in Communications*, vol. 20, no. 6, pp. 1247–1257, 2002.

[26] A. F. Molisch, J. R. Foerster, and M. Pendergrass, "Channel models for ultrawideband personal area networks," *IEEE Wireless Communications*, vol. 10, no. 6, pp. 14–21, 2003.

[27] V. Hovinen, M. Hamalainen, and T. Patsi, "Ultra wideband indoor radio channel models: preliminary results," in *Proceedings of IEEE Conference on Ultra-Wideband Systems and Technologies (UWBST '02)*, pp. 75–79, Baltimore, Md, USA, May 2002.

[28] B. Vucetic and J. Yuan, *Space-Time Coding*, John Wiley & Sons, New York, NY, USA, 2003.

[29] A. Hottinen, O. Tirkkonen, and R. Wichman, *Multi-antenna Transceiver Techniques for 3G and Beyond*, John Wiley & Sons, New York, NY, USA, 2003.

[30] W. C.-Y. Lee and Y. S. Yeh, "Polarization diversity system for mobile radio," *IEEE Transactions on Communications*, vol. 20, no. 5, pp. 912–923, 1972.

[31] R. G. Vaughan, "Polarization diversity in mobile communications," *IEEE Transransactions on Vehicular Technology*, vol. 39, no. 3, pp. 177–186, 1990.

[32] B. Lindmark and M. Nilsson, "On the available diversity gain from different dual-polarized antennas," *IEEE Journal on Selected Areas in Communications*, vol. 19, no. 2, pp. 287–294, 2001.

[33] C. Degen and W. Keusgen, "Performance evaluation of MIMO systems using dual-polarized antennas," in *Proceedings of 10th International Conference on Telecommunications (ICT '03)*, vol. 2, pp. 1520–1525, Papeete, Tahiti, French Polynesia, February–March 2003.

[34] S. M. Alamouti, "A simple transmit diversity technique for wireless communications," *IEEE Journal on Selected Areas in Communications*, vol. 16, no. 8, pp. 1451–1458, 1998.

[35] R. van Nee and R. Prasad, *OFDM for Wireless Multimedia Communications*, Artech House, Norwood, Mass, USA, 2000.

[36] S. Hara and R. Prasad, *Multicarrier Techniques for 4G Mobile Communications*, Artech House, Norwood, Mass, USA, 2003.

[37] A. Saleh and R. Valenzuela, "A statistical model for indoor multipath propagation," *IEEE Journal on Selected Areas in Communications*, vol. 5, no. 2, pp. 128–137, 1987.

[38] *IEEE 802.15 WPAN High Rate Alternative PHY Task Group 3a (TG3a)*, August 2005, available at: http://www.ieee802.org/15/pub/TG3a.html.

[39] *Automatic selection of receiving channels*, US patent no. 1747218, February 1930.

[40] W. C. Jakes, *Microwave Mobile Communications*, John Wiley & Sons, New York, NY, USA, 1974.

[41] M. Weisenhorn and W. Hirt, "Performance of binary antipodal signaling over indoor UWB MIMO channel," in *Proceedings of IEEE International Conference on Communications (ICC '03)*, vol. 4, pp. 2872–2878, Anchorage, Alaska, USA, May 2003.

[42] C. Roblin, S. Bories, and A. Sibille, "Characterization tools of antennas in the time domain," in *Proceedings of International Workshop on Ultra Wideband Systems (IWUWBS '03)*, Oulu, Finland, June 2003.

[43] D. Cassioli, M. Z. Win, and A. F. Molisch, "The ultra-wide bandwidth indoor channel: from statistical model to simulations," *IEEE Journal on Selected Areas in Communications*, vol. 20, no. 6, pp. 1247–1257, 2002.

[44] K. Kunisch and J. Pamp, "Measurement results and modeling aspects for the UWB radio channel," in *Proceedings of COST 273 5th Management Committee Meeting (MCM '02)*, Lisbon, Portugal, September 2002, Document TD(02)105.

[45] V. Hovinen, M. Hamalainen, and T. Patsi, "Ultra wideband indoor radio channel models: preliminary results," in *Proceedings of IEEE Conference on Ultra Wideband Systems and Technologies (UWBST '02)*, pp. 75–79, Baltimore, Md, USA, May 2002.

[46] D. Cassioli and A. Durantini, "A time-domain propagation model of the UWB indoor channel in the FCC-compliant band 3.6-6 GHz based on PN-sequence channel measurements," in *Proceedings of IEEE 59th Vehicular Technology Conference (VTC '04)*, vol. 1, pp. 213–217, Milan, Italy, May 2004.

[47] R. J.-M. Cramer, R. A. Scholtz, and M. Z. Win, "Evaluation of an ultra-wide-band propagation channel," *IEEE Transactions on Antennas and Propagation*, vol. 50, no. 5, pp. 561–570, 2002.

[48] K. Haneda and J.-I. Takada, "An application of SAGE algorithm for UWB propagation channel estimation," in *Proceedings of COST 273 8th Management Committee Meeting (MCM '03)*, Prague, Czech Republic, September 2003, Document TD(03)182.

[49] C. Prettie, D. Cheung, L. Rusch, and M. Ho, "Spatial correlation of UWB signals in a home environment," in *Proceedings of IEEE Conference on Ultra Wideband Systems and Technologies (UWBST '02)*, pp. 65–69, Baltimore, Md, USA, May 2002.

[50] A. Durantini, W. Ciccognani, and D. Cassioli, "UWB propagation measurements by PN-sequence channel sounding," in *Proceedings of IEEE International Conference on Communications (ICC '04)*, vol. 6, pp. 3414–3418, Paris, France, June 2004.

[51] S. Bories, C. Roblin, and A. Sibille, "Ultra-wideband monocone antenna for UWB channel measurements," in *Proceedings of International Workshop on Ultra Wideband Systems (IWUWBS '03)*, Oulu, Finland, June 2003.

[52] L. Yang and G. B. Giannakis, "Space-time coding for impulse radio," in *Proceedings of IEEE Conference on Ultra Wideband Systems and Technologies (UWBST '02)*, pp. 235–239, Baltimore, Md, USA, May 2002.

[53] A. Sibille, "Time-domain diversity in ultra-wideband MIMO communications," in *Proceedings of COST 273 5th Management Committee Meeting (MCM '02)*, Lisbon, Portugal, September 2002, Document TD(02)105.

[54] E. Zollinger, "Extremely wideband antennas," in *Digital Mobile Radio Towards Future Generation Systems*, DG XIII, Ed., chapter 3, pp. 80–82, European Commission EUR 18957, Brussels, Belgium, 1999, COST 231 final report.

[55] V. Murino, A. Trucco, and A. Tesei, "Beam pattern formulation and analysis for wide-band beamforming systems using sparse arrays," *Signal Processing*, vol. 56, no. 2, pp. 177–183, 1997.

[56] M. G. M. Hussain, "Principles of space-time array processing for ultrawide-band impulse radar and radio communications," *IEEE Transransactions on Vehicular Technology*, vol. 51, no. 3, pp. 393–403, 2002.

[57] F. J. Harris, "On the use of windows for harmonic analysis with the discrete Fourier transform," *Proceedings of IEEE*, vol. 66, no. 1, pp. 51–83, 1978.

[58] B. Steinberg, *Principles of Aperture and Array System Design*, John Wiley & Sons, New York, NY, USA, 1976.

[59] A. Papoulis, *Signal Analysis*, McGraw-Hill, New York, NY, USA, 1985.

[60] S. Ries and T. Kaiser, "On the Influence of Prefiltering on the Sidelobe Level for Broadband Impulse Beamforming," 2004, submitted for publication.

[61] E. J. Bond, X. Li, S. C. Hagness, and B. D. Van Veen, "Microwave imaging via space-time beamforming for early detection of breast cancer," *IEEE Antennas and Propagation Magazine*, vol. 51, no. 8, pp. 1690–1705, 2003.

[62] M. Ghavami and R. Kohno, "Recursive fan filters for a broad-band partially adaptive antenna," *IEEE Transactions on Communications*, vol. 48, no. 2, pp. 185–188, 2000.

[63] M. Ghavami and R. Kohno, "Improvement in the DOA estimation of broadband signals using partially IIR beamformers," *IEEE Transactions on Communications*, vol. 50, no. 6, pp. 897–901, 2002.

[64] R. G. Pridham and R. A. Mucci, "Digital interpolation beamforming for low-pass and bandpass signals," *Proceedings of IEEE*, vol. 67, no. 6, pp. 904–919, 1979.

[65] D. Rathjen, G. Bödecker, and M. Siegel, "Omnidirectional beamforming for linear antennas by means of interpolated signals," *IEEE Journal of Oceanic Engineering*, vol. 10, no. 3, pp. 260–268, 1985.

[66] T. Blu, P. Thevenaz, and M. Unser, "MOMS: maximal-order interpolation of minimal support," *IEEE Transactions on Image Processing*, vol. 10, no. 7, pp. 1069–1080, 2001.

[67] S. Ries, "On the reconstruction of signals by a finite number of samples," *Signal Processing*, vol. 23, no. 1, pp. 45–68, 1991.

[68] J. R. Higgins, *Sampling Theory in Fourier Analysis and Signal Analysis: Foundations Vol. 1*, Clarendon Press, Oxford, UK, 1996.

[69] T. Blu, P. Thevenaz, and M. Unser, "Linear interpolation revitalized," *IEEE Transactions on Image Processing*, vol. 13, no. 5, pp. 710–719, 2004.

[70] C. Buchholz and T. Kaiser, "Is DoA estimation feasible for dense multipath UWB indoor channels?" in *Proceedings of 16th International Conference on Wireless Communications*, pp. 420–425, Calgary, Alberta, Canada, July 2004.

[71] A. F. Molisch, J. R. Foerster, and M. Pendergrass, "Channel models for ultrawideband personal area networks," *IEEE Wireless Communications*, vol. 10, no. 6, pp. 14–21, 2003.

[72] A. I. Zayed, *Advances in Shannon's Sampling Theory*, CRC Press, Boca Raton, Fla, USA, 1993.

[73] P. L. Butzer and R. J. Nessel, *Fourier Analysis and Approximation Vol. 1*, Birkhäuser, Basel, Switzerland, 1971.

[74] J.-C. Guey, M. P. Fitz, M. R. Bell, and W.-Y. Kuo, "Signal design for transmitter diversity wireless communication systems over Rayleigh fading channels," *IEEE Transactions on Communications*, vol. 47, no. 4, pp. 527–537, 1999.

[75] V. Tarokh, N. Seshadri, and A. R. Calderbank, "Space-time codes for high data rate wireless communication: performance criterion and code construction," *IEEE Transactions on Information Theory*, vol. 44, no. 2, pp. 744–765, 1998.

[76] S. M. Alamouti, "A simple transmit diversity technique for wireless communications," *IEEE Journal on Selected Areas in Communications*, vol. 16, no. 8, pp. 1451–1458, 1998.

[77] V. Tarokh, H. Jafarkhani, and A. R. Calderbank, "Space-time block codes from orthogonal designs," *IEEE Transactions on Information Theory*, vol. 45, no. 5, pp. 1456–1467, 1999.

[78] B. M. Hochwald and T. L. Marzetta, "Unitary space-time modulation for multiple-antenna communications in Rayleigh flat fading," *IEEE Transactions on Information Theory*, vol. 46, no. 2, pp. 543–564, 2000.

[79] D. Agrawal, V. Tarokh, A. Naguib, and N. Seshadri, "Space-time coded OFDM for high data-rate wireless communication over wideband channels," in *Proceedings of 48th IEEE Vehicular Technology Conference (VTC '98)*, vol. 3, pp. 2232–2236, Ottawa, Ontario, Canada, May 1998.

[80] R. S. Blum, Y. G. Li, J. H. Winters, and Q. Yan, "Improved space-time coding for MIMO-OFDM wireless communications," *IEEE Transactions on Communications*, vol. 49, no. 11, pp. 1873–1878, 2001.

[81] H. Bölcskei and A. J. Paulraj, "Space-frequency coded broadband OFDM systems," in *Proceedings of IEEE Wireless Communications and Networking Conference (WCNC '00)*, vol. 1, pp. 1–6, Chicago, Ill, USA, September 2000.

[82] W. Su, Z. Safar, M. Olfat, and K. J. Ray Liu, "Obtaining full-diversity space-frequency codes from space-time codes via mapping," *IEEE Transactions on Signal Processing*, vol. 51, no. 11, pp. 2905–2916, 2003, Special issue on MIMO systems.

[83] W. Su, Z. Safar, and K. J. Ray Liu, "Systematic design of space-frequency codes with full rate and full diversity," in *Proceedings of IEEE Wireless Communications and Networking Conference (WCNC '04)*, vol. 3, pp. 1436–1441, Atlanta, Ga, USA, March 2004.

[84] A. H. Tewfik and E. Saberinia, "High bit rate ultra-wideband OFDM," in *Proceedings of IEEE Global Telecommunications Conference (GLOBECOM '02)*, vol. 3, pp. 2260–2264, Taipei, Taiwan, November 2002.

[85] J. Balakrishnan, A. Batra, and A. Dabak, "A multi-band OFDM system for UWB communication," in *Proceedings of IEEE Conference on Ultra Wideband Systems and Technologies*, pp. 354–358, Reston, Va, USA, November 2003.

[86] The UWB Multi-Band Coalition, Internet: www.uwbmultiband.org.

[87] *IEEE 802.15WPAN High Rate Alternative PHY Task Group 3a (TG3a)*, Internet: http://www.ieee802.org/15/pub/TG3a.html.

[88] R. A. Scholtz, "Multiple access with time-hopping impulse modulation," in *Proceedings of IEEE Military Communications Conference (MILCOM '93)*, vol. 2, pp. 447–450, Boston, Mass, USA, October 1993.

[89] M. Z. Win and R. A. Scholtz, "Impulse radio: how it works," *IEEE Communications Letters*, vol. 2, no. 2, pp. 36–38, 1998.

[90] M. L. Welborn, "System considerations for ultra-wideband wireless networks," in *Proceedings of IEEE Radio and Wireless Conference (RAWCON '01)*, pp. 5–8, Waltham, Mass, USA, August 2001.

[91] J. R. Foerster, "The performance of a direct-sequence spread ultrawideband system in the presence of multipath, narrowband interference, and multiuser interference," in *Proceedings of IEEE Conference on Ultra Wideband Systems and Technologies (UWBST '02)*, pp. 87–91, Baltimore, Md, USA, May 2002.

[92] N. Boubaker and K. B. Letaief, "Ultra wideband DSSS for multiple access communications using antipodal signaling," in *Proceedings of IEEE International Conference on Communications (ICC '03)*, vol. 3, pp. 2197–2201, Anchorage, Alaska, USA, May 2003.

[93] R. A. Horn and C. R. Johnson, *Matrix Analysis*, Cambridge University Press, New York, NY, USA, 1985.

[94] L. Yang and G. B. Giannakis, "Space-time coding for impulse radio," in *Proceedings of IEEE Conference on Ultra Wideband Systems and Technologies (UWBST '02)*, pp. 235–239, Baltimore, Md, USA, May 2002.

[95] M. Nakagami, "The *m*-distribution—A general formula of intensity distribution of rapid fading," in *Statistical Methods in Radio Wave Propagation*, W. G. Hoffman, Ed., pp. 3–36, Pergamon Press, Oxford, UK, 1960.

[96] M. Z. Win and R. A. Scholtz, "Ultra-wide bandwidth time-hopping spread-spectrum impulse radio for wireless multiple-access communications," *IEEE Transactions on Communications*, vol. 48, no. 4, pp. 679–689, 2000.

[97] J. Proakis, *Digital Communications*, McGraw-Hill, New York, NY, USA, 4th edition, 2001.

[98] M. K. Simon and M.-S. Alouini, *Digital Communication over Fading Channels: A Unified Approach to Performance Analysis* , John Wiley & Sons, New York, NY, USA, 2000.

[99] W. P. Siriwongpairat, M. Olfat, and K. J. Ray Liu, "Performance analysis and comparison of time-hopping and direct-sequence UWB-MIMO systems," *EURASIP Journal on Applied Signal Processing*, vol. 2005, no. 3, pp. 328–345, 2005, Special issue on UWB-State of the art.

[100] S. S. Ghassemzadeh, L. J. Greenstein, T. Sveinsson, and V. Tarokh, "A multipath intensity profile model for residential environments," in *Proceedings of IEEE Wireless Communications and Networking Conference (WCNC '03)*, vol. 1, pp. 150–155, New Orleans, La, USA, March 2003.

[101] J. Zhang, R. A. Kennedy, and T. D. Abhayapala, "New results on the capacity of M-ary PPM ultra-wideband systems," in *Proceedings of International Workshop on Ultra WideBand Systems (IWUWBS '03)*, Oulu, Finland, June 2003.

[102] L. Zhao and A. M. Haimovich, "The capacity of an UWB multiple-access communications system," in *Proceedings of IEEE International Conference on Communications (ICC '02)*, vol. 3, pp. 1964–1968, New York, NY, USA, April–May 2002.

[103] L. Zhao and A. M. Haimovich, "Capacity of M-ary PPM ultra-wideband communications over AWGN channels," in *Proceedings of IEEE VTS 54th Vehicular Technology Conference (VTC '01)*, vol. 2, pp. 1191–1195, Atlantic City, NJ, USA, October 2001.

[104] G. J. Foschini and M. J. Gans, "On limits of wireless communications in a fading environment when using multiple antennas," *Wireless Personal Communications*, vol. 6, no. 3, pp. 311–335, 1998.

[105] I. E. Telatar, "Capacity of multi-antenna Gaussian channels," *European Transactions on Telecommunications*, vol. 10, no. 6, pp. 585–595, 1999.
[106] I. E. Telatar, "Capacity of multi-antenna Gaussian channels," Tech. Rep., AT&T Bell Laboratories, Murray Hill, NJ, USA, 1995.
[107] M. J. Gans, N. Amitay, Y. S. Yeh, et al., "Outdoor BLAST measurement system at 2.44 GHz: calibration and initial results," *IEEE Journal on Selected Areas in Communications*, vol. 20, no. 3, pp. 570–583, 2002.
[108] A. F. Molisch, M. Steinbauer, M. Toeltsch, E. Bonek, and R. S. Thomä, "Capacity of MIMO systems based on measured wireless channels," *IEEE Journal Selected Areas in Communications*, vol. 20, no. 3, pp. 561–569, 2002.
[109] A. van Zelst and T. C. W. Schenk, "Implementation of a MIMO OFDM-based wireless LAN system," *IEEE Transactions on Signal Processing*, vol. 52, no. 2, pp. 483–494, 2004.
[110] D. Cassioli, M. Z. Win, and A. F. Molisch, "The ultra-wide bandwidth indoor channel: from statistical model to simulations," *IEEE Journal on Selected Areas in Communications*, vol. 20, no. 6, pp. 1247–1257, 2002.
[111] H. Hashemi, "The indoor radio propagation channel," *Proceedings of IEEE*, vol. 81, no. 7, pp. 943–968, 1993.
[112] M. Z. Win, R. A. Scholtz, and M. A. Barnes, "Ultra-wide bandwidth signal propagation for indoor wireless communications," in *Proceedings of IEEE International Conference on Communications (ICC '97)*, vol. 1, pp. 56–60, Montreal, Quebec, Canada, June 1997.
[113] H. Zhang, T. Udagawa, T. Arita, and M. Nakagawa, "A statistical model for the small-scale multipath fading characteristics of ultra wideband indoor channel," in *Proceedings of IEEE Conference on Ultra Wideband Systems and Technologies (UWBST '02)*, pp. 81–85, Baltimore, Md, USA, May 2002.
[114] J. R. Foerster, M. Pendergrass, and A. F. Molisch, "A channel model for ultrawideband indoor communication," Tech. Rep. TR-2003-73, Mitsubishi Electric Research Laboratories (MERL), Cambridge, Mass, USA, 2003, available at: http://www.merl.com/reports/docs/TR2003-73.pdf.
[115] J. G. Proakis, *Digital Communications*, McGraw-Hill, Singapore, 4th edition, 2001.
[116] I. S. Gradshteyn and I. M. Ryzhik, *Table of Integrals, Series, and Products*, 5th Corrected and Enlarged Edition, Prepared by A. Jeffrey, Academic Press, New York, NY, USA, 1980.
[117] R. G. Gallager, *Information Theory and Reliable Communication*, John Wiley & Sons, New York, NY, USA, 1968.
[118] F. Zheng and T. Kaiser, "On the evaluation of channel capacity of multi-antenna UWB indoor wireless systems," in *Proceedings of IEEE 8th International Symposium on Spread Spectrum Techniques and Applications (ISSSTA '04)*, pp. 525–529, Sydney, Australia, August–September 2004.
[119] R. J. Muirhead, *Aspects of Multivariate Statistical Theory*, John Wiley & Sons, New York, NY, USA, 1982.
[120] E. Biglieri, J. Proakis, and S. Shamai, "Fading channels: information-theoretic and communications aspects," *IEEE Transactions on Information Theory*, vol. 44, no. 6, pp. 2619–2692, 1998.
[121] D. Gesbert, "Multipath: curse or blessing? A system performance analysis of MIMO wireless systems," in *Proceedings of IEEE International Zurich Seminar on Communications (IZS '04)*, pp. 14–17, Zurich, Switzerland, February 2004.
[122] A. V. Oppenheim and R. W. Schafer, *Discrete-Time Signal Processing*, Prentice-Hall, Englewood Cliffs, NJ, USA, 1989.

Thomas Kaiser: Department of Communication Systems, Faculty of Engineering, University of Duisburg-Essen, 47048 Duisburg, Germany

Email: thomas.kaiser@uni-duisburg.de

Jürgen Kunisch: IMST GmbH, 47475 Kamp-Lintfort, Germany

Email: kunisch@imst.de

Werner Sörgel: Institut für Höchstfrequenztechnik und Elektronik (IHE), Universität Karlsruhe (TH), 76131 Karlsruhe, Germany

Email: werner.soergel@ihe.uka.de

Christian Waldschmidt: Institut für Höchstfrequenztechnik und Elektronik (IHE), Universität Karlsruhe (TH), 76131 Karlsruhe, Germany
Email: christian.waldschmidt@ihe.uka.de

Werner Wiesbeck: Institut für Höchstfrequenztechnik und Elektronik (IHE), Universität Karlsruhe (TH), 76131 Karlsruhe, Germany
Email: werner.wiesbeck@ihe.uka.de

F. Argenti: Department of Electronics and Telecommunications, University of Florence, 50139 Florence, Italy
Email: argenti@lenst.det.unifi.it

T. Bianchi: Department of Electronics and Telecommunications, University of Florence, 50139 Florence, Italy
Email: bianchi@lenst.det.unifi.it

L. Mucchi: Department of Electronics and Telecommunications, University of Florence, 50139 Florence, Italy
Email: mucchi@lenst.det.unifi.it

L. S. Ronga: Consorzio Nazionale Interuniversitario per le Telecomunicazioni (CNIT), Università degli Studi di Firenze, 50139 Firenze, Italy
Email: ronga@lenst.det.unifi.it

Alain Sibille: École Nationale Supérieure de Techniques Avancées (ENSTA), 32 Boulevard Victor, 75739 Paris Cedex 15, France
Email: alain.sibille@ensta.fr

Sigmar Ries: Fachhochschule Südwestfalen, Hochschule für Technik und Wirtschaft, Frauenstuhlweg 31, 58644 Iserlohn, Germany
Email: ries@fh-meschede.de

Christiane Senger: Department of Communication Systems, Faculty of Engineering, University of Duisburg-Essen, 47048 Duisburg, Germany
Email: senger@nts.uni-duisburg.de

W. Pam Siriwongpairat: Department of Electrical and Computer Engineering and Institute for Systems Research, University of Maryland, College Park, MD 20742, USA
Email: wipawee@glue.umd.edu

Masoud Olfat: Department of Electrical and Computer Engineering and Institute for Systems Research, University of Maryland, College Park, MD 20742, USA
Email: molfat@eng.umd.edu

Weifeng Su: Department of Electrical and Computer Engineering and Institute for Systems Research, University of Maryland, College Park, MD 20742, USA
Email: weifeng@isr.umd.edu

K. J. Ray Liu: Department of Electrical and Computer Engineering and Institute for Systems Research, University of Maryland, College Park, MD 20742, USA
Email: kjrliu@eng.umd.edu

Feng Zheng: Department of Electronic and Computer Engineering, University of Limerick, Limerick, Ireland
Email: feng.zheng@ul.ie

6 UWB ranging

Domenico Porcino, Jürgen Sachs,
Rudolf Zetik, and Andy Ward

6.1. Introduction

Ultra wideband technology has been identified as one of the most promising techniques to enhance a mobile terminal or a sensor with accurate ranging and tracking capabilities.

In simple words, the basic idea behind most accurate positioning systems under development today is to determine the time that a radio wave takes to propagate from the transmitter to the receiver and then convert that measurement into a distance to enable the estimation of the *range* between the two devices. The initial estimate of this range distance is often called the pseudorange. By calculating the pseudorange from the querying device to multiple devices at known locations, (technique often called trilateration) it is possible to identify with high accuracy the position of a device itself (*positioning*). Finally, it is also possible to keep calculating these range estimates over time and follow the device over a given time window while it is moving inside the area covered by the ranging system (*tracking*).

The system just described only gives a simplistic view of what needs to be done to tackle a substantial number of technical challenges. Complex mathematical algorithms will be used in support of the ranging and tracking calculations. In fact, in the first place, it is necessary to be able to measure with a good accuracy a very low-power signal in any potential condition of operation (severe multipath included). This signal might additionally be composed of the intentional combination of multiple signals transmitted by a number of parallel antennas or nearby transmitters. Then it is necessary to distinguish inside the received signal a sufficient number of characteristics to allow an informed estimate of the distance between the receiver and the transmitter(s). Finally it might be necessary to combine the information from multiple (and possible redundant) sources to be able to provide the application layer with usable information on the position of the node and an estimate of the reliability of such information.

The obstacles in the detection and processing of the radio-wave signals are many, including significant constraints on the maximum power allowed over air (*regulatory constraints*), constraints on the radio architecture (*standards and cost constraints*), constraints on the maximum processing power (*technology constraints*), and time needed to derive the information (*quality-of-service constraints*). Ranging systems based on UWB technology face all these challenges that need to be appropriately addressed. But the step forward offered with respect to narrowband technologies is significant and comes from the same definition of ultra-wideband signals. In fact, the transmission of a substantial bandwidth (a minimum of 500 MHz to comply with FCC definitions and regulations) gives UWB receivers the possibility to achieve an extremely narrow (i.e., precise) temporal resolution with no precedence in the history of radio communications in any band below 10 GHz.

Making a correct use of such property has allowed the development of practical systems which are offering today ranging resolutions in the order of few tens of centimeters and coverage of areas as large as 60 meters with a single set of UWB beacons/base stations.

This chapter offers an introduction to this important and unique feature of UWB systems, guiding the reader to an understanding of some of the abovementioned challenges and potential solutions that will drive future UWB positioning systems.

6.2. UWB location system techniques, architectures, and analysis

In general, location systems operate by sensing some physical relationship (e.g., range or bearing) between a set of reference points and the object to be located, or some marker attached to that object.

Some location sensors give *position* location information, that is to say, they report the location of an object as a point in some coordinate space. Other location sensors give *proximity* information, that is, some indication of how near an object is to another object or some point in space.

6.2.1. Positioning methods in theory

Triangulation systems use measurements of the bearings of objects from known points to find their locations. Similarly, *trilateration* (or multilateration) schemes find object positions by determining their ranges from known points. Hybrid triangulation/trilateration schemes using both bearing and range information are also possible.

The number of independent bearings or ranges required to fix the position of an object depends on the number of degrees of freedom of the solution. For example, in a 2D triangulation system, at least two independent bearings must be found between an object and known points in the environment to calculate the object's position, because the tag's position is represented by coordinates in

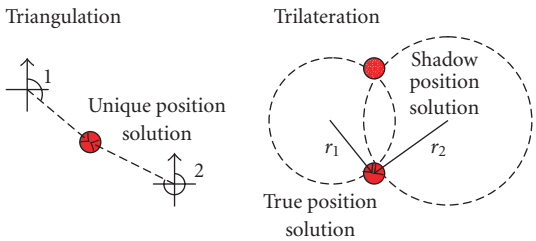

FIGURE 6.1. Triangulation and trilateration in 2D using two measurements.

two orthogonal dimensions. Similarly, in a 3D triangulation system, at least three independent bearings must be found. In general, *multilateration* systems require an additional measurement to fully resolve ambiguities in the position calculation, as shown in Figure 6.1.

6.2.2. Practical positioning systems

It is possible to implement practical multilateration systems using UWB technology. In these systems, ranges are determined between the object (or a tag marker placed on it) and the known points by measuring the time of flight of an UWB signal between a transmitter and a receiver (with either the transmitter being placed at the object to be tracked, and receivers at known points, or vice versa). The measured signal times-of-flight can be converted into ranges by multiplication by the (known) speed of light.

Time-of-arrival (TOA) systems measure the signal time of flight between transmitter and receiver directly. A practical problem arises in these systems: how should the transmitter and receiver be synchronized in order for the receiver to measure this time of flight? Note that because the speed of light is very high, this synchronization must be very tight if accurate ranges are to be measured, and often it is required that the tracked objects have unimpeded mobility (precluding the use of timing cables of known length for synchronization).[1]

One solution to this problem involves *bidirectional* ranging . A signal is sent from a transceiver at one point to a transceiver at another point, which then sends a signal in response back to the first transceiver. By measuring the round-trip time of the signal, the first transceiver can determine the distance to the second transceiver and back, that is, twice the range between the transceivers. In this arrangement, the relative timing of signal emission and detection occurs only at the first transceiver, and only local synchronization between transmitter and receiver is required—this is, of course, a relatively simple proposition.

Once a number of ranges from an object to known points have been determined, a nonlinear model can be fitted to the data to estimate the object's location.

[1]TOA systems that use lower-velocity signals can be very simple. See, for example, ultrasonic systems [1].

The nonlinear model for a 2D TOA system would be

$$l_i = \sqrt{(x_i - u)^2 + (y_i - v)^2} + \varepsilon_i \quad (i = 1, \ldots, n), \tag{6.1}$$

where (x_i, y_i) is the position of the ith known point, l_i is the measured range of the object to the ith known point, (u, v) is the estimate of the object's location, and ε_i is a term which can account for the errors (residuals) in the fitted model.

In some circumstances, it might not be desirable to equip the object, or its tag marker, with both an UWB transmitter and receiver, and bidirectional ranging cannot be used. *Time-difference-of-arrival (TDOA)* systems are suitable in these situations. A TDOA system uses a mobile transmitter and a set of synchronized receivers placed at known points, or a mobile receiver and set of synchronized transmitters placed at known points. In either case, the mobile and infrastructure components of the system are unsynchronized, but the infrastructure components are synchronized—because these components tend to be static a variety of wired or wireless techniques can be used to achieve synchronization.

TDOA systems are unable to directly measure the time of flight of a signal from a transmitter to a receiver, because these two system components are unsynchronized, and there exists an unknown offset between the clocks of the mobile unit and the surrounding infrastructure. Rather than convert the time-of-arrival of a signal at a receiver directly into a transmitter-receiver range, the receiver in a TDOA system converts the time-of-arrival into a *pseudorange* (by multiplication by the speed of light). The pseudorange encapsulates both the range and clock offset information.

To compute the unknown position of an object in the TDOA system, a nonlinear model is fitted to multiple pseudoranges and the positions of the known points. The nonlinear model for a 2D TDOA system would be

$$p_i = \sqrt{(x_i - u)^2 + (y_i - v)^2} + c \cdot t + \varepsilon_i \quad (i = 1, \ldots, n), \tag{6.2}$$

where (x_i, y_i) is the position of the ith known point, p_i is the pseudorange between the object and the ith known point, (u, v) is the estimate of the object's location, c is the speed-of-light, t is the unknown transmitter-receiver clock offset, and ε_i is a term which accounts for the errors in the fitted model. Note that the TDOA system must estimate an additional unknown parameter (the clock offset) as compared to a TOA system, and therefore a TDOA system must measure at least one more pseudorange than the equivalent TOA system measures ranges.

Practical triangulation sensors, or *angle-of-arrival* (AOA) systems, can also be implemented using UWB technology. Bearings can be determined by employing arrays of receivers and measuring differences in the signals received by each antenna (such as signal phase or time-of-signal-arrival). By using 2D antenna arrays, a single receiver unit can determine bearings of the signal transmitter in both azimuth and elevation.

It is of course possible to develop hybrid TOA/AOA and TDOA/AOA systems, which capture and make use of both range (or pseudorange) and angular information to determine the position of an UWB transmitter or receiver.

6.2.3. Proximity versus positioning

Proximity location sensors are naturally simpler than positioning sensors, because they essentially need to determine only a single quantity (the range between two objects), whereas a 2D position location sensor must determine at least two quantities (because the solution has two degrees of freedom), and a 3D position location sensor must determine at least three. The methods used in UWB proximity sensing systems are often similar to those employed in TOA position sensors—that is, two-way ranging between cooperating devices.

However, the information reported by a proximity sensor is often less useful than that reported by a positioning system. Consider, for example, a service deployed in an office which used location information to send a document from a user's laptop to a nearby printer. It might be the case that the closest printer to the user was in the room immediately above them on an adjacent floor of the building. A proximity-based solution would suggest this printer as being the most suitable, but this choice might be very inconvenient to the user. In contrast, a position-based solution might determine the coordinates of the user and candidate printers, and software could relate this information to the known architecture of the building to select the most appropriate printer.

6.2.4. Symmetric versus asymmetric architectures

Symmetric location systems architectures are those in which the entities involved in the location-finding process have identical (or very similar) capabilities. *Asymmetric* architectures typically involve a mobile component and an infrastructure component with different characteristics.

The bidirectional-ranging TOA system described above has a symmetric architecture, because both the mobile and known system components are capable of transmission and reception of UWB signals. An architecture of this type might be most suitable when UWB-enabled communications devices (such as those in PAN and LAN environments) are augmented with location-finding capability—in this situation, all system components will already be capable of bidirectional UWB communications.

In TDOA and AOA systems, the mobile and infrastructure components of the system have different capabilities and levels of functionality, and system designers are free to exploit this asymmetry to improve the overall performance of the system. For example, UWB receivers are often more complex and power-hungry than their transmitter counterparts (as can be seen also from commercial solutions discussed within the IEEE 802.15 working groups). In an UWB TDOA system, it might therefore be advantageous to make the mobile component (which must

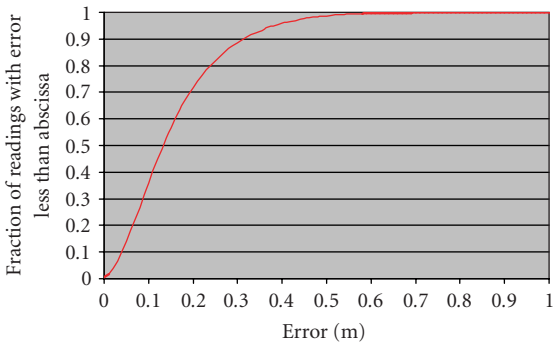

FIGURE 6.2. A cumulative probability graph describing 3D location system accuracy.

meet size and power constraints) the transmitter, and the infrastructure component (where form factor is less important, and mains power may be available) the receiver.

6.2.5. Analysis location system accuracy

Developers of location sensor systems often describe their systems as being "accurate to x cm," but statements like this provide only a rough indication of how well a system will work in practice. For example, it is very unlikely that the system will *always* be accurate to within x centimeters, because most sensor systems generate a small proportion of very large outlying readings.

Typically, quoted figures refer to either the root-mean-square (RMS) error of the system , or the accuracy level that 50% of the readings will meet. However, neither of these measures give the system designer a good idea of what the outlying error distribution looks like, and it is frequently these errors that determine how effective a sensor system is in practice. Consider, for example, a system that requires the location of an object to be found within one meter of its true position for successful operation. A location sensor with an "RMS accuracy of 75 cm" might seem quite appropriate for this task. However, if only 80% of all readings lie within one meter of the true position (a figure that could be entirely consistent with the quoted accuracy), then one in five attempts to use the system will fail. This level of service might be adequate for some applications, but would be unlikely to be sufficient for, say, a safety-critical system.

An informative way of describing location system accuracy is via the use of a cumulative probability graph showing the fraction of readings having an error less than or equal to some value.

A typical cumulative probability graph (often called *cumulative distribution function of errors* or cdf) for an UWB location system can be seen in Figure 6.2. For example, it can be seen that 50% of the 3D readings produced by the system lie within 14 cm of the true 3D position, and 95% lie within 39 cm. Comparing data in this graphical form, designers of different systems can therefore use the

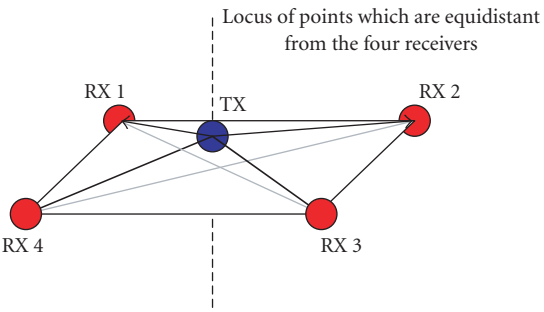

FIGURE 6.3. Pathological geometric dilution of precision in a TDOA system.

same graph to determine whether or not the sensor is suitable for their needs and applications.

When assessing a sensor system that gives 3D information about the position of an object, it is also important to consider whether quoted accuracy figures refer to the full 3D position, or only to a 2D component of that position. For example, a 3D system may be very accurate in two axes, but substantially less accurate in the third (e.g., the global positioning system [2], GPS, is very accurate in horizontal position, but relatively inaccurate in height). Manufacturers may quote performance in the accurate plane only.

6.2.6. Geometric dilution of precision

A further complication in the analysis and use of location systems is the *geometric dilution of precision*. This effect relates the fundamental ranging or bearing accuracy of the components of a location sensor to its positioning accuracy at some point in space.

Consider a TDOA system with a mobile transmitter and four receivers as shown in Figure 6.3. As can be seen, all receivers are equidistant from the transmitter, and so all will report the same pseudorange. However, this condition (that all reported pseudoranges are equal) exists at all points along the dashed line, and variations in the value of the pseudorange might be because of changes in the transmitter-receiver distance or variations in the unknown clock offset, so the location system will be unable to determine where along this line the transmitter lies. Therefore, the location system will be very inaccurate in the Z dimension with the transmitter in this X-Y position, because the particular geometry of the transmitters and receivers leads to magnification (in this case, infinite magnification!) of ranging errors.

Given a particular location system architecture and deployment, it is possible to calculate in advance the geometric dilution of precision at any point in space—the geometric dilution of precision depends only on the relative positions of the transmitter and receivers, and the chosen location system architecture. For example, in the example given above, it is not necessary to consider the technology

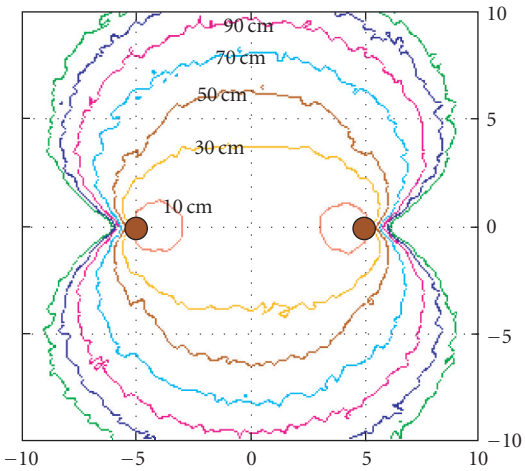

FIGURE 6.4. Simulated 2D location accuracy contours for a hybrid TDOA/AOA system. The simulated receivers covering the 20 m × 20 m space (marked as big dots) are placed at coordinates (−5 m, 0 m) and (5 m, 0 m). The area within a particular location accuracy contour represents the region in which the 2D accuracy of the system will be better than the value marked on the contour.

involved in measurements, or the measurement accuracy, to identify the inability of the TDOA system to determine the z-coordinate of a transmitter somewhere on the dashed line.

The graphs in Figure 6.4 show the expected 2D accuracy of a hybrid TDOA/AOA system within a 20 m × 20 m space.[2] Note that in practice, the *positioning* accuracy tends to be much worse than might be expected from the ranging (or bearing) accuracy.

6.3. Comparison of UWB and alternative radio-based systems

Radio-based positioning systems have several general advantages over alternative systems using optical, acoustic, inertial, or magnetic technology. These advantages include non-line-of-sight operation, compact and physically robust implementation, and minimal disruption to existing environments.

Radio location systems have been extremely successful in the wide area, and systems like GPS and LORAN [3] have been used for many years for applications such as navigation, asset tracking, and surveying. Unfortunately, the traditional techniques of radio location are difficult to use in indoor environments, because multipath signals are inevitably present—radio frequency (RF) energy sent from a transmitter bounces off walls, windows, supporting structures, equipment, and so on, causing receivers to detect a confusing superposition of signals. Furthermore, electromagnetic radiation travels at very high speed, and any system attempting to

[2]The simulation assumes that the TDOA/AOA system can measure ranges accurate to +/ − 5 cm and bearings accurate to +/ − 1°.

determine the propagation time of a signal from a transmitter to a receiver must be able to make measurements with extremely high time resolution.

Having said this, several in-building radio location systems have been developed.

Assisted GPS (A-GPS) is a technique that enables GPS receivers to detect satellite signals even when the line of sight to the satellites is obscured by the structure of a building [4]. Whereas most GPS receivers are self-contained, an A-GPS unit receives aiding information from another source (e.g., the cellphone network operator) to allow it to lock on to the severely attenuated GPS signals found inside buildings. Several US cellphone carriers have selected this method for use in enhanced 911 services, but accuracy could be significantly worse than the ˜10 m accuracy (95%, 2D) of GPS outdoors, and the receiver/aiding-channel combination is relatively complex and power-hungry. This technique is one of the methods that might be used for cellular device location [5].

Signal strength systems that estimate transmitter-receiver distances from the received strength of a reference signal have been developed to allow the location of wireless LAN nodes within buildings. Unfortunately, received signal strength varies not only with distance, but also with composition of the media through which the signal has passed (which may be air, concrete, metal, etc.), and the relative orientations of the transmitting and receiving antennae. Some systems are set up to give a simple indication of proximity to other nodes, others use a fixed infrastructure of base stations to provide a positioning capability, but reported accuracy is around 10 m (95%, 2D) [6]. Some other systems, such as *Ekahau* positioning system [7], use standard IEEE 802.11 access points, but require extensive surveys of the building to get enough statistics of the received signal strength (RSSI) to be able to fingerprint the position of the tag to a claimed accuracy of 1 m.

Systems based on narrowband RF detection. Examples include the following.

(i) The *WhereNet* location system, a TDOA system operating in the 2.4 GHz industrial, scientific, and medical (ISM) band [8]. Active tags are attached to the objects to be located, and their signals are detected by a set of receivers placed at known points. The manufacturers suggest that this system has an accuracy of a few meters in in-building environments.

(ii) The *PinPoint* system, which measures the round-trip time of flight of a spread-spectrum radio signal sent in the ISM bands (2.4 GHz and 5.8 GHz) from a fixed infrastructure of transceivers placed around a building to active transponders placed on equipment [9]. Again, this type of system is accurate to within a few meters indoors.

(iii) *Bluetooth* location systems, which use timing of RF signals between cooperating nodes, and which are being commercialized by companies like *Bluesoft* [10]. Some modifications to the Bluetooth radio and protocols are required to implement this functionality. Accuracy is similar to the other ISM band systems described above.

Other RF technologies can be used to provide some indication of the proximity of an object to some point in space.

Passive RFID systems (e.g., [11]) infer the presence of nearby objects using small, passive transponder tags attached to those objects. A reader unit energizes transponders in its vicinity via electromagnetic coupling, causing the tags to respond with a radio message containing their unique identifier. The tags are cheap and virtually indestructible, but they must be placed very close to a reader antenna (within a few meters) to be detected, and no precise information regarding the tag's location in relation to the reader can be deduced.

Active RFID systems (e.g., [12]) use battery-powered tags which transmit signals coded with each tag's unique identifier. Because they do not rely on electromagnetic coupling to provide power to the tag, they operate over much longer ranges (up to a few hundred meters) than passive RFID systems, but the tags are much more expensive.

6.3.1. UWB and indoor location systems

As noted above, one of the major limiting factors in the use of RF positioning systems within buildings is the presence of multipath signals. UWB location systems have a great advantage in this regard over other RF positioning technologies, because they are able to make use of bandwidths in the multi-GHz range, rather than, say, the 80 MHz bandwidth available to systems operating in the 2.4 GHz ISM band.

As the bandwidth of a transmitter-receiver link increases, so does the ability of the receiver to distinguish between one incoming signal and a second arriving a short time afterwards. Because multipath signals must travel a longer distance from the transmitter to the receiver than the direct path signal, they will arrive at the receiver later. Therefore, the increased bandwidth available to UWB systems allows them to better distinguish between line-of-sight signals and those which have reached a receiver after one reflection (or several reflections) from surfaces in the environment. Since only the direct path signal conveys useful information for the purposes of location, the increased system bandwidth results in improved location accuracy.

6.3.2. UWB location systems outdoors

UWB location systems may also have advantages over other RF-based positioning techniques in outdoor environments. In the areas around buildings (the so-called "urban canyon"), an UWB location system could supplement other wide-area techniques such as GPS which have difficulty in those environments due to RF shadowing. And although systems like GPS can provide very high (centimeter or even millimeter) accuracy positioning through the use of carrier-phase techniques, these methods can require continuous tracking and might require a long time to achieve their first position fix from a cold start. An UWB system can often provide similar tracking accuracy with lower power consumption at the mobile device and better dynamic response.

6.3.3. Disadvantages of UWB location systems

When compared to other RF-based positioning technologies, UWB location systems do have some disadvantages.

Although they can make use of very wide operating bandwidth, the transmitted signal powers permitted by regulation are typically very low, limiting the operating range of UWB location systems compared to traditional RF location technologies.

Potential interference concerns have also lead to regulation (in the US, at least), which shifts the permitted operating frequencies of UWB systems away from the congested 0–3 GHz band. However, higher frequencies propagate through construction materials less easily than lower frequencies, and so the effect of this aspect of the regulations is to further decrease the ability of UWB location systems to operate over long ranges indoors.

6.4. A typical RF link budget for UWB positioning systems

The radio frequency (RF) characteristics of the link between an UWB transmitter and an UWB receiver have a very significant influence on key parameters of a correspondent ranging system. Important system parameters such as the area of coverage, the needed receiver sensitivity, the noise figure of the receiver, the gains on the antennas, the path dynamics are all connected and interrelated with the final quality (accuracy, reliability) and convenience (maximum range, minimum infrastructure) that the positioning system will be able to offer.

Looking at the positioning system as any wideband radio link between two UWB devices, we can start a simple analysis considering the constraints under which our positioning system will need to operate. Table 6.1 will guide the reader through this simple exercise. In particular, we will need to comply with

(i) international recognized definitions of UWB systems,
(ii) power emission restrictions,
(iii) feasibility of the corresponding UWB parts of the system.

As for the first constraint, we will adhere to the only official definition of UWB systems which is widely recognized (i.e., the UWB definition given in the FCC First Report and Order [13]). Considering that definition and the likely developments in other region of the world, we assume a bandwidth for the system larger than 500 MHz. Given that the positioning system is designed with range resolution as an important target, we set for this link budget a goal of 1800 MHz bandwidth for the UWB system, with a center frequency around 4 GHz.

The second constraint (power limit) is very important to ensure adequate coverage at feasible receiver sensitivity. To keep within the FCC recommendation, we fix the average EIRP level to -41.2 dBm/MHz, which, integrated over the 1.8 GHz chosen for transmission, allows us to send over air about -8.74 dBm (which is about 0.14 mW).

Other parameters, which are usually very significant on the communications side, such as the throughput or the coding of the system, are a secondary element

in our link budget as this is considered an auxiliary function to the positioning system rather than a founding block. For sake of simplicity, we limit our desired throughput to a modest 60 kbps (just slightly faster than PC analog modems).

Very important are the considerations on the path characteristics. One of the targets to keep in mind is the maximization of the link distance, with a realistic set of propagation characteristics (typically far from ideal line of sight). We select a target of 70 m distance between the transmitter and the receiving units. We then distinguish three separate elements in the path characterization: a close-in path loss factor P_0, a far-field path loss at distance $d(P_L)$, correlated to the decay exponent of the signal attenuation, and a lognormal shadowing contribution (P_S). The formulae applied for the close-in and far-field pass loss are reported

$$\begin{aligned} P_0 &= 20\log\left(\frac{1}{4\pi d_0}\cdot\lambda\right), \\ P_L &= 10\cdot n\cdot\log\frac{d}{d_0}. \end{aligned} \tag{6.3}$$

The parameters selected for the propagation part of this simple exercise are in line with current models and reported indoor measurements for UWB systems. The path loss exponent we consider is $n = 2.5$, and the standard deviation of the lognormal shadowing distribution is about 2 dB (i.e., lower than the narrowband equivalent). The resulting signal loss in the air channel will be

$$P_{L\text{tot}} = P_0 + P_L + P_s = 44.48\,\text{dB} + 46.12\,\text{dB} + 4\,\text{dB} = 94.6\,\text{dB}. \tag{6.4}$$

Considering two omnidirectional antennas with zero dBi gain, we can see that the average power arriving to the receiver will be in the order of -103.35 dBm (i.e., a tiny 46.23 pW).

Considering a thermal noise floor, KTB, of $4.002 * 10^{-21}$ Watts (or equivalently in log form $= -174$ dBm), our data rate of 60 kbps and a receiver noise figure of 10 dB (adequate given the low-cost target in mind), we can calculate the received noise power per bit P_N as -116.2 dBm.

Adding the spectral characteristics of a simple binary antipodal modulation (such as BPSK) with a BER target of 10^{-3} ($Eb/N_0 = 6.6 - (-1.59)$ dB $= 8.19$ dB) and further implementation losses, as written in (6.5), we still manage to save (see (6.5)) over 1 dB (L_M) of link margin from our original budget, achieving the target link distance of 70 m

$$L_M = P_R - P_N - P_{EB} - P_{IL} = -103.357\,\text{dB} - (-116.218)\,\text{dB} - 8.19\,\text{dB} - 3\,\text{dB} = 1.67\,\text{dB}. \tag{6.5}$$

The corresponding UWB positioning system would have access to a spatial resolution inversely proportional to the usable bandwidth resulting in a discrimination to the level of 17 cm, very good to provide accurate range information to the applications using the positioning information.

Table 6.1. A typical RF link budget for an UWB positioning system.

TX system parameters	Value	Units
Throughput(Rb)	60	Kbps
Bandwidth(B)	1800	MHz
Average Tx power(Pt)	−8.7473	dBm
TX antenna gain(GT)	0	dBi
Geometric center frequency(Fc)	4000	MHz
Path characteristics		
Link distance(d)	70	m
Path loss at 1 m(P_0)	44.483	dB
Path loss exponent(n)	2.5	—
Path loss at distance d(P_L)	46.1275	dB
Lognormal shadowing standard deviation	2	dB
Worst-case shadowing loss(P_S)	4	dB
RX system parameters		
RX antenna gain(Gr)	0	dBi
RX received power(Pr)	−103.36	dBm
Noise-related factors		
Average noise power per bit	−126.22	dBm
Receiver noise figure	10	dB
Average RX noise power per bit(PN)	−116.22	dBm
Modulation minimum Eb/N_0 (at BER = 10^{-3})(PEB)	8.19	dB
Implementation losses(PIL)	3	dB
Budget		
Link margin at distance d(L_M)	1.6708	dB
Temporal resolution	0.16667	m

Many are of course the potential tradeoffs that could be considered with changes to this simple UWB positioning link budget for a low data rate system with positioning capabilities. But the essence of this simple exercise is to show that building a low cost, low data rate system with accurate positioning feature is feasible with a set of relatively standard ultra-wideband parameters.

6.5. Characteristics of a fine-grained UWB positioning system

The Ubisense location system [14] is one example of a fine-grained UWB indoor location system. The system is primarily designed to track people and objects in support of "smart space" applications —these applications involve computing and communications systems which react to the locations of objects in the environment to make work processes faster, safer, and easier. An example smart space application might be a "corporate memory" application which automatically records who meets who, where and when, within an office environment to allow employees

(a) (b)

FIGURE 6.5. Ubisense tag (a) and base station (b).

to more easily recall details of meetings at a future date. Of course, the fundamental UWB tracking technology used in the Ubisense system to support smart space applications can also be used to solve other (more basic) tracking problems both indoors and outdoors.

The Ubisense location technology (shown in Figure 6.5) uses small UWB transmitter tags, which are attached to objects and carried by people. The signals from these tags are detected by a set of base stations placed at known points around the area to be instrumented—base stations are networked using the standard structured cabling found in many modern buildings. Base stations are capable of determining both pseudoranges and bearings to tags, and so the system represents a hybrid TDOA/AOA location technology.

Many features of the Ubisense system result from the desire to support smart space applications.

High accuracy. Smart space applications use a model of the environment built using location information, and make automatic decisions based on the relative and absolute positions of objects in that model. If the application's model of the environment differs significantly from the user's mental model (constructed using their senses), then the decisions made by the application could differ from those which the user would make, leading quickly to user disillusionment with the smart space application. It is therefore important that the smart space applications sense the world as well, or nearly as well, as the human user does. The Ubisense system is designed to achieve 3D positioning accuracy of 15 cm (95% confidence level, averaged across the space covered by the system)—the raw pseudoranges and angles measured by the TDOA/AOA technology are accurate to around 5 cm and 1°.

Figure 6.6 shows the results of measurements taken using a prototype Ubisense system in late 2003. Two base stations were used to cover a 10 m × 10 m test space, and a tag was placed at points on a 1 meter grid within that space—the tag positions were determined in three dimensions, although the projection shows only the 2D (x-y) locations of the tags. The area over which readings are distributed around each point on the unit meter grid gives an indication of the

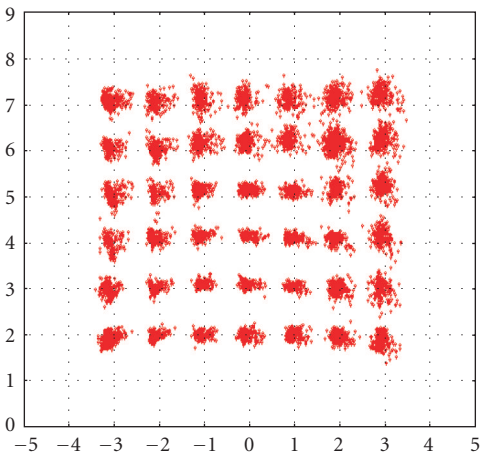

FIGURE 6.6. Tracking results from prototype Ubisense system in a 10 m × 10 m space.

accuracy of the system at each of those grid points, and illustrates the differing magnification of errors due to geometric dilution of precision across the measurement space.

Flexible tracking. Many smart space applications demand real-time performance, because they perform user-interface functions. An example of this type of smart space application is a "mobile desktop" process in an office environment, which automatically moves a user's personal desktop to any display which they approach. Real-time performance demands high tracking rates, so that applications can respond instantly to changes in the environment. However, it would be wasteful of tag battery power to demand that they transmit continuously at the highest rate which might be appropriate for *any* smart space application, because that update rate might only be required for a short period of time in specific circumstances. The Ubisense system is therefore designed to allow applications to request (via the location system) different tracking rates for individual tags. Smart space applications can change the activity rates for tags depending on the current state of the environment—for example, persons might be located only once every few seconds if they were sitting down, but if they were moving, they might be located a few times each second. In this way, smart space applications can balance their requirements for real-time location information with power management requirements.

Unlimited scalability. Smart space applications are often the most useful in large environments where there are many people and many computing and communications devices which interact frequently. Examples of these types of environment might be large hospitals and office buildings, which can cover tens or hundreds of thousands of square meters, and house thousands of people and items of equipment. These characteristics demand that tracking systems intended to support smart space applications in these environments must be designed to scale in terms of the area of coverage and the number of tracked objects. The Ubisense

location technology achieves this scalability using cellular techniques—large areas are covered using a number of unit cells, each of which tracks objects over a smaller area of space. In the Ubisense system, each unit cell uses a small number of base stations (typically four) and can cover an area of up to around 1000 m^2 (depending upon the degree of obstruction within the space). Because each cell operates essentially independently from neighboring cells, and is capable of tracking many objects within that cell per second, the total area which can be covered by the system is essentially unlimited, and as the number of cells involved in the system increases, so does the aggregate tracking capacity of the whole system. A control system links the cells and ensures that tags hand over from one cell to the next as they move around the covered space to permit seamless, continuous tracking.

Hybrid TDOA/AOA architecture. Because many smart space applications are driven by position data relating to people, it is important that the sensor system supporting those applications can locate people effectively. However, the microwave signals suitable for use in UWB systems do not propagate well through the human body, which tends to shadow emissions from a body-worn tag, and a tag worn by a person will therefore only "see" the limited set of base stations which happen to lie in the unobstructed direction. Although it would be possible to compensate for this shadowing by deploying more base station infrastructure, it is desirable for reasons of cost and complexity to keep the level of system infrastructure to a minimum. Therefore, it is important to ensure that the location system can track a tag even when only a very few base stations can detect its signal. The hybrid TDOA/AOA architecture employed by the Ubisense system enables a tag's 3D position to be determined using information from only two base stations, making the technology particularly well suited to the locations of people in cluttered indoor environments.

6.6. Positioning techniques in harsh environments

One of the myths that surrounded the evolution of UWB technology to the commercial world was that this fantastic technology was multipath-free and would allow the existence of joint data communications and positioning in almost any environment. While it is undeniable that the temporal resolution of UWB signals is much higher than the one offered by typical narrowband systems, it is clear to any engineer that this resolution is finite and fading effects will be registered in any relatively dense multipath area. From a positioning point of view, the presence of multipath might create difficulties in distinguishing the leading trail of a series of return signals from its reflections off walls or close-by objects. This will render the estimation of the time of flight between transmitter and receiver (and consequently the estimation of the relative distance) much more complicated than in free-space propagating conditions. Fundamental importance in the dense multipath case has to be given to the exact propagation characteristics of the UWB signals over air, which is usually simulated with the help of a channel model.

A radio channel is in fact a complex mathematical attempt to describe the propagation phenomena trough air, physical objects, and people. The interaction among electromagnetic waves and the real world is extremely difficult to predict reliably and is clearly strongly dependent on the very precise details of the propagation scenario chosen to represent the typical case under analysis.

The radio-mobile channel has to physically represent the sum of all the effects of loss and distortion that the signals undergo during their propagation from a transmitter to a receiver. In the case of studies of UWB propagation through non-line-of-sight conditions, we will be interested in knowing how the UWB signals will propagate through air and how this might affect our link budget.

The main effects that a radio wave encounters during its propagation can be divided into the following.

(i) *Long-term (path loss)* characteristics. The long-term characteristics of the radio-mobile channel describe how the *mean* signal will behave in function of the distance at a given frequency. The loss is gradual with received power decreasing almost as an exponential decay in logarithm scale (represented by the decay facto n introduced in Section 6.4).

(ii) *Medium-term (shadow fading)* characteristics. The shadow fading shows the time-varying factors, such as shadowing from buildings or big objects. It is added on top of the path loss and represented as a random fluctuation with a lognormal distribution, with a standard deviation σ dependent on propagation conditions.

(iii) *Short-term (multipath or fast fading)* characteristics. The short-term characteristics (fast fading) describe the sudden variations on the received signal strength due to multipath and reflections coming off buildings and objects. This factor is superimposed on the long-term variation. These variations will typically happen for very small movements of the mobile antenna: a few wavelengths are enough to cause fast fading (as an example, at 4 GHz, the wavelength is just 7.5 cm).

These three effects will of course be summed together and will not easily be discernible in environments where the propagation conditions are cluttered.

A more formal classification of environments based on the propagation conditions can be done with postprocessing and analysis of the path loss characteristics as registered in loco. In particular, from the path loss analysis, we can define three different cases.

(i) *Line of sight (LOS)* is a case when a signal reaches the receiver directly from the transmitter, that is, when there are no obstacles in the transmission path. In this case, the leading path is clearly distinguishable from reflections and its energy is above 80% of any potential reflection.

(ii) OBS (obstructed line of sight), or *soft (NLOS) soft non-line-of-sight* is a situation in which the transmission path is lightly obstructed but energy is still recoverable from the direct path. In this case, the power coming from reflections is dominant with respect to the power coming from the direct path, (energy from reflected path energy from direct path).

(iii) *Hard NLOS* is a situation of almost total absence of any penetration in a direct path. In this case, the direct path between transmitter and receiver is totally obstructed and the energy from reflected path is greater than 90% of total recovered energy.

The nice features of UWB systems are usually simulated or demonstrated in environments where line of sight (or at worst soft line of sight) is guaranteed, but many of the interesting applications for UWB as an asset tracking system will need to be able to handle much more challenging conditions and combat the multipath. Severe multipath makes in fact the process of estimating the time of flight extremely difficult and its effects need to be removed.

As in the case of narrowband technologies (see [15]) also for UWB systems, there is a clear need to guarantee reasonable performance in harsh conditions and it is therefore necessary to develop appropriate and reliable techniques for signal detection in multipath.

Two different families of signal detection in dense multipath can be applied:

(i) techniques based on equalization,

(ii) techniques based on statistics.

Techniques based on equalization usually estimate the multipath delays introduced by the radio channel and compensate the received signal for them, trying effectively to remove any spurious echoes from the received signal. A critical element in this receiver structure will be the channel sounder, which will determine the coefficients and weights of the reflected paths and consequent signal processing to apply to them to recover a reasonable estimate of the leading edge of the direct signal.

Techniques based on statistics rely on a large number of measures (ideally statistically independent) to derive statistical data on the temporal variation of received signals. They can use all or only the part of collected data on which the level of confidence is higher. Statistics can be of first order (averaging) or higher orders (such as those used in MUSIC or ESPIRIT algorithms, [16, 17]).

A good example of an UWB positioning system designed to be reliable in extremely harsh conditions is the precision asset location (PAL) system developed by Multispectral Solutions (MSSI) for the Office of Naval Research (ONR) Naval Total Asset Visibility (NTAV) Program. This governmental study [18] investigated technologies for asset visibility and tracking on board of navy ships where hundreds of containers are transported at any time.

As shown in Figure 6.7, the conditions in the container ship are extremely difficult for radio wave propagation, with floor-to-ceiling metal walls surrounding every room. The experiments carried out by the University of Southern California to characterize this environment [19] report very problematic propagation conditions. The severe attenuation and numerous reflections of these environments cause deep nulls (30–40 dB) in the received signals and very long delay spreads (3 μsec at the -20 dB points), over 10 times longer than what is recorded in any office conditions. In such harsh operating conditions, very numerous are the occurrences of total blockage of the signal, and this will cause severe strain to the signal processing algorithms designed into the PAL signal recovery.

(a)

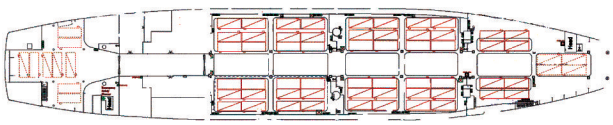

(b)

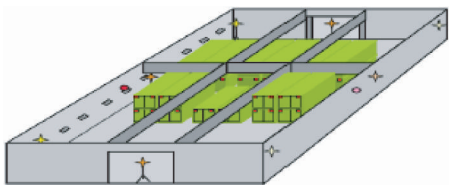

(c)

FIGURE 6.7. Harsh environments for UWB positioning systems (from [18, 19]).

The initial prototype PAL system consisted of a set of four passive UWB receivers, an UWB reference tag (positioned at a known location), and a collection of UWB active tags. It transmitted short pulses over an instantaneous bandwidth of approximately 400 MHz. The average energy sent over air was 5 nW, equivalent to 1.25×10^{-11} Watts/MHz (-79 dBm/MHz; i.e., well below FCC limits) in the L-band (frequencies centered around 1.5 GHz). The following commercial developments of the PAL system into the Sapphire Precision Asset Location System lead to a higher operation frequency of 6.1–6.6 GHz and FCC certification, but still maintained a great resilience to harsh conditions.

Even in these challenging conditions, the UWB technology implemented in the PAL system was reportedly able to measure positions in open space with an RMS accuracy between 0.9 and 1.5 m. It also achieved 1 meter accuracy in the measurements of single-high stacked containers and about 3.5 meter accuracy with double-high stacked containers (under heavy blockage).

6.7. UWB precise ranging with an experimental antenna-array system

Another example of an indoor location system is an experimental antenna-array localizer developed at Technical University of Ilmenau. The system is designed to

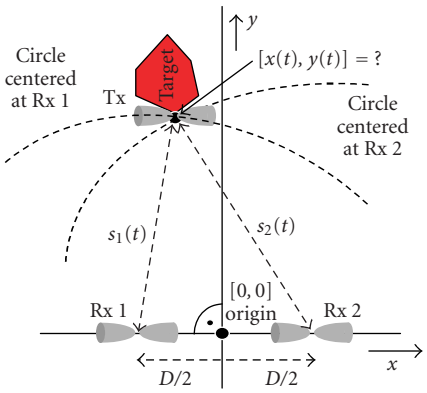

FIGURE 6.8. Active positioning using two reference antennas at known positions.

investigate the precision of UWB ranging and positioning with colocated and spatially distributed antennas and to push the accuracy close to its limits in a controlled environment.

The localization techniques subjects of this section allow two different positioning approaches: an active and a passive approach. In the following pages, the fundamentals of both methods will be considered in more detail and experimental results carried out with UWB transmissions in the frequency range 0.8 to 5 GHz will be shown.

6.7.1. Positioning—active and passive approaches

The *active* method presumes that the target device (which is the device to be tracked) "cooperates," that is, actively interacts with the positioning device. In order to cover this proactive role, the target has to include also a transmit or receive unit and collaborate in the ranging measurements. The passive approach in contrast is based on a standalone positioning system exploiting "simple" wave scattering by the (unaware) target as in the case of a radar system. Both approaches are dealing with trilateration principles, as briefly introduced at the beginning of this chapter (see Figure 6.1 and (6.1), (6.2)).

Figures 6.8 and 6.9 represent the fundamental layout of the active and passive positioning techniques based on time-delay measurements. In both arrangements, simple uniform linear antenna arrays can be used if the up-down ambiguity (as shown in Figure 6.1) is not in the focus of the investigations. In the case of necessity to avoid this ambiguity, the linear antenna configuration has to be replaced by a triangular one for 2D positioning (or a tetrahedron for 3D positioning). The actual number of antennas used in a practical system usually exceeded the required minimum, as shown in the figures. This redundancy allows working with an overdetermined system of equations resulting in solutions with a statistically improved confidence. For simplicity, the figures are restricted to the 2D case.

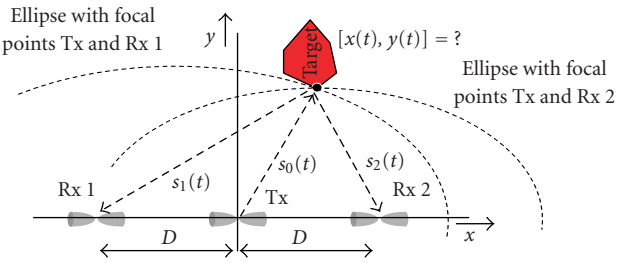

FIGURE 6.9. Passive positioning by a three-element linear array.

Figure 6.8 represents the geometrical basics of the active approach. In this example it was assumed that the target object is carrying a radio transmitter and the positioning unit (which would be the master in a master/slave configuration) contains the receiver with a two-element antenna-array. The positioning unit estimates the times of flight τ_{a1} and τ_{a2} of the electromagnetic waves arriving from the transmitter (target) to each of the antenna-array elements. Each of these time intervals determines the radius of a circle centred at the corresponding receive antenna element. The target will be standing on both circles, and therefore will need to be also at the interception point of the two. The radiuses of the two circles are referred to as $s_1(t)$ and $s_2(t)$. The position of the target is determined as one of the two intersections of the circles above described. Finding the position of the target, that is, solving its cartesian coordinates [x(t),y(t)] will therefore be equivalent to solving the equations

$$\begin{aligned}\left(x(t)+\frac{D}{2}\right)^2+y(t)^2 &= s_1(t)^2 = \left(c\tau_{a1}(t)\right)^2,\\ \left(x(t)+\frac{D}{2}\right)^2+y(t)^2 &= s_2(t)^2 = \left(c\tau_{a2}(t)\right)^2.\end{aligned} \tag{6.6}$$

Note that the indicated arrangement presumes an exact synchronization between the transmitter and the receivers. In a laboratory experiment, this hypothesis can be met by synchronizing transmitter and receiver units by wire (using a cable connecting both units). In practical situations, the synchronization problem will need to be dealt with and consequently an additional receive channel is required in order to measure the time-difference of arrival. The corresponding equations in such unsynchronized case will be slightly more complicated as mentioned in Section 6.2.

In the case of the passive approach, the target (at an unknown position) acts as a scatterer and the positioning device works in a radar-type mode without any cooperation from it. In these conditions, the round-trip time Tx-target-Rx is measured. This information will give access to the target locus. If two independent monostatic radar systems (i.e., with identical receive and transmit antennas) are used, the target locus can also be calculated from (6.6) replacing the time of flight by half of the round-trip time.

From the viewpoint of device complexity, it is easier to deal with multistatic radar arrangement consisting of one transmit element and a number of receive elements at different locations. Figure 6.9 demonstrates the simplest possible configuration.

Obviously, the measured round-tripe times τ_{p1} and τ_{p2} determine two ellipses; those focal points are determined by the locus of the transmit antenna and the loci of the corresponding receive antennas. Thus, the target position results from the intersection of both ellipses:

Tx-Rx1:

$$\left(\frac{x(t)+D/2}{a_1(t)}\right)^2+\left(\frac{y(t)}{b_1(t)}\right)^2=1, \tag{6.7}$$

Tx-Rx2:

$$\left(\frac{x(t)-D/2}{a_2(t)}\right)^2+\left(\frac{y(t)}{b_2(t)}\right)^2=1. \tag{6.8}$$

The length of the main axis $2a_i$ is given by the appropriate round-trip time τ_{pi},

$$2a_i(t)=s_0(t)+s_i(t)=c\tau_{pi}(t) \tag{6.9}$$

and the length of the minor $2b_i$ axis calculates from

$$\left(\frac{D}{2}\right)^2+b_i^2(t)=a_i^2(t). \tag{6.10}$$

Each of the two mentioned approaches, the active and the passive ones, has its specific advantages and disadvantages.

In the case of the active approach.

(i) the cooperation of the object to be localized is required,

(ii) an exact synchronization between transmitter and receiver is necessary unless a time-difference-of-arrival approach is applied. This would restrict the sophisticated demands on synchronization to the receivers only,

(iii) the signal could be made more easily detectable compared with the passive case,

(iv) covering of larger areas is possible (depending on the regulatory constraints on max emitted power).

In the case of the passive approach, there exist the following.

(i) There is no need for object cooperation. That is, the objects to be localized do not have to be equipped beforehand and the system is working in a noncooperative environment.

(ii) There are no synchronization problems since all system components can be mutually wired (at least in an experimental setup).
(iii) The precision of position is limited by the size of the target unless its scattering behavior is known and can be respected by solving the positioning equations.
(iv) The signal detection is quite more demanding due to interference with scattering at unwanted and mostly dominant objects.
(v) Compared to the active approach, the covered area is restricted due to higher path loss due to the double path length (transmitter target plus target receivers) necessary before detection.

Generally speaking, the precision of the positioning estimate depends heavily on the array geometry in connection with the actual locus of the target, the precision of the time delay estimator, and also on the design of the localizer unit provide a stable ultra-wideband sounding signal. In the case of passive approach, the scattering behavior of the target will also play a significant part in the detection and relative accuracy. Furthermore, appropriate antenna models and correction methods are needed if the required precision comes down to the antenna size or even below. As can be seen, the large bandwidth and good temporal resolution of UWB localization systems are an essential base for an accurate positioning calculation, but are not sufficient when the requirements call for extremely accurate devices.

6.7.2. Localization unit using ultra-wideband M-sequences

The theoretical calculation and system considerations done up to now are the basis for the design of an accurate antenna-array localization system, as used in our practical trials. The following section shortly considers the functioning of the UWB electronics used in the experiments and some related aspects. Besides a wide bandwidth, the UWB measuring system has to meet the following requirements:

(i) a high data-recording rate in order to be a match for the time variance of the target to be positioned,
(ii) a multichannel arrangement capability in order to provide data for 2D or 3D target localization,
(iii) a high degree of hardware configuration flexibility to adapt the system performance to the actual requirements of the individual user.

There are different possibilities to generate excitation signals covering a wide spectral band:

(i) chirp signals,
(ii) stepped sine wave,
(iii) short-impulse signals,
(iv) pseudorandom binary sequences and others.

However, not all of these signals are suitable to be used in the real-time localizing systems. For example, besides its cost, the network analyzer (stepped sine wave signals) can easily meet the UWB bandwidth demand (even if not the instantaneous bandwidth demands of the FCC regulations). But, although suitable

multichannel arrangements might exist, the real-time operation is prohibited by the slow measurement rate of typical network analyzers. Other systems, for example, the short-impulse- based systems, offer real-time operation but they are often subject to a higher susceptibility to jitter and drift.

The key to a powerful UWB localizer is the use of an appropriate stimulus signal because the whole device hardware and signal processing depend upon it. Some of the key points considering a suitable stimulus are the following.

(i) The stimulus must be an UWB signal that allows real-time operation. Sequentially stepped narrowband signals are not suitable because they prevent real-time operation due to the dead time during the system settling.

(ii) The stimulus must be generated in a stable manner by simple means up to several GHz bandwidth.

(iii) The stimulus must be periodic in order to apply cost-effective subsampling methods for signal recording and to avoid a spectral bias error. It should be allowed to work with a certain degree of subsampling without loss of data due to the time variation of the channel.

(iv) The stimulus must have a low crest factor. The crest factor is defined by the ratio between the RMS value and the peak value of a signal. Low crest factor signals distribute their energy uniformly over the time. This maximizes signals energy even at low peak voltages. However, impulse compression (e.g., by correlation) is required in order to gain the impulse response on which the delay-time estimation is based. Impulse compression further improves the SNR due to the correlation gain.

(v) The stimulus must follow the FCC rules concerning the covered frequency band and restrictions on power emission.

A family of signals that meets most of these strict requirements is formed by the pseudorandom binary sequences, for example, M-sequence (maximum-length binary sequence—MLBS) . An M-sequence can be easily generated up to dozens of GHz of bandwidth via a digital shift register, which is clocked by a stable single-tone RF oscillator. Besides the advantage of having a reasonable correlation gain, the M-sequence signals are characterized by small binary voltage amplitudes that allow extremely fast digital switching in integrated circuit technology to meet the demanding requirements on bandwidth and low jitter.

Figure 6.10 shows one channel of the UWB localizer, which was used for the positioning experiments. It is working in the baseband covering the spectral band from DC up to $f_c/2$. Controlled by a single tone clock, a digital shift register generates the M-sequence. Since the M-sequence signal is periodical and the measurement scenario can be assumed to be locally stationary, it is possible to acquire the MLBS signal by an undersampling approach. Here, the binary divider (2^m) determines the undersampling factor and provides the receiver sampling clock. The measurement data are captured by a track-and-hold circuit (T&H), transformed into the digital domain (ADC), optionally synchronously averaged (p is number of averages), and finally stored (MEM) for offline processing or online processing (DSP).

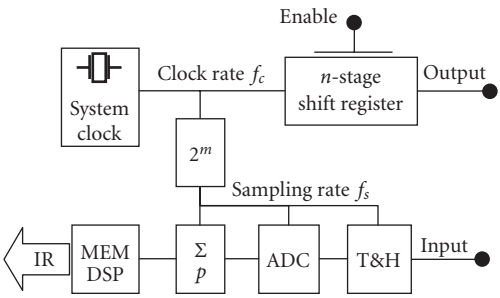

Figure 6.10. Basic block diagram of the UWB RF interface.

As mentioned above, the impulse response (IR) results from an impulse compression, which is performed by the fast Hadamard-transform (FHT). The FHT-algorithm is very close to a fast Fourier transform algorithm except that it is based on a pure summing of data samples, which promises very fast operation in a custom hardware implementation.

The architecture illustrated in Figure 6.10 represents only one channel of the UWB localizer. For the position estimation (2D, or 3D), a multichannel arrangement is necessary. As seen from Figure 6.10, the circuits for signal generation and signal capturing have a very simple structure. Since it is built from cost-effective large-scale components or custom integrated circuits, minimizing the number of components is not a fundamental target for the overall system. With this consideration, it looks possible to build a true multichannel and multiarray UWB locationing system at reasonable cost.

Figure 6.11 shows one possibility of a multichannel UWB localizer architecture. In this version, all receiving channels work continuously in parallel providing the shortest measurement time. The transmitter modules work sequentially in time by activating only one shift-register output per measurement cycle. Thus, the overall measurement time increases with the number of transmitter channels and does not depend on the number of receiver channels. It should be noted that usually even one single transmitter is sufficient for most localizers applications.

In order to meet the FCC rules completely with the M-sequence approach, the operational band has to shift to the range from 3 to 10 GHz approximately. Figure 6.12 represents a possible schema of such accurate measurement device. It is based on a homodyne concept, which allows for operation in arbitrary bands. Additionally, the usable bandwidth doubles compared to the baseband concepts shown earlier and it corresponds now to the clock rate of the shift register.

The system used for experiments of extremely accurate positioning was an M-sequence multichannel UWB device [20, 21] operating in the frequency band from DC up to 5 GHz . It was built from custom integrated circuits in SiGe:C-technology (shift register, binary divider, and T&H) that have been designed at Ilmenau University of Technology in cooperation with MEODAT.

The extremely linear time axis and the superior jitter and drift behaviour (compared to traditional sequential sampling oscilloscopes) are the result of the

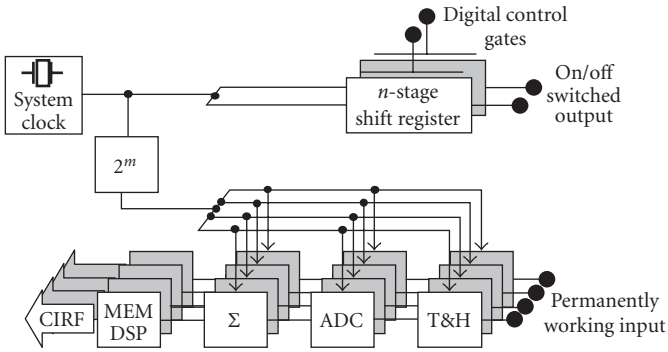

FIGURE 6.11. Multichannel UWB localizer.

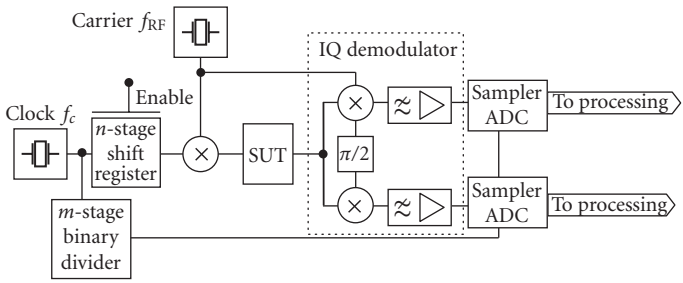

FIGURE 6.12. Extended UWB localizer for operation at arbitrary frequency bands. The scenario under test (SUT) covers the antennas and the propagation path.

synchronous digital controlled sampling. The DSP module of the described experimental systems is based on standard off-shelf PCB products. The ADC was a 12-bit-video ADC and the sampling frequency was 17.68 MHz (depending on the adjusted undersampling factor). An example of the complete RF electronics of a device with 3 transmitter units and 4 receiver units is illustrated in Figure 6.13.

Initially, the UWB electronic components were developed for a mine-detection radar. Due to its sufficient large ambiguity range, it could also be used for very accurate positioning purposes. Since the transmit and receive units are jointly designed on one board, the system is better suited for passive positioning tasks than for active one. Nevertheless under laboratory conditions, it can also be applied to analyze the active approach by connecting the moving antennas via long cables.

6.7.3. Experimental results

The experimental UWB system described in the previous section can demonstrate the potential performance expressed in terms of the range resolution and precision of the 2D/3D position estimation using both an active and a passive approach.

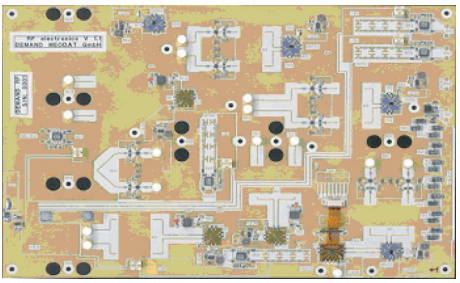

FIGURE 6.13. Experimental UWB localizer RF electronics (courtesy of MEODAT GmbH Ilmenau).

Range estimation. The accuracy of the range estimation is the most critical parameter of a positioning procedure. A first experiment demonstrated the excellent range resolution of an UWB system under idealized propagation conditions. The expression describing the typical range resolution in transmit and back-scatter mode, respectively, is given by

(i) transmit mode (active approach):

$$\delta_{Rt} \approx \frac{c}{B}; \tag{6.11}$$

(ii) back-scatter mode (passive approach):

$$\delta_{Rs} \approx \frac{c}{2B}, \tag{6.12}$$

where c represents the speed of propagation of radio waves (assumed equal to the speed of light) and B the bandwidth of our system.

A positioning device having a bandwidth of about 5 GHz (as in the case of this example) provides a range resolution of $\delta_{Rt} = 6$ cm (active approach) and $\delta_{Rs} = 3$ cm (passive approach) according to (6.11) and (6.12). But this range resolution can be drastically improved by exploiting super-resolution techniques, on the condition that there is some knowledge about the expected received signal. The following example will show how accurate an UWB system can be made beyond the natural range resolution. In a simple experiment, the transmitter and receiver were connected through a mechanical delay line allowing 200 μm distance adjustments. The standard deviation of the mechanical distance adjustment was estimated to between 50 and 100 μm. Thirty eight measurements were taken at different delays adjusted by the delay line (20 measurements with 200 μm delay increments, 9 measurements with 2 mm delay increments, and 9 measurements with 2 cm delay increments). Since the variable (perfect) delay line does not affect the time shape of the propagating wave, the temporal pulse position can be estimated by means of a high-resolution maximum-likelihood (ML) estimator as used for wideband channel sounding [22]. Beside the noise, the only unknown signal which degrades the resolution was initiated by the cross-coupling within the RF electronics. Intentionally, this was not removed from the measurement signal with a prior calibration.

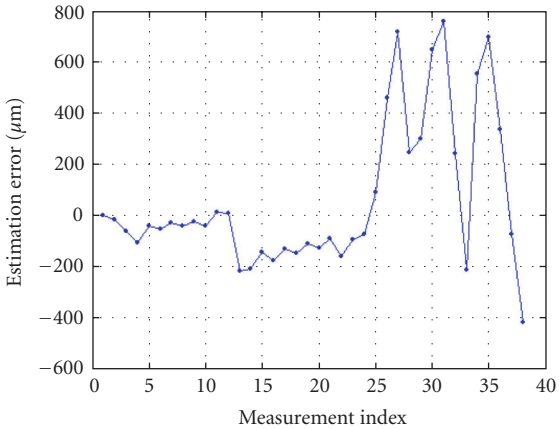

Figure 6.14. Error in the distance estimation with the experimental multiarray UWB system.

The estimation error resulting from this experiment is presented in Figure 6.14. It can be seen that for small delay steps (first 20 scans), the total positioning estimation error is well below 200 mm. This is more than 300 times better than predicted by (6.11). It is to be noted also that the total error covers the error of the delay estimation as well as the mechanical adjustment error. The error increases at larger delay increments since the cross-coupling gains more power on the overall signal. By respecting the cross coupling signal, the estimation error can be reduced and kept constant for different delay increments.

This experiment indicates that a quite high precision can be achieved if the transmit signal is known by the processing unit and altered by the propagation. This is close to the case of a real transmission in the active approach mode under line-of-sight conditions, provided that the impulse response function of the involved antennas is independent from the radiation angle (which is not easy to guarantee). In any other nonideal case, the resolution will degrade in function of how much information is missing from the target. Some of the elements that will make difficult the development of a very precise positioning system are

(i) non-line-of-sight propagation conditions (radiation through walls, edge diffraction, diffraction at wires, tubes colons, etc),
(ii) back scattering from objects of limited size (passive approach) except for purely specular scattering which only changes the sign of the amplitude but not the signal shape,
(iii) angle-dependent radiation behavior of the antennas.

2D position estimation. The experimental multi-array UWB system introduced in the previous section has also been used for further accuracy testing. The following two examples demonstrate the UWB localizer ability to estimate 2D object position using both the passive and active positioning techniques. In both cases, the objects to be tracked were mounted on a positioning unit [23] in order to have a

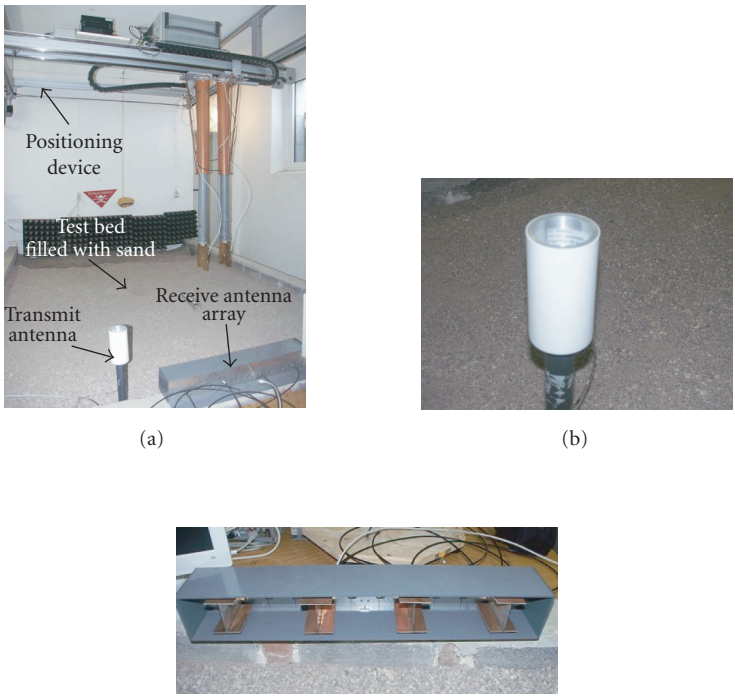

FIGURE 6.15. (a) Experimental positioning device in the measurement laboratory and (b), (c) pictures of the antennas used in the measurements ((c) the Vivaldi antenna array and (b) the biconical antenna).

precise reference for error determination. The maximum inaccuracy of the positioning system was quantified in 0.75 mm for all axis within an area of 2 meters by 4 meters. Continuous sweeps can be carried out with a maximum displacement speed of about 130 mm/s in the x-direction and 170 mm/s in the y-direction, respectively. The measurement laboratory with the positioning test bed and antenna arrays used for the experiments can be seen in Figure 6.15. The scanner was mounted at the ceiling level above a sandbox since its original purpose was radar imaging of buried objects.

The objects were moved along a predefined track (corner points in m: $[0;0]$, $[0;2.5]$, $[0.8;2.5]$, $[0.8;1.5]$, $[-0.9;1.5]$, and $[-0.9;0]$) with the maximum velocity allowed by the positioning unit. The data was collected and processed by the UWB localizer described above. The measurement rate was reduced to about 11 scans per second which was sufficient given the slow movements. The whole measurement lasted about 90 seconds. A linear antenna array containing four Vivaldi antennas was used for receiving and a biconical omnidirectional antenna (Figure 6.15) was introduced as the transmit antenna (for both active and passive approaches).

Passive approach. In the case of passive positioning approach, the object was a metal box of the size 0.5 m × 0.5 m × 0.1 m. The radiation pattern of the box was not taken into account. Thus, the positioning accuracy is comparable only with the box size since its radiation pattern (and by that, the shape of the back-scattered signals) is strongly angle-dependent. The result of the positioning using the ML based estimator is illustrated in Figure 6.16(a). The solid line represents the actual object track. The estimated positions are represented by dots. Obviously, there are some differences between the two tracks, but the accuracy was very good. The main cause of positioning errors was the scattering behavior of the tracked object.

Active approach. In the case of active positioning, the metal box was replaced by the biconical antenna, which was connected via a long cable with the positioning device. Thus problems of the transmitter-receiver synchronization were neglected.

The estimation results using the ML-based estimator are displayed in Figure 6.16(b). Here, the estimated positions follow the real track much better than it was in the case of the passive approach. The main reason was that the radiation center of the antenna used in the second experiment was well defined (note, this will change by going into the third dimension), and thus the shape of the LOS signal was not varying. The standard deviation of the position error of the second experiment was about 1.5 cm in both x- and y-directions. The maximum error of azimuth angle ranged about one degree.

3D position estimation. The Technical University of Ilmenau experimental UWB multiarray test bed was also used for 3D positioning measurements. An example of 3D positioning is illustrated in Figure 6.17. Here, the transmit antenna was moved by hand in the air writing the year "2003." The dotted line represents the estimated positions. In the right part of the figure, the written track is zoomed out. To improve the understanding, the contours of the laboratory space (big cube) and the sandbox (smaller cube) were added to the picture.

The technical description and practical experiments shown in this paragraph provide a useful reference to understand the potential precision of UWB multiarray positioning systems. Even if some limits are registered in practical situations, the test bed designed by the Technical University of Ilmenau and MEODAT clearly shows that UWB multiarray active localization units can be the solution to the problem of extreme accuracy, when resolution to the level of 1 cm is needed.

6.8. Systems integration and UWB positioning technology

When considering deployment of UWB location technology across a large area (such as that shown in Figure 6.18), it is important to consider the system-level issues associated with such deployments (as opposed to the technical issues related to individual ranging or angle measurements). If systems-level issues are not dealt with adequately in the design of the location sensor, performance will suffer, especially as the system scales beyond the simplest configurations.

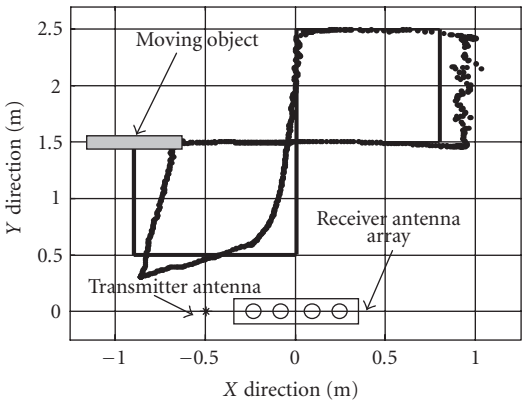

(a)

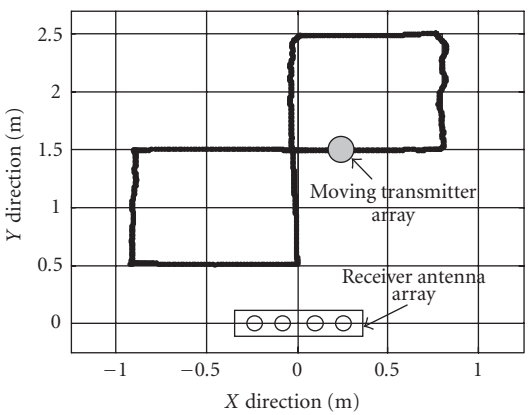

(b)

FIGURE 6.16. (a) Results of the 2D position estimation with a passive approach; (b) results of the same estimation with an active approach.

6.8.1. The role of infrastructure

The organization of the location system, and in particular the role of infrastructure within it, governs many of the system-level design decisions. Two distinct system organizations are frequently discussed—infrastructure-based and ad hoc. Infrastructure-based location systems involve a static set of equipment whose purpose is to support the tracking of a population of mobile devices. In ad hoc systems, on the other hand, the devices to be located also perform the function of locating other devices—the devices interacting in the system do not necessarily *have* to be mobile, but the location system has the property that if they are moved, then the system will continue to operate correctly.

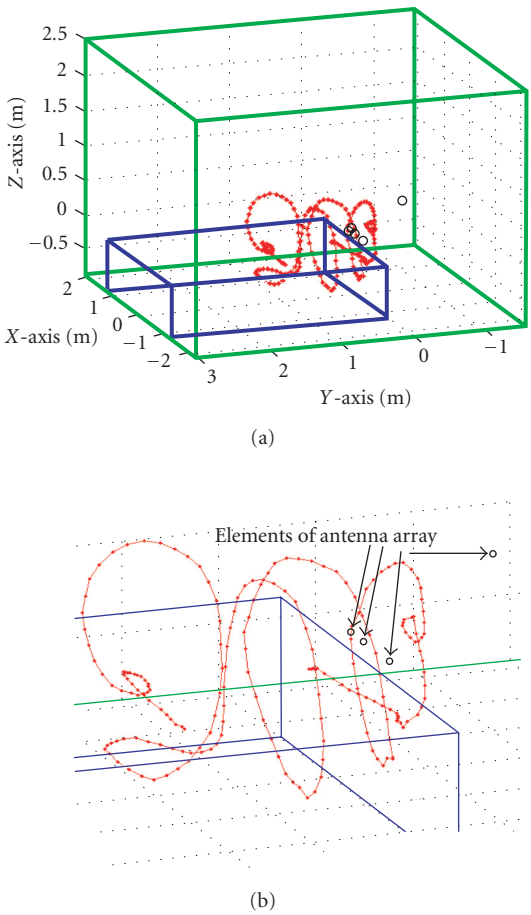

FIGURE 6.17. (a) The 3D position estimation with active approach; (b) a detailed view.

Each of these two system organizations has advantages and disadvantages. There is clearly a cost involved in installing infrastructure within an environment. However, this cost can be reduced by an appropriate design (quantified before the system is installed), and a properly designed infrastructure which will have minimal maintenance requirements once installed. Fixed infrastructure also lets the system designers give predictions and guarantees about system performance and give users confidence that the system will be robust. Furthermore, in many environments where UWB location technology will be deployed, infrastructure is already accepted. Hospitals and offices, for example, have substantial infrastructure in the form of electrical wiring, air conditioning, pipework, telephone cabling, computer networking, and so on. In these target environments, there already exist well-developed processes for managing infrastructure, and it is likely that similar processes can and will be used to support installed location sensor technology.

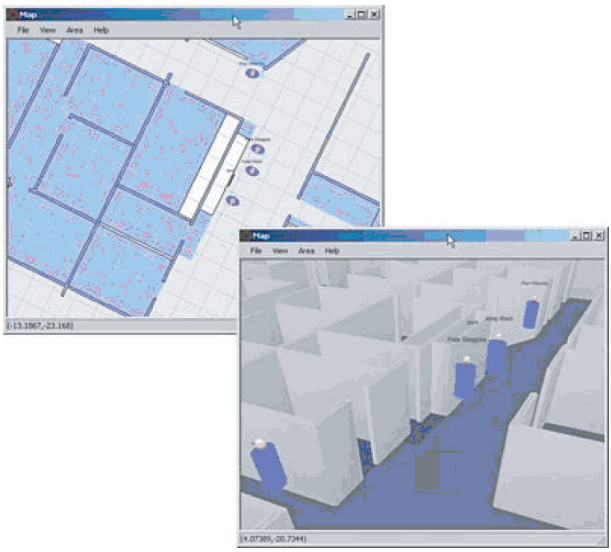

FIGURE 6.18. Example of Ubisense smart localization in a complex office infrastructure.

Of course, some environments, such as denied territory during warfare, may not be amenable to the deployment of sensor infrastructure. Proponents of ad hoc systems architectures point to applications in these environments as being well suited to ad hoc techniques. On the other hand, systems with ad hoc architectures can be more unpredictable—the system performance at any particular point in time will depend on the current physical organization of the system (because of effects like geometric dilution of precision, discussed earlier in this chapter). Consequently, ad hoc systems do not have an *inherent* cost of deployment, but may involve a significant maintenance cost if a minimal level of performance must be guaranteed over time.

6.8.2. Surveying techniques

All the positioning techniques discussed in this chapter involve determining the location of a mobile object by measuring properties such as its range or bearing from points in space which are already known. Surveying of sensors is therefore an important step in the deployment of any location system, because a poor survey will result in poor accuracy during operation.

Infrastructure-based location systems involved fixed sensor components, which must be surveyed only once (to create survey maps such as those shown in Figure 6.19). It will normally be possible to complete the survey using equipment which would not normally be considered for the location task because of constraints of cost, size, power, and so on. For example, an infrastructure-based UWB location system might be surveyed with a laser total station, a tripod-mounted device that uses two-way laser ranging to measure the position of a point in 3D

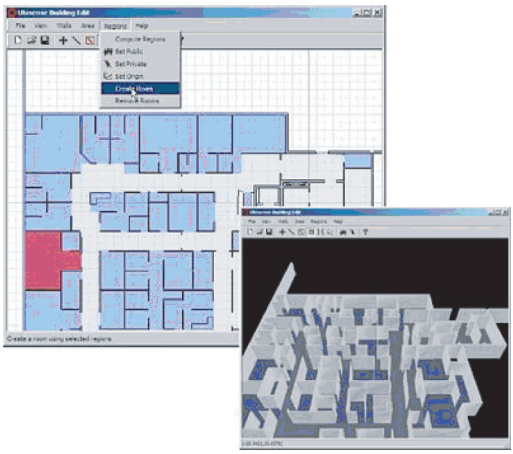

FIGURE 6.19. 3D mapping of building infrastructure.

space to an accuracy of one or two millimeters. A laser total station would be totally impractical as a sensing tool for many tracking applications—although it is very accurate, it is power-hungry, line of sight only, large, and fragile—but its use (once) to survey the system enables the known points to be located very accurately.

It is also possible to survey UWB location systems using measurements of tracked devices which have been placed at known points in space—in effect, "self-surveying" the system by applying the nonlinear models discussed earlier in this chapter in reverse. Of course, location systems with ad hoc architectures must rely on these techniques, because they cannot depend on an external surveying mechanism to operate if a component of the system moves. Although these approaches are theoretically attractive, the limited accuracy of UWB location systems (when compared to technologies such as laser total stations) leads to worse survey accuracy, and hence worse operational accuracy.

Whichever survey route is taken, the surveying process must be robust to the effects of geometric dilution of precision (as described earlier) and multipath, which both introduce into the surveyed position systematic errors which cannot be mitigated by simple averaging.

6.8.3. System scalability

A sensor system deployed across a large building such as a hospital could involve very high aggregate data rates, potentially up to tens of thousands of events per second. At the same time, several applications may be running simultaneously on top of the common sensor infrastructure—for example, a hospital may want applications for security, office productivity, and intelligent building infrastructure, in addition to specific healthcare applications. Furthermore, many of those

applications, such as the smart space applications mentioned previously, could demand real-time performance.

Maintaining low latency in a system whilst processing and distributing large volumes of location information represents a significant challenge. Centralized approaches to data management, such as those used by traditional Geographic Information System (GIS) databases are unlikely to be sufficiently scalable, and distributed system techniques must be used to partition the data processing and transfer tasks. These methods will likely be used in any case to support multiple applications that share the same sensor system, and to integrate the sensor system and location management platform with other software systems in the target environment.

6.8.4. Sensor independence

Whichever variety of UWB technology is used to implement a large-scale sensor deployment, it is desirable to make the applications of the system and the particular sensors being used independent of one another . By separating these components of the system, it becomes possible to replace the underlying sensor system without requiring significant (and costly) changes to the applications themselves. Changes in the fundamental sensor system may become desirable as UWB technology matures and the regulatory landscape changes.

The Ubisense system described earlier, as an example, employs a location-aware middleware layer to isolate applications and sensors. One of the middleware's tasks is to convert the raw location information from the sensor system (which will tend to have sensor-specific characteristics) into application-relevant but sensor-independent spatial facts (such as "The user is standing in front of the workstation."). By writing code which only deals with sensor-independent spatial relationships, developers can ensure that their applications are future-proofed against changes in the sensor technology further down the system stack.

Bibliography

[1] A. Harter, A. Hopper, P. Steggles, A. Ward, and P. Webster, "The anatomy of a context-aware application," in *Proceedings of 5th ACM/IEEE International Conference on Mobile Computing and Networking (MOBICOM '99)*, pp. 59–68, Seattle, Wash, USA, August 1999, ACM Press.

[2] I. A. Getting, "Perspective/navigation—The Global Positioning System," *IEEE Spectrum*, vol. 30, no. 12, pp. 36–38, 43–47, 1993.

[3] G. J. Sonnenberg, *Radar and Electronic Navigation*, Butterworths, London, UK, 1998.

[4] G. M. Djuknic and R. E. Richton, "Geolocation and assisted GPS," *IEEE Computer*, vol. 34, no. 2, pp. 123–125, 2001.

[5] D. Porcino, "Location of third generation mobile devices: a comparison between terrestrial and satellite positioning systems," in *IEEE 53rd Vehicular Technology Conference (VTC '01)*, vol. 4, pp. 2970–2974, Rhodes, Greece, May 2001.

[6] P. Bahl and V. N. Padmanabhan, "RADAR: an in-building RF-based user location and tracking system," in *Proceedings of 19th Annual Joint Conference of the IEEE Computer and Communications Societies (INFOCOM '00)*, vol. 2, pp. 775–784, Tel Aviv, Israel, March 2000.

[7] Ekahau Incorporated website, 2005, http://www.ekahau.com/.

[8] WhereNet website, 2005, http://www.wherenet.com/.

[9] C. Lanzl and J. Webb, Position Location Finds Applications. Wireless System Design, June 1998.

[10] Bluesoft Incorporated website, 2001, http://www.bluesoft-inc.com/.
[11] R. Want and D. M. Russell, "Ubiquitous electronic tagging," *IEEE Distributed Systems Online*, vol. 1, no. 2, 2000.
[12] Wavetrend Technologies Limited website, 2005, http://www.wavetrend.net/.
[13] Federal Communications Commission (FCC), "Revision of Part 15 of the commission's rules regarding ultra-wideband transmission systems," *First Report and Order*, ET Docket 98-153, FCC 02-8, adopted/released February 14/April 22, 2002.
[14] Ubisense Limited website, 2005, http://www.ubisense.net/.
[15] D. Porcino and A. Yule, "Positioning Technology for cellular mobile devices," in *IEEE Vehicular Technology Conference (VTC '01)*, Rhodes, Greece, May 2001.
[16] H. Saarnisaari, "TLS-ESPRIT in a time delay estimation," in *IEEE 47th Vehicular Technology Conference (VTC '97)*, vol. 3, pp. 1619–1623, Phoenix, Ariz, USA, May 1997.
[17] M. Feder and E. Weinstein, "Parameter estimation of superimposed signals using the EM algorithm," *IEEE Transactions on Acoustics, Speech, and Signal Processing*, vol. 36, no. 4, pp. 477–489, 1988.
[18] R. J. Fontana and S. J. Gunderson, "Ultra-wideband precision asset location system," in *Proceedings of IEEE Conference on Ultra Wideband Systems and Technologies*, pp. 147–150, Baltimore, Md, USA, May 2002.
[19] S. J. Gunderson, R. Scholtz, K. Chugg, et al., "Shipboard Environment Characterization," Appendix A, Technical Report: Naval Total Asset Visibility Tests on the USS Curtiss, Port Hueneme, CA, 25 December–6 October 2000.
[20] M. Roßberg, J. Sachs, P. Rauschenbach, et al., "11 GHz SiGe circuits for ultra wideband radar," in *Proceedings of Bipolar/BiCMOS Circuits and Technology Meeting*, pp. 70–73, Minneapolis, Minn, USA, September 2000.
[21] J. Sachs, P. Peyerl, and M. Roßberg, "A new UWB-principle for sensor-array application," in *Proceedings of 16th IEEE Instrumentation and Measurement Technology Conference (IMTC '99)*, vol. 3, pp. 1390–1395, Venice, Italy, May 1999.
[22] A. Richter, M. Landmann, and R. S. Thoma, A Gradient Based Method for Maximum Likelihood Channel Parameter Estimation from Multidimensional Channel Sounding Measurement, XXVIIth URSI General Assembly, Maastricht, NL, pp. CD, August 2002.
[23] R. Zetik, J. Sachs, and B. Schneegast, "Non-destructive testing with imaging radar: first experience with a laboratory equipment," in *Proceedings of Internationales Wissenschaftliches Kolloquium (IWK '98)*, vol. 3, pp. 317–322, Ilmenau, Germany, September 1998.

Domenico Porcino: Philips Research Laboratories, Cross Oak Lane, Redhill, Surrey RH1 5HA, UK
Email: porcino@iee.org

Jürgen Sachs: Technical University Ilmenau, 98684 Ilmenau, Germany
Email: jurgen-sachs@gmx.de

Rudolf Zetik: Technical University Ilmenau, 98684 Ilmenau, Germany
Email: rudolf.zetik@tu-ilmenau.de

Andy Ward: Ubisense, St. Andrews House, 90 St. Andrews Road, Cambridge CB4 1DL, UK
Email: andy-ward@ubisense.net

7 Regulation and standardization

Christian Politano, Walter Hirt, Nils Rinaldi,
Gordana Drakul, Romeo Giuliano, and Franco Mazzenga

7.1. Introduction

Ultra-wideband (UWB) radio techniques have been extensively described in the previous chapters, and we emphasize in this section the most fundamental parameter that characterizes UWB radio, which is the capability of UWB devices to operate over a very large frequency range (several GHz bandwidth).

Since typical UWB radio may use spectrum already assigned to operative primary or secondary radio services, UWB radio devices—despite their extremely low transmission output power—may be a potential source of interference for incumbent radio services, and should provide the ability to coexist with legacy radio services.

In this section, we provide the reader with a comprehensive description of the worldwide UWB regulation and standardization framework under completion in order to elaborate novel and effective means of spectrum management based on coexistence mechanisms, instead of using conventional frequency-sharing mechanisms.

The first section, dedicated to regulation aspects, is introducing the UWB regulation framework elaborated under ITU-R to allow UWB devices, in particular UWB communication and positioning applications, to operate without requirement for individual right to use radio spectrum ("license-exempt") and on a "no protection, no harmful interference" basis. Then a detailed overview on the European regulation framework is provided to explain how prudent but constructive regulation rules are elaborated in this region.

The second section presents a UWB standardization overview in the USA and in Europe. It provides the global overview of IEEE working groups mandated for wireless personal area network (WPAN) including high-data-rate (IEEE802.15.3a) and low-data-rate (IEEE802.15.4a) communication applications, and introducing the most popular UWB technology candidates identified during the year 2004. The European standardization process is also presented in this section with an overview of the ETSI-TG31 task group mandated by the ECC for the definition

of "harmonized standards for short-range devices (SRDs) using UWB technology."

The last section describes a methodology applicable to "compatibility studies" for evaluating UWB interference risks with incumbent radio services. It provides some results of compatibility studies conducted for a few coexistence scenario between UWB and UMTS, fixed services. The particular interest in this section is the description of the UWB characteristics impacting compatibility studies (activity factors, traffic characteristics, radio access modes), and how interference risks may be reduced by applying these features, allowing incumbent radio receivers to coexist with UWB devices.

The results of such compatibility studies have been used for the elaboration of interference mitigation techniques (proposed for standardization) in order to specify coexistence mechanisms to reduce UWB interferences with incumbent radio services.

7.2. Regulation

7.2.1. Introduction

The FCC's (Federal Communications Commission) introduction of rules in early 2002 in the USA to authorize ultra-wideband (UWB) radio devices to be deployed and marketed as "unlicensed devices" has generated studies and considerations of radio spectrum implications within many administrations around the world. As a result, the ITU-R (International Telecommunication Union-Radiocommunication Sector) created Task Group 1/8 (TG 1/8) to study UWB radio coexistence issues.

As a technology, UWB does not fit into a classical radio regulatory process, which is based on the allocation of dedicated spectrum bands for the different radiocommunication services. Since UWB radio signals spectrally overlap with frequency bands occupied by other services, the incumbent spectrum users are concerned about possible interference effects from single UWB devices. In addition, concerns exist about the cumulative effect of UWB signals (aggregated power) by raising the background noise for the different radiocommunication services.

The regulatory process driven by the work program within ITU-R TG 1/8, initially intended to be completed by end of 2004, has been extended to 2005 with the objective to complete an ITU recommendation for international UWB regulation before the end of 2005.

Figure 7.1 provides an overview of the selected frequency bands for short-range devices using UWB radio technologies. While the frequency band below 1 GHz will be only allocated to UWB devices deployed within the USA, the frequency band between 3.1 to 10.6 GHz is intended to become the common band allocated to UWB radio devices on a worldwide basis. Thus, the band between 3.1 to 10.6 GHz is of most interest for short-range communication devices. In the medium term, the main emerging application will be wireless personal area networks (WPANs) offering high data rates of up to 480 Mbps, for which a standardization process is already well engaged (IEEE802.15.3a). UWB radio is

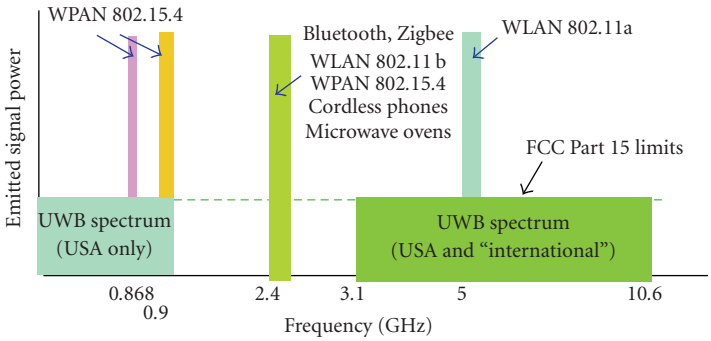

Figure 7.1. Proposed frequency bands for UWB radiocommunication devices.

also providing advantages for future WPAN enabling low-data-rate applications featuring location-tracking capability; for this type of UWB devices, technical proposals have been submitted and a selection process has started within the IEEE803.15.4a Standardization Group. Furthermore, there exist research programs considering broadband evolutions towards data rates of 1 Gbps and beyond.

In the light of the large application potential of UWB radio technology and the broad interest from the wireless industry worldwide, intensive efforts towards a globally compatible UWB regulation have started. In particular, regulatory work has started to investigate all potentially affected radiocommunication services. Under this harmonization process, the initial studies by the FCC are being extended within the ITU, the CEPT (European Conference of Postal and Telecommunications Administrations) in Europe, and by the Japanese as well as other Asian regulatory bodies.

In the following, a specific focus is provided on the regulatory status within the ITU-R and the European regulation work within CEPT, where a specific UWB Task Group 3 (TG3) has been created under a mandate issued by the European Commission. This mandate orders the CEPT to undertake all necessary work to enable identification of the most appropriate technical and operational criteria for the harmonized introduction of UWB radio applications in the European Union.

7.2.2. Worldwide status—International Telecommunication Union

In July 2002, the Study Group 1 (SG1) of the Radiocommunication Sector of the ITU (ITU-R) decided to form a Task Group 8, named ITU-R TG 1/8, to carry out relevant studies to answer two questions (ITU-R 226/1 and ITU-R 227/1) adopted by SG1 on ultra-wideband technology.[1] These questions concern the proposed introduction of UWB devices and the implications of compatibility with radiocommunication services:

[1]International Telecommunication Union (ITU), Report of the second meeting of Task Group 1/8, Geneva, 27–31 October, 2003.

(i) Question 226/1: spectrum management framework related to the introduction of ultra-wideband (UWB) devices;
(ii) Question 227/1: compatibility between ultra-wideband (UWB) devices and radiocommunication services.

The work load within ITU-R TG 1/8 was divided among four working groups:

(i) WG-1: UWB characteristics (Questions 226/1 and 227/1);
(ii) WG-2: UWB compatibility (Question 227/1);
(iii) WG-3: spectrum management framework (Question 226/1);
(iv) WG-4: measurement techniques (Decision 1/95).

The deliverables expected from these working groups have been defined as follows [1]:

(i) ITU-R recommendation on the characteristics of UWB;
(ii) ITU-R recommendation(s) addressing compatibility between UWB and radiocommunication services;
(iii) ITU-R recommendation providing guidance to administrations on a spectrum management framework for UWB;
(iv) ITU-R recommendation on measurement techniques for UWB.

For each ITU-R TG 1/8 meeting, the Chairman issues a report (e.g., see [1]) with a number of annexes produced by the working groups listed above. Thus far, these documents must be considered continued working documents of a technical nature from which—at this time—no final conclusions can (or should) be drawn. However, from the material available thus far, it is evident that particularly the UWB compatibility issues dealt with in WG-2 pose key working and discussion areas. For example, similar to within CEPT/ECC-TG3, a major discussion point in TG 1/8 is to what extent coexistence-related results based on relevant field measurements should be admitted into the technical documents to allow verification and "calibration" of theoretical results obtained from corresponding (worst-case) modelling studies. As a result of these ongoing debates and other types of work, it has been recognized that the four originally planned meetings of ITU-R TG 1/8 until end of 2004 will not suffice to complete the work as anticipated. At its third meeting in June 2004 in Boston, USA, the leadership of TG 1/8 already indicated that a total of at least up to seven TG 1/8 meetings will be necessary to produce the final deliverables. Thus, final globally applicable recommendations for UWB radio as worked out by ITU-R TG 1/8 should not be expected before the end of 2005.

7.2.3. European regulatory process

The precedence set in the USA by the FCC in early 2002 has stimulated some considerable activities and to some extent competitive pressure in Europe to establish a similar ruling for the deployment and use of devices based on UWB radio technology (UWB-RT). The European regulatory process started in early 2000 inspired by the FCC's proposal for regulating UWB devices as adopted on May 10, 2000. A number of interest groups and industrial parties have been active in the last few

years to assess and verify potential interference issues between UWB devices and existing radio services. In this context, two main organizations are particularly relevant in Europe:

(i) CEPT (European Conference of Postal and Telecommunications Administrations) focused on the harmonization of telecommunications regulations across its member countries;

(ii) ETSI (European Telecommunications Standards Institute) created in 1988 by the CEPT as a new organization to which its telecommunication standardization activities were transferred.

However, as of this writing (late 2004), given the innovative and somewhat disruptive nature of UWB-RT, significant work in the areas of UWB device characterization, measurement techniques, compatibility, as well as frequency management and regulation is still pending. Whereas some experts still question the interference potential of a single UWB signal source in a typical home or office environment, many others express great concerns should UWB devices proliferate and become truly ubiquitous. It is feared that the simultaneous operation and aggregation of a large number of UWB transmitters within a confined area may pose a significant risk of harmful interference to incumbent radiocommunication services, such as for navigation, rescue and communications, fixed wireless access services, and even radio astronomy. The industrial UWB community spends great efforts to address these legitimate concerns by proposing and designing systems that prevent interference under all practical and reasonable conditions. However, only a large research effort and scrutinizing analysis and, in particular, measurements will be able to help establish the most appropriate set of rules for this very low-power and yet disruptive spectral underlay technology. In Europe, efforts are under way to assess and define the required protection measures for all potentially affected services, for example, fixed wireless access (FWA) within the bands 3.5 GHz, 3.6–4.2 GHz, 4.4–5.0 GHz; cellular systems in the bands 915 MHz, 1800–2100 MHz; space scientific services with bands 406–406.1 MHz, 1400–1427 MHz, 1544–1545 MHz, 5250–5460 MHz. In particular, relevant field measurements that will help assess various pending issues on coexistence between UWB radio devices and existing active and passive radio systems or services are pending. Such measurement campaigns will allow to assess the validity of results already obtained from corresponding theoretical (worst-case) modelling studies involving single and multiple UWB radio devices and incumbent radio services. The inclusion of results based on actual measurements into the regulatory decision process may help define a globally compatible European regulatory framework for UWB radio, which accommodates both the incumbent radio services and the deployment of technically and economically viable UWB radio applications. The UWB radio regulatory process in Europe is mainly driven by Task Group 3 (TG3) of the Electronic Communications Committee (ECC) within the European Conference of Postal and Telecommunications Administrations (CEPT) and Task Groups 31A and 31B (TG31A/B) of the European Telecommunications Standards Institute (ETSI). Historically, CEPT was founded on 26 June, 1959, in Montreux,

Switzerland, uniting 19 administrations from Western Europe; today, CEPT encompasses 46 European countries and one of the key achievements of CEPT was the establishment of ETSI in 1988.[2] CEPT and ETSI are both working on UWB radio matters under respective mandates issued to them by the European Commission [2, 3].

In particular, the recent mandate to CEPT is an order to identify the conditions relating to the harmonized introduction in the European Union (EU) of radio applications based on UWB-RT, that is, "*... pursuant to Art. 4 of the Radio Spectrum Decision, CEPT is mandated to undertake all necessary work to identify the most appropriate technical and operational criteria for the harmonized introduction of UWB-based applications in the European Union*" [2]. Among other reasons, the EC provides the following justification for this mandate: "*UWB technology may provide a host of applications of benefit for various EU policies. However, its characteristic broad underlay over spectrum already used by other radio services may also have an impact on the proper operation of radio services of significance for the successful implementation of EU policies. It is therefore important to establish conditions of the use of radio spectrum for UWB which will allow UWB to be introduced on the market as commercial opportunities arise, while providing adequate protection to other radio services.*" As explained below, in response to the EC mandate, the CEPT has reorganized their ongoing UWB work in a new task group (ECC-TG3).

The earlier EC mandate forwarded to ETSI calls for *harmonized standards covering ultra-wideband (UWB) applications* and derives from the *R&TTE Directive* which defines the essential requirements equipment must meet to be placed on the market and to be put into service for its intended purpose [3]. The mandate points out that "*... as a technology, UWB radio does not fit in the classical radio regulatory paradigm, which bases itself on a subdivision of the spectrum in bands and allocated for specific usage(s).*" A stipulation of the mandate is to align the work with equivalent activities within the ITU and ISO/IEC while due account should be taken of (draft) regulations adopted in other economies, so as to ensure a global market for UWB devices.

At the seventh CEPT/ECC meeting held in Vilnius, Lithuania, on 15–19 March, 2004, a decision based on the European Commission's "UWB mandate" issued to CEPT resulted in the final approval of engaging in the work required for the "harmonization of frequency bands for UWB applications." The plenary session decided consequently to establish a specific task group to report to the ECC, called Task Group 3 (ECC-TG3), which will take charge of the respective developments. The ECC's working methods were also modified accordingly to reflect the principle that all ECC documents that are meant to respond to Commission mandates need to be approved by part of the ECC plenary session.

[2]ETSI has a memorandum of understanding with CEPT, which allows ETSI to (a) provide direct input to most of the drafting groups (project teams) of the ECC, and (b) give an indication of the balance of views among ETSI members to the working groups; this function is carried out by the ETSI liaison officer.

7.2.3.1. Radio spectrum management in Europe

In Europe, radio frequencies are administered on a national basis, where national administrations cooperate via CEPT and in particular the Electronic Communications Committee (ECC), which is administered by the European Communications Office (ECO). The ECC publishes decisions and recommendations to be followed by national administrations in making their national frequency regulations; however, these recommendations and decisions of CEPT are not always adopted in their entirety in every country. The European Commission is in the process of implementing its "Radio Spectrum Decision," which has the objective of providing legal certainty to spectrum allocations which support EU policies. Within ETSI see also http://portal.etsi.org/erm/kta/Spectrum/spectrum.asp, TC ERM is the technical committee responsible for EMC and Radio Spectrum Matters (RM). Within TC ERM, the working group RM is the centre of expertise on radio spectrum matters and is mandated to coordinate and support the needs and interests of the entire ETSI membership on radio spectrum matters. In particular, liaison to CEPT ECC according the MOU between ECC and ETSI is required. TC ERM has the primary responsibility for coordination of ETSI positions on the efficient use of the radio spectrum and spectrum allocations. TC ERM has created working group ERM RM to carry out the detailed preparation work on its behalf. CEPT/ECC has three working groups concerned with radio spectrum management:

(i) Frequency Management (FM), including the Short-Range Device Maintenance Group (SRDMG);
(ii) Radio Regulatory (RR);
(iii) Spectrum Engineering (SE).

In addition, CEPT/ECC has project teams to cover specific issues. In general, project teams are established to draft proposed decision and recommendation documents. These are formally adopted by a corresponding working group (i.e., FM, RR, or SE), a process which includes a period of public consultation.[3] Based on the Radio Spectrum Policy Decision (Decision no. 676/2002/EC of the European Parliament and of the Council of 7 March, 2002, on a regulatory framework for radio spectrum policy in the European Community), the European Commission seeks to

(i) relate spectrum demands to EU policy initiatives, supported by a Radio Spectrum Policy Group, a Committee of Member States, chaired by the European Commission, with ETSI and CEPT as permanent observers;
(ii) introduce legal certainty for technical harmonization measures carried out by CEPT in areas of EU Community policy; the Commission, in consultation with a Radio Spectrum Committee (RSC), will place mandates on the CEPT; the resulting spectrum allocations will be codified in Commission Decisions, applicable throughout the European Community;

[3]CEPT/ECC is currently reorganizing the structure of its working groups; for the latest information, please see the web site of the European Radiocommunications Office (http://www.ero.dk).

(iii) increase transparency and information on the use of spectrum by requiring Member States to publish spectrum tables and other relevant information in a common format accessible to all interested parties;
(iv) support the CEPT on the promotion of European interests in international negotiations.

In support of this activity, the Commission has established two advisory groups:

(i) The Radio Spectrum Policy Group (RSPG; Commission Decision 2002/622/EC), to advise the Commission on radio spectrum policy issues, and where the Commission should take spectrum harmonization measures in support of other policies;
(ii) The Radio Spectrum Committee (RSC), which advises the European Commission on mandates to be given to the CEPT in support of harmonization measures and the measures that should be taken to provide legal certainty within the Community.

Some of the key services that have been identified for study by CEPT are as follows:

(i) aeronautical radionavigation service;
(ii) amateur service;
(iii) amateur satellite service;
(iv) earth exploration satellite service (active);
(v) fixed service;
(vi) fixed satellite service;
(vii) land mobile service (including 5 GHz radio LAN);
(viii) mobile satellite service;
(ix) radio astronomy;
(x) radio determination service;
(xi) radio navigation service.

7.2.3.2. ECC-TG3

The first meeting of ECC-TG3, whose main function is to prepare all aspects of CEPT's response to the European Commission's mandate requesting the "harmonization of spectrum used by ultra-wideband (UWB) systems in Europe," took place on 19 April, 2004, in Maisons-Alfort, France [4]. This first meeting of ECC-TG3 aimed at setting the organization of the Task Group as well as the general objectives for future meetings in the light of its mandate. While limited to CEPT administrations, the meeting was also attended by representatives from the European Commission, the European Radiocommunications Office (ERO), the Chairman of ETSI ERM[4] (Electromagnetic Compatibility and Radio Spectrum Matters)

[4]ETSI ERM is a "horizontal" technical committee responsible for the standardization of Electromagnetic Compatibility (EMC) and Radio Spectrum Matters on behalf of all other technical bodies of ETSI. The Radio Matters (RM) working group is responsible for cooperation with the European Radiocommunications Committee (ERC) to secure appropriate spectrum allocations in the CEPT countries for standardized systems, in order to ensure coexistence between different communications systems standardized by ETSI. ERM has a number of task groups established on a short-term basis to deal with particular issues; they disband on the resolution of the task. Concerning UWB radio matters, the current ERM structure includes the following task groups: Standardization of Land-Mobile Radio, including Ultra-Wideband for Telecommunications and Radio locations Activities (TG31A), and Automotive, including Ultra-Wideband Radar (TG31B).

Work Group TG31A, and a representative from the "UWB Cluster." The latter is an industry-led interest group that includes representatives of UWB radio-related European RTD (Research and Technology Development) projects supported by the European Commission; the leading European RTD project within the UWB Cluster is the Integrated Project PULSERS (Pervasive Ultra-wideband Low Spectral Energy Radio Systems). Members of PULSERS have been instrumental in supporting the Commission and its Radio Spectrum Committee[5] (RSC) during preparation of the "UWB mandate" issued to CEPT. As a result, subsequent ECC-TG3 meetings are open for participation to recognized CEPT observers, representatives of the European industry, and telecommunication operators. It was also concluded that, as the main deliverable of ECC-TG3, a "Draft ECC Report on UWB" would be developed, essentially in the form of a technical document, together with whatever else is deemed necessary. A further task is the coordination of European positions and contributions within the Task Group 1/8 (TG 1/8) dealing with UWB matters in the Radiocommunication Sector of the International Telecommunications Union (ITU-R).

The first ECC-TG3 meeting considered the current state of European activities on UWB. It was decided to make use of the documentation already developed by the Project Teams SE21 and SE24 of the CEPT/ECC Working Group for Spectrum Engineering (WGSE), to obtain a description of the work already achieved and to highlight areas seen as mature and to identify where further work is needed. In particular, the Chairman of ETSI ERM TG31A offered its continued support to the activity of ECC-TG3 on UWB, indicating that an ETSI system reference document (SRDoc) on UWB imaging systems (wall probing radars and ground probing radar systems) is to be approved by ETSI ERM RM at its September 2004 meeting while the SRDoc on UWB communication applications has been published and submitted to CEPT. Moreover, ECC-TG3 had received a liaison from the Chairman of WGFM Project Team FM22 (a project team covering monitoring issues of CEPT's Frequency Management Working Group), indicating that a subject on "ultra-wideband measurements" was added to the work program of FM22 on spectrum monitoring; FM22 offered its willingness to assist ECC-TG3 in conducting measurements related to UWB.

The mandate to CEPT as issued by the European Commission requests to report on actual or planned real-life testing within the European Union (EU) and to consider the possible benefits of experimental rights to use radio spectrum for UWB applications. In this and other relevant areas of the mandate, the Commission encourages CEPT to make use of ongoing activities and know-how of EU RTD projects on UWB radio (see footnote 2 in [2]). At this first ECC-TG3 meeting, a representative from the ERO presented a report on the second meeting of ITU-R TG 1/8 (UWB) held in Geneva, Switzerland, 27–31 October, 2003, underlining in particular the difficulties within its Work Group 3 (WG3) on defining a "UWB spectrum management framework." Finally, the Chairman of SE24

[5]European Radio Spectrum Committee; http://europa.eu.int/information_society/topics/radio_spectrum/all_about/rsc/index_en.htm.

offered a statement as to the FCC regulations on UWB, initially adopted 14 February, 2002, indicating that SE24 had studied in detail the impact of the FCC limits on radiocommunication services and concluded that CEPT could not endorse these limits.[6]

The general objectives of ECC-TG3 on UWB as mandated are

(i) to develop the draft ECC report on UWB;
(ii) to develop the draft ECC responses to the European Commission mandate to CEPT to harmonize radio spectrum use for ultra-wideband systems in the European Union;
(iii) to coordinate European positions in preparation for ITU-R TG1/8 on ultra-wideband issues.

The deliverables of ECC-TG3 in response to the EC mandate, which may be generally referred to as the "Draft ECC Responses to the EC Mandate on UWB," will be submitted by ECC-TG3 for consideration at the ECC plenary meetings in July 2004 (Draft First Report), November 2004 (Draft Interim Report), and March 2005 (Draft Final Report). ECC-TG3 liaises with and consolidates outputs from other working groups (e.g., WGFM and WGSE). ECC-TG3 will be open to ETSI members in accordance with the terms of the CEPT/ETSI MOU and the group will consult with relevant European organizations, in particular ETSI. As a result of the technical work on UWB initially carried out within SE24 and transferred to ECC-TG3, a "Draft ECC Report" will be submitted to WGSE for preliminary adoption at its October 2004 meeting and WGSE will handle the consultation process, relying on TG3 in case of substantial comment to the draft ECC report, and finally adopt the report at its first meeting in 2005. This "Draft ECC Report" will serve as the technical basis for the "Draft ECC Responses to the EC Mandate on UWB."

From the minutes reported in [4], it is interesting to observe that the EC's representative expressed his wish to follow the work of ECC-TG3 and help whenever necessary with the interpretation on the objectives of the mandate. He also insisted on the need for rapid progress due to growing industrial demands for regulating this (UWB) technology and explained that the tight and challenging schedule of the mandate was aimed at providing viable solutions in a timely fashion. Moreover, the EC's counselor also underlined that a large amount of funding is invested by the European Union in various research projects on UWB,[7] indicating that the Commission strongly encourages CEPT to use the resources available in these RTD activities to validate, where possible, UWB compatibility studies by a campaign of experimental testing.

ECC-TG3 constituted itself into three working groups:

(i) WG1: UWB Characteristics and Measurement Techniques;
(ii) WG2: UWB Compatibility;
(iii) WG3: Frequency Management and Regulatory Issues.

[6]See, for example, the FCC mask for communication applications in [5].

[7]EC supported RTD projects related to UWB radio technology are, for example, whyless.com (http:/www.whyless.org), UCAN (http://www.ucan.biz/), ULTRAWAVES (http://www.ultrawaves.org), and PULSERS (http://www.pulsers.net).

ECC-TG3/WG1: UWB Characteristics and Measurement Techniques. The general terms of reference (TORs) of WG1 are to provide the following deliverables, for approval by ECC-TG3:

(i) prepare chapter on "technical characteristics of UWB devices" for insertion in the "Draft ECC Report on UWB;"
(ii) prepare chapter on "operational characteristics of UWB applications" for insertion in the "Draft ECC Report on UWB;"
(iii) prepare draft contributions intended for WG-1 of ITU-R TG1/8 on "UWB characteristics;"
(iv) prepare draft contributions intended for WG-4 of ITU-R TG1/8 on "UWB measurement techniques."

In the course of this mandate, ECC-TG3/WG1 should

(i) consider operational characteristics of UWB applications, that is, communication equipment (Type 1) and radar imaging systems (Type 2);
(ii) consider technical characteristics of devices using UWB technology;
(iii) consider UWB measurement techniques;
(iv) identify the technical parameters of UWB systems to be included in the overall harmonized regulatory approach;
(v) consider where design guidelines for existing and new radio standards could improve coexistence between UWB devices and radiocommunication devices.

ECC-TG3/WG2: UWB Compatibility. The general TORs of WG2 are to provide the following deliverables, for approval by ECC-TG3:

(i) prepare the Draft ECC Report on UWB;
(ii) prepare draft contributions intended for WG-2 of ITU-R TG1/8 on "UWB compatibility."

In the course of this mandate, ECC-TG3/WG2 should

(i) clarify relevant methodologies for compatibility analysis between devices using UWB technology and radiocommunication services (single interferer and aggregate interference), including the definition of reference UWB deployment scenarios dependent on the type of UWB applications;
(ii) clarify relevant propagation models for use in compatibility studies;
(iii) report on actual or planned real-life testing within the European Union;
(iv) define protection requirements for radiocommunication services;
(v) identify the conditions of use of radio spectrum by UWB required to protect other radio services from harmful interference, including the potential impact of UWB out-of-band emissions on other services.

WG2 is also expected to coordinate the liaison with WGFM Project Team FM22 as well as the "UWB Cluster" and take into consideration results from experimentation campaigns.[8]

[8]The first meeting of ECC-TG3, a contribution was presented on the "UWB Cluster" (TG3#1_-03R0) for further consideration by WG2 of TG3. The UWB Cluster, initiated by EU project members, proposed to contribute as an industry association providing contributions relying on UWB theoretical

ECC-TG3/WG3: Frequency Management and Regulatory Issues. The general TORs of WG3 are to provide the following deliverables, for approval by ECC-TG3:

(i) prepare the draft ECC responses to the European Commission mandate;
(ii) prepare draft contributions intended for WG-3 of ITU-R TG1/8 on "UWB spectrum management framework."

In the course of this mandate, ECC-TG3/WG3 should

(i) consider the existing and developing regulatory environment, in particular ongoing ITU activities, and the extent of convergence which is feasible with non-EU regulation, including the application across the EU of ITU RR Article 4.4, but also the implications of UWB emissions in frequency bands covered by ITU RR footnote 5.340;
(ii) consider the applicability and impact of existing relevant definitions in the radio regulations to UWB;
(iii) define where necessary relevant specific terminology for UWB (e.g., UWB emission, center frequency, necessary bandwidth, fractional bandwidth, unwanted out-of-band emissions, etc.);
(iv) consider the possible benefits of experimental rights to use radio spectrum (or licenses) for UWB applications;
(v) consider the designation of one or more harmonized frequency band(s) for generic or specific UWB uses, and alternatively develop different (technical) "options" for possible introduction of UWB devices;
(vi) consider what could be the possible elements of a monitoring and review mechanism aimed at ensuring that regulation of radio spectrum for UWB remains responsive to technical and societal developments, and to actual or perceived changes in the risk of harmful interference with other radio services.

In the course of its work, WG3 is also expected to provide recommendations to ECC-TG3 on the overall approach to UWB regulation, possibly consisting of

(i) short-range device annex in ERC/Recommendation 70-03 covering generic UWB communications equipment;
(ii) ECC recommendation or ECC decision for imaging systems including ground penetrating radar.

Nearly all possible UWB applications, in particular UWB communication and positioning applications, are expected to be operated without requirement for an individual right to use radio spectrum ("license-exempt") and on a "no protection, no harmful interference" basis. The regulatory regime for radar imaging systems is however likely to differ; regarding regulatory enforcement matters, ECC-TG3/WG3 is expected to primarily focus on this type of UWB applications. The schedule outlined in the Commission's mandate to CEPT calls for deliverables according to the following schedule: First Report from CEPT by 15 July, 2004; Interim Report by 15 November, 2004; Final Report by April, 2005. In addition, CEPT is requested to report on the progress of its work pursuant to the mandate

studies and on UWB experimentation campaigns already defined and supported by the EU projects' work plans or by individual member contributions.

at all meetings of the Radio Spectrum Committee taking place during the course of the mandate.

7.2.3.3. ETSI-TG31A/B

The task of TG31A is to investigate and develop generic and/or specific ETSI radio standards for short-range devices (SRDs) using UWB technology see also http://portal.etsi.org/erm/ERMtg31A_ToR.asp. Considered UWB applications include, but are not limited to, high-speed short-range wireless communications links, security and movement/location detectors, electronic fences, proximity alarms, medical sensors, intelligent automotive systems, and ground penetrating radars. TG31A will also identify spectrum requirements to ensure spectrum efficiency and compatibility with other radio services. Inputs will be prepared for TC-ERM Working Group ERM-EMC on EMC aspects relevant to devices covered by TG31A. The TG31A Group issued a technical report (TR 101 994 [6]) that covers the intended applications, proposed technical parameters, and radio spectrum requirements for UWB. The report includes necessary information to support the cooperation under the MOU between ETSI and the European Radiocommunications Committee (ERC) of CEPT for amending the ERC Recommendation 70-03. Another report (TR 101 994-2) covers the technical characteristics of short-range ground, wall, and through-wall probing radars using UWB technology. The progress made within ETSI-TG31A in the last three years includes the discussion of a so-called "sloped" power spectral density (PSD) emission mask for UWB communication devices [7]. However, note that the emission limits indicated by this mask are not an official proposal nor are they a recommendation. Instead, they are merely under discussion as a possible means to obtain additional out-of-band protection for existing radiocommunication services in Europe, when compared with the corresponding FCC. The task of TG31B involves the area of UWB automotive radar, to develop standards, system reference documents, or other technical documents for short-range devices as covered by the ECC SRD Recommendation 70-03 and the relevant ECC decisions in the field of automotive UWB radar applications. TG31B also investigates spectrum parameters for use in automotive radar systems in order to ensure the efficient use of the radio spectrum, considering global harmonization[9] see also http://portal.etsi.org/erm/ERMtg31B_ToR.asp.

7.3. Standardization

7.3.1. Introduction

In today's information society, new technologies affect our life significantly. Technology makes things quicker, easier, better, but also more complex. Standardization can be seen as an essential requirement for an open exchange of information

[9]Special state-of-the-art measurement equipment may be capable to measure power levels of perhaps as low as −90 dBm in a bandwidth of 1 MHz.

enabling interoperability between different services/technologies. Standards need to be produced at a speed that is consistent with market demand; they have to be considered by all involved parties, otherwise they may not be widely accepted.

Since standardization and innovation go hand in hand, standards in certain way allow those innovative ideas to reach the market. And one innovative idea that has emerged in the latest years is the use of ultra-wide band (UWB) for civil applications. UWB targets a broad spectrum of radiocommunications and localization applications, and is foreseen to be integrated in low-power low-cost devices.

In the following sections, UWB standardization efforts across the world are presented. Next section will discuss the standardization activities carried out by the IEEE in the US. In particular, two task groups are of interest: IEEE802.15 TG3a and IEEE802.15 TG4a. Section 7.3.3 discusses UWB standardization progress made in Europe by the ETSI. Standardization efforts in Japan (ARIB) are presented in Section 7.3.4, while international standardization activities are presented in Section 7.3.5 (GRSC).

It is to be mentioned that the presented standardization activities are ongoing, and that the status of these may have become obsolete. The current chapter presents the standardization status as of spring 2004.

7.3.2. IEEE

The Institute of Electrical and Electronics Engineers (IEEE) Standards Association is a leading developer (based in the US) of global industrial standards in various industries. The IEEE created in May 1999 the IEEE802.15 Wireless Personal Area Network (WPAN) Working Group (formerly the WPAN Study Group (SG), formed in March 1998) [8]. The IEEE802.15 WG aims to provide, in the IEEE802 family, standards for low-complexity and low-power consumption wireless connectivity. As of today, there are several task groups (TGs) and study groups (SGs) identified within IEEE802.15:

(i) TG1: 1 Mbps WPAN/Bluetooth,
(ii) TG1a: WPAN 15.1 Revisions to Bluetooth v1.2,
(iii) TG2: Recommended Practice for Coexistence in Unlicensed Bands,
(iv) TG3: 20+ Mbps High Rate WPAN for Multimedia and Digital Imaging,
(v) TG3a: 110+ Mbps Higher Rate Alternative PHY for 802.15.3,
(vi) TG3b: WPAN 15.3 Maintenance,
(vii) SG3c: mmWave,
(viii) TG4: 200 kbps for Interactive Toys, Sensor, and Automation Needs,
(ix) TG4a: WPAN Low Rate Alt PHY,
(x) TG4b: WPAN 15.4 Revisions and Enhancements,
(xi) TG5: WPAN Mesh Networking.

Two of the standards projects are of interest for the reader, the IEEE802.15.3a TG3a and the IEEE802.15 TG4a, as they are both susceptible of adopting UWB as radio technology. These two TGs' activities will be presented in the next sub-sections.

7.3.2.1. IEEE802.15 TG3a

The IEEE802.15 High Rate Alternative PHY Task Group (TG3a) for Wireless Personal Area Networks (WPANs) [9] became a TG in December 2002, when its Project Authorization Request (PAR) [10] was approved. It aims to provide a higher-speed PHY enhancement amendment to 802.15.3 for applications involving imaging and multimedia. Hence, the medium access control (MAC) as defined within 802.15.3 will be kept for 802.15.3a systems; only the PHY will change. The 802.15.3 MAC is based on a centralized network topology, that is, organized in piconet fashion, with one piconet coordinator and devices synchronized to it; the common air interface is shared by implementing time-division multiplex access (TDMA).

In December 2002, the TG3a issued a Call for Intent/Call for Proposals (CFI/CFP) [11], in order to open the discussion about the 802.15.3a standard proposers. The TG3a also issued (between December 2002 and January 2003) three important documents fixing the rules for the standardization procedure: the technical requirements [12], the PHY selection criteria [13], and the down selection voting procedure [14].

The PHY selection criteria document defines among other things the throughput performances to be achieved (110 Mbps at 10 meters, 200 Mbps at 4 meters, and 480 Mbps at undefined range), performance requirements with simultaneously operating piconets (SOPs); signal acquisition performance requirements; link budget and sensitivity calculation; power management modes, power consumption requirements; antenna practicality.

A common channel model to be used for system simulations from all proposers has been established by the TG3a [15]. It is a channel model based on the Saleh-Valenzuela channel model [16], with slight changes.

The first TG3a meeting where the first proposals were presented (25 proposers) was held in March 2003. The vast majority of the proposals were based on UWB radio technology. These UWB proposals could be divided into two technical approaches: the mono- or dual-band approach and the multiband approach.

The down selection voting procedure during the March 2003 meeting eliminated several proposals. Alliances between proposers were also formed, and as a result the number of proposals presented during the next meeting (held in May 2003) was reduced from 25 to 13. After further down selection, the number of proposals squeezed to 7 in July 2003, to finally end with 2 main proposals in September 2003. These two proposals are the multiband OFDM (orthogonal frequency-division multiplex) proposal and the DS-CDMA (direct-sequence code-division multiple access) proposal. Since September 2003, the standardization process has been stalled, as none of the two proposals have reached the 75% of the votes required for a proposal to become a standard. These two proposals are presented in the following sections.

Multiband OFDM physical layer proposal. The Multiband OFDM Alliance (MBOA [17]) is a group of companies that has gained more and more momentum during the down selection process. Its PHY proposal is currently the majority-holding

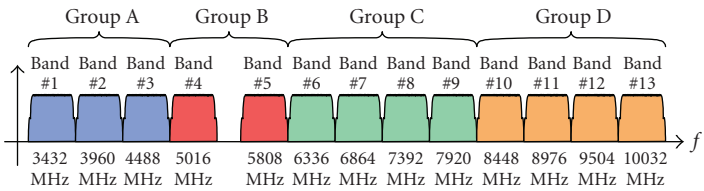

Figure 7.2. Spectrum division into groups, as proposed by MBOA.

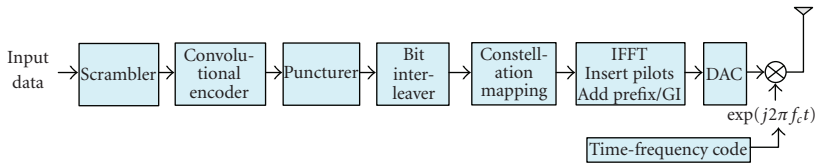

Figure 7.3. Block diagram of an example MBOA TX architecture.

proposal at the IEEE802.15.3a meetings, reaching roughly 2/3 of the votes (which is not enough as 75% are required).

The basic principle of the MBOA proposal is to divide the spectrum into several subbands of 528 MHz, on which the OFDM symbols are transmitted. The current proposal band plan divides the bands into several groups, as illustrated in Figure 7.2.

Subbands of Group A are recommended for first generation devices; it includes 3 bands in the bandwidth 3.1 to 4.9 GHz. Subbands of Group B (4.9–6.0 GHz) are reserved for future use; subbands of Group C (6.0–8.1 GHz) are reserved for devices with improved SOP performance; subbands of Group D (8.1–10.6 MHz) are also reserved for future use.

Information is transmitted using OFDM symbols on each subband. OFDM carriers are being efficiently generated using a 128-point IFFT/FFT. By limiting the constellation size of the modulation to QPSK (quaternary phase-shift keying), the internal precision requirement is reduced.

The OFDM symbols consist of 128 QPSK modulated tones: 100 data tones, used to transmit information; 12 pilot tones, used for carrier and phase tracking; 10 user-defined tones; 4 NULL tones. The modulation is performed through signal mapping to tones and then IFFT operation. A 60.6-nanosecond prefix is added for robustness against multipath. A 9.5-nanosecond guard interval is inserted in order to provide sufficient time for switching between bands. The symbols are then mixed up to the right subband, according to the time-frequency code. In this way, information is coded across all bands in order to exploit frequency diversity, and to provide robustness against multipath and interference. Figure 7.3 depicts an example of a MBOA transmitter (TX).

The raw bit rate (bit rate over the air) of the MBOA system is 640 Mbps. Channel coding and frequency spreading techniques will reduce the information bit rate (bit rate at MAC-PHY interface), depending on channel conditions; this will yield information bit rates between 55 Mbps and 480 Mbps.

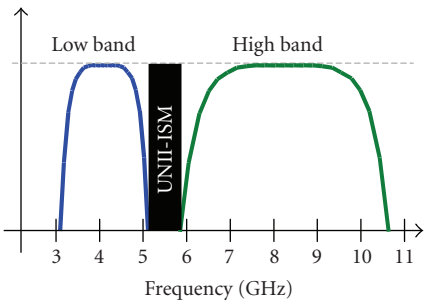

FIGURE 7.4. The two subbands as defined in the DS-CDMA proposal.

The MBOA claims that this OFDM-based solution is spectrally efficient, that it has inherent robustness against narrowband interferers, and that it has excellent robustness in multipath environment. Furthermore, by dividing the UWB band into several subbands, sensitive subbands and tones can be turned off (in order to comply with changing regulations, or for enhanced coexistence with other devices) when needed. Hence, ability of this system to comply with worldwide regulations is claimed by the MBOA; coexistence with current and future systems is also assured this way. Finally, the MBOA proposal claims to offer multimode devices, hence scalability.

DS-CDMA physical layer proposal. The DS-CDMA proposal was presented initially by Xtreme Spectrum Inc. [18], a startup company that was later bought by Motorola [19]. Along the way, the proposal has gained support by other companies as well. It is the second standing proposal in the IEEE, collecting the remaining third of the votes.

The DS-CDMA proposal envisions a dual-band approach: 3 spectral modes of operations are proposed. One is the low-band mode, from 3.1 to 5.15 GHz; it provides information bit rates between 28.5 and 400 Mbps, and is designed to support lower-rate, longer-range devices. The second is the high-band mode spanning from 5.825 to 10.6 GHz; it accommodates information bit rates from 57 to 800 Mbps, and targets high-rate, short-range devices. Finally, the last mode is the multiband mode, which combines the bandwidth of the previous two modes. It can achieve up to 1.2 Gbps in information bit rate, and supports low-rate, longer-range, high-rate, short-range devices.

The proposed spectrum division avoids carefully the UNII and ISM bands (unlicensed national information infrastructure and industrial, scientific, and medical radio bands, spanning roughly from 5.25 to 5.85 GHz), as illustrated in Figure 7.4. This spectrum division proposal is adjustable, in case future spectral allocation requires it. The DS-CDMA proposal uses two types of modulations: binary phase shift keying (BPSK, mandatory) and quaternary phase shift keying (QPSK, optional). For spreading, CDMA is used via low cross-correlation MBOK (M-ary biorthogonal keying) ternary code sets (1, 0, +1). There are 4 CDMA code sets per frequency band. CDMA also provides a selection of logical channels (4 logical channels per frequency band, that is, up to 8 piconets accommodated

when both subbands are used). The chip rate is 1.368 GHz for the low-band mode, and 2.736 GHz for the high-band mode. For both modes, the CDMA code length is 24 chips/symbol.

The DS-CDMA proposal is claimed to handle SOP conditions well, by using frequency-division multiplexing (FDM, via 2 defined subbands), code-division multiplexing (CDM, for spreading), and time-division multiplexing (TDM, via 802.15.3 MAC implemented as TDMA protocol). It is also claimed to be capable to be robust against narrowband interference via its CDMA codes, and via tunable notch filters.

7.3.2.2. IEEE802.15 TG4a

The IEEE802.15 Low Rate Alternative PHY Task Group (TG4a) for Wireless Personal Area Networks (WPANs) became an official Task Group in March 2004 [20]; with its committee work tracing back to November 2002, when an interest group was formed. TG4a has defined a project for an amendment to 802.15.4 for an alternative PHY. While the 802.15.3 MAC is targeting centralized network topology with TDMA, the 802.15.4 MAC uses a distributed architecture, where clear channel assessment (CCA) is preferred for sharing the radio medium.

The main goals of WP4a are to provide communications and high precision ranging/location capability (1 meter accuracy or better), high aggregate throughput, and ultra-low power; as well as adding scalability to data rates, longer range, and lower power consumption and cost. These additional capabilities over the existing 802.15.4 standard are expected to enable significant new applications and market opportunities.

TG4a meets every other month, during the 802.15 plenary or interim meetings. TG4a is very young; the Call for Application (CFA) has already been issued, but the TG4a Call for Proposals (CFP) has not been issued yet (expected to be issued in May 2004). Other activities such as the definition of selection criteria and of the technical requirements have been initialised.

UWB is one strong candidate for the alternative PHY to be selected within 802.15.4a, due to its inherent low-power low-complexity characteristics, along with precise localization capabilities. In fact, UWB channel model activities have already been started. But as of today no proposal has been presented yet, as the CFP is still to be issued in its final version.

7.3.2.3. Other IEEE groups related to UWB

Other groups interested in UWB technology are the IEEE802.15 TG5 (WPAN Mesh Networking), the IEEE802.15 SG3c (mmWave), and the IEEE802.19 (Coexistence Technical Advisory Group).

The IEEE802.15 TG5 is a Task Group whose charter is to define recommended practices for implementing mesh networking of WPANs [21]. Mesh topologies can be used to increase the reliability and range of network, with focus on special needs of WPAN application such as very low energy consumption and very low cost. The TG5 may in this respect be of interest for UWB, as UWB's PHY is well adapted to mesh networking.

The IEEE802.15 SG3c mmWave Study Group was formed to explore the use of the 60 GHz band for WPANs. This little-used band (as defined in the Federal Communications Commission (FCC) Article 47 CFr 15.255) provides 5 GHz of bandwidth and avoids interference with nearly all electronic devices, given the high attenuation of these wavelengths by walls and floors, hence allowing more WPANs to occupy the same building. The intention of the SG3c is to consider mobile and networked applications, network protocols and performance, mobile and ad hoc networking, mobile and ubiquitous systems, network security, internet computing, wireless networks, multimedia distribution, last-mile applications. Again, UWB may become the PHY of choice for this Study Group, as the very large available bandwidth would enable UWB operation.

The IEEE802.19 Coexistence Technical Advisory Group (TAG) develops and maintains policies defining the responsibilities of 802 standards developers to address issues of coexistence with existing standards and other standards under development [22]. Due to the very large bandwidth of UWB, several coexistence scenarios for UWB devices have been submitted to the IEEE802.19 TAG. The following scenarios have been envisaged in order to study single interferer coexistence issues

(i) *Home usage:*
  (1) a UWB digital video camera streams video to a multimedia hub in the home that also forwards the stream to an HDTV monitor, while the same multimedia hub is streaming MP3 audio to a remote audio terminal;
  (2) the multimedia hub in a home is located 1 meter away from a cellphone or WLAN base station; the user may be talking on the phone or the hub is supporting web browsing or email while uploading video or still images.

(ii) *Enterprise usage:*
  (1) a UWB video projector is used in a conference room to allow attendees to stream their presentations from their laptops, but all attendees want to use the corporate network simultaneously using 802.11b/g/a/n.

(iii) *Kiosk/hot-spot usage:*
  (1) a laptop computer equipped with 802.11b/g/a/n uploads photos to a kiosk while a digital still camera (DSC)/digital video camera (DVC) with a UWB device also uploads photos to the same kiosk;
  (2) in an airport hot spot, several users upload their DSC/DVC to their laptop computers, then forward these images via WLAN to a central server for storage.

(iv) *Mobile usage:*
  (1) mobile phone incorporating UWB technology and GPS;
  (2) mobile phone with either DSC or DVC capability that uploads video or still images to kiosk or A/V hub while maintaining 3G connection.

7.3.3. ETSI

The European Telecommunication Standards Institute (ETSI) is responsible for development of standards for radiocommunications systems and equipment [23]. Radio standards contain by their nature several requirements which relate to efficient use of radio spectrum, including compatibility between different radio services.

In order to ensure the planning of an efficient use of radio frequency spectrum, a memorandum of understanding (MOU) has been elaborated between ETSI and the Conférence Européenne des Postes et Télécommunications (CEPT) Electronic Communications Committee (ECC), for cooperation in development of radio technical specifications. In the development of harmonized standards containing technical specifications for radio equipment, the provisions of the ETSI-CEPT MOU will be applied, to the extent that the MOU applies to the particular equipment. Compliance within essential requirements (Radio & Telecommunications Terminal Equipment (R&TTE) Directive) will ensure free circulation of radio products within the European Environment Agency (EEA).

In general, assumptions are necessary for spectrum management purposes concerning the performance of transmitters, receivers and control functions in the areas of signalling, code-domain consideration and frequency sharing, and so forth.

In this sense, the European Commission (through the ECC Telecommunication Conformity Assessment and Market Surveillance Committee (TCAM)) has given a mandate (M/329) to the European Standardization Organization on March 19th, 2003, with the goal to establish a set of harmonized standards covering UWB applications under the R&TTE Directive. In response to that, the ETSI Electromagnetic compatibility and Radio Spectrum Matters Task Group 31A (ERM TG31A) [24] started developing a set of harmonized standards for short-range devices (SRDs) using UWB technology.

The ERM TG31B, on the other side, has the task to develop standards, system reference document or other technical documents for short-range devices as covered by the ECC SRD Recommendation 70-03, and the relevant ECC decision in field of automotive ultra-wideband radar applications in relation with efficient use of radio spectrum, considering global harmonization.

ERM TG31A and B are described in more details in the following two sections.

7.3.3.1. ETSI ERM TG31A

In order to support cooperation between ETSI and ECC, the TG31A produced a technical report as system reference document [25], which provides information on the intended applications, the technical parameters and radio spectrum requirements for UWB communications equipment in the frequency range from 3.1 GHz to 10.6 GHz. In this document, it was indicated that there is a potential for variety of UWB communication applications as well as an increasing number of sensing and positioning applications.

In Annex A1 of the mentioned document, a variety of communication applications are described, like wirelessly distributed services such as phone, cable, and computer networking throughout a building or home. UWB has potential in both home and business markets, based on its low cost as well as high-speed data transmission capability (100 Mbps–500+ Mbps), and could be well suited to for various video distribution applications (DVD player/recorder to TV or transmitting images/video from digital camera/camcorder to TV) and, generally, new high-speed consumer SRDs.

Particularly, UWB technology is a potential cable replacement for applications where USB 2.0/Firewire resides, for example,

(i) USB 2.0 allows data rates up to 480 Mbps;
(ii) IEEE1394 [18] (Firewire 400 Mbps and 800 Mbps);
(iii) USB 1.1 at 12 Mbps.

Other identified UWB applications are low data rate with very low activity factors, and are typically used in sensor networks and RFID (radio frequency identification) systems. For example, the FCC recently approved a tagging system for UWB precision asset location systems.

Since technology is still advancing, it is very unlikely that only one single type of signaling and modulation will be used for this large variety of applications. The UWB communication devices based on single impulse radio technology (as shown in Figure 7.5) and on multiband OFDM pseudocarrier approach (illustrated in Figure 7.6) have been given as two examples of UWB implementations [25]. Since in time of publishing the Technical Report (January 2004) consensus was not reached by ETSI delegates for power limits within the band 3.1 GHz to 10.6 GHz, the values given in Annex B2 of the Technical Report are supported by the UWB industry within ETSI as a starting point, representing rather general emission (power spectral density) limits requested for UWB devices, with no relation to the particular modulation scheme.

TG31A is also in charge of providing a system reference document covering ground probing radars and wall probing radars applications [26], in support to the cooperation under the MOU between ETSI and ECC. This document provides information on the intended applications, technical parameters, and the radio spectrum requirements. The scope is limited to short-range devices, in which the system is in close proximity to the materials being investigated (e.g. earth materials, highway pavement,). The system is designed to radiate a sequence of pulses into the ground and capture a waveform corresponding to the received signal scattered by objects in the ground. The pulse repetition frequency (PRF) of the transmitted pulse may vary widely dependent upon the application, with a range between 1kHz and 10 MHz operating in the band from 30 MHz to 12.4 GHz. It is proposed that such kind of devices will be covered by a generic standard for unintentional radiation with radiation limits up to 1 GHz specified in EN 55022 for Class A, and new amended limits up to 6/18 GHz as proposed in CISPR/I/105/CDV and CISPR/I/106/CDV.

Besides producing the Technical Reports mentioned above, TG31A is working on drafting a harmonized standard: EN 302 065, which deals with UWB devices

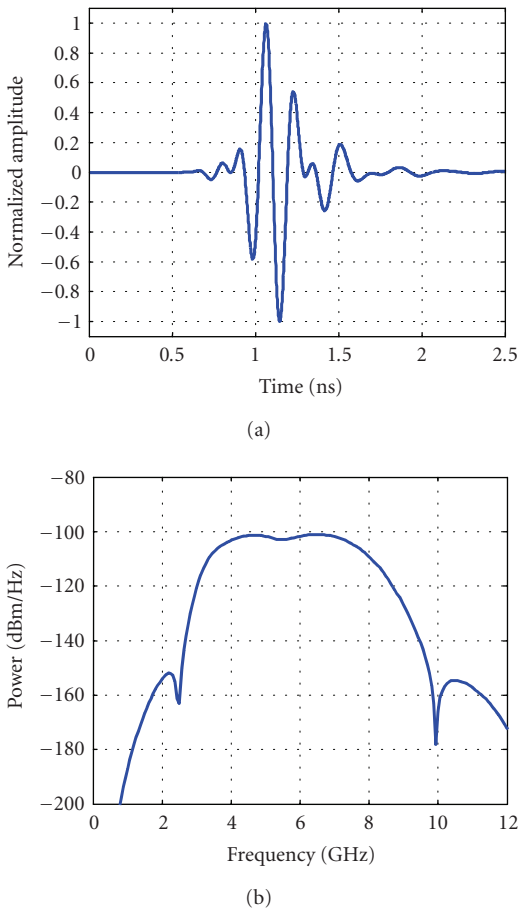

FIGURE 7.5. Pulse shape with corresponding spectrum.

for communication purposes operating between 3.1 GHz and 10.6 GHz. Part 1 of this draft standard deals with technical characteristics, while Part 2 provides parameters deals with the R&TTE Directive and is currently concentrating on measurement methods (this work is done with the ERM Task Group 33, which is in charge of measurement methods for discontinuous transmission).

7.3.3.2. ETSI ERM TG31B

TG31B has the task to develop standards, system reference document, or other technical documents for short-range devices as covered by the ECC SRD Recommendation 70-03, and the relevant ECC decision in field of automotive ultra-wideband radar applications in relation with efficient use of radio spectrum, considering global harmonization.

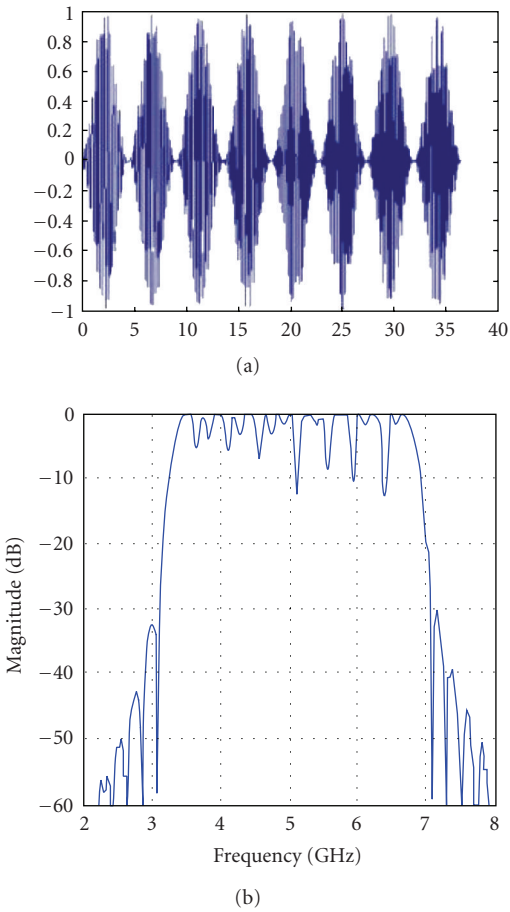

Figure 7.6. Amplitude and frequency spectrum characteristics for a multiband implementation.

Automotive short-range radar (SRR) systems have been identified by the EU policy eSafety initiative as significant technology for the improvement of road safety in Europe addressing overall transport policy goal of cutting road fatalities in Europe by half by 2010, detecting the location and movement of objects near a vehicle, enabling features such as near collision avoidance, improved airbag activation, and suspension systems that better respond to road conditions (see Figure 7.7).

Work in this group has been concentrated on SRR equipment for road safety and intelligent transport systems (automotive collision warning), temporarily operating in the 24 GHz band and permanently in the 77 GHz to 81 GHz band [27]. The industry has been working towards an early introduction of equipment due to interest to reuse the same technology during the lifetime of the model lines (usually 6–7 years in Europe), so it is expected that new car lines will already use

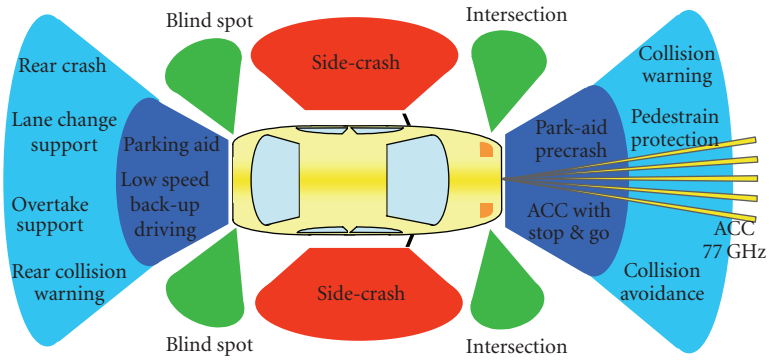

FIGURE 7.7. Short-range radar functions for vehicle.

long-term frequency equipment. Possible deployment at 24 Ghz will be not only time limited but also overall car park penetration is restricted to below 10% as an outcome of CEPT's compatibility studies.

Another activity of TG31B is related to adaptive cruise control using automotive long-range radar (LRR) operating in the 76 GHz to 77 GHz band. Adaptive cruise control today uses LRR operating with maximum bandwidth of 1 GHz. It uses distance scanning, which requires an operating range of approximately 150 m and is used at vehicle velocities above 30 km/h. One or multiple narrow lobes control or scan the driving path in front of the car to determine the distance to the vehicle driving ahead for maintaining a constant minimum safety distance.

ETSI is also supporting activity foreseen by the International Telecommunications Union (ITU) and CEPT using unconventional channel arrangements much larger than those foreseen so far, in frequencies up to 58 GHz. The goal is to carry at least a fully transparent 1 Gbps signal, to support interfaces like Gigabit Ethernet or Fibre Channel, and to use only one radio equipment with expected goal of covering at least 1–2 km in line-of-sight (LOS) scenario.

7.3.4. ARIB/MMAC

The Association of Radio Industries and Businesses (ARIB) is a Japanese standardization and radio spectrum regulation body [28]. Since 2002, standardization activities on "Ubiquitous homelinks: 1394 over UWB" have been initiated in the Multimedia Mobile Access Communication (MMAC) Wireless Home-Link Ad-Hoc Group, combining spectrally efficient UWB impulse radio technology and flexibility and mobility of a broadband wireless access solution in and around the home.

7.3.5. Global radio standardization collaboration

The Global Radio Standardization Collaboration (GRSC) Group (initially RAST [29]) was formed in November 1994 at the initiative of ETSI, for the purpose of

providing an informal multinational information exchange focused on radio standardization trends and developments in the delegates' various regions. GRSC was foreseen to facilitate assessing the potential for harmonization and to complement the more formal processes of other bodies, and particularly the ITU, in the work of developing international standards recommendations. It enables regular exchange of information between work programs and others, in a number of agreed high-interest technical areas like UWB and software-defined radio, attracting a growing number of participants from around the world.

7.4. Coexistence with radio systems

7.4.1. Introduction

To protect existing systems against UWB emissions, the FCC and successively ETSI restricted the UWB operating bands for communications in the 3.1–10.6 GHz frequency range by regulating UWB power emission with frequency-power masks for each specific UWB application/device [30].

Even considering FCC (or ETSI) restrictions, the evaluation of interference caused by UWB devices on existing narrowband terminals is important to guarantee nonconflicting coexistence and to gain acceptance of UWB technology worldwide. In fact, as shown in [31], coexistence among UWB and fixed wireless systems may be critical even when FCC (or ETSI) rules are fully respected. However, the analysis in [31] was too simplistic. In particular, the calculation of UWB interference on fixed systems receivers was carried out considering UWB terminals as electromagnetic radiators transmitting at their maximum allowable power for 100% of time; the UWB signal spectrum was assumed to be flat and, finally, no realistic communication system architecture was considered for the UWB. Other results on the coexistence between UWB and fixed wireless systems operating in the 3–5 GHz band have been presented in the open literature as well as in regulatory forums [32–36]. Some of the assumptions in [31] have been relaxed in [33, 34, 36] and different conclusions were reached. As an example, it could be noted that using 100% activity factors contrasts with the typical deployment scenarios envisaged for UWB devices where it is estimated that in any case the aggregate percentage of time that any single device transmits is to be considered not exceeding 10% [33, 34, 36].

Coexistence analysis was further extended to other existing and licensed narrowband and wideband systems. In [37], UWB interference on GSM, UMTS, and GPS was analyzed even though results were obtained by considering baseband UWB signals and not including any realistic system architecture for the UWB. In [32] UWB interference on UMTS base stations was assessed introducing the equivalent cumulative path gain parameter. However, even in this case, only the UWB single terminal case transmitting at fixed power level was considered. Finally, several coexistence studies have been reported in the current literature for the IEEE802.11a,b and Bluetooth standards [38–40].

In this section, coexistence between a UWB hot spot located inside a building and fixed wireless systems FWA and PP as well as UMTS and DCS 1800 is

analyzed. In order to render results comparable with those presented in the current literature, the scenario in [31] is considered but UWB interference is evaluated accounting for the most important system parameters such as the UWB network architecture, power control, traffic characteristics (e.g., the UWB device activity factor), and the spectral characteristics of the UWB signals. The direct-sequence (DS) and the time-hopping (TH) UWB signals are considered and their spectra are used to evaluate the fraction of UWB power leaking in the band of the victim receivers.

The procedure adopted for coexistence assessment can be divided in the following four steps:

(1) calculation of the maximum allowable UWB interference limits for each of the considered victim receivers;
(2) definition of the UWB hot-spot interference scenario;
(3) analytical calculation of the average interference due to UWB devices on the victim receivers accounting for several features of the UWB signals and system;
(4) comparison of the average UWB interference with the limits obtained in point 1.

The proposed procedure is quite general and provides a unique framework to analyze coexistence of UWB with several classes of victim terminals.

The main aim is to demonstrate that by proper selection of few UWB system features, victim receivers can coexist with UWB terminals without any dangerous interference even in very critical operating conditions where the victim receiver is interfered by several UWB terminals. The organization of this section closely follows the steps of the procedure used for coexistence assessment. In Section 7.4.2 the maximum allowable UWB interference for each one of the considered victim receivers is evaluated. In Section 7.4.3 the interference scenario and the characteristics of the UWB system are detailed. In Section 7.4.4 the power spectral densities of the DS and TH UWB signals are obtained and are used in Section 7.4.5 to calculate the fraction of UWB interference power leaking in the band of the victim receiver. In the same paragraph, several results are provided for the two cases of power and non-power controlled UWB devices. Finally, conclusions are drawn.

7.4.2. Calculation of UWB interference limits

Considering one generic victim receiver, the degradation due to UWB interference can be expressed in terms of the signal to noise ratio reduction r in the receiver, that is,

$$r = \frac{I_{\mathrm{UWB}} + N}{N}, \tag{7.1}$$

where I_{UWB} is the interference due to UWB devices in the area on the victim receiver and N, in the simplest case, is the thermal noise power which depends

on the receiver characteristics. Using standard formulas, N in (7.1) can be expressed as

$$N = -144 + 10\log_{10}(B_{\mathrm{RX}}) + N_F[\mathrm{dBW}], \tag{7.2}$$

where B_{RX} is the victim receiver bandwidth in MHz and N_F is the corresponding noise figure.

Starting from the specifications on the maximum allowed degradation r for each of the considered victim receivers using (7.1) and (7.2), the maximum allowable UWB interference power $\hat{I}_{\mathrm{UWB}}$ is calculated. This value is then used as reference to assess coexistence between UWB and the selected victim terminal.

7.4.2.1. Fixed wireless systems interference specifications

To evaluate the maximum allowable UWB interference on the existing fixed wireless systems (FWA and PP), the ITU-R requirements in [41] have to be considered. They report on the limits of the interference power, I, due to unwanted emissions from sources other than fixed services or services sharing the same band on primary bases. In [41] the total interference I on a fixed service link is partitioned as 89 % for the intra service interference; 10% for the co-primary services interference. The remaining 1% is for the aggregation of interference due to radio services sharing frequency allocations on a non-primary basis, unwanted emissions (i.e., out-of-band and spurious emissions such as energy spread from radio systems, etc.) in non-shared bands and finally unwanted radiations (e.g., industrial scientific medical (ISM) applications).

The previous percentages only apply to the performance objectives [42, 43] and degradation allowance refers to the aggregation of the whole secondary services transmitters and unwanted signals.

In order to ensure not conflicting coexistence, ITU-R defined long and short term interference criteria among generic wireless devices. For our purposes only the long-term criteria are of interest. In particular, while for co-primary sharing a degradation of $r = 0.5\,\mathrm{dB}$, corresponding to $I/N = -10\,\mathrm{dB}$, is admitted, for secondary service interference and unwanted emissions, the performance degradation shall not exceed $r \leq 0.05\,\mathrm{dB}$ corresponding to $I/N \leq -20\,\mathrm{dB}$. The previous values for I/N represent generic objectives and refer to the average interference which is the case analyzed in this section. However, due to the pulsed characteristic of UWB signals, separate considerations would be needed for both average and peak interference objectives in the victim receiver band.

It should be noted that the allocation of 99% of the interference margin to intra-service and/or co-primary services (89%+10%) might also be too pessimistic with today's technology and in more realistic conditions higher margins than 1%, in particular I/N closer to 0 dB, could be tolerated by fixed links for secondary services. As an example, $I/N = -10\,\mathrm{dB}$ have been proposed in [33, 34, 36], as more realistic estimates of interference margins against UWB for today's FWA and PP technologies.

To calculate the FWA or PP receiver noise power N in (7.2), the receiver characteristics of the considered FWA and PP systems need to be specified.

The considered FWA systems operate in the 3.5–4.2 GHz and 4.4–5.0 GHz bands. They include two communicating devices: the FWA central station (CS) and an FWA terminal station (TS). When the FWA receiver operates at 3.5 GHz, with $N_F \cong 5$ dB, and $B_{RX} \cong 50$ MHz or as an alternative $B_{RX} \cong 14$ MHz. Using (7.2), $N \cong -122$ dBW is obtained for 50 MHz at 3.5 GHz and $N \cong -127.5$ dBW for 14 MHz at 3.5 GHz. When the FWA systems transmits in the 4.4–5.0 GHz band with $N_F \cong 6$ dB and $B_{RX} \cong 50$ MHz, $N \cong -121$ dBW is obtained for $B_{RX} = 50$ MHz. As an example, the corresponding UWB interference limit is $\hat{I}_{UWB} = -142$ dBW for $N_F = 5$ dB at 3.5 GHz.

To evaluate the UWB interference I_{UWB} on the FWA receiver, it is necessary to account for the FWA-TS antenna radiation patterns envelopes in both horizontal and vertical planes. Typically a 90° sectorial antenna with mainlobe gain of 16 dB is deployed. The FWA receiver antenna characteristics are indicated in [44] and for brevity are not repeated.

Finally, a representative PP link operating at 4.0 GHz is considered. Its receiver noise figure is $N_F = 6$ dB and its bandwidth is about 40 MHz [31]. Using (7.2), the noise power of the PP receiver is $N \cong -122$ dBW and the corresponding UWB interference limit is $\hat{I}_{UWB} = -142$ dBW.

Also in the PP case, to evaluate the UWB interference I_{UWB} on the PP receiver, the antenna characteristics for the PP have been be specified. As reported in [45], a parabolic approximation for the antenna mainlobe is assumed with a gain of 43.6 dB and a 3 dB beam width of 1 degree.

7.4.2.2. DCS1800, UMTS interference specifications

As indicated in [35], UWB interference is considered to be harmful when the signal-to-noise ratio degradation is about $r = 1$ dB. Assuming $N_F = 9$ dB for the UMTS terminal [46] and using (7.2), $N = -128$ dBW, $\hat{I}_{UWB} = -134$ dBW is obtained.

For the GSM and DCS-1800 the same performance specifications as for the UMTS are considered. A target $N_F = 9$ dB is assumed[10] [48] thus obtaining $\hat{I}_{UWB} = -148$ dBW.

The limits on the allowable UWB interference for the victim systems considered in this section have been listed in Table 7.1. Also the DCS-1800 case with $N_F = 5$ dB has been included.

7.4.3. UWB interference scenario

In this section, the main characteristics of the UWB interference scenario used to assess coexistence are detailed. The UWB system is located inside a commercial/industrial building and interferes with the victim receiver that can be inside or outside the building.

[10] In [47] a noise figure goal of $N_F = 5$ dB is indicated for the DCS receiver.

Table 7.1. UWB allowable interference limits for FWA, PP, UMTS, DCS1800.

System	Parameters	$\hat{I}_{\text{UWB}}$	f_{low}	f_{high}
FWA	$N_F = 5$ dB, $r = 0.05$ dB	-142 dBW	3.475 GHz	3.525 GHz
PP	$N_F = 6$ dB, $r = 0.05$ dB	-142 dBW	3.980 GHz	4.020 GHz
UMTS	$N_F = 9$ dB, $r = 1$ dB	-134 dBW	2.165 GHz	2.170 GHz
DCS-1800	$N_F = 9$ dB, $r = 1$ dB	-148 dBW	1.805 GHz	1.8052 GHz
	$N_F = 5$ dB, $r = 1$ dB	-152 dBW		

The geometry of the selected interference scenario is shown in Figure 7.8. The UWB devices communicate in accordance with a master-slave network architecture. We assume that any UWB device (master or slave) is equipped with an omnidirectional antenna with 0 dB gain. The UWB slaves are randomly located on each building floor according to a uniform distribution while UWB masters are positioned on a regular grid as shown in Figure 7.8(c). The floor dimensions are 120 m $\times$ 60 m and the vertical distance between two adjacent floors is 3 m. The building is 10 floors high. The evaluation of the UWB interference on the victim receivers is detailed in the following sections. Both power and non-power controlled UWB devices are considered in the analysis including the spectral characteristics of the UWB signals used for multiple access. Only interference due to UWB upstream communications is considered.

7.4.4. Calculation of the UWB power spectral density

In this section, a closed-form expression for the power spectral density (PSD) of the DS and TH UWB signals is obtained. The PSD is then used to evaluate the fraction of UWB interference power leaking in the band of the selected victim receiver.

7.4.4.1. UWB signal models

Two different pulse amplitude modulated UWB signals are considered: the DS-UWB and the TH UWB [37].

The baseband DS UWB signal $s_{\text{DS}}(t)$ can be written as

$$s_{\text{DS}}(t) = \sum_{k=-\infty}^{\infty} c_k w(t - kT_c), \tag{7.3}$$

where $w(t)$ is the baseband pulse transmitted in each chip interval of duration T_c; c_k is the amplitude of the modulated chip, that is, $c_k = b_{\lfloor k/N_c \rfloor} d_k$, where b_k is the transmitted symbol, N_c is the number of chips per symbol, and $\{d_k\}$ is the code sequence assigned to the generic UWB slave. Finally, $\lfloor x \rfloor$ denotes the largest integer lower than x. The code sequence $\{d_k\}$, $d_k \in \{-1, 1\}$, has duration longer than the symbol period $T = N_c T_c$ and can be approximated as an ideal random white sequence.

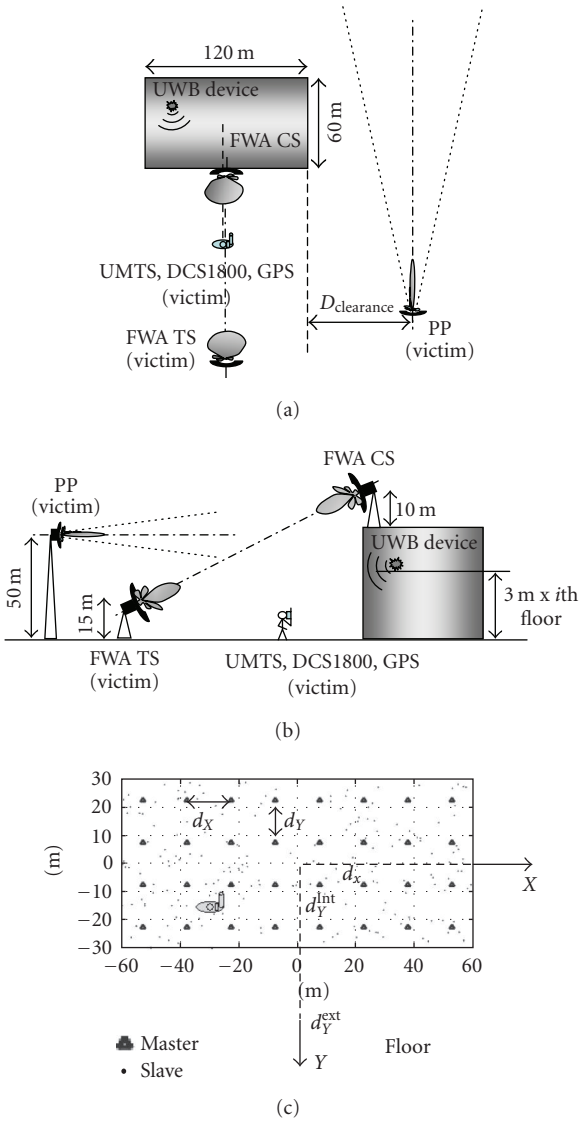

FIGURE 7.8. UWB hot-spot interference scenario. (a) Upper view. (b) Side view. (c) Floor view.

The TH UWB signal can be written as

$$s_{\text{TH}}(t) = \sum_{k=-\infty}^{\infty} b_k p_k(t - kT), \tag{7.4}$$

where b_k is the transmitted symbol in the kth time interval of duration T; $p_k(t)$ is the corresponding pulse waveform. The random symbol sequence $\{b_k\}$ is white,

with zero mean and variance σ_b^2. The $p_k(t)$ is

$$p_k(t) = \sum_{n=0}^{N_f-1} w(t - nT_f - c_{k,n}T_c), \tag{7.5}$$

where T_f is the frame period and $N_f = T/T_f$ is the number of frames per period and the sequence $\{c_{k,n}\}$, $k = -\infty, \ldots, +\infty$ and $n = 0, 1, \ldots, N_f - 1$, is the code word segment accounting for the pulse time shift for each frame in the kth symbol time interval. The $\{c_{k,n}\}$ takes integer values in $\{0, 1, \ldots, N_h - 1\}$, where $N_h = T_f/T_c$.

For the signals in (7.3) and (7.4), the Gaussian pulse $w(t)$ is considered:

$$w(t) = \frac{1}{\sqrt{2\pi}\sigma} e^{-(t-\mu)^2/2\sigma^2}, \tag{7.6}$$

where the parameter σ in (7.6) is the standard deviation of the Gaussian pulse waveform which can be related to the practical duration of the pulse $w(t)$ and to its bandwidth;[11] μ is the mean value indicating the pulse peak position within the chip time interval T_c.

7.4.4.2. Spectral analysis for the selected UWB signals

Considering $\{c_k\}$ in (7.3) as an ideal random bipolar zero-mean white sequence with standard deviation σ_c^2, the power spectrum of the baseband DS UWB signal is [49]

$$S_{\mathrm{DS}}(f) = \frac{\sigma_c^2}{T_c} \left| W(f) \right|^2, \tag{7.7}$$

where $W(f)$ is the Fourier transform of the pulse waveform $w(t)$, for example,

$$W(f) = e^{-2\pi^2 f^2 \sigma^2} e^{-j2\pi f\mu}. \tag{7.8}$$

The power spectrum of the TH UWB signal in (7.4) can be conveniently approximated as (see [50])

$$S_{\mathrm{TH}}(f) = \frac{\sigma_b^2}{T} \left| W(f) \right|^2 \left[N_f (1 - B(f)) + B(f) \left| \frac{\sin^2(\pi f N_f T_f)}{\sin^2(\pi f T_f)} \right|^2 \right], \tag{7.9}$$

where $B(f)$ is

$$B(f) = \frac{\sin^2(\pi f N_h T_c)}{\sin^2(\pi f T_c)} \cdot \frac{1}{N_h^2} \tag{7.10}$$

[11] In the following, the UWB signal bandwidth W_{UWB} is defined as the -10 dB bandwidth of the corresponding Gaussian pulse signal.

and $W(f)$ is given in (7.8). The above expression for the TH UWB spectrum is independent on the specific code sequence assigned to each user. The dependence of the TH UWB spectrum from the generic code sequence $\{c_{k,n}\}$ assigned to the user has been averaged out assuming that the period of the code sequence $\{c_{k,n}\}$ is much longer than the symbol period and can be approximated as a white sequence.

To comply with the FCC requirements, the transmitted UWB signal can be obtained as harmonic modulation of the baseband signal in (7.3) or (7.4), that is,

$$s_{\mathrm{UWB}}(t) = s(t)\cos\left(2\pi f_0 t\right), \tag{7.11}$$

where f_0 is the UWB center frequency that can vary from 0 (e.g., baseband UWB signal) up to several GHz. Using standard formulas [49], the spectrum of the UWB signal in (7.11) is

$$S_{\mathrm{UWB}}(f) = \frac{1}{2}\left\{S_{\mathrm{DS,TH}}(f - f_0) + S_{\mathrm{DS,TH}}(f + f_0)\right\}. \tag{7.12}$$

When the signal in (7.11) is transmitted, it is linearly distorted by the antenna. As outlined in [37] for baseband transmissions, the antenna acts as a derivative filter on the transmitted signal. However, when the UWB center frequency f_0 increases, the derivative effect tends to disappear and a nondistorting behavior of the antenna can be assumed. Starting from the previous considerations, antenna distortion is modelled with a highpass filter with transfer function $H_a(f)$ that, in the simplest case, can be approximated as

$$H_a(f) = \begin{cases} j2A\pi f, & |f| < f_{co}, \\ j, & |f| \geq f_{co}, \end{cases} \tag{7.13}$$

where f_{co} is the cutoff frequency and A is a normalization constant such that $H_a(f_{co}) = j$. For frequencies $f \geq f_{co}$, the antenna is modelled as all pass.

Due to antenna filtering, the spectrum of the transmitted UWB signal is

$$S_{\mathrm{UWB-TX}}(f) = S_{\mathrm{UWB}}(f) \cdot \left|H_a(f)\right|^2, \tag{7.14}$$

where $S_{\mathrm{UWB}}(f)$ is given in (7.12).

Neglecting for the moment the attenuation due to propagation, the average interference due to a single UWB terminal in the victim receiver band is

$$I_{\mathrm{UWB,single}} = 2\int_{f_{\mathrm{low}}}^{f_{\mathrm{high}}} S_{\mathrm{UWB-TX}}(f)df, \tag{7.15}$$

where $f_{\mathrm{low}} \geq 0$ and $f_{\mathrm{high}} \geq f_{\mathrm{low}}$ are the two extremes of the victim band (uplink or downlink).[12] These values have been indicated in the last two columns of Table 7.1 for each one of the selected victim receivers.

[12]To evaluate the maximum allowed UWB interference, the frequency response of each victim receiver was assumed as an ideal brick-wall filter with band equal to that assigned to the specific service, for example, 5 MHz for the UMTS, and so on.

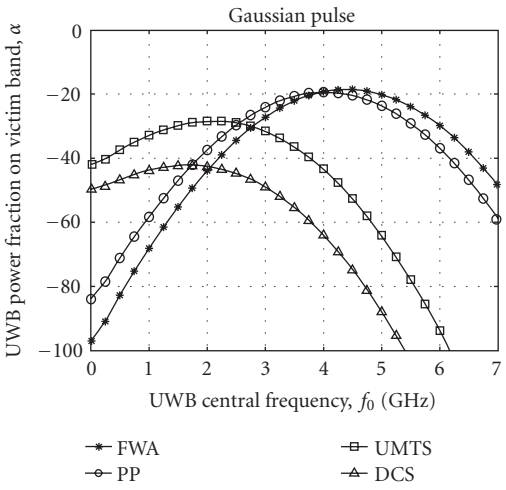

FIGURE 7.9. α versus the UWB center frequency as a function of the UWB center frequency; DS UWB signal, Gaussian pulse, $W_{\text{UWB}} = 3$ GHz; $f_{co} = 1$ GHz.

Indicating with P_T the power transmitted by the UWB device, the interfering power in (7.15) can be conveniently rewritten as

$$I_{\text{UWB single}} = \alpha P_T, \tag{7.16}$$

where $\alpha \leq 1$ is the fraction of UWB power in the band of the victim receiver and $\alpha = 2\int_{f_{\text{low}}}^{f_{\text{high}}} \bar{S}_{\text{UWB-TX}}(f)df$, where $\bar{S}_{\text{UWB-TX}}(f)$ is the normalized UWB spectrum, that is, $\int_{-\infty}^{\infty} \bar{S}_{\text{UWB-TX}}(f)df = 1$. From (7.12) and (7.14), α depends on f_0, on the UWB spectrum shape, and on the antenna characteristics, for example, f_{co} in this case.

In Figure 7.9, α is plotted as a function of UWB center frequency assuming a Gaussian pulse with -10 dB bandwidth of 3 GHz.[13] In Figure 7.10, the values of α obtained for different values of N_f and N_h in (7.9) are plotted in the DS and TH UWB cases. The FWA case is considered.

As shown in Figure 7.10, α is practically independent on N_h and N_f and the more significative variations are on the order of 3 dB and have been obtained for $N_f/N_h = 8$. Still in Figure 7.10, the values of α obtained for both DS UWB and TH UWB signals have been superimposed. The difference between the two curves is negligible and for this reason, in the following, only α for the DS UWB signals are considered.

The dependence of α on the UWB signal bandwidth has been analyzed and results have been shown in Figure 7.11 for the FWA and UMTS cases. For brevity, the α corresponding to the other victim systems have not been indicated.

Finally, in Figure 7.12, α for different values of the antenna cutoff frequency f_{co} is plotted in the FWA and UMTS cases.

[13]The -10 dB UWB bandwidth is $W_{\text{UWB}} = 2f_B$ with f_B such that $|W_0(f_B)|^2 = 0.1$.

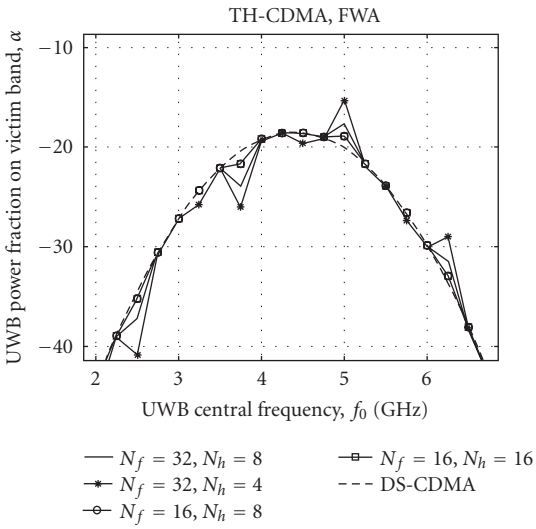

FIGURE 7.10. α versus the UWB center frequency for different values of N_f and N_h; FWA case; Gaussian pulse, $W_{\text{UWB}} = 3\,\text{GHz}$; $f_{co} = 1\,\text{GHz}$, $f_0 = 4.5\,\text{GHz}$.

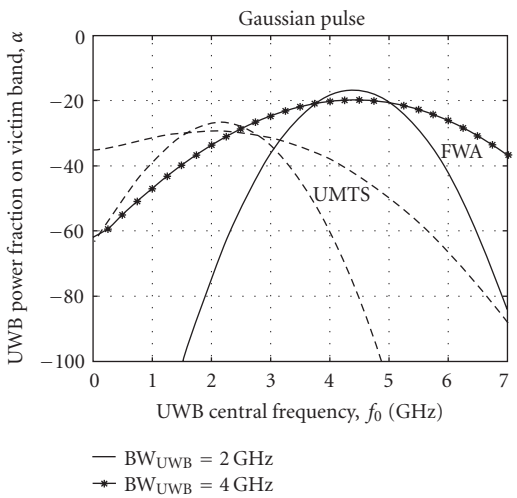

FIGURE 7.11. Fraction of the UWB power in the receiver band as function of the UWB carrier frequency; UWB signal with variable Gaussian pulse bandwidth; $f_{co} = 1\,\text{GHz}$; FWA and UMTS victim systems.

The increase of α for lower values of f_0 and for $f_{co} = 3\,\text{GHz}$ in the UMTS case is due to the derivative distortion introduced by the antenna which leads to a shift of the UWB spectral components towards higher frequencies.

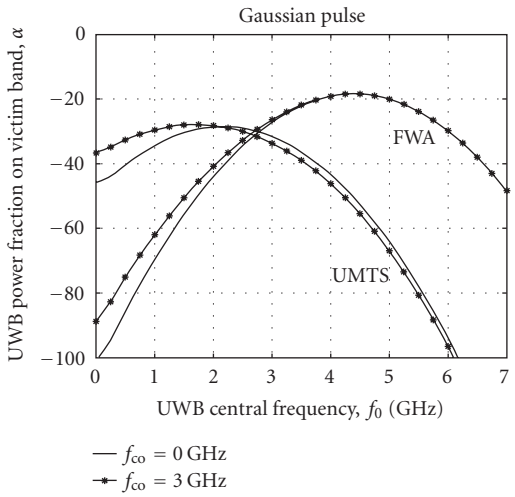

FIGURE 7.12. Fraction of the UWB power in the receiver band as function of the UWB carrier frequency; UWB signal with 3 GHz Gaussian pulse bandwidth; variation of antenna cutoff frequency f_{co}; FWA and UMTS systems.

7.4.5. Calculation of UWB average interference

Using (7.16), the aggregate UWB interference in the victim band can be calculated as

$$I_{\mathrm{UWB}} = \alpha \sum_{m=1}^{M} \chi_m P_{T_m} A(d_m), \tag{7.17}$$

where M is the number of UWB active terminals in the hot spot, P_{Tm} is the power transmitted by the mth UWB slave. The χ_m are binary random variables accounting for the activity of the mth user, for example, $\mathrm{Prob}(\chi_m = 1) = p$ and $\mathrm{Prob}(\chi_m = 0) = 1 - p$, where p is the activity factor of the UWB device.

The terms $\{A(d_m)\}$, $m = 1, 2, \ldots, M$, in (7.17) account for both indoor and (possible) outdoor propagations and includes the antenna gain of the victim receiver. The $A(d)$ can be expressed as

$$A(d) = G_{\mathrm{TX_{UWB}}} G_{\mathrm{RX}} L(d) S_{\mathrm{INT}} S_{\mathrm{OUT}}, \tag{7.18}$$

where $G_{\mathrm{TX_{UWB}}}$ and G_{RX} indicate the antenna gains of the UWB transmitter and of the victim receiver, respectively.

In the FWA and PP cases, the antenna gain of the victim receiver depends on the relative orientation and on the distance between the generic UWB slave inside the building and the FWA or PP receiver outside the building. The S_{INT}, S_{OUT} are two log-normal random variables accounting for shadowing effects for both indoor and (possibly) outdoor propagations. Finally, $L(d)$ is the overall path

loss whose model is taken from [34], that is,

$$L_{dB}(d) = -L_{fs_{(dB)}} - L_{B_{(dB)}} - 10\gamma_{\text{INT}}\log_{10}(d_{\text{int}}) - 10\gamma_{\text{OUT}}\log_{10}\left(\frac{d_{\text{out}}+d_{\text{int}}}{d_{\text{int}}}\right), \tag{7.19}$$

where $L_{fs} = (4\pi/\lambda)^2$ is the free-space attenuation at distance $d = 1$m and L_B is the building penetration loss. The γ_{INT} and γ_{OUT} are the path loss exponents for indoor and outdoor propagations, respectively.

Referring to the scenario in Figure 7.8 for the FWA and PP, d_{int} is the distance of the UWB slave from the external wall of the building which is in front of the victim receiver; d_{out} is the distance (in 3D) between the point indicating the projection of the UWB slave on the external wall in front of the victim receiver (see Figure 7.8) and the victim receiver itself. The victim receiver antenna gain G_{RX} in (7.18) is evaluated along the direction connecting the projection point for the UWB and the victim receiver.

When the UMTS and DCS terminals are considered $L(d)$ in (7.18) only accounts for the internal path loss model, that is, $L_{dB}(d) = -L_1 - 10\gamma_{\text{INT}}\log_{10}(d)$ and d is the distance between the generic UWB transmitter and the victim receiver.

The UWB interference in (7.17) depends on the (instantaneous) geometry of the UWB terminals inside the building, on their state (active or not) and on the transmitted power P_T required to the UWB slave to be received with a specified signal-to-noise ratio to its serving master. In the power controlled case, $\{P_{T_m}\}$ depend on the interference among the UWB devices in the area which in turn depend on the relative position of the UWB devices. The UWB interference power for each floor is obtained after averaging (7.17), for example,

$$I_{\text{UWB}} = \alpha M p E\{P_T A(d)\}. \tag{7.20}$$

The calculation of $E\{A(d)\}$ can be easily reformulated as the average with respect to the spatial coordinates (x, y, z) of the generic UWB device. Assuming that UWB devices have omnidirectional antennas with 0 dB gain, the average interference produced by the UWB devices at floor height h_F is

$$I_{\text{UWB}}(h_F) = \alpha M p E\{P_T \cdot L(x, y, h_F) G_{\text{RX}}(x, y, h_F)\} E\{S_{\text{INT}}\} E\{S_{\text{OUT}}\}. \tag{7.21}$$

Using standard formulas, $E\{S\} = e^{0.5\sigma_S^2}$ for $S = S_{\text{INT}}$ and S_{OUT}. As shown in the following, a simplified expressions for (7.21) can be obtained in the non-power control case. In the power control case, the exact calculation of $E\{P_T \cdot L(x, y, h_F) G_{\text{RX}}(x, y, h_F)\}$ in (7.21) seems to be difficult and it is necessary to resort to simulation. The total UWB interference to be compared with the allowable limits in Table 7.1 is obtained summing (7.21) over the floors, for example,

$$\tilde{I}_{\text{UWB}} = \sum_{h_F} I_{\text{UWB}}(h_F) = \alpha M p \eta_I \eta_O \sum_{h_F} i(h_F), \tag{7.22}$$

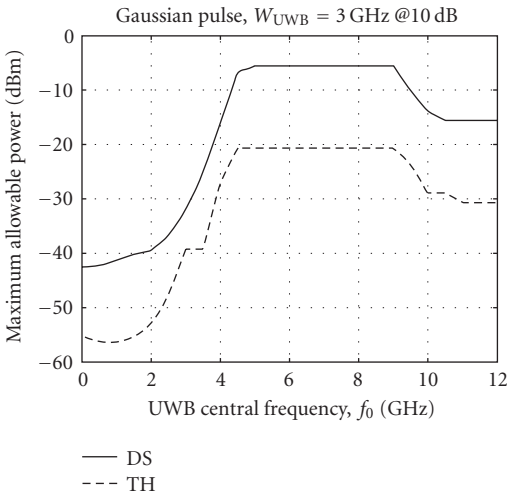

FIGURE 7.13. Maximum transmitting power for DS and TH UWB signals in accordance with the FCC limitations as a function of the UWB signal center frequency; $f_{co} = 1$ GHz; $N_f = 32$, $N_h = 4$ for the TH UWB case.

where $\eta_I = E\{S_{\text{INT}}\}$, $\eta_O = E\{S_{\text{OUT}}\}$, and $i(h_F)$ is the coefficient accounting for the interference produced by the UWB devices located at floor height h_F, that is, $i(h_F) = E\{P_T \cdot L(x, y, h_F)G_{\text{RX}}(x, y, h_F)\}$. By definition, the $i(h_F)$ is independent of the UWB traffic characteristics as well as of number of UWB users in the area and of the shadowing characteristics. It accounts for the (average) geometry of the link. To obtain (7.22), it was implicitly assumed that the number of UWB slaves M for each floor is the same and floors are isolated.

7.4.5.1. Non-power control case

In the non-power control case, the UWB devices transmit at their maximum allowable power which is fixed in accordance with their spectral characteristics and accounting for the spectral emission masks issued by FCC (or ETSI).

The maximum transmitted power $P_{T_{\max}}$ respecting the FCC/ETSI restrictions depends on the UWB center frequency f_0. In Figure 7.13, $P_{T_{\max}}$ as a function of f_0 is plotted for both the DS and TH UWB signals. In the non-power controlled case, the average UWB interference per floor in (7.20) can be rewritten as

$$I_{\text{UWB}}(h_F) = \alpha\rho_{\text{UWB}}MpP_{T_{\max}}E\{\cdot L(x, y, h_F)G_{\text{RX}}(x, y, h_F)\}\eta_I\eta_O. \tag{7.23}$$

The (7.23) can be inserted in (7.22) to obtain the total interference on the victim receiver.

Results for the non-power controlled case. The additional scenario parameters adopted for the evaluation of $\widehat{I}_{\text{UWB}}$ in the non-power control case are $f_0 = 4.5$ GHz corresponding to a $P_{T_{\max}} = -6.2$ dBm for the DS and TH UWB cases with -10 dB

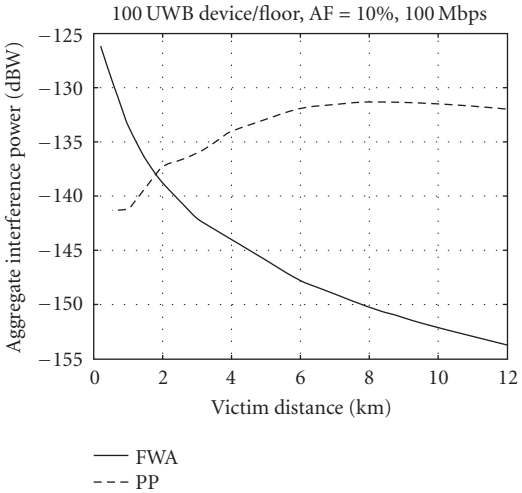

FIGURE 7.14. Average UWB interference as a function of the distance of the victim receiver from the building; non-power control case; PP and FWA.

bandwidth $W_{\text{UWB}} = 3\,\text{GHz}$; the standard deviations $\sigma_{S_{\text{INT}}} = 4\,\text{dB}$ and $\sigma_{S_{\text{OUT}}} = 0\,\text{dB}$ (e.g., no shadowing) have been considered.

In Figure 7.14, the average UWB interference (7.23) is plotted as a function of the distance of the victim receiver from the building. The behavior of the PP curves in Figure 7.14 can be explained looking at the scenario in Figure 7.8. It can be observed that, for a fixed clearance X by varying the distance of the PP receiver from the UWB hot spot, the antenna gain under which the PP sees the hot-spot increases up to the maximum (43.6 dBi). This leads to an increase in the interference power as also indicated in Figure 7.14. By further increasing the PP-UWB distance, the attenuation due to propagation becomes dominant and interfering power restarts to decrease. Thus, differently from the FWA to reduce UWB interference, it should be more convenient to locate the PP receiver in the close proximity of the UWB hot spot.

From Figures 7.14 and 7.15, it can be observed that for a fixed distance between the hot spot and the victim receiver, when it is impossible to reduce the UWB transmitting power to respect the interference limits in Table 7.1, the only viable alternative is to reduce the (average) number of active UWB terminals indicated by the product Mp in (7.22). This may lead to a significant reduction of the UWB system capacity due to coexistence requirements.

7.4.5.2. Power control case

As shown in this section, the adoption of power control in the UWB allows to obtain a consistent reduction of the (average) power transmitted by the UWB devices. In the first generation of UWB devices, power control is not included in order to reduce the UWB modem complexity and thus costs. However, as shown

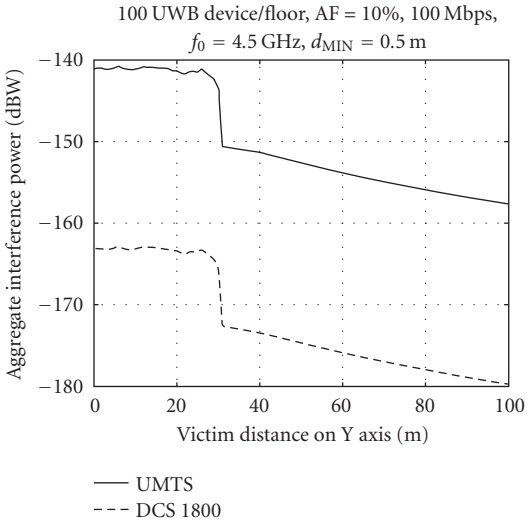

FIGURE 7.15. Average UWB interference as a function of the x position of the victim receiver inside the building; non-power control case; UMTS and DCS-1800.

in the following, the adoption of power control introduces additional degrees of freedom for the UWB network designer and allows to safely improve UWB system capacity without incurring in coexistence problems also in very critical scenario such as the one considered in this section.

A UWB system with a master-slave architecture is considered. Masters are uniformly located over a regular rectangular grid while the power controlled UWB slaves are randomly located in the floor area in accordance with a uniform distribution. Unless otherwise noted, in the following, 32 masters per floor are assumed. To evaluate the power transmitted by each slave (e.g., P_{T_m} in (7.20)), computer simulation is adopted. The principle of operation of the simulation program is illustrated in the flow chart in Figure 7.16. At the beginning of each outer loop iteration, a new scenario is generated. Scenario generation consists in randomly placing the slaves in the area according to a uniform spatial distribution. Each slave is connected to the master with the lowest indoor overall loss including shadowing. The inner loop is used to simulate an iterative power control procedure. In each inner iteration, the power of each transmitter is increased or decreased in accordance with the result of the comparison between the received power-to-interference ratio C/I, calculated for each slave in the area, and the target C/I, that is, $(C/I)_{\text{Target}}$.[14] The power updating procedure is halted when the power transmitted by each active UWB device is practically constant or the maximum allowable transmission power has been reached. At the end of the inner loop, all the relevant parameters, such as the power level transmitted by each user, the number of terminals in outage and so forth, are collected. The powers $\{P_{T_m}\}$ transmitted by the

[14]The target carrier to interference ratio is evaluated as $(C/I)_{\text{Target}} = (E_b/N_0)_{\text{Target}} - PG$, where PG is the processing gain that varies with the UWB slave bit rate.

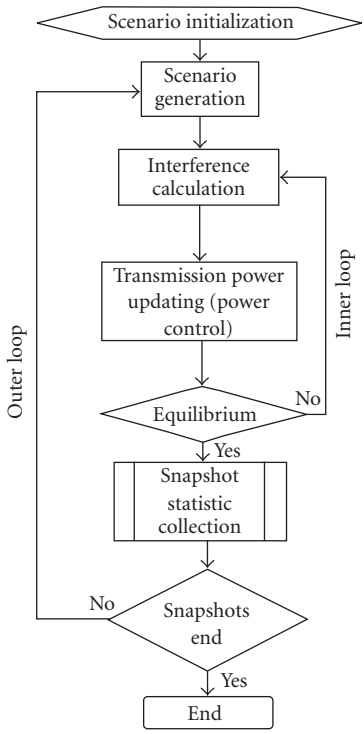

Figure 7.16. Simulator flowchart; upstream simulation.

mth UWB slave at equilibrium are then used in (7.21) to evaluate the interference on the victim receiver. In the (C/I) calculation, the effects of the interference due to the narrowband systems on the UWB are assumed to be negligible. However, they could be easily included in the simulation by suitably increasing the UWB receiver noise power by an amount depending on the spectral characteristics of the UWB signal and of the narrowband systems. The simulations results presented in this section have been obtained considering variable UWB device density as well as different bit rates for the UWB slaves.

In Figure 7.17, the histogram on the UWB transmitted power is plotted in the case of terminals operating at 2, 25, and 100 Mbps. From Figure 7.17, it can be observed that due to power control action the UWB transmitting power is always well below the maximum allowable limits indicated by FCC. As expected, in this case, the total average UWB interference power rapidly decreases as also shown in the following. In Figure 7.18, the aggregate UWB interference power is reported as a function of the distance of the FWA and PP receivers from the UWB hot spot. From Figure 7.18, it can be observed that in every practical case the UWB interference is well below the limits in Table 7.1. Results in Figure 7.18 were obtained considering the largest values for α corresponding to $f_0 = 4.5$ GHz in the FWA and PP cases. Results in Figure 7.18 can be easily recalculated for different UWB

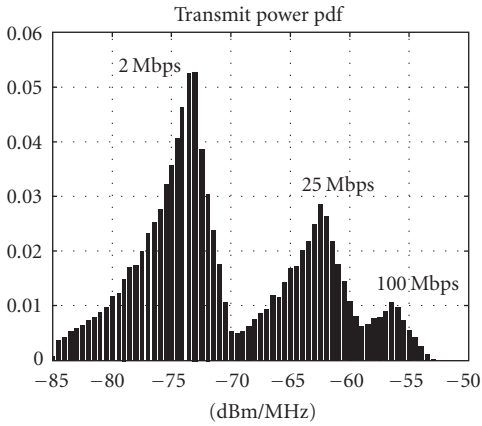

FIGURE 7.17. Power distribution for power controlled devices transmitting at 2, 25, and 100 Mbps, 400 UWB devices/floor.

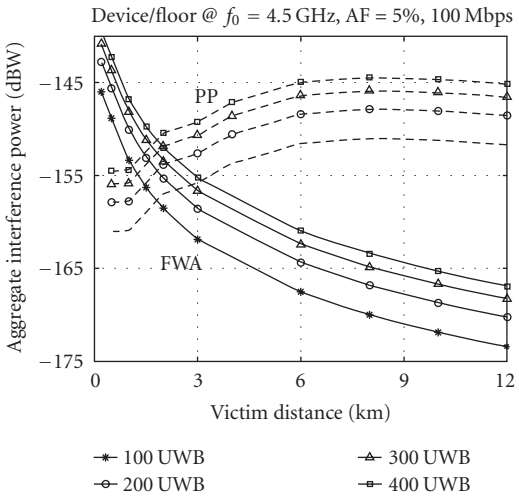

FIGURE 7.18. Aggregate UWB interference power as a function of the victim receiver distance from the UWB hot spot; FWA, PP victim systems; UWB carrier frequency $f_0 = 4.5$ GHz.

center frequencies by scaling them with the factor $\alpha(f_0)/\alpha_R$, where α_R is the interference fraction at $f_0 = 4.5$ GHz and $\alpha(f_0)$ is the fraction at frequency f_0 which can be easily obtained from the curves in Figure 7.9. As expected, by changing f_0, it is possible to reduce the interference well below the limits in Table 7.1 also for every distance between the UWB hot spot and the fixed victim device.

In Figure 7.19, the aggregate UWB interference for the UMTS and DCS-1800 cases is shown. The oscillating interference pattern in Figure 7.19 is due to the position of the UWB masters on the regular grid in Figure 7.8. The discontinuity in the plots is due to the building penetration loss (10 dB was assumed) when passing from indoor to outdoor (or vice versa).

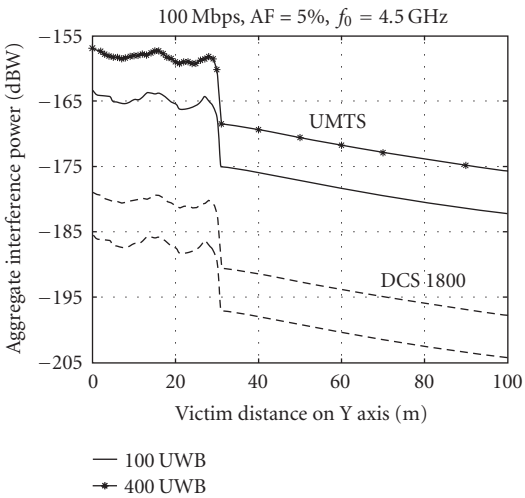

FIGURE 7.19. Aggregate UWB interference power as a function of the victim receiver distance from the UWB hot spot; UMTS, DCS-1800; UWB center frequency $f_0 = 4.5$ GHz.

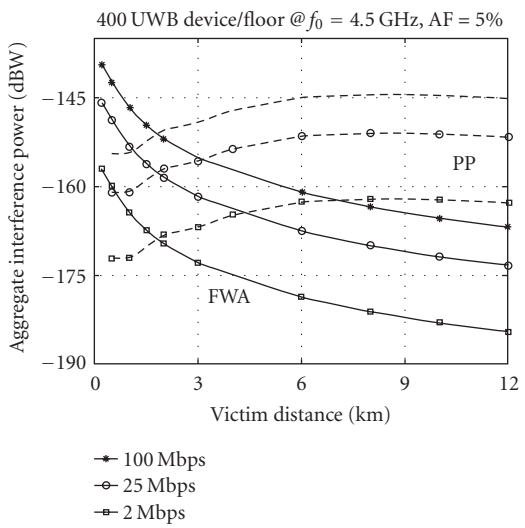

FIGURE 7.20. Aggregate UWB interference power as a function of the victim receiver distance from the UWB hot spot; FWA and PP systems; UWB carrier frequency $f_0 = 4.5$ GHz; 400 UWB devices/floor; variation of the bit rate.

From the results in Figures 7.18 and 7.19, it is evident that when the UWB system operates within the allowed FCC band, the systems that could be impaired from UWB are PP and FWA systems. As indicated in Figure 7.19, the selection of $f_0 = 4.5$ GHz leads to a significative reduction of the UWB interfering power for UMTS and DCS also for very large UWB device densities. For this reason in the following, only the FWA and PP systems are analyzed in detail.

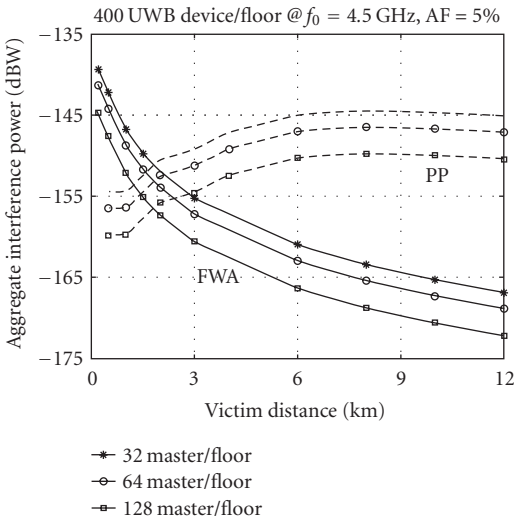

FIGURE 7.21. Aggregate UWB interference power as a function of the victim receiver distance from the UWB hot spot; FWA and PP systems; UWB carrier frequency $f_0 = 4.5$ GHz; variation of the number of masters; 400 UWB devices/floor.

Figure 7.20 evidences the reduction of UWB interference considering UWB transmissions at bit rates lower than 100 Mbps. It can be observed that the bit rate reduction allows to increase the receiver processing gain thus leading to a corresponding reduction in the UWB slave transmitter power and thus in the interference on the victim receivers.

Finally, in Figure 7.21, $\tilde{I}_{\mathrm{UWB}}$ is reported for different number of UWB master stations in the area. As expected, the increase in the number of master stations can lead to a significative reduction of UWB interference. This may represent an additional degree of freedom for the UWB system designer at the expense of an increased complexity of the overall system architecture.

7.4.6. Summary

The assessment of the potential interference caused by UWB devices is of great importance to guarantee nonconflicting coexistence between UWB technology and any other existing and future wireless systems as well as to gain acceptance of UWB technology worldwide. Any study on this aspect needs to go beyond simplistic models and should adopt realistic scenario deployments for UWB. Similarly to many other wireless local area network systems, UWB terminals will be in sleep mode for the large percentage of time, will not run continuously, and will not emit constantly at the maximum allowed power. In this section, the potential harmful interference of UWB on many categories of victim receivers was analyzed. Both non-power controlled and power controlled UWB terminals were considered. UWB interference on the narrowband systems was evaluated including the

spectral characteristics of the transmitted UWB signal including antenna distorting effects and different UWB carrier frequencies. Differently from the results presented in the open literature, mainly focusing on the non-power controlled single terminal case, it was shown that by considering some simple system features for the UWB system such as its architecture, the activity factor, power control, and so forth, even for very large UWB terminal densities, there is no practical risk for the selected victim receivers especially when the carrier frequency of the UWB is selected in the 3.1–10.6 GHz band. The coexistence issues of power controlled UWB with fixed wireless systems (FWA and PP) have been analyzed in detail when the UWB operates in the 3.1–10.6 GHz band. Even in this case, there is no practical risk for the FWA and PP operations. Further margins on UWB interference, not even considered, still exist such as admission control techniques, antenna polarization mismatches, deep NLOS, and multiple through-wall indoor losses.

Bibliography

[1] International Telecommunication Union (ITU)Radiocommunication Study Groups: Chairman Task Group 1/8, "Report of the second meeting of Task Group 1/8 (Geneva, 27–31 October 2003)," ITU-R Document 1-8/59-E, 2 December 2003.

[2] Mandate forwarded to CEPT to harmonize radio spectrum use for ultra-wideband systems in the European Union, DG INFSO/B4, 18 February 2004; http://europa.eu.int/information_society/policy/radio_spectrum/docs/current/mandates/rscom0408_mandate_uwb.pdf.

[3] Mandate forwarded to CEN/CENELEC/ETSI in the field of information technology and telecommunications, DG ENTR/G/3, 25 February 2003; http://portal.etsi.org/public-interest/Documents/mandates/M329EN.pdf.

[4] Report of the First Meeting of ECC-TG3, Maisons-Alfort, France, 19 April 2004, Document TG3#1_10R1, approved and issued 23 April 2004.

[5] Federal Communications Commission (FCC), "Revision of Part 15 of the commission's rules regarding ultra-wideband transmission systems," First Report and Order, ET Docket 98-153, Federal Communication Commission 02-8, Washington, DC, USA, adopted on 14 February 2002, and released on 22 April 2002.

[6] ETSI-TG31A Technical Report: Electromagnetic compatibility Radio spectrum Matters (ERM); Short Range Devices (SRD), "Technical characteristics for SRD communication equipment using Ultra-Wideband technology (UWB)," TR 101 994-1 V1.0.0 (2003-8); also available as document SE24M21_42.

[7] International Telecommunication Union (ITU)Radiocommunication Study GroupsDocument 1-8/TEMP/XX-E17 June 2004: Annex 1 to TG 1/8 Chairman's Report (Working Document), "Characteristics of ultra-wideband technology (Questions ITU-R 226/1 and ITU-R 227/1)."

[8] IEEE 802.15 Overview web site, http://standards.ieee.org/wireless/overview.html#802.15.

[9] IEEE 802.15 WPAN High Rate Alternative PHY Task Group 3a (TG3a) web site, http://ieee802.org/15/pub/TG3a.html.

[10] IEEE 802.15.3a Project Authorization Request, December 2002, http://standards.ieee.org/board/nes/projects/802-15-3a.pdf.

[11] Task group 3a Call For Intent and Proposals (CFI/CFP), December 2002, http://grouper.ieee.org/groups/802/15/pub/TG3a_CFP.html.

[12] TG3a Technical Requirements, December 2002, http://grouper.ieee.org/groups/802/15/pub/2003/Jan03/03030r0P802-15_TG3a-Technical-Requirements.doc.

[13] P802.15.3a Alt PHY Selection Criteria, December 2002, http://grouper.ieee.org/groups/802/15/pub/2003/Jan03/03031r6P802-15_TG3a-PHY-Selection-Criteria.doc.

[14] TG3a Down Selection Voting Procedure, January 2003, http://grouper.ieee.org/groups/802/15/pub/2003/Jan03/03041r7P802-15_TG3a-Down-Selection-Voting-Procedure.doc.

[15] Channel Modeling Sub-committee Report Final, November 2002.
[16] A. A. Saleh and R. A. Valenzuela, "A statistical model for indoor multipath propagation," *IEEE Journal on Selected Areas in Communications*, vol. 5, no. 2, pp. 128–137, 1987.
[17] MultiBand OFDM Alliance web site, http://www.multibandofdm.org.
[18] Xtreme Spectrum web site, http://www.xtremespectrum.com.
[19] Motorola's UWB web site, http://www.motorola.com/uwb/.
[20] IEEE 802.15 WPAN Low Rate Alternative PHY task group 4a (TG4a) web site, http://www.ieee802.org/15/pub/TG4a.html.
[21] IEEE 802.15 WPAN^{TM} Task Group 5 (TG5) web site, http://www.ieee802.org/15/pub/TG5.html.
[22] IEEE 802.19 Coexistence Technical Advisory Group (TAG) web site, http://grouper.ieee.org/groups/802/19/.
[23] European Telecommunications Standards Institute web site, http://www.etsi.org/.
[24] ERM TG31A: Ultra Wide Band for Short Range Devices, Terms of References, http://portal.etsi.org/erm/ermtg31a_tor.asp.
[25] ETSI TR 101 994-1 V1.1.1 (2004-01) Technical characteristics for SRD equipment using Ultra Wide Band technology (UWB) Part 1: Communications applications.
[26] ETSI TR 101 994-2 V1.0.0 (2004-03) Technical characteristics for SRD equipment using Ultra Wide Band technology (UWB) Part 2: Ground-and Wall- Probing radar applications; System reference Document.
[27] ETSI TR 101 982 Electromagnetic compatibility and Radio spectrum Matters (ERM); Radio equipment to be used in the 24 GHz band; System Reference Document for automotive collision warning Short Range Radar.
[28] Association of Radio Industries and Businesses web site, http://www.arib.or.jp/.
[29] Global Radio Standardization Collaboration (GRSC) web site, http://www.rast.etsi.org/.
[30] Federal Communications Commission (FCC), "Revision of Part 15 of the Commission's Rules Regarding Ultra-Wideband Transmission Systems," First Report & Order, ET Docket 98-153, Federal Communication Commission 02-48, Washington, DC, USA, adopted on 14 February 2002, and released on 22 April 2002.
[31] R. Macchi (Siemens), "Revision of UWB and FS coexistence report (Annex 5-1)," in *Proceedings of Conference of European Post and Telecommunication Administrations SE24 Meeting 17*, Mainz, Germany, September 2002.
[32] J. Huschke, "Aggregated UWB interference into the uplink of UMTS," in *Proceedings of Conference of European Post and Telecommunication Administrations SE24 Meeting 17*, Mainz, Germany, September 2002.
[33] R. Giuliano, G. Guidoni, F. Mazzenga (Radiolabs), and D. Porcino (Philips), "Study of the coexistence UWB—Fixed Wireless Access (FWA) systems (with power control variation analysis)," in *Proceedings of Conference of European Post and Telecommunication Administrations SE24 Meeting 18*, Copenhagen, Denmark, December 2002, IST ULTRAWAVES.
[34] J. Foerster and A. Stephens (Intel), "Response to the Revision of UWB and FS coexistence report (Annex 5-1) concerning aggregate UWB interference into FS systems," in *Proceedings of Conference of European Post and Telecommunication Administrations SE24 Meeting 18*, Copenhagen, Denmark, December 2002.
[35] J. Huschke, "Generic power spectral density limits for a single UWB interfer into the uplink of UMTS," in *Proceedings of Conference of European Post and Telecommunication Administrations SE24 Meeting 18*, Copenhagen, Denmark, December 2002.
[36] R. Giuliano, G. Guidoni, F. Mazzenga, and F. Vatalaro, "On the coexistence of UWB with fixed wireless access systems," in *Proceedings of IEEE Personal Wireless Communications (PWC '03)*, pp. 101–113, Venice, Italy, September 2003.
[37] M. Hamalainen, V. Hovinen, R. Tesi, J. H. J. Iinatti, and M. Latva-aho, "On the UWB system coexistence with GSM900, UMTS/WCDMA, and GPS," *IEEE Journal On Selected Areas in Communications*, vol. 20, no. 9, pp. 1712–1721, 2002.
[38] D. Landi and C. Fischer, "UWB interference to IEEE 802.11a/b WLAN," Swisscom Innovations, D4.2v1.0, 18/08/03.

[39] M. Hamalainen, J. Saloranta, J.-P. Makela, I. Oppermann, and T. Patana, "Ultra wideband signal impact on IEEE802.11b and bluetooth performances," in *Proceedings of 14th IEEE International Symposium on Personal, Indoor, and Mobile Radio, Communications (PIMRC 2003)*, vol. 3, pp. 2943–2952, Beijing, China, September 2003.
[40] D. Landi and C. Fischer, "UWB interference with bluetooth," Swisscom Innovations, D4.3v1.0, 20/08/03.
[41] ITU-R F.1094-1 (10/95), "Maximum allowable error performance and availability degradations to digital radio-relay systems arising from interference from emissions and radiations from other sources".
[42] ITU-R F.1397, "Error performance objectives for real digital radio links used in the international portion of a 27500 km hypothetical reference path at or above the primary rate."
[43] ITU-R F.1491, "Error performance objectives for real digital radio links used in the national portion of a 27500 km hypothetical reference path at or above the primary rate."
[44] ITU-R F.1336, "Reference radiation patterns of omnidirectional, sectoral and other antennas in point-to-multipoint systems for use in sharing studies in the frequency range from 1 to about 70 GHz."
[45] ETSI EN 300 833 V1.4.1, "Fixed Radio Systems; Point-to-point antennas; Antennas for point-to-point fixed radio systems operating in the frequency band 3 GHz to 60 GHz," (2002-07).
[46] 3GPP TR 25.942 V6.1.0 (2003-09) Technical Specification Group Radio Access Networks, "Radio Frequency (RF) system scenarios," (Release 6).
[47] ETS(I) 300 190, "(GSM 05.05 version 5.4. 1): Digital cellular communication system (Phase 2+); Radio transmission and reception," European Telecommunications Standards Institute, Sophia Antipolis, Cedex, France, August 1997.
[48] J. Janssens and M. Steyaert, *CMOS Cellular Receiver Front-Ends: From Specification to Realization*, Kluwer Academic, Dordrecht, the Netherlands, 2002.
[49] J. G. Proakis, *Digital Communications*, McGraw-Hill, New York, NY, USA, 4th edition, 2001.
[50] D. Cassioli and F. Mazzenga, "Spectral analysis of UWB multiple access schemes using random scrambling," *IEEE Transactions on Wireless Communications*, vol. 3, no. 5, pp. 1637–1647, 2004.

Christian Politano: STMicroelectronics, 1228 Plan-les-Ouates, Geneva, Switzerland
Email: christian.politano@st.com

Walter Hirt: IBM Research GmbH, Zurich Research Laboratory, 8803 Rüschlikon, Switzerland
Email: hir@zurich.ibm.com

Nils Rinaldi: STMicroelectronics, 1228 Plan-les-Ouates, Geneva, Switzerland
Email: nils.rinaldi@st.com

Gordana Drakul: STMicroelectronics, 1228 Plan-les-Ouates, Geneva, Switzerland
Email: gordana.drakul@st.com

Romeo Giuliano: RadioLabs, Consorzio Università Industria-Laboratori di Radiocomunicazioni, Via del politecnico 1, 00133 Rome, Italy
Email: romeo.giuliano@radiolabs.it

Franco Mazzenga: Dipartimento di Ingegneria Elettronica, Università di Roma Tor Vergata, via del politecnico 1, 00133 Rome, Italy
Email: mazzenga@ing.uniroma2.it

Index